STRONG MICROWAVES IN PLASMAS

1996

Volume 2

Institute of Applied Physics
Nizhny Novgorod

RUSSIAN ACADEMY OF SCIENCES
INSTITUTE OF APPLIED PHYSICS

STRONG MICROWAVES IN PLASMAS

PROCEEDINGS
OF THE INTERNATIONAL WORKSHOP

Nizhny Novgorod,
7 – 14 August 1996

Edited by
A.G. Litvak

In two volumes
Volume 2

Nizhny Novgorod – 1997

License No 020235 of 20.01.97

ISBN 5-201-09305-1

NONLINEAR PROCESSES IN PLASMAS

CYCLOTRON MASERS IN SPACE: NEW APPROACHES AND APPLICATIONS

V. Y. Trakhtengerts

Institute of Applied Physics, Nizhny Novgorod, Russia

1 Introduction

Cyclotron masers (CM) are widely spread in space plasmas. Practically any space object with magnetic field and an internal or external source of energy can be a candidate for CM operation. In the simplest case a space cyclotron maser (SCM) is a magnetic flux tube filled with a cold plasma, with a small addition of charged energetic particles, electrons or ions, which serve as a working substance for a space generator. This magnetic flux tube can belong to planetary magnetospheres, solar corona or other stellar or nebular objects. SCM has many common features with its nearest laboratory analog — gyrotron. The cyclotron resonance lies in the base of SCM operation, and cyclotron instability (CI) of energetic particle population with transverse anisotropy of velocity distribution causes stimulated electromagnetic emission.

At the same time there are some important differences. At first, it concerns wave eigenmodes. In the presence of rather dense cold plasma those are whistler mode waves and alfven waves, which are strongly ducted by the magnetic field. Second, natural sources supply SCM with energetic particles with large pitch angle and energy dispersion. And third, the magnetic field in space changes its value by several orders along the magnetic flux tube. All these circumstances together with quasioptical scales of electrodynamical systems stimulated application of the quasilinear (QL) theory to description of wave-particle interaction in SCM. The QL approach was found very fruitful for analysis of stationary and quasistationary regimes of SCM operation, when the characteristic time, τ, of wave intensity and energetic particle flux changes was much more than period T_g of wave

group oscillations between reflected mirrors (conjugate ionospheres in the feet of the magnetic flux tube) and the period of particle bounce oscillations, T_b, between magnetic mirrors:

$$\tau \gg (T_g, T_b) \qquad T_g = \oint \frac{dz}{v_g} \qquad T_b = \oint \frac{dz}{v_z}, \tag{1}$$

where z is coordinate along the magnetic field line, v_g is wave group velocity, and v_z is particle velocity component along the magnetic field.

Many features of the Earth radiation belt dynamics and generation of natural ELF (Extreme Low Frequency) and VLF (Very Low Frequency) waves in the frequency range $f \sim 0.1$–10 kHz were described successfully on the base of the QL theory. At the same time essential discrepancies with QL approach were revealed under analysis of the fine structure of ELF-VLF emission spectra, which were observed by satellites and on the ground. A pulsating aurora could be the most bright illustration to this discrepancy. The matter is that Nature invented a very interesting phenomenon, so-called pulsating auroral patches, which turned out to be very convenient for experimental verification of the SCM theory. Detailed experimental and theoretical investigations have shown that these patches, which are seen as periodically flashed bright spots in the night sky, are the result of electron CM operation inside a separate magnetic flux tube with enhanced cold plasma density [1, 2]. This tube serves as a cavity for cyclotron waves and at the same time it creates favorable conditions for CI development. Optical emission is the result of energetic electron precipitation into the atmosphere under the action of cyclotron (whistler mode) waves.

Many macroscopic features of this phenomenon (connection with a cold plasma duct, ELF wave generation and energetic electron precipitation, periodicity of generation) were described very well on the base of the QL theory. However, patches revealed a very pronounced fine structure in dynamical spectra of waves and in temporal behavior of precipitated electron fluxes, which could not be explained by the QL theory. This fine structure appeared at the maximum phase of the flash and manifested itself as discrete ELF-VLF signals with rising frequency, which grew from the noise-like radiation background and followed each other with period T_f less then T_g and T_b (1). The

precipitated particle fluxes showed the same deep temporal modulation. Actually, these facts testified specific self-organization effects, which appeared in process of QL relaxation.

It is shown below that such a fine structure can be connected with formation, at the QL stage, of a specific step-like deformation on the energetic electron distribution function and transition to the hydrodynamic stage of CI, when coherence effects become important. These effects lead to new generation regimes with discrete structure of the dynamic spectrum of radiation.

Another new tendency in the theory of cyclotron masers in space concerns interaction of hot and cold plasma components in SCM through the electromagnetic radiation generated. This interaction is considered principal in some important applications. Below such an interaction is investigated on the example of a solar flare. It is shown that the fast transfer of energy from hot to cold plasma component, which takes place in CM operating in the solar corona, produces strong heating of coronary plasma and can lead to mass ejection of coronary matter into the interplanetary space. In conclusion, some consequences of SCM investigations are discussed, which could be interesting to apply in laboratory plasma magnetic traps.

2 Self-organization effects and discrete dynamical spectrum structure of SCM radiation

In this section we consider some self-organization effects, which arise at the final stage of quasilinear relaxation and determine a discrete dynamical spectrum structure of SCM electromagnetic emission. These effects are connected with formation of a step-like deformation in a distribution function of energetic particles at the boundary between resonance and nonresonance particles. In the case of CM this boundary is determined from the cyclotron resonance condition, written for the central crossection of the magnetic flux tube:

$$\omega_m - \omega_{BL} = k_m v_{zL} \tag{2}$$

where ω_{BL} is gyrofrequency of energetic electrons, v_{zL} is velocity component along the magnetic field direction, ω_m is maximum frequency in the spectrum of generated whistler waves, wave vector k_m and frequency ω_m are connected by the dispersion relation for whistler-mode

waves. In general case ω_m and k_m are slowly changing (in comparison with the period of the wave) functions of time. The idea about step-like deformation of a distribution function and possible transition to hydrodynamic stage of instability was formulated at first in [3, 4] in application to one-dimensional beam-plasma interaction. In a sense, transition to the hydrodynamic stage of instability testifies some self-organization process, when phase effects become important.

At that time this interesting idea did not find further applications. We came back to this idea under the influence of experimental facts. Satellite measurements of so-called ELF chorus emissions, which were attributed to CM generation, showed [5, 6] that chorus were always a mixture of noise-like and discrete emissions, moreover, the periodic succession of discrete signals formed the high-frequency part, which was growing from noise background. Period T_f of this succession was less then T_g and T_b, so it was clear that this fine structure could not be explained in the framework of the QL theory only, but the QL stage played an important role in preparation of the situation when formation of discrete signals was possible. Detailed analytical and computational analysis of SCM operation was undertaken on the base of the QL theory, which showed the formation of a step-like deformation in the distribution function for conditions close to real SCM systems [7]. In fact, it was generalization of the results of [4] on the case of two-dimensional QL relaxation with sources and sinks of energetic particles and waves taken into account.

Figures 1–3 illustrate the computational results, which were obtained by [7]. In particular, Fig. 1 shows the behavior of the CI amplification (solid line) and wave energy density (dashed line) in the process of QL relaxation, and in Fig. 2 the tendency to hydrodynamic stage of instability is seen, when the ratio of growth rate, γ, to the spectrum width, Δ_ω, goes to unity. Figure 3 demonstrates the appearance of a step-like deformation in the distribution function as a function of pitch angle sine x ($x = \sqrt{1-(v_{zL}/v)^2} = \sin\theta_L$, where θ_L is pitch angle in the central cross-section of the magnetic mirror).

Transition to the hydrodynamic stage of CI leads to a principally new generation regime in SCM, when coherence effects begin to prevail [8]. This regime is the so-called backward-wave-oscillator generation regime. It is well-known in electronics dealing with well-

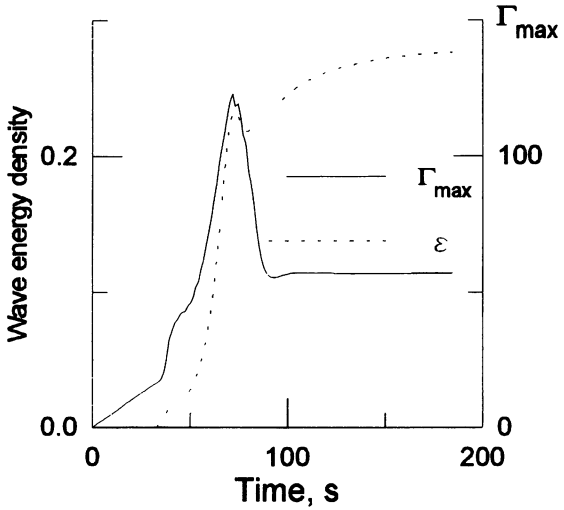

Figure 1. The temporal evolution of amplification $\Gamma = 0.5 \oint (\gamma / v_g)\, dz$ and the whistler wave energy density $\mathcal{E}$ (computational results [7]).

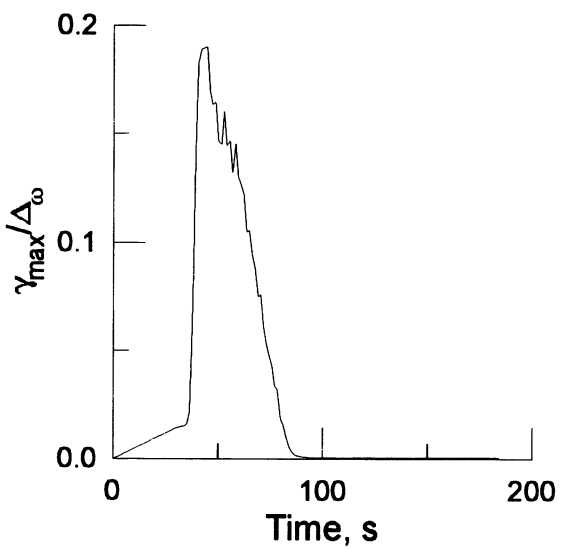

Figure 2. The temporal evolution of the ratio of γ to the amplification frequency bandwidth at half power Δ_ω (computational results [7]).

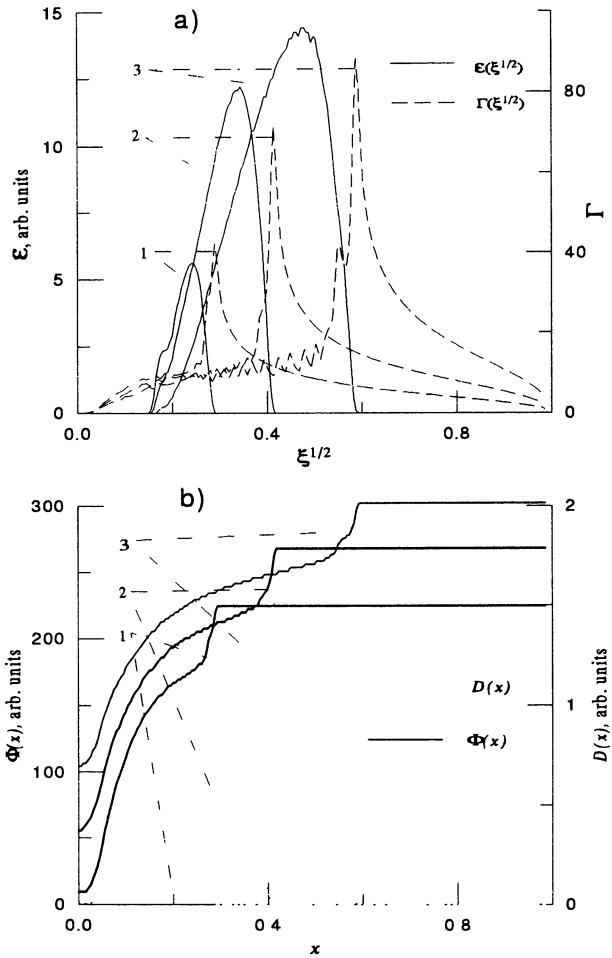

Figure 3. The dependencies of the averaged growth rate, γ (dashed line), and the whistler wave energy density, $\mathcal{E}$ (solid line), on the dimensionless frequency $\xi = 1 - \omega_0/\omega$, and of the distribution function, F (bold line), and the diffusion coefficient, D (dotted line), on $x = \sin\theta_L$ at different times (from [7]). Curve labels (1–3) refer to the time points: 1 denotes $t = 52.5$ s, 2 denotes $t = 63.5$ s, and 3 denotes $t = 70$ s. The formation of the step and wavelet generation are seen.

organized electron beams with small velocity dispersion (see, for example, [9]). The important property of this regime is that it is excited in open electrodynamical systems without reflecting mirrors. The positive feedback connection appears in such generators through interaction of the cold–plasma wave mode with the "beam" mode, which has to propagate against a cold mode. This case takes place, when $\omega \leq \omega_B$. the "beam" mode exists only in the case of hydrodynamic instability. Both these conditions are fulfilled in SCM with the step-like distribution function, the difference is only quantitative. If in the case of a well-organized beam (δ-function in the velocity space) the growth rate, γ, which characterizes the temporal scale in the generator, is proportional to $N_h^{1/3}$, N_h is beam density, so for a step distribution $\gamma \sim N_h^{1/2}$. Computational modeling and experimental investigation of laboratory devices [9] show, that the BWO regime is excited, when the beam density overcomes some threshold value. When the beam density is growing, a generator comes through several bifurcations from stationary generation to the periodic regime and further to the stochastic one. Taking into account the common physical basis, we have grounds to expect the same regimes in SCM. More detailed consideration is given in [8], where it has been shown, that the fine structure of radiation in SCM can be attributed to periodic and stochastic BWO generation regimes with a step distribution function. In particular, the period of the fine dynamical spectrum structure is equal to

$$T_f = l\left(v_{\text{st}}^{-1} + v_g^{-1}\right) \tag{3}$$

where v_{st} is velocity of a step, v_g is group velocity of waves, the characteristic scale, l, of SCM along the magnetic field is determined by the cyclotron resonance mismatching due to the magnetic field inhomogenity and is equal to [8]

$$l = a/(ka)^{1/3}, \tag{4}$$

where a is characteristic length of a magnetic flux tube, k is wave vector, $(ka)^{1/3} \gg 1$.

According to (1) and (3), $T_{g,b} \sim 2a/v_{g,z}$, so $T_f \ll T_g, T_B$; that is in good accordance with experiment. It is borne in mind, that the

present theory of a fine structure has mainly the qualitative character, though it explains many important features of SCM generation. In future it is necessary to develop a strict nonlinear theory, which could include an appearance of phase coherence and nonlinear dynamics of particles and waves at this stage. In real conditions the influence of magnetic field inhomogenity can be very important [10].

3 Fast energy exchange between hot and cold plasma components in SCM

In the previous section a cold plasma played passive role in SCM, determining cold electromagnetic eigenmodes. In real conditions hot and cold components can strongly interact with each other. In particular, a cold component can serve as a nonlinear element, which determines the quality of the CM electrodynamical system and, consequently, generation regimes in SCM. Such a situation is realized in so-called alfven sweep masers (ASM), operating in the frequency range of geomagnetic pulsations ($f \sim 0.1$–10 Hz) and using energetic protons as an active substance. ASM generates alfven waves with the wavelength comparable with thickness of the ionosphere. Thus the conjugate ionospheres serve in ASM as Fabry-Perot cavities, which determine the resonance (nonmonotonous) dependence of the wave reflection coefficient on frequency. When ASM begins to operate, generated alfven waves cause precipitation of energetic protons into ionosphere, which create additional ionization and change the reflection coefficient. As the result, specific periodic regimes are excited, which can explain the important type of geomagnetic pulsations in the frequency range $f \sim 0.1$–10 Hz [11, 12].

The point of view on the cold plasma component as a nonlinear element in CM was very fruitful for explanation of some experiments with laboratory magnetic traps, where burst-like whistler wave generation and energetic electron precipitation were observed [13, 14]. Here we pay attention to the experiment of [15], which is important for further consideration. In this experiment the plasma was prepared by magnetic compression, which was accompanied by appearance of energetic electrons. At some phase of compression the bursts of electromagnetic radiation appeared on the frequency less then the minimum gyrofrequency in the magnetic trap. At the same time intense

optical emission from plasma volume was observed, which testified strong pulse heating of the background plasma.

The explanation of this experiment given in [13] is based on the consideration of a cold plasma as a nonlinear absorbing element, which determines the CI threshold in CM and is switched off in process of CI development. Actually, in the presence of a dense cold plasma with a sufficiently high degree of ionization the CI threshold is determined by damping of whistler waves due to electron-ion collisions and can be written as

$$\gamma = (\omega/\omega_{BL})\,\nu_{ei} \tag{5}$$

where $\gamma \sim \omega_B(N_h/N_c)$ is CI growth rate, ω is frequency of cyclotron waves, N_h and N_c are densities of hot and cold plasma components, respectively, ν_{ei} is electron-ion collision frequency, which is equal to

$$\nu_{ei} \approx 50 N_c T_c^{-3/2} \quad [\mathrm{s}^{-1}], \tag{6}$$

where T_c is the electron temperature of a cold plasma (in ^{o}K), and N_c is measured in cm^{-3}.

When in the process of slow evolution of CM parameters the CI threshold (5) is reached, generated whistler waves begin to heat a cold plasma, and ν_{ei} is decreased according to (6). As the result, CI develops as a very short burst of waves, which is accompanied by fast heating of a cold plasma. The similar situation can be repeated in space plasma, in a solar corona particularly. It is well-known, that on the preflare stage a coronary magnetic loop, which is connected with a solar flare, is filled with a very dense and relatively cold plasma. Simultaneously a reconfiguration of the magnetic field takes place in this region. However, these processes by themselves can not provide for the explosive beginning of a solar flare, when very strong heating of corona takes place during parts of a second in the central crossection of this magnetic loop, and intense energetic electron precipitation appears in its feet.

A possible physical mechanism of such an explosion can be connected with operation of CM inside a flaring magnetic loop. A new scenario for a solar flare could be the following. During the preflare stage plasma injection from the chromosphere and magnetic reconfiguration (reconnection and compression) lead to formation of two-component plasma, consisting of cold dense plasma and hot addition

with small density but large energy supply, which are conditions for CM operation. In principle, this process is quite real: energetic electrons appear due to the running-away effect in the increasing magnetic field [16], background plasma remains cold due to additional ionization process and to radiative losses, which are very strong in the conditions of the solar corona [17, 18]. At a certain stage of evolution the CI threshold (5) is achieved. It occurs at first in the equatorial crossection of the magnetic loop, where the threshold is minimal. In this region explosive accumulation of whistler wave energy and growth of plasma temperature occur for a very short time, $\sim \gamma^{-1}$. The initial spatial scale of the heated region along the magnetic flux tube is determined by heat conductivity length, l_T, which is much less than the scale of magnetic loop. This length determines the front width of two nonlinear thermal waves, which propagate along the magnetic flux tube from the central crossection. Thus the energy of energetic electrons is gathered from all volume of a magnetic loop and accumulated inside a very small volume in the form of thermal energy of the background plasma. The energy density of this plasma can overcome the local magnetic energy density, what can lead to mass ejection to the interplanetary space. More detailed quantitative calculations [19] make it possible to explain many important features of a solar flare.

4 Some consequences for laboratory plasma

The most important problem in the SCM theory now seems to be the fine structure of SCM radiation. This problem includes the principal questions, such as self-organization effects, which are arising in the process of QL relaxation and are connected with formation of some specific deformations in the distribution function of energetic particles. The most natural of them is a step-like deformation, which can be the embryo of coherent states in plasma. New wave generation regimes caused by these coherent states could be the universal mechanism of the spectral fine structure of radiation from natural sources. Experiments with man-made sources of electromagnetic radiation are very fruitful here. A unique example of such an experiment is operation of the american transmitter "Siple" in the frequency range $f \sim$ 2–12 kHz, which is just the range of natural CM in the Earth

magnetosphere [20]. The very important results were obtained in this experiment, which dealt with so-called triggered ELF-VLF emissions [20, 10]. Unfortunately, the investigations ceased because Siple was destroyed by a hurricane and would not be restored due to its very high cost. At the same time, laboratory modeling could give valuable results and would be much cheaper than construction of a special transmitter for space experiments.

The creation of CM with a background plasma of full value would be very useful for modeling new applications, such as fast energy transfer from the hot to the cold plasma component. It would be possible to verify in laboratory conditions the full chain of a new scenario of a solar flare from creation of the two-component plasma to explosive heating of a cold plasma.

These experiments could have relation to controlled thermonuclear fusion (CTNF). Actually, accumulation of small addition of energetic electrons inside a magnetic trap with cold plasma is often an easier problem than heating and confinement of dense thermonuclear plasma. CM operation permits, in principle, to put very fast the considerable part of energy of energetic electrons from all the volume of magnetic trap into a small volume of background cold plasma, which could be a thermonuclear plasma. In fact, we have some modification of inertial CTNF. More detailed consideration of this question is beyond the frame of this paper.

Acknowledgment This work was supported in part by the Russian Foundation for Basic Research, grant 96-02-16473a.

References

1. Trakhtengerts V.Y., Tagirov V.R., Chernous S.A., *Geomagn. Aeron.* 1986, **26**, 99
2. Demekhov A.G., Trakhtengerts V.Y., *J. Geophys. Res.* 1994, **99**, 5831
3. Ivanov A.A., Rudakov L.I., *Zhurn. Exp. i Teor. Fiz.* 1966, **51**, 1522 (In Russian)
4. Ivanov A.A., *Physics of strongly nonequilibrium plasmas* (in Russian), Energoatomizdat, Moscow 1977

5. Hattori K., Hayakawa M., Shimakura S., Parrot M., Lefeuvre F., in *Proceedings of the NIPR Symposium on Upper Atmospheric Physics*, vol. 2. National Inst. of Polar Res., Tokyo 1989, p. 84
6. Hattori K., Hayakawa M., Lagoutte D., Parrot M., Lefeuvre F., *Planet. Space Sci.* 1991, **39**, 1465
7. Trakhtengerts V.Y., Rycroft M.J., Demekhov A.G., *J. Geophys. Res.* 1996, **101**, 13,293
8. Trakhtengerts V.Y., *J. Geophys. Res.* 1995, **100**, 17,205
9. Ginzburg N.S., Kuznetsov S.P., in *Relativistic HF Electronics*, Inst. of Appl. Phys., Gorky, USSR, 1981 pp. 101–144, In Russian
10. Omura Y., Nunn D., Matsumoto H., Rycroft M.J., *J. Atmos. Terr. Phys.* 1991, **53**, 351
11. Belyaev P.P., Polyakov S.V., Rapoport V.O., Trakhtengerts V.Y., *Geomagn. Aeron.* 1987, **27**, 652
12. Demekhov A.G., Trakhtengerts V.Y., Polyakov S.V., Belyaev P.P., Rapoport V.O., An alfven sweep maser model for pc 1 pearls: Theory, Tech. Rep. 405, Radiophysical Research Institute, Nizhny Novgorod, Russia 1994
13. Gaponov-Grekhov A.V., Glagolev V.M., Trakhtengerts V.Y., *ZhETF* 1981, **80**, 2198
14. Demekhov A.G., Trakhtengerts V.Y., *Radiophys. and Quantum Electr.* 1986, **29**, 848
15. Perkins W.A., Barr W.L., in *Proc. Int. Conf. Plasma Phys. and Controlled Nucl. Fusion Res.*, vol. 2. IAEA, Vienna 1966, 1966 pp. 115–134
16. Bogomolov Y.L., Demekhov A.G., Trakhtengerts V.Y., Scher E.M., Yunakovsky A.D., *Sov. J. Plasma Phys.* 1988, **14**, 316, FP-rus: v.14, No.5, p.539–546
17. Priest E.R., *Solar Magnetohydrodynamics*, D. Reidel, Dordrecht, Holland 1982
18. Khodachenko M.L., *Izv. Vuzov — Radiofizika* 1996, **39**, 53
19. Trakhtengerts V.Y., *Izv. Vuzov — Radiofizika* 1996, **39**, 699
20. Helliwell R.A., *Mod. Radio Sci.* 1993, p. 189

INHOMOGENEOUS PLASMA PARAMETRIC INSTABILITY DRIVEN BY FREQUENCY MODULATED PUMP

V.I.Arkhipenko, V.N.Budnikov[*], *E.Z.Gusakov*[*], *V.A.Pisarev*, *V.L.Selenin*[*], *L.V.Simonchik and B.O.Yakovlev*[*]

Institute of Molecular and Atomic Physics, Minsk, Beylorussia

[*]Ioffe Physico-Technical Institute, St Petersburg, Russia

Abstract

The inhomogeneous plasma parametric decay instability driven by frequency modulated pump is studied both theoretically and experimentally. A strong decrease of the threshold of decay instability of the Trivelpiece-Gould wave in a magnetized plasma is observed in a narrow range of the pump frequency modulation rates. The decay point motion due to the pump frequency modulation is shown to be responsible for this effect, which occurs when the decay point velocity is equal to the ion acoustic velocity. Effective instability suppression is demonstrated for larger decay point velocities. The time evolution of the decay wave amplitude is investigated for different pump frequency modulation rates.

Introduction

According to [1,2] plasma inhomogeneity has a strong stabilizing effect on parametric decay instabilities. The decay condition

$$\kappa_0(x) = \kappa_1(x) + \kappa_2(x) \qquad (1)$$

for projections κ_j (j=0,1,2) of wavevectors in the inhomogeneity direction, can be satisfied only at isolated points $x = x_d$ in a

nonuniform plasma. The parametric interaction occurs in the vicinity of these points with the size

$$l = \left| \frac{d}{dx} \left(\kappa_0(x) - \kappa_1(x) - \kappa_2(x) \right) \right|^{-1/2} \qquad (2)$$

Convection of the decay waves out of narrow interaction regions is the loss mechanism that saturates the instability. In fact, we have here amplification of the decay waves with the amplification coefficient given by

$$S = \exp\left(\frac{\pi \gamma_0^{\,2} l^2}{|v_1 v_2|} \right) \qquad (3)$$

where γ_0 is the instability maximal growth rate in the homogeneous plasma theory and v_1 and v_2 are components of the daughter wave group velocity in the inhomogeneity direction.

The plasma nonstationarity also produces a stabilizing effect on decay instabilities due to violation of the frequency decay condition [3]

$$\omega_0(t) = \omega_1(t) + \omega_2(t) \qquad (4)$$

However these factors acting simultaneously can reduce the stabilizing effect, as has been shown theoretically for decay **t→l+s** [4]. In this case the decay point $x_d(t)$, at which the decay conditions (1) and (4) are satisfied, moves with the velocity $v = dx_d/dt$. When the velocity of the decay point approaches one of the group velocities v_1 or v_2, the convection of the daughter wave out of drifting interaction region vanishes and the amplification coefficient formally goes to infinity. This resonance can modify the fluctuation spectra of parametrically driven waves in inhomogeneous and nonstationary plasma and could be used, in principal, for selective excitation of plasma waves. In spite of this, the above effect has not been verified experimentally yet, probably due to difficulties in controlling the

parameters of nonuniform and nonstationary plasmas and performing fine wave measurements in such conditions.

However the required motion of the decay point can be achieved in much more convenient way by using a frequency modulated pump wave. The time variation of the pump frequency $\omega_0 = \omega_0(t)$ results in a change in the decay point position $x_d = x_d(\omega_0) = x_d(\omega_0(t))$. Unlike the nonstationary plasma case, this drift of the decay point can be easily controlled by variation of the frequency modulation rate. The first experimental observations of the effect of enhancement of parametrically produced waves due to the pump frequency modulation were reported in [5,6]. In the present paper the theoretical analysis will be given as well as the results of experimental investigation of dependence of the decay instability threshold on the pump modulation rate. The time evolution of parametric decay at different pump frequency modulation rates is also investigated.

Theoretical analysis

The decay instability driven in inhomogeneous plasma by frequency modulated pump is investigated in the framework of coupled wave equations for slowly varying amplitudes of parametrically excited waves

$$\begin{aligned} \frac{\partial a_1(x,t)}{\partial t} + v_1 \frac{\partial a_1(x,t)}{\partial x} &= \gamma_0 a_2(x,t) e^{i\phi(x,t)} \\ \frac{\partial a_2(x,t)}{\partial t} + v_2 \frac{\partial a_2(x,t)}{\partial x} &= \gamma_0^* a_1(x,t) e^{-i\phi(x,t)} \end{aligned} \qquad (5)$$

where the phase mismatch $\phi = \frac{x^2}{2\ell^2} + \alpha_0 (x - v_0 t)^2$ consists of two terms. The first is related to the plasma inhomogeniety, where as the second describes the pump frequency modulation with the period

τ and deviation Δf, $\alpha_0 = -\frac{1}{v_0^2}\frac{\pi\Delta f}{\tau}$, v_0 is the pump group velocity projection in the inhomogeneity direction. Supposing that all the frequency variation of the pump is taken by the high frequency daughter wave a_1 we use a quadratic phase substitution for a_1

$$a_1 = \tilde{a}_1 \exp\left\{-i\alpha_0 \frac{v_0(v_0 - v)}{v_1(v_1 - v)}(x - v_1 t)^2\right\} \qquad (6)$$

$$\text{where } v = -\frac{2\alpha_0 \ell^2 v_0(v_1 + v_0)}{2\alpha_0 \ell^2(v_1 + v_0) + v_1} \qquad (7)$$

Introducing a new variable $\eta = x - vt$ we represent the equations (5) in the standard form

$$\begin{aligned} \frac{\partial \tilde{a}_1(\eta,t)}{\partial t} + u_1 \frac{\partial \tilde{a}_1(\eta,t)}{\partial \eta} &= \gamma_0 a_2(\eta,t) e^{i\eta^2/2\tilde{\ell}^2} \\ \frac{\partial a_2(\eta,t)}{\partial t} + u_2 \frac{\partial a_2(\eta,t)}{\partial \eta} &= \gamma_0^* \tilde{a}_1(\eta,t) e^{-i\eta^2/2\tilde{\ell}^2} \end{aligned} \qquad (8)$$

in which $u_1 = v_1 - v$, $u_2 = v_2 - v$, $\tilde{\ell}^2 = \ell^2 \frac{(v_1 - v)(v_0 - v)}{v_1 v_0}$

Equations (8) describe the parametric decay in the inhomogeneous plasma. These equations were studied in [1,2], where no absolute instability, but spatial amplification of plasma fluctuations was found. The amplification coefficient for the low frequency wave a_2 which dose not change the frequency, according to [1,2], takes a form

$$S = \exp(\pi Z) = \exp\left(\frac{\pi\gamma_0^2 \tilde{\ell}^2}{|v_1 - v||v_2 - v|}\right) \qquad (9)$$

This coefficient formally goes to infinity for modulation rates $\alpha_0 \to \frac{v_1 v_2}{2\ell^2 (v_0 - v_2)(v_1 - v_0)}$, for which the decay point velocity v approaches the group velocity v_2. The physical reason for this effect is that convection of the decay wave out of the drifting interaction region vanishes when v equals its group velocity. This is similar to some extent to the increase of the amplification near the cut off, where $v_2 \to 0$. However, in the cut off case the amplification length $\ell \cong \left| \frac{d\kappa_2}{dx} \right|^{-1/2}$ vanishes together with v_2 in such a way that the amplification coefficient remains finite. In our case, in the absence of convective losses the decay wave energy will concentrate within the drifting decay region. The energy growth in this region can be limited by a number of mechanisms, in particular by the violation of the resonance condition $v = v_2$, or by small convective losses caused by the effect of wave dispersion. Another limiting factor of importance under the experimental condition is the finite modulation period. The analysis of the transient phenomena after the pump switch on made for equations (8) in [7,8] shows that for $v_2 > v$ the amplitude $a_2|_{\eta=0}$ growth exponentially in time with the growth rate

$$\gamma = \gamma_0 \frac{(v_2 - v)^{1/2} (v - v_1)^{1/2}}{v_2 - v_1} \qquad (10)$$

The growth rate decreases when approaching the resonance $v \to v_2$. The saturation time for exponential growth is

$$t_{sat} \cong \frac{\pi \gamma_0 \tilde{\ell}^2 (v_2 - v_1)}{(v_2 - v)^{3/2} (v - v_1)^{3/2}} \qquad (11)$$

In the resonance case, for $v \to v_2$, the saturation time goes to infinity, which is explained by the growth of the interaction length $L \cong \tilde{\ell}\sqrt{Z}$ and decrease of the convective losses $t_{sat} \cong \dfrac{L}{v_2 - v}$. When the saturation time is longer than the modulation period $t_{sat} > \tau$ the wave amplitude will grow exponentially during all the modulation period, so that close to the resonance the amplification will be given not by (9), but by

$$S = \exp\{\gamma\tau\} = \exp\left\{\gamma_0 \frac{(v - v_1)^{1/2}(v_2 - v)^{1/2}}{v_2 - v_1}\tau\right\} \qquad (12)$$

In the opposite case $t_{sat} < \tau$ (far from resonance) the exponential growth saturates due to the convective losses so that expression -9th is valid. The decay point velocity, providing the largest amplification is given by condition $t_{sat} \approx \tau$ .For large decay point velocities $v > v_2$, no exponential growth in time is predicted at $\eta = 0$. The convective instability occurs instead.

Experimental observations

The experiment was carried out in the linear plasma device [9] shown in fig.1. The argon plasma was produced using the electron cyclotron discharge in a tube 2cm in diameter and 100cm long placed in an uniform magnetic field of 3kG. The plasma was inhomogeneous both across and along the magnetic field $n_e=n_e(r,z)$. The maximum density was $n_e \approx 10^{12} cm^{-3}$, electron temperature $T_e \approx 2eV$ and argon pressure $2 \cdot 10^{-2}$Torr. The Trivelpiece-Gould (TG) pump wave was excited in the plasma with a waveguide. The saw-tooth frequency modulation of the pump was used with the frequency variation given by $f = f_0 - \dfrac{t}{\tau}\Delta f$. In the experiment we had $f_0 - \Delta f = 2300 MHz$,

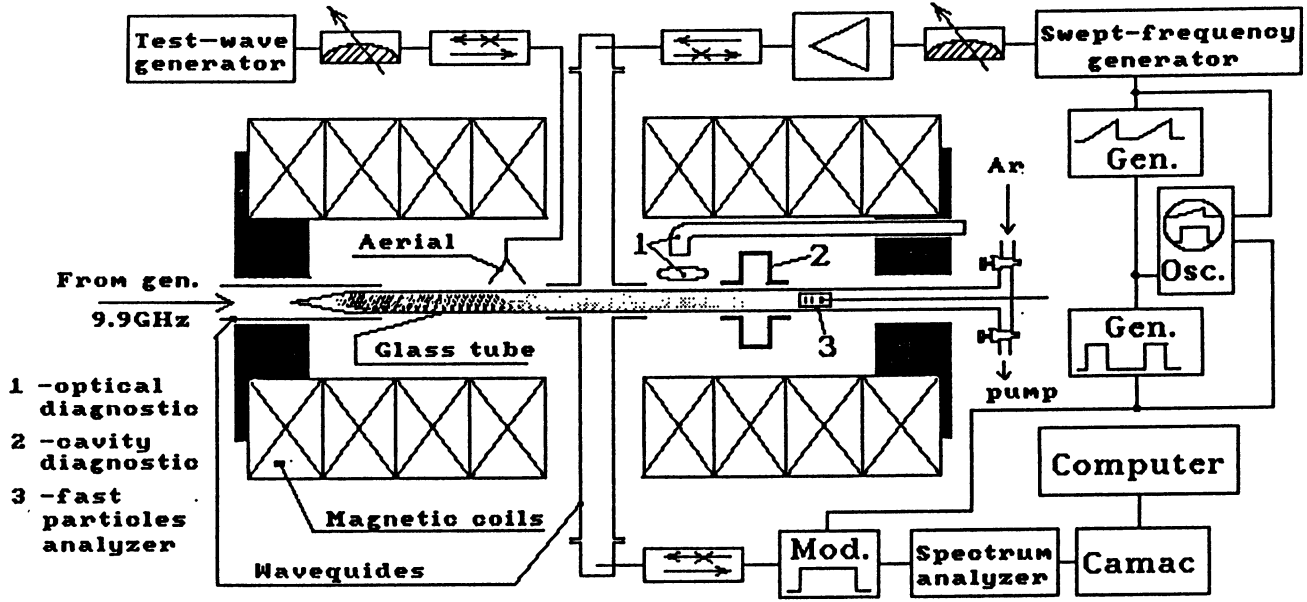

Fig.1 Experimental set up.

the frequency deviation $\Delta f \le 800MHz$ and $\tau > 10^{-6}s$. According to the dispersion relation for the TG mode $k_\perp{}^2 = \left[\frac{\omega_{pe}{}^2(r,z)}{\omega^2} - 1\right] k_{II}{}^2$, the overcritical plasma density region represents a waveguide for this mode (see fig.2). Propagating along this weakly inhomogeneous channel towards decreasing plasma density the pump gradually slows down. Its electric field and parallel wavenumber sharply increase near the point where the critical density surface $n_e(r,z)=n_c$ intersects the chamber axis and where the hybrid resonance is situated [9].Close to the resonance the pump parallel wavenumber k_0 is given by equation

$$3r_d{}^2 k_0{}^2 - \frac{z}{a} - \frac{2}{k_0 b} = 0 \qquad (13)$$

where $a \approx 4cm$ and $b \approx 0.4cm$ are the density scale lengths along and across the magnetic field. The backscattering parametric instability **l→l'+s**, excited in the near vicinity of the hybrid resonance was observed in previous experiments [9], utilizing a monochromatic pump $(\Delta f = 0)$. As it was shown in [9] at small power level $P_0 < 20mW$ the inhomogeneous plasma convective decay instability was excited, described by the amplification coefficient (3). The ion acoustic wave involved in this decay propagate along the magnetic field in the direction of decreasing density.

The homodyne and heterodyne detection of the backscattered pump wave used in these experiments for studying the decay instability is not applicable in the frequency modulation case. The enhanced microwave scattering diagnostics was used instead to study the ion acoustic decay wave [9,10]. For this purpose a small power $(P < 5mW)$ probing TG mode was launched into the plasma by the same waveguide. The probing wave frequency was chosen $f_p = 2250MHz$ less than the minimum pump frequency, so that its backscattering by the decay ion acoustic wave occurs out of the

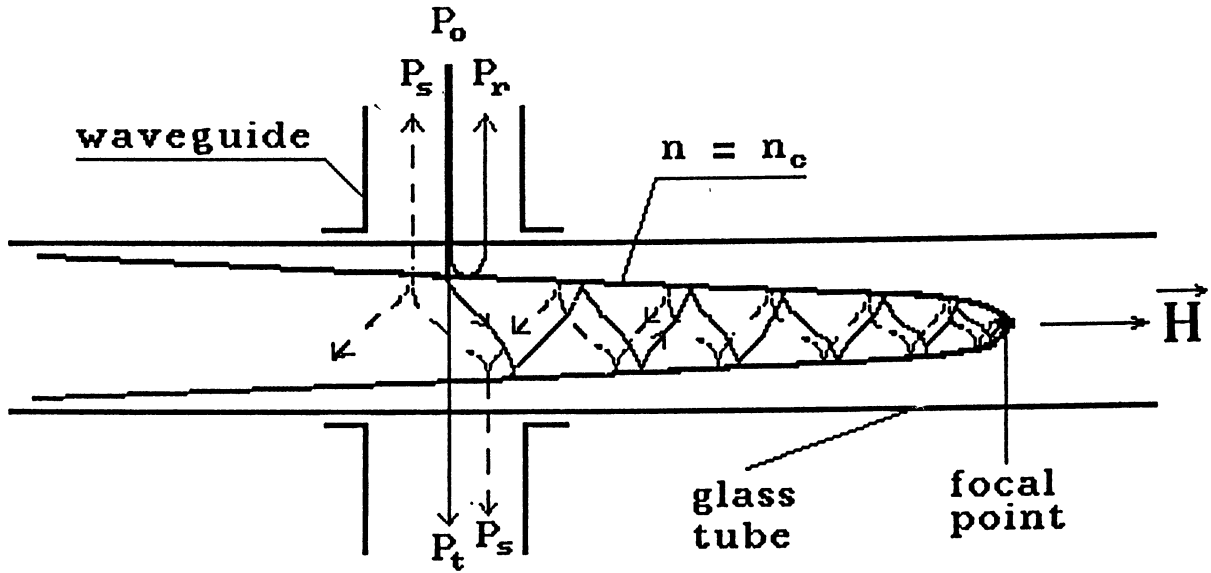

Fig.2 The pump electron plasma wave propagation scheme. P_t, P_r and P_s are the transmitted, reflected and scattered powers, respectively.

instability region, providing information on the decay wave amplitude and spectra.

The first experiments have shown the possibility of parametric excitation of ion acoustic waves at frequency 2-3 MHz by frequency modulated pump. The probing wave backscattering spectrum A_{ps} consisted of a single line down-shifted by 2MHz and 1MHz broad. The sequence of such spectra for modulation periods from 3.5μs to 10.5μs and frequency deviation Δf=350MHz is shown in fig.3. The line amlitude is suppressed for slow and fast modulation and has a maximum for τ=5.5μs. The dependence of the threshold of ion acoustic wave observation on the modulation rate $\Delta f/\tau$ is shown in fig.4. This dependence has a deep minimum for optimum rate $\Delta f/\tau \approx 50\, MHz/\mu s$. The threshold here is a factor of 5 smaller than in the stationary pump case $(\Delta f = 0)$. The modulation rate for which the destabilization occurs is close to that predicted by theory. From condition $v = c_s$ one obtained for the **l→l'+s** backscattering decay $\left.\frac{\Delta f}{\tau}\right|_{res} = f_0 \frac{c_s}{2a} \approx 60 \frac{MHz}{\mu s}$. The instability observation threshold increases drastically for the fast modulation case taking the value a factor of 10 higher for $\frac{\Delta f}{\tau} \approx 120 \frac{MHz}{\mu s}$. For higher modulation rates the instability excitation was not observed in the experiment.

The temporal evolution of the instability was studied in the special experiment in which the modulation period was varied at constant modulation rate and $f_0 - \Delta f$. The different behaviour was observed for slow and optimum modulations. For slow modulation $(\Delta f_{max} = 400 MHz$ for $\tau_{max} = T = 12\mu s)$ the dependence of acoustic wave amplitude A_s, proportional to the spectral line A_{ps} maximum, on time τ consists of two different parts (see fig.5). It is exponential for small τ and then saturates at the level, which exponentially depends on

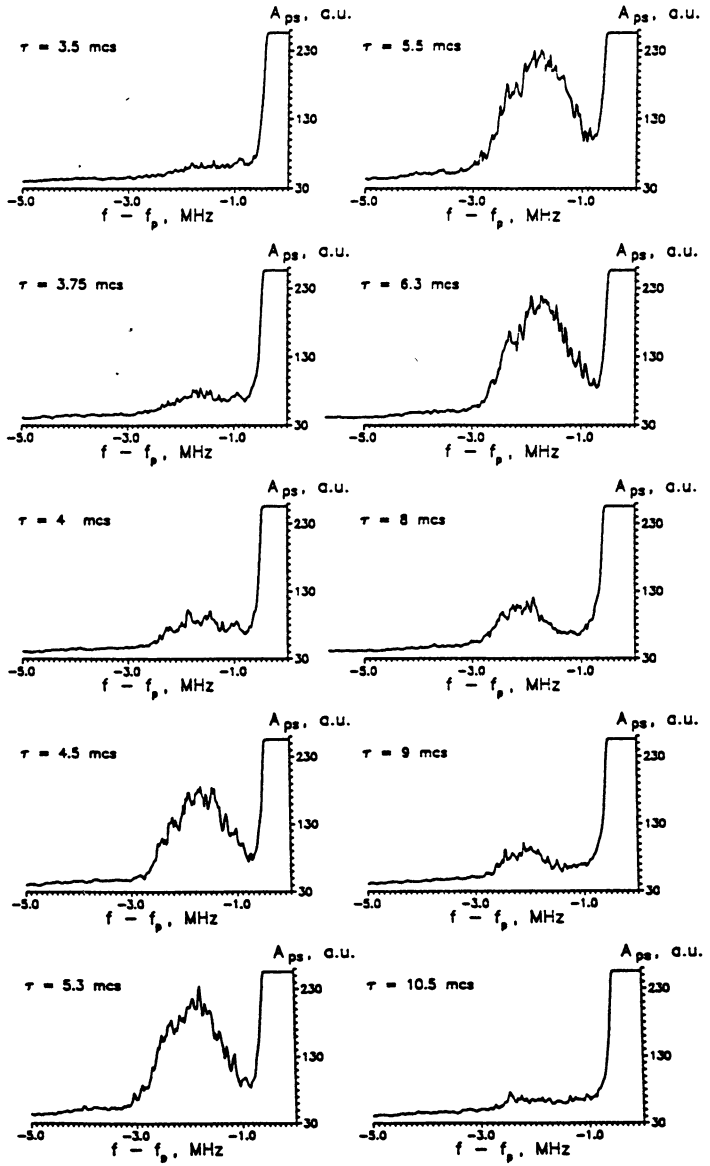

Fig.3 The probing wave backscattering spectra $A_{ps}(f\text{-}f_p)$ for different pump frequency modulation rates.

the pump power P. Such a dependence agrees well with the theoretical prediction for the case of $\tau > t_{sat}$ in which the convective losses are essential for the instability saturation. On contrary in the optimum case for $T = 8\mu s$ shown in fig.6, only exponential growth is observed and no saturation takes place. The growth rates here are lower than in the previous case for the same power level (see fig.7).

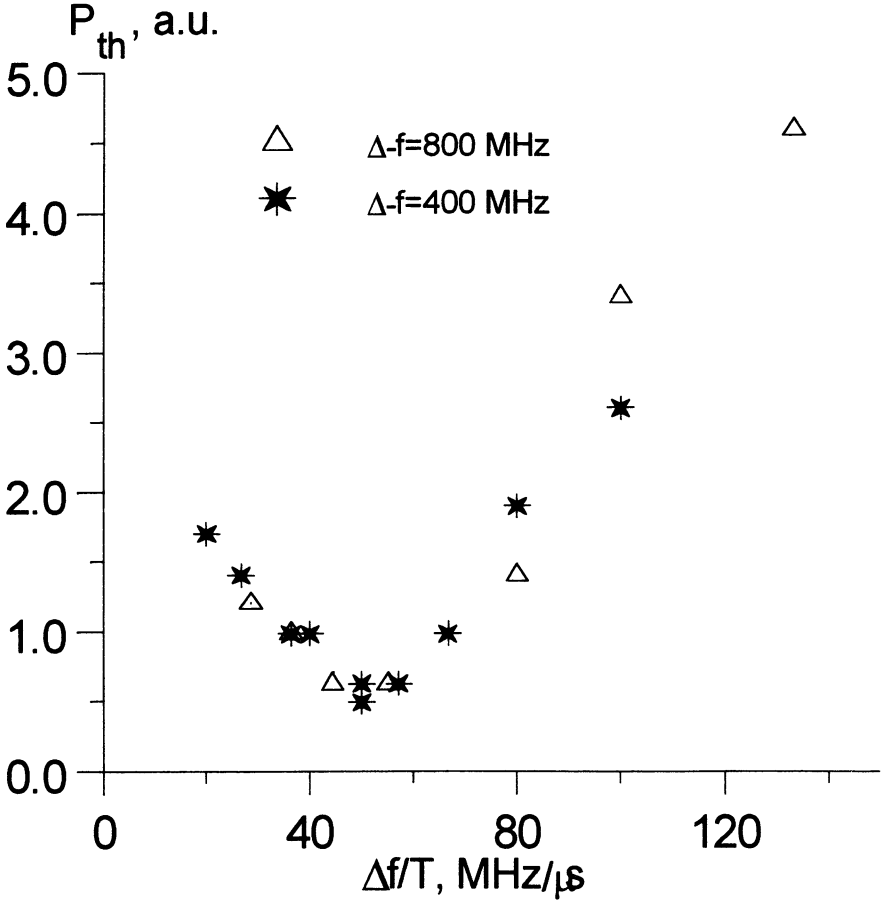

Fig.4 Threshold dependence on modulation rate

This observations are explained by the increase of the saturation

time and decrease of the growth rate which should occur according to equations (10), (11) when the decay point velocity increases and approaches c_s.

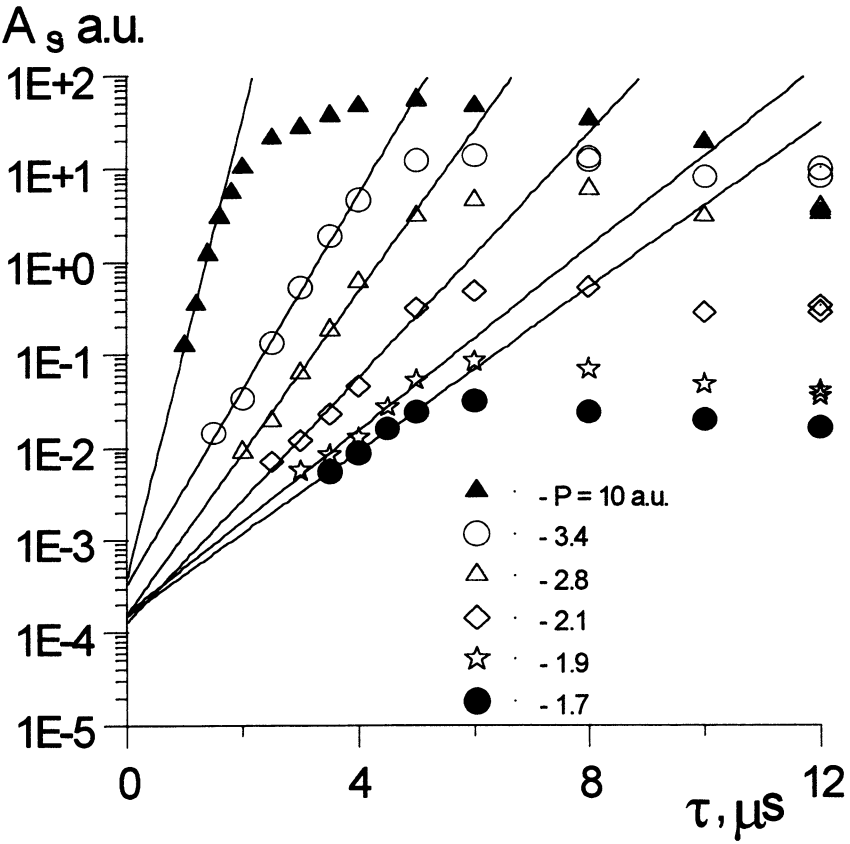

Fig.5 IA wave evolution for slowly modulated pump

At higher modulation rates for $T = 6\mu s$ the growth rate decreases drastically as it is seen in fig.7. and the saturation dose not exist, which is in agreement with predictions of theoretical analysis.

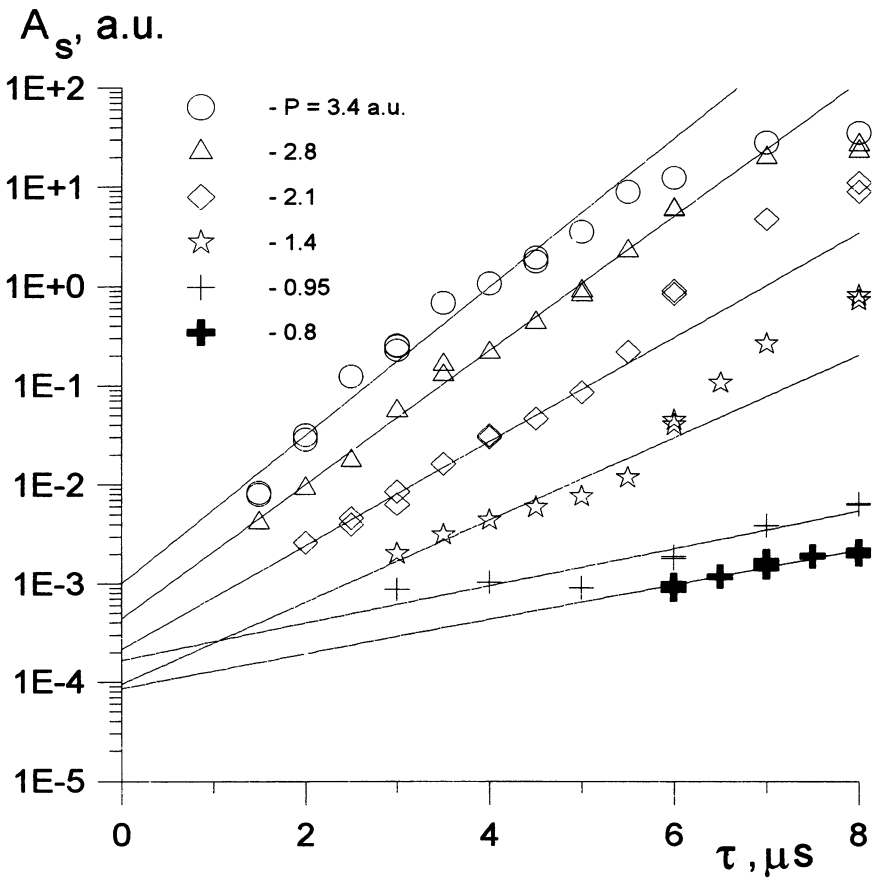

Fig.6 IA wave evolution for optimum modulation

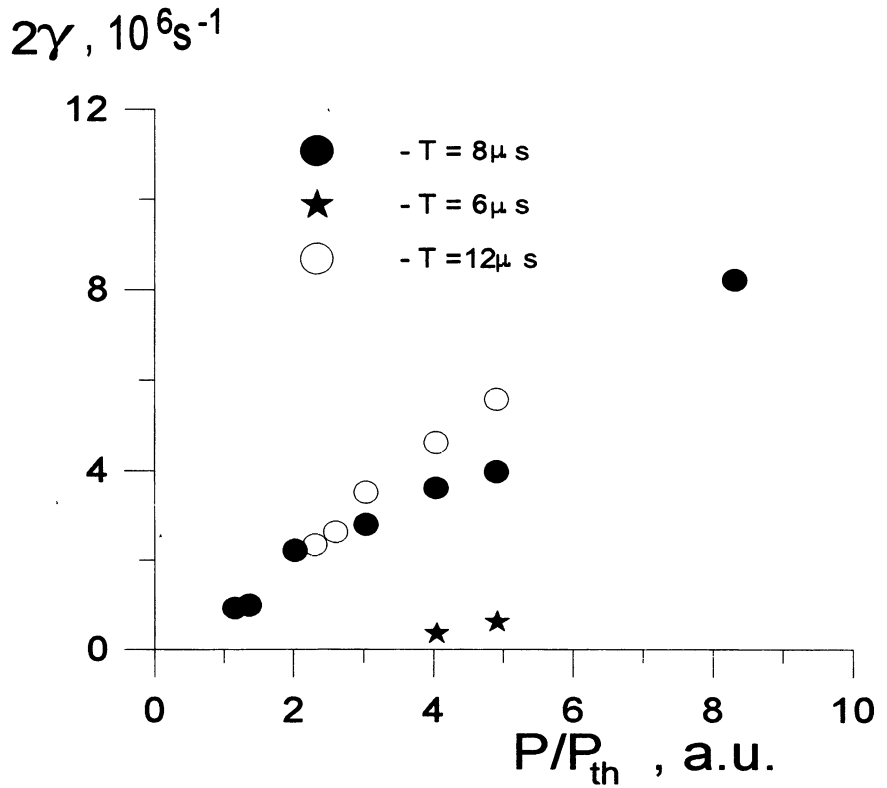

Fig.7 Instability growth rate versus pump power

Acknowledgments

This work was performed within the activities of RFBR Grant 95-02-05421

References

1. Piliya A.D. Proc. X Int. Conf. on Phenomena in Ionised Gases, Oxford 320 (1971)
2. M.N.Rosenbluth Phys. Rev. Lett. **29,** 565 (1972)
3. L.M.Gorbunov, A.N.Starodub Pis'ma v zhurnal tekhnicheskoi fiziki **3,** 820 (1977)

4. A.A.Andreev, V.I.Fedorov Fizika plasmy **5,** 1058 (1979)
5. V.I.Arkhipehko et al Zh.E.T.Ph.Lett. **60,** 829 (1994)
6. V.I.Arkhipehko, V.N.Budnikov, E.Z.Gusakov et al Plasma Phys. Contrl. Fusion **37,** 1353 (1995)
7. A.D.Piliya Zh.E.T.Ph. **64,** 793 (1973)
8. M.N.Rosenbluth, R.B.White, C.S.Liu Phys. Rev. Lett. **31,** 1190 (1973)
9. V.I.Arkhipenko, V.N.Budnikov, E.Z.Gusakov et al Sov. J. Plasma Physics **13,** 398 (1987)
10. K.M.Novik, A.D.Piliya Plasma Physics Control Fusion **35**, 357 (1993)

THEORY OF STIMULATED ELECTROMAGNETIC EMISSIONS IN IONOSPHERIC RADIO MODIFICATION EXPERIMENTS

*E. Mjoelhus, E. Helmersen**

Institute of Mathematical and Physical Sciences, University of Tromsø, N–9037 Tromsø, Norway

*Present address: SINTEF, N–7034 Trondheim, Norway

Abstract

First a brief overview of electrostatic excitations in ionospheric radio modification experiments is given, including the Stimulated Electromagnetic Emissions (SEE). Then a simplified model for their generation by upper hybrid oscillations trapped in plasma density striations, is formulated. This model permits new kinds of parametric processes. Two such processes are introduced. Numerical results showing SEE source spectra from these instabilities, are shown, and their relation to observed SEE features discussed.

1. Introduction

This report will discuss processes which occur when powerful HF waves are launched from ground into the ionosphere, the so-called ionospheric radio modification experiments. Thus we discuss electromagnetic waves of wavelength $\sim$ 50–200 m, propagating into the ionospheric plasma, and thus our waves are certainly not microwaves. However, many of the processes of interaction between an incident electromagnetic wave and a plasma are quite generic. This is in particular true for the aspect of *electrostatic excitations,* which is the primary interest of the present authors. Namely, when the electromagnetic wave penetrates into the plasma, electrostatic oscillations may be excited in various ways. This must be at the expense of the energy of the incident wave, and so, when the electrostatic oscillations are eventually absorbed in the plasma, it amounts to an additional, or "anomalous" absorption of the incident electromagnetic waves.

The ionospheric modification experiments have been an active field of research since the 1960's, and since about 1970, an extensive literature on experimental and theoretical investigations of processes

of electrostatic excitations in these experiments has occurred. In the next section, a brief overview of this field will be given. However, our main focus of interest in this report is certain particular manifestations of these electrostatic excitations, which have been detected in a long series of experiments starting about 1980: When the reflected HF wave is frequency-analysed, it shows a rich sideband structure, which has proved to be highly reproducible, although it depends strongly on the applied frequency. This has been termed *Stimulated Electromagnetic Emissions (SEE).* Experiments of this kind have been performed at Tromsø, Northern Norway [1], near Niznyi Novgorod, Russia [2], at the Arecibo Observatory, Puerto Rico [3], and near Fairbanks, Alaska [4]. A brief account of these experiments will be given in sect. 3.

However, our main objective is to present a (fairly novel) theoretical model and point of view on the theoretical explanation of these manifestations. In sect. 4 we formulate the theoretical model. Our main point of view is that the sidebands are due to parametric processes of electrostatic (upper hybrid) oscillations across the magnetic field lines which are trapped in magnetic-field-aligned plasma density irregularities. These parametric processes are discussed in sect. 5. Sect. 6 contains a concluding summary.

2. Electrostatic excitations in ionospheric radio modification experiments

For most aspects of the theoretical discussion of these experiments, the Earth's magnetic field must be included in the theoretical model. Then, the incident electromagnetic wave will be a superposition of an ordinary polarized wave (O-mode) and an extraordinary wave (X-mode). The O-mode will be reflected at the height where the applied frequency ω_0 equals the electron plasma frequency $\omega_{pe} = 4\pi e^2 n/m_e$, where n is the electron density, while the X-mode is reflected at a lower altitude. As a result, only the O-mode can excite high-frequency electrostatic waves near the applied frequency ω_0; this can take place in a height interval roughly given by

$$\begin{aligned} &1 > X > 1 - Y^2 \\ &X = \omega_{pe}^2(h)/\omega_0^2\,, \qquad Y = \Omega_e/\omega_0\,, \end{aligned} \tag{1}$$

where $\Omega_e = eB_0/cm_e$ is the electron gyrofrequency. The X-mode does not have access to this height range. Thus, electrostatic excitations have the signatures (i) $\omega_0 < \max\omega_{pe}$, and (ii) it occurs only for O-mode incident wave. We mention the following three major classes of phenomena of electrostatic excitations:

(i) *Linear mode conversion.* The incident O-mode wave can be converted into electrostatic waves by a purely linear process, although plasma inhomogeneity must be taken into account in the theoretical model. For a version of the theory relevant for the ionospheric experiments, the magnetic field must be included; then, the relevant process is penetration through the radio window near critical incidence. For further information, it is referred to [5] and references therein. From a theoretical point of view, there is good reason to expect this process to take place during the experiments. However, it is not readily accessible to experiments, and it does not play a major role in explaining observed phenomena, although it has been invoked in some cases. Note that this process has recently been reported in experiments in a stellarator [29].

(ii) *Ponderomotive parametric instabilities.* The parametric decay instability, in which the electromagnetic wave ω_0 excites a Langmuir wave (ω_l, k) and an ion-acoustic wave $(\omega_i, -k)$ where $\omega_0 = \omega_l + \omega_i$ and $\omega_0 \simeq \omega_l$, $\omega_i \ll \omega_l$, as well as the so-called "Oscillating Two-Stream Instability" (OTSI), were theoretically predicted to be excitable in the ionospheric experiments in the late 1960's, and subsequently observed using the UHF radar of the Arecibo facility [6]. Due to the excellent experimental possibilities using VHF/UHF radars at Arecibo and later at EISCAT, Tromsø, these processes have received extensive attention up to the present date. This attention may also be due to the interesting theoretical issues involved, and we include here a brief historical account. A saturation theory of the parametric decay process was presented in refs. [7,8] in terms of further cascading, using the formalism of weak turbulence theory. A well-known theoretical contribution [9] pointed out a certain theoretical paradox in the weak turbu-

lence description of Langmuir turbulence, and together with certain laboratory experiments [10], and certain observational surprises, in particular concerning measurements of the height in the ionosphere from which the radar echo came [11,12], led to interest in alternative explanations of the observations in terms of "strong" Langmuir turbulence processes involving various kinds of cavitation phenomena and "solitons". Improved resolution in the experiments as well as a new generation of computers to simulate nonlinear models of the processes, has recently led to a detailed correspondence between theoretical predictions and experimental observation. On the theoretical side, driven and damped models were considered instead of the conservative model of ref. [9]. As a result, localized cavitation phenomena were seen as a result of (driven) cavity resonance (analogous to what will be discussed later in this paper). On the other hand, cascades also proved to play a role, although not in agreement with weak turbulence results [13,14]. In an elegant experiment at Arecibo [15], various different spectral features predicted by theory [13,14] were identified, originating from separate heights, in agreement with theoretical predictions. The same can be said to be true at Tromsø [16], although the features associated with cavitation are not always observed.

(iii) *Magnetic field-aligned density striations.* It was discovered in experiments in Platteville, Colorado, USA, that density irregularities with a small scale perpendicular to the Earth's magnetic field and very elongated along the field lines, were developed during radio modification experiments. They were detected by means of radar backscatter perpendicular to the magnetic field lines [17,18]. Similar experiments have later been performed at Sura, Tromsø, and Arecibo. Their transverse dimension is of the order of metres (as determined by the wavelength of the diagnostic radars), while their parallel dimension is expected to be of the order of several kilometres. In all current theoretical efforts, this phenomenon is considered as a feature of electrostatic excitation, because it has the features of being excitable only with O-mode polarization. The current theoretical picture which is promoted by the present authors, is briefly as follows:

(a) The time scale of the phenomenon of striations is of the order of seconds. All theoretical efforts therefore have concentrated on slow transport and heat conduction processes. This also is the essence of the explanation of the strong anisotropy, since electron transport goes much easier along than across the magnetic field. (b) The driving of these thermal processes, is provided by the ohmic heating of the electrons due to damping of electrostatic excitations. These excitations come about due to already existing striations. (c) In order to have a theoretical explanation, there must be a positive feedback between the electrostatic excitations and the striations. In some of the theoretical contributions [19–22] this is achieved by pointing out that the striations can both trap and generate upper hybrid oscillations in a certain height range. These oscillations will exist in the density depletions, and there they lead to heating and excess pressure. Then plasma is blown out of the density depletions, mainly along the magnetic field lines. The most recent of these contributions [22] extends this into a saturation theory.

3. Stimulated electromagnetic emissions

When $\omega_0 < \max \omega_{pe}$ of the ionosphere, the incident O-mode wave is totally reflected at $\omega_0 = \omega_{pe}$. As already mentioned in the introduction, the SEE experiments consist in spectral-analysing the returned wave. At first, the objective was to use the ionospheric set-up to study direct stimulated scattering processes, such as stimulated Brillouin scattering or stimulated Raman scattering. However, the spectra that were actually obtained, could not be explained this way. One then turned to invoking electrostatic excitations as intermediate stages, and see the generation of electromagnetic sidebands as a nonlinear mixing of these excitations. At the early stage of development, the ponderomotive parametric instabilities were considered this way. Since these processes had been well documented through the extensive radar studies, this was a rather natural choice. Ref. [23] is an attempt at a rather complete explanation along these lines.

However, since about 1988, it has become clear that the main

features of the SEE most probably have their origin in the striations. First, it was detected that the spectra behave in particular ways when the applied frequency is near a harmonic of the electron gyrofrequency [24]. This invokes the electron Bernstein waves, which exist only for wave vectors nearly perpendicular to the magnetic field. Since the striations also involve electrostatic excitations perpendicular to the magnetic field, the association is obvious. Another result which points in the same direction, is that the main SEE features need a time of order seconds to develop [25], just as the striations do. It is very reasonable also from a theoretical point of view that striations play a role in producing SEE: as will be demonstrated in sect. 5, they serve as *resonators* for electrostatic excitations.

There are two main features of SEE which will be of concern in this paper: (i) The *Downshifted Maximum* (DM), which is a hump in the spectrum downshifted by $\sim$ 8–15 kHz from the applied frequency $f_0 = \omega_0/2\pi$. The upper limit, ~ -8 kHz, is fairly invariant, and it has been pointed out long ago [26] that it corresponds to the lower hybrid frequency $\Omega_{LH} = (\Omega_i \Omega_e)^{1/2}$ where $\Omega_{i,e}$ are the ion and electron gyrofrequencies. This is a third feature that points towards the striations, since lower hybrid waves are also perpendicular waves. (ii) The other main feature is the *Broad Continuum* (BC), which is a broad feature, mainly downshifted, extending down to ~ -150 kHz.

Common to the DM and BC is that they disappear when the applied frequency is near a gyroharmonic, and they need a time of order seconds to develop. An explanation of this, compatible with the above theoretical explanation of the striations, occurred in ref. [27]. There are other features that occur when the applied frequency is near a gyroharmonic; and there is a narrow continuum (NC) which shows up also in short time experiments. These features are, however, thought to involve processes outside of the scope of this paper.

4. A general theoretical framework for SEE generation

The general theoretical framework within which it is proposed to investigate the SEE generation, was developed in ref. [28], and will be briefly described below. The basic achievement of the approach of ref. [28] is to apply the averaging method to the space dependence, so as to separate the problem into (i) electrostatic excitation, (ii) calculation

of source, and (iii) electromagnetic generation and propagation. The electric field is represented as

$$\mathbf{E} \longmapsto \frac{1}{2}\left[\mathbf{E}(\mathbf{x},t)\exp(-i\omega_0 t) + \text{c.c.}\right] \tag{2}$$

where the dependence of the complex envelope $\mathbf{E}(x,t)$ on t is slow. Then, the method of average induces a decomposition of this envelope into

$$\mathbf{E} = \mathbf{E}_0 + \nabla\phi \tag{3}$$

where the electrostatic part ϕ varies on the short, local, spatial scale $\mathbf{x}$.

(i) *The electrostatic excitation* is then governed by the *local* equation

$$\nabla\cdot\left[\left(i\left(\frac{\partial}{\partial t}+\nu*\right)\nabla\phi + \frac{3}{2}\omega_0\lambda_D^2\nabla^2\nabla\phi + \left(\Delta\Omega - \frac{\omega_0}{2}\frac{\delta n}{n_0}\right)\right)\nabla\phi\right]$$
$$-\frac{1}{2}\frac{\Omega_e^2}{\omega_0}\nabla_\perp^2\phi = \frac{\omega_0}{2}\mathbf{E}_0\cdot\nabla\left(\frac{\delta n}{n_0}\right). \tag{4}$$

In (4), the electromagnetic wave field $\mathbf{E}_0(\bar{\mathbf{x}})$ varies on the global spatial scale $\bar{\mathbf{x}}$, and is considered a constant in (4). The same is true of the mismatch parameter $\Delta\Omega(\bar{\mathbf{x}}) = \omega_0 - \omega_{pe}(\bar{\mathbf{x}})$. The damping operator ν can contain both the collisional and Landau damping

$$\nu(\mathbf{k}) = \frac{\nu_{ec}}{2} + \gamma_L(\mathbf{k}) \tag{5}$$

where ν_{ec} is the effective frequency of collisions between electrons and heavy particles. The remaining quantities in (2) are $\lambda_D = v_{te}/\omega_{pe}$, v_{te} electron thermal velocity, and Ω_e electron gyrofrequency.

To close the electrostatic part of the model, one has to add an equation for the plasma density perturbation. That will be further discussed at the end of this section.

(ii) *The source term.* The interaction between the local (electrostatic) and global (electromagnetic) level, is taken care of by

$$\bar{\mathbf{j}}_2(\bar{\mathbf{x}}) = i\frac{1}{4\pi}\omega_0\overline{\frac{\delta n}{n_0}\nabla\phi} \tag{6}$$

where the bar denotes average over the local space variable.

(iii) *Electromagnetic generation and propagation.* On the global level, the relevant set of equations can now be written as

$$i\underset{\sim}{\alpha}\cdot\frac{\partial \mathbf{E}_0}{\partial t} + \underset{\sim}{\varepsilon}_0\cdot\mathbf{E}_0 - \frac{c^2}{\omega_0^2}\bar{\nabla}\times(\bar{\nabla}\times\mathbf{E}_0) = -i\frac{4\pi}{\omega_0}\bar{\mathbf{j}}_2 \tag{7}$$

where

$$\underset{\sim}{\alpha} = \frac{1}{\omega_0}\frac{\partial}{\partial\omega_0}\left(\omega_0\,\underset{\sim}{\varepsilon}(\omega_0)\right)$$

In ref. [28] it was demonstrated that the source term $\bar{\mathbf{j}}_2$ takes consistently care of the energy loss from the electromagnetic wave into the electrostatic turbulence. In addition, its spectral sidebands will drive up sidebands in $\mathbf{E}_0$ according to equation (7).

This formalism is sometimes called the *mean field approximation.*

Eqs. (4) + an equation for the ponderomotive density modification, (6), and (7), constitute our general theoretical framework for the study of SEE generation. However, this is presently a fairly intractable model even numerically. For the results to be presented in this paper, we shall specialize to a much more restricted model:

(i) We do not consider the generation process, involving eq. (7). Instead, we shall solve the local equations at constant values of $\mathbf{E}_0$ and $\Delta\Omega$, compute the spectrum of the source $\bar{\mathbf{j}}_2$, and consider that as a contribution to the sideband spectrum.

(ii) For the local (electrostatic excitation) part, we consider a *one-dimensional* (slab) model, in which all space variation is across the magnetic field.

In normalized variables, our equations are

$$i\left(\frac{\partial}{\partial t}+\nu\right)E+\frac{\partial^2 E}{\partial x^2}+(\Omega-(N+n))\,E$$
$$=E_0(N+n)-j_2(t) \tag{8a}$$

$$\frac{\partial^2 n}{\partial t^2}+2\nu_i*\frac{\partial n}{\partial t}-\frac{\partial^2 n}{\partial x^2}+\Omega_{LH}^2\,n=\frac{\partial^2}{\partial x^2}\,|E+E_0|^2 \tag{8b}$$

$$j_2(t)=\overline{(N+n)E} \tag{8c}$$

In (8) the units are

$$\begin{aligned}
T&=\frac{3}{2\eta_\perp}\,\frac{M}{m}\,\frac{1}{\omega_0} && \text{(time)}\\
X&=\frac{3}{2}\sqrt{\frac{M}{m}}\,\lambda_D/\sqrt{\eta_\perp} && \text{(space)}\\
\varepsilon&=\left(\frac{64}{3}\,\pi\eta_\perp\,\frac{m}{M}\,n_0T_e\right)^{1/2} && \text{(electric field)}\\
\hat{N}&=\frac{4}{3}\,\eta_\perp\,\frac{m}{M}\,n_0 && \text{(density)}
\end{aligned} \tag{9}$$

where m, M are the electron and ion masses, $\lambda_D=v_{te}/\omega_{pe}$ the Debye length ($v_{te}=(T_e/m_e)^{1/2}$ electron thermal velocity), $\eta_\perp=2+3T_i/T_e$ (using $\gamma_e=2$ and $\gamma_i=3$ for the adiabatic exponents), and $T_{e,i}$ are the electron and ion temperatures. The parameters of the model (8) are

$$\begin{aligned}
\Omega&=\frac{3}{2\eta_\perp}\,\frac{M}{m}\left(\frac{\Delta\Omega}{\omega_0}-\frac{1}{2}\,Y^2\right) && \text{(mismatch)}\\
E_0&=(\mathbf{E}_0\cdot e_x)\,/\varepsilon && \text{(drive)}\\
\Omega_{LH}^2&=\frac{9}{4\eta_\perp^2}\,\frac{M}{m}\,Y^2 && \text{(normalized lower hybrid frequency squared)}\\
\nu&=\frac{3}{4\eta_\perp}\,\frac{M}{m}\,\nu_{ec}/\omega_0 && \text{(collisional damping)}
\end{aligned} \tag{10}$$

One can, without loss of generality, assume E_0 real and positive in (8) (remove a common phase in E_0 and E).

In addition, we have the lower hybrid Landau damping operator, which in wave space representation is

$$\begin{aligned}
&\gamma_i(k) = \gamma_{LH}(k) = (1/2)(\pi/2)^{1/2}\bar{\omega}_r(k)r^3\exp(-r^2/2)\,,\\
&\bar{\omega}_r(k) = (k^2 + \Omega_{LH}^2)^{1/2}\,,\\
&r = (\bar{\omega}_r(k)/|k|)\delta\,,\\
&\delta = (3 + 2T_e/T_i)^{1/2}\,.
\end{aligned} \tag{11}$$

In (8), the density perturbation has been separated into two parts:

$$\frac{\delta n}{n_0} \longmapsto n(x,t) + N(x) \tag{12}$$

where $N(x)$ is a preexisting depletion representing the striation, which is assumed to have formed as a result of slow transport processes not accounted for in model (8), and assumed to be maintained by, e.g., pressure balance; while $n(x,t)$ represents the perturbation due to the ponderomotive force.

5. Some results

In this section we shall report some numerical and analytic results for the model (8), and interpret them relative to SEE observations, in particular the DM and BC features. In all of our numerics, we solve (8a,b) with periodic boundary conditions using a spectral method described in [14], with some obvious modifications due to the change of model. For $N(x)$ we have used a depletion

$$N(x) = \left(-N_0 \exp\left(-(x/l)^2\right)\right) - \bar{N} \tag{13}$$

where $\bar{N}$ is the mean value of the first term. In all the cases we are going to discuss, we have used $N_0 = 55.0$ and $l = 1.5$, which for typical parameter values correspond to an electron density depletion of $\sim 1\%$ and halfwidth ~ 1.4 m. We have used 4096 Fourier modes and system length 204.8, so that $N(x)$ comes very near to being an isolated irregularity. Even so, we have included the term $\bar{N}$ in (13) so that $N(x)$ has vanishing mean value in the periodic system, in accordance with the formulation in ref. [28]. For the nondimensional lower hybrid frequency, we have used the value $\Omega_{LH}^2 = 375$.

Our primary objective is to determine the spectrum

$$S(\omega;\Omega) = \langle |\hat{J}_2(\omega)|^2 \rangle \tag{14}$$

where $\hat{J}_2(\omega)$ is the Fourier transform of $J_2(t)$ as determined by (8), and the brackets denote average over subspectra. We shall call (14) the *source spectrum.*

(i) *Stationary solution.* The first finding we wish to describe, is that nontrivial source spectra (i.e., spectra with contributions away from $\omega = 0$) is a *threshold* phenomenon. For sufficiently small E_0, eqs. (8a,b) have a stationary solution. (This can be proved rigorously using fixed point theorems of mathematical analysis.) In the simplest case, when the ponderomotive modification of the density is neglected, the stationary electrostatic response $\hat{E}(x)$ satisfies

$$\frac{d^2\hat{E}}{dx^2} + (\Omega + i\nu - N(x))\hat{E} = E_0 N(x)\,, \tag{15a}$$

$$\hat{E}(x) \longrightarrow 0\,, \qquad |x| \longrightarrow \infty\,. \tag{15b}$$

In order to obtain this, we have also assumed an isolated irregularity $N(x)$ so that the average terms vanish.

(ii) *Trapped mode resonances.* Since the operator $L = -(d^2/dx^2) + N(x)$ with boundary condition (15b) is self-adjoint, it has only real eigenvalues. Consequently, (15) has unique solution as long as $\nu \neq 0$. However, when $N(x)$ is negative, L has (a finite number of) eigenvalues, $0 > \Omega_j > \min N(x)$, $j = 0, 1, ..., n$. The eigenfunctions represent undamped, undriven standing oscillations trapped in the density depletions. When ν is small and $\Omega \simeq \Omega_j$, the solution to (15) may attain a large amplitude. We shall call this the *trapped mode resonances.* For $N(x)$ as defined in this section, they occur at $\Omega_0 \simeq -50.2$, $\Omega_2 \simeq -32.4$, $\Omega_4 \simeq -17.8$, and $\Omega_6 \simeq -6.8$. These are the eigenvalues of the undamped and undriven problem which have even eigenfunctions. In addition, there are eigenvalues $\Omega_1 \simeq -41.0$, $\Omega_3 \simeq -24.8$, and $\Omega_5 \simeq -11.9$. having odd eigenfunctions. The corresponding trapped mode resonances are not excited in the present case, because the driving term is even.

(iii) *Trapped mode decay instability.* Nontrivial SEE spectra occur as a result of some instability of the stationary wave structures. We have found the following instability mechanism: The stationary wave structure can decay to a *trapped mode resonance* which exists at a lower frequency; at the same time the frequency difference must be near (i.e., slightly larger than) the lower hybrid frequency. Linearizing around the stationary solution to (8a,b) and Fourier-analysing as $\sim \exp(-i\omega t)$ the following approximate dispersion relation for decay to trapped resonant mode j can be derived:

$$\omega = -i\nu + \Omega_j - \Omega + E_0^2 W_j(\omega) \tag{16}$$

where

$$E_0^2 W_j(\omega) = \frac{\lambda}{2} \int_{-\infty}^{\infty} \int_{-\infty}^{\infty} \hat{V}_j(x) \hat{V}_j^*(x') \exp(-\lambda|x - x'|) dx\, dx' - \int_{-\infty}^{\infty} |\hat{V}_j(x)|^2 dx\,, \tag{17}$$

and $\lambda = (\Omega_{LH}^2 - \omega^2)^{1/2}$, $\hat{V}_j(x) = (\hat{E}(x) + E_0) e_j(x)$; $e_j(x)$ is a normalized eigenfunction for eigenmode j, $\int_{-\infty}^{\infty} e_j^2(x) dx = 1$. For $|\omega| < \Omega_{LH}$, W_j is real-valued. Invoking causality, (17) has to be continued to $|\omega| > \Omega_{LH}$ via the upper complex ω half plane. It can be shown that this gives W_j a positive (negative) imaginary part for $\omega < -\Omega_{LH}$ ($\omega > \Omega_{LH}$), and thus an instability exists for $\omega < -\Omega_{LH}$. For sufficiently small E_0, $\hat{E}(x)$ can be determined by (15), implying that $W_j(\omega)$ is independent of E_0. Fig. 1 shows an example of W_0 for values of ω around $\omega = -\Omega_{LH}$ computed this way. Fig. 1 demonstrates that (i) $\mathrm{Im}\, W_0 \geq 0$ for $\omega < -\Omega_{LH}$; (ii) $\mathrm{Im}\, W_0 = 0$ for $-\Omega_{LH} < \omega$; (iii) $\mathrm{Im} W_0 \to 0$ as $\omega \to -\infty$ (fairly quickly). For E_0^2 small, $\mathrm{Re}\,(\omega) \simeq \Omega_j - \Omega$. At the same time $\mathrm{Im} W_j > 0$ for $\omega \lesssim -\Omega_{LH}$. This gives roughly the condition

$$\Omega \simeq \Omega_j + \Omega_{LH} \tag{18}$$

for the excitation of the instability.

In Fig. 2 we show source spectra obtained by solving (8a,b)

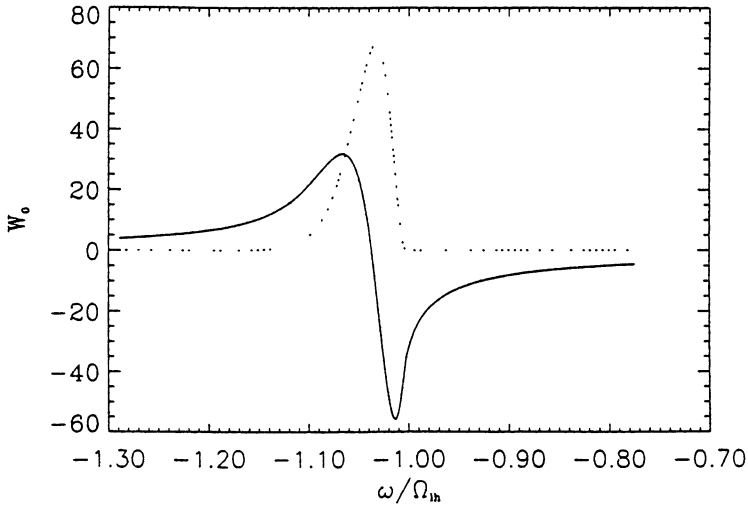

Figure 1: The function $W_0(\omega)$ computed for $\Omega = -29.8$, $\nu_e = 0.5$. Full line: Re (W_0), dotted line: Im (W_0).

numerically for $\Omega = -29.8 - \bar{N}$, and for three different values of E_0: 0.1, 0.3, and 0.5. At $E_0 = 0.075$ (not shown), the solution approached the stationary state, and no nontrivial source spectrum resulted. The theoretical threshold derived from Fig. 1 is about $E_0 = 0.09$. At $E_0 = 0.1$, regular oscillations at frequency $-\hat{\omega}$, where $\hat{\omega} \simeq 20.4$, resulted, and this frequency is observed in the source spectrum. At $E_0 = 0.2$ (not shown), regular oscillations at the same frequency upon a slowly oscillating mean value resulted. At $E_0 = 0.3$, these slow modulations (corresponding to the spectrum near $\omega = 0$) became more irregular. At $E_0 = 0.5$, a fairly erratic and irregular behaviour was found, although the spectrum still peaked at $\omega \simeq -20.4$. At $E_0 = 1.0$ (not shown), no such peak could be observed. Note also that peaks at $-2\hat{\omega}$, $-3\hat{\omega}$ and $+\hat{\omega}$ occur in Fig. 2, and that they increase greatly by passing from $E_0 = 0.1$ to $E_0 = 0.3$.

We have also identified the trapped mode decay instability for the trapped mode resonances Ω_1 and Ω_2. Decay to odd modes does not give nontrivial SEE spectrum, at least not just above threshold.

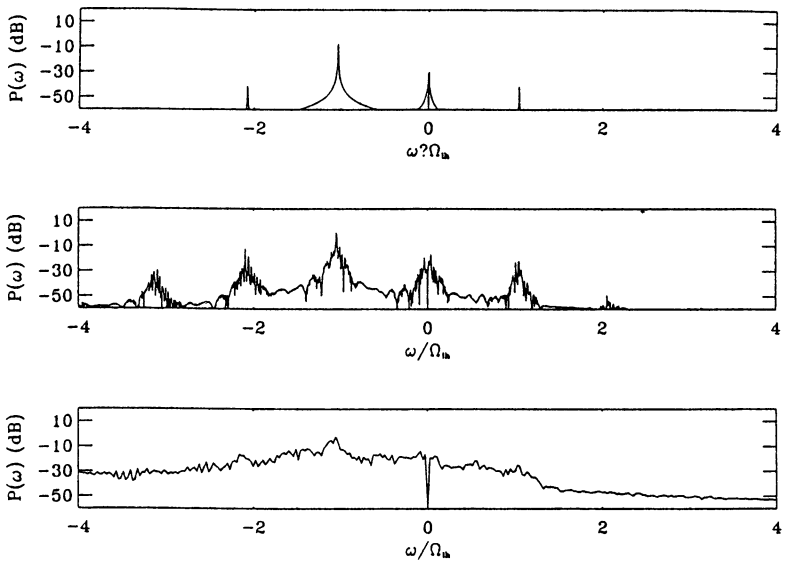

Figure 2: Source spectra computed according to (1c) and (2) with $\Omega = -29.8 - \bar{N}$, $\nu_e = 0.5$. (a) $E_0 = 0.1$, (b) $E_0 = 0.3$, (c) $E_0 = 0.5$. In each case, 120 000 values sampled with time step $\delta t = 0.0005$ were used. In (a) and (b), one spectrum was used, while in (c) the plotted spectrum is an average of 5 subspectra.

(iv) *Application to Downshifted Maximum feature.* In order to apply the process of trapped mode decay instability, we interpret the model (8) as local and quasi one-dimensional, and consider Ω as dependent on height. Then in some height regions, (18) is satisfied, and at each value of Ω in these regions, a source $S(\omega;\Omega)$ is produced according to (14) which contributes to the observed spectrum. In some, but not all, cases, features called UM (upshifted maximum), 2DM, and 3DM, have been observed. The spectral features at $+\hat{\omega}$, $-2\hat{\omega}$, $-3\hat{\omega}$ in Fig. 2 are compatible with these observations.

(v) *A Stokes–antiStokes instability.* Another instability, which can be seen as related to the OTSI instability, can be excited when Ω is midway between two trapped mode resonances, i.e., $\Omega \lesssim \frac{1}{2}(\Omega_n + \Omega_m)$. Its mechanism can be described as a

resonance between the Stokes component of mode Ω_n, which is at $\omega \simeq \Omega_n - \Omega$ with the antiStokes component of mode Ω_m, $\omega \simeq -(\Omega_m - \Omega)$. For an isolated irregularity $N(x)$, the approximate dispersion relation

$$(\omega + i\nu - \tilde{\omega}_n)(\omega + i\nu + \tilde{\omega}_m) = E_0^4 |W_{nm}|^2 \tag{19}$$

can be derived, where

$$\tilde{\omega}_j = \Omega_j - \Omega + E_0^2 W_j(\omega)\,, \qquad j = n, m \tag{20}$$

and

$$E_0^2 W_{nm}(\omega) = \frac{1}{2}\lambda \int_{-\infty}^{\infty}\int_{-\infty}^{\infty} \hat{V}_n(x)\hat{V}_m(x') \exp(-\lambda|x - x'|)dx\,dx' - \int_{-\infty}^{\infty} \hat{V}_n(x)\hat{V}_m(x)dx\,. \tag{21}$$

For the situation ω real and $|\omega| < \Omega_{LH}$, W_n is real. Then, for $\omega = \tilde{\omega}_n$ and $\omega = -\tilde{\omega}_m$ simultaneously, we obtain from (19) the threshold condition

$$|W_{nm}| E_0^2 = \nu\,, \tag{22}$$

so clearly an instability exists. The conditions imply

$$\Omega \simeq \frac{1}{2}(\Omega_n + \Omega_m) + \frac{1}{2} E_0^2 (W_n + W_m)\,, \tag{23}$$

$$\omega \simeq \frac{1}{2}(\Omega_n - \Omega_m) + \frac{1}{2} E_0^2 (W_n - W_m)\,. \tag{24}$$

In addition, for $N(x)$ even, both resonances must be either even or odd. It is easily shown that solutions $\hat{E}(x)$ to (15) are even when $N(x)$ is even; then it readily follows that $W_{nm} = 0$ for combinations of odd and even resonances.

In Fig. 3 we show examples of source spectra where this instability is active. The model was run at a fixed Ω, while increasing E_0 in steps of 0.1 every 30 time units. At $E_0 = 0.4$ and 0.5 the stationary structure was stable, while the instability

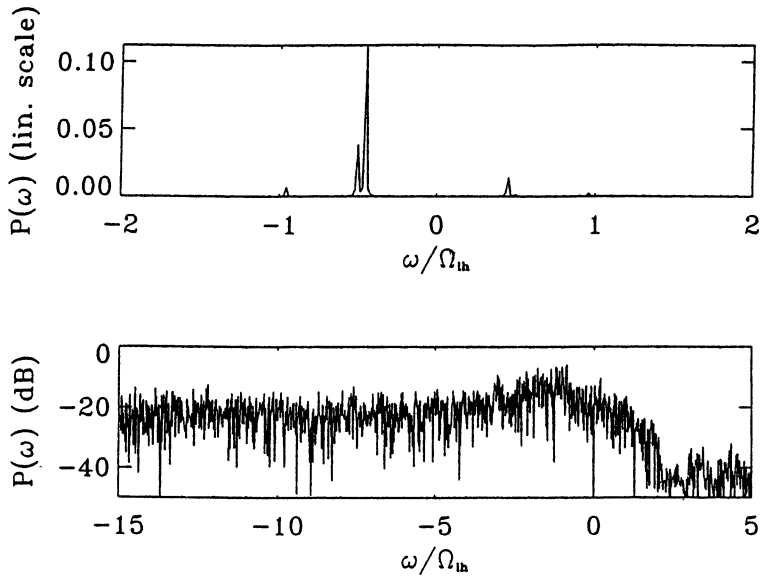

Figure 3: Results from a numerical run with $\Omega = -42.06 - \bar{N}$, $\nu_e = 0.2$, where E_0 was increased by 0.1 every 30 time units, starting at $E_0 = 0.4$ and ending at $E_0 = 0.8$. Upper panel: source spectrum for $100 \leq t \leq 120$ ($E_0 = 0.7$). Lower panel: source spectrum for $130 \leq t \leq 150$ ($E_0 = 0.8$) (no averaging over subspectra).

set in at $E_0 = 0.6$. Results at $E_0 = 0.7$ and 0.8 are shown. In particular, when increasing E_0 from 0.7 to 0.8, the average of $U = \int |E|^2 dx$ increased by a factor ~ 8.5, and the time variation of U was of the order of, or larger than, this mean value itself. The source spectrum for this case (lower panel) shows an extremely broad spectrum, mainly downshifted.

(vi) *The Broad Continuum.* The extremely broad spectrum of Fig. 3, lower panel, is compatible with the observed phenomenon of Broad Continuum (BC), though, the spectrum shown here (as well as many other cases that we have obtained) appears to be even broader than those reported, in terms of the width expressed as numbers of Ω_{LH}. As the observed spectrum, it is mainly downshifted. From studies of HF-generated Langmuir

turbulence, it has been concluded that cavitation processes lead to broad SEE spectra [28]. This spectrum should be understood this way. We are not ready to say whether the onset of this cavitation should be associated with the Stokes–antiStokes instability described above, or whether it should be understood as some independent transition, such as, e.g., loss of equilibrium, or nonlinear resonance.

6. Discussion

We have demonstrated how $N(x)$ in model (8) can act as a resonator, to produce SEE source spectra (8c) compatible with experimental observations. The model (8) is extremely rich in dynamical behaviour, as already the above theoretical and numerical results indicate. We have obtained numerical solutions for a large set of parameter values. We have demonstrated phenomena that can explain the occurrence of Downshifted Maximum and Broad Continuum. In particular, the processes behind the two appear as independent, with DM having a considerably lower threshold than BC.

It should not be underscored that (8) represents a considerable simplification from the real situation. For example, the existence of the trapped mode resonances implies that the solutions will be very sensitive to $\Omega(z)$; therefore, a model with consistent height dependence may be more appropriate, though, at the boundary of what can be treated numerically. This also implies a considerable extension of (8b) for the density response. Another omission that may be critical, is the Z-mode leakage [19]. Of course, the generation process according to (7), deserves attention; a simple example was discussed in [28].

References

1. B. Thidé, H. Kopka, and P. Stubbe, *Phys. Rev. Lett.*, **49**, 1561, 1982.

2. G. N. Boiko et al., *Radiophys. Quantum Electron.*, English transl., **28**, 259, 1985.

3. B. Thidé et al., *Geophys. Res. Lett.,* **16,** 369, 1989; B. Thidé et al., *J. Geophys. Res.,* **100A,** 23887, 1995.

4. W. T. Armstrong et al., *Radio Sci.,* **25,** 1283, 1990.

5. E. Mjølhus, *Radio Sci.,* **25,** 1321, 1990.

6. H. C. Carlson, W. E. Gordon, and R. L. Showen, *J. Geophys. Res.,* **77A,** 1242, 1972.

7. F. W., Perkins, C. Oberman, and E. J. Valeo, *J. Geophys. Res.,* **79A,** 1478, 1974.

8. J. A. Fejer and Y.-Y. Kuo, *Phys. Fluids,* **16,** 1490, 1973.

9. V. E. Zakharov, *Sov. Phys. JETP,* English transl., **35,** 908, 1972.

10. H. C. Kim, R. L. Stenzel, and A. Y. Wong, *Phys. Rev. Lett.,* **33,** 886, 1974.

11. D. B. Muldrew and R. L. Showen, *J. Geophys. Res.,* **82A,** 4793, 1977.

12. B. Isham et al., *J. Geophys. Res.,* **92A,** 4629, 1987.

13. D. F. DuBois, A. Hanssen, H. A. Rose, and D. Russell, *J. Geophys. Res.,* **98A,** 17543, 1993; *Phys. Fluids,* **5B,** 2616, 1993.

14. A. Hanssen, E. Mjølhus, D. F. DuBois, and H. A. Rose, *J. Geophys. Res.,* **97A,** 12073, 1992.

15. M. P. Sulzer and J. A. Fejer, *J. Geophys. Res.* **99A,** 15035, 1994.

16. H. Kohl and M. Rietveld, *J. Geophys. Res.,* **101A,** 5391, 1996.

17. P. A. Fialer, *Radio Sci.,* **9,** 923, 1974.

18. J. Minkoff, P. Kugelman, and I. Weissman, *Radio Sci.,* **9,** 941, 1974.

19. K. B., Dysthe, E. Mjølhus, H. Pecseli, and K. Rypdal, *Physica Scripta,* **T2/2,** 548, 1982.

20. B. Inhester, *J. Atm. Terr. Phys.*, **44**, 1049, 1982.

21. V. V. Vaskov and A. V. Gurevich, *Geomagn. Aeron.*, **24**, 350, 1984.

22. A. V. Gurevich, K. P. Zybin, and A. V. Lukyanov, *Phys. Rev. Lett.*, **75**, 2622, 1995.

23. P. Stubbe, H. Kopka, B. Thidé, and H. Derblom, *J. Geophys. Res.*, **89A**, 7523, 1984.

24. T. Leyser et al., *Phys. Rev. Lett.*, **63**, 1145, 1989.

25. M. Waldenvik, dr. thesis, University of Uppsala, Sweden, 1994.

26. T. Leyser et al., *J. Geophys. Res.*, **99A**, 19555, 1994.

27. E. Mjølhus, *J. Atm. Terr. Phys.*, **55**, 907, 1993.

28. E. Mjølhus, A. Hanssen, and D. F. DuBois, *J. Geophys. Res.*, **100A**, 17527, 1995.

29. V. Erckmann, this issue.

LOWER-HYBRID TURBULENCE EXCITED BY A TRANSVERSE ION BEAM IN A MAGNETIZED PLASMA

E.V. Suvorov, A.B. Burov, Y.A. Dryagin, S.E. Fil'chenkov, A.A. Fraiman, L.V. Lubyako, D.A. Ryndyk, N.K. Skalyga, O.B. Smolyakova, V. Erckmann, H. Laqua*, T. Geist*, M. Kick*, W VII-AS Team*, ECRH Team*, CX Diagnostics Team*, E. Holzhauer†, W. Kasparek†*

Institute of Applied Physics, Nizhny Novgorod, Russia
*Max-Planck-Institute für Plasmaphysik, Garching, Germany
†Institute für Plasmaforschung, Universitet Stuttgart, Germany

Microinstabilities arising in a magnetized plasma due to the presence of charged particles with some kind of the non-equilibrium distribution function constituted an important subject in the early days of fusion researches since they were related to the problem of anomalous transport in experiments on the magnetic plasma confinement. Considerable progress has been achieved with respect to theoretical investigations (see, e.g. [1]) where the instability growth-rates for different types of oscillations can be obtained from the dispersion relation for small amplitude fluctuations provided that the non-equilibrium distribution function of electrons and ions is known. Experimental investigations of these instabilities are intrinsically more difficult due to the fact that in the experiment usually only parameters of the fully developed (saturated) stage of the instability can be measured, which results from some nonlinear saturation mechanisms (e.g. nonlinear mode coupling); besides, the initial undisturbed nonequilibrium distribution function is often known only approximately and is, therefore, the subject of more or less justified speculation. A number of laboratory plasma experiments have been reported on the excitation of instabilities by ion beams (e.g. [2,3]). Recently these instabilities have been invoked to explain enhanced emission at the ion cyclotron harmonics of fusion products [4-8].

In this paper we present results of experimental and theoretical investigations of lower hybrid (LH) turbulence excited in a magnetized plasma by a transverse ion beam. This turbulence was initially detected in experiments on collective Thomson scattering of powerful gyrotron radiation at W7-AS [9-11] and is closely correlated with injection of a charge-exchange (CX) diagnostic neutral hydrogen beam into the plasma transversely to the magnetic field; later it was also confirmed by measurements

with a magnetic loop antenna located close to the plasma edge. An attractive feature of these experiments at the W7-AS stellarator is the fact that the non-equilibrium distribution function of the ion beam can be considered as well defined. In addition, the detected turbulence is characterized by a very narrow frequency spectrum and a very narrow angular spectrum in the wavenumber space which allows a straightforward theoretical analysis.

Experimental results

In Collective Thomson Scattering (CTS) experiments at the W7-AS stellarator the frequency of probing radiation is 140 GHz; the geometry is close to back-scattering (see Fig.1). With a plasma diameter about 20 cm and probing and receiving antenna beam cross-sections about 4 cm practically no spatial resolution is achieved. For this scattering geometry the characteristic scale of detected electron density fluctuations is close to that corresponding to twice the vacuum wave-number of probing radiation: $k_p \approx 2k_0 = 2\omega_i / c$. When a diagnostic neutral hydrogen beam is injected into the plasma transversely to the magnetic field, a sharp increase in the scattered signal power from turbulent density fluctuations propagating transversely to the magnetic field is observed in the LH frequency range (see Fig.2). The dependence of measured frequency on plasma density closely follows the linear LH dispersion relation [10-11]. The turbulence is characterized by both a narrow frequency spectrum (of the order of 2-3% of LH frequency) and a narrow angular spectrum (clearly even narrower than the intrinsic angular resolution of 1-2 deg. of the scattering system determined by the emitting and receiving antennae). The intensity of scattered radiation is very high and could reach several MeVs in terms of the equivalent black-body radiation temperature (see Fig.3). With a magnetic loop antenna positioned close to the plasma edge similar signals correlated with launching of the diagnostic neutral beam into the plasma were also registered in the appropriate frequency range; an example of the spectrum analyzer output at the centered frequency of 900 MHz is presented in Fig.4a together with the monitor for a CX neutral beam (Fig.4b). Simulta-

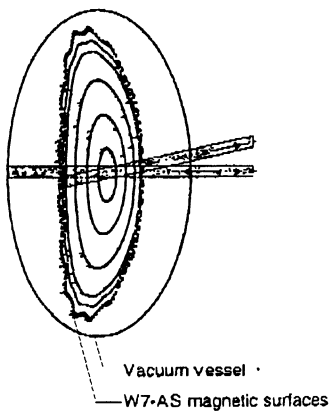

Fig. 1
CTS geometry at W7-AS

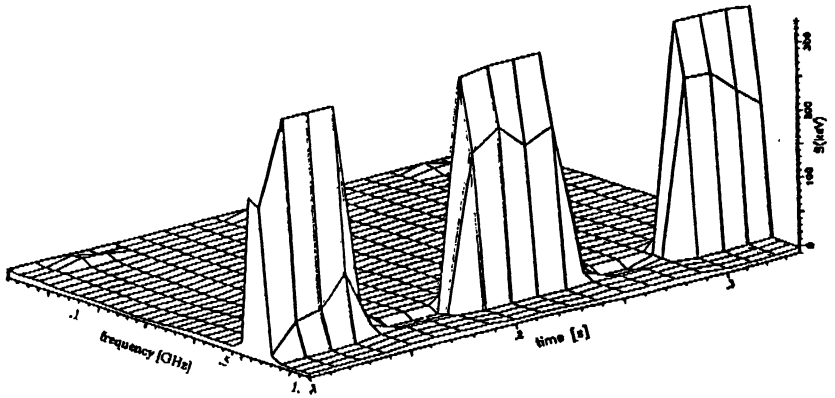

Fig. 2

neously with LH turbulence and with the charge exchange diagnostics the appearance of a fast ion component with a quasi-maxwellian distribution function ("tail" temperature about 2 keV) could be also observed.

The main part of CTS results on LH turbulence is obtained for deuterium plasma with electron cyclotron resonance heating (ECRH) at the second harmonic (radiation frequency 140 GHz, magnetic field 2.5 T) with electron density ranging within $(3-8)\bullet 10^{13} cm^{-3}$, electron temperature 1-2 keV and ion temperature 200-400 eV. The diagnostic hydrogen beam is injected vertically into the vacuum chamber at a toroidal position where the plasma column has an elliptical shape strongly elongated in the vertical

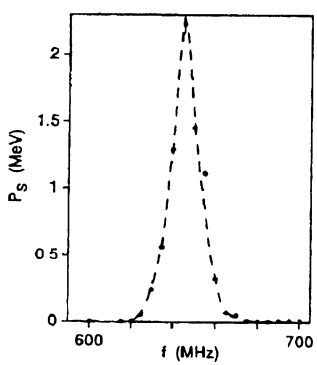

Fig. 3
Frequency dependence of scattered signal

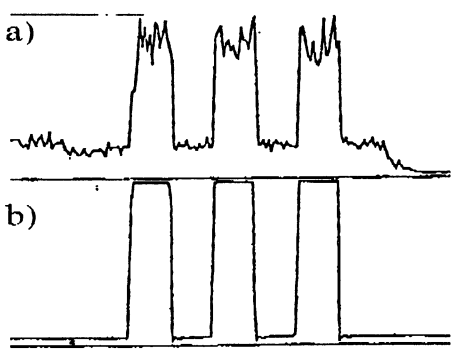

Fig. 4

direction. Over the plasma cross-section the magnetic field is nearly transverse to the direction of propagation of the probing microwave beam. It possesses low shear and the magnetic field intensity undergoes radial variation with scale length of about 1.5 m. The neutral beam aperture in the plasma, a_b, is about 5 cm with angular divergence about 1.5 deg. It is composed of 3 monoenergetic fractions with energies E_o = 22 keV, $E_o/2$ and $E_o/3$ and approximate mixing ratio 45:30:25; the total beam current is about 5 A. The neutral beam is injected at the toroidal position separated by approximately 2 m from the position where the CTS antenna block is installed.

Ion beam in the plasma

The ion beam in the plasma is the result of the charge exchange process between plasma ions and injected neutral atoms, whereby hydrogen ions are created in the plasma with the same energy and direction of motion as the original neutral beam. The life-time of beam ions is determined by the vertical drift in the nonuniform magnetic field:

$$\tau_b \approx \frac{2aR\omega_{ci}}{V_b^2}, \qquad (1)$$

where a and R are minor and major plasma radii correspondingly, ω_{ci} is gyrofrequency of beam ions, and V_b is velocity of beam ions transverse to the magnetic field. For W7-AS parameters and given values of the beam energy the estimate for the beam life-time yields the value in the 100 microsecond time scale which is considerably less than the inverse collision frequency of beam ions in the relevant range of plasma parameters. The fraction of neutral atomstrapped into the plasma as beam ions, α_b, is defined as the product of the resonant charge exchange cross-section and line-integrated density of plasma ions: $\alpha_b = \sigma_{CX} \bullet n_l$ (with $\alpha_b \le 1$). This value approaches unity for plasma densities about $0.5 \bullet 10^{14} cm^{-3}$. Taking into account angular divergence of the neutral beam and the low value of the rotational transform it is possible to estimate beam density in the plasma and its spatial distribution. Due to combined action of vertical drift with drift velocity $V_d \approx V_b^2 / 2R\omega_{ci}$ and beam transport along the magnetic field with velocity $V_{//} \approx V_b \bullet \Delta\vartheta$, where $\Delta\vartheta$ is angular beam divergence in the toroidal direction; beam ions fill a plasma volume which extends along the

magnetic field by approximately $L_b = 2a(V_{//}/V_d)$ in both directions from the injector position; for the values under consideration L_b amounts to 3-5 m. Density of the ion beam may be estimated as the total electric charge injected into the plasma by NB during ion beam life-time divided by the elementary electric charge and by the volume filled with the ion beam. With $\alpha_b \leq 1$ beam density normalized to the background plasma density equals

$$\alpha = \frac{n_b}{n_0} \approx \frac{\alpha_b I_{NB} \tau_b}{2eaL_b a_b n_0} \approx \frac{\sigma_{CX} I_{NB}}{ea_b V_b \Delta \vartheta_b}, \qquad (2)$$

where I_{NB} is the neutral beam current and e is the electric charge of a beam ion. For the beam parameters used in experiments, from Eq.(2) it follows that $n_b \approx (2-4) \bullet 10^{-4} n_o$.

Thus, the spatial distribution of beam ions is defined by geometrical factors only, such as the beam aperture in the direction of major radius, angular beam divergence in toroidal direction and by the major plasma radius, which determines the inhomogeneity scale of the toroidal magnetic field. Beam life-time in the plasma is defined by the scale of the magnetic field inhomogeneity and beam energy. Beam density normalized to background plasma density is independent of plasma parameters and defined by the parameters of injected neutral beam with taking into account CX cross-section.

Dispersion relation for LH perturbations

Here we consider the dispersion relation for LH waves in the electrostatic approximation, which is justified by the considerable slowing-down of the experimentally observed turbulence which corresponds to the value of the transverse refractive index of a few hundred. Since the wavelength of LH turbulence is small as compared to the characteristic radial inhomogeneity scales of plasma parameters, we start with a homogeneous plasma model (i.e. local approximation). Later we shall discuss what may be expected for the inhomogeneous case. Following /10/ we investigate the possibility that LH turbulence is originating due to the instability driven by a transverse ion beam in the plasma.

As is well known (see, e.g. [1]),the dispersion relation for small perturbations in the electrostatic approximation may be presented in the following form:

$$\varepsilon_{//} = 1 + \sum_{\alpha} \varepsilon_{//}^{(\alpha)} = 0, \tag{3}$$

where $\varepsilon_{//}$ is dielectric tensor component in the direction of $\boldsymbol{k}$-vector of perturbations under consideration and $\varepsilon_{//}^{(\alpha)}$ is contribution into dielectric tensor from the α -th specie of plasma charged particles which in the case of magnetized plasma with arbitrary distribution functions of charged particles $F_\alpha(\upsilon_\perp, \upsilon_z)$ may be presented as [1]:

$$\varepsilon_0^{(\alpha)} = -\frac{4\pi e_\alpha^2}{m_\alpha k^2} \int \left(\frac{\partial F_\alpha}{\partial \varepsilon_\perp} - \left[(\omega - k_z \upsilon_z) \frac{\partial F_\alpha}{\partial \varepsilon_\perp} + k_z \frac{\partial F_\alpha}{\partial \upsilon_z} \right] \bullet \sum_{n=-\infty}^{\infty} \frac{J_n^2(\xi)}{\omega - n\omega_{c\alpha} - k_z \upsilon_z} \right) \upsilon_\perp d\upsilon_\perp d\upsilon_z, \tag{4}$$

where $\upsilon_\perp$ and υ_z are velocity components transverse and parallel to the magnetic field, respectively, ω and $\boldsymbol{k}$ are frequency and wave-vector of considered small perturbations, e_α, m_α and $\omega_{c\alpha}$ are respectively charge, mass and gyrofrequency of the α-th plasma specie, $\varepsilon_\perp = \upsilon_\perp^2/2$, and the argument of the Bessel function is $\xi = k_\perp \upsilon_\perp / \omega_{c\alpha}$.

For the maxwellian distribution function,

$$F_\alpha = n_\alpha \left(\frac{m_\alpha}{2\pi T_\alpha} \right)^{3/2} \exp\left(-\frac{m_\alpha \upsilon^2}{2T_\alpha} \right)$$

it follows from Eq. (4) that

$$\varepsilon_0^\alpha = \frac{1}{k^2 d_\alpha^2} \left[1 + i\sqrt{\pi} \frac{\omega}{k\upsilon_\alpha \cos\theta} \sum_n W\left(\frac{\omega - n\omega_{c\alpha}}{k\upsilon_\alpha \cos\theta} \right) e^{-z_\alpha} I_n(z_\alpha) \right], \tag{5}$$

where d_α is Debye length of the α -th specie, $\upsilon_\alpha^2 = 2T_\alpha / m_\alpha$, W is plasma dispersion function, the argument of modified Bessel function is $z_\alpha = T_\alpha k^2 \sin^2\theta / m_\alpha \omega_{c\alpha}^2$, and ϑ is angle between the $\boldsymbol{k}$-vector and the magnetic field.

For the plasma parameters considered here it is possible to simplify the contribution of the main plasma species to the dielectric tensor in the LH frequency range. Restraining ourselves to quasi-perpendicular propagation ($\cos\vartheta << 1$) and assuming maxwellian distributions for electrons and bulk plasma ions we have:

for electrons ($\omega << \omega_{ce}, k\upsilon_e << \omega_{ce}, z_e << 1$)

$$\varepsilon_0^e = \frac{\omega_{pe}^2}{\omega_{ce}^2} - \frac{\omega_{pe}^2 \cos^2\theta}{\omega^2} - \frac{3}{8}\frac{\omega_{pe}^2}{\omega_{ce}^2} r_{ce}^2 k^2 + i\frac{\sqrt{\pi}\omega}{k^3 \upsilon_e d_e^2 \cos\theta} \exp\left(-\frac{\omega^2}{k\upsilon_\alpha \cos\theta}\right), \tag{6}$$

where ω_{pe} is electron plasma frequency and r_{ce} is mean electron gyroradius;

for ions ($\omega >> \omega_{ci}, k\upsilon_i; z_i >> 1$)

$$\varepsilon^{(i)} = -\frac{\omega_{pi}^2}{\omega^2} - \sum_m \frac{\omega_{pi}^2}{\omega_{ci}^2} \frac{mI_m(z_i)\exp(-z_i)}{z_i(\omega - n\omega_{ci})}, \tag{7}$$

where ω_{pi} is ion plasma frequency. The last term in (7) is specified separately because it may be of importance in the close vicinity of the multiple cyclotron resonance, in other cases this term can be neglected.

For the distribution function of beam ions we shall use the following expression:

$$F(\upsilon_\perp, \upsilon_z) = \frac{\alpha n_0 \delta(\upsilon_z)}{\upsilon_\perp} \begin{bmatrix} 0.45\delta(\upsilon_\perp - \upsilon_1) + 0.3\delta(\upsilon_\perp - \upsilon_2) \\ +0.25\delta(\upsilon_\perp - \upsilon_3) \end{bmatrix}, \tag{8}$$

where the numerical factors represent the mixing ratio in the ion beam used and transverse velocities υ_1, υ_2 and υ_3 correspond to the beam fractions with different energy. Then the beam contribution to the dielectric tensor can be written as follows:

$$\varepsilon^{(b)} = \alpha \frac{\omega_{pi}^2}{\omega_{ci}} \sum_n \frac{nG_n}{\omega - n\omega_{cb}}, \tag{9}$$

where the value of G_n is found by substitution of distribution function (8) into Eq.(4) and integration by parts:

$$G_n = -\frac{2}{\xi_0} \begin{bmatrix} 0.45J_n(\xi_0)J_n'(\xi_0) + 0.3\sqrt{2}J_n(\xi_0/\sqrt{2})J_n'(\xi_0/\sqrt{2}) + \\ 0.25\sqrt{3}J_n(\xi_0/\sqrt{3})J_n'(\xi_0/\sqrt{3}) \end{bmatrix} \tag{10}$$

and quantity ξ_o corresponds to the most energetic beam fraction: $\xi_o = k_\perp \upsilon_1 / \omega_{cb}$.

LH wave instability under double resonance condition

Below we consider the frequency range close to some cyclotron harmonic of beam ions ($|\omega - n\omega_{cb}| << \omega_{cb}$),,so that from contributions of both background ions (7) and beam ions (9) to the dielectric tensor only one

harmonic of infinite sum can be taken into account. With this approximation the dispersion equation can be written in the dimensionless form as follows:

$$1+q_e-\frac{1+\varphi^2}{\Omega^2}-\frac{3}{4}q_e^2K^2+i\sqrt{\frac{\pi}{2}}\frac{\Omega}{K^3\varphi}\exp\left(-\frac{\Omega^2}{2K^2\varphi}\right)+\frac{H_n}{\Omega-n\Omega_{cb}}=0, \qquad (11)$$

where $\Omega=\omega/\omega_{pi}$ and $\Omega_{cb}=\omega_{cb}/\omega_{pi}$ are wave frequency and ion beam gyrofrequency normalized to ion plasma frequency, respectively, $K=kd_e$ is wave number normalized to the inverse electron Debye length, and $q_e=\omega_{pe}^2/\omega_{ce}^2$. Angle $\varphi=\left(\omega_{pe}/\omega_{pi}\right)\cos\vartheta$ gives the deviation of wave propagation from the perpendicular normalized to its natural scale for LH waves, propagating nearly transverse to the magnetic field. The last term in (11) includes

$$H_n=\frac{1}{\Omega_{ci}}\left[\alpha nG_n-\frac{m}{z_i}I_m(z_i)\exp(-z_i)\right] \qquad (12)$$

with $m=n$ for a hydrogen beam in hydrogen plasma and $m = 2n$ for a hydrogen beam in deuterium plasma, $\Omega_{ci}=\omega_{ci}/\omega_{pi}$. For k-numbers under consideration the value of K is rather small (few units times 10^{-1}) and the fourth term in Eq.(11), which represents a thermal correction may be omitted without serious modification of the dispersion relation (see also [9]). The imaginary term in (11) describes Landau damping of LH waves due to electrons and may be of importance even for propagation angles rather close to transverse to the magnetic field. A similar ion term is negligibly small for quasi-transverse propagation and is already omitted in (7).

The solution of Eq.(11) without beam contribution produces the well-known result for angular dependence of the LH wave frequency:

$$\Omega^2=\Omega_{LH}^2=\frac{1+\varphi^2}{1+q_e}, \qquad (13)$$

where the imaginary term due to Landau damping is not taken into account.

Next we consider the solution of Eq.(11) under the so-called double resonance condition,

$$\Omega_{LH}=n\Omega_c.$$

It is difficult to realize this in a perfectly uniform plasma but such a condition can be naturally realized (locally) under realistic experimental conditions due to the inhomogeneity of magnetic field and plasma density.

Since the last term in (11) constitutes a small correction everywhere outside the resonance, we look for the solution in the form $\Omega = \Omega_{LH} + \delta$ with $|\delta| << \Omega_c$. With no account for Landau damping (which is justified for $\varphi \to 0$) this small correction is given by (see [1]).

$$\delta^2 = -\frac{\Omega_{LH} H_n}{2(1+q_e)}, \tag{14}$$

from which it follows that for positive H_n there is a solution with $\mathrm{Im}\,\delta > 0$ which corresponds to an unstable mode with the growth-rate $\gamma = \mathrm{Im}\,\delta$. This is an instability of hydrodynamic type which is described by the dispersion relation without the negative imaginary part in the explicit form. If the contribution of background ions to the last term of Eq.(11) can be neglected, then the instability growth-rate is proportional to the square root of $\alpha = n_b / n_o$.

In a similar way the angular dependence of the instability growth-rate may be obtained with the Landau damping term taken into account. The instability also takes place when $H_n > 0$:

$$\delta = -i\frac{L\Omega_{LH}}{4(1+q_e)} + \sqrt{-\frac{L^2\Omega_{LH}^2}{16(1+q_e)^2} - \frac{\Omega_{LH} H_n}{2(1+q_e)}}, \tag{15}$$

here the Landau damping term in Eq.(11) is denoted by iL. It is interesting to note that the instability still exists even when the Landau term is so large that weakly damped LH waves (with $|\gamma| << \omega$) are absent without ion beam. In this case the instability growth-rate is proportional to the first power of the small parameter $\alpha = n_b / n_o$.

A more general result can be obtained taking into account the effect of both Landau damping and small detuning from the exact double resonance condition. The instability takes place when the normalized detuning does not exceed the square root of the maximum normalized growth-rate obtained under the exact double resonance condition.

In order to find the conditions of instability and values of its growth-rate it is necessary to investigate the value of H_n. All the contributing quantities (see (10), (12)) are negative until the arguments in the Bessel functions are smaller than their indexes; so the instability can arise only for a large enough wave number and beam energy. In Fig.5 the dependence of G_n on n for $\xi_o = 50$ (which corresponds to typical plasma and beam parameters in the CTS experiment) demonstrates that in principle a large

number of cyclotron harmonics may become unstable. A small variation in ξ_o (for example, due to variation of $k_\perp$) shifts this oscillating dependence along n axis changing the regions of stable and unstable harmonics. A similar dependence of H_n on ξ_o for a fixed value of $n=20$ is presented in Fig.6, which illustrates the sequence of stable and unstable ξ_o regions.

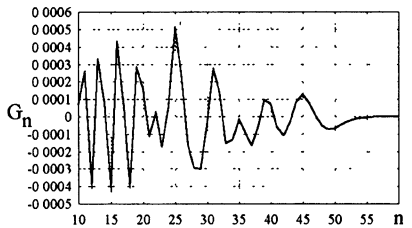

Fig. 5

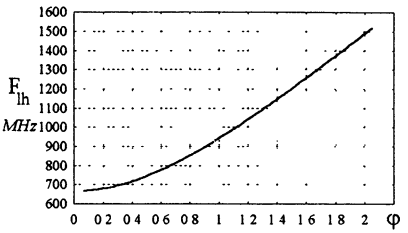

Fig. 7a

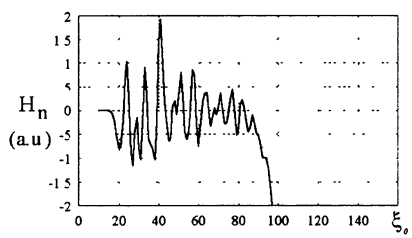

Fig. 6

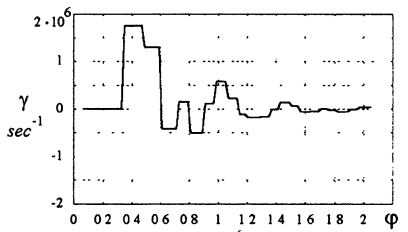

Fig. 7b

For a fixed given background ion temperature and beam-to-ion density ratio (in our case T_i=200eV and α=10^{-4}) there is some maximum value of ξ_o, after which instability regions cease to exist due to negative contribution of background ions in (12). Note that at fixed plasma and beam parameters ξ_o-dependence is equivalent to k-dependence and gives spatial spectrum of unstable modes.

An example of the angular dependence of the instability growth-rate is presented in Fig.7b, where all plasma parameters and the wave number of LH wave are assumed to be fixed ($n_e = n_i = 10^{13}\,cm^{-3}$, $B_0 = 2.5T$, $T_e = 2\,keV$, $T_i = 0.2\,keV$, $k_p \approx 2k_0$, $\alpha = 10^{-4}$) and the only parameter varying is the propagation angle. There are again some angular regions, in which instability takes place. It is clear that the angular width of the first theoretical unstable region considerably exceeds the experimentally observed angular range of excited LH waves. Furthermore, within the same

unstable region the theoretical variation of LH frequency (see Eq.(13)), which is shown in Fig.7a is considerably greater than the experimentally observed spectral width (compare with Fig.3). This means that the narrow width of propagation angles close to perpendicular to the magnetic field for the detected LH waves cannot be explained by the angular dependence of the linear instability growth-rate.

A possible qualitative explanation may be proposed by investigating the development of instability in the case of inhomogeneous plasma in the W7-AS stellarator experiment. The group velocity of LH waves can be estimated from dispersion relation (11) with both resonance and Landau damping terms omitted. The dimensionless components of group velocity (i.e. components of group velocity normalized to $d_e\omega_{pi}$) are:

$$V_{gr\perp} \approx \frac{3}{4}\frac{q_e^2}{1+q_e}\Omega_{LH}K_\perp - \frac{1}{1+q_e}\frac{\varphi^2}{\Omega_{LH}K_\perp},$$
$$V_{gr//} \approx \frac{3}{4}\frac{q_e^2}{1+q_e}\Omega_{LH}K_{//} + \frac{1}{1+q_e}\frac{\varphi^2}{\Omega_{LH}K_{//}}, \qquad (16)$$

where it is assumed that the thermal correction is small. For the plasma parameters considered here the transverse group velocity is of the order of 10^6 cm/sec for $\varphi=0$, diminishes to zero at $\varphi=\varphi^*$, which is comparable to dimentionless wavenumber K, and then changes its sign and continue to increase in magnitude with φ. The longitudinal group velocity is rapidly increasing with φ deviating from zero and for $\varphi=\varphi^*$ is by 2-3 orders of magnitude higher than $V_{gr\perp}(\varphi=0)$. Using typical values of instability growth-rate of the order of $10^7 sec^{-1}$ one can expect practically absolute instability within "quasi-homogeneous" region with the radial scale of the order of 1 cm and the propagation directions very close to transverse to the magnetic field. The above strong dependence of group velocity on the propagation direction may be proposed as a possible mechanism for explanation of the narrow angular and frequency range of measured LH turbulence based on the propagation effects in the nonuniform plasma. LH waves propagating not transverse to the magnetic field are rapidly swept out of the interaction region without noticeable amplification.

Ion diffusion in the velocity space

As established by Carney [12,13] the interaction of magnetized ion with LH wave of finite amplitude may be of stochastic character provided

that the transverse ion velocity is greater than the phase velocity of the wave and the wave amplitude is large enough. A gyrating ion gets "a kick" from the wave at the point on its trajectory, where the component of ion velocity parallel to the wave-vector, $\boldsymbol{k}$, equals the wave phase velocity. This results in the variation of both the transverse ion velocity ($\Delta v_\perp$) and the phase of ion gyration in the external magnetic field, $\Delta\varphi$; these values are related as

$$\Delta v_\perp \approx -\frac{\omega_{ci}}{k_{LH}}\Delta\varphi \approx 2\sqrt{2\pi}\,\frac{eE_0\omega}{m_i\omega_{ci}^2}\left(\frac{\omega_{LH}}{k_{LH}v_\perp}\right)^{3/2}\cos\varphi, \qquad (17)$$

where φ is unperturbed phase of ion-wave interaction; e and m_i are electric charge and mass of ion; ω_{LH}, k_{LH} and E_o are the frequency, the wave-number and the amplitude of LH wave, respectively. Eq.(17) is valid only in the case of $v_\perp > \omega_{LH}/k_{LH}$; in the opposite case the values of both $\Delta\varphi$ and $\Delta v_\perp$ are zero since there is no point of resonance interaction on the ion trajectory. So inequality

$$v_\perp > \omega_{LH}/k_{LH} \qquad (18)$$

may be considered as the condition of resonance interaction. Stochastic behaviour takes place if the averaged phase variation of the ion motion after one rotation is larger than approximately $\pi/2$.

In the following we investigate the case of LH turbulence with the $\boldsymbol{k}$-vectors isotropically distributed in all directions transverse to the magnetic field and covering some range in k-numbers. This assumption is natural for the locally homogeneous model. Although our scattering experiment does not allow to check this assumption in full extent, it is partially supported by the experimental observation of waves propagating in two opposite directions which were identified by the sign of the corresponding frequency shift in the scattering spectrum. To estimate the total phase variation of ion during one gyro-rotation we consider interaction of a single ion with a large enough number of LH waves and take the limit of continuous spectrum. We assume that all LH waves have random phases, so that the mean squared phase variations may be added to each other; the sum should be taken over all waves satisfying the resonance condition (18). Thus we obtain:

$$\left\langle \Delta\varphi_i^2 \right\rangle = \int d^3k \left\langle \Delta\varphi_{ik}^2 \right\rangle = 8\pi \frac{e^2\omega_{LH}^5}{m_i^2\omega_{ci}^6 v_\perp^3}\int \frac{d^3k}{k}|E|_k^2\,\theta\left(v_\perp - \frac{\omega_{LH}}{k}\right), \qquad (19)$$

where $|E|_k^2$ is spectral density of the squared LH wave amplitude (for the sake of simplicity we assume that the LH wave frequency is not dependent on *k)* and the Heaviside function, θ, (which equals zero for the negative argument and unity for the positive argument) takes into account condition (18) of resonance interaction; the full energy density in LH turbulence is defined as:

$$\langle W_{LH} \rangle = \frac{1}{8\pi} \int |E|_k^2 d^3k \ . \tag{20}$$

It is evident that if an ion after interaction with many waves gets large enough squared average phase variation during one rotation, then the effect of this interaction will be the same as in the case of one wave with large enough amplitude, namely stochastic behaviour and diffusion in the velocity space. When the squared averaged phase variation, $\sqrt{\langle \Delta\varphi_i^2 \rangle}$, is larger than approximately $\pi/2$, then the ion after orbiting once in the magnetic field "forgets" about the phase of previous interaction with the LH wave and its stochastic behaviour can be described in terms of the diffusion equation in the velocity space with the diffusion coefficient $D = \langle \Delta v_\perp^2 / 2 \rangle \cdot \langle \omega_{ci} / 2\pi \rangle$. From Eq.(19) it follows that for a fixed shape of the LH wave spectrum there exists a threshold value of LH wave energy density, beyond which ions demonstrate stochastic behaviour in some finite region of the velocity space. The evolution of the averaged ion distribution function is then defined by the well known Fokker-Plank equation:

$$\frac{\partial f(v_\perp, t)}{\partial t} = \frac{1}{v_\perp} \frac{\partial}{\partial v_\perp} \left(v_\perp D(v_\perp) \frac{\partial f}{\partial v_\perp} \right), \tag{21}$$

with the diffusion coefficient with accounting for (17), (19) is equal to :

$$D(v_\perp) = \frac{\omega_{ci}}{2\pi} \left\langle \frac{\Delta v_\perp^2}{2} \right\rangle = 2 \frac{e^2 \omega^2}{m_i^2 \omega_{ci}^3} \int d^3k |E|_k^2 \left(\frac{\omega_{LH}}{k v_\perp} \right)^3 \theta \left(v_\perp - \frac{\omega_{LH}}{k} \right). \tag{22}$$

Note that the diffusion coefficient should be taken equal to zero in the region of large velocities, for which the value $\langle \Delta\varphi_i^2 \rangle$ defined by (19) does not exceed $\pi^2/4$.

The ultimate goal for the problem under investigation is to find a steady-state spectrum of saturated LH turbulence for which steady-state distribution function of ions (including beam ions) results in zero growth-rate for initially unstable LH waves. The effect of phase breaking is also to

be taken into account. However, this kind of theoretical treatment is beyond the scope of the present paper. In the following we will qualitatively discuss the possible mechanisms of instability saturation, which reduce the instability growth-rate to zero. There is experimental evidence which may help to identify the type of the mechanism: measurements show that the frequency of fully developed LH turbulence corresponds to the value calculated for the linearly unstable wave. A similar result is obtained for the wave propagation direction. One may be sure at least, that noticeable "wave diffusion" over the propagation direction with respect to the magnetic field is absent. Unfortunately, the same cannot be stated for diffusion in the wavenumber space due to the fact that the scattering experiment could only be operated for a fixed value of $k_\perp$.

Instability saturation mechanism

We shall briefly discuss here two possible mechanisms of instability saturation. One of them is the transport of LH wave energy from the region where the instability is driven. As it has been pointed out before, the group velocity for the propagation direction transverse to the magnetic field is rather small; from (16) it follows that its typical value is about $10^6\ cm/sec$. The transition time of waves travelling through a region of "homogeneous" plasma (about 1 cm) seems to be enough for the exponential increase of the initial noise with the instability growth-rate about $10^7\ sec^{-1}$. The power level of turbulence is determined in this case by the geometrical factor. This is a rather qualitative argument because it assumes a process of wave amplification when the wave is travelling through the instability region; such an approach is appropriate for the convective type of instability. Strictly speaking, it is not true for the instability under consideration because it is of the hydrodynamic type and the relation between time and spatial growth-rates is not trivial. The mechanism of development of an absolute hydrodynamic instability requires a special approach for a weakly inhomogeneous plasma and will not be pursued further here.

We would like to draw attention to another mechanism of the instability saturation, which seems to be more relevant and is based on the developed above idea of stochastic ion behaviour in the isotropically distributed transverse to the magnetic field LH turbulence with the random phases. This mechanism has a threshold which is obviously dependent on the LH turbulence distribution over wave numbers. It results in the instability satu-

ration and puts the limit on the turbulent energy density. The initial exponential growth of small-amplitude LH waves is present only in the linear case when the "bunching" of beam ions provides independently phased interaction with every unstable wave. With a sufficiently high turbulence level every ion of the beam gets an additional phase shift due to the interaction with all LH waves satisfying the resonance condition (18). This additional phase shift disturbs the phasing, which is necessary for the exponential growth of unstable waves. The upper limit when this is expected to occur is the threshold of stochastic phase breaking for the beam ions. The threshold may be estimated from Eq.(19) for the average squared phase shift, if the spatial spectrum of LH turbulence is known. Since this is not the case, one may use some reasonable assumptions. We assume that

$$\left\langle E_{LH}^2 \right\rangle_k = W_{LH}\delta(k_{//})f(k_\perp), \tag{23}$$

where W_{LH} is total LH turbulence energy density and for $f(k_\perp)$ we assume smooth dependence within $\Delta k_\perp$, which is of the order of $k_\perp$ measured in the CTS experiment (this assumption is supported by linear analysis). It should be noted that this $k_\perp$ together with the beam energy satisfies the condition of resonance interaction (18) for all measured frequencies of LH turbulence excited within the plasma density range investigated. Under the assumption made in (23) phase shift (19) reaches the threshold value of about $\pi^2/2$ already with a fairly low level of LH turbulent energy, $W_{LH}/nT_e \approx 10^{-6}$. This level does not contradict the measured scattering signal power. Such a low level of saturated LH turbulence justifies the approach, in which other nonlinear mechanisms of instability saturation are not taken into consideration. The proposed mechanism is equivalent to the existence of some nonlinear collisions disturbing phase coherence between beam ions and LH waves, with frequency $\nu_{NL}(W_{LH})$ determined by the total level of LH turbulence and by the shape of its spatial spectrum.

Conclusions

Lower-hybrid turbulence detected in the experiments on collective Thomson scattering of powerful gyrotron radiation at W7-AS is triggered by launching of a rather weak diagnostic neutral beam (the beam energy about 20 keV, beam current about 2 *A*) into the plasma transversely to the magnetic field of the stellarator. The registered turbulence has the frequency which follows the dispersion relation for LH waves propagating

transverse to the magnetic field rather nicely and possesses a unique peculiarity. Practically in back-scattering geometry without any spatial resolution in the direction of the major torus radius the registered scattered signal has a very narrow bandwidth (2-3% of plasma turbulence frequency) and a very narrow angular spectrum in the toroidal direction (less than the radiation patterns of the emitting and receiving antennas, which are about 1-2 deg.). Having in mind that there is line integration of the scattered signal practically throughout the whole plasma volume along the major radius, the only possibility to explain this rather fine selectivity of plasma with respect to the generated frequency is to assume that the turbulence is generated at some intrinsic plasma frequency (e.g. some definite number of the ion cyclotron harmonic or the LH frequency or something else) in a very narrow region along the major radius. In other cases the bandwidth will be essentially wider due to natural inhomogeneity of plasma parameters (characteristic scales along major radius are of the same order for the both mentioned frequencies and are of the order of the integration length).

To provide this, an instability mechanism for LH waves, which takes place in the presence of transverse ion beam under double resonance condition, has been proposed. This rather strong instability of the hydrodynamic type with the growth-rate proportional to the square root of the beam density takes place in the regions where the LH frequency is rather close to some integer number multiplied by the beam gyrofrequency. The investigation of the dispersion relation in the homogeneous plasma approximation shows that the instability is rather easily realized in the experimentally observed frequency and wave number range with the reasonable assumptions about the ion beam distribution function. But the instability exists in a noticeable range of propagation angles, close to transverse to the magnetic field. The very narrow angular range experimentally observed for excited LH turbulence can be qualitatively explained by propagation effects in the nonuniform plasma of a stellarator. It has been proposed that the instability saturates due to a modified effect of stochasticity, which arises in the beam ion motion when the level of LH turbulence exceeds some threshold value, which is rather low under the discussed experimental conditions.

To confirm theoretical speculations developed here, it could be very useful to perform local measurements of LH turbulence (e.g. in the 90 degree scattering geometry). If they are close to reality, some additional fine structure should be revealed in the spatial and temporal distribution of LH turbulence. In the case of fine spatial resolution it will be possible to

determine with the good accuracy ratio $\omega_{pi}^2/\omega_{pe}^2$, which provides additional information on plasma ion composition as compared to routine measurements of Z_{eff}.

The work has been supported by the German Bundesministerium fur Forschung und Technologie.

References

1. A.B.Mikhailovsky, "Theory of plasma instabilities", 1974, Vol.1, New York - London.
2. R.P.H. Chang, "Lower-hybrid beam-plasma instability", Phys. Rev.Letters, 1975, **v.35**, pp.285-288.
3. S.Seiler, M.Yamada, and H.Ikezi, "Lower hybrid instability driven by spiraling ion beam", Phys.Rev.Letters, 1976, **v.37**, pp.700-703.
4. C.N.Lashmore-Davis, *et.al.*, "Electromagnetic ion-cyclotron instability driven by a hot minority ion species with temperature anisotropy", 1993, Plasma Phys. Contr. Fusion, **v.35**, pp.1529-1540.
5. R.O.Dendy, *et.al.*, "The excitation of obliquely propagating fast Alfven waves at fusion ion cyclotron harmonics", Phys.Plasmas, 1994, **v.1**, pp.1918-1928.
6. R.O.Dendy, *et.al.*, "A mechanism of beam driven excitation of ion cyclotron harmonic waves in the Tokamak Fusion Test Reactor", Phys.Plasmas, 1994, **v.1**, pp.3407- 3413.
7. R.O. Dendy, *et.al.*, "Interpretation of ion cyclotron emission from sub-alfvenic fusion products in TFTR", 22-nd EPS Conf. on Contr. Fusion and Plasma Phys., Contributed Papers, Part II, pp.229-232, Bournemouth, 3rd-7-th July, 1995.
8. S.Cauffman, *et.al.*, "Observations of ion cyclotron emission from charged fusion products in TFTR", 22-nd EPS Conf. on Contr. Fusion and Plasma Phys., Contributed Papers, Part II, pp.405-408, Bournemouth, 3rd-7-th July, 1995.
9. Suvorov E.V., *et.al.*, "First results on ion temperature measurements at W7-AS by collective scattering of 140 GHz gyrotron radiation", Proc. of the 9-th Joint Workshop on ECE and ECH, Borrego Springs, Clifornia, 23-26 January 1995, ed. by John Lohr, pp.501-508.

10. Suvorov E.V., *et.al.*, "Collective scattering of powerful 140 GHz radiation at W7-AS", 22-nd EPS Conf. on Contr. Fusion and Plasma Phys., Contributed Papers, Part I, pp.429-432, Bourne-mouth, 3rd-7-th July, 1995.
11. Suvorov E.V., *et.al.*, "Ion temperature and beam-driven plasma waves from collective scattering of gyrotron radiation in W7-AS", 1995, Plasma Phys. Control. Fusion, **v.37**, pp.1207-1213.
12. C.F.F. Karney, "Stochastic ion heating by a lower hybrid wave", 1978, Phys. Fluids, **v.21**, pp.1584-1599.
13. C.F.F. Karney, "Stochastic ion heating by a lower hybrid wave (II)", 1979, Phys. Fluids, **v.22**, pp.2188-2208.

THEORY OF THE DECAY PARAMETRIC INSTABILITY EXCITED BY FREQUENCY MODULATED PUMP.

E.Z.Gusakov, B.O.Yakovlev

Ioffe Physico-Technical Institute, St.Petersburg, Russia

According to [1] plasma inhomogeneity produces a stabilizing influence on the parametric decay instability, leading to the mismatch of the wavenumber decay condition. The plasma nonstationarity and the pump frequency modulation appear to be a stabilizing factor as well because of mismatch of the decay condition for frequencies [2] . However simultaneously acting these two factors can interfere leading, in theory, to the singularity of the convective amplification coefficient, describing the parametric interaction in the inhomogeneous plasma [3],[4]. Predicting the possibility of decrease of the decay instability threshold this theory fails to explain the detailed picture observed in the experiment [4] .

The present paper is devoted to development of more elaborated theory taking into account effects removing the singularity of the amplification coefficient, such as nonlinearities of the wavenumber mismatch profile and pump frequency modulation or the wave dispersion.

The decay instability excited in inhomogeneous plasma by frequency modulated pump is described by coupled equations for slowly varying amplitudes of parametrically excited waves

$$\begin{aligned} \frac{\partial a_1(x,t)}{\partial t} + \nu_1 \frac{\partial a_1(x,t)}{\partial x} &= \gamma_0 a_2(x,t) e^{i\phi(x,t)} \\ \frac{\partial a_2(x,t)}{\partial t} + \nu_2 \frac{\partial a_2(x,t)}{\partial x} &= \gamma_0^* a_1(x,t) e^{-i\phi(x,t)} \end{aligned} \qquad (1)$$

where γ_0 is the maximal instability growth rate in the homogeneous plasma, ϕ is the phase mismatch given by $\phi = x^2/2\ell^2 + \alpha_0(x - \nu_0 t)^2$, where the first term is related to the plasma inhomogeneity $\ell = \left| d\left(\kappa_0(x) - \kappa_1(x) - \kappa_2(x)\right)/dx \right|_{x=0}^{-1/2}$, while the second term describes the plasma frequency modulation with period τ and deviation $\delta\omega = -2\alpha_0 \nu_0^2 \tau$; k_0 and $k_{1,2}$, ν_0 and $\nu_{1,2}$ are correspondingly projections of

the wavenumbers and group velocities of the pump and daughter waves in the inhomogeneity direction. After substitution

$$a_j = \tilde{a}_j \exp\left\{ i(-1)^j \alpha_j \left(x - v_j t\right)^2 \right\} \quad j = 1,2 \qquad (2)$$

with

$$\alpha_1 = -\frac{1}{2\ell^2} \frac{v v_2}{(v_1 + v)(v_1 + v_2)} + \alpha_0 \frac{(v_0 - v)(v_0 - v_2)}{(v_1 + v)(v_1 + v_2)}$$

$$\alpha_2 = \frac{1}{2\ell^2} \frac{v_1 v}{(v_2 - v)(v_1 + v_2)} - \alpha_0 \frac{(v_0 - v)(v_1 + v_0)}{(v_2 - v)(v_1 + v_2)} \qquad (3)$$

equations (1) take the following standard form

$$\frac{\partial \tilde{a}_1(\eta,t)}{\partial t} + u_1 \frac{\partial \tilde{a}_1(\eta,t)}{\partial \eta} = \gamma_0 \tilde{a}_2(\eta,t) e^{i\psi(\eta)}$$

$$\frac{\partial \tilde{a}_2(\eta,t)}{\partial t} + u_2 \frac{\partial \tilde{a}_2(\eta,t)}{\partial \eta} = \gamma_0^* \tilde{a}_1(\eta,t) e^{-i\psi(\eta)} \qquad (4)$$

in which $\psi(\eta) = \frac{\eta^2}{2\tilde{\ell}^2}$, $\eta = x - vt$, $u_1 = v_1 - v$, $u_2 = v_2 - v$ and

$\tilde{\ell}^2 = \frac{1}{2} \frac{(v_1 + v)(v_2 + v)}{(v_0 - v_2)(v_1 - v_0)} \left[\alpha_0 - \frac{1}{2\ell^2} \frac{v_1 v_2}{(v_0 - v_2)(v_1 - v_0)} \right]^{-1}$ is a new characteristic size of the phase mismatch. Equations (4) were investigated in [1], where no instability, but the spatial amplification of waves was found. According to [1] the amplification coefficient is given by

$$S = \exp\left(\frac{\pi \gamma_0^{\,2} \tilde{\ell}^2}{u_1 u_2} \right) = \exp\left(\frac{\pi \gamma_0^{\,2}}{2(v_0 - v_2)(v_1 - v_0)} \left[\alpha_0 - \frac{1}{2\ell^2} \frac{v_1 v_2}{(v_0 - v_2)(v_1 - v_0)} \right]^{-1} \right) \qquad (5)$$

This coefficient does not depend on decay point velocity v and has a singularity for modulation rate $\alpha_0 \to \frac{v_1 v_2}{2\ell^2 (v_0 - v_2)(v_1 - v_0)}$. This singularity corresponds to the complete interference of the phase mismatch terms in $\phi(x,t)$ and infinite growth of the interaction region width, proportional to $\tilde{\ell}^{3/2}$. The linear mechanism which can limit this growth

and thus remove the singularity of the amplification coefficient is related to the higher order terms in the phase mismatch which were neglected in system (4). Taking them into account one readily obtain the phase mismatch in the following form

$$\phi(x,t)=\frac{x^2}{2\ell^2}+\frac{x^3}{6L^3}+\alpha_0\left(x-v_0t\right)^2+\beta_0\left(x-v_0t\right)^3$$

where $L=\left|d^2\left(\kappa_0(x)-\kappa_1(x)-\kappa_2(x)\right)/dx^2\right|_{x=0}^{-1/3}$ describes a nonlinear wavenumber mismatch due to plasma inhomogeneity and β_0 is related to small frequency sweep nonlinearity. After phase substitution $a_j=\tilde{a}_j\exp\left\{i(-1)^j\alpha_j\left(x-v_jt\right)^2+i(-1)^j\beta_j\left(x-v_jt\right)^3\right\}$ j=1,2 coupled equations for slowly varying amplitudes could be transformed to the standard form (4) in which now $\psi(\eta)=\frac{\eta^2}{2\tilde{\ell}^2}+\frac{\eta^3}{6\tilde{L}^3}$, $\frac{1}{\tilde{L}^3}=\frac{1}{L^3}\frac{{v_1}^2v_2}{\left({v_1}^2-v^2\right)\left(v_2-v\right)}$ and $v=\frac{v_1}{1-\frac{v_2}{\left(v_1-v_2\right)}\frac{1}{12L^3\beta_0}}$ is the decay point velocity. In order to simplify the solution, we assumed here that as in the backscattering decay v_0=-v_1. After making the Laplace transform in time of equations (4) with p the Laplace variable and putting $a_1=a\exp\left\{i\frac{\eta^3}{12\tilde{L}^3}-\frac{p}{2}\left(\frac{1}{u_1}-\frac{1}{u_2}\right)\eta\right\}$ we find

$$\frac{d^2a}{d\xi^2}+\left\{\frac{1}{4}\left[\frac{\xi^2}{2}+ip\tilde{L}\left(\frac{1}{u_1}-\frac{1}{u_2}\right)\right]^2-\frac{i}{2}\xi-\frac{{\gamma_0}^2\tilde{L}^2}{u_1u_2}\right\}a=0 \qquad (6)$$

where $\xi=\eta/\tilde{L}$ is a dimensionless variable and $\tilde{\ell}^2\to\infty$ is supposed. The expression for the maximal spatial amplification coefficient, obtained from (6) for p=0, under assumption ${\gamma_0}^2\tilde{L}^2/\left|u_1u_2\right|>>1$, is given by

$$S = \exp\left\{ \frac{\Gamma^2(1/4)}{3\sqrt{2\pi}} \frac{\gamma_0^{3/2} L^{3/2} (v_1 - v)^{1/2}}{(v_1 + v)^{1/4} (v_2 - v)^{1/4} (v_1^2 v_2)^{1/2}} \right\} \qquad (7)$$

It is finite, unless the case $v \to v_2$, in which it still posses a singularity. The physical reason for this singularity is suppression of convective losses from the vicinity of the moving decay point.

Equation (6), unlike the standard system analyzed in (4), possess unstable normal modes which exist in the case $u_1 u_2 < 0$. Assuming, as in the previous case, the pump power to be high enough, so that $\gamma_0^2 \tilde{L}^2 / |u_1 u_2| >> 1$, one can reduce the equation (6) to the form

$$\frac{d^2 a}{d\xi^2} - 2i \sqrt{\frac{\gamma_0^2 \tilde{L}^2}{u_1 u_2}} \left[\frac{\xi^2}{2} - i \left(p\tilde{L} \frac{u_1 + u_2}{u_1 u_2} - \sqrt{\frac{\gamma_0^2 \tilde{L}^2}{u_1 u_2}} \right) \right] a = 0 \qquad (8)$$

valid in the vicinity of the "turning points" defined by

$$\xi = \pm \left\{ -ip\tilde{L} \left(\frac{1}{u_1} + \frac{1}{u_2} \right) \pm 2i \sqrt{\frac{\gamma_0^2 \tilde{L}^2}{u_1 u_2} - i\xi} \right\}^{1/2}$$

The localized solutions of the equation (6) are possible only for

$$p_n = \gamma_0 \frac{(v_1 + v)^{1/2} (v_2 - v)^{1/2}}{v_1 + v_2} \left[1 - \left(n + \frac{1}{2} \right) e^{i\pi/4} \frac{(v_1 v_2)^{1/2} (v_1 + v)^{1/4} (v_2 - v)^{1/4}}{\gamma_0^{3/2} L^{3/2}} \right] \qquad (9)$$

where n=0,1...This solutions correspond to the unstable normal modes with the growth rate given by p_n. One can conclude that the mode is unstable only for the decay point velocity satisfying condition $-v_1 < v < v_2$. The growth rate approaches zero for $v \to v_2$, because the wave convection out from the decay region vanishes in this case. The threshold of this instability is determined by the wave damping

$$\gamma_0 > \frac{(v_2 - v)^{1/2} (v_1 + v)^{1/2}}{2} \left(\frac{\Gamma_1}{v_1 + v} + \frac{\Gamma_2}{v_2 - v} \right)$$

which could be found by adding the damping terms $\Gamma_i a_i$ to the system (4) The domain of validity of the results obtained above is determined by the

condition of the daughter wave amplitude slow variation on the scale of its period or wave length. As it is obvious from (2) and (3), these conditions are most likely to be violated in the resonance case, when $\nu \to \nu_2$ and the phase of incident and amplified wave a_2 varies rapidly. To describe the amplification of the incident wave a_2, possessing the constant frequency we should put a limitation $\alpha_2=0$ on the phase in the substitution (3). In this case we suppose that all the pump phase variation is taken by the high frequency wave a_1. The modified substitution for a_1 looks as follows

$$a_1 = \tilde{a}_1 \exp\left\{ -i\alpha_0 \frac{\nu_0(\nu_0-\nu)}{\nu_1(\nu_1-\nu)}(x-\nu_1 t)^2 \right\}$$

where $\nu = -\dfrac{2\alpha_0 \ell^2 \nu_0(\nu_1+\nu_0)}{2\alpha_0\ell^2(\nu_1+\nu_0)+\nu_1}$ is relation which defines the dependence of the decay point velocity on frequency deviation. The spatial amplification in this case is still described by (5). This amplification coefficient has the singularity for $\nu \to \nu_2$, when the convective losses are suppressed. This effect takes place simultaneously for all frequencies, which could be no longer true when the wave dispersion is taken into account. The slow wave equation in this case takes the form

$$\frac{\partial \tilde{a}_2(\eta,t)}{\partial t} - u_2 \frac{\partial \tilde{a}_2(\eta,t)}{\partial \eta} + D\frac{\partial^2 \tilde{a}_2(\eta,t)}{\partial \eta^2} = \gamma_0^* \tilde{a}_1(\eta,t) e^{-i\eta^2/2\tilde{\ell}^2} \qquad (10)$$

where $D = i\partial^2\omega_2/\partial\kappa^2$. Solution of the new equations could be represented in the integral form

$$a_2(x,\Omega) = \sum_j \int_{C_j} e^{-i\tilde{\ell}^2 p^2/2} (p-p_1)^{-1-\sigma}(p-p_2)^{-1-\sigma}\left(\frac{p-p_1}{p-p_2}\right)^{9/p_1-p_2} e^{px}dp,$$

where, $\sigma = \frac{\Omega \upsilon_2 \tilde{\ell}^2}{2\upsilon_1 D}$, $\vartheta = -\frac{\upsilon_2}{D}\sigma + i\frac{\tilde{\ell}^2\left(\Omega^2 + \gamma_0{}^2\right)}{\upsilon_1 D}$ and $p_{1,2}$ - roots of the equation $p^2 - \frac{\nu_2}{D}p + i\frac{\Omega}{D} = 0$

The amplification coefficient is easily obtained from this integral representation in the form

$$S = \exp\left(-\frac{\pi\gamma_0{}^2\ell^2}{(\nu_1 - \nu)\sqrt{(\nu_2 - \nu)^2 - 4D\Omega}}\right)$$

The singularity of the amplification coefficient is removed here for all frequencies but $\Omega = (\nu - \nu_2)^2/4D$, for which the convective losses are still suppressed. Instead of conclusion it is worth to underline that different mechanisms discussed above reduce the domain of parameters for which the amplification coefficient singularity exists, but fail to remove it completely. Under this circumstances the transient phenomena and the finite time of experiment could be of importance, determining the level of parametric amplification in the system. This mechanism is analyzed in detail in the another paper in this book.

References

[1] Piliya A.D. Proc. X Int. Conf. on Phenomena in Ionised Gases, Oxford 320 (1971)

[2] L.M.Gorbunov, A.N.Starodub Pis'ma v zhurnal tekhnicheskoi fiziki **3,** 820 (1977)

[3] A.A.Andreev, V.I.Fedorov Fizika plasmy **5,** 1058 (1979)

[4] V.I.Arkhipehko, V.N.Budnikov, E.Z.Gusakov et al Plasma Phys. Contrl. Fusion **37,** 1353 (1995)

NONLINEAR DYNAMICS OF LASER INTERACTION WITH HIGH Z PLASMA[1]

*Zhang Jiatai, Su Xiumin, Chang Tieqiang, N.E. Andreev**

Institute of Applied Physics and Computational Mathematics
P.O. Box 8009, Beijing 100088, P.R. China

*High Energy Density Research Center,
Joint Institute for High Temperatures of Russian Academy of Sciences,
Moscow 127412, Russia

Abstract

The formation and evolution of a plasma in the interaction of laser radiation with gold targets are studied by computer simulations using MHD code (ESC-CASTOR). The nonlinear features of the interaction including the absorption of laser radiation, heating of the plasma components, and the deformation of the density profile under the action of the ponderomotive force are discussed. The role of these nonlinear effects together and in the influence of the density profile is discussed basing on the numerically obtained two dimensional dynamical structures of the hydrodynamic parameter (electron density n_e, ion density n_i, electron temperature T_e, ponderomotive force profile, and the space-time dependences of the absorption efficiency and the ionization rates. The radiation spectrum is analyzed and the regularities in the motion of the critical density surface are clarified.

[1] Project supported by the National High-Technology Inertial Confinement Fusion Committee, in China, NSFC, and PFBR.

1 Equations

Two-dimensional cylinder geometry (r-z) is assumed. The laser target is assumed to be a single element of atomic Z and mass number M. There are the principal variables ρ (mass density), $\rho\vec{u}$(momentum), T_e (electron temperature), T_i (ion temperature), T_r (radiation temperature), $\vec{B}$ (magnetic field), ϵ (internal energy), and $\vec{f}$ (ionization ratio). The additional variables are C_{ve} (electron specific heat), C_{vi} (ion specific heat), p (pressure) and $\frac{\partial p}{\partial \epsilon}$.

The principal equations solved are following [1][2][3].

The equation of mass conservation is

$$\frac{\partial \rho}{\partial t} + \nabla \cdot \rho\vec{u} = 0, \tag{1}$$

The equation of momentum conservation is

$$\frac{\partial \rho\vec{u}}{\partial t} + \nabla \cdot \rho\vec{u} + \nabla p - \vec{J} \times \vec{B} - \frac{1}{c}\frac{\partial F_L}{\partial z} = 0 \tag{2}$$

the electrical current

The equation of electron energy is

$$C_{ve}\frac{\partial T_e}{\partial t} = -\nabla \cdot \vec{F}_e - \nabla \cdot F_L - S_r - P_{bb} + \vec{E} \cdot \vec{J} - K, \tag{3}$$

the ion energy equation

$$C_{vi}\frac{\partial T_i}{\partial t} = -\nabla \cdot \vec{F}_i + K, \tag{4}$$

and radiation energy equation ($\epsilon_R = aT_r^4$)

$$\frac{\partial \epsilon_R}{\partial t} = -\nabla \cdot \vec{F}_R + S_r, \tag{5}$$

where the laser flux F_L is in the z direction, P_{bb} is the radiation rates from bound-bound(bb), K is the transfer rate of energy between the electron and the ion, S_r is the transfer rate of energy between the electron and the radiation field, c is the speed of light. A fraction $1 - (n_e/n_{el})^2$ of the line radiation is assumed to escape the plasma for $n_e < n_{el}$, where n_{el} is a density chosen below the solid density (typically n_{el} is about 15% of the solid density). For $n_e > n_{el}$ the line radiation is assumed to be reabsorbed.

The transfer rate of energy $\vec{E} \cdot \vec{J}$ between the magnetic field and electrons is calculated from

$$\frac{\partial \vec{B}}{\partial t} - \nabla \times \vec{u} \times \vec{B} = -\nabla \times \vec{E} \quad , \tag{6}$$

where the electric field is

$$\vec{E} = \eta \cdot \vec{J} + E_s \quad , \tag{7}$$

$$\vec{E}_s = -\frac{kT_e}{en_e}\nabla n_e - \frac{k}{e}\beta \nabla T_e + \frac{1}{en_e}\vec{J} \times \vec{B} \tag{8}$$

In the cylinder symmetry geometry $B = B_\theta$, so that (20) reduces to scalar equation.

The vector $\vec{f} = (f_0, f_1, \cdots, f_z)$ obeys the equation

$$\frac{\partial \vec{f}}{\partial t} + (\vec{u} \cdot \nabla)\vec{f} = A \cdot \vec{f} \quad , \tag{9}$$

where the matrix A contains the ionization and recombination rates.

2 Simulation Model

The target plasma material is gold, atomic weight $M = 196.9665$, atomic number $A_z = 79$, solid density $\rho_s = 19300 kg/m^3$. The initial conditions are follows: $T_{e0} = 1eV$, $T_{i0} = 1eV$, $T_{r0} = 0.03eV$; $u_{z0} = u_{r0} = 0$; $B_0 = 0$; The initial average ionization number $\bar{Z} = 1.019$. The radius direction distribution of the initial density ρ_{0r} is homogeneous, the axis direction distribution is variables as a exponential function

$$\rho_{0z} = a\rho_s exp(\frac{Z-b}{L}) \tag{10}$$

where model parameters a, b and L are given. The MHD equations are solved on Eulerian grid using the flux-corrected transport method, the orthogonal(r,z) mesh is of dimensions $20(N_r) \times 80(N_z)$.

A straight-line approximation is used such that the laser beam travels parallel to the z axis. At $t = 0$, the laser light ($I_L = 10^{14} \sim 5 \times 10^{14} W/cm^2, \lambda_L = 1.053 \mu m$) incident on the target turns on. It has a flux $F_0^+ = F^+(r, z = z_1, t)$ and absorption occurs via inverse bremsstrahlung at electron densities below the critical density

$$n_c = \frac{\epsilon_0 me}{e^2}(\frac{2\pi c}{\lambda_L})^2 \tag{11}$$

The classical absorption coefficient A written in the form

$$A = \frac{2\pi me)^{1/2} e^2 c}{\epsilon_0 k^{3/2} T_e^{3/2}} \frac{< z >}{\lambda_L^2} \frac{\xi^2 ln\Lambda}{(1-\xi)^{1/2}} \tag{12}$$

here ϵ_0 is vacuum dielectric constant, $\xi = n_e/n_c$, $ln\Lambda$ is Coulomb's logarithm. The flux reaching the critical depth z_c at which $n_e = n_c$ is

$$F_c = F_0^+ exp(-\int_{z_1}^{z_c} Adz) = F_0^+(1 - A_0) \tag{13}$$

F_c can be split into two parts. $A_c F_c$ deposited at z_c and a reflected flux $(1 - A_c)F_c$. The flux reflected by the plasma is

$$F_0^- = F_0^+(1 - A_c)(1 - A_0)^2 \tag{14}$$

3 X-ray spectrum and transform efficiency

As laser light is absorbed by the target plasmas, the electron temperature in the corona region rises gradually. Results in computer simulation have shown that before the peak value of laser pulse, the electron temperature rises throughout, at $t = 0.15ns$, $T_e \simeq 40eV$, at $t = 0.5ns$, $T_e \simeq 100eV$, and temperature in the corona region reaches equivalent, the maximum temperature is about $1500eV$. The ion temperature in the corona rises very slowly, at $t = 0.15ns$, it reaches equivalent, the maximum temperature is about $100eV$.

The radiation temperature in the corona region is very low, because of radiation loss. The maximum radiation temperature reaches $100eV$ in critical density and overdense density region. The strong laser absorption occurs near the critical density surface, the absorption efficiency is about 55%.

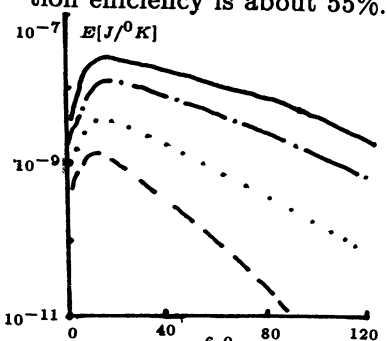

Fig. 1 X-ray spectrum

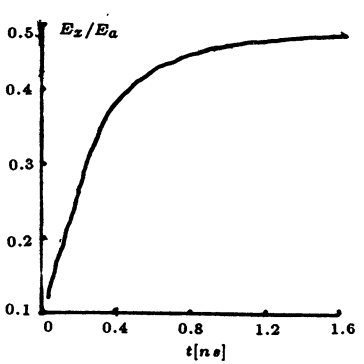

Fig. 2 Laser X-ray transform efficiency as a function of time

X-ray are divided 30 group between $0 - 10.05KeV$, time-space integration X ray spectrum is obtained (Fig. 1), the spectrum value decreases as energy increases, excepting first and second group of lower energy. It is the folding spectrum of bremsstrahlung and line spectrum. Its tail of the high energy decreases quickly. These results are comparable with experimental and other computational results. Figure 2 shows the laser X-ray transform efficiency as a function of time, At $t = 0.05ns$, transform efficiency $\eta = \frac{\text{X-ray Energy}}{\text{Asorption Eergy}} = 10\%$; at $t = 0.45ns$, $\eta = 43\%$; after this transform efficiency increases very slowly and saturates; in the end $\eta = 55\%$. This result is comparable with the computational result of Turner, R. E et al. [4]. The rate of energy between the line radiation and the continuum radiation is about 5. The rate decreases as time increases.

4 Motion Regularities of Critical Surface

Figure 3 a–d show the density contour as a function of time.

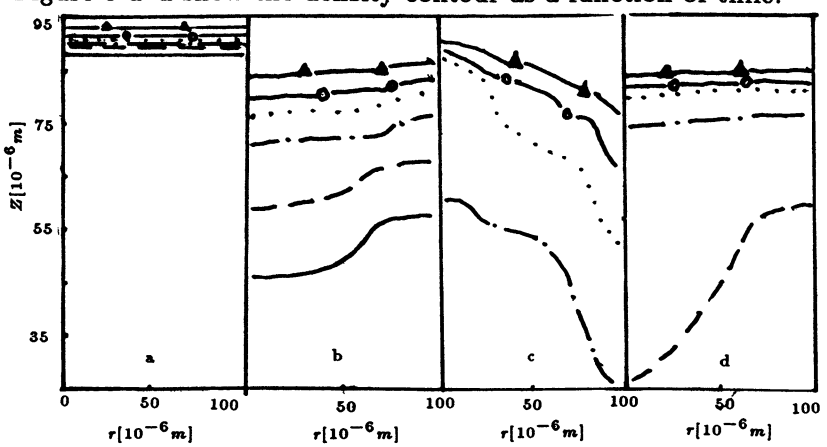

Fig. 3 The density contour
a. $t = 0$, b. $t = 0.255ns$. c. $t = 1.555ns$. d. $t = 2.355ns$.

Figure 3a shows the density contour at $t = 0$. The x-axis denotes the radial coordinate(r), the y-axis denotes the axial coordinate(z). The initial density distribution is homogeneous in the radial direction, the density value increases with the axial coordinate (z), they are $0.11n_c$, $0.22n_c$, $0.55n_c$, $0.88n_c$, n_c and $1.32n_c$ respectively, n_c is the critical density. Because absorbed laser energy in the focus centre is much more, the expansion is faster. Figure 3b has shown two-dimensional characteristic of the density contour, the lower density, the bigger difference of the distance in z direction between the centre and the border of r–coordinate, the difference is $6.5\mu m$ at $n = 0.11n_c$,

the difference is $2\mu m$ at $n = n_c$. Because the motion picture of the density contour are determined by competition between hydrodynamic motion and ionization, the pictures closely related to the fluid velocity u and the ionization rates $< z >$. At the time in laser peak, the shape of the density contour (Fig.3c) is different from that of early time, because the ionization at the centre is very strong, the fluid velocity is very high. In the end , the centre in the density contour of lower density is protuberant, the density contour of high density is smoothing. The critical density surface becomes steep because of ponderomotive force. The results of computer simulation show that the critical density surface maintain immovable basically during early time, after $t = 0.5ns$, it moves toward the direction -z of the lower density, the maximum motion range is about $15\mu m$, the motion velocity is $10^6 \sim 10^7 cm/s$. Fig.7 shows the critical density surface of the electron density ($n_e = 10^{21}/cm^3$) as a function of time, where solid line denotes $r = 0$, line of dashes denotes $r = 50\mu m$.

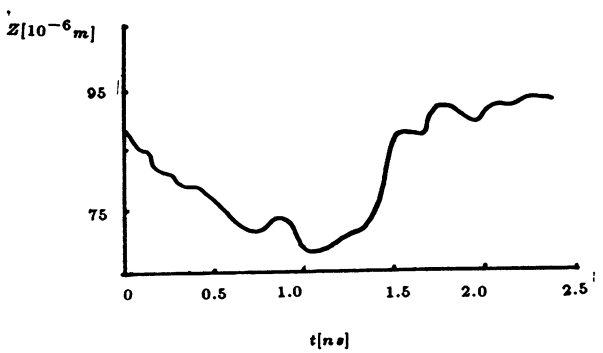

Fig. 4 Critical density surface as a function of time

References

[1] J.P. Christiansen et al., Comput..Phys. Comm. 17(3), 412(1979); 23(1), 1981(112).

[2] Zhang Jiatai et al., Comput. Phys. Comm. (in Chinese) 1, (1985)7; Zhang jiatai et al., Nuclear Fusion abd Plasma Physics (in Chinese) 8(1), (1988)1.

[3] Zhang Jiatai, Nie Xiaobo and Su Xiumin, Acta Physica Sinica (in Chinese)43(1), (1994)112

[4] R.E. Turner et al., UCRL(50021), (1982)6.

DESCRIPTION OF WAVE PROPAGATION IN AN ANISOTROPIC DISPERSIVE MEDIUM INCLUDING REFRACTION, DIFFRACTION, AND WEAK ABSORPTION

A.G. Peeters

Max Planck Institut für Plasmaphysik
Euratom-IPP Association, Boltzmannstraße 2 85748 Garching Germany

Abstract

In this paper the geometric optics approximation is extended. A consistent set of ray equations for wave propagation in an anisotropic dispersive medium with weak and localized absorption is derived.

Introduction

The research presented in this paper can have many applications. It has been developed to describe the propagation of wave beams in magnetized plasmas used for thermonuclear fusion research. Often focused wave beams are used for either localized heating or to obtain small scatter volumes. In these experiments not only refraction but also diffraction and absorption can play a role.

In the literature several methods to include diffraction effects in the description of wave propagation in a magnetized plasma are given. A generalization of the complex eikonal method of S.Choudary and L.B. Felsen [1,2] was developed by E. Mazzucato [3]. This method will be investigated in detail in this paper.

In this paper an anisotropic medium in steady state is considered. Consequently the real part of the wave frequency is constant. Both the absorption and diffraction are assumed weak, i.e. the length scale over which the electric field amplitude changes is much larger than the wave length.

The extension of geometric optics

The propagation of waves for which the wave length is small compared to the length scale over which the medium changes can be treated within geometric optics. The goal of this paper is to extend this formalism to include diffraction and absorption. Therefore, first the geometric optics approximation will be discussed.

In the geometric optics approximation the electric field is written in the form

$$\mathbf{E} = \mathbf{E}_0 \exp(\mathrm{i}\mathbf{k}_r\mathbf{x} - \mathrm{i}\omega t), \tag{1}$$

where $\mathbf{E}_0$ determines the electric field amplitude and polarization, and $\mathbf{k}_r$ is the (real) wave vector. These quantities are assumed to vary only slightly over a wave length, i.e $|\partial \mathbf{E}_0/\partial \mathbf{x}|/|\mathbf{k}_r| \ll 1$, $|\partial \mathbf{k}_r/\partial \mathbf{x}|/|\mathbf{k}_r| \ll 1$. A solution of the form of Eq. (1) can be obtained by substituting this expression in the wave equation $\nabla\times(\nabla\times\mathbf{E})-(\omega^2/c^2)\bar{\epsilon}\mathbf{E}=0$, where $\bar{\epsilon}$ is the dielectric tensor. The terms involving the gradients of $\mathbf{E}_0$ and $\mathbf{k}_r$ can be neglected, and an equation is obtained which has the form $\bar{\Lambda}(\mathbf{k},\omega,\mathbf{x})\cdot\mathbf{E}=0$. Non trivial solutions for the electric field exist when

$$D = \det\bar{\Lambda} = 0, \tag{2}$$

which is the dispersion relation of the wave. It depends only on the wave vector and frequency and on the spacial coordinates through the dependence on the dielectric tensor. The dispersion relation states that the propagating wave at any position has the form of a plane wave propagating in a homogeneous plasma with the local plasma parameters. As the wave propagates through the (inhomogeneous) plasma its characteristics change such that it again satisfies the local dispersion relation, i.e.

$$\frac{\mathrm{d}D}{\mathrm{d}\mathbf{x}} = \frac{\partial D}{\partial \mathbf{x}} + \frac{\partial D}{\partial \mathbf{k}_r}\frac{\mathrm{d}\mathbf{k}_r}{\partial \mathbf{x}} = 0. \tag{3}$$

From this equation the ray equations

$$\frac{\mathrm{d}\mathbf{x}}{\mathrm{d}\tau} = \frac{\partial D}{\partial \mathbf{k}_r} \qquad \frac{\mathrm{d}\mathbf{k}_r}{\mathrm{d}\tau} = -\frac{\partial D}{\partial \mathbf{x}} \tag{4}$$

which describe the wave propagation can be derived.

In the geometric optics approximation the wave beam is represented by a number of rays which are traced independently through the plasma. When the beam is focused the rays propagate towards another and can cross. In the point where the rays cross the beam width is zero and, consequently, the electric field amplitude infinite. This erroneous result can occur because the gradient of the electric field amplitude is neglected. To describe the wave beam correctly one should include effects caused by the electric field profile, which is possible through the introduction of a complex wave vector in (1), where the imaginairy part equals the inverse gradient length of the electric field profile

$$\mathbf{k}_i = \frac{1}{|\mathbf{E}_0|}\frac{\partial|\mathbf{E}_0|}{\partial \mathbf{x}}. \tag{5}$$

Note that both the electric field profile of the wave beam and absorption are described by this imaginary part.

The same derivation that gave the ray equations of geometric optics can now be repeated. A dispersion relation is obtained which depends on the electric field profile. From this dispersion relation ray equations, which include diffraction effects, are obtained.

The dispersion relation

To be able to expand various quanitities in the same dimensionless small parameter δ, the velocity of light c and a frequency ω_0 close to the wave frequency will be used to make all length and time scales dimensionless.

Three different length scales are discerned, the wave length λ, the width w of the beam, and the length scale L over which the plasma parameters change. It is assumed that these length scales can be ordened in the following way

$$L \ : \ w \ : \ \lambda \ \sim \ \delta^{-2} \ : \ \delta^{-1} \ : \ 1, \tag{6}$$

The imaginairy part of the wave vector $\mathbf{k}_i$ is of the order δ compared with the real part $\mathbf{k}_r$. Consistency with $w \approx \delta^{-1}$ demands that the beam focusing is moderate. It turns out that the gradient $\mathrm{d}\mathbf{k}_r/\mathrm{d}\mathbf{x}$, which is related to the curvature of the phase front, must be taken of the order δ^2 to satisfy this demand. The imaginairy part of the wave vector $\mathbf{k}_i$, its gradient $\mathrm{d}\mathbf{k}_i/\mathrm{d}\mathbf{x}$, and $\mathrm{d}\mathbf{k}_r/\mathrm{d}\mathbf{x}$ are allowed to vary over the width of the beam, i.e. $\mathrm{d}^n\mathbf{k}_i/\mathrm{d}\mathbf{x}^n = \mathcal{O}(\delta^{n+1})$ with $n \geq 0$, and $\mathrm{d}^n\mathbf{k}_r/\mathrm{d}\mathbf{x}^n = \mathcal{O}(\delta^{n+1})$ with $n \geq 1$.

In this paper the absorption is assumed to be weak, and localized in a region in space with a size of the order of the beam width. This ordering is relevant for the treatment of electron cyclotron waves in thermonuclear plasmas. The imaginairy part of the wave vector which is due to absorption satisfies the same ordering as the component of $\mathbf{k}_i$ that describes the electric field amplitude perpendicular to the beam. Finally, the length scale over which the plasma parameters change, together with the weak absorption changing over a length scale of the order δ^{-1} makes that the spatial derivative of the dispersion function $\partial\omega(\mathbf{k},\mathbf{x})/\partial\mathbf{x}$ is of the order δ^2. Higher order derivatives satisfy $\partial^n\omega(\mathbf{k},\mathbf{x})/\partial\mathbf{x}^n = \mathcal{O}(\delta^{n+1})$ with $n \geq 2$, because the absorption is assumed to vary over the length scale δ^{-1} rather than the length scale $L = \mathcal{O}(\delta^{-2})$.

The dispersion relation is obtained through the substitution of the ansatz (1) with complex wave vector in the wave equation. If the gradients of the wave vector are negelected one derives at a dispersion relation

$$\omega = \omega(\mathbf{k}_r + \mathrm{i}\mathbf{k}_i, \mathbf{x}). \tag{7}$$

First it will be discussed to what order in the smallness parameter δ the dispersion relation (7) must be expanded to describe diffraction effects. Here, a non absorbing plasma is considered. In lowest order one obtains

$$\omega = \omega(\mathbf{k}_r, \mathbf{x}), \tag{8}$$

which is the usual dispersion relation used in the geometric optics description. This dispersion relation, therefore, describes refraction but no diffraction. In next order one obtains

$$\omega = \omega(\mathbf{k}_r, \mathbf{x}) + \mathrm{i}\mathbf{k}_i \cdot \frac{\partial \omega(\mathbf{k}_r, \mathbf{x})}{\partial \mathbf{k}_r}. \tag{9}$$

The second term on the right hand side of this equation is a pure imaginairy correction, whereas the first term is purely real. Consequently, the correction does not influence the ray trajectories which are completely determined by the first term. The correction term imposes a restriction on the imaginairy part of the wave vector. Because the partial derivative in the second term is the group velocity, the second term demands that the imaginairy part of the wave vector is in any point perpendicular to the direction of energy propagation. In this order refraction and the evolution of the electric field profile are described, but the rays can still cross and, consequently, diffraction effects are not described. In second order one obtains

$$\omega = \omega(\mathbf{k}_r, \mathbf{x}) + \mathrm{i}\mathbf{k}_i \cdot \frac{\partial \omega(\mathbf{k}_r, \mathbf{k}_r)}{\partial \mathbf{x}} - \frac{1}{2}\mathbf{k}_i\mathbf{k}_i : \frac{\partial^2 \omega(\mathbf{k}_r, \mathbf{x})}{\partial \mathbf{k}_r \partial \mathbf{k}_r} \tag{10}$$

In this order a real correction of the order δ^2 to the zeroth order dispersion relation is obtained. and in this order diffraction effects are properly described.

It is clear that all terms of the order δ^2 in the dispersion relation can generate effects of the same order. Because a consistent ordering of terms requires that both $\mathrm{d}\mathbf{k}_r/\mathrm{d}\mathbf{x}$ and $\mathrm{d}\mathbf{k}_i/\mathrm{d}\mathbf{x}$ are of the order δ^2, gradients of the wave vector can not be neglected. It is assumed that the dispersion relation including absorption and gradients of the wave vector can be written in the general form [4]

$$\omega = \omega_0(\mathbf{k}, \mathbf{x}) + \mathrm{i}F_{\alpha\beta}(\mathbf{k}, \mathbf{x})\frac{\partial k_\alpha}{\partial x_\beta}, \tag{11}$$

where $\omega = \omega_0(\mathbf{k}, \mathbf{x})$ is the usual dispersion relation of the homogeneous medium with constant wave vector. The tensor $F_{\alpha\beta}$ is assumed to be real and is, like ω_0, of the order δ^0. Therefore, the second term

on the right hand side of Eq. (11) is a correction of the order δ^2 to the usual dispersion relation.

The ray equations

To write the ray equations in a convenient form the following functions are defined $\omega_i = \Im[\omega_0(\mathbf{k}_r, \mathbf{x})] = \mathcal{O}(\delta)$, $\omega_r = \Re[\omega_0(\mathbf{k}_r, \mathbf{x})] = \mathcal{O}(1)$. The function ω_i is related to the wave absorption. The second order real and imaginairy part of the dispersion relation are

$$\omega = \omega_r(\mathbf{k}_r, \mathbf{x}) - \frac{1}{2}\mathbf{k}_i\mathbf{k}_i : \frac{\partial^2\omega_r(\mathbf{k}_r, \mathbf{x})}{\partial\mathbf{k}_r\partial\mathbf{k}_r} - \mathbf{k}_i \cdot \frac{\partial\omega_i}{\partial\mathbf{k}_r} - \overline{\mathbf{F}}_r(\mathbf{k}_r, \mathbf{x}) : \frac{\partial\mathbf{k}_i}{\partial\mathbf{x}} \quad (12a)$$

$$0 = \omega_i(\mathbf{k}_r, \mathbf{x}) + \mathbf{k}_i \cdot \frac{\partial\omega_r(\mathbf{k}_r, \mathbf{x})}{\partial\mathbf{k}_r} + \overline{\mathbf{F}}_r(\mathbf{k}_r, \mathbf{x}) : \frac{\partial\mathbf{k}_r}{\partial\mathbf{x}}. \quad (12b)$$

The ray equations can be derived from these expressions by demanding that they are satisfied in any point, i.e. that the total derivative towards the spatial coordinate is zero. If the direction of propagation of the ray is defined through

$$\frac{\mathrm{d}x_\alpha}{\mathrm{d}\tau} = \frac{\partial\omega_r}{\partial k_{r,\alpha}}, \quad (13)$$

then the total derivative of Eqs. (12a-b) yields

$$\frac{\mathrm{d}k_{r,\alpha}}{\mathrm{d}\tau} = -\frac{\partial\omega_r}{\partial x_\alpha} + k_{i,\gamma}\frac{\partial^2\omega_r}{\partial k_{r,\gamma}\partial k_{r,\eta}}\frac{\mathrm{d}k_{i,\eta}}{\mathrm{d}x_\alpha} + F_{r,\gamma\eta}\frac{\mathrm{d}^2k_{i,\gamma}}{\mathrm{d}x_\eta\mathrm{d}x_\alpha} + \frac{\partial\omega_i}{\partial k_{r,\gamma}}\frac{\mathrm{d}k_{i,\gamma}}{\mathrm{d}x_\alpha} \quad (14a)$$

$$\frac{\mathrm{d}k_{i,\alpha}}{\mathrm{d}\tau} = -\frac{\partial\omega_i}{x_\alpha} - k_{i,\gamma}\frac{\partial^2\omega_r}{\partial k_{r,\gamma}\partial x_\alpha} - k_{i,\gamma}\frac{\partial^2\omega_r}{\partial k_{r,\gamma}\partial k_{r,\eta}}\frac{\mathrm{d}k_{r,\eta}}{\mathrm{d}x_\alpha} - F_{r,\gamma\eta}\frac{\mathrm{d}^2k_{r,\gamma}}{\mathrm{d}x_\eta\mathrm{d}x_\alpha} \quad (14b)$$

The Eqs. (13-14) are the extension of the equations given in Ref. [4], including a weak and localized absorption. The right hand side of Eq. (13), and the first term on the right hand side of Eq. (14a), are the terms of geometric optics. The direction of propagation of a ray is equal to that of geometric optics. The diffraction effects appear indirectly through a modification of the real part of the wave vector which is driven by the electric field profile through $\mathbf{k}_i$, $\mathrm{d}\mathbf{k}_i/\mathrm{d}\mathbf{x}$, and $\mathrm{d}^2\mathbf{k}_i/\mathrm{d}\mathbf{x}^2$. If the width of the beam decreases the gradient of the electric field profile increases and the second and third terms on the right hand side of Eq. (14a) become larger, causing more bending of the rays away from each other. The rays will, therefore, never cross and no caustics will be formed.

The equation (14b) determines the evolution of the imaginary part of the wave vector such that equation (12b) is always satisfied.

Neglecting the tensor F this equation states that the decrease in the electric field amplitude in the direction of energy propagation is given by the absorption of the medium. The term involving the tensor F generates a change in the electric field amplitude that is due to a focusing of the wave beam [4].

A word of caution regarding Eqs. (13-14) is required. These equations describe the evolution of the wave vector along a certain path correctly, but it has not been shown that this path coincides with the flow of wave energy.

The Gaussian beam

One important special case of wave beams used in the experiment is the Gaussian beam of lowest order. If the Gaussian beam is defined by the relations $\mathrm{d}^n\mathbf{k}_i/\mathrm{d}\mathbf{x}^n = \mathcal{O}(\delta^{2n})$ and $\mathrm{d}^n\mathbf{k}_r/\mathrm{d}\mathbf{x}^n = \mathcal{O}(\delta^{2n})$ with $n \geq 2$, it can be shown [4] that for a non absorbing plasma a Gaussian beam remains Gaussian as it propagates through the plasma. In this case the beam can be described entirely with a few parameters (width and radius of curvature of the phase front). A reduced set of equations can be derived that gives the evolution of these parameters. Such a set is discussed in Refs. [4-6].

In the case of weak and localized absorption, it can be shown by differentiating the Eq. (14b) twice towards position that

$$\frac{\partial}{\partial\tau}\left[\frac{\mathrm{d}^2\mathbf{k}_i}{\mathrm{d}\mathbf{x}^2}\right] \propto \frac{\partial^3\omega_i}{\partial x^3} = \mathcal{O}(\delta^4) \tag{15}$$

Therefore, after integrating over the length scale δ^{-1} in which absorption occurs the beam is no longer a Gaussian beam. The physical reason can easily be understood. The absorption is allowed to vary over the width of the beam. Therefore, a localized absorption in a part of the beam can easily change the electric field profile of the wave beam. This result makes that no simple set of equations involving a few parameters can be derived.

References

[1] S. Choudhary, L.B. Felsen, IEEE Trans. Antennas Propagation, **Ap-21** 827 (1973).
[2] S. Choudhary, L.B. Felsen, Proc. IEEE **62**, 1530 (1974).
[3] E. Mazzucato, Phys. Fluids B **1**, 1855 (1989).
[4] A.G. Peeters, *Extension of the ray equations of geometric optics to include diffraction effects*, accepted for publication in Phys. Plasmas.
[5] G.V. Pereverzev, Reviews of Plasma Physics **19** (Consultants Bureau, New York, 1996).
[6] A.V. Timofeev, Plasma Phys. Reports **21**,646 (1995).

INFLUENCE OF ELECTRON BUNCH ENERGY AND DURATION ON WAKE-FIELD DYNAMICS IN PLASMA

I. N. Onishchenko, G. V. Sotnikov, A. N. Storozhenko
NSC "Kharkov Institute of Physics & Technology,
Kharkov, Ukraine

Introduction

The method of acceleration with plasma wave, excited by an electron bunch or the train of bunches should be provided by the condition of exceeding of wake-field over the electric field in a bunch. There are several ways to satisfy this requirement: bunch profiling [1], displacement of driving and accelerated bunches in space [2], specific succession of bunches or varied duration of bunches in collision plasma [3], using space harmonics in periodic plasma waveguide [4], nonlinear plasma wave [5-8].

The latter way is considered as a most perspective. In [5, 6] it is shown that maximum intensity of the wake-field is realized due to the plasma-wave nonlinearity for the bunch of density n_{b0} equal to the one half of plasma density n_0. The bunch profile is rectangular and nonchanged and electrons are ultrarelativistic ($\beta_0 = v_{b0}/c = 1$). The accelerating field intensity for these conditions [6] $E_{ac} \sim L_{b0}^{1/2}$ ($L_{b0} = \omega_p \mathcal{L}_{\lfloor\prime}/\rfloor \gg \infty$, $\omega_p = 4\pi n_0 e^2/m$ – plasma frequency, $\mathcal{L}_{\lfloor\prime}$ – bunch length). From the other side for the fixed bunch energy and $\beta_0 \neq 1$ wake-field is proportional $(\gamma_{b0} - 1)^{1/2}$ [5]. The latter result is obtained at the approximation that the electric field inside bunch is equal zero.

In the present work the nonlinear plasma wake excitation by dense electron bunch ($n_{b0} = n_0/2$) is being investigated numerically. Simulation was carried out for varied finite energy γ_{0b} and length L_{b0} of the electron beam.

The excitation of the stationary nonlinear plasma wave by relativistic electron bunch

Let an electron bunch of velocity $v_{b0} = \beta_{b0}c$ and density n_{b0} is injected into cold collisionless plasma. Beam-plasma system is proposed infinite and homogeneous in transverse direction. For this case the excitation of the stationary nonlinear plasma wave is described by the following set of the nonlinear equation:

$$\frac{d\beta}{d\tau} = \frac{\beta_b}{(1-\beta^2)^{3/2}} \frac{\epsilon}{\beta_b - \beta}, \quad \frac{d\epsilon}{d\tau} = -\beta_b \left(\frac{\beta}{\beta_b - \beta} + \frac{n_b(\tau)}{n_p} \right), \qquad (1)$$
$$n_p = n_0 \frac{\beta_b}{\beta_b - \beta},$$

where $\varepsilon = eE/mc\omega_p$ – dimensionless value of the electric field, $\tau = \omega_p(t - z/v_{b0})$, $\beta = v/c$ – dimensionless velocity of the plasma electrons, n_p – plasma density, $n_b(\tau)$ describes the profile of the electron bunch.

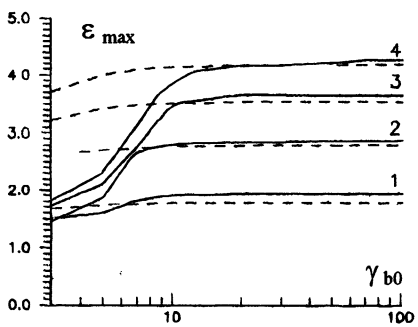

Fig. 1.

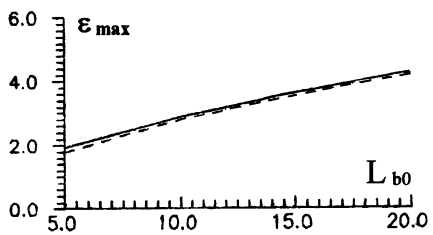

Fig. 2.

The set of nonlinear equations at $\beta_b = 1$ has been analyzed in [5, 6] for various profiles of the bunch. For the rectangular form of the bunch of the density $n_b = n_0/2$ the excited wake-field behind bunch is proportional to squared root of bunch length, and electric field inside bunch $|\varepsilon| \to 1$. So the transformation ratio is proportional to squared length of the bunch.

At first we investigate the dependence of the excited wake-field value upon initial energy and length L_{b0} of the bunch. The bunch profile is supposed to describe by the expression:

$$n_b(\tau) = \begin{cases} n_0/2, & 0 \le \tau \le L_{b0} \\ 0, & \tau > L_{b0},\ \tau < 0. \end{cases} \qquad (2)$$

Boundary conditions are taken in the form: $\beta|_{\tau=0} = 0, \qquad \varepsilon|_{\tau=0} = 0.$

In Fig.1 the dependence of wake-field amplitude maximum ε_{max} upon relativistic factor γ_{b0} for various dimensionless length L_{b0} (1, 2, 3, 4 for $L_{b0} = 5, 10, 15, 20$) of the bunch is represented. Curves(dotted lines) show a slight dependence of the field amplitudes on the bunch energy. The dependence $\varepsilon_{max}(\gamma_{b0})$ is rapidly saturated at the value ε_{sat} determined by bunch length L_{b0}. The amplitude dependence on bunch length for $\gamma_{b0} = 100$ is represented in Fig.2 (dotted line). It is seen that this dependence is described by $\varepsilon_{max} \sim \sqrt{L_{b0}}$ in accordance with [6].

The excitation of nonstationary nonlinear plasma wake-field

Now we take into consideration selfconsistent changing of the bunch profile and velocity. For the investigation of the bunch dynamics and wake-field excitation we use closed set of equations consisting of the hydrodynamic motion and continuity equations and Maxwell equation for the longitudinal electric field:

$$\begin{aligned}
&\frac{\partial n_p}{\partial t} + \frac{\partial}{\partial z}(n_p v_p) = 0, \quad \frac{\partial}{\partial t}(n_p p_p) + \frac{\partial}{\partial z}(n_p p_p v_p) = e n_p E, \\
&\frac{\partial n_b}{\partial t} + \frac{\partial}{\partial z}(n_b v_b) = 0, \quad \frac{\partial}{\partial t}(n_b p_b) + \frac{\partial}{\partial z}(n_b p_b v_b) = e n_b E, \qquad (3) \\
&\frac{\partial E}{\partial t} + 4\pi e(n_p v_p + n_b v_b) = 0,
\end{aligned}$$

where n_b, n_p are the variable beam and plasma densities, $v_{b,p}$, $p_{b,p}$ are beam and plasma velocities and moment, correspondingly $v_{p,b} = p_{p,b}/[m(1 + (p_{p,b}/mc)^2]$.

For numerical investigations of equations set (3) it is convenient to introduce dimensionless variables:

$$\begin{aligned}
&\beta_{p,b} = v_{p,b}/c, \quad \nu_{p,b} = p_{p,b}/mc, \quad \tau = \omega_p t, \\
&\zeta = \omega_p z/c, \quad \varepsilon = eE/mc\omega_p, \quad \nu_{p,b} = n_{p,b}/n_0.
\end{aligned}$$

In this variables equations set (3) takes the following view:

$$\frac{\partial \nu_p}{\partial \tau} + \frac{\partial}{\partial \zeta}(\nu_p \beta_p) = 0, \quad \frac{\partial}{\partial \tau}(\nu_p \rho_p) + \frac{\partial}{\partial \zeta}(\nu_p \rho_p \beta_p) = e \nu_p \varepsilon,$$
$$\frac{\partial \nu_b}{\partial \tau} + \frac{\partial}{\partial \zeta}(\nu_b \beta_b) = 0, \quad \frac{\partial}{\partial \tau}(\nu_b \rho_b) + \frac{\partial}{\partial \zeta}(\nu_b \rho_b \beta_b) = e \nu_b \varepsilon, \qquad (4)$$
$$\frac{\partial \varepsilon}{\partial \tau} + \nu_p \beta_p + \nu_b \beta_b = 0.$$

This set has been solved by method FCT [9] with essentially nonlinear algorithm to exclude nonphysical riple and numerical diffusion.

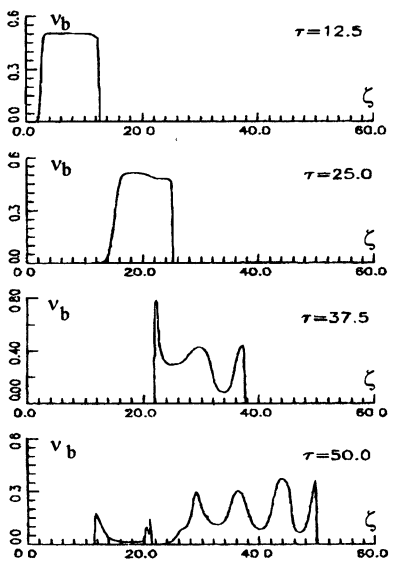

Fig. 3.

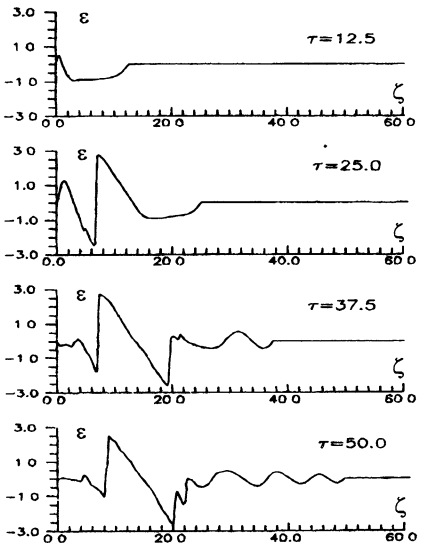

Fig. 4.

For simulation the grid was chosen with $\Delta\zeta = 0,1$ in space ($\zeta = 1 \ldots 100$) and time step $\Delta\tau = 0,05$ for time duration injection $\tau_0 = \omega_p t_0$. Boundary conditions were symmetrical, i.e. values of all parameters calculated at the terminal point of considered region were given to the boundary point outside of region: $S_0 = S_1$, $S_{N+1} = S_N$, where S – any calculated parameter, 0 and $N+1$ corresponds to left and right boundary. It should be noted the slighter qualitative dependence of the the results upon boundary conditions. Particularly for the periodic boundary conditions the wake-field dependence on γ_{b0} and L_{b0} is the same as for the symmetrical one's.

Obtained results are the followings. For small values γ_{b0} ($\gamma_{b0} \lesssim L_{b0}$) rapid decay of the bunch occurs at the flight time of the initial bunch length. During this time interval field amplitude reaches its maximum value. With relativistic factor γ_{b0} increasing ($10 \lesssim \gamma_{b0} \lesssim 40$) flight length to decay occurring increases to several bunch lengths. In Fig.3 the example of such bunch spatial dynamics is represented for $\gamma_{b0} = 20$ and various time moments. It is seen that initially rectangular profile of the bunch begins to diffuse at the bunch front ($\tau = 25.0$), then it is being modulated $\tau = 37.5$) conserving approximately its initial length. Later ($\tau = 50.0$) bunch is devided into several microbunches.

Longitudinal distribution of the wake-field for the same time moments is represented in Fig.4. Excited nonlinear wave is located behind the bunch over the distance of plasma wave order.

For beginning with $\gamma_{b0} \approx 40$ for bigger γ_{b0} the bunch is stable in the calculated region and excited wake-field has regular character.

Simulation of the wake-field dependence on energy and length of the the bunch were performed for $\gamma_{b0} = 3 \div 1000$ and $L_{b0} = 5 \div 20$. In Fig.1 (continious lines) the $\varepsilon_{\max}$ dependencies on γ_{b0} at various L_{b0} are represented. They are qualitatively coincided with stationary for "strict" bunch (dotted lines). For the values $\gamma_{b0} < L_{b0}$ wake-field amplitude increases with γ_{b0} increasing, then reaches its saturation value at $\gamma_{b0} = \gamma_{cr}$ and further γ_{b0} increasing doesn't change. Difference with stationary model at $\gamma_{b0} \ll L_{b0}$ is explained by the breaking of the stationary conditions in this region [7]. In Fig.2 the wake-field maximum amplitude ε_{max} dependence on the bunch length L_{b0} is depicted by continuous curve for the relativistic factor $\gamma_{b0} = 100$. Represented dependence is coincident with the dependence obtained for the ultrarelativistic case $\beta_{ph} = 1$ (dotted line) for the stationary model and is described analytically by the expression $\varepsilon_{max} \sim \sqrt{L_{b0}}$ [6] for the $L_{b0} \gg 1$.

Conclusion

In the frame of the one-dimensional model it is studied the process of the stationary and nonstationary nonlinear plasma wave excitation by an electron bunch in a cold collisionalless plasma and their using

possibility for wake-field acceleration. The main accent is made on the investigation of the influence of the bunch energy and its length on the principal characteristics of the excited nonlinear plasma wave and electron bunch. It is shown that at using bunch with density $n_b = n_0/2$ (n_0 is initial plasma density) the basic characteristics of the bunch, determining the wake-field amplitude and, correspondingly the accelerating gradient, is the the bunch length. Qualitatively the dependence of the maximum of the wake-field amplitude on the bunch length is described by formula $\varepsilon_{max} \sim \sqrt{L_{b0}}$. The initial energy of the bunch determines mainly its stability. Stationary and nonstationary models are coincided for $\gamma_{b0} \gtrsim L_{b0}$. At the lower energy of the bunch $\gamma_{b0} < L_{b0}$ results for two models differ, bunch is instable and decays rapidly at the distance $\Delta\zeta < L_{b0}$. Maximum field amplitude is considerably less than for the case $\gamma_{b0} \gtrsim L_{b0}$. The dependence of ε_{max} on γ_{b0} shows that ε_{max} is growing with bunch energy increasing for $\gamma_{b0} \ll L_{b0}$, at $\gamma_{b0} \sim L_{b0}$ it saturated and doesn't change with further γ_{b0} increasing.

This work is partly supported by ISF Grant N U27200.

References

1. Katsouleas T., Phys.Rev.A, 1986, **33**, 2056
2. Balakirev V.A. e.a., Preprint KFTI 87-51, Kharkov; KFTI, 1987
3. Vedenin P.V., Nikulin M.G., Rozanov N.E., Thesis of Conf. on physics of cosmic plasma, Erevan; 1989, p.117
4. Balakirev V.A., Onishchenko I.N., Sotnikov G.V., Fizika Plazmy (Rus.), 1988, **14**, 1313
5. Amatuni A.C., Sekhposyan E.V., Elbakyan S.S., Fizika Plazmy (Rus.), 1979, **5**, 85
6. Rozenzweig J.B., Phys.Rev.Lett., 1987, **58**, 555
7. Voropaev M.V., Rozanov N.E., Fizika Plazmy (Rus.), 1991, **17**, 600
8. Batischev O.V. e.a., Fizika Plazmy (Rus.), 1994, **20**, 650
9. Oran E., Boris G., Simulation of reactive flows, Moskow: Mir, 1990, 662 p.

EXPERIMENTAL LARGE PLASMA SET-UP FOR MODELING SPACE PHENOMENA

G.Yu. Golubyatnikov, S.V. Egorov, B.G. Eremin, A.V. Kostrov, M.V. Starodubtcev, A.V. Strikovsky, O.N. Tolkacheva, A.V. Shaykin

Institute of Applied Physics RAS, N.Novgorod, Russia

Modern intense progress in investigation of the near and far space has made laboratory modeling of some space phenomena most important. Scientific results of such studies can help solve fundamental problems of plasma physics and realize practical applications, such as: active space experiments and satellite communications. Of great interest are laboratory experiments on modeling acceleration of charged particles with electrostatic oscillations. Recently the problem of significant influence of self-consistent nonlinear formations (of the caviton type) in the lower-hybrid-resonance (LHR) frequency band on the processes of particle acceleration has been also given much attention. The newly arisen interest to solar phenomena provides the possibility for laboratory modeling of the processes running on the Sun itself, in the upper layers of the photosphere, and in space down to the Earth surface.

In order to solve these problems, IAP has developed and built a large-scale experimental set-up called "KROT" that furnishes the possibility to produce both isotropic and magnetized plasmas. The general scheme of the set-up is shown in Figure 1. The vacuum chamber of the set-up is 3 m in diameter and 10 m long. Dimensions of the solenoid having the trap configuration and shown in Figure 1 are $l \sim 3.5$ m and $d \sim 1.5$ m.

The process of modeling requires homogeneous calm plasma with no external sources. That is why the experiments were performed in the afterglow plasma. Since dimensions of the plasma are sufficiently large, diffusion of it is rather slow and sufficient for studying many physical problems.

This presentation describes results of studying experimentally the process of inductance plasma production in the presence of the magnetic field and without it under pressures $p \sim 10^{-4}$–10^{-3} Torr in a large

volume. The problem of matching the self-generator with the discharge was considered, as well as achievement of stable discharge parameters at the maximal efficiency. Plasma parameters were studied in the afterglow stage.

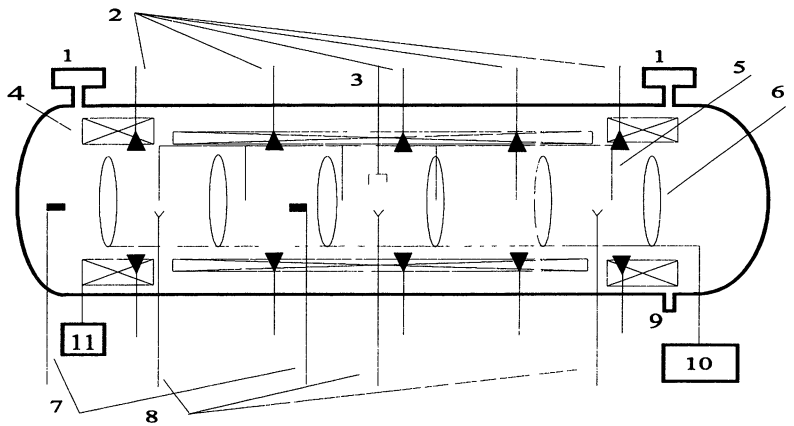

Fig. 1. Scheme of large-scale experimental set-up "KROT". 1 - vacuum pumps, 2 - 5 channel 8 mm interferometer, 3 - rf antenna, 4 - solenoid, 5 - system for moving double probes along the chamber, 6 - current loops, 7 - grid probes, 8 - system for moving double probes across the chamber, 9 - gas injector, 10 - rf-generators, 11 - generator of the pulse magnetic field

The isotropic plasma was produced by four RF generators operating at the frequency $f = 5$ MHz. Duration of RF pulses was $\sim 10^{-3}$ s, and their power, ~ 1 MW each. To each generator a second inductor $\sim$ 240 cm in diameter was connected via a 50 Ω cable. To measure inductor impedance and to control the degree of matching the RF generator with the load, a scheme of a common reflectometer with the Rogovsky belt was used. One of the main problems in producing inductance plasmas is optimal matching of the generator with the load. The gas is ionized mainly by a vortex electric field; however, at the inductor inputs there arises a powerful quasi-potential field, which is extremely undesirable. In this case the discharge is localized near the inputs. Hence, to reduce potential fields and improve discharge parameters, an inductor covered with a dielectric layer was used. To raise the current in the inductor, and, correspondingly, the vortex field, an adjustment capacitor was connected in series with the inductor. It was used to tune the serial contour to match the optimal conditions for ionization of the neutral gas. The frequency of

a serial contour before a breakdown must be lower than the frequency of the self-generator, and its impedance must have the inductance character. As the plasma appears and evolves, inductance of the inductor begins decrease, and the resonance frequency of the contour draw near the frequency of the self-generator. At this moment the maximum value of RF current, which flows through plasma is achieved. As plasma density grows further, reactance of the inductor acquires the capacity character and is actually determined by the impedance of the adjustment capacitor. Figure 2 shows the current and impedance of the inductor. As the result, we obtained the system "self-generator–plasma" with self-tuning, which makes it possible to achieve maximum plasma densities. Measurement results showed that when a plasma with $Ne \approx 10^{12}$ cm^{-3}, $Te \sim 5 \div 10$ eV is produced in the volume of 80 m^3, it absorbs about 2500 kW of RF power. Hence, efficiency of generator operation with the load was about 50%. The dependence of electron density in the plasma produced in the operating volume of the chamber under pressure about 10^{-4} Torr on the fed power is shown in Figure 3.

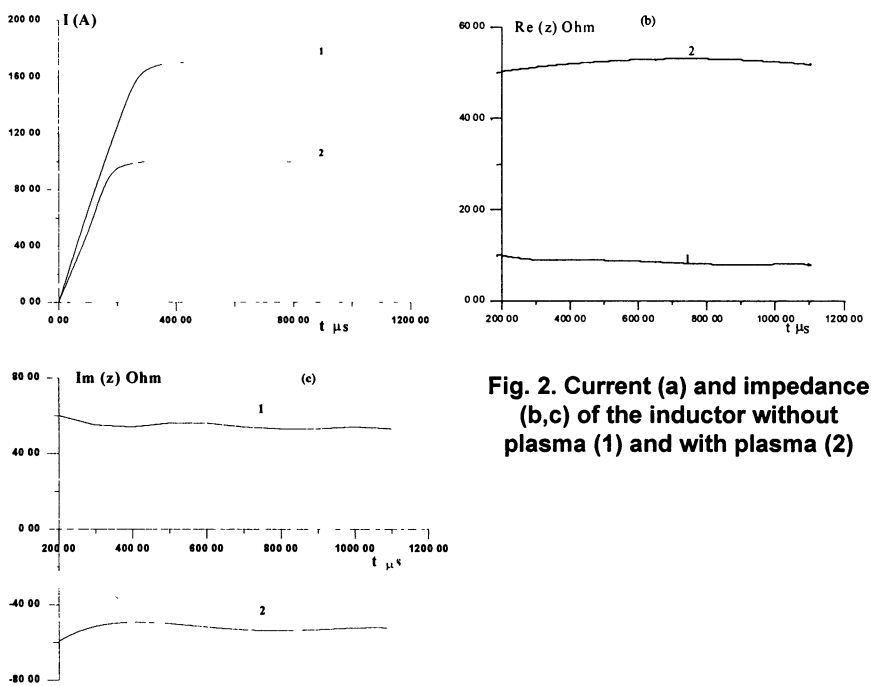

Fig. 2. Current (a) and impedance (b,c) of the inductor without plasma (1) and with plasma (2)

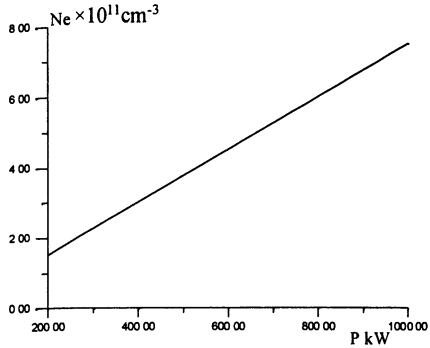

Fig. 3. The dependence of electron density in the plasma produced on the fed power

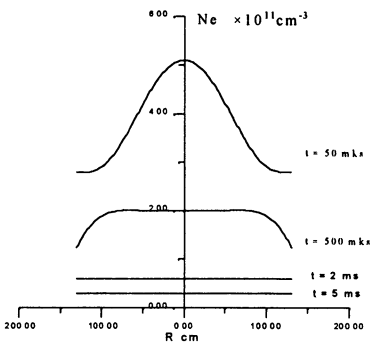

Fig. 4. Transverse distribution of electron density at continuous flow

The maximum plasma density grows linearly with power growth:

$$P \approx \frac{N_e(T_e + U_i)}{t} V \text{ , and } \frac{1}{t} = \frac{1}{t_N} + \frac{1}{t_T} .$$

Parameters of the isotropic plasma were diagnosed using double probes moving along the chamber radius and allowing measurements of relative plasma density distribution over the chamber volume, as well as of electron temperature. The transverse distribution of electron density at continuous flow (argon was used as the gas medium) at $p \sim 2 \cdot 10^{-4}$ Torr is shown in Figure 4. Decay electron density and electron temperature versus afterglow time obtained from double probe traces are shown in Figure 5 and 6 respectively. Estimations show that in this case free collisionless spreading of plasma is realized, since $l_{ia} \geq L$, where l_{ia} is length of the free run of ion-molecules, and L is characteristic chamber length. Calculated life times τ_e and τ_N coincided with the measured values and were about 1.5 ms.

Of the greatest interest is the problem of producing and using magnetoactive plasmas in large volumes, since such plasma makes it possible to model specific ionospheric physical phenomena in the laboratory. Currently our main research line here is investigation of interaction and propagation of intense waves in the LH frequency range in magnetoactive plasmas ($\omega_H \leq \omega_0 << \omega_{He} << \omega_{pe}$), where ω_H is LH frequency, ω_0 is wave frequency, ω_{He} and w_{pe} are cyclotron and plasma frequency, respectively.

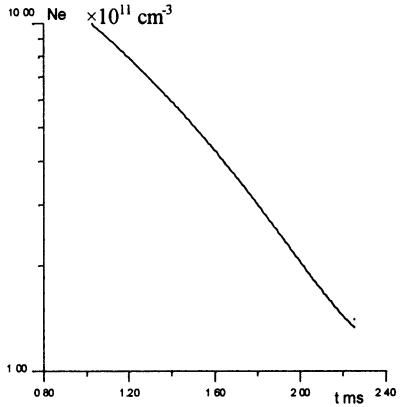

Fig. 5. Decay electron density

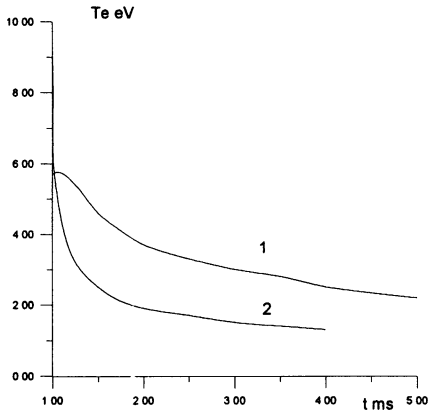

Fig. 6. Temperature versus afterglow time obtained from double probe traces: (1) $P \approx 10^{-3}$ Torr and (2) $P \approx 10^{-4}$ Torr.

To produce a magnetic field of the trap configuration (trap ratio ~ 2, pulse duration ~ 20 ms), a special solenoid 3.5 m long and 1.5 m in diameter was manufactured. It was fed by a generator of the pulse magnetic field.

Figure 7 shows the path of relative electron density along the radius at the center of the trap at different time moments. The time was counted from the end of RF generator operation. It is seen that at the magnetic field of about 400 G and pressure of the operating gas (argon) about $6 \cdot 10^{-4}$ Torr the discharge was localized near the inductors. The trap center is filled in the process of plasma diffusion across the magnetic field. In about 4–5 ms after the plasma source stops operating, density distribution along the chamber radius becomes sufficiently homogeneous. Figure 8 presents characteristic time dependencies of ion saturation current to the double probe at different distances from the chamber axis. The characteristic time of plasma decay, as seen from Figure 8, is about 1 ms. Plasma density after $t \sim 4$ ms was about $5 \cdot 10^{11}$ cm^{-3}, and the temperature of electrons was about 0.5–1 eV.

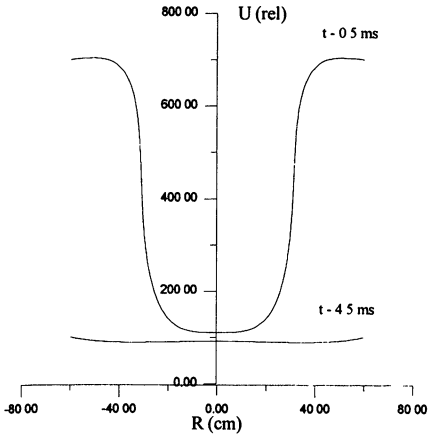

Fig. 7. Path of relative electron density along the radius at the center of the trap at different time moments

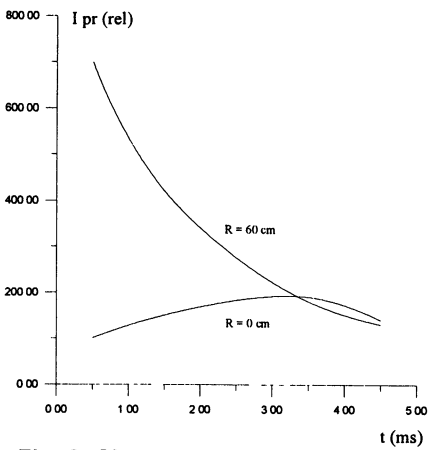

Fig. 8. Characteristic time dependencies of ion current to the double probe at different distances from the chamber axis

Thus, the "Krot" set-up developed and built at IAP produces magnetized plasmas in the volume about 8 m^3 with parameters mentioned above. Such a great volume of plasmas provides the unique possibility of studying physical phenomena in an "unboundary" plasma.

The work was performed with support of RFFI (grant 96 - 02 - 16471 - A), and with financial support of Russian Department of Science on "Krot" set-up (registr. 01 - 18).

PLASMA DYNAMICS IN VICINITY OF A STRONG OBLIQUE LANGMUIR WAVE RESONANCE

V.I.Arkhipenko, V.N.Budnikov†, E.Z.Gusakov†, V.A.Pisarev, L.V.Simonchik

Institute of molecular and atomic physics ASB, Minsk, Belarus
†Ioffe physical - technical institute RAS, St-Petersburg, Russia

In present work the dynamics of the partly ionized and magnetized argon plasma inhomogeneous both in radial and axial direction is investigated at incidence of the short (hundreds of nanoseconds) microwave impulse, when the oscillatory energy of electron in the wave field is significantly higher than ionization energy of working gas atoms. The experiments were performed in a linear plasma device "Granite" [1] with the following parameters: intensity of an external magnetic field H - 3500 Oe, the pressure of working gas - argon - $p = 10^{-2}$ Torr, the longitudinal and cross scale of plasma inhomogeneity - $a = 5$ cm and $b \approx 0.4$ cm accordingly, electron concentration - $n_e < 10^{11}$ cm^{-3}, electron temperature - $T_e = 1 \div 2$ eV.

The microwave power P was launched to plasma sideways by waveguide (Fig.1). An oblique Langmuir wave (OLW) mainly in the form of the fundamental Trivelpiece-Gould mode was excited in plasma by influence of a electromagnetic wave with frequency $f = \omega/(2\pi) = 2{,}84$ GHz essentially smaller than electron cyclotron frequency, but higher than the ion plasma frequency. The dispersion relation for this wave is $k_\perp^2 = [\omega_{pe}^2(r, z) / \omega^2 - 1]\, k_{||}^2$, where $k_{||}$ and $k_\perp$ are the components of the wave vector parallel and transverse to the magnetic field, $\omega_{pe}^2(r, z) = 4\pi n_e e^2/m_e$ - electron plasma frequency, n_c - critical concentration. The plasma with density higher than the critical value ($n_e(r,z) > n_c$) is a plasma waveguide for OLW with a week axial inhomogeneity. Propagating in direction of

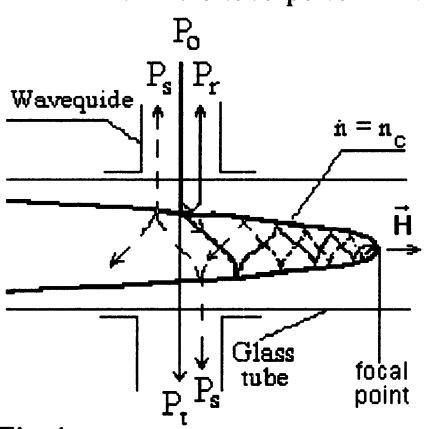

Fig.1

decreasing electron density to a point of a plasma resonance (focal point) $\omega = \omega_{pe}(r, z)$ the wave slows down and its electric field increases. In focal point the linear transformation of OLW into "warm plasma wave" happens and its field reaches the maxima values, assigned by relation [2]:

$$E_0 = \left(\frac{P'}{\omega}\right)^{1/2} \frac{k_0^{3/2}}{\left(3r_d^2 b k_0 + 1\right)^{1/2}} \exp\left[-i\int_{-\infty}^{z}\left(k_0 + ik_0''\right)dz' - \frac{k_0}{2b}r^2 - i\,t\,\omega\right] + c.c., \quad (1)$$

where $P' = \kappa P$ is the part of incident power P, which is transfered by excitation of the fundamental radial TG mode (according to [1], $\kappa \approx 0.2$); $\nu_{ea} = 4 \times 10^7$ s^{-1} - the collision frequency of the electrons and argon atoms in initial plasma, r_d - electron Debye length in focal point, k_0 - is the component of wave vector **k** along the exterior magnetic field direction. It is defined in neighbourhood of focal point at m=0 from the equation:

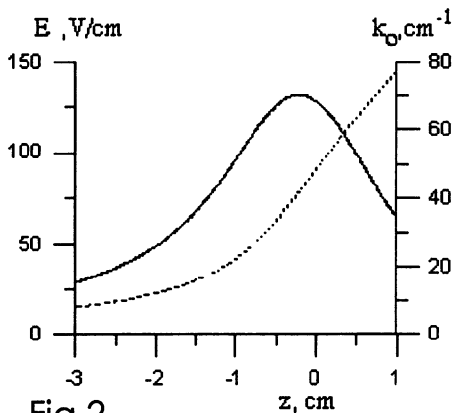

Fig.2

$$3r_d^2 (k_m + ik_m'')^2 - \frac{z}{a} - \frac{2(2m+1)}{(k_m + ik_m'')b} + i\eta'' = 0,$$

were η is the longitudinal dielectric plasma permeability:

$$\eta = 1 - \frac{\omega_{pe}^2(r,z)}{\omega^2} + i\eta'' = \frac{z}{a} + \frac{r^2}{b^2} + i\eta'', \eta'' = \frac{\nu_{ea}}{\omega} - \pi\frac{\omega_{pe}^2}{k_o^2}\frac{\partial f_e}{\partial v}\bigg|_{v=\frac{\omega}{\kappa_o}},$$

where $f_e(v)$ - is the electron distribution function on longitudinal velocities. The damping of oblique electrostatic wave given by:

$$lnb_\ell = -\int_{-\infty}^{z} k''dz' = -(\frac{\nu_{ea}}{\omega})k_o a - \pi a\omega f_e(\omega/k_o).$$

The calculated dependencies of electric field amplitude for $P = 20$ mW (solid curve) and wave vector of OLW are shown on Fig. 2.

The increasing of wave electric field amplitude (in hundreds times in comparison with field in exciting waveguide) occurs because of the group velocity decreasing and propagation channel contraction. It is in the neighbourhood of the focal point that the electron-plasma collision wave absorption and the wave interaction with electrons by Landau damping mechanism are occurred.

The direct measurements of electric field in focal point were not performed, but nonlinear processes, which become apparent at incident power about several milliwatts, are confirming the high value of electric field. So at $P > 10$ mW the parametric decay instability $l \rightarrow l' + s$ develops in vicinity of focal point [3,4].

According to (1), one can evaluate the oscillatory electron energy in OLW field:

$$W_{\sim} = \frac{P'}{\pi\omega n_e} \frac{k^3 exp(-2ak\nu_{ea} / \omega)}{3r_d^2 bk^3 + 1},$$

For the $k \sim 40$ cm^{-1} (it is usual value for OLW in focal point) the $W_{\sim}$(eV) $\approx$ 3,2P(W). If $P = 5$ W the oscillatory energy is equal $W_{\sim} = 16$ eV, that already higher than ionization energy for argon atoms $E_i = 15{,}76$ eV.

Because of longitudinal decelerations, which happens in vicinity of focal point, the phase velocity reaches the values $\omega/k < 4 \times 10^8$ cm/s that is close to electron thermal velocity in initial plasma $v_{Te} \approx 10^8$ cm/s. When $P \sim 20$ W, the electron oscillatory velocity become equal to phase velocity. At this conditions the resonance interaction with plasma electrons and capture of electrons by wave can active occur. The energy of captured electrons one can estimate as W^* (eV) $\approx 90\, P^{0.4}$ (W).

Parameters of microwave pump in experiment: impulse power $P \leq$ 10 kW, impulse duration $t \sim 0{,}1 \div 7$ μs, impulse front duration $t_f \sim 40$ ns, repetition frequency - 300 Hz.

In this investigation we have used the following diagnostics: cavity diagnostic allowing to measure the electron plasma density distribution; optical diagnostics giving the information about the change of the intensity of the integral plasma radiation in visible spectrum range; registration of light radiation spectrum in the range of 400 - 500 nm; multigrid analyzer of charged particles allowing to control the distribution function of the electron component. The information about plasma wave processes was taken from the spectral analysis of scattered microwave signals as well.

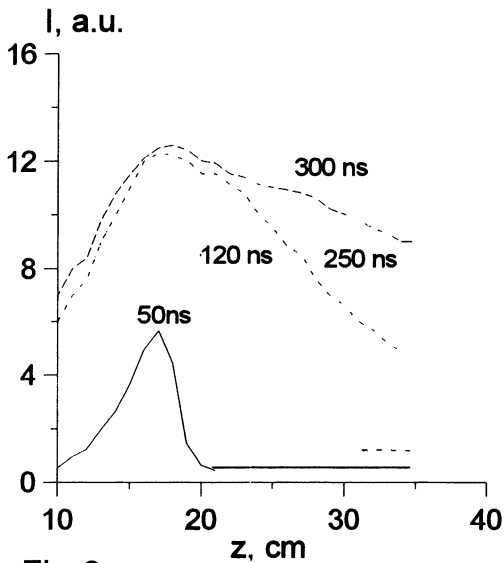

Fig.3

At initial moment (t < 150 ns) the longitudinal distribution maximum of the integral plasma light radiation is located in the area of the critical concentration (Fig. 3). At t > 150 ns there is the growth of the light radiation intensity in the region of smaller concentration of initial plasma. The uniform luminous channel is formed at the impulse end. In a cross direction the distribution of plasma light radiation have the length ~1 mm and then extends by 1,5 - 2 times.

There are low-frequency fluctuations (Fig.4) with frequency 10-20 MHz in detected scattered microwave signal at the moment of formation of the luminous channel (150 ns). Then to the impulse end their frequency decreases to 1 MHz. The similar oscillations are observed on the impulses both of the light radiation and charged particle analyzer current. The low-frequency fluctuations after detection are the result of beating of two waves: wave passed through plasma P_t and wave reradiated to the waveguide tract from plasma P_s (Fig. 1). At spectral analyzis of the signal from waveguide one can observe in spectrum the blue satellite, i.e. the frequency of wave coming out from plasma is higher than pump frequency. The appearance of this effects, as we consider, connected to the modulation of parameters of plasma waveguide at channel formation and with the properties of OLW propagating in it.

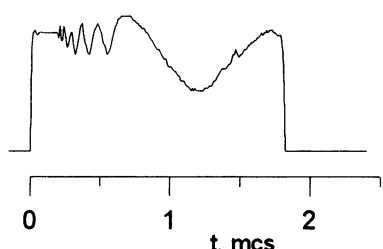

Fig.4

At the start-up of impulse the multigrid analyzer registers a quasi-Maxwell's tail of the accelerated electrons with $T_h \sim 500$ eV. The dependencies of accelerated electron temperature T_h on pump wave power in various time moment from start of impulse are shown on Fig.5. Until $P \sim 0{,}5$ W T_h increases as linear function of P, then the growth rate falls.

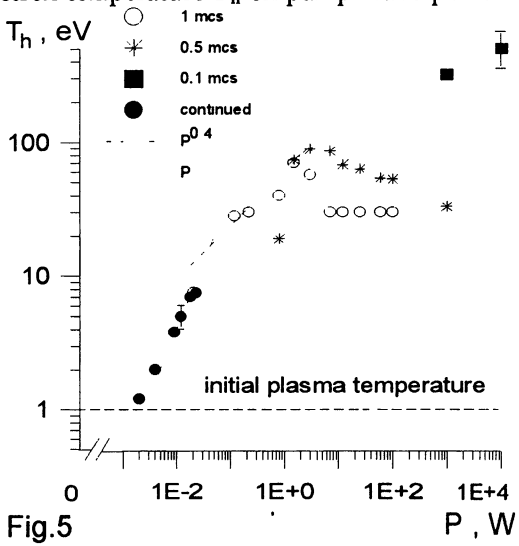

Fig.5

The electron concentration at short impulses (< 400 ns) practically don't varied, when the pump power changes up to some hundreds watt (Fig.6). At the same time the electron concentration has a tendency to the permanent increase during the impulse at duration about few microseconds at lower powers (~ 20 W) . The concentration increase continues after the microwave impulse during the tens microseconds, and then slow plasma decay is observed.

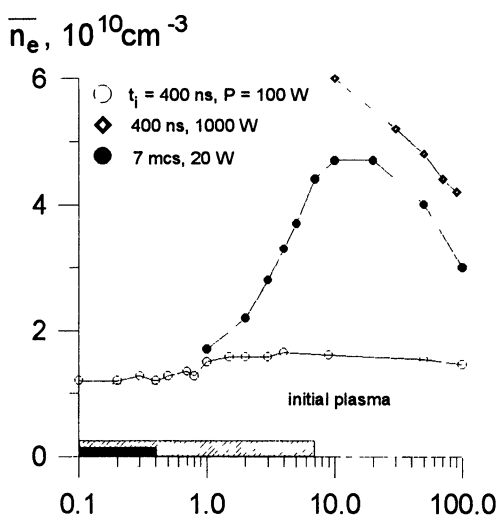

Fig.6

The ion lines are the most intensive at the beginning of impulse (t < 100 ns) and the spectrum is practically consists of Ar^+ lines. The ion lines intensity fall at the impulse end and become weaker than Ar atom lines. One can relate this effect to the decreasing of energy of the accelerated electron at impulse end. The excitation of ions and atoms is likely to happen from the basic state of argon atoms after collisions with accelerated electrons.

The longitudinal

spectral line intensity distribution for ion Ar^+ (454,5 nm ($4s^2P$ -$4p^2P^0$)) in various time moment from start of impulse is presented in Fig.7 (curve 1 - t = 70 ns, 2 - 80 ns, 3 - 100 ns, 4 - 110 ns, 5 - 130 ns, 6 - 180 ns).

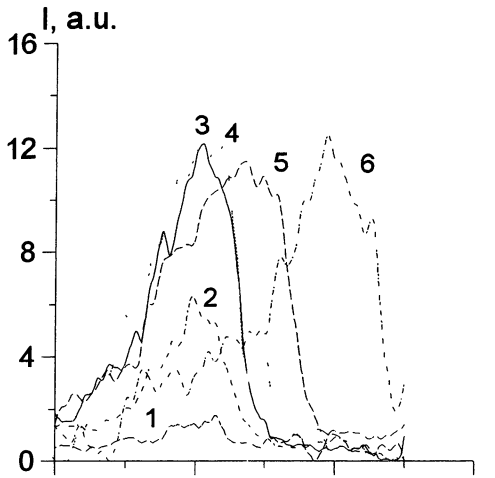

Fig.7

At t < 110 ns, the maximum of intensity is located in the area of focus of initial plasma, similar to the integral light distribution (Fig.3). However, in this case distribution curves have an obviously expressed maximum and their forms are similar to the theoretical picture of electrical field distribution of wave in the area of focus (Fig.2).

Since t > 110 ns, maximum of distribution begins to displace, that is likely to relate with growth of electron concentration and, as a consequence, with displacement of focus point. Knowing the electron concentration distribution in initial plasma n_{eo} and time of displacement of longitudinal intensity distribution maximum τ, it is possible to estimate the ionization frequency in plasma: $\nu_i/p \sim \ln(n_e/n_{eo})/(\tau p) \approx 3\times10^9$ $s^{-1}Torr^{-1}$.

The estimation of ionization frequency have been carried out also, basing on change in time of intensity of a spectral line of ion component I. According to the plasma crown model $I \sim n_e$ and for ionization frequency was received the following value: $\nu_i/p \approx 3{,}5\times10^9$ s^{-1} $Torr^{-1}$, that is close to value already above received from the analysis of focal point displacement.

References

1. Arkhipenko V.I. et al., Sov. J. Plasma Physics, 1981, 7, 396.
2. Budnikov V.N. et al., Sov. J. Plasma Physics, 1980, 6, 1050.
3. Arkhipenko V.I. et al., Sov. J. Plasma Physics, 1987, 13, 693.
4. Arkhipenko V.I. et al., Sov. J. Exp. Theor. Phys., 1987,93, 1221.

NONLINEAR INTERACTIONS OF KDV SOLITONS

G.M.Fraiman [1] and D.N.Ivanychev
Institute of Applied Physics, Russian Academy of Sciences
N.Novgorod, Russia

1 Introduction

One of the most important questions which appears during the analysis of nonlinear nearly integrable systems describing by the partial differential equations, is to develop the perturbation theory to investigate the character of solitons interactions in such systems. At present such methods for investigation of one solitary wave interaction are developed well enough [1]. All of them are based on the "shortcut" differential equations on the solitons parameters (those like solitons mass centers or their velocities etc) obtained in one or another way. The asymptotical methods of the perturbation theory are multivariant but as a rule all of them are based on the assumption about the solitons stability in the consideration of the weak perturbations of them. Herewith, the variational principle which was developed by Whitham [2] acquired the greatest popularity because of its simplicity. The content of its method can be described in the following way. To investigate the nonlinear system dynamics with weakly changing parameters it is necessary to use the variational principle of the corresponding nonperturbed problem generalized to the case of the weak perturbation:

$$\delta S = \delta Q, \tag{1}$$

where $S \equiv \int_{-\infty}^{t} L\,dt$, L is Lagrange function of the nonperturbed problem, and Q is dissipative function which depends on the parameters of the nonperturbed problem. Having made the coefficients standing in front of the corresponding independent variations equal, we immediately obtain the required shortcut equations, which describe the weak evolution of previously standing parameters of nonperturbed problem.

[1] e-mail:fraiman@appl.sci-nnov.ru

The main problem of such an approach is the absence of strong criteria of convergence and the consequent perturbation theory. As far as single-soliton problems are considered, appropriateness of the variational approach for nearly integrable systems was demonstrated by comparing the shortcut equations with those obtained by the exact perturbation theory (IST) in the first order. However, as it will be shown in this paper, this method can fail already when applied the problem of soliton pair interactions.

Constructively in this paper we will demonstrate it on the example of soliton interactions within the frame of equations which are closed to the KdV equation. It's well known that equation

$$u_t + c\,u_x + uu_x + \beta u_{xxx} = 0 \tag{2}$$

describes a wide class of nonlinear wave processes. It generalizes the usual wave equation,

$$u_{tt} - c^2 u_{xx} = 0, \tag{3}$$

for unidirectional waves propagating to the right-hand side of the numerical axis if we take into account the presence of weak media nonlinearity and dispersion. It was shown in [3, 4] that the KdV equation appears in some types of weakly nonlinear and dispersive systems. If we take into account weak viscosity, we immediately obtain the BKdV equation:

$$u_t + c\,u_x + uu_x + u_{xxx} = \mu u_{xx}. \tag{4}$$

Processing the linear substitution of variables in (2) we obtain its more preferable form:

$$u_t - 6uu_x + u_{xxx} = 0. \tag{5}$$

The advantage of this form is in the simplicity of obtaining numerical coefficients in the solution. The processes taking place in this simple system are well studied [10, 7]. The evolution of the initial condition looks like fragmentation into solitary waves moving to the right-hand side of the numerical axis and oscillating tails moving to the left-hand side. If initial condition $u(x,0)$ in the model of equation (5) satisfies the following condition: $\int_{-\infty}^{+\infty} u(x,0)\,dx < 0$, then the oscillating tails will add insufficient deposit to all motion integrals if the ratio

of nonlinearity and dispersion is a big parameter of the problem [7]. If these requirements are satisfied, then we can consider our system using the terms of solitons. Asymptotically, when we tend t to $\pm\infty$, field distribution $u(x;t)$ is splitted into a sequence of infinitely separated solitons with the shape of the single-soliton solution of the KdV-equation with different values of velocities and amplitudes. So we see that the field allows us to describe it using the terms of quasiparticles. The similar approach was demonstrated, for example, in article [1], where the approximation of closed velocities used and the motion equations for soliton-particles are obtained. The authors of this paper considered pair interactions of solitons with closed velocities. It is well known (in the framework of the KdV equation) that in the case of closed velocities, v_1 and v_2, the maximums of the interacting solitons are situated farther than a logarithmical big distance on parameter $v_2 - v_1$. In this case the wave packets can be approximated as a sum of two pure single-soliton solutions of KdV (5):

$$u_{s_j}(x,t) = \frac{-2\kappa_j^2}{\cosh^2 \kappa_j(x - \xi_j(t))}, \qquad \xi \equiv -4\kappa_j^2 t. \tag{6}$$

In the obtained model the authors discovered that solitons repulse and change their initial momentums during interaction. It appeared that in such a model of interaction the asymptotical results are well matched with the results of the exact solution. Namely, the relative soliton shifts before and after interaction are equal to the same shifts yielded by the exact theory in the main order of the perturbation theory by the small parameter of the problem. The weak place of such an approach is as follows: it takes into account only exponentially weak interactions between solitons, so it required particular attention during its application (more completely this question will be discussed in the discussion of the main results).

The reasons for writing this paper were the results of numerical simulations of soliton interaction in the framework of the BKdV equation (7) with weak viscosity.

$$u_t - 6uu_x + u_{xxx} = \mu u_{xx}. \tag{7}$$

We expected that even weak dissipation $\mu \ll \kappa_{1,2}$ (where $k^2 = -\kappa_{1,2}^2$ are lines of discrete spectrum of the Shrödinger's equation

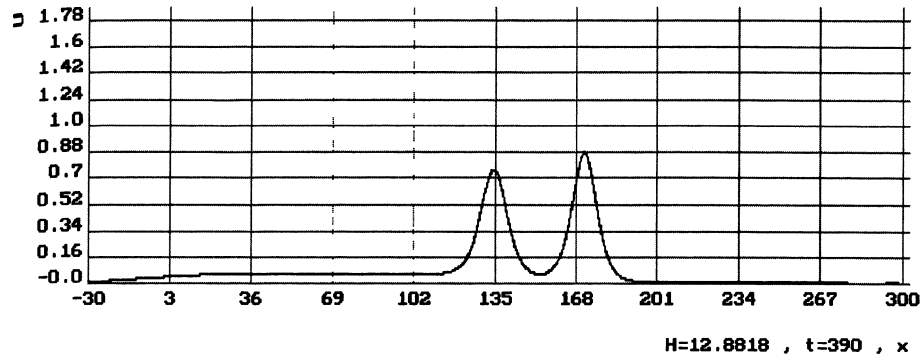

Figure 1: Pair of KdV-solitons

$\psi'' + [k^2 - u(x;t)]\psi = 0$) could decrease relative velocity of solitons if $\mu \sim |\kappa_2 - \kappa_1|$ because of the increasing of gradients of solitons velocitities in the interaction area. In this case a couple of solitons can be born. We saw the predicted effect during numerical simulations: $\kappa_1 = 0{,}5$, $\kappa_2 = 0{,}6$, $\mu = 0{,}05$. In the same experiment but with $\mu = 0{,}001$ the solitons didn't couple and we saw two solitons like in the model of KdV-equation. When making the dissipation coefficient, μ , greater than it was in the first case the coupling were always taking place. The coupling solitons are always construct two-hills nonsymmetrical field distribution with the big front hill like in plot 1.

Such distribution moves and retains its shape. Of course it dissipates in time with a small tail radiating ($|h| \ll 4\kappa_{1,2}^2$) but very slowly. The characteristic cut of time T of dissipation is more greater than characteristic time τ of soliton coupling.

The attempt to describe this effect using the variational method with application of the single-soliton approximation of exact two-solitons solution leads us to the wrong result. The coupling in this model is absent. Thus, we should consider the exact two-solitons solution of (5) to develop a perturbation theory.

In paper [11] the authors developed a perturbation theory for equation (10) based on the IST method and as a simple application

they demonstrated it on a single KdV soliton

$$u_s(x;t) = -2\kappa(t)^2 \operatorname{sech}^2 \kappa(t)(x - s(t)). \tag{8}$$

As the result of this application, two differential equations were obtained. In this paper the soliton parameters were chosen in the same way:

$$u_s = \frac{-2(\kappa_2^2 - \kappa_1^2)}{(\kappa_2 \coth \kappa_2(x-\xi_2) - \kappa_1 \tanh \kappa_1(x-\xi_1))^2} \times \\ \times \left(\frac{\kappa_1^2}{\cosh^2 \kappa_1(x-\xi_1)} + \frac{\kappa_2^2}{\sinh^2 \kappa_2(x-\xi_2)} \right), \tag{9}$$

where $\xi_{1,2} \equiv 4\kappa_{1,2}^2 t$, and $\kappa_2 > \kappa_1$. As the result, the system of four first-order differential equations was obtained. They describe time evolution of parameters $\kappa_{1,2}$ ($4\kappa_{1,2}^2$ mean soliton velocities) and $\xi_{1,2}$ (means solitons coordinates). After some transformations this system can be transformed to the system of two differential equations, which describes fast coupling of solitons.

2 The adiabatic perturbation theory for exact tow-solitons solution of the equation KdV

2.1 IST method

In this section we using the method described in [11] are to develop the perturbation theory for (9) for KdV equation (5) with the weak perturbation term in the right-hand side of it:

$$u_t - 6uu_x + u_{xxx} = \varepsilon R[u]. \tag{10}$$

The weakness of perturbation means that corresponding term is always much less than all other terms in the equation for all values of t and x . In the zero order it is possible to ignore the effect of the perturbation term so we have exact two solitons solution of (5). Evolution of soliton parameters can be described by the following equations: $\dot{\kappa}_{1,2} = 0$ and $\dot{\xi}_{1,2} = 4\kappa_{1,2}^2$. In the next order these

equations will be written in a more exact form. And if the perturbation is weak enough (the soliton velocities weakly change in the time, which solitons move their widths), then this order will be enough to describe coupling effects.

As is well known, equation (5) is the condition of compatibility of auxiliary differential linear equations (11)-(12):

$$\hat{L}\psi = \lambda\psi, \quad \hat{L} = -\frac{\partial^2}{\partial x^2} + u(x,t) \tag{11}$$

$$\psi_t = \hat{A}\psi, \quad \hat{A} = -4\frac{\partial^3}{\partial x^3} + 6u\frac{\partial}{\partial x} + 3u_x. \tag{12}$$

If it is, then the eigenvalues of Shrödinger's operator don't depend on time t. Perturbated equation (10) in terms of operators $\hat{L}$ and $\hat{A}$ is rewritten in this way:

$$\hat{L}_t + [\hat{L}, \hat{A}] = \varepsilon R[u]. \tag{13}$$

In the perturbated case we have the same Shrödinger's equation but now potential function $u(x;t)$ doesn't satisfy the KdV-equation so eigenvalues $-\kappa_{1,2}^2$ now have the temporal dependence (remember that t is only an external parameter in the Shrödinger's equation and not a time).

Let us consider the problem of evaluating the eigenvalues of adjoined Shrödinger's operator $\hat{L}^+$:

$$\hat{L}^+\psi = \lambda^*\psi. \tag{14}$$

Let us suppose that we know the solution of the problem (14): $\tilde{\psi}$. Let us suppose also that $(\tilde{\psi}, \psi) \neq 0$. And now let us multiply equation (13) by $\tilde{\psi}$ from the left side. Following the definition of adjoined operator $(\hat{L}\psi, \tilde{\psi}) = (\psi, \hat{L}^+\tilde{\psi})$ we obtain the following expression:

$$\lambda_t = \varepsilon\frac{(\tilde{\psi}, R[u_s]\psi)}{(\tilde{\psi}, \psi)}. \tag{15}$$

We can observe that if $\varepsilon = 0$ equation (15) gives us the result of nonperturbated case $\frac{\partial}{\partial t}\kappa_{1,2}^2 = 0$. It is not very difficult to check that operator $\hat{L}$ is self-adjoined. In this case we can choose functions

ψ and $\tilde{\psi}$ as Yost's functions of Shrödinger's equation (11) with $\lambda = k^2$: $f(x,k;t)$ and $g(x,k;t)$.

Let us remind some properties of Yost's functions(for more detail see [9, 15, 19]):

$$g(x,k;t) = c_{11}(k)f(x,k;t) + c_{12}f(x,-k;t) \quad (16)$$

$$f(x,k;t) = c_{21}(k)g(x,-k;t) + c_{22}g(x,k;t). \quad (17)$$

Substituting Yost's functions to (15) and setting $\lambda = -\kappa_{1,2}^2$ we obtain the following:

$$\dot{\kappa}_{1,2} = -\frac{\varepsilon}{2\kappa_{1,2}} \frac{\int_{-\infty}^{+\infty} f(x,i\kappa_{1,2};t)R[u_s]g(x,i\kappa_{1,2};t)\,dx}{\int_{-\infty}^{+\infty} f(x,i\kappa_{1,2};t)g(x,i\kappa_{1,2};t)\,dx}. \quad (18)$$

Equations (18) are insufficient to describe the dynamics of the two-solitonian system. We should find also the equations for $\xi_{1,2}$.

Let us differentiate equation (11) with respect for t . We obtain $\hat{L}_t\psi + \hat{L}\psi_t = \lambda_t\psi + \lambda\psi_t$. Substituting the value of $\hat{L}_t\psi$ from (13) we obtain the following equation:

$$(\hat{L} - \lambda)(\psi_t - \hat{A}\psi) = \lambda_t\psi - \varepsilon R[u_s]\psi. \quad (19)$$

Let us consider function $\Phi \equiv \psi_t - \hat{A}\psi$. It satisfies the following linear nonhomogeneous differential equation:

$$(\hat{L} - \lambda)\Phi = \lambda_t - \varepsilon R[u_s]\psi \quad (20)$$

The homogeneous equation corresponding to (20), $(\hat{L} - \lambda)\Phi = 0$, looks like Shrödinger's equation $\frac{\partial^2\Phi}{\partial x^2} + (k^2 - u)\Phi = 0$ with unknown potential $u(x;t)$. All we know about it now is $u(x,t)|_{x\to\pm\infty} \to 0$. In this case operator $\hat{A}$ has the following asymptotical value: $\hat{A}\Big|_{x\to\pm\infty} = -4\frac{\partial^3}{\partial x^3}$. Let us consider the solution of the nonhomogeneous equation corresponding to Yost's function $g(x,k;t)$, which possess the following property: $\lim\limits_{x\to-\infty} g(x,k;t) = e^{-ikx}$. Writing ψ in the form $h(t)g(x,k;t)$ and setting $x \to -\infty$ we obtain

$$\Phi = \psi_t - \hat{A}\psi = (h_t + 4ik^3h)e^{-ikx}. \quad (21)$$

Let us suppose that $h(t)$ has the form of $h(0)e^{ik^3t}$. In this case Φ tends to zero if $x \to -\infty$. If the perturbation coefficient tends to zero then equation (20) gives us the solution: $\lambda_t = 0$.

On the other hand, setting $x \to +\infty$ and using Yost's functions' properties (16) we obtain the following form for function Phi :

$$\Phi \to h(t)[c_{12t}e^{-ikx} + (c_{11t} - 8ik^3c_{11})e^{ikx}]. \tag{22}$$

For the arbitrary values of x we can write the solution of non-homogeneous equation in the form of linear combination of Yost's functions $f(x,k;t)$ and $g(x,k;t)$:

$$\Phi = \alpha(x,k;t)f(x,k;t) + \beta(x,k;t)g(x,k;t). \tag{23}$$

Varying arbitrary constants α and β we obtain the following differential equations for them:

$$\alpha = \frac{h(t)}{2ikc_{12}} \int_{-\infty}^{x} (\lambda_t - \varepsilon R[u_s])[g(x',k;t)]^2\,dx' \tag{24}$$

$$\beta = -\frac{h(t)}{2ikc_{12}} \int_{-\infty}^{x} (\lambda_t - \varepsilon R[u_s])f(x',k;t)g(x',k;t)\,dx' \tag{25}$$

Now let us use the boundary conditions (22) for function Φ with found coefficients α and β . If $x \to +\infty$, then

$$\Phi = \alpha e^{ikx} + \beta(c_{11}e^{ikx} + c_{12}e^{-ikx}) =$$
$$= \tfrac{h(t)}{2ikc_{12}} \left[e^{ikx} \textstyle\int_{-\infty}^{+\infty} e^{ikx}(\lambda_t - \varepsilon\ R[u_s])g(g - c_{11}f)\,dx + \right.$$
$$\left. + e^{-ikx}c_{12} \textstyle\int_{-\infty}^{+\infty} (\lambda_t - \varepsilon R[u_s])fg\,dx'.\right.$$

Equating the coefficients before the same exponents from the last equation and from (22) we obtain the differential equations for scattering coefficients $c_{11}(k;t)$ and $c_{12}(k;t)$:

$$c_{11t} - 8ik^3c_{11} = -\frac{i}{2k}\int_{-\infty}^{+\infty} (\lambda_t - $$
$$-\varepsilon R[u_s])f(x,-k;t)g(x,k;t)\,dx, \tag{26}$$

$$c_{12t} = \frac{i}{2k}\int_{-\infty}^{+\infty} (\lambda_t - \varepsilon R[u_s])f(x,k;t) \times$$
$$\times g(x,k;t)\,dx. \tag{27}$$

Function $f(x-k;t)$ has a singularity with $k = i\kappa_{1,2}$ (for the example see [15]). It will be clear when we write functions f and g in the obvious form. Using equation (16) for $g(x,k;t)$ we obtain

$$f(x,-k;t) = \frac{g(x,k;t) - c_{11}(k;t)f(x,k;t)}{c_{12}(k;t)}. \tag{28}$$

As we see, this fraction is of the $\frac{0}{0}$ type. Solving it and tending k to $i\kappa_{1,2}$ we find the following equations for c_{11} :

$$\begin{aligned} c_{11t} - 8ik^3 c_{11} \quad = \quad & -\frac{\varepsilon}{2\kappa_{1,2}\dot{c}_{12}(i\kappa_{1,2})}\int_{-\infty}^{+\infty} R[u_s]g(i\kappa_{1,2}) \times \\ & \times \frac{d}{dk}[g(k) - c_{11}(i\kappa_{1,2})f(k)]_{k=i\kappa_{1,2}}\,dx, \end{aligned} \tag{29}$$

where the dot means differentiating by k for brevity.

If $k = i\kappa_{1,2}$ then the Yost's functions aren't linear independent

$$g(x,i\kappa_{1,2};t) = c_{11}f(x,i\kappa_{1,2};t). \tag{30}$$

We can find Yost's functions of nonperturbated problem and giving $k = i\kappa_{1,2}$ we automatically obtain the value of $c_{11}(i\kappa_{1,2}$. For the last one we have differential equation (29) but c_{11} depends of $\xi_{1,2}$ so we find the differential equations for them. Now we found a full system of differential equations, which describes the dynamics of the two-solitonian solution of the KdV equation in the media with weak dissipation. Now we have to do some evaluations for the BKdV model.

Let us find Yost's functions of the two-solitonian potential. We use Crum's method to find them. As you know, Yost's functions of Shrödinger's equation with a trivial potential $u(x;t) \equiv 0$ have the following form: $f_0(x,k;t) = e^{+ikx}$, $g_0(x,k;t) = e^{-ikx}$. After applying Crum's transformation of the second order for them, we obtain the linear independent functions satisfying the Shrödinger's equation with the two-solitonian potential (9):

$$\begin{Bmatrix} \tilde{f}_2(x,k;t) \\ \tilde{g}_2(x,k;t) \end{Bmatrix} =$$

$$\left\{\begin{matrix}\mathcal{A}\\ \mathcal{B}\end{matrix}\right\} e^{\pm ikx} \frac{\begin{vmatrix} \cosh\kappa_1(x-\xi_1) & \sinh\kappa_2(x-\xi_2) & 1 \\ \kappa_1\sinh\kappa_1(x-\xi_1) & \kappa_2\cosh\kappa_2(x-\xi_2) & \pm ik \\ \kappa_1^2\cosh\kappa_1(x-\xi_1) & \kappa_2^2\sinh\kappa_2(x-\xi_2) & -k^2 \end{vmatrix}}{\begin{vmatrix} \cosh\kappa_1(x-\xi_1) & \sinh\kappa_2(x-\xi_2) \\ \kappa_1\sinh\kappa_1(x-\xi_1) & \kappa_2\cosh\kappa_2(x-\xi_2) \end{vmatrix}}. \tag{31}$$

If we find constantants $\mathcal{A}$ and $\mathcal{B}$ from the following conditions:

$$\mathcal{A}\tilde{f}_2\Big|_{x\to+\infty} = e^{ikx} \quad , \quad \mathcal{B}\tilde{g}_2|_{x\to-\infty} = e^{-ikx}, \tag{32}$$

then $\tilde{f}$ and $\tilde{g}$ are the Yost's functions which we are interested in. They can be written in the following form:

$$f(x,i\kappa_1;t) = \frac{\kappa_2-\kappa_1}{2}e^{-i\kappa_1\xi_1}\frac{\sinh z_2}{\gamma}, \tag{33}$$

$$g(x,i\kappa_1;t) = -\frac{\kappa_2-\kappa_1}{2}e^{i\kappa_1\xi_1}\frac{\sinh z_2}{\gamma}, \tag{34}$$

$$f(x,i\kappa_2;t) = \frac{\kappa_2-\kappa_1}{2}e^{-i\kappa_2\xi_2}\frac{\cosh z_1}{\gamma}, \tag{35}$$

$$f(x,i\kappa_2;t) = \frac{\kappa_2-\kappa_1}{2}e^{i\kappa_2\xi_2}\frac{\cosh z_1}{\gamma}, \tag{36}$$

$$\gamma \equiv \kappa_2\cosh z_1\cosh z_2 - \kappa_1\sinh z_1\sinh z_2.$$

Then, following our method, which we already discussed, it is necessary to evaluate coefficients $c_{11}(i\kappa_1)$ и $c_{11}(i\kappa_2)$:

$$c_{11}(i\kappa_1) = \frac{g(x,i\kappa_1;t)}{f(x,i\kappa_1;t)} = -e^{2\kappa_1\xi_1}, \tag{37}$$

$$c_{11}(i\kappa_2) = \frac{g(x,i\kappa_2;t)}{f(x,i\kappa_2;t)} = e^{2\kappa_2\xi_2}. \tag{38}$$

Expression $\frac{1}{c_{12}(k)}$ is nothing but passing coefficient $T(k)$ for the wave going with wave vector k through the two-solitonian potential, $u_s(x;t)$. Formula for $T(k)$ for the nonreflective potentials is well known:

$$T(k) = \frac{1}{c_{12}(k)} = \frac{(k+i\kappa_1)(k+i\kappa_2)\dots(k+i\kappa_N)}{(k-i\kappa_1)(k-i\kappa_2)\dots(k-i\kappa_N)}. \tag{39}$$

In our case the value of $\dot{c}_{12}(k)$ given with $k = i\kappa_{1,2}$

$$\left.\frac{dc_{12}(k)}{dk}\right|_{k=i\kappa_1} = -\frac{\kappa_2-\kappa_1}{\kappa_2+\kappa_1}\frac{1}{2i\kappa_1}, \tag{40}$$

$$\left.\frac{dc_{12}(k)}{dk}\right|_{k=i\kappa_2} = \frac{\kappa_2-\kappa_1}{\kappa_2+\kappa_1}\frac{1}{2i\kappa_2}. \tag{41}$$

We will skip very long evaluations of expressions $\frac{d}{dk}[g(k) - c_{11}(i\kappa_{1,2})f(k)]_{k=i\kappa_{1,2}}$ and just write the result:

$$\xi_{1t} = 4\kappa_1^2 + \frac{\varepsilon}{8\kappa_1^4}\int_{-\infty}^{+\infty} R[u_s]u_1(x,t)\{z_1 + \\ + \frac{1}{2}\frac{\kappa_2^2+\kappa_1^2}{\kappa_2^2-\kappa_1^2}\sinh 2z_1 - \frac{2\kappa_1\kappa_2}{\kappa_2^2-\kappa_1^2}\coth z_2\cosh^2 z_1\Big\}\,dx, \tag{42}$$

$$\xi_{2t} = 4\kappa_2^2 + \frac{\varepsilon}{8\kappa_2^4}\int_{-\infty}^{+\infty} R[u_s]u_2(x,t)\{z_2 + \\ + \frac{1}{2}\frac{\kappa_2^2+\kappa_1^2}{\kappa_2^2-\kappa_1^2}\sinh 2z_2 - \frac{2\kappa_1\kappa_2}{\kappa_2^2-\kappa_1^2}\tanh z_1\sinh^2 z_2\Big\}\,dx, \tag{43}$$

where functions $u_1(x;t)$ and $u_2(x;t)$ are defined as following:

$$u_1(x,t) \equiv -8\kappa_1^2\frac{\kappa_1+\kappa_2}{\kappa_1-\kappa_2}f(x,i\kappa_1;t)g(x,i\kappa_1;t) \tag{44}$$

$$u_2(x,t) \equiv -8\kappa_2^2\frac{\kappa_2+\kappa_1}{\kappa_2-\kappa_1}f(x,i\kappa_2;t)g(x,i\kappa_2;t) \tag{45}$$

Transformed equations (18) in the new terms have the following form:

$$\kappa_{1t} = \frac{\varepsilon}{8\kappa_1^2}\int_{-\infty}^{+\infty} R[u_s]u_1(x,t)\,dx \tag{46}$$

$$\kappa_{2t} = \frac{\varepsilon}{8\kappa_2^2}\int_{-\infty}^{+\infty} R[u_s]u_2(x,t)\,dx. \tag{47}$$

Together equations (46), (47), (42) and (43) are the full system of differential equations which describes dynamic of two solitons in dissipative medias. We will point out the properties of functions $u_{1,2}$ [19]:

1. Two-solitons solution $u_s(x;t)$ is the exact sum of field clots $u_1(x;t)$ and $u_2(x;t)$.

2. Asymptotically, with $t \to \pm\infty$, functions $u_{1,2}(x;t)$ have the form of pure single-solitonian solutions of the KdV equation:

$$u_1(x,t)|_{t\to\pm\infty} = \frac{-2\kappa_1^2}{\cosh^2(\kappa_1 x - 4\kappa_1^3 t \mp \ln \frac{1}{2}\frac{\kappa_2+\kappa_1}{\kappa_2-\kappa_1})}, \quad (48)$$

$$u_2(x,t)|_{t\to\pm\infty} = \frac{-2\kappa_2^2}{\cosh^2(\kappa_2 x - 4\kappa_2^3 t \pm \ln \frac{1}{2}\frac{\kappa_2+\kappa_1}{\kappa_2-\kappa_1})}. \quad (49)$$

3. Field clots $u_{1,2}(x;t)$ save wave momentums of each soliton:

$$\int_{-\infty}^{+\infty} u_{1,2}(x,t)\,dx = -4\kappa_{1,2}. \quad (50)$$

4. The soliton coordinates defined as the average value of x with distribution functions $u_{1,2}(x;t)$ have the following dependence on time:

$$< x_1 > \equiv \frac{\int_{-\infty}^{+\infty} x u_1(x,t)\,dx}{\int_{-\infty}^{+\infty} u_1(x,t)\,dx} = 4\kappa_1^2 t - \frac{1}{2\kappa_1}\ln\frac{\kappa_2+\kappa_1}{\kappa_2-\kappa_1} \times$$
$$\times \tanh\left[c_2(\kappa_1,\kappa_2)(\kappa_2-\kappa_1)t\right], \quad (51)$$

$$< x_2 > \equiv \frac{\int_{-\infty}^{+\infty} x u_2(x,t)\,dx}{\int_{-\infty}^{+\infty} u_2(x,t)\,dx} = 4\kappa_2^2 t + \frac{1}{2\kappa_2}\ln\frac{\kappa_2+\kappa_1}{\kappa_2-\kappa_1} \times$$
$$\times \tanh\left[c_2(\kappa_1,\kappa_2)(\kappa_2-\kappa_1)t\right], \quad (52)$$

where $c_2(\kappa_1,\kappa_2)$ is a certain function, which is symmetrical by places exchanging of its arguments.

If we understand these coordinates as solitonian ones, then in this system solitons are attracting during interaction (see fig. 2).

All of these properties can be generalized for the N–solitonian case but field clots $\{u_1, u_2, \ldots, u_N\}$ now must be defined as follows:

$$u_j \equiv -8\kappa_j^2 \left(\prod_{\substack{s=1\\ s\neq j}}^{N} \frac{\kappa_j+\kappa_s}{\kappa_j-\kappa_s}\right) f(x,i\kappa_j;t)g(x,i\kappa_j;t) \quad , \quad j = 1\ldots N, \quad (53)$$

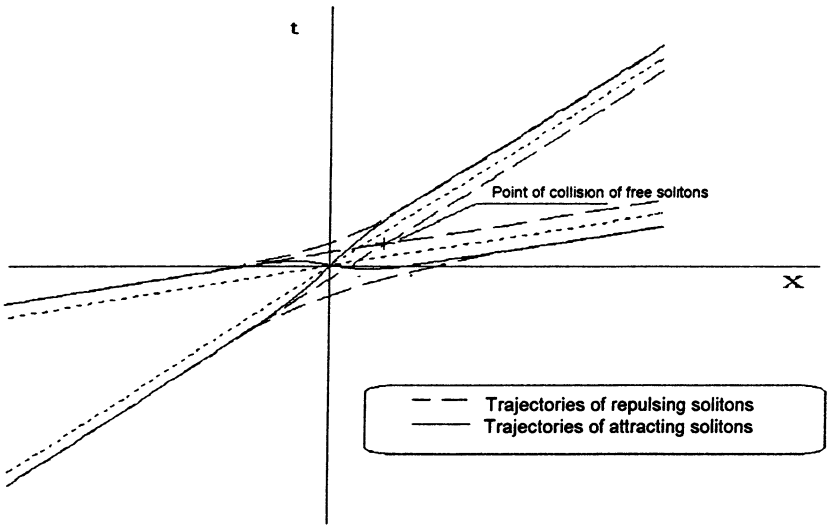

Figure 2: Solitons trajectories

where f and g now are Yost's functions of the N–solitonian potential of Shrödinger's equation. Using the terms of ψ –functions the previous property can be rewritten as the following theorem

Theorem 1 *The arbitrary nonreflective potential* $u(x;t)$ *of Shrödinger's equation* $\psi'' + (-\kappa^2 - u(x,t))\psi = 0$, *where* t *is external parameter, can be represent in the following combination of* υ *– functions of the discrete spectrum:*

$$u(x;t) \equiv -4 \sum_{s=1}^{N} \kappa_s |\psi_s(x,t)|^2, \tag{54}$$

where N *is number of discrete levels and* $-\kappa_s^2$ *are discrete levels in potential* $u_s(x;t)$.

This property was pointed by Deift and Trubowitz [20]. Indeed, because the eigenfunctions of operator $\hat{L}$ are the full closed system of functions, their squares are the full closed system of functions too. So the arbitrary function, which satisfies some conditions [20] on the

infinity can be written in the form of these functions series. This function can be $u(x;t)$ too. Property 4 needs to be slightly redefined. N solitonian coordinates $< x_J >$, $j = 1 \ldots N$ defined in analogy with the property 4 ($\kappa_1 < \kappa_2 < \ldots < \kappa_N$) have the following evolution:

$$< x_j >= 4\kappa_j^2 t + \frac{1}{2} \sum_{\substack{s=1 \\ s \neq j}}^{N} \ln \left| \frac{\kappa_j + \kappa_s}{\kappa_j - \kappa_s} \right| \tanh \left[c_N(\kappa_j, \kappa_s)(\kappa_j - \kappa_s)t \right],$$

$$j = 1 \ldots N. \tag{55}$$

Thus in terms of soliton mass centers the exact N–solitons problem in the framework of the KdV equation the soliton interaction is constructed of pair solitons interactions. Previously this result was known for asymptotical data about solitons coordinates' shifts [10].

2.2 Whitham's variational method

Let us find the Lagrangian function of the KdV equation (5). We need consider not function $u(x;t)$ but potential function $\Phi(x;t)$ which could be defined as the follows: $u(x,t) = \frac{\partial \Phi(x,t)}{\partial x}$. In new definitions equation (5) has the following form:

$$\Phi_{xt} - 6\Phi_x \Phi_{xx} + \Phi_{xxxx} = 0. \tag{56}$$

It is clear that the Lagrangian function has to depend on the following variables: Φ_x , Φ_t and Φ_{xx} . If it is right, then the minimal action principle $\delta \int_0^t \int_{-\infty}^{+\infty} L(\Phi_t, \Phi_x, \Phi_{xx})\, dxdt = 0$ gives us the following Euler's equation:

$$- \frac{d}{dt} \frac{\partial L}{\partial \Phi_t} - \frac{d}{dx} \frac{\partial L}{\partial \Phi_x} + \frac{d^2}{dx^2} \frac{\partial L}{\partial \Phi_{xx}} = 0. \tag{57}$$

Having compared equations (56) and (57) we can immediately write the Lagrangian function in which we are interested in:

$$L = \int_{-\infty}^{+\infty} \left(-\frac{1}{2} \Phi_x \Phi_t + \Phi_x^3 + \frac{1}{2} \Phi_{xx}^2 \right) dx. \tag{58}$$

And now, to obtain the motion equations for solitons, we should substitute the N–solitonian solution of the KdV equation $u_s(x;t)$ to

the Lagrangian function, which we have found. In our case we should substitute two-solitonian solution. After evaluation of all integrals we obtain the following Lagrangian function of the two-solitonian system:

$$L = \frac{8}{3}\kappa_1^3\dot{\xi}_1 - \frac{32}{5}\kappa_1^3 + \frac{8}{3}\kappa_2^3\dot{\xi}_2 - \frac{32}{5}\kappa_2^3 = L_1 + L_2, \qquad (59)$$

where L_1 and L_2 are Lagrangian functions of single-solitonian systems. We can see that in these generalized coordinates the solitons are independent because there is no interaction term in the Lagrangian function of two solitons. Varying L by soliton parameters we obtain:

$$\delta \int_0^t L\,dt = \int_0^t \left[8\kappa_1^2(\dot{\xi}_1 - 4\kappa_1^2)\delta\kappa_1 - \frac{d}{dt}\left(\frac{8}{3}\kappa_1^3\right)\delta\xi_1 + \right.$$
$$\left. + 8\kappa_2^2(\dot{\xi}_2 - 4\kappa_2^2)\delta\kappa_2 - \frac{d}{dt}\left(\frac{8}{3}\kappa_2^3\right)\delta\xi_2\right] dt = 0 \qquad (60)$$

Having equated coefficients standing before the independent variations to zero we obtain the motion equations:

$$\dot{\kappa}_{1,2} = 0 \qquad (61)$$
$$\dot{\xi}_{1,2} = 4\kappa_{1,2}^2. \qquad (62)$$

It was the result for nonperturbated system of two solitons. But the small perturbation term standing in the right-hand side of equation (10) changes the form of obtained equations (61) and (62). If the perturbation term can be written in the form of full variation of certain function L_{int}, then our problem could be solved exactly using the previously discussed concept. But it is necessary to change L to $\tilde{L} \equiv L - L_{int}$ everywhere.

In the majority of cases the perturbation term cannot be presented like variation of L_{int} and we have to develop the sequential approximations method to obtain the motion equations. If the right-hand part of (10) is weaker than other terms in it, then in the zero approximation we can consider the nonperturbed KdV equation. As a solution we take of course the two-solitonian solution $u_s(x;t)$. In the next approximation the solitonian parameters become weak functions of time t (we already discussed the meaning of weakness). We

cannot find the motion equation using the minimal action principle. It doesn't work for our equation (10). But it can be generalized to this way: $\delta L = \delta' Q$, where $\delta' Q$ is incomplete variation of dissipative function Q :

$$\delta' Q = \int_{-\infty}^{+\infty} \varepsilon R[u_s]\delta\Phi\, dx = \varepsilon \int_{-\infty}^{+\infty} R[\Phi_s] \left(\frac{\partial \Phi_s}{\partial \kappa_1}\delta\kappa_1 + \right.$$
$$\left. + \frac{\partial \Phi_s}{\partial \kappa_2}\delta\kappa_2 + \frac{\partial \Phi_s}{\partial \xi_1}\delta\xi_1 + + \frac{\partial \Phi_s}{\partial \xi_2}\delta\xi_2 \right) dx, \qquad (63)$$

where potential Φ can be evaluated directly after integrating $u_s(x;t)$ The partial derivatives in the right-hand side of (63) can be evaluated very simply:

$$\frac{\partial \Phi_s}{\partial \kappa_1} = \frac{(-2)(\kappa_2^2 - \kappa_1^2)}{\cosh^2 z_1 (\kappa_1 \tanh z_1 - \kappa_2 \coth z_2)^2} \times$$
$$\times \left[\frac{1}{2} \frac{\kappa_2^2 + \kappa_1^2}{\kappa_2^2 - \kappa_1^2} \sinh 2z_1 - \frac{2\kappa_1\kappa_2}{\kappa_2^2 - \kappa_1^2} \coth z_2 \cosh^2 z_1 + z_1 \right], \qquad (64)$$

$$\frac{\partial \Phi_s}{\partial \kappa_2} = \frac{(-2)(\kappa_2^2 - \kappa_1^2)}{\sinh^2 z_2 (\kappa_1 \tanh z_1 - \kappa_2 \coth z_2)^2} \times$$
$$\times \left[\frac{1}{2} \frac{\kappa_2^2 + \kappa_1^2}{\kappa_2^2 - \kappa_1^2} \sinh 2z_2 - \frac{2\kappa_1\kappa_2}{\kappa_2^2 - \kappa_1^2} \tanh z_1 \sinh^2 z_2 + z_2 \right], \qquad (65)$$

$$\frac{\partial \Phi_s}{\partial \xi_1} = -u_1(x,t), \qquad (66)$$

$$\frac{\partial \Phi_s}{\partial \xi_2} = -u_2(x,t). \qquad (67)$$

And now, having written the generalized minimal action principle we immediately obtain the final motion equations:

$$\dot{\kappa}_1 = \frac{\epsilon}{8\kappa_1^2} \int_{-\infty}^{+\infty} R[u_s]u_1(x,t)dx,$$
$$\dot{\kappa}_2 = \frac{\epsilon}{8\kappa_2^2} \int_{-\infty}^{+\infty} R[u_s]u_2(x,t)dx, \qquad (68)$$

$$\dot{\xi}_1 = 4\kappa_1^2 + \frac{\varepsilon}{8\kappa_1^4} \int_{-\infty}^{+\infty} R[u_s]u_1(x,t)\,\{z_1 +$$

$$+\frac{1}{2}\frac{\kappa_2^2+\kappa_1^2}{\kappa_2^2-\kappa_1^2}\sinh 2z_1 - \frac{2\kappa_1\kappa_2}{\kappa_2^2-\kappa_1^2}\coth z_2 \cosh^2 z_1\Bigg\} dx,$$

$$\dot{\xi}_2 = 4\kappa_2^2 + \frac{\varepsilon}{8\kappa_2^4}\int_{-\infty}^{+\infty} R[u_s]u_2(x,t)\{z_2+$$

$$+\frac{1}{2}\frac{\kappa_2^2+\kappa_1^2}{\kappa_2^2-\kappa_1^2}\sinh 2z_2 - \frac{2\kappa_1\kappa_2}{\kappa_2^2-\kappa_1^2}\tanh z_1 \sinh^2 z_2\Bigg\} dx, \tag{69}$$

which are fully analogous to those we obtained in the previous section.

Thus, we obtained the equivalent results using two methods for the KdV solitons in dissipative media. It is obvious that the variational method yielded results quicker and easier. Karpman's theory way is rather difficult from the technical point of view and its difficulty increases very strongly when the number of solitons increases.

3 Solitons coupling in the BKdV equation

In this section we will apply our common results to the case of BKdV-equation (7). In this case perturbation term $R[u_s]$ standing in equations (42), (43), (46), (47) has the form μu_{sxx} . We will consider the case of close soliton velocities: $\ln\frac{\kappa_2+\kappa_1}{\kappa_2-\kappa_1} \gg 1$.

First, let us consider the case of the exact 2-solitons solution approximation by the sum of sufficiently distanced exact KdV-solitons.

$$u_s(x,t) = -\frac{2\kappa_1^2}{\cosh^2\kappa_1(x-s_1)} - \frac{2\kappa_2^2}{\cosh^2\kappa_2(x-s_2)} \tag{70}$$

The lagrangian of this problem has the following form [1]:

$$L = \frac{8}{3}\kappa_1^3\dot{s}_1 + \frac{8}{3}\kappa_2^3\dot{s}_2 - \frac{32}{5}\kappa_1^5 - \frac{32}{5}\kappa_2^5 - 256\bar{\kappa}^5 e^{-2\bar{\kappa}|s_2-s_1|}. \tag{71}$$

Here $\bar{\kappa} = (\kappa_1+\kappa_2)/2$ is constant of time and $s = s_2-s_1$ is less than zero all time. The exponential term corresponds to the potential energy of solitons interaction and it corresponds to their repulsing when viscosity is absent. Having calculated the variation of the dissipative function using formula (63) and applying the variational method we

obtain after some transformations:

$$\dot{\kappa}_\delta = -\frac{8}{5}\mu\bar{\kappa}^2\kappa_\delta + 64\bar{\kappa}^4(\bar{\kappa}s)e^{-2\bar{\kappa}|s|}, \quad (72)$$

$$\dot{s} = 8\bar{\kappa}\kappa_\delta - 32\mu\bar{\kappa}(\bar{\kappa}s)^2 e^{-2\bar{\kappa}|s|}. \quad (73)$$

The stationary point of such problem is absent.

The situation can be saved if we consider the existence of nonsolitonian tails between interacting solitons. If we consider the tail which is radiated by the right-hand soliton in the form, $-\kappa_2 \tanh \kappa_2(x-\xi_2)$ then the system transforms to the following one:

$$\dot{\kappa}_\delta = -\frac{8}{5}\mu\bar{\kappa}^2\kappa_\delta + 64\bar{\kappa}^4(\bar{\kappa}s)e^{-2\bar{\kappa}|s|}, \quad (74)$$

$$\dot{s} = 8\bar{\kappa}\kappa_\delta + \frac{2}{5}\mu\bar{\kappa}. \quad (75)$$

The last system possesses two stationary points of different type of stability, which need to observe the coupling.

Now we consider the exact 2-soliton solution in the perturbation theory. In the case of closed velocities the right-hand parts of the motion equations can be simplified. Let us subtract equation (47) from equation (46). We obtain

$$\dot{\kappa}_\delta = \frac{\mu}{8\bar{\kappa}^2}\int_{-\infty}^{+\infty}(u_2 - u_1)u_{sxx}\,dx = -\frac{\mu}{8\bar{\kappa}^2}\int_{-\infty}^{+\infty}(u_{2x}^2 - u_{1x}^2)\,dx. \quad (76)$$

If the solitons are sufficiently distanced then we can talk about independent solitons. Taking into account relation $\kappa_2 > \kappa_1$ we could say that the integral standing in the right-hand side of equation (76) is positive. During the interaction of solitons this integral can change its sign if the eigenvalues $-\kappa_1^2$ and $-\kappa_2^2$ are close enough. This fact can be explained in the following way. If $\kappa_1 \approx \kappa_2$ and $t \approx 0$ then functions $u_{1,2}(x;t)$ have approximately the identical shape. The area of sufficiently different behavior placed near the point of their symmetry as you can see in plot 3, where $\kappa_1 = 0{,}3$, $\kappa_2 = 0{,}305$, $t = 0$. Function u_1 equal to zero in the certain point on the x - axis (when $t = 0$ it is point $x = 0$) and function u_2 has no such points at all. This fact follows from the oscillating theorem of quantum mechanics because the eigenvalue $-\kappa_2^2$ corresponds to

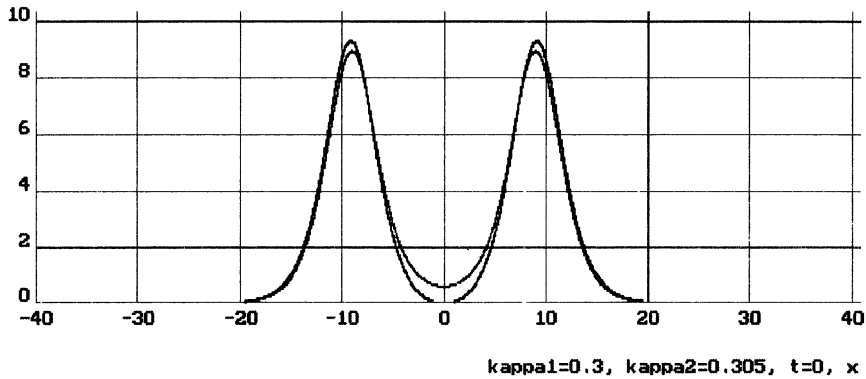

Figure 3: Functions $-u_{1,2}$ in the interaction area

the lowest discrete level and $-\kappa_1^2$ corresponds to the next one. In the area, which we mentioned before, the value of u_{1x}^2 is mainly greater than u_{2x}^2 , so the integral in (76) can be negative sometimes. Evaluating it, within our approximation of closed velocities we obtain

$$\dot{\kappa}_\delta = \frac{8}{5}\mu\bar{\kappa}^2\kappa_\delta \ln\frac{4\bar{\kappa}}{\kappa_\delta}. \tag{77}$$

Equation (76) can be rewritten in the following way:

$$\dot{\kappa}_\delta = -\frac{8}{5}\mu\bar{\kappa}^2\kappa_\delta F(\bar{\kappa},\delta), \tag{78}$$

where function F were calculated by us and has the shape of a bell. You can see in plot4($\kappa_1 = 0{,}3$, $\kappa_2 = 0{,}301$). Here are some properties of this function:

- If $|\bar{\kappa}(\xi_2 - \xi_1)| \gg 1$, then $F = -1$. If $\xi_2 - \xi_1 = 0$, then $F \approx \frac{1}{3}\ln\frac{4\bar{\kappa}}{\kappa_\delta}$.
- The characteristic scale of function F is $\bar{\kappa}^{-1}$ and it does not depend on κ_δ . This fact was checked by us during a great number of numerical simulations.

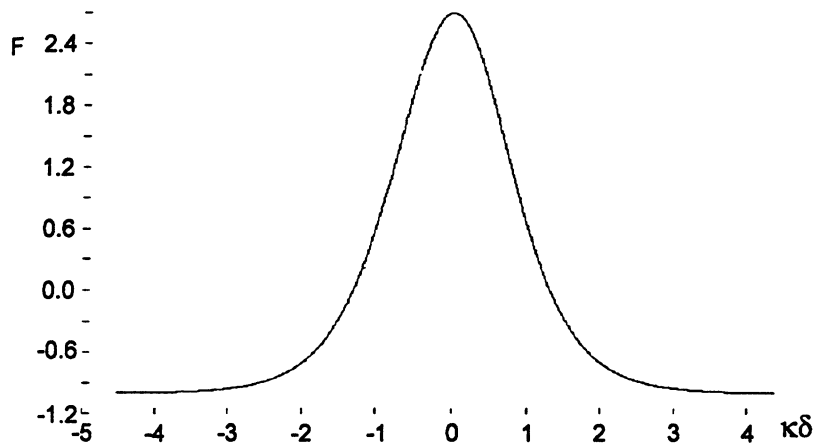

Figure 4: Function F

Equating the right part of equation (78) to zero we obtain motionless point δ^* : $F(\bar{\kappa}, \delta^*) = 0$.

And now let us subtract equation (42) from equation (43) but before this we should point out, that if solitons velocities are closed we can say that the shapes of functions $u_{1,2}(x;t)$ are approximately identical in the small neighborhood of point $\delta = 0$ ($|\delta| \ll \bar{\kappa} \ln \frac{2\bar{\kappa}}{\kappa_\delta}$), the value of expression in brackets is changing more sufficiently in this neighborhood of $\delta = 0$. So this part will determine the dependence of integral on δ :

$$\dot{\delta} = 8\bar{\kappa}\kappa_\delta + \mu G(\bar{\kappa}\delta). \tag{79}$$

The integral standing in the right-hand side of (79) is not calculated analytically too. Function G is shown in Fig. 5. It has characteristic scale $\bar{\kappa}\delta$ in the framework of our assumptions about soliton velocities. Let us approximate the linear part of function G in the neighborhood of point $\delta = 0$. If $|\delta| \ll \bar{\kappa} \ln \frac{4\bar{\kappa}}{\kappa_\delta}$ then u_1 and u_2 have practically the identical shape so we assume that $u_1 = u_2 = u/2$. The dependence of the integral on δ is defined by the expressions

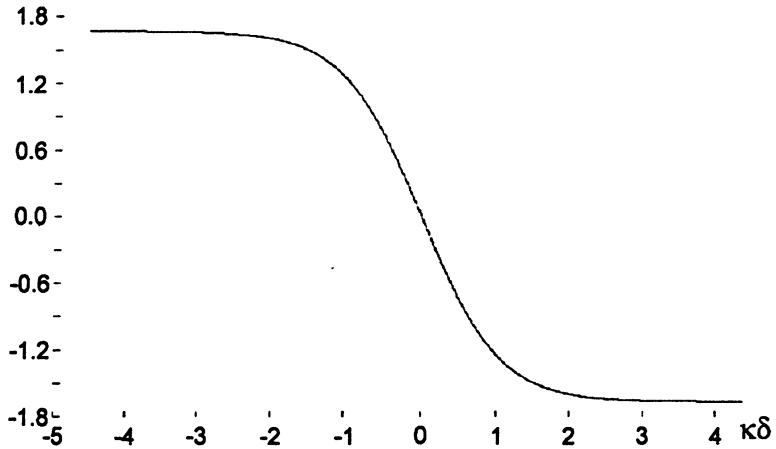

Figure 5: Function G

standing in brackets under the integral, so:

$$\dot{\delta} = 8\bar{\kappa}\kappa_\delta - \frac{8\mu}{15}\left(\frac{\bar{\kappa}}{\kappa_\delta}\right)^2 \bar{\kappa}(\bar{\kappa}\delta). \tag{80}$$

Having equated the right-hand part of the obtained equation to zero we find

$$\kappa^* = \left(\frac{\mu\bar{\kappa}^3\delta^*}{15}\right)^{1/3}. \tag{81}$$

Now we are evaluating the coordinates of motionless points . If we linearize equations (78) and (80) in the neighborhood of this point $(\kappa^*_\delta, \delta^*)$ we obtain the following system of linear differential equations:

$$\frac{d}{dt}\tilde{\kappa}_\delta = -\frac{8}{15}\mu\bar{\kappa}^2\kappa^*_\delta\left(\frac{\partial F}{\partial\delta}\Big|_{\delta=\delta^*}\right)\tilde{\delta}, \tag{82}$$

$$\frac{d}{dt}\tilde{\delta} = 24\bar{\kappa}\tilde{\kappa}_\delta - \frac{8}{15}\mu\frac{\bar{\kappa}^4}{\kappa^{*2}_\delta}\tilde{\delta}. \tag{83}$$

Let us rename the derivative of F calculated in motionless points $\delta^*_{1,2}$ via $\alpha_{1,2}$. It is clear that $\alpha_1\alpha_2 < 0$ and $|\alpha_1| = |\alpha_2|$ because

function F has two zeros and has derivatives with different signs there. Let us investigate stability of the motionless points. To make it we will find the solution of our linear system in this form: $e^{\lambda t}$. After substitution of this exponent in system (82)-(83) we obtain the following algebraic equation:

$$\lambda^2 + \frac{8}{15}\mu\frac{\bar{\kappa}^4}{\kappa_\delta^{*2}}\lambda + \frac{64}{5}\mu\bar{\kappa}^3\kappa_\delta^*\alpha_{1,2} = 0. \tag{84}$$

For our estimations let us set $\bar{\kappa}\delta^* = 1$. After it we can find from equation (81) that $\kappa_\delta^* = \left(\frac{\mu\bar{\kappa}^2}{15}\right)^{1/3}$. The previous equation can be rewritten as:

$$\lambda^2 + 3{,}2\mu^{1/3}\bar{\kappa}^{8/3}\lambda + 5{,}2\mu^{4/3}\bar{\kappa}^{11/3}\alpha = 0. \tag{85}$$

It has the following roots:

$$\lambda_{1,2} = -1{,}6\mu^{1/3}\bar{\kappa}^{8/3} \pm 1{,}6\mu^{1/3}\bar{\kappa}^{8/3}\sqrt{1 - 2{,}1\left(\frac{\mu}{\bar{\kappa}}\right)^{2/3}\frac{\alpha}{\bar{\kappa}}}. \tag{86}$$

In our case of weak dissipation coefficient μ is small, so parameter $\frac{\mu}{\bar{\kappa}} \ll 1$. We have two motionless points: $(\tilde{\kappa}_\delta, \tilde{\delta})$. If $\delta^* > 0$, then it is stable, and if $\delta^* < 0$, then it is unstable.

The stable motionless point, of course, corresponds to solitons coupling which we observed in experiment. The distance between the hills of solitons is approximately equal to the characteristic scale of one soliton multiplied by $\ln\frac{2\bar{\kappa}}{\kappa_\delta}$ in the case of closed velocities. After coupling this distance can change only due to dissipation of the whole envelope. The rate of this change has the same order as solitons couple dissipation and that rate is much less than that of coupling. The process of coupling, as we can see from (86), is very quick because $\mu^{-1/3}\bar{\kappa}^{-8/3} \ll \mu^{-1}\bar{\kappa}^{-2}$.

It is necessary to add the following. We were comparing the results of numerical calculations of the exact BKdV equation and its model, which we have obtained and we found their good matching (see Fig. 6). The coupling time in the both cases are approximately equal to each other. The only difference is a small spatial shift of the double soliton, which is caused by the influence of the weak tail in the exact model.

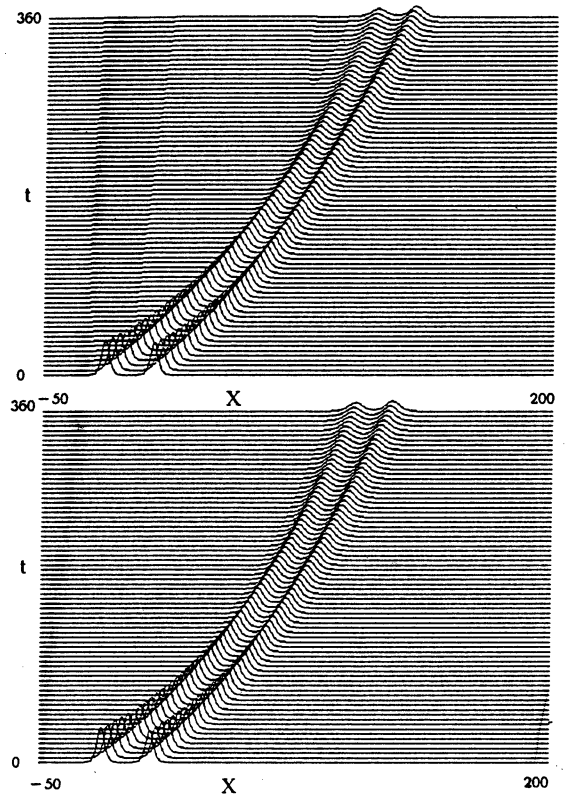

Figure 6: Results of numerical simulations of the BKdV equation (7): exact solution(to the top), solution of the sortcut equations (68), (69), (to the bottom). The initial condition in both cases is the exact two-soliton solution of the KdV equation, $\mu = 0.05$, $\kappa_1 = 0.3$, $\kappa_2 = 0.35$

4 Resume

It is necessary to add that we compared the results of numerical calculations of the shortcut equations and the exact solution of BKdV. They were found to be a perfect matching (see Fig. 6).

The analysis of such model of nonelastic processes in the system with weak dispersion and nonlinearity has shown that taking into account even weak viscosity completely changes the structure of solutions. The coupling processes are sufficiently faster than the dissipation of the whole solution. We are assured that the considered property is not specific one of our system. The soliton coordinates we introduced in this paper are not coordinates of soliton maximums, which we can observe in experiment but distanced to constant $\leq \frac{1}{\bar{\kappa}} \ln \frac{2\bar{\kappa}}{\kappa_\delta}$ from them. It can be found from property 4 of functions $u_{1,2}$. If δ is fixed, then the distance between solitons fixes too.

5 Acknowledgments

This work was supported by Russian foundation for basic Research (Grant 95-02-04997-a) and ISSEEP (Grant s96-3094).

References

[1] K.A. Gorshkov, L.A. Ostrovsky. "Interactions of solitons in nonintegrable systems : direct perturbation method and applications". Physica–3D(1981) 1&2, 428—438.

[2] Уизэм Дж. "Линейные и нелинейные волны", 1977, М: Мир
Whitham G.B. (1974) "Linear and Nonlinear Waves", New York: John Willey.

[3] Su C.S. and Gardner C.S. (1969) "The KdV equation and generalizations. III. Derivation of Korteweg-de Vries equation and Burger's equation", J. Math. Phys., 10, 536-539

[4] Taniuti T. and Wei C.—C. (1968) "Reductive perturbation method in nonlinear wave propagation", J. Phys. Soc. Japan, 24, 941—6

[5] Y. Kodama "Nearly Integrable Systems", Physica 16D(1985) 14—26
Y. Kodama and T.Taniuti, "Higher order approximation in the reductive perturbation method I. The weakly dispersive system", J. Phys. Soc. Jpn. 45 (1978) 298
Y. Kodama "Normal Forms for Weakly Dispersive Wave Equations", Phys. Lett. 112A. number 5, 193—196
Y. Kodama "On Solitary-Wave Interaction" Phys. Lett., A 123(1987) 276.

[6] Hershkowitz N., Romesser T. and Montgomery D. (1972) "Multiple soliton production and the KdV equation" Phys. Rev. Lett., 29, 1586—9.

[7] В.И. Карпман. "Нелинейные волны в диспергирующих средах". М. Наука. 1973.

[8] Korteweg D.J. and Vries G. (1895) "On the change of form of long wavesadvancing in rectangular canal, and on a new type of long stationary waves", Phil. Mag., 39, 422—443

[9] Р. Додд , Дж. Эйлбек, Дж. Гиббон, Х. Моррис. "Солитоны и нелинейные волновые уравнения", Москва, "Мир", 1988

[10] А. Ньюэлл. "Солитоны в математике и физике", Москва, 1989, "Мир"

[11] В.И. Карпман, Е.М. Маслов. "Теория возмущений для солитонов". ЖЭТФ 1977 том. 73 стр .537.

[12] Gardner C.S., Greene M.J., Kruskal M.D. aqnd Miura R.M. and (1967) "Method for solving the Korteweg-de-Vries equation", Phys. Rev. Lett., 19, 1095—1097.

[13] Lax P.D.(1968) "Integrals of nonlinear equations of evolution and solitary waves" Commum. Pure and Appl. Math., 21, 467—490.

[14] Гельфанд И.М., Левитан Б.М. (1951) "Об определении дифференциального уравнения по его спектральной функции". — Изв. АН СССР (сер. мат.), т.15, #4, 309—360.
Агранович З.С., Марченко В.А. (1960) "Обратная задача теории рассеяния" Изд. Харьковского университета, Харьков.

[15] Lamb G.R., Jr.(1980) "Elements of Soliton Theory", New York: John Willey.

[16] V.B. Matveev, M.A. Salle "Darboux Transformations and Solitons" Springer 1991.

[17] Wahlquist: in Bäcklund Transformationsed. by Miura, Lect. Notes Math. Vol 515. (Springer, Berlin Heidelberg 1976) pp. 162—175

[18] M.Crum: Quat. J. Math., 6, 121—128(1955).

[19] Иванычев Д.Н. "Неупругие столкновения КдВ-солитонов" Дипломная работа на соискание степени бакалавра, Нижегородский Государственный Университет, 1995.

[20] Deift P. and Trubowitz E. (1979) "Inverse scattering on line", Comm. Pure Appl. Math., 32, 121—251.

FRACTAL COLLAPSE IN NORMAL DISPERSIVE MEDIA

A.G. Litvak, V.P. Slipenchuk, G.M. Fraiman

Institute of Applied Physics, Russian Academy of Sciences,
46 Ulyanov Street, Nizhny Novgorod, Russia

Recently a great attention of researchers has been given to the problem of nonlinear interaction of intense ultra-short laser pulses with plasma and plasma-like media. The longitudinal dimension of such a pulse is usually significantly smaller than the interaction space, so one can assume that the self-action process has the 3-D character. Besides, at this durations the process is governed by the Kerr-type local nonlinearity. It is well known (for detail see [1]..[3]), that in the co-moving with linear groups velocity coordinate system for complex amplitude of wave packet, having averaged one can get:

$$i\Psi_z + \Delta_\perp \Psi - \frac{\partial^2 \Psi}{\partial t^2} + |\Psi|^2 = 0 \qquad (1)$$

The main specific feature of this problem that differs it from the problem of critical wave collapse, which was widely discussed in the 80ths, is that the nonlinearity influences the processes in the transverse ($\Delta_\perp\Psi$ in Eq. (1)) and longitudinal (Ψ_{tt}) directions in a different way. Namely, in the transverse direction the nonlinearity is a focusing, and in the longitudinal, a defocusing one.

That is why beginning from [1] all the discussions connected with the possibility to realize the singularity regime in Eq. (1) reduce actually to the problem of competition of these two processes. In this paper we will analyze the recent results (first of all, those of [2] and [3]) and discuss possible scenarios for realization of singular behavior of solution (1).

The main outline of the discussion is as follows. First we will present the results for self-similar solutions that will be necessary for further consideration [2]. By that, we assume that realization of the singularity regime requires transverse self-focusing, at least. Then the profile formed fast in the transverse direction is close to the self-similar one but has a somewhat over-critical character. Further the process of transverse compression may go on only if the power in the transverse cross-section (at $t = const$) tends to P_{cr}(5). As shown in [4], at purely transverse compression this power decrease may go on only by means of "tunnel" leakage. However, within the problem considered here the process of power decrease in the cross-

section with the minimum size goes on due to defocusing (energy flow) towards t. By that, near the maximum the field became smoother over t.

Further the splitting instability become evident, that is caused by specific degeneration of two-dimensional defocusing problem [5],[6] (due to existence four-parametric manifold solution of self-similar channels). The main characteristics of this instability (parameter range, growth rate , etc.) will be discussed in paragraph 3 in the frame of variation approach. Contrary to [2],[3], this method allow us to find interested functions for all scales, and not for long-wave region only. Having obtained the results of paragraphs 2 and 3 we will then discuss possible scenarios for the self-focusing process at all z. At least three variants prove to be possible in principle: finite number of splitting and consequent blurring with no singularity formed [2], formation of a singularity after a finite number of splitting [3], and fractal regime proper with formation of singularities after an infinite number of splittings. However, having done analysis shows, that first regime can be realized only for long enough waves with a not large subcritical power, and the second one, evidently, does not exists either. For sufficiently subcritical wave packets the regime of fractal collapse occurs.

2. In this paragraph we will discuss the main properties of the manifold of self-similar solutions for the problem of transverse self-focusing ($\partial/\partial t=0$). From theory of 2-D self-focusing it is well-known that the main process when coming closer to the singularity is the process of separating a self-similar solution at the peculiarity point. This solution is an element of the four parametric manifold with the following parameters:

$$\vec{\alpha} = (a, \dot{a}, \beta, \varphi_0) \tag{2}$$

where a is width in the transverse direction, $\dot{a} = \partial a/\partial z$ is value responsible for the wave front curvitude, $\beta = -\ddot{a}a^3$ is parameter determining the excess of the power over P_{cr}, and φ_0 is phase at the beam axis.

Equations of this manifold can be obtained from Eq. (1) by means of the following replacement:

$$\begin{cases} \Psi = \dfrac{1}{a} V(\tau, \xi) \exp\, i(\tau + \dot{a} a \xi^2) \\ \xi = \dfrac{\vec{r}}{a}, \tau = \displaystyle\int_0^t \frac{dt}{a^2} \\ i\dfrac{\partial V}{\partial \tau} + \Delta_\xi V + (|V|^2 - 1 + \beta \xi^2) V = 0 \end{cases} \tag{3}$$

By that, the self-similar manifold in Eq. (3) is corresponded by the solutions of the type of inhomogeneous beams a in the (r,t) representation of function $a(t), \beta(t), \varphi_0(t)$ in [4]:

$$\begin{cases} \dfrac{d\varphi_0}{dz} = \dfrac{1}{a^2} \\ \dfrac{d^2 a}{dz^2} = \beta \\ \dfrac{d\beta}{dz} \cong -\dfrac{A}{a^2}\exp - \dfrac{\pi}{\sqrt{\beta}}, \quad A \sim 1 \end{cases} \tag{4}$$

Thus, parameter β corresponds to the degree of the excess of the power over the critical value ($\beta > 0$, $P > P_{cr}$). Qualitative dependence P/P_{cr} from β is shown in Fig. 1.

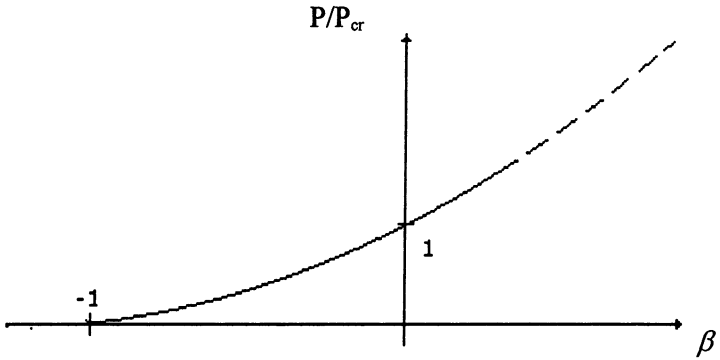

Fig. 1.

According to Eq. (4), at $\beta \geq 1$ there happen strong radiation losses. At $\beta << 1$

$$P(\beta) \approx P_{cr} + \beta r_{eff}^2, P_{cr} = 11.87, r_{eff} = 13.8 \tag{5}$$

It is clear from Eq. (4), particularly, that at $z \to z_0$ (where z_0 is point of peculiarity) that

$$\beta(z) \sim \ln\ln\frac{1}{\sqrt{z_0 - z}} \tag{6}$$

$$a(z) = \sqrt{\frac{z_0 - z}{\ln\ln(z_0 - z)}} \tag{7}$$

Correspondingly,

$$\varphi_0(z) \sim \tau \sim ln\ \frac{1}{z_0 - z} \sim ch\ \tau,\ \text{at}\ z \to z_0\ (\tau \to \infty)\ \text{at}\ \beta > 0 \qquad (8)$$

$a(z) \sim z,\ \varphi_0 \to const$ at $\beta < 0$, and $z \to 0$.

3. When dynamics over t is taken into account, splitting - instability begins to become evident. It is significant that it is parameter degeneration that determines this instability. Unlike [2] and [3] we will use the following method to estimate basic characteristics of the instability. As it has been mentioned in the Introduction, the fastest way is formation of a self-similar profile in the transverse cross-section. Taking this into consideration we will assume that the solution will have the following form:

$$\Psi = A(z,t)\ V\left(\frac{r}{a(z,t)}, P_\perp\right) \exp\ i\ \frac{\dot{a}}{a}\ r^2 + \delta \qquad (9)$$

where

$$|A(z,t)|^2 = P_\perp(z,t) \qquad (10)$$

is power corresponding to the self-similar profile, and

$$V\left(\frac{r}{a}, \dot{a}\right) = \frac{1}{a\sqrt{\pi}} V_0\left(\frac{r}{a}, P_\perp\right) \exp\ i\ \frac{1}{a}\ \frac{\partial a}{\partial z}\ \frac{r^2}{2} \qquad (11)$$

$$\frac{1}{a^2} \int |V_0|^2\ d\vec{r}_\perp \equiv 1 \qquad (12)$$

Here V_0 is self-similar solution of (3) normalized to unity, and $a(z,t)$ is local width of the beam. For further analysis let us use variation method. Having substituted Eq.(10) into expression for action of initial problem and integrating over $\vec{r}_\perp$, one can get for shortcut Lagrangian the following formula:

$$L = \frac{i}{2}(A_z A^* - \kappa.c.) + |A|^2\ a\ a_{zz} + \frac{1 - |A|^2/4\pi}{a^2} |A|^2 - |A_t|^2 \qquad (13)$$

It is important to note that dynamics $A(z,t)$ corresponding to this Lagrangian agrees qualitatively with the results of modeling complete problem (1) . By that, the latter is essentially simpler and can be analyzed up to the end.

Now we will pass over to the analysis of the splitting instability basing our consideration on Eq. (13) for the homogeneous profile. To do this, let us make a series of assumptions simplifying the matter further.

Namely, we take into account well known aberrationless approach, where exact transverse profile is substituted by gaussian profile with the same proportion between amplitude and width, i.e. in Eq.(10) we apply:

$$V_0 = \frac{1}{\sqrt{\pi}} e^{-\frac{r^2}{2a^2}} \tag{14}$$

By that we may lose some details in the structure of the transverse mode; however, all the results stay qualitatively valid. Moreover, our instability estimations, when compared to accurate ones, [2] and [3], prove to agree well with the latter up to coefficients of the order of unity. At the same time, this way, unlike the method described in [2] and [3], makes it possible to analyze characteristics of the instability for the whole range of perturbation wave lengths. Specifically, for beams with a small excess over the critical value,

$$P \approx P_{cr} = 4\pi \tag{15}$$

(remember that the value of the critical power is P_{cr} =*11.84*) the problem can be linearized in the vicinity of the distributions corresponding to homogeneous beams:

$$A = (A_0 + \delta)\exp(i\frac{z}{a_0^2}) \tag{16}$$

$$a = (a_0 + b) \tag{17}$$

Searching for solution in the form of a plane wave,

$$\mathrm{Re}\,\delta,\ \mathrm{Im}\,\delta,\ \ b \ \sim \exp(ihz/a_0^2 + i\Omega t/a_0) \tag{18}$$

one can obtain the following dispersion relation for dimensionless Ω and h:

$$h^2 = -4\frac{\Omega^2}{h^2} + 2(\Omega^4 - \Omega^2) \tag{19}$$

Analysis of this relation shows that in the long-wave region (Ω<<1) there are two unstable modes, the instability growth rate s of which correspond to the results of [2,3]. Besides, at Ω>>1, the instability is absent.

The dependence of the instability growth rate on Ω is shown in Fig. 2.

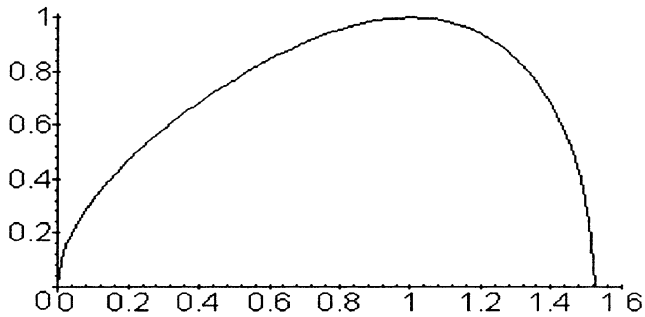

Fig. 2.

Thus, the maximum of the growth rate corresponds to the region of $\Omega \sim 1$ (Fig. 1). Similar results can be obtained also for the case of an arbitrary excess over the critical value.

Qualitatively the instability mechanism is as follows. Let us consider the field distribution at $z=0$ with width :

$$a(0,t) \approx a_0 + \delta a \cos \Omega t, \quad \Omega << 1 \qquad (20)$$

It corresponds to a self-consistent wave beam with a slightly (and smoothly) modulated boundary. Then, if $0 \cdot \beta(0,t)=\beta_0 \cdot 1$ is constant along the whole beam, then in each cross-section the collapse process begins. By that, in the regions where the width is narrower, this process will run faster, so that the relative depth of width modulation will be growing. As the result of phase modulation growing over t the energy will flow over the waveguide from one cross-section to another. It is significant that for long-wave modulations it is width variation that is the determining process for phase modulation. The latter, in its turn, leads to a growth of transverse power over critical value in the regions with narrower widths, and to its decrease in wider regions.

That is, the process in the narrower regions looks like additional focusing of the power and the compression effect becomes stronger. The aforesaid can be conveniently represented by the following scheme:

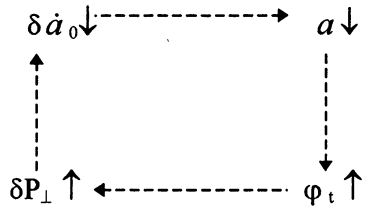

(21)

Here solid arrows correspond to the growth or fall of parameter modulation in the t direction, and the dashed ones, to the process in the z direction. This scheme is convenient also because it makes it possible to replay all stages of our consideration beginning from any element. Note, that the presence of four links in chain (21) corresponds precisely to the presence of four-parametric manifold of self-similar solutions (3). Note also, that instability phenomena does not depend on longitudinal dispersion sign, and, formally, it is consequence of degeneration of self-similar solutions only. The dispersion sign, it will be shown below, is significant only for nonlinear regimes.

4. Basing on the general scenario of an elementary instability phenomenon we will discuss here possible models of "long-term" evolution of solutions of the collapse problem in media with normal dispersion. One can single out the three following scenarios:

1. Finite number of splitting instabilities with further defocusing as the transverse power at its maximum becomes less than P_{cr} [2]. A similar picture is really often realized in numerical experiments. However, we are of the opinion that in numerical calculations a usual limitation here is additional grid dispersion that is a mandatory consequence of actually any numerical algorithm. A formal drawback of this scenario is the presence of the following sufficient criterion for impossibility of blurring of a sufficiently intense field cluster:

$$\min_z \max_t \left(\frac{P}{P_{cr}}\right) \geq -\frac{H_\perp(z)}{F_\perp} \tag{22}$$

where

$$H_\perp = \int dt \left(|\nabla_\perp \Psi|^2 - \frac{|\Psi|^4}{2}\right) dxdydz \tag{23}$$

$$F_\perp = \int |\nabla_\perp \Psi|^2 dxdydt \quad P_\perp = \int |\Psi|^2 dxdy \tag{24}$$

Nonequality (22) followed from (23) when using well known estimation for nonlinear term (see [4]):

$$\int \frac{|\Psi|^4}{2} d\vec{r} \le \int |\nabla_\perp \Psi|^2 \, d\vec{r} \, \frac{\int |\Psi|^2 \, d\vec{r}}{P_{cr}} \tag{25}$$

One can see, that if for all z $H_\perp < 0$, than $\min_z \max_t P_\perp \ge P_{cr}$. This means, that sufficiently nonlinear regime must exist (capture regime) for all z, but this is in contradiction with first scenario. The next question is of importance: is it possible that at all z (in the region where a solution exists) $H_\perp < 0$? We have not managed yet to find a rigid sufficient condition for that possibility. However, we can give the following qualitative ideas to benefit the above statement.

As is known (see, e.g. [2]) from Eq. (1) one can obtain the following expression:

$$8H_\perp = \frac{d^2}{dz^2} r_{eff}^2 \quad , \text{ where } \quad r_{eff}^2 = \frac{\int r^2 |\Psi|^2 \, d\vec{r}_\perp \, dt}{\int |\Psi|^2 \, d\vec{r}_\perp \, dt} \tag{26}$$

Under the assumption that at each cross-section over t the transverse profile is close to the self-similar one, and the phase profile, at $z = 0$, is plane, the right-hand part of this correlation can be transformed in the following way:

$$8H_\perp \sim \int \frac{(1 - P_\perp / P_{cr}) \, P_\perp (z,t)}{a^2 (z,t)} dt \tag{27}$$

Hence it is seen that the whole region of $P(t) > P_{cr}$ corresponds to a negative value of $H_\perp(z) < 0$, and the region of $P < P_{cr}$, to a positive one. Moreover, due to efficient "locking" of the field in the transverse direction one can show that variation of $H_\perp$, and, consequently, outflow of the field can happen only through the boundaries (over t) of a 3-D resonator with a sufficiently high Q-factor.

Therefore, one can expect that a sufficient condition for fractal collapse, $H_\perp(0)$, is

$$H_\perp (0)|_{z=0} < 0 \tag{28}$$

that means, that subcritical region in t-direction must be large enough.

2. Another scenario runs as follows. Let there have been one splitting (see paragraph 3). Can it end with monotonous collapse [3]? Evidently, the answer is no. Really, when considering the instability we took into account only long-wave (in the t direction) effects. Formally it is associated with

the fact that unlike in [3], when the t-directed diffraction is taken into account, stabilization of the instability manifests itself for sufficiently small sizes (Fig. 2), i.e. there appear structures similar, in the t-direction, to the solitons of the onedimensional nonlinear Schrodinger equation.

3. Further, in our opinion, only the fractal scenario of the collapse can take place. Namely, in the t-direction the field cluster affected by the defocusing nonlinearity will be blurring until the next splitting begins.

At whole, it was shown, that the first regime can be realized for long enough waves with a not large subcritical power only, and the second one, evidently, does not exists either; and for sufficiently subcritical wave packets the regime of fractal collapse occurs.

To conclude, we would like to note that the whole plot in the framework of the complete 4-D model (1) can be hardly observed. Therefore we hope that a numerical experiment can be more conveniently built on simplified model based on Lagrangian (13) and reducing to the onedimensional problem.

This work was supported Russian Foundation for Basic Research grants 95-02-04997-a, 96-02-19482.

References

1. N.A.Zharova, A.G.Litvak, T.A.Petrova, A.M.Sergeev and A.D.Yunakovksy, Pis`ma Zh. Eksp. Teor. Fiz. **44**, 12 (1986) [JETF Lett **44**, 13 (1986)]
2. L. Berge, J.J. Rassmussen, Phys. Plasmas 3 (3), March 1996.
3. G.Fibich, V.Malkin, G.Papanicolau, Phys.Rev. A, **52**, (1995)
4. G.M.Fraiman, Zh. Eksp. Teor. Fiz., **88**, 390 (1985)
5. A.I.Smirnov, G.M.Fraiman, Physica D, **52**, (1991)
6. A.G.Litvak, V.Yu.Trakhtengerts, T.N.Fedoseeva, G.M.Fraiman, Pisma v Zh. Eksp. Teor. Fiz., **20**, 544, (1974)

PENETRATION OF RELATIVISTICALLY STRONG ELECTROMAGNETIC RADIATION INTO OVERDENSE PLASMA

V.A. Mironov, A.B. Kim, and L.A. Abramyan

Institute of Applied Physics, Russian Academy of Sciences 46 Ulyanov Street, 603000 Nizhny Novgorod, Russia

Radiation-plasma interaction due to relativistic dependence of the electron mass on its oscillations in the field within the nonlinear wave theory [1] became the object of interest long ago. The progress made in creating powerful electromagnetic generators of various frequency ranges makes it possible to discuss peculiarities of relativistically strong radiation-plasma interaction. Now the quiver electron velocities of the light velocity order are achieved by focus of compact multiterawatt laser systems radiation [2]. To investigate dynamics of interaction of such radiation with plasma numerically, the particle in-cell simulation method is usually employed [2, 3]. However, the obtained information often proves to be too detailed and the picture of interaction is too complicated. So, to simulate the physical processes one has to construct simple models describing the situation adequately.

Let us consider relativistically strong electromagnetic waves reflected by the overdense plasma in one-dimensional case.

1. The analysis is based on hydrodynamic description of plasma. Another simplifying assumption is connected with consideration of circularly polarized wave-plasma interaction. In this case generation of electromagnetic radiation harmonics is absent and, in order to describe the dynamics of field penetration into half-bounded plasma, one can use slow-varying (on the scale of the field variation period) complex amplitude of the vector potential. The initial set of equations in dimensionless variables have the following form:

$$\frac{\partial n}{\partial t} + \frac{\partial}{\partial z}\frac{np}{(1+p^2+A^2)^{\frac{1}{2}}} = 0, \tag{1}$$

$$\frac{\partial p}{\partial t} = \frac{\partial}{\partial z}(\varphi - (1+p^2+A^2)^{\frac{1}{2}}), \tag{2}$$

$$\frac{\partial^2 \varphi}{\partial z^2} = \frac{\omega_p^2}{\omega^2}(n-1), \tag{3}$$

$$2i\frac{\partial A}{\partial t} + A_{zz} + (1 - \frac{\omega_p^2}{\omega^2}\frac{n}{(1+p^2+A^2)^{\frac{1}{2}}})A = 0. \tag{4}$$

Here n is electron concentration normalized on its value when the field is absent; p, φ, A are momentum of electrons, potential and vector potential of the electromagnetic field, respectively, in the gauge $div\mathbf{A} = 0$, normalized on m_0c and m_0c^2/e, m_0 is electron mass of rest; ω_p is plasma frequency and ω is field frequency. Plasma is supposed to be cold. The relativistic peculiarity of the problem is taken into account in Eq. (4). The wave refraction index is determined both by variation of plasma concentration and by variation of relativistic electron mass. In the set of equations (1)-(4) the following dimensionless variables for time and coordinate were used: $t = \omega t_{ct}$, $z = z_{ct}\omega/c$. Futher we will suppose that plasma occupies the half-space ($z > 0$) with constant density. In the case of a wave falling normally to the plasma boundary ($z = 0$) it is easy to obtain the following boundary condition:

$$A + iA_z = 2iA_0(t). \tag{5}$$

It correlates the field in plasma with the field in the incident wave, $A_0(t)$.

First we will consider the stationary regime of interaction of relativistically strong electromagnetic radiation and half-bounded plasma and then present the results of numerical investigations of the dynamics of the field penetration into the medium.

2. In the stationary case ($\frac{\partial}{\partial t} = 0$) the initial set of equations will have the following form:

$$\frac{\partial^2 \varphi}{\partial z^2} = \frac{\omega_p^2}{\omega^2}(n-1)\,, \tag{6}$$

$$\frac{\partial^2 A}{\partial z^2} + (1 - \frac{\omega_p^2}{\omega^2}\frac{n}{(1+A^2)^{\frac{1}{2}}})A = 0, \tag{7}$$

$$\varphi = (1+A^2)^{\frac{1}{2}} - 1\,. \tag{8}$$

Here relationship (8) betwen the wave field (A) and the potential (φ) is written for field distribution localized near the interface ($z = 0$), ($A(z \to \infty) \to 0, \varphi(z \to \infty) \to 0$). In this case we have the analytical solution of the considered set of equations (6)-(8) of the soliton type:

$$A = \frac{[8|\epsilon_0|(1+|\epsilon_0|)]^{\frac{1}{2}}(1 + ch2\sqrt{|\epsilon_0|}(z+z_0))^{\frac{1}{2}}}{(1+|\epsilon_0|)ch2\sqrt{|\epsilon_0|}(z+z_0) + (1-|\epsilon_0|)}\,, \tag{9}$$

where $\epsilon_0 = 1 - \omega_p^2/\omega^2$ is permittivity of unperturbed plasma. Constant z_0 is determined by boundary condition (5). In the linear regime ($A_0 \to 0$) the value z_0 tends to infinity and expression (9) describes the field distribution in the skin-layer ($A \sim exp(-\sqrt{|\epsilon|}z)$. Together with increasing of the incident wave intensity the field distribution in plasma is modified (9). It is important to note that the soliton amplitude is

$$A_{max} = (4|\epsilon_0|(1+|\epsilon_0|))^{\frac{1}{2}}\,, \tag{10}$$

i.e. the maximum value of the field in the medium is determined by the density of the unperturbed plasma. It means that the stationary regime is possible only at field amplitudes of the incident wave not exceeding some threshold value corresponding to the soliton amplitude,

$$A_{cr} = (|\epsilon_0|(1+|\epsilon_0|))^{\frac{1}{2}}\,. \tag{11}$$

If the field in the incident wave exceeds the threshold value ($A_0 > A_{cr}$), then the regime of relativistically strong radiation and plasma interaction becomes dynamical.

3. Further the results of numerical solution of the initial set of equations (1)-(4) under boundary conditions (5) at $|\epsilon_0| = 1$ will be presented. Calculations were carried out for the momentum radiation of the form $A_0 = A_m/ch(t/\tau)$. The dependence of transmissivity of the electromagnetic radiation into plasma on the amplitude of the incident wave is demonstrated in Fig. 1.

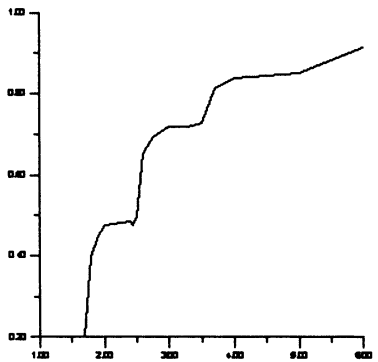

Fig.1. The part of energy which penetrates an overdense plasma at $N/N_c = 2$ as a function of the field amplitude of the incident pulse

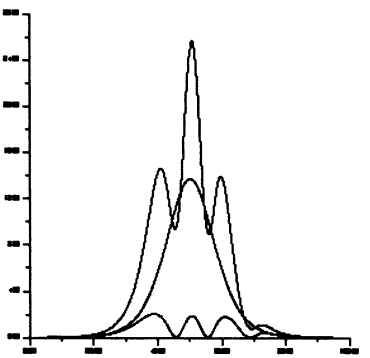

Fig.2. Temporal profiles of the incident pulse (solid line, pulse with amplitude $A_j = 3.7$ reflected pulse (dashed), and the intensity of electric field on the boundary of a plasma at $N/N_c = 2(thinline)$

One can observe the existence of the expressed threshold of plasma penetration corresponding to the above-mentioned estimation (11). Under the conditions considered before (for $\omega_p^2/\omega^2 = 2$) $A_{kp} = \sqrt{2}$. First "saturation" of the transient index at $A_0 \simeq 2$ is accompanied by excitation of one soliton in the region of the nonlinear skin-layer and by its motion into plasma. The results for a certain amplitude ($A_0 = 3.7$) are presented in Fig. 2. The most representative is the reflected momentum

structure (Fig. 2). It practically consists of four pulses. Each of the decreasing amplitudes of the incident wave is accompanied by soliton excitation. As a result, the field in plasma represents a sequence of three solitons (Fig. 3) moving into the medium. The solitons have the form decscribed by (9) but they correspond

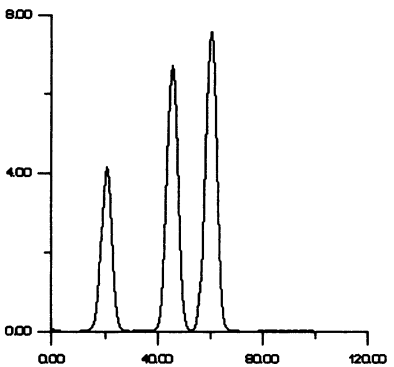

Fig. 3. Snapshot of a field structure inside the plasma region for the pulse with amplitude $A_j = 3.7$ falling from vacuum $x < 0$ on a sharply edged overdense plasma at $N/N_c = 2$

to the lower frequency. It is connected with the fact that in the process of soliton excitation the effective boundary reflecting the radiation moves into plasma. As a result, both the spectrum of the reflected momentum and the spectrum of the soliton turn out to be red-shifted with respect to the spectrum of radiation.

To conclude, within the considered approximation the dynamics of interaction of relativistically strong electromagnetic radiation and overdense plasma is qualitatively the same as in the case of other media with nonlinear response inertia [4]. Electromagnetic radiation penetrates the overdense plasma due to excitation of solitons close to the interface medium boundary. By the way, the refraction index proves to be noticeably less than in the linear case.

This work was supported in part by the Russian Basic Research Fondation under Grant N 96-02-19482.

References

[1] V.A. Kozlov, A.G. Litvak, and E.V. Suvorov, Zh. Eksp. Teor. Fiz. **7**, 148 (1979

2,5-DIMENSIONAL NUMERICAL SIMULATION OF PROPAGATION OF THE FINITE SEQUENCE OF RELATIVISTIC ELECTRON BUNCHES (REB) IN UNDERDENSE AND OVERDENSE PLASMAS*

Ya.B. Fainberg, V.I. Karas',
V.D. Levchenko+ and Yu.S. Sigov+

Kharkov Institute of Physics and Technology, NSC, Kharkov, Ukraine
+M.V. Keldysh Institute of Applied Mathematics, Moscow, Russia

Introduction

Charged particle acceleration by means of charge density waves both in plasmas and in noncompensated charge particle beams is the major trend in collective acceleration methods [1, 2, 3]. The charge density variable part can be made very high (up to n_e); consequently, the accelerating field can reach values on the order of $10^7 - 10^9 V/cm$. Chen et al. [4] suggested a modification of Fainberg's acceleration method [1] consisting of the use of wave trains. Katsouleas [5] considered this problem for different electron bunch profiles with aim of transformation coefficient increasing.

Nonlinear model experiments on acceleration by means of wake fields emphasized the importance of the 2D and 3D effects [6, 7]. In approximation of immobile ions [8, 9] a channel of uncompensated positive charge is formed when the plasma electrons are ejected in response to the incoming REB.

As it is shown in presented paper on relative phenomena, the ion dynamics should be obligatory taken into account for it plays the decisive role in a real formation of such "ion channel" being the significant factor of transverse bunches' focusing.

*This work was performed with partial support from the Russian Foundation for Fundamental Research Grant No 94-02-06688 and the International Scientific Foundation Grant No U27200.

Computer simulation

The wake field excitation was studied using 2D3V axially symmetric electromagnetic code COMPASS [10]. Previously, this code was used to simulate an induction accelerator [11], modulated REB [12] and a single relativistic electron bunch or a sequence of such bunches in plasma [13]. Note that, as in experiments [7], the bunch initial transversal R_0 and longitudinal L_0 dimensions were smaller than c/ω_p at the REB density $n_b = \frac{1}{2}n_e$ (n_e is plasma density). The computer simulation [13] showed the transversal dimension of a bunch, propagating in plasma, to vary over a wide range.

run id		Var1	Var2	Var3	Var4	Var5
bunch density	n_b cm^{-3}	$2\cdot 10^{10}$	$2\cdot 10^{10}$	$4.86\cdot 10^{10}$	$4.86\cdot 10^{10}$	$2.\cdot 10^{11}$
plasma density	n_e cm^{-3}	$4\cdot 10^{10}$	$4\cdot 10^{11}$	$9.72\cdot 10^{10}$	$8.75\cdot 10^{11}$	$1.\cdot 10^{12}$
plasma frequency	ω_p c^{-1}	$1.13\cdot 10^{10}$	$3.57\cdot 10^{10}$	$1.76\cdot 10^{10}$	$5.27\cdot 10^{10}$	$5.76\cdot 10^{10}$
skin-depth	c/ω_p cm	2.66	0.84	1.71	0.57	0.52
particles per bunch	N	$6.28\cdot 10^{9}$	$6.28\cdot 10^{9}$	$1.53\cdot 10^{10}$	$1.53\cdot 10^{10}$	$6.28\cdot 10^{9}$
bunch sizes	$Z_0 \times R_0$ cm	0.4×0.5				0.4×0.1

Table 1. Parameters of the runs.

This caused substantial changes in its density (more then order of magnitude) as well as a change in the excited wake field. It is also shown that the amplitudes of longitudinal and transversal fields increase upon additional bunch injection. However these amplitudes are not proportional to the number of injected bunches (as it should be in case of "rigid" bunches). For future experimental researches in the domain of intense microwave (wake) field excitation in plasmas and for use of these fields for charged particle acceleration it is expected to employ a new electron accelerator being constructed at KhIPT. Its parameters are as follows: energy $W = 20MeV$; num-

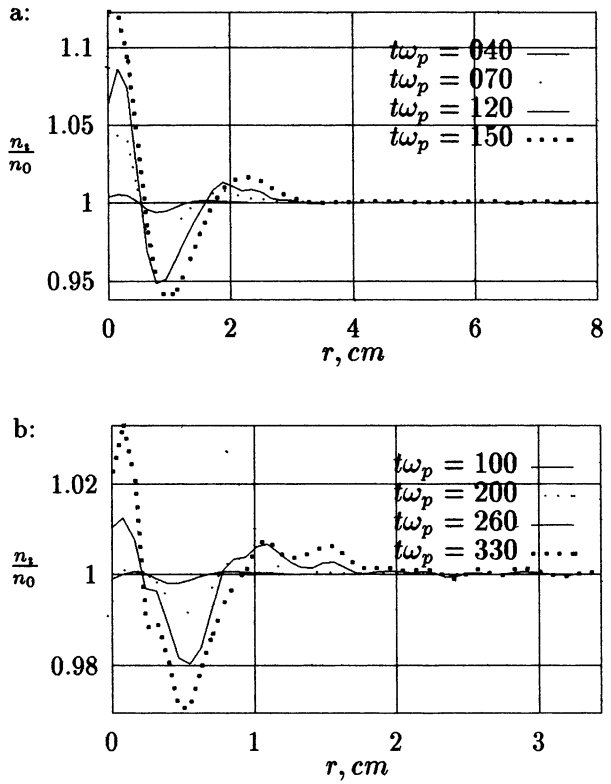

Fig. 1: Dependence of the ion density n_i upon the radial coordinate r ($z = 10.cm$): a–Var1, b–Var4

ber of electrons per bunch $N \sim 10^{10}$; number of bunches from 10 to 20; bunch repetition rate is $2797.16MHz$. The electron bunches will be injected into plasma of the following sizes: the length $L = 1m$ and the radius $R = 10cm$ (plasma density will be variable within $n_e = 10^{10} - 10^{14} cm^{-3}$) with a minimum density longitudinal gradient. In our numerical simulation we shall keep in mind these parameters.

The REB dynamics is described by Vlasov relativistic equations (the Belyaev–Budker equations) for the distribution function $f_\alpha(\vec{r}, \vec{p})$ of each plasma specie $\alpha = e, i, b$ and by the Maxwell equation set for self–consistent electric $\vec{E}$ and magnetic $\vec{B}$ fields. The initial and boundary conditions and numerical scheme are the same to [14] ones.

Five runs were considered to study the dependence of the ecxited

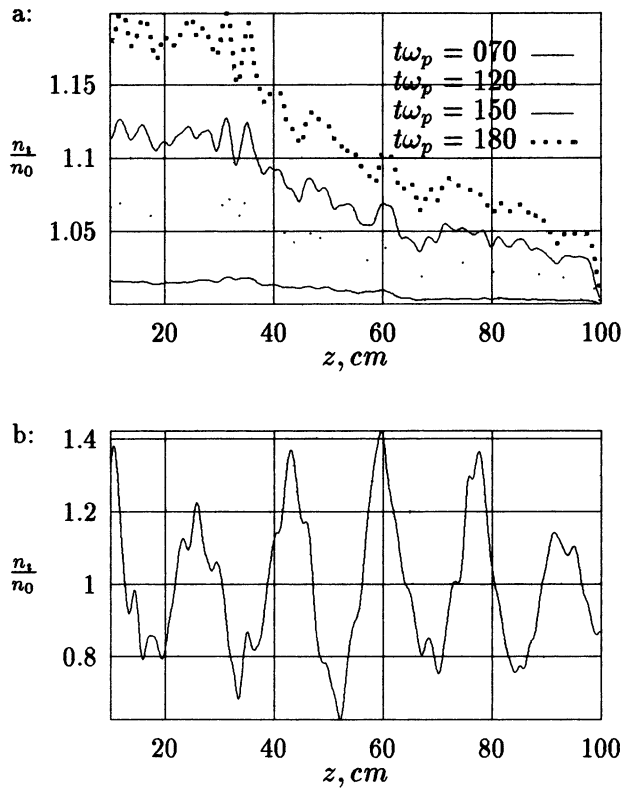

Fig. 2: Ion density n_i (a) and electron density n_e (b) via longitudinal coordinate z (Var1, $r = 0.5cm$, $t\omega_p = 180$)

fields: upon the number N of bunches injected into plasma; on the density ratio of bunch and plasma; on the bunch repetition rate; on the ratio of the bunch size R_0 and skin–depth c/ω_p. The parameters of these runs are listed in the table 1.

The weight of model particles was assumed to be a function of their radial position. The plasma was assumed to have smaller numbers of particles in the less disturbed region distant from the axis. The total number of model particles was about 10^6. Note that all the calculations were carried out using a PC/Pentium–66 computer and a high-speed particle–in–cell technique.

Computational results

The computer simulation showed the transversal dimension of the bunch, propagating in plasma, to vary over a wide range at the conditions $R_0 < c/\omega_p$ and $L_0 < c/\omega_p$. Contrary to common consideration (with $L_0 \gg c/\omega_p > R_0$ or $R_0 \gg c/\omega_p > L_0$), we considered the conditions $L_0 \sim R_0 < c/\omega_p$ or $L_0 \sim R_0 \sim c/\omega_p$, in relation to the experimental situation [15]. In these cases significant nonlinearities in both plasma and beam behavior have been observed. As we shall see subsequently in our simulation the ion motion plays significant role in the REB propagation in the plasmas. Formation of the ion channel in time is shown in Fig. 1–2.

The dependence of the ion density n_i upon the radial coordinate r for sequential time moments is presented in Fig. 1. One can see that ions form the plasma channel due to their transversal motion in self–consistent fields. The channel parameters are determined by density ratio of bunch and plasma, and by size ratio of bunch radial size R_0 and skin–depth c/ω_p (Fig. 1 a, b).

As it shown in figures, the channel's effective size and depth monotonically increase in time as well as along the z–direction. By comparision in Fig. 2 b is given the electron density depending on z. It is easy to see its significant oscillations caused by the longitudional wave.

The formed ion channel considerable effects the REBs' transportation due to their additional focusing in regions of incresed ion density.

Conclusions

The amplitudes of the longitudinal electric field component and the radial one increase with injection of each of consequent additional bunches. But, these amplitudes are not proportional to the number of injected bunches as it should be in the case of "rigid" bunches. The shape of bunches is not close to Bennet equilibrium case. However, as it is shown in the presented full–scale computer experiments, the REB expansion is appreciably retarded by the formation of the plasma channel with the ion radial motion.

The planned consideration of the three–dimensional nonlinear bunch–plasma behavior should be useful for better understanding

of fundamental physics of the plasma wake–field acceleration and focusing.

References

[1] Ya. B. Fainberg, *Proc. Symp. CERN* (CERN, Geneva, 1956), Vol. 1, p. 84.

[2] Ya. B. Fainberg, Sov. J. Plasma Physics **13**, 350 (1987).

[3] Ya. B. Fainberg, Plasma Physics Reports **20**, 549 (1994).

[4] P. Chen, J. M. Dawson, R. W. Huff, and T. Katsouleas, Phys. Rev. Lett. **54**, 693 (1985).

[5] T. Katsouleas, Phys. Rev. A **33**, 2056 (1986).

[6] A. T. Amatuni *et al.*, Sov. J. Plasma Physics **11**, 417 (1985).

[7] J. B. Rosenzweig, *FERMILAB Conf. 90/40* (FNAL, Batavia, Illinois, 1990).

[8] J. B. Rosenzweig *et al.*, Phys. Rev. A **44**, 6189 (1991).

[9] N. Barov and J. B. Rosenzweig, Phys. Rev. E **44**, 4407 (1994).

[10] O. Batishchev, V. Karas', V. Levchenko, and Yu. Sigov, Plasma Physics Reports **20**, 587 (1994).

[11] V. I. Karas', O. V. Batishchev, Yu. Sigov, and Ya. Fainberg, Particle Accelerators **37-38**, 281 (1992).

[12] O. V. Batishchev, Yu. Sigov *et al.*, Sov. J. Plasma Physics **19**, 738 (1993).

[13] O. Batishchev, V. Karas', Yu. Sigov, and Ya. Fainberg, Plasma Physics Reports **20**, 583 (1994).

[14] V. Karas', Ya. Fainberg, V. Levchenko, and Yu. Sigov, Bulletin of the American Physical Society **40**, 1141 (1995).

[15] N. Aizatskii *et al.*, Plasma Physics Reports **20**, 603 (1994).

COLLISIONLESS SHOCK WAVES IN DUSTY PLASMAS

S.I.Popel (a), M.Y.Yu (b), V.N.Tsytovich (c)
(a) Institute for Dynamics of Geospheres, Moscow, Russia
(b) Theoretical Physics, Ruhr University Bochum, Germany
(c) General Physics Institute, Moscow, Russia

Shock waves often arise in nature because of a balance between wave breaking nonlinear and wave damping dissipative forces [1]. Collisional or collisionless shock waves can appear in ion acoustic wave propagation because of friction between the particles or wave–particle interaction [2,3]. It has recently been found [4–7] that linear ion-acoustic waves in a dusty plasma can be damped because of an anomalous dissipation originating from the dust charging process. The latter involves microscopic electrons and ions currents flowing into the micron sized variable–charge dust grains because of the potential difference between the grain surface and the adjacent plasma. It is thus of interest to investigate if this dissipation can also give rise to shock waves. Here, we show analytically that weak, grain–charging driven ion acoustic shock waves can indeed occur for a limited range of the propagation speed.

The average radius a of the dust grains in a typical dusty plasma is much smaller than the electron Debye length λ_D, the spatial scale of the perturbations, and the distance between the plasma particles. The grains are negatively and heavily charged (with an average charge $q_d(x) = -Z_d e$ of $-10^4 e$ or more). As they are also massive ($m_i Z_d \ll m_d$, where $m_{i,d}$ are the ion and dust masses), the dust can be considered as stationary and their density n_d constant in the ion acoustic time scale [6]. Furthermore, in the absence of perturbations the quasineutrality condition $n_{i0} = n_{e0} + Z_{d0} n_d$, where $n_{i,e}$ are the

ion and electron densities and the subscript 0 denotes unperturbed quantities, holds.

Under the assumption of equilibrium electrons and kinetic ions, according to the orbit–limited probe model, we have the following expressions for the electron and ion currents flowing into the dust grain [4]

$$I_e \approx -\pi a^2 e \left(\frac{8T_e}{\pi m_e}\right)^{1/2} n_e \exp\left(\frac{eq_d}{aT_e}\right), \tag{1}$$

and

$$I_i = \sqrt{\frac{\pi}{2}} a^2 v_{Ti} e n_i \left[2\exp\left(-\frac{v_i^2}{2v_{Ti}^2}\right)\right.$$
$$\left. + \sqrt{2\pi}\frac{v_{Ti}}{v_i}\left(1 + \frac{v_i^2}{v_{Ti}^2} - \frac{2eq_d}{am_i v_{Ti}^2}\right)\mathrm{erf}\left(\frac{v_i}{\sqrt{2}v_{Ti}}\right)\right], \tag{2}$$

where m_e is the electron mass, T_j and v_{Tj} are the temperature, and thermal speed of the species j $(= i, e)$, $v_i \mathbf{e}_x$ is the ion fluid velocity, and $\mathrm{erf}(x)$ is the error function. Here, the complete formula for I_i is used in order to account for the slow ions, which should be included for consistency. This is related to the fact that the cold ion limit $T_i = 0$ used for the ion acoustic waves cannot be applied in considering the charging processes. The ions and electrons entering the dust grain recombine into neutral atoms, which then re–enter the plasma and re–ionize, thus preserving the number of ions and electrons.

The average charge of the stationary dusts is governed by the equation [4–7]

$$\partial_t q_d = I_e(q_d) + I_i(q_d), \tag{3}$$

for charge conservation.

We consider a quasi–stationary structure moving with a speed V in the x direction, satisfying $v_{Ti} \ll V \ll v_{Te}$. Thus, all parameters depend only on $\xi = x - Vt$. We shall also assume $v_i \gg v_{Ti}$, which imposes a lower limit on the magnitude of the electrostatic potential φ of the nonlinear waves. From the ion conservation equations, one obtains

$$n_i = M n_{i0} (M^2 - 2\varphi)^{-1/2}, \quad v_i = c_s(M - \sqrt{M^2 - 2\varphi}), \qquad (4)$$

where we have used the normalization $e\varphi/T_e \to \varphi$, $V/c_s \to M$, and $\xi/\lambda_D \to \xi$. Here, $c_s = (T_e/m_i)^{1/2}$ is the ion acoustic speed.

From the Poisson equation we can obtain

$$d_\xi^2\varphi = \exp(\varphi) + \left(1+\frac{\delta z}{z_0}\right) Z_{d0} d - \frac{M(1+Z_{d0}d)}{\sqrt{M^2-2\varphi}}, \qquad (5)$$

where $d = n_{d0}/n_{e0}$ and $z_0 = Z_{d0}e^2/aT_e$. The normalized charge perturbation $\delta z = -e\delta q_d/aT_e$ is governed by

$$d_\xi \delta z = j \equiv \frac{A}{\sqrt{M^2-2\varphi}} \left[\sqrt{\frac{2}{\pi}} \exp(-\gamma^2) + \left(\frac{1+2\gamma^2}{\sqrt{2}\gamma} + \frac{\sqrt{2}(z_0+\delta z)T_e}{\gamma T_i}\right) \mathrm{erf}(\gamma)\right] - \sqrt{\frac{8}{\pi}} \frac{A}{M} \left(1 + z_0 \frac{T_e}{T_i}\right) \exp(\varphi - \delta z), \qquad (6)$$

where $A = a[(1 + Z_{d0}d)/4\lambda_D](T_i/T_e)^{1/2}$, $\gamma = [M - (M^2 - 2\varphi)^{1/2}] \times (T_e/2T_i)^{1/2}$, and we have used (1)–(3). Note that j is the normalized perturbed total current density. Clearly, all solutions must satisfy $\varphi \le M^2/2$.

Equations (5) and (6) can be numerically integrated provided that the existence conditions for shock solutions are known. For the latter to exist, there must be two distinct asymptotic values for φ (say at $\xi \to \pm\infty$), and the derivatives of the perturbed quantities must vanish there. In this limit, we obtain from (5) and (6)

$$\delta z = f_1(\varphi) \equiv -z_0 + \frac{z_0}{Z_{d0}d}\left[\frac{M(1+Z_{d0}d)}{\sqrt{M^2-2\varphi}} - \exp(\varphi)\right], \quad j = 0. \qquad (7)$$

The set of equations (7) have two different solutions $\varphi = 0$ and $\varphi = \varphi_A$ only if

$$M^2 > M_0^2 \equiv \left(1 + \frac{1+Z_{d0}d}{Z_{d0}d} z_0 G\right) \left(\frac{z_0 G}{1+Z_{d0}d}\right)^{-1}, \qquad (8)$$

where $G = (1+z_0T_e/T_i)/[1+(z_0+1)T_e/T_i]$. We note that M_0 satisfies $1 < M_0^2 < 1+Z_{d0}d$. As an example, for the typical parameters $Z_{d0}d = 2$, $T_e/T_i = 10$, $a/\lambda_D = 0.01$, and $M = 1.7$, one finds $z_0 \approx 1.23$ and $\varphi_A \approx 0.935$. Thus, the inequality (8) is necessary for the existence of two asymptotic solutions, namely $\varphi = 0$ and $\varphi = \varphi_A$ (say at $\xi \to +\infty$ and $-\infty$, respectively).

A solution bridging these two asymptotic ones can be obtained by making the Ansatz that the second derivative in (5) is negligible. In this case we obtain from (5) and (6)

$$d_\varphi \xi = \frac{1}{j} d_\varphi \delta z = \frac{z_0}{Z_{d0} j d} \left[\frac{(1+Z_{d0}d)M}{(M^2-2\varphi)^{3/2}} - \exp(\varphi) \right], \tag{9}$$

which can be integrated. The zeros of the denominator on the right hand side of (9) correspond to $j = 0$, or the asymptotic values of $\varphi(\xi)$. Within the range $0 < \varphi < \varphi_A$ the function j is negative (see Fig. 1).

A solution for φ can now be obtained. An analysis of (9) (with taking into account that $j < 0$ for $0 < \varphi < \varphi_A$) shows that such a solution existing for all ξ: $-\infty < \xi < \infty$ takes place only if

$$M^2 \leq 1 + Z_{d0}d. \tag{10}$$

This solution corresponds to positive value of $\delta z_A = \delta z(\varphi_A)$. In fact, for the parameters in our example we obtain $\delta z_A \approx 0.31$. The solution of (9) in the case (10) is a decreasing function with $\varphi \to \varphi_A > 0$ for $\xi \to -\infty$, and $\varphi \to 0$ for $\xi \to +\infty$. In Fig. 2 the profile of the potential $\varphi(\xi)$ satisfying (9) is shown. A similar profile for the normalized charge perturbation δz can be deduced from (6) by recalling that j is always negative in the region of interest.

In the analysis we have neglected the second derivative d_ξ^2 in (5), equivalent to assuming quasineutrality in the wave dynamics. For waves with amplitude φ_A near or exceeding unity, this Ansatz is valid if the the width of the shock front $\Delta\xi$ greatly exceeds unity. For the shock wave in Fig. 2, we have $\Delta\xi \sim 100 \gg 1$, so that the Ansatz is well justified.

Thus, shock solutions are possible for Mach numbers satisfying both (8) and the condition (10). The shock amplitude φ_A is an

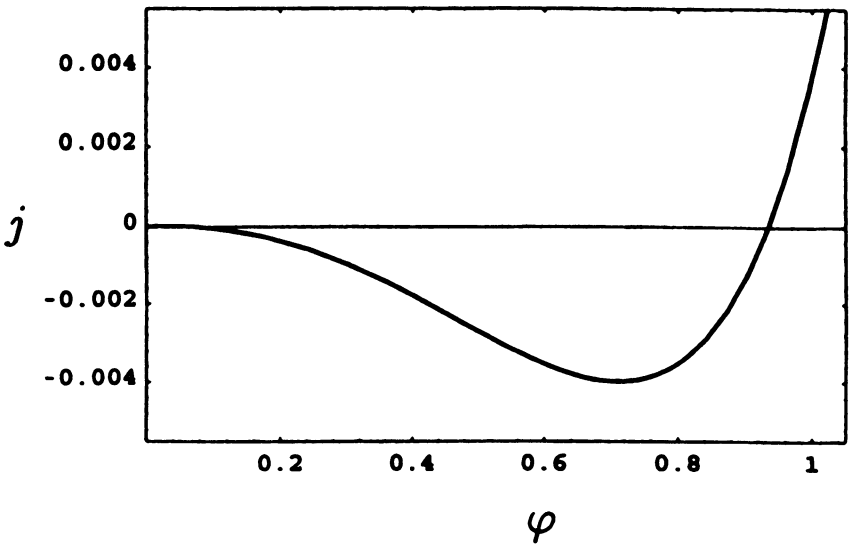

Figure 1: The dependence of j on φ for $Z_{d0}d = 2$, $T_e/T_i = 10$, $a/\lambda_D = 0.01$, and $M = 1.7$. The solutions of the equation $j = 0$ are $\varphi = 0$ and $\varphi = \varphi_A \approx 0.935$.

increasing function of M. The maximum value of the amplitude corresponds to $M^2 = 1 + Z_{d0}d$, and is given by $\varphi_A|_{\max} \sim (1 + Z_{d0}d)/2$. The shock solutions are inherent in the collisionless situation where one can neglect electron–electron, electron–ion, and ion–ion collisions and has to take into account only charging collisions of electrons and ions with the dust particles. This situation can occur because the charging frequency $\nu_q = \omega_{pi}^2 a(1 + z_0 + T_i/T_e)/\sqrt{2\pi}v_{Ti}$ (where ω_{pi} is the ion plasma frequency) is much larger than the ion-ion collision frequency and also exceed the electron collision frequencies [4]. Thus the shock waves in the plasma containing the dust grains with variable charges can be treated as collisionless. The character of dissipation in these waves significantly differs them from the usual collisionless shock waves (in impurity–free plasmas) [2].

This work is partially supported by the Russian Foundation for Fundamental Research (grant no. 96-02-16456-a) and by the Sonderforschungsbereich 191 Niedertemperatur Plasmen.

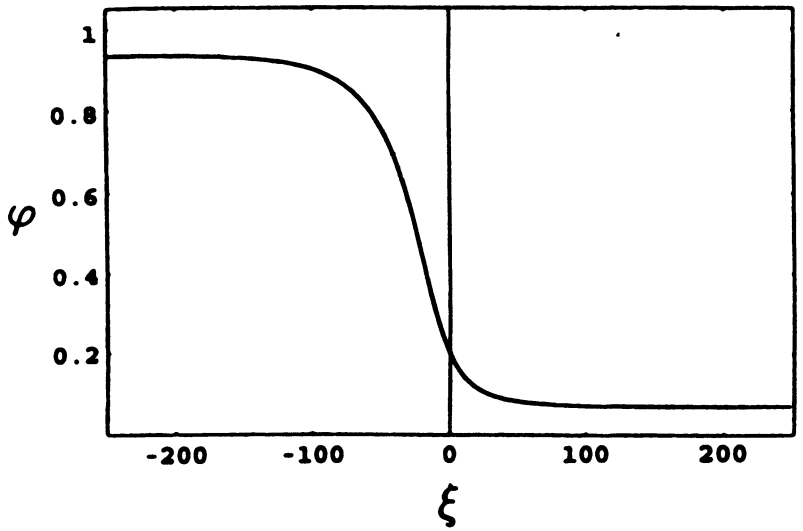

Figure 2: The $\varphi(\xi)$ profile for the nonlinear wave structure. The parameters are the same as those of Fig. 1.

References

1. Zel'dovich Ya.B. and Raizer Yu.P., Physics of Shock Waves and High-Temperature Hydrodynamic Phenomena. New York: Academic, 1967.
2. Sagdeev R.Z., in Reviews of Plasma Physics, edited by M.A. Leontovich, Vol. 4. New York: Consultants Bureau, 1966, p. 23.
3. Chen F.F., Introduction to Plasma Physics. New York: Plenum, 1974, Chap. 8.
4. Tsytovich V.N. and Havnes O., Comments Plasma Phys. Controlled Fusion, 1993, **15**, 267.
5. Vladimirov S.V., Phys. Plasmas, 1994, **1**, 2762.
6. Popel S.I. and Yu M.Y., Phys. Rev. E, 1994, **50**, 3060; *ibid*, Contrib. Plasma Phys., 1995, **35**, 103.
7. Ma J.X. and Yu M.Y., Phys. Plasmas, 1995, **1**, 3520.

HIGH-POWER MICROWAVE SOURCES

MEGAWATT POWER LEVEL LONG-PULSES 110 GHz AND 140 GHz GYROTRONS

V.E. Mjasnikov, M.V. Agapova, V.V. Alikaev, A.S.Borshchegovsky, G.G. Denisov, V.A. Flyagin, A.Sh. Fix, V.I. Ilyin, V.N. Ilyin, A.P. Keyer, V.A. Khmara, D.V. Khmara, A.N. Kostyna, V.O. Nichiporenko, L.G.Popov, V.E. Zapevalov

GYCOM Ltd., Nizhny Novgorod, RUSSIA
Phone: (8312) 365810, Telex: 151129 FIZIK SU, FAX: (8312) 362061

Abstract

The new design of the gyrotron, which was intended for operation in long-pulse and (in future) CW regime needed for electron cyclotron plasma heating (ECH) have been completed by GYCOM (Toriy SRPC Moscow, IAP N.Novgorod, KIAE Moscow) in the end of 1993. Since that time a series of gyrotrons based on the original design and its modifications, has been built to provide ECH in W7-AS stellarator, ASDEX Upgrade tokamak (both IPP, Germany) and D III-D tokamak (GA, USA). A set of convincing results was obtained during the gyrotron testing and operation. An output power approaching to 1 MW was achieved in 140 GHz frequency range with pulse duration of 1.2 s and in 110 GHz frequency range with pulse duration of 2 s. In 3 s pulse 140 GHz gyrotron produced output power in excess of 0.5 MW.

Introduction

In the end of 1993 GYCOM Ltd. has completed development of the new design for gyrotron which could operate in long-pulse or even CW regime in above 100 GHz frequency range. At the same time first 140 GHz gyrotron of new design was successfully tested [1]. It produced 535 kW output power in 3 s pulse.

New design of gyrotron base oneself upon the main subassemblies, which are developed for CW operation with the thermal stabilization time less than 2 s. Gyrotron scheme is presented in Fig. 1. The only unit, which limits advance of gyrotron from long-pulse operation to CW regime, is now an output window built on the basis of pyrolitic boron nitride (BN) disk. The energy, which this window is capable to pass through, is about 2 MJ.

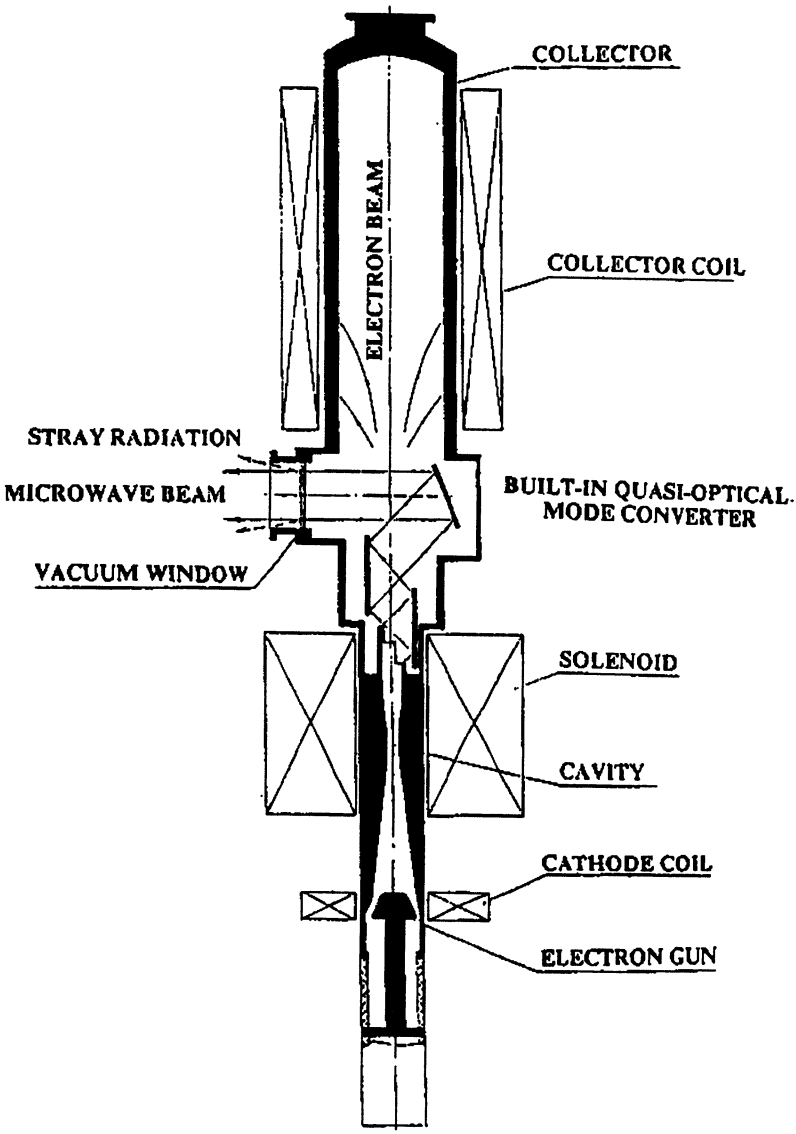

Fig .1. Gyrotron overall scheme.

One can distinguish the principal peculiarities, which are habitual for all the gyrotrons of new design.

- For the cavity made of dispersion-strengthen copper the high-effective cooling system is used, which provides cavity inner surface to have the temperature not exceeding 250 ^{0}C under heat loading up to 5 kW/cm^2.
- For the electron gun, which produce electron beam of so-called boundary type with relatively low velocity spread, metal-porous cathode is used. Cathode emitting performances while manufacturing of each one are carefully checked by original methods.
- Built-in quasi-optical converter, which transforms cavity operation mode to Gaussian beam, shapes the radiation with flattened power distribution over the window surface. This kind of wave beam pattern allows in assigned frequency range to pass through BN single disc window the radiation with power up to 1 MW and pulse duration within 1 s to 3 s.
- Collector is equipped with a sweep coil supplied by saw-tooth current to move an electron beam along the specially shaped collector wall. It gave the possibility to extend sufficiently surface scanned with electron beam and to provide the heat loading not to exceed 1 kW/cm^2 under megawatt level electron beam deposition.
- High accuracy of gyrotron assembly on a whole is foreseen with the design of each gyrotron unit, and technological processes applied for gyrotron manufacturing give the possibility to maintain the conditions, which are needed for reliable and long-lived gyrotron operation.

Slight modifications of the original design and optimization of operation regime for higher output power made it possible to create gyrotrons with about 1 MW power level in 110 GHz and 140 GHz frequency ranges [2,3]. Both gyrotrons demonstrated near 40% efficiency, and last one is intended for operation in the complicated (for gyrotron collector) ambient magnetic conditions under lateral magnetic field up to 6 Gs exposure. The most important information about GYCOM gyrotrons is summarized in the Table 1.

Table 1
GYCOM gyrotrons of 110 GHz and 140 GHz frequency ranges.

Gyrotron type (called as first gyrotron in series)	HERCULES	ZODIAC	CENTAUR
Frequency, GHz	140	140	110
Total radiated power, MW	≥ 0.5	0.65 - 1.0	1.0
TEM_{00} mode power fraction in the total radiation	0.85	0.85	≈ 0.9
Pulse duration, s	3	1 - 2	2
Cavity mode	$TE_{22\,6}$	$TE_{22\,6}$	$TE_{19\,5}$
Efficiency, %	≥ 30	≥ 30	≥ 35
Beam voltage, kV	75	75	80
Beam current, A	30	35	40
Users installation	W7-AS IPP Germany	ASDEX Upgrade IPP Germany	D III-D GA USA
Manufacturing period	1993-95	1995-96	1995

Design

Cavity

The advanced non-linear theory of the electron beam interaction with RF field of the cavity mode is used to compute the cavity and RF radiation parameters.

Choice of optimal cavity mode for (0.5-1) MW gyrotrons is determined by admissible RF ohmic losses in the cavity wall, mode selection and mode competition conditions for single-mode operation and beam voltage depression.

Considering all these conditions the $TE_{22\,6}$ operating mode was chosen for 140 GHz gyrotron.

Fig.2 demonstrates so-called "tuning curves" for ZODIAC type gyrotron, i.e., dependencies of the efficiency, output power and RF ohmic losses on the magnetic field in the cavity. Two sets of the curves are

presented. The first set corresponds to 5.2 kV space charge depression in the electron beam potential. The second one is valid, when the space charge is compensated by ions of residual gas.

The calculations were done taking into account velocity spread $\delta v_\perp$ in the electron beam. The ohmic losses in cavity walls are given for the cavity center where they are maximal. The cavity maximal ohmic losses are not exceeding 2.4 kW/cm^2 at output power of 1 MW and efficiency of about 40%.

In accordance with calculations of the electron gun the velocity spread $\delta v_\perp$ in the electron beam is expected to be near 0.20-0.3

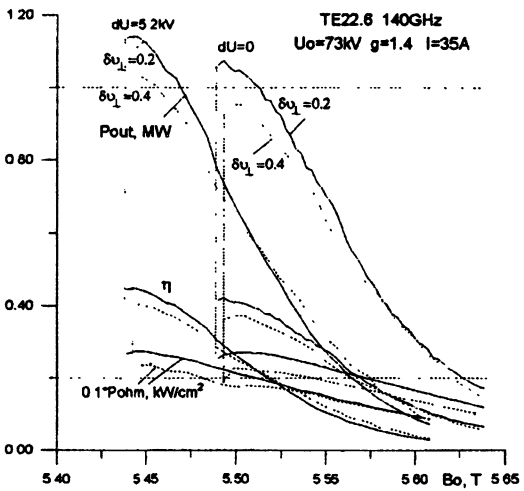

Fig.2. Calculated output power, efficiency and RF ohmic losses vs. Magnetic field (with and without space charge depression) for 140 GHz gyrotron.

The cavity mode of 110 GHz gyrotron is $TE_{19.5}$. For the optimized cavity profile of CENTAUR gyrotron the results of calculations of the output power P_{out}, efficiency η and thermal load of the cavity p_{ohm} as the functions of the beam current I are presented in Fig.3. Calculations show possibility to attain 1MW output at the beam current below 40 A with maximum ohmic load of 2.25 kW/cm^2.

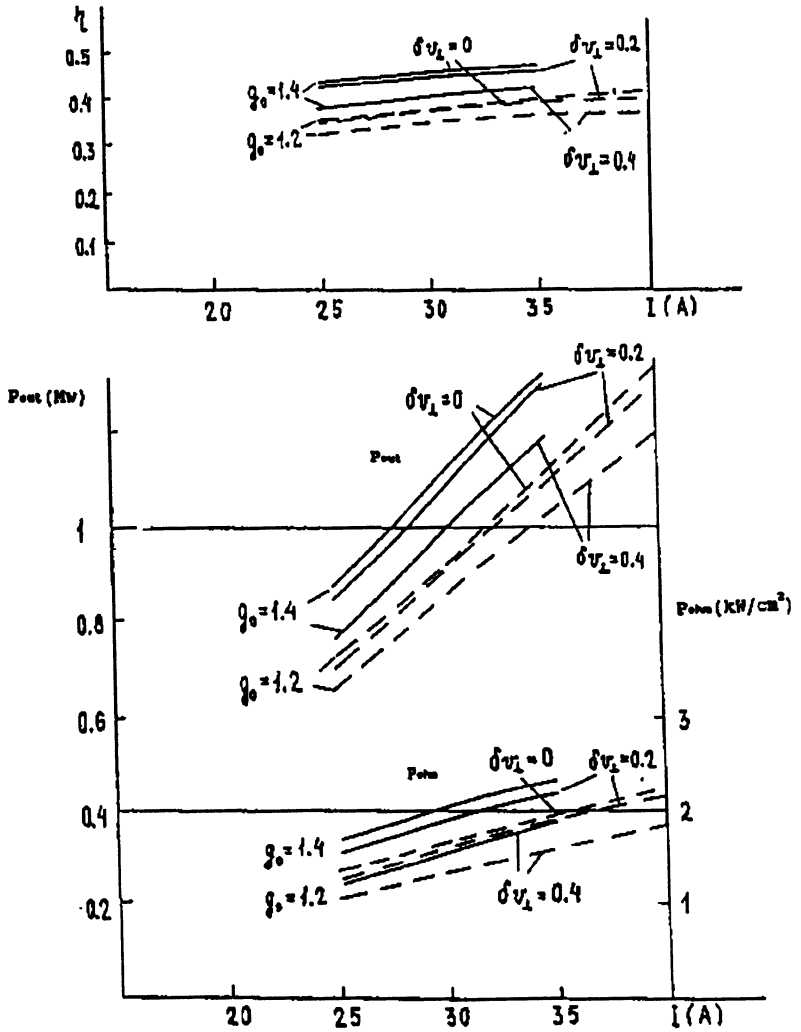

Fig.3. Calculated efficiency η, output power P_{out} and density of ohmic losses in cavity p_{ohm} depending upon electron beam current I at pitch factors g equal to 1.2 and 1.4 and electron velocity spread $\delta v_\perp$ equal to 0, 0.2 and 0.4 .

Due to a high-effective cooling system with porous structure the inner cavity surface can withstand the ohmic losses of 2.5 kW/cm^2 with its calculated temperature level not more than 250^{0}C. The cooling system consumes 40 l/min water flow, 4 bar of input pressure. The thin cavity wall envelope is made of dispersion-strengthened copper.

Electron gun and cathode technology

For the megawatt power level gyrotrons the gun with operating current of (30-40) A and decent velocity spread is required. The electrical field at working emitting surface ~6 kV/mm is typical for gyrotron gun. Optimal value of pitch factor should be (1.3-1.4) taking into account the conflicting factors of beam space stability and achieving as high as possible beam-wave interaction efficiency in the cavity. Pointed properties are similar for HERCULES, ZODIAC and CENTAUR types gyrotron guns and, hence, they are equipped with the same type of cathode. Main distinctions of gun design are determined by difference in cavity operating modes, frequency ranges and, consequently, the cavity beam radii.

At the design stage the numerical calculations with trajectory analysis was carried out. In both gyrotron frequency ranges the diode-type magnetron-injection gun has been chosen. Calculation results show the rather high beam quality with $\delta v_\perp$~20% even at the maximal current. This fact allows in principle to achieve the beam-wave interaction efficiency near 40%.

Azimuthal homogeneity of electron beam is an important factor of tube proper operation. The electron beam is produced by metal-porous cathode with its temperature of about 1050^{0}C. The width of emitting belt is 5 mm, average diameter is 83 mm, the current density is (3-4)A/cm^2 at operation regime. To achieve rather uniform distribution of the emitting current, special attention has been paid to the cathode technology.

Before mounting into tube the quality control of cathode unit is carried out by checking of temperature and current emission azimuthal homogeneity in original installation. Investigations are performed in current density saturation mode at near operation temperature in pulse regime.

Current measurements are made by means of current-collection microprobe, inserted into special anode. Scanning of probe is executed by anode or cathode rotation. Space resolution is about 1 mm^2.

Typical azimuthal distribution of current density are plotted in Fig.4.

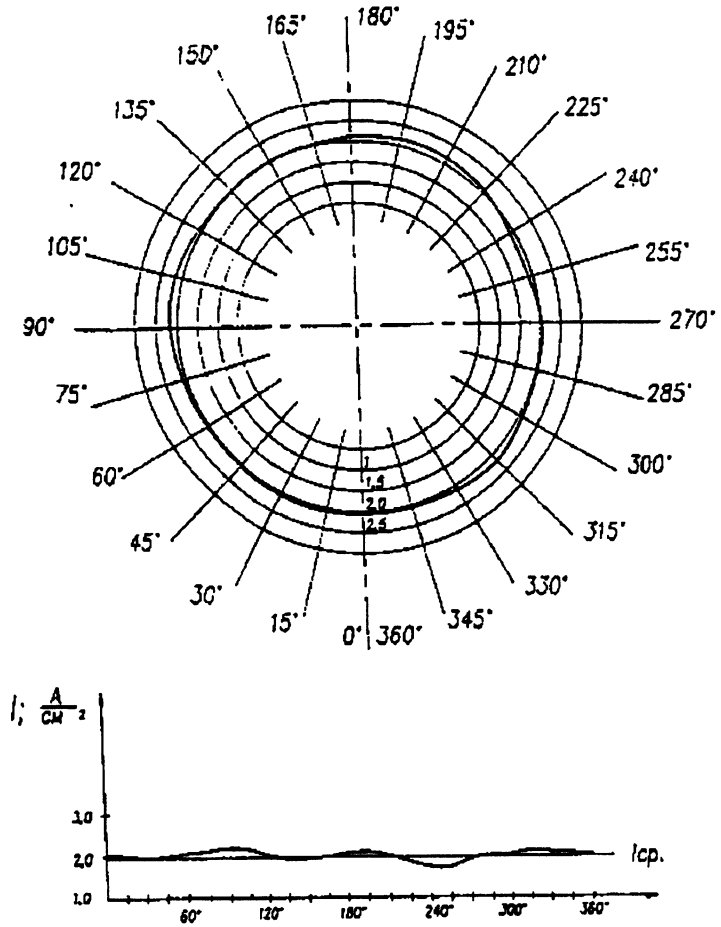

Fig.4. Cathode current density distribution (T=1040°C).

After exhaustive search it was determined that gyrotron cathode based on so-called "plasma" metal-porous emitter has current density inhomogeneity level below ±10% of its average value.

The homogeneity of secondary emission from emitting surface is checked too. Using the scanning microscopy method the secondary emission mapping of cathode surface was got with azimuthal resolution

~1^0 and space one along the axis of about(0.05-0.1)mm. Typical examples of secondary emission mappings of cathode surface at different stages of activation are presented in Fig.5. It is necessary to note that the secondary emission mapping of cathode surface has a good correlation with its current density azimuthal distribution.

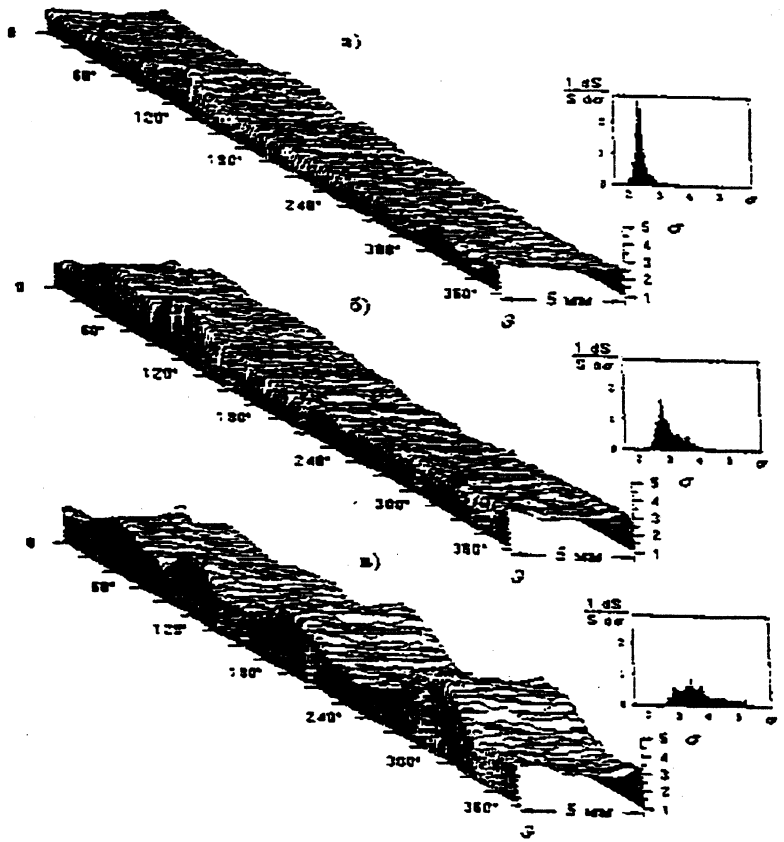

Fig.5. The secondary emission current homogeneity at different stages of activation process.

To find out the reasons of observed inhomogeneities the checkup method of cathode temperature field azimuthal homogeneity was developed. This method is used together with emitter chemical composition

analysis, carrying out with well-known Auger spectroscopy and X-ray spectral analysis methods.

The main point of new method is visualization of distribution of emitting surface brightness in range of $\lambda=(0.7\text{-}1.0)\mu m$ by use of PC-controlled videosystem. Designed special equipment allows to checkup the temperature in $(400\text{-}1200)^0C$ range with space resolution of 0.2 mm and temperature resolution of 0.7^0C. Typical example of cathode temperature field is presented in [4]. Developed method demonstrated that the cathode based on "plasma" metal-porous emitter has inhomogeneity level of temperature field of about $(3\text{-}4)^0C$.

Developed checkup methods integrated into technology allows to make reliable cathodes with mentioned above parameters.

Mode converter

The mode converter is an important part of gyrotron internal electrodynamic system. It allows to separate the RF radiation from the worked-out electron beam, transform a cavity mode to a paraxial linear-polarized wave beam, minimize harmful action of possible reflections of RF power to a gyrotron.

The build-in quasi-optical (QO) converter, which consists of an irradiator and 3 beam- forming mirrors, has a diffraction losses due to finite reflectors dimension and the window aperture. Owing to negligible absorption inside the tube the output wave beam consists of paraxial wave beam and stray radiation which is, as a matter of fact, converter diffraction losses.

The advanced computer codes were used for optimization of the converter to increase the Gaussian mode content in paraxial wave beam, decrease the diffraction losses, provide optimal RF distribution over the output window.

According to the calculation and experimental results for ZODIAC and CENTAUR gyrotrons the TEM_{00} mode contents in paraxial wave beam is at least 90% and the relative stray radiation power is (7-10)%. Thus, the Gaussian mode content in the output RF radiation is about 85%.

Both calculated and measured by infrared camera RF field patterns are shown in Fig.6,7 for gyrotron of ZODIAC type. One can see a good agreement between the measurements and calculations.

a)

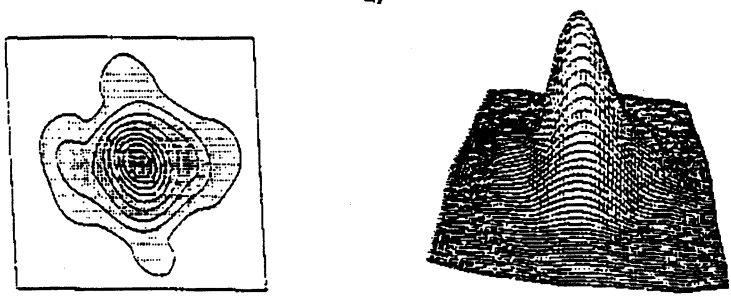

b)

Fig.6. Calculated field amplitude distributions at the distance (a) Z=0 mm and (b) Z=1000 mm from the gyrotron window.

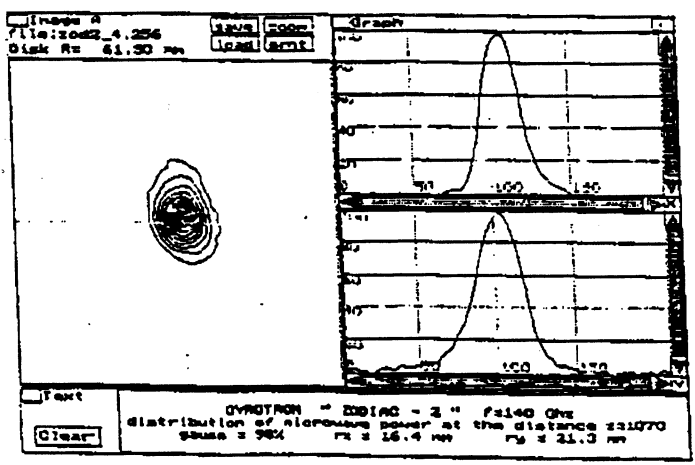

Fig.7. Measured distribution of microwave power at the distance Z=1070 mm from the gyrotron window for Zodiac 2 gyrotron.

Output window

For output windows the pyrolytic boron nitride single disc brazed into a metal cylinder with water cooling along its edges is used. The physical parameters of BN materials are (1) $\tan\delta \sim (0.9\text{-}1)*10^{-3}$; $\varepsilon \sim (4.4\text{-}4.7)$ for frequency range of 110 GHz and (2) $\tan\delta \sim (1.1\text{-}1.4)*10^{-4}$; $\varepsilon \sim (4.4\text{-}4.7)$ for frequency range of 140 GHz depending on a specimen quality. Since the thermal relaxation constant of window is several tens of seconds, its thermal regime is characterized mainly by absorbing energy accumulation with weak effect of heat conductivity. This defines a special requirement for as uniform as possible RF energy distribution over the window, still having in mind .

To reach combination of maximal output power level and pulse duration one had to follow two ways:

- the first one was increasing of the window diameter from 80 mm to (123-145) mm for ICAR (HERCULES type tube), ZODIAC and CENTAUR gyrotrons.

-the second one was improving the RF power distribution over the window by means of using nonquadratic last inside mirror in gyrotrons of ZODIAC and CENTAUR types.

As remark, the quadratic last internal mirror was used in gyrotron of HERCULES type.

Output power and pulse duration limits were defined during the gyrotron test with special developed videosystem taking into account the RF absorption properties of the BN disk and its admissible temperature of 700^0C [4]. The start temperature of the oxidation process for pyrolytic BN is 1200^0C. Experimental dependencies of maximal temperature of BN window surface versus pulse energy at various pulse power and pulse duration are given in Fig.8 showing that the maximal temperature did not exceed 700^0C at specified regimes of 140 GHz tube.

The maximal energy passing through the window is estimated as 1.5 MJ for 140 GHz gyrotrons and 2 MJ for 110 GHz ones.

Collector

The collectors withstanding the (1.5-2)MW electron beam deposition are necessary to provide the proper operation of megawatt level gyrotrons. The base design cylindrical shape collector with average inner diameter~250mm and overall length ~1000mm, equipped with special coil for sweeping an electron beam along the axis, has been designed. Both its

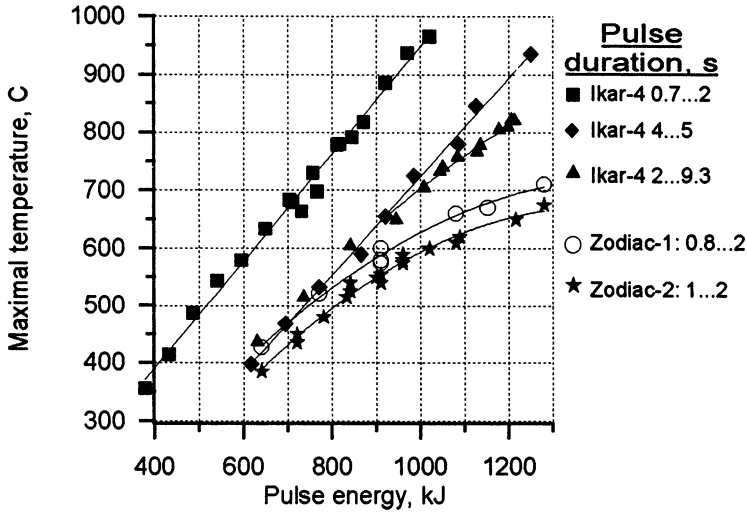

Fig.8. Maximal temperature of BN window surface vs. pulse energy at various pulse power and pulse duration

inner surface and own magnetic field distribution are optimized to reduce thermal load and make it as homogenious as possible. Collector is water cooled, its exchange thermal coefficient is about $10W/(cm^2*K)$. Varying the type of collector coil, its current parameters and some subassemblies of the base design, the multimegawatt collectors, operated in different frequency ranges and ambient magnetic conditions, can be created.

The calculated data are indirectly verified by the collectors reliable operation.

The gyrotrons of HERCULES type are operated in simple ambient magnetic conditions with lateral stray field up to $3*10^{-4}T$. These tubes are equipped with base design collector, which scaned length is of 800 mm. Maximal local steady temperature of inner surface reaches 250^0C at 1.5MW electron beam deposited at 3Hz sweeping frequency. Average heat load is less than 0.5 kW/cm^2. Due to some temperature reserve these gyrotrons reliably operate even if the breakdown of cavity oscillation is occures.

ZODIAC gyrotrons, operated in more complicated ambient magnetic conditions, equipped with the collector, withstanding the exposure of lateral stray magnetic field up to $6*10^{-4}T$ at 1.5 MW electron beam deposition. The simplest way to provide proper operation in this case was reducing of scaned length to make reserve zone for deflected electron beam

and creation of sharper slope of collector magnetic field. Due to increased up to 7Hz sweeping frequency and fitted distribution of collector coil magnetic field, the scaned length was shortened to 520mm without noticeable temperature level increasing in the simple ambient magnetic conditions case. If the lateral stray magnetic field up to $6*10^{-4}$T is present, the maximal scaned length reaches 800 mm, but maximal local steady temperature of inner surface is not exceed 290^0C. Average heat load is slightly over a level of 0.5 kW/cm^2.

In CENTAUR gyrotron the electron beam can be practically twice as powerful, as mentioned above. But the ambient magnetic conditions are simple. This gyrotron was equipped with base design collector, withstanding the deposition of 2 MW electron beam, due to fitting the collector coil magnetic field distribution and beam sweeping frequency to make the temperature field smoother. At sweeping frequency of 5Hz and scaned length of 800 mm, the average heat load reaches the 0.7kW/cm^2 level. But the maximal local steady temperature of inner surface does not exceed 260^0C.

If the oscillation breakdown occures in HERCULES cavity, the 3MW electron beam will come to collector, and its inner surface temperature will exceed the reliable operation level of 300^0C and more. To avoid overheating of collector, the interlock system have to switch off the beam voltage within 50 ms.

Tests results

Testing procedure

Gyrotron testing is carried out aiming to attain its reliable operation with specified pulse duration, output power, efficiency, frequency range and output radiation mode. To reach the operation reliability exceeding 90% with pulse duration up to 3s gyrotron conditioning is needed. During the gyrotron testing its beam voltage and current, main magnet and cathode coil currents are optimized for highest efficiency at necessary power level. Structural scheme in Fig.9 shows the set of equipment units involved in a gyrotron testing and conditioning procedure.

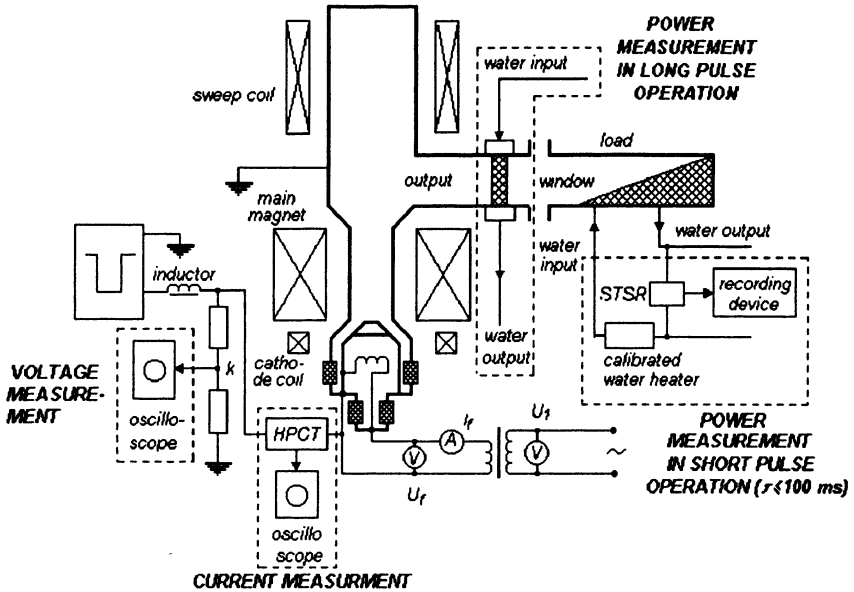

Fig.9. Structural scheme of gyrotron test equipment.

During long-pulse testing gyrotron RF power usually is transmitted to a brick load, which is capable to absorb large energy, and can not be measured directly. Output power measurement in this case is performed by the "window calorimetry". The output power is calculated from the calorimetricaly measured power absorbed by the window through the window losses coefficient. To find out this coefficient, which value is typically within 3% to 5%, a set of simultaneous output power and window absorbed power measurements has preliminary to be carried out. Usually these calibrating measurements are performed at pulse duration of 100 ms, when the energy absorbed in a window is sufficient for measurement accuracy and the energy absorbed in a dummy load is not so large that cooling water starts to boil.

The reliability of gyrotron RF power data obtained by "window calorimetry" at pulse duration up to 3s have been proved by direct measurement of certain small power fraction separated from output radiation by corrugated mirror. It was checked by RF detector signal stability too.

The testing equipment must be supplied with a set of interlocks to prevent gyrotron's damage while running. For instance, if a breakdown

inside a gyrotron have occurred, the interlock tripping should limit the energy deposition inside the gyrotron at the level not more than 10 J. Another interlock should protect a window from overheating. Recently developed videosystem is used now for a window temperature monitoring[4] to set the level of interlock tripping.

Window absorbed power and hence its temperature depends not only on an output power but on a reflected one too. Reflected power is often the reason for gyrotron arcing or oscillations breakdown. That is why any significant reflections should be avoided. Power reflection can be caused by imperfection of either load or wave transmission line or matching mirrors. The effect of reflected power on gyrotron of HERCULES type behavior was observed during initial transmission line matching at IPP. When mirrors with incorrect surface shape were used, it caused large fraction of stray radiation inside the mirror box. This radiation, being not carefully absorbed, was reflected and thus prevent stable gyrotron operation. Exactly the off-designed increasing of window absorbed power during gyrotron operation was considered as the first sign of output power reflection.

Before installing a gyrotron into a magnet's bore it is necessary to align the centers of the top and the bottom fitting flanges, which are intended to fix gyrotron radial position, with the axis of the magnetic field. This alignment is performed with the special tool equipped with two Hall probes to measure the azimuthal symmetry of a magnetic field distribution inside the bore. The permissible misalignment of the magnetic axis and the centers of both fitting flanges is of 0.1 mm.

Gyrotron performances

Despite the fact that the considered gyrotrons are of three modifications due to their different frequency range, output power level and pulse duration their performances, when some operating regime needs to be changed, are very similar.

Fig.10 shows measured output power and efficiency as a function of a beam current for CENTAUR gyrotron. With the beam current increasing an output power rose up to about 1 MW at efficiency approaching 40%.

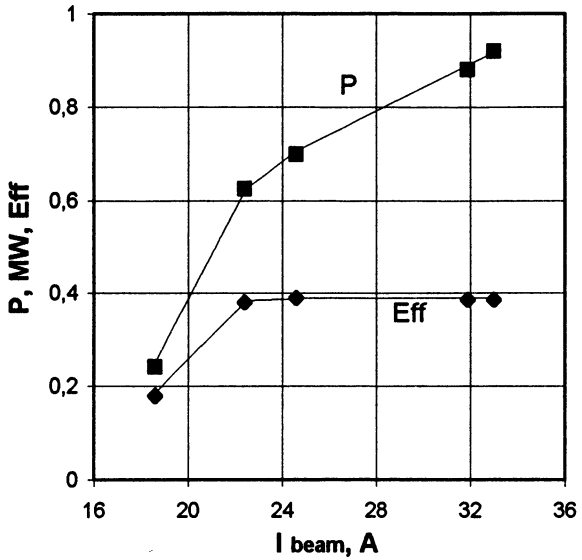

Fig.10..Output power and efficiency of CENTAUR gyrotron vs. beam current.

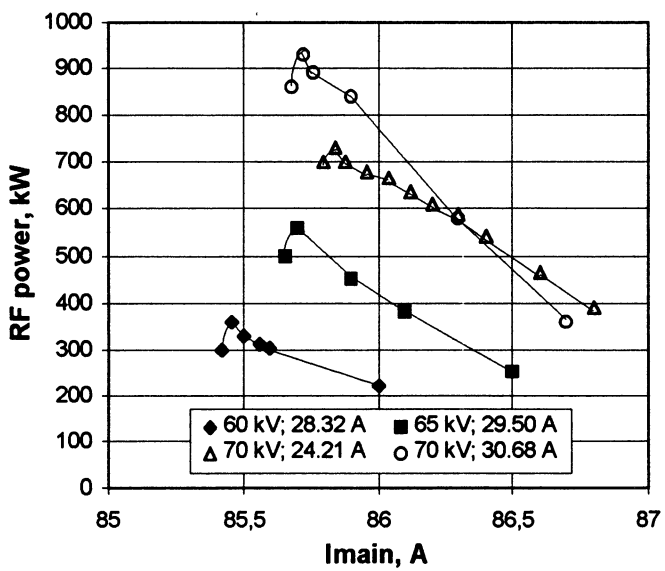

Fig.11. Output power of ZODIAC gyrotron vs. main magnet current at different beam voltages and currents.

In Fig.11 an output power of ZODIAC gyrotron is plotted against the main magnet current. To drive the gyrotron from the nominal regime to the optional one it was enough to increase the beam current from ~24 A to ~ 30 A and adjust a main magnet current value at the same beam voltage of 70 kV.

To confirm the gyrotron ability to run in the power modulated regime the power measurement was carried out at the beam voltage reducing from 70 kV to 55 kV and fixed all the other settings for both the nominal and the optional regimes. It is seen from the plot in Fig.12 that output power dropped much faster with voltage lowering than in the case in Fig.11, when the magnet current was adjusted to its optimal value.

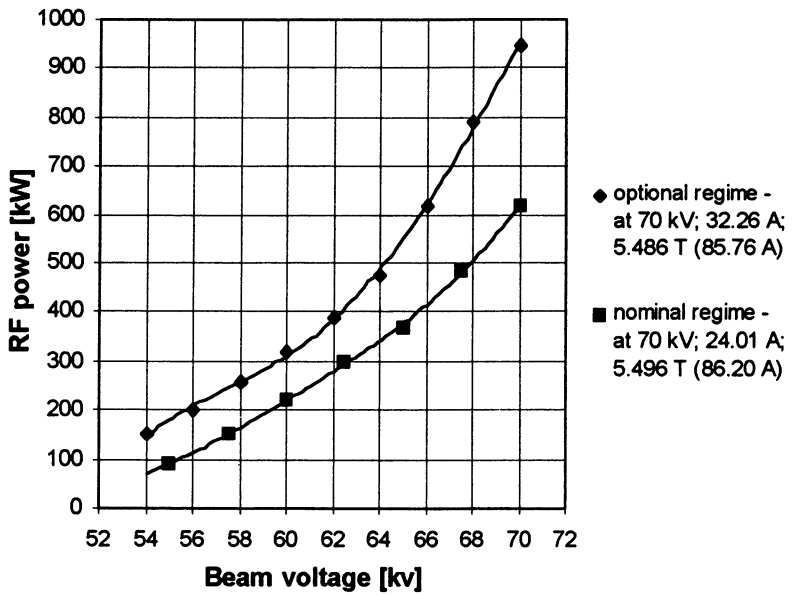

Fig.12. Output power of ZODIAC gyrotron in nominal and optional regimes dropping with beam voltage reducing.

Some unwanted effects

Usage in gyrotrons of high- voltage large-current electron beams, catching with a strong magnetic field can lead under certain conditions to excitation of some secondary oscillations or to particular discharge arising. These conditions either could appear during gyrotron manufacturing due to slight fluctuations in its technology, or may be initialized later on with some external reasons during gyrotron running. The misalignment of

gyrotron and magnetic field axes as well as sufficient power reflection from the wave transmission line should mainly be considered in the last case.

Parasitic oscillation was met for the first time during testing of the HERCULES type gyrotron as a kind of pickup on several monitored and control signals. The frequency range of this oscillation with its harmonics is typically 20 MHz to 150 MHz. The radiated power is negligible if compared with gyrotron output one but it is well enough to be the serious obstacle for testing equipment operation. The nature of this oscillation is not completely studied. Obviously it occurs due to electrons with the high starting pitch angle trapping between the cathode and the magnetic mirror. . For HERCULES gyrotron it was possible to damp this oscillation after hard conditioning but then the oscillation burst out again. With the special kind external capacitive filter shunted the HV insulator on a gyrotron's body the radiated power was reduced at least on 20 dB. It puts to an idea that HV power supply and its connecting cables probably take part in this oscillation excitation too. In any case the EMI problem should be solved by both gyrotron and testing equipment debugging.

During the testing of few gyrotrons it was met a new phenomenon, which for a long enough time could not be satisfactory accounted. Outwardly it looked like usual breakdown inside a gyrotron but without any throw of vac-ion current. It occurred at pulse duration about 30 ms and defied conditioning. Under the careful examination of beam voltage and current behavior it became clear that this breakdown is not a real arcing. This type of breakdown (so-called "soft breakdown") has a significant discharge voltage (20% to 100% of rated beam voltage) and discharge current, which is 2 to 3 times more than beam current. Current and voltage fluctuations forestalling the crowbar are presented in Fig.13. This fluctuations are determined not only by a nature of "soft breakdown" but by large dynamic output impedance of HV power supply too. The current initial fast increasing results in cathode voltage reduction and, thus, damping of discharge. Therefore, cathode voltage starts to grow again. Sometimes several cycles of that kind were observed before crowbar protected the tube.

An interesting result was obtained under interior gyrotron pressure changing within 10^{-7} to 10^{-5} torr by getter heating. The pulse duration, when "soft breakdown" occurred, depended inversely on the pressure.

The hypothesis was proposed that outlined "soft breakdown" take place in the space below the cathode. In this region electrical and magnetic fields combining forms a trap for electrons, which could be born for instance with Penning discharge. Electron accumulation in the trap should result in a breakdown. Somehow the ceramic insulator being bombarding with electrons and ions should take part in this phenomenon too.

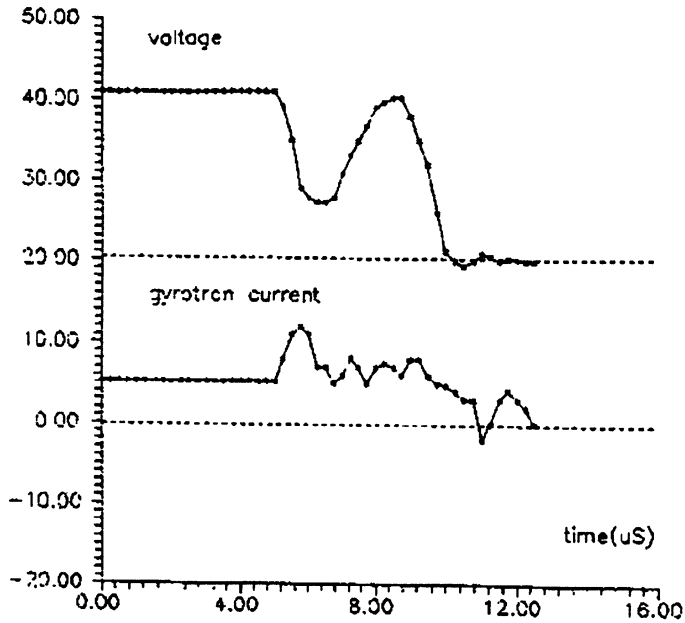

Fig.13. Voltage and current fluctuations under a "soft breakdown".

The easiest way to destroy this trap in the already existing gyrotron was mounting of the magnetic shield in cathode region to disturb the magnetic field distribution. Fig.14 shows calculated electrical equipotential and magnetic strength lines as well as electron trajectories before (a) and after (b) iron shield installing. (Numerical simulation was made by A.Kuftin and V.Lygin).

Exactly the iron shield usage have allowed to get over considered breakdowns without gyrotron design changing.

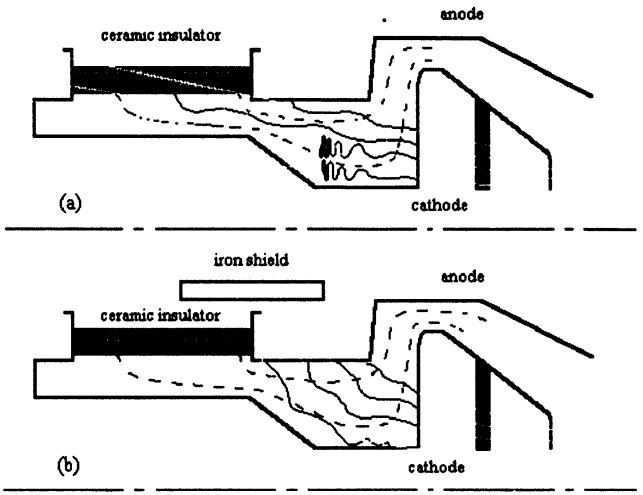

Fig.14. Electron trajectories (solid lines) without (a) and with (b) iron shield installed below the cathode. Dashed curves-

Main parameters

During the tests of gyrotrons of HERCULES, ZODIAC and CENTAUR types a set of convincing results on their operation parameters have been achieved.

HERCULES was the first one in series of 140 GHz gyrotrons producing RF power in excess of 0.5 MW with pulse duration up to 3s. HERCULES itself generated in 3s pulse output power of 535 kW with efficiency about 40%. The Gaussian beam contents in the HERCULES gyrotron output radiation was of 82%. The output radiation quality have later on been improved in next gyrotrons of HERCULES type and its following modifications. Gaussian beam fraction is now within 85% to 88%.

ZODIAC type 140 GHz gyrotrons had to radiate higher power but in shorter pulses. The power of 620 kW with efficiency of 39% was attained in nominal regime at pulse duration up to 2.5s. In optional regime power was increased to 960 kW and efficiency reached 44%. Maximal pulse duration was of 1.2s.

For CENTAUR type 110 GHz gyrotron power level of about 1 MW was available at longer pulses due to lower window losses in its frequency

range. Power of 926 kW was obtained at specified pulse duration of 2s with efficiency of 38%.

All the parameters listed above were obtained for the gyrotrons delivered within the contracts to IPP(Germany) and GA(USA).Contract specifications limit maximal beam voltage with 75 kV or 80 kV. All the mentioned gyrotrons were tested under beam voltage less than 75 kV.

A special test of the HERCULES type gyrotron was carried out to check the limit power passing possibility of a BN single disk window. Owing to imperfect wave beam structure of tested gyrotron it was rather small spot on the window with high power density. In this test window temperature was limited with setting of a window light interlock to the usual constant level. Pulse duration at different output power was increasing up to interlock tripping. But this tripping took place at a different maximal window temperature due to heterogeneity of power distribution over the window and involving of a heat spread process at large pulse duration. Nevertheless pulse duration of 5s at power of 250 kW and that of 9.3s at 140 kW were achieved.

Conclusion

Developed gyrotrons in 110GHz and 140GHz frequency ranges are generate the output power of about 1 MW level at (2-3)s pulse duration with ~40% efficiency. The gyrotrons are used at W7-AS, Asdex-Upgrade (Garching, Germany) and D III-D (San-Diego, USA) installations.

References

1. Agapova M.V. et al. XIX International Conference on infrared and Milimeter Wawes, 1994, 79
2. Agapova M.V. et al. XX International Conference on infrared and Milimeter Wawes, 1995, 205
3. Mjasnikov V.E. et al. XXI International Conference on infrared and Milimeter Wawes, 1996, AThl
4. Ilyin V.N. et al. - this Conference

ACHIEVEMENT OF STABLE OPERATION OF POWERFUL GYROTRONS FOR FUSION

V.E.Zapevalov

Institute of Applied Physics, Russian Academy of Sciences,
46 Ulyanov Street, 603600 Nizhny Novgorod, Russia

Abstracts. The paper reviews some problems of physical electronic of high power gyrotron and possible solution, results of calculation and experimental study of gyrotrons for fusion operating in a wide frequency range and at the 1 MW power level. Effects of beam potential depression in gyrotrons, effects of mode interaction (competition and cooperation) and methods of mode selection including multibeam and complex cavity systems are presented. The dependence of gyrotron parameters on the beam current and magnetic field is analyzed. The experimental results are compared with the calculated data.

Introduction. Gyrotrons of the mm wavelength band are used for ECR heating and active plasma diagnostics and recently they have been used also in technological application. For electron-cyclotron heating and current control in existing and planned plasma set-ups gyrotrons with CW power up to 1 MW and frequency from 25 up to 170 GHz are required. The possibility to make such gyrotrons is proved by calculations and experiments [1,2]. It is very important to provide stable operation of such gyrotrons.

At present the main problems of powerful gyrotrons in the terms of their stable operation are as follows:

- development of electron guns that form stable helical electron beams with power up to 3 MW at minimal velocity spread;
- transportation of these electron beams up to the operating region without disturbance;
- selection of a high-efficiency operating mode in oversized resonators.

Electron beams. Designing and optimization of gyrotrons require the reliable information on the parameters of the active medium: helical electron beams (HEB), and also on the factors and processes affecting

these parameters. In the field of electron optics the main efforts go along the following lines:

- development of the theory for formation and transportation of helical electron beams (HEBs) of high intensity, including the study of instabilities and methods of their suppression [3, 4];
- experimental investigation of HEB properties in the scale-down regimes [3, 5].

Achievement of 1MW output power of gyrotron with the operating voltage U =80 kV and the efficiency ≈ 35 % requires a beam with a current I ≈40 A and a pitch-factor g ≈1.25 ($g = v_\perp / v_z$, $v_\perp$, v_z - oscillatory and longitudinal velocity in operating space). Thus, a magnetron-injection gun (MIG) should provide formation of a beam with such parameters. When selecting the optimum configuration of electrodes the value of velocity spread $\delta v_\perp$ was not allowed to exceed 30 %. The specified restrictions were accepted with account for specific guns for gyrotrons with different operating modes. Very important for the beam stability is the influence of electrons catched in adiabatic trap between the cathode and magnetic mirror.

For experiments the method of a retarding field [6] was usually applied. The measurements were carried out for a gun in the scale-down regime on an automated installation [3,5], both at presence of influence electrons catched in the adiabatic trap between the cathode and magnetic mirror, and at excepting such electrons. The received dependencies, $\delta v_\perp$ and $t_\perp$, are compared with results of numerical simulation and good correlation for the optimized gun usually is observed.

Effects of beam potential depression in gyrotrons Other important factors is HEB potential depression in the gyrotron cavity caused by the eigen space charge of the beam [7,8]. This factor exerts a considerable influence in superpowerful gyrotrons when intense HEB and space-developed operating modes of oversized open cavities are used. The peculiarities of the effect of potential depression for HEB are studied theoretically in a number of papers. The calculated models of different complexity show that the effect of depression on HEB parameters is stronger than in the case of straight electron beams. However, the

conclusions of the theory have not been verified experimentally and even the procedure of such verification has not been proposed.

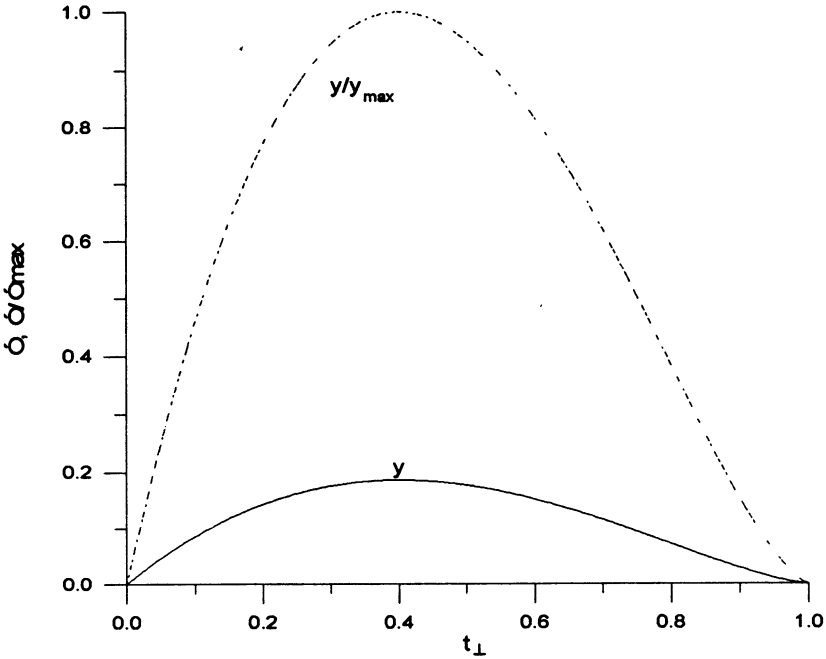

Fig. 1. Relative maximum gyrotron power vs. $t_\perp$

The main effects of beam potential depression in gyrotrons are:

1. Limiting current and power of gyrotrons. The power of gyrotrons can be written as

$$P_{out} = I \cdot U \cdot t_\perp \cdot \eta_\perp \eta_c \cdot \frac{Q_{ohm}}{Q_{ohm} + Q_d}, \qquad (1)$$

where I and U are current and accelerating voltage, $\eta_\perp$ and η_c are transverse efficiency and efficiency of transformation of the built-in converter, $t_\perp$ is relation of transverse energy of electrons to the complete one ($t_\perp = g^2/(1+g^2)$, and Q_d and Q_{ohm} are diffraction and ohmical Q-factor. Limiting current [7,8] and power, limited by the potential depression are:

$$I_{\max} = 0.4 \cdot U^{3/2} \cdot k / ((1+g^2)^{3/2} \cdot \ln(R_c / R_b)), \qquad (2)$$

$$P_{\max} = 0.4 \cdot U^{5/2} \cdot \eta_c \cdot \eta_\perp \cdot k \cdot \frac{Q_{ohm}}{Q_{ohm} + Q_d} \cdot y(t_\perp) / \ln(R_c / R_b), \quad (3)$$

where k is factor dependent on velocity spread ($k(0)=1$)

$$y(t_\perp) = t_\perp (1 - t_\perp)^{3/2} .$$

We shall note, that at typical values of the pitch-factor and velocity spread the value of k equals 0.5-0.7 and the maximum power is 1.5-2 time lower. Achievement of the power level of 1 MW in modern gyrotron using spatially advanced modes ($Rb/Rc \sim 0.5$) for reduction of ohmic losses instead of whispering gallery modes ($Rb/Rc \sim 1$) used earlier requires the accelerating voltage 80 kV and higher.

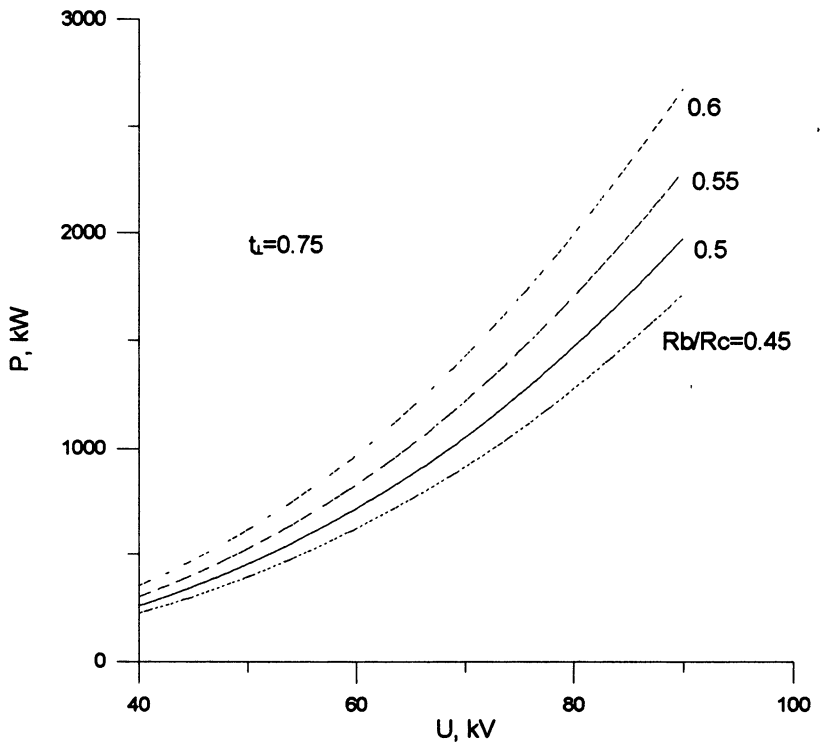

Fig. 2. Dependence of the maximum achievable gyrotron power on an accelerating voltage ($Q_{ohm}/(Q_{ohm} + Q_d)$=0.95, $t_\perp$=0.75, $\eta_\perp$=0.6, η_c=0.83, k=1 (zero velocity spread)).

2. Reduction of a starting current displacement of the zone of self-excitation. The second effect is reduction of a starting current at self-excitation of oscillations in the gyrotron and displacement of the zone of self-excitation towards lower magnetic fields that is caused by decrease of effective potential and increase of drift time.

3. Displacement tuning curve (dependencies of efficiency and power on the magnetic field) towards lower magnetic fields, that is also caused by reduction of effective potential and increase of drift time. The optimum drift angle, thus, at the presence of potential depression corresponds to lower magnetic fields and achievable efficiency can change.

4. Ion compensation (power change and reduction of frequency). In long pulse and CW gyrotrons during the time of the order of 100 ms there is practically complete compensation of the space charge of a beam by positive ions and corresponds to the absence of potential depression.[9]. Thus, the optimum magnetic field of tuning curves at the presence of potential depression B_1 corresponds short-pulse regime ($T_p << 100$ ms), and at the absence of potential depression B_0 -CW regime ($T_p >> 100$ ms). Meanings of a magnetic field smaller B_0 result in restriction of duration of a pulse. At pulse duration $T_p \sim 100$ ms the constant magnetic field cannot be established on optimum meaning and in these regimes achievable efficiency is usually less than in short pulse or long pulse, that corresponds to the well known empirical facts. We shall note that in process ion compensation occurs not only power change, but also reduction of frequency of generation (electronic tuning).

5. Mode interaction. The effects of potential depression and ion compensation can essentially affect processes of mode interaction, which depend on parameters of the electron beam, detuning of a magnetic field, and it requires their correct account at numerical modeling of processes of mode interaction.

6. Coaxial cavities. The analogous calculation performed for the case of coaxial cavities have shown that the depression effect in them is essentially weak.

From the above considerations it is evident, that there has ripened the necessity to develop a technique for experimental determination of potential depression influence on HEB parameters and realization of experiments and their comparison to settlement data.

The first opportunity for indirect experimental estimation of the influence of potential depression consists in measurement of the drift of gyrotron frequency during a pulse. Such measurements were repeatedly carried out on different gyrotrons. As an example in Fig. 4 measurements of frequency of the 140GHz/0.5 MW/3s gyrotron [10] carried out by Th.Geist at IPP (Garching) in May 1996 are shown.

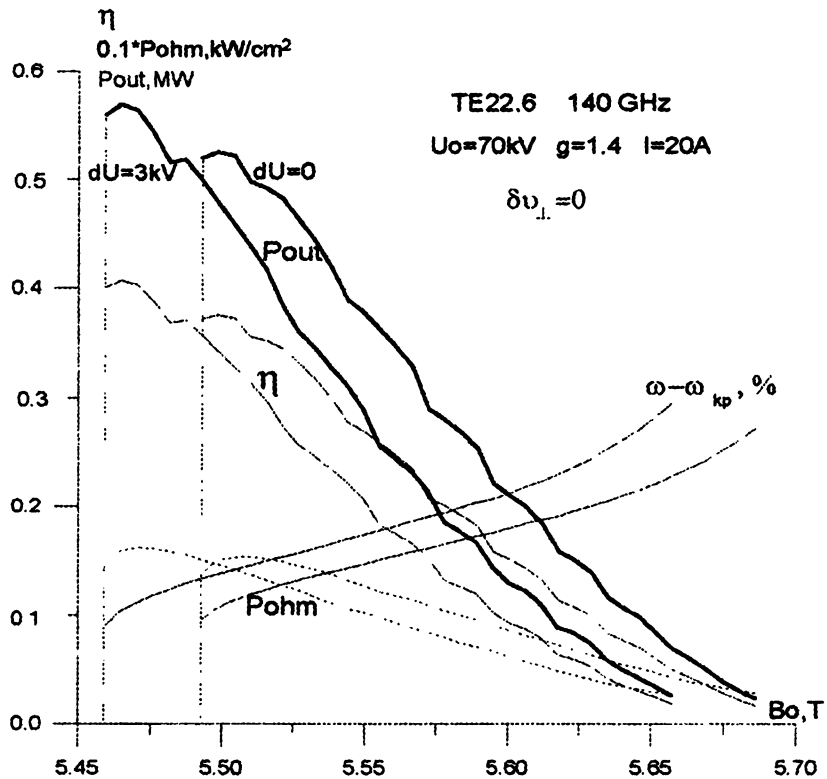

Fig. 3. Tuning curves for typical gyrotron at the presence and absence of potential depression

Those experiments showed essential influence of effects of voltage depression on parameters of HEB and necessity of essential development of the theory and technique of experiments both. On the basis of the received results possible directions for further theoretical and experimental

researches of the voltage depression problem, in particular influences of effects of beam potential depression on function of distribution electron on transverse and longitudinal velocities are planned

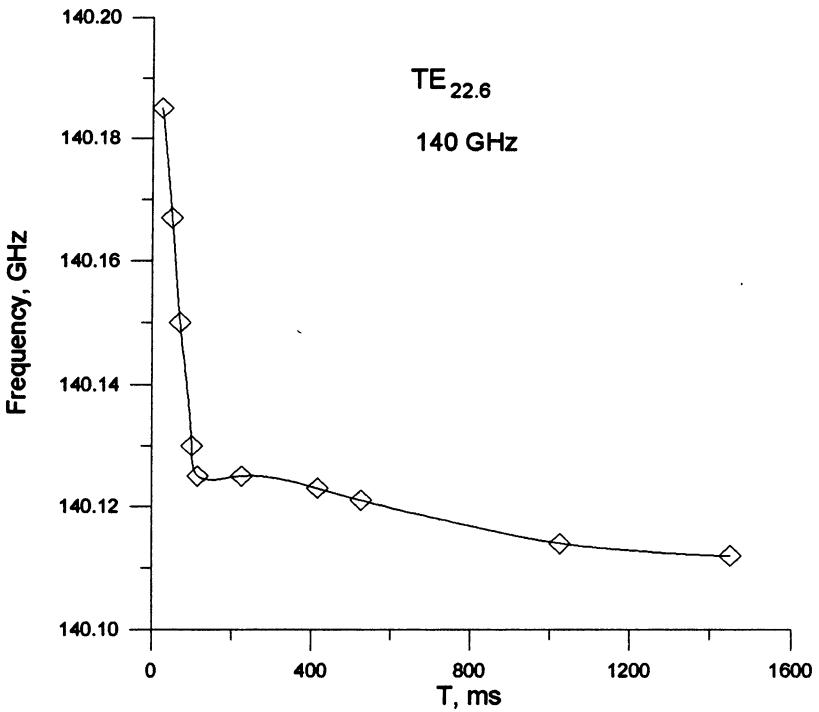

Fig. 4. Frequency measurements on a 140GHz/0.5 MW/3s gyrotron.

The problem of providing of stable single-mode generation

The problem of providing of stable single-mode generation in an oversized resonator at sufficiently high efficiency and a near-1MW level of output power becomes more complicated at high working frequencies. An essential circumstance here is that this problem has to be solved within a number of limitations. The basic one is the limitation of density of ohmic losses in resonator walls - energy load is limited by possibilities of the cooling system, which are, as a rule, not higher than 2–3 kW/cm^2. Stability of operation is analyzed theoretically for more and more accurate models with consideration of two-mode and three-mode interaction.

Besides stability of stationary regimes, nonstationary processes of mode interaction are studied, including those under variation of the electron beam parameters.

The problem of mode interaction was investigated for the simplest model in [11], and it was shown that for the usual case (the same field distribution and Q-factors, not very high beam current and so on) as a rule we have in gyrotron a single-mode stable operating regime. But even for a slightly complicated model we can observe a lot of possibilities. For example, for the model of two mode interaction with the equal parameters (dimensionless currents $I_1Q_1=I_2Q_2=IQ$) except frequency detuning [12] possible situation are shown in Fig. 5 (F_1 and F_2 are dimensionless amplitudes of modes). Fig. 5a shows the effect of force excitation of the second mode when dimensionless current IQ=1.1 (for optimal efficiency regime IQ=0.03). Figures.5b-to 5e. corresponds the evolution of the system when dimensionless current IQ exeeded values 0.7, 0.85, 1.25, 3.13, 4.16 in the following order: 5b, 5c, 5d , 5c (in general), 5e.

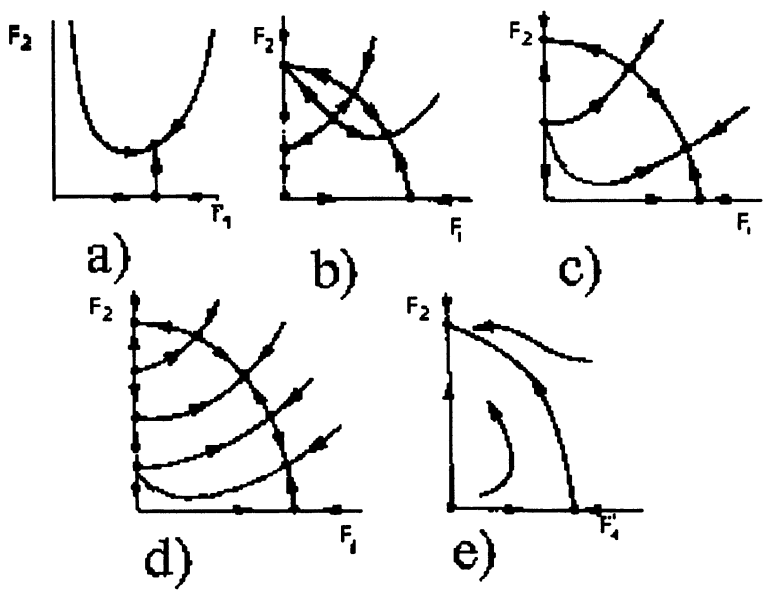

Fig.5. Evolution of the system when dimensionless current *IQ* grows.

For a more complicated model of mode interaction (selfconsistent system with nonfixed structure of RF field, real property of electron beam,

etc.) we have got a very serious problem even near the optimal current [2]. Parameters of RF radiation from the cavity have been computed basing on the advanced non-linear theory of interaction of the electron beam with RF field of the cavity mode. The calculations were done taking into account velocity spreads $\delta v_{\perp}$ in the electron beam. The thermal load is given for the cavity center where it is maximal. From investigations of the electron gun the velocity spread, $\delta v_{\perp}$ in the electron beam is expected to be near 0.3. Calculations show the possibility to attain 1 MW output at the beam current below 40 A with an acceptable thermal load in the cavity. Special theoretical investigation has confirmed the stability of operation of the $TE_{28.7}$ ($TE_{31\,8}$) mode at its high-efficiency regimes, but if we exceed optimal current we face a very serious problem.

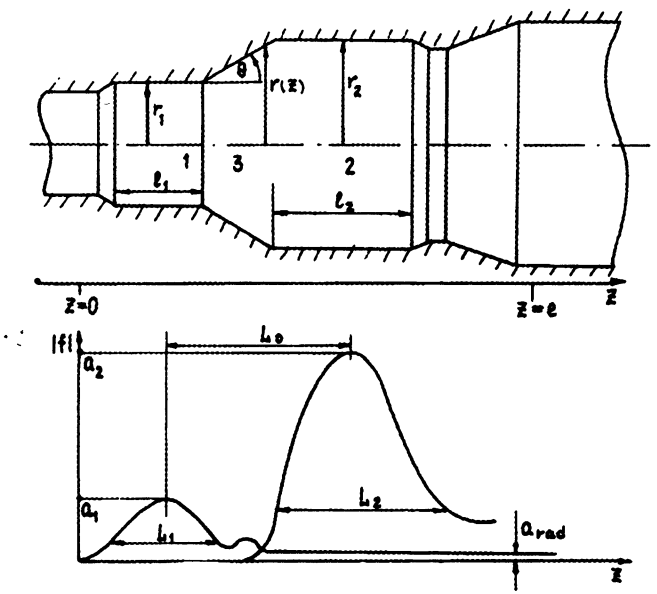

Fig.6a. Longitudinal cross-section of CCMC, and longitudinal distribution of the electric field for operating mode pair

The mode converter is a part of the internal electrodynamic system of the tube including the cavity as well. The converter separates the RF radiation from the worked-out electron beam, transforms a complicated cavity mode to an easier transportable wave beam and allows to minimize harmful action of possible reflections of RF power to the gyrotron.

Stability of the operating mode to undesirable mode conversion has to be achieved by optimization of the cavity output up-tapering waveguide connecting. Calculation has shown that in the optimized up-tapering waveguide connecting the cavity with the mode converter a parasitic RF power transformation of the $TE_{28.7}$ ($TE_{31.8}$) mode to other is below 1%.

There are different ways to increase mode selection in order to provide a stable single-mode regime such as quasioptical gyrotrons, coaxial cavity [13], coupled cavity with mode conversion (CCMC) [14-16], etc. Figure 6a shows the typical coupled cavity with mode conversion (CCMC) for the gyrotron and Fig. 6b.- presents the typical dependencies of basic CCMC parameters on a relative frequency mismatch of partial cavities. Increasing of the Q-factors correspond to the electrodynamics selection, and preferences in the RF field amplitude of input cavity for operating couple modes as compared to the neighbor one corresponds to electron selection by prebunching of an electron beam. Using this system we can make the starting current of the operating mode 3-10 times lower and achieve nonlinear suppression of the undesirable mode.

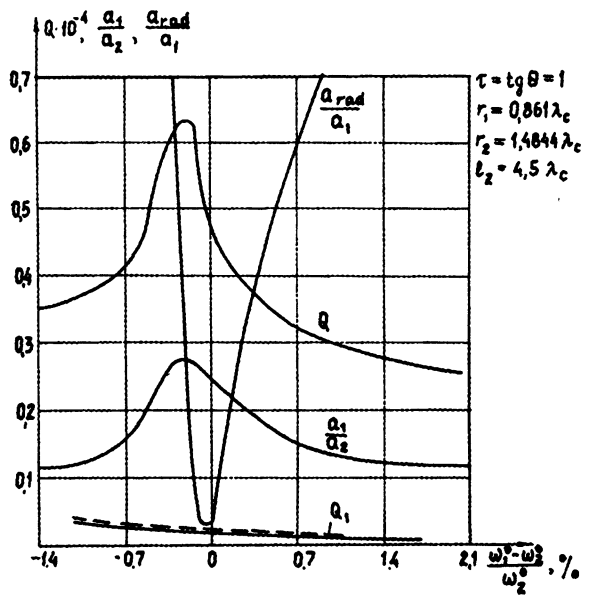

Fig.6b. Q-factors, ratios of resonance field amplitudes in CCMC regions 1 and2, relative amplitude of the radiation field at the lower mode out of CCMC plotted versus a relative frequency mismatch of partial cavities.

The possibility to use spatially-developed electrodynamic structures with large volume of the active medium in gyrotrons creates conditions for the further increase of the frequency and the output power but poses a number of serious problem. One of the most difficult ones is the problem of mode selection and especially mode selection on transverse indices. The operation at the cyclotron frequency harmonics appears to be most critical, since the modes synchronous with the beam at all lower harmonics, the starting currents of which are usually lower, become also competing.

One of the promising methods of selection is application of helical electron beams (HEB) additional to the main one , i.e. realization of multibeam gyrotrons [17,18]. According to the parameters (mainly the oscillatory and drift velocities in space of interaction) the supplementary electron beams may be either radiating or may perform the function of the electron absorber.

The basic results of the theory of multibeam gyrotron are reduced to the following [19].

The introduction of supplementary radiating **HEB** weekly connected with the parasitic mode field essentially increases the resource of stability of generation at the operating mode, even if the currents of supplementary beams constitute a small part of the main beam, which has the greatest cross-section for ensuring the maximum gyrotron output power and, correspondingly, strongly depends on the parasitic mode fields. In practically important cases, as a rule, one manages to choose the parameters of multi-beam systems in such a way that the efficiency of the multi-beam gyrotrons is at the level of the best one-beam gyrotron. The space separation of partial beams makes the influence of the space charge on the velocity spread weaker. Therefore, the total current in a multi-beam system may essentially exceed the current of one-beam gyrotrons without worsening the beam quality.

Absorbing electron beams should have the parameters which can ensure the maximum cyclotron absorption of the parasitic mode, when the interaction with the operating mode field is minimum. A smooth (nonoscillating) beam introduced into the node of the operating mode is the ideal absorber. The electron Q-factor (quality) characterizing the losses due to introduction of the absorbing beam is proportional to its resistance to the direct current, therefore it is preferable to use absorbing

beams with small energy of electrons. Note, however, that as the energy decreases, detuning of electron cyclotron frequencies with respect to the gyrofrequency of the radiated beams increases and the band of the cyclotron radiation becomes narrower. Absorbing beams are of special interest for the gyrotrons operating at the second harmonic of gyrofrequency. In this case nonoscillating beam does not interact with the operating mode field.

The two-beam system is the simplest one for practical realization [20]. There are several alternatives of the design of two-beam magnetron-injector guns (MIG) and the conditions which they should satisfy are analyzed.

The results of the trajectory analysis for a two-beam EOS optimized numerically in operating regimes are given. The main beam in the region of the gun is laminar and the supplementary one is a regularly-intersecting one. The results of measuring the parameters of beams in the modeling regime by the retarding field method agree satisfactorily with calculations.

In the experiments with two-beam gyrotrons, the single-beam gyromonotron operating at the second harmonic of gyrofrequency (wavelength 12 mm, accelerating voltage 60 kV, mode TE_{031}) [21] is taken as the basic one.

a) The active supplementary beam is formed in the optimized two-beam system described above. The choice of the operating mode, the wavelength and the numbers of the gyrofrequency harmonic defines the electron beams radii in the operating space $R_{0(1)}$ =13 mm, $R_{0(2)}$ =5.6 mm. The design of the two-beam gun provides separate heating of the emitter, which allows practically the independent control of the currents of both beams. The potential to the first anode was feel from the variable high-voltage divider. The potential of the second anode was set equal to the cavity potential.

If only one (the main) beam was used the gyrotron output power did not exceed 0,5 MW and was limited mainly by the competition of the TE_{411} mode (the fundamental harmonic of gyrofrequency). Two-mode generation at the TE_{031} and the TE_{411} modes is observed, as will as at the pair of the TE_{031} and TE_{231} modes. When the current of the supplementary beam was great enough, the operating mode was stable, and the parasitic generation was absent [21]. Figure 7

shows results of measurements of the output power, and efficiency depending on the electron beam current for the short pulse experimental model of gyrotron. The maximum efficiently of 40% was registered at the current of the main beam 6.2 A, the current of the main beam 24 A and the output power 0.87 MW (current 13A and 44A, efficiency 25%). Thus it is obvious that the effect of the supplementary beam is stabilizing.

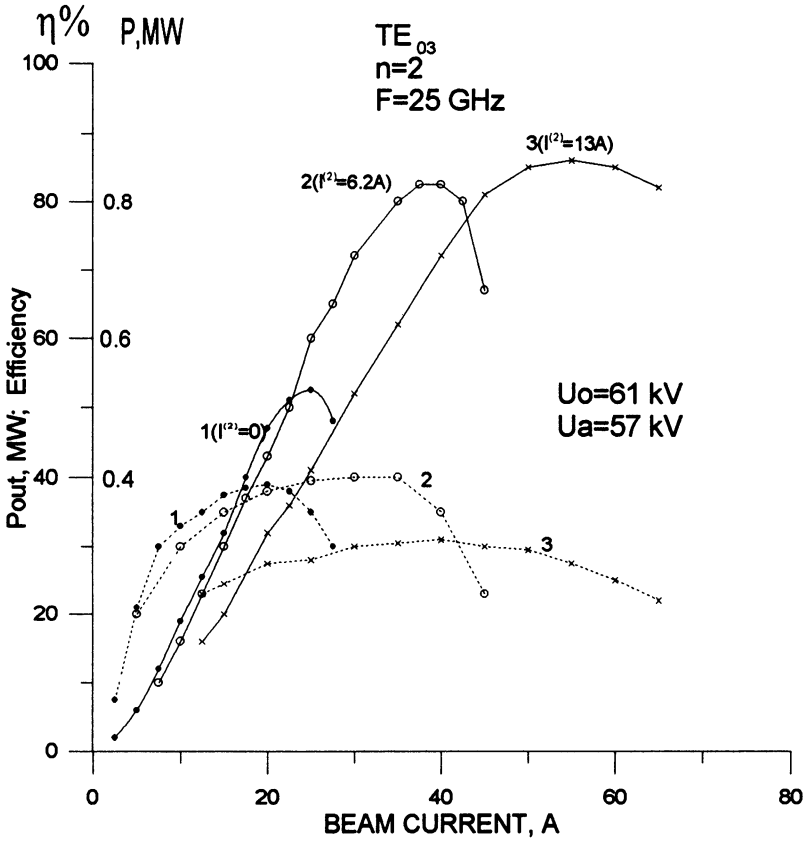

Fig.7. Results of measurements of the output power, and efficiency of gyrotron depending on the beam current.

The absorbing supplementary beam was formed with the aid of a simple modification of the existing cathode without optimizing the electron optic system. The maximum output power of 0.6 MW achieved experimentally

at the total current in the operating space of a two-beam gyrotron 70A (U_0=47kV) and efficiency 18%. Elimination of the supplementary emitter decreases the maximum output power down 360kW. In this case limitation of the output power was the result of the instabilities caused by mode competition [22].

Conclusion. The possibility to make a stable 1 MW power level gyrotron for fusion is proved by calculations, numerical modeling and series of experiments. Supplementary beams can provide the possibility to increase mode stability of gyrotron oscillation. Calculation results and experimental data are in good correlation. Successfully tested short-pulse gyrotrons are a reliable basis for elaboration of an industrial tube operating in the full-scale regime.

References:

1. Flyagin V.A.,.Goldenberg A.L, Zapevalov V.E.., Conference Digest, 18 International Conference on Infrared and Millimeter Waves, 6-10 September, University of Essex Colchester, United Kingdom , 1993, 581.
2. Denisov G.G., Flyagin V.A., Zapevalov V.E. Conf. Proc. 20 Int. Conf. on IR & MM waves. Orlando, USA. 1995,.197
3. Kuftin A.N, et al. Int. J. Electronics, 72, (1992), 1145-1151.
4. Lygin V.K, Int. J. of Infrared and Millimeter waves, 16 (1995), 363-376.
5. Andronov A.N., et al., Conference Digest , 20 International Conference on Infrared and Millimeter Waves 11-14 December, Orlando, Florida, 1995, 141.
6. Avdoshin E.G., Goldenberg A.L. Izv. Vish.Uch. Zav, Radiofisika, 1973.**16**, 1605.
7. Drobot A. T., Kim K.. Int. J. Electronics, 1981,.**51**, 351.
8. Tsimring Sh. E. "Radiotekhnika and electronika ", 1990, **6**, 1284.
9. Varentsov V.A., Tsimring Sh.E. Journal of technical physics, 1983. V.53,.**2**., 264
10. Zapevalov V.E. et al.. Electronic industry, 1991, **6**,.71.
11. Moiseev M.A., Nusinovich G.S. Izv. Vish.Uch. Zav, Radiofisika, 1974.**11**, 1709.

12. Zapevalov V.E., Nusinovich G.S. Izv. Vish.Uch. Zav, Radiofisika, 1984.**16**, 117.
13. Flyagin V.A. et al., Conference Digest, 19 International Conference on Infrared and Millimeter Waves, Sendai, Japan, 1994, 75
14. Gaponov A.V. et al,.. Int. J. Electronics, 1981,.**51**, 277.
15. Fix A.Sh. et al,. Int. J. Electronics, 1984,.**57**, 821
16. Zapevalov V.E., et al. Izv. Vuzov. Radiofisika 1984 , **12**, 1194.
17. Zapevalov V.E. et al Inventor's certificate N786677 USSR with priority from 25.07.79, Cyclotron-Resonance Maser., Published in Bull. Isobret. 1989,. **7**
18. Wang Hui, Zho Jin-lin et al. Conf. Digest 10 th. Int. Conf. Infrared and Millimeter Waves. Orlando, USA, 1985, 265.
19. Zapevalov V. E., Tsimring Sh.E. Izv. Vuzov. Radiofisika 1990 , vol.33, no.11, p.1288.
20. Zapevalov V.E., Manuilov V.N., Tsimring Sh.E. Izv. Vuzov. Radiofisika 1991, vol.34, no.2, p.205.
21. Zapevalov V.E. Manuilov V.N., Malygin O.V., Tsimring Sh.E. Izv. Vuzov., Radiofisika, 1994., vol.37, no. 3, p.387.
22. Zapevalov V.E., Malygin S.A., Tsimring, Sh. E. Izv. Vuzov. Radiofizika, 1993, vol.36, no.6, p.543.

EXPERIMENTAL RESULTS OF 1.5 MW COAXIAL CAVITY GYROTRONS IN THE FREQUENCY RANGE 115-170 GHZ

M. Thumm[1], *O. Braz*[1], *G. Dammertz, C.T. Iatrou, S. Kern*[1], *M. Kuntze, A. Möbius*[2], *B. Piosczyk*

Forschungszentrum Karlsruhe, Association EURATOM-FZK,
Institut für Technische Physik, P.O. Box 3640, D-76021 Karlsruhe, Germany
[1] also Universität Karlsruhe, Institut für Höchstfrequenztechnik und Elektronik
Kaiserstrasse 12, D-76128 Karlsruhe, Germany
[2] IMT GmbH, Luisenstr. 23, D-76344 Eggenstein, Germany

V.A. Flyagin, V.I. Khishnyak, V.I. Malygin, A.B. Pavelyev, V.E. Zapevalov

Institute of Applied Physics, RAS, Nizhny Novgorod, 603600, Russia

1.5 MW gyrotron oscillators with coaxial cavities designed for operation in the $TE_{28,16}$ and $TE_{31,17}$ modes at 140 and 165 GHz are under development and test at FZK in collaboraton with IAP. A maximum output power of 1.17 MW has been measured at 140 GHz in the design mode with an efficiency of 27.2 % (pulse duration 0.15 to 0.5 ms). Single mode operation has been found over a wide range of operating parameters. The experimental values agree well with the results of multimode calculations. The design operating point with 1.5 MW output power and 35 % efficiency is not accessible in this tube with axial output, probably because of enhanced mode competition due to window reflection. Frequency step tuning has been performed successfully. With a constant magnetic compression, 20 modes have been excited in single mode operation in the frequency range between 115.6 and 164.2 GHz. In particular, an output power of 0.9 MW has been measured in the $TE_{25,14}$ mode at 123.0 GHz and 1.16 MW in the $TE_{32,18}$ mode at 158.9 GHz. The selection of the operating frequency and mode of the 165 GHz version are based on limitations imposed by the maximum magnetic field of the existing superconducting magnet and the use of the inverse magnetron injection gun of the 140 GHz, $TE_{28,16}$ coaxial gyrotron. In particular, a maximum output power of 1.17 MW with an efficiency of 26.7 % has been measured in the design mode $TE_{31,17}$. A maximum efficiency of 28.2 % has been observed at an output power of 0.9 MW. Modes with high window reflection are important competitors. Single mode oscillation was also achieved in the $TE_{32,17}$ mode at 167.1 GHz, in the $TE_{33,17}$ mode at 169.5 GHz and in the $TE_{34,17}$ mode at 171.8 GHz with an output power of 1.02 MW, 0.63 MW and 0.35 MW, respectively. The power and efficiency decrease towards higher frequencies is due to the maximum achievable magnetic field of 6.6 T.

1. Introduction

Conventional cylindrical-cavity gyrotrons are limited in output power and operating frequency ($\approx$ 1 MW at 170 GHz) due to ohmic wall loading, mode competition, and limiting beam current [1]. The problem of ohmic wall loading can be reduced by increasing the cavity diameter and using volume modes. The increased cavity diameter and the high operating frequency require operation in high-order modes, where the mode spectrum is dense and mode competition could prevent the gyrotron from stable single-mode operation. Furthermore, the use of volume modes, which do not load significantly the cavity walls, leads to lower limiting currents and reduced total efficiency because of the increased voltage depression. These limiting factors can be considerably reduced by the use of coaxial resonators [1,2], which, by tapering the inner conductor, offer the possibility of selective influence on the diffractive quality factor of different modes, allowing operation in high-order volume modes with reduced mode competition problems. In addition, the presence of the inner conductor practically eliminates the restrictions of voltage depression and limiting current. Gyrotrons with coaxial cavities have the potential to generate, in cw operation, rf output powers in excess of 1 MW at frequencies above 140 GHz. In general, two methods are available in a coaxial-cavity configuration for an effective control of the total Q factor, and hence of the starting current, of different modes: (a) the use of a longitudinally corrugated tapered inner conductor [2,3], and (b) the use of a resistive inner conductor [1,4]. The first method seems preferable for high-power operation and it has been followed in the development of coaxial gyrotrons for fusion applications at FZK and IAP.

A 1.5 MW gyrotron oscillator with coaxial cavities designed for operation in the $TE_{28,16}$ and $TE_{31,17}$ modes at 140 and 165 GHz is under development in a collaboration between the FZK and the IAP Nizhny Novgorod [3,5]. The development has been planned to be performed in two steps. The first step, in which the gyrotron has an axial waveguide output with 100 mm diameter, has already been realized and experiments have been performed with pulse length $\leq$ 0.5 ms due to the limited heat load capability of the collector, which is part of the output waveguide.

In a second step a tube design relevant for cw operation with a radial rf output will be investigated. Especially because of the present power limit of rf vacuum windows the mm-wave power will be split into two

beams and coupled out radially through two windows. In addition, a single-stage depressed collector will be used in order to enhance the total efficiency and to reduce the power loading at the collector surface.

In the following the design consideration and the components of the 1.5 MW, 140 GHz and 165 GHz coaxial cavity gyrotrons including the quasi optical (q.o.) output systems for the tubes with radial dual rf - beam output, are described. Operating experience and results of rf measurements obtained with the axial tubes are presented and compared with the results of numerical simulations.

2. 140 GHz, $TE_{28,16}$ coaxial cavity gyrotron with axial output

A schematic layout of the gyrotron with the axial waveguide output is shown in Fig. 1. The main design parameters are summarized in Tab. 1.

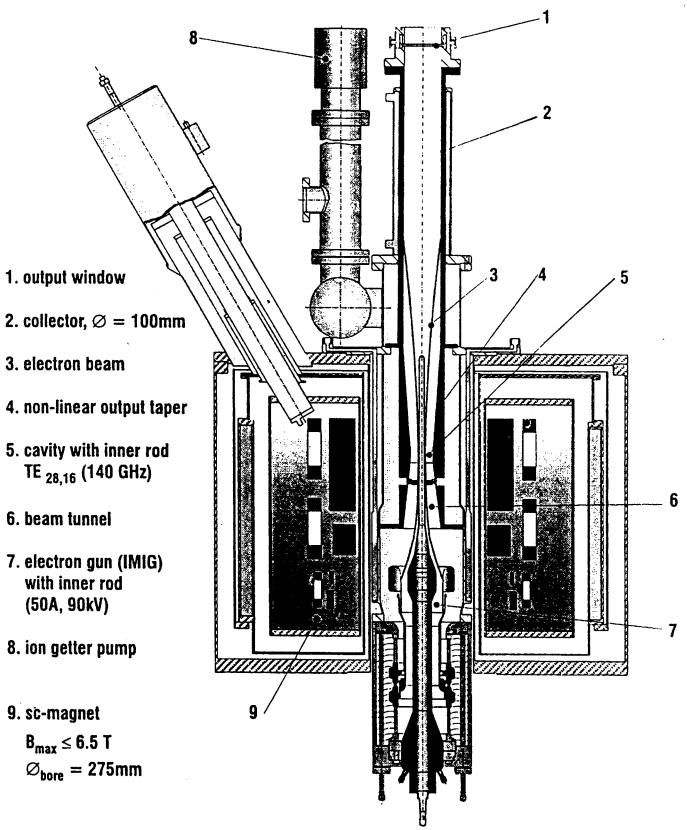

Fig. 1: Schematic layout of the coaxial cavity gyrotron with axial rf-output.

Tab. 1: Design parameters of the 140 GHz-$TE_{28,16}$ coaxial gyrotron.

frequency f / GHz	140
rf output power P_{out} / MW	1.5
cathode voltage U_c / kV	90
beam current I_b / A	50
velocity ratio α	1.35
cavity radius R_{cav} / mm	29.81
beam radius R_b / mm	10.0
voltage depression ΔU_b / kV	1.6
limiting current I_{lim} / A	≈ 400
peak wall loading (ideal copper) p_Ω / kWcm^{-2}	0.63

The low realistic wall loading which is about twice the ideal value, $p_\Omega(\text{real}) \approx 2\, p_\Omega(\text{ideal})$ is very attractive for technical realization. The peak ohmic losses at the inner rod are calculated to be about 10% of the cavity wall losses and are not considered to be a technical problem. The main features of the gyrotron components are described in the following.

2.1 The superconducting magnet and the electron gun

For the operation of the coaxial gyrotron an existing superconducting (sc) magnet with a maximum magnetic field of 6.6 T and a warm bore hole having a diameter of 275 mm is used. In addition to the solenoidal coils the magnet has a set of dipole coils which permits a radial shift of the electron beam in the region of the cavity. With the help of these coils the alignment of the beam with respect to the inner rod can be verified and redone if necessary in the fully installed tube.

The 4.5 MW electron gun is of the diode type having a central rod surrounded by the cathode ring (inverse magnetron injection gun, IMIG) [6]. The inner rod is electrically isolated but is held close to ground potential. It is supported and cooled from the gun side. The part of the rod within the cavity can be radially adjusted under fully assembled conditions between two shots. At the design beam current $I_b = 50$ A the emitter current density is $j_e = 2.8$ A/cm^2. The design operating voltage is $U_c = 90$ kV. The emitter consists of LaB_6 and has an average radius of 56 mm. The properties of the electron beam, such as the velocity ratio α

and the velocity spread $\delta\beta_{\perp rms}$, have been measured by the method of retarding fields. The average value of α was found to be in reasonable agreement with numerical results. The measured velocity spread $\delta\beta_{\perp rms} \cong 9\%$ is relatively high but sufficient for reliable operation at the design parameters. For generation of the magnetic field in the gun region two coils (ES1 and ES2) are available, which allow a variation of the direction of the magnetic field lines relative to the emitter surface. Depending on the ratio of the coil currents the velocity ratio α changes at the design conditions from 1.15 (I_{ES1}=0) up to about 1.4 (I_{ES2} = 0).

2.2 Cavity and output taper

The co-rotating $TE_{-28,16}$ mode with an eigenvalue $\chi = 87.35$ was chosen as the working mode for operation at 140 GHz. When selecting this mode it was considered that for the dual beam q.o. output a two-step mode conversion scheme, $TE_{-28,16}$ to $TE_{+76,2}$ to TEM_{00}, which generates two narrowly-directed (60° at the launcher) output wave beams is foreseen. In order to allow a simple transformation of the cavity mode into the intermedite $TE_{76,2}$ whispering gallery mode (WGM) the two modes have to be degenerate [7].

For the resonator (Fig. 2) a cavity with a cylindrical outer wall and a radially tapered and corrugated inner rod is used. The cavity has a length of 20 mm and the inner rod has a negative taper (radius decreases towards the collector, $dR_{rod}/dz < 0$) of 1^0. For a negatively tapered inner rod, a positive/negative slope in the eigenvalue curve $\chi(C)$ of any mode will increase/decrease its diffractive quality factor [2,8]. $C = R_{cav}/R_{rod}$ is the ratio of the cavity radius R_{cav} to the radius of the inner rod R_{rod}. The longitudinal impedance corrugation on the inner rod is introduced in order to avoid an increase of the quality factor of some competing modes. The corrugation consists of small longitudinal slots which imply no mode conversion because the period s is small compared to $\lambda/2$, the free-space half-wavelength. In particular, 72 slots with a depth d = 0.5 mm and a width l = 0.4 mm are taken. The influence of the corrugation on the eigenvalue is shown in Fig. 3. The normalized surface impedance w of the corrugated wall given by [2]: $w = (l/s)\tan(2\pi d/\lambda)$ has a value > 2 within the resonator.

Appropriate tapering of the rod together with the impedance corrugation results in a significantly decreased diffractive quality factor

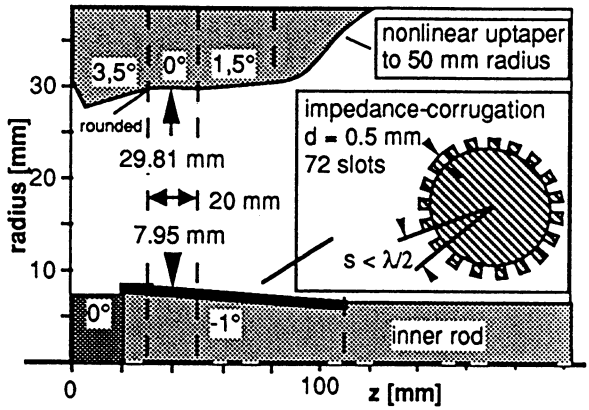

Fig. 2: Geometry of the $TE_{28,16}$ coaxial cavity with tapered and longitudinally corrugated inner rod.

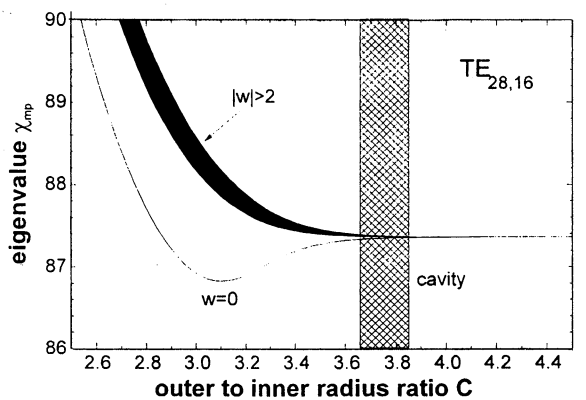

Fig. 3: Influence of longitudinal corrugations of the inner rod on the mode eigenvalue. The C-range within the cavity is indicated.

of any mode which is influenced by the rod. The range of C in the cavity is: $3.66 < C < 3.82$. It is chosen such that the working mode is only slightly influenced by the inner rod. Then its Q-factor remains high while the diffractive Q factors of all other modes with higher radial index are reduced and consequently the starting currents are increased. Modes with lower radial index couple significantly less to the electron beam and therefore also have a high starting current. The mode spectrum of the product Q • (relative coupling coefficient) is given in Fig. 4. Only the azimuthal neighbours $TE_{-27,16}$ and $TE_{-29,16}$, which have almost the same caustic radius as the operating mode and which therefore are only slightly

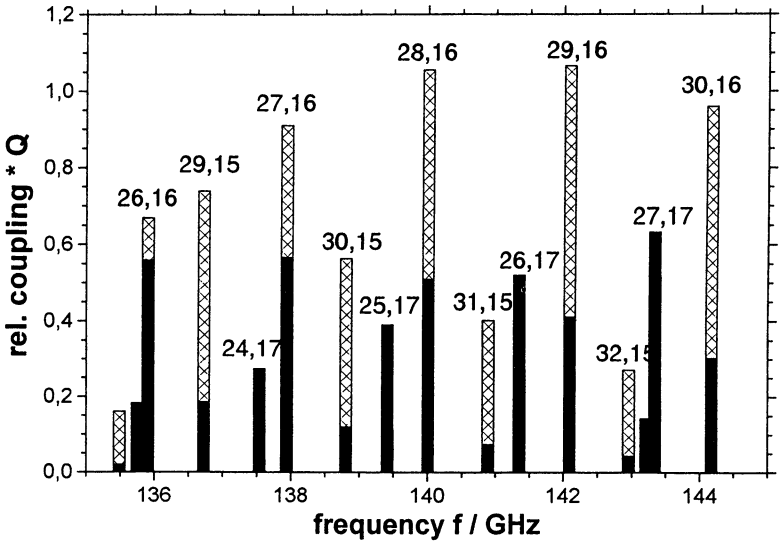

Fig. 4: Mode spectrum of the product of Q factor and relative coupling coefficient for the coaxial cavity. Co-rotating and counter-rotating modes are given with filled and hatched columns, respectively.

influenced by the inner conductor, remain as serious competitors. Their Q factor is almost the same as that of the operating mode and thus mode competition through the phase-amplitude interaction can occur. Self-consistent codes, which compute the electron beam - rf wave interaction, predicted an output power of 1.5 MW at 139.97 GHz in the $TE_{-28,16}$ mode at a beam current of 42 A with an overall efficiency of 40%. The peak ohmic losses (ideal copper at room temperature) are calculated to be 0.63 kW/cm^2 on the outer wall of the resonator and 0.07 kW/cm^2 on the inner conductor wall.

A nonlinear output taper (Fig. 1) having low mode conversion adapts the diameter of the cavity to the diameter of the electron beam collector. Mainly because of voltage depression the inner rod ends above the nonlinear part of the output taper about 250 mm above the cavity.

2.3 Collector and output window

The investigated coaxial gyrotron has an axial waveguide output with a fused silica window of 100 mm diameter and a thickness of 4.61 mm corresponding to $7\lambda_\varepsilon/2$ of the $TE_{28,16}$ mode at 140 GHz. The window is transparent for the design mode. However, there is power reflection of

about 15% at the frequencies of the nearest competitors, the $TE_{27,16}$ and $TE_{29,16}$ modes. The collector is part of the output waveguide with a diameter of 100 mm. At the design parameters the estimated electron beam power density at the collector surface is as high as 50 kW/cm^2 thus limiting the maximum allowable pulse length to about 0.5 ms.

The gyrotron version with lateral dual beam output will have a single-stage depressed collector with an inner diameter of 300 mm allowing a maximum pulse length of several 10 ms. Two fused silica output windows transparent for the Gaussian mode at 140 and 165 GHz will be used (d = 6.045 mm).

2.4 Experiments in the design mode at 140 GHz

The measurements have been performed in short pulse operation. Most data have been taken with a pulse length of 0.15 ms. The repetition rate was 1 to 2 Hz. However, with lower repetition rate single pulses have been performed up to 0.5 ms. The available HV-power supply delivered a maximum voltage of about $U_c \approx 86$ kV at a beam current $I_b = 50$ A. The shape of the high voltage pulse was characterized by an overshooting of about 4%. The rf power has been measured as an average over typically 30 pulses with a ballistic calorimeter. With a contiguous filter bank consisting of ten 2 GHz channels a down converted signal of the generated rf has been observed simultaneously in the different frequency channels giving information about single or multi-mode oscillation in the cavity. The time dependence of the frequency during a pulse was measured with a time frequency analyzer. For investigation of the mode purity, measurements of the near and far-field pattern of the rf power radiated from the open output waveguide have been performed using an infrared (IR) camera [9]. The far-field pattern has been measured using the following setup. A nonlinear uptaper was connected behind the output window to increase the diameter from 100 mm to 140 mm in order to optimize the Brillouin angle of the mode. A quartz glass plate, longitudinally mounted on the axis of the output waveguide, was used to produce a standing wave pattern of the rotating cavity mode and a teflon lens with 165 mm focal length focused the radiation at a dielectric target plate, which was observed by the IR camera.

Before assembling the gyrotron tube all parts were aligned mechanically. However, it turned out that a realignment of the inner rod

with respect to the hollow electron beam became necessary under operating conditions in the fully installed tube. For doing this, the dipole coils in the sc magnet, which enable one to shift the electron beam radially in the cavity region, are very useful. Using this method, the position of the electron beam relative to the inner rod was measured giving the necessary information about the mechanical shift. The result of the alignment of the inner rod relative to the beam is shown in Fig. 5. The deviation from concentricity is less than 0.1 mm.

An unstable behaviour of the electron beam has been observed at a velocity ratio above $\alpha \approx 1.2$. When the gyrotron was operated in modes with frequencies having high window reflections the beam stability limit was shifted towards even lower α values. The occurence of beam instabilities is thought to be related to electrons reflected at the magnetic mirror. The mechanism of the reduction of the stability due to reflected rf power flowing towards the gun is not yet clear.

The design working mode $TE_{28,16}$ was found to oscillate stably over a wide parameter range. This prooves the suppression of possible competing modes by the tapered and corrugated inner rod. A maximum rf-output power of 1.17 MW with an output efficiency $\eta_{out} = 27.2\ \%$ has

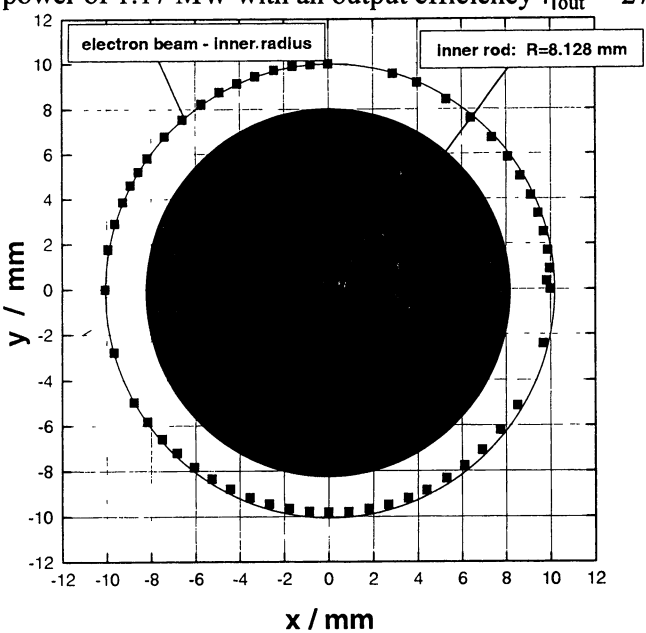

Fig. 5: Position of the electron beam relative to the inner rod at the entrance of the cavity.

been measured in the $TE_{28,16}$ mode in single mode operation at $U_c = 86$ kV, $I_b = 50$ A and $B_{cav} = 5.63$ T. According to numerical calculations the corresponding transverse efficiency $\eta_\perp$ is around 57 % since the velocity ratio is only 1.0 having a numerically calculated spread $\delta\beta_{\perp rms} = 8$ %. The measured frequency of 139.96 GHz is very close to the calculated value. The internal losses in the cavity, the output taper and the window are estimated to be about 5.5%.

Figure 6 shows as an example the measured and the numerically calculated rf-output power versus the beam voltage for a magnetic field of $B_{cav} = 5.62$ T and a beam current between 50 A and 52 A. The calculations have been performed with a multi-mode code [10] using the geometry of the cavity and the operating parameters without any fitting. For the velocity spread $\delta\beta_{\perp rms} = 6\%$ has been taken. As expected from the numerical calculations the azimuthal neighbours $TE_{29,16}$ at 142.02 GHz and $TE_{27,16}$ at 137.86 GHz, which are the remaining competitors, are limiting the stability region of the working mode in the U_c - B_{cav} parameter space. The experimentally observed regions with single and multi-mode oscillation are indicated at the top of Fig. 6. At a given magnetic field the $TE_{29,16}$ mode oscillates at a voltage below and the

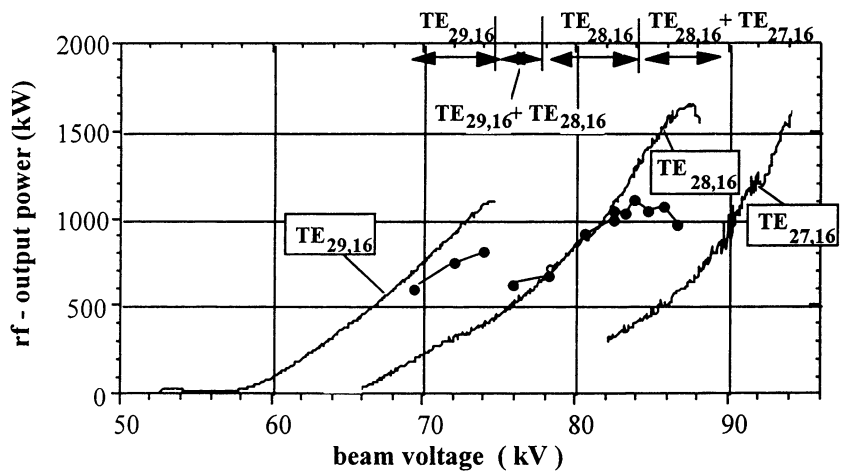

Fig. 6: RF output power versus beam voltage. $I_b = 50$-52 A, $B_{cav} = 5.62$ T. Experimental results are given as points, with oscillating modes indicated at top. Solid lines are stable single mode operation points from multi mode calculations performed with experimental parameters and $\delta\beta_{\perp rms} = 6\%$.

$TE_{27,16}$ above the oscillating range of the $TE_{28,16}$ mode. Single mode oscillation of the $TE_{28,16}$ mode is found within several kV of U_c. The regions of oscillations of the three measured modes agree well with the numerical predictions. Only the experimental transition region is wider than expected. According to calculations the rf power should rise up with its maximum at $U_c = 87$ kV while the measured values reach a maximum around 84 kV and above $\approx$ 86 kV the $TE_{27,16}$ mode is oscillating. In the region between $U_c = 84$ to 86 kV there is a small amount of the $TE_{27,16}$ mode present simultaneously with the $TE_{28,16}$ mode. This gives an explanation for the reduced efficiency and output power in that region. However, this multimoding is not predicted by the numerical calculations. One reason for the discrepancy is thought to be caused by window reflections, which support the competing $TE_{27,16}$ mode. Another reason for the loss of single mode stability at higher voltages is the overshooting of the accelerating voltage. At the peak of the voltage the competing mode starts oscillations, and after the voltage dropped again these oscillations may remain. The influence of the window reflections on the gyrotron operation is mainly a problem of tubes with an axial rf-output. This effect is expected to be of no importance in the tube with radial output, as has already been proven experimentally with conventional hollow-waveguide cavity gyrotrons.

2.5 Frequency step tuning

The possibility of frequency step tuning has been proven over a wide frequency range from 115.6 GHz to 164.2 GHz. Frequency step tuning was performed by changing the magnetic field with constant magnetic compression corresponding to a beam radius R_b=10.0 mm. The beam radius was not optimized for maximum output power at the different modes except for the $TE_{28,16}$ mode. Under that condition single mode operation has been achieved in 20 different modes as indicated in Fig. 7. Output powers around 1 MW and output efficiencies above 25% have been achieved near frequencies where the window reflection is minimal (122 GHz, 140 GHz and 158 GHz).

Fig. 8 shows the maximum output power P_{out} measured in the different modes together with the output and transverse efficiencies, η_{out} and $\eta_\perp$, the rf-power reflection coefficient R of the window, the caustic radius R_{caust} and the velocity ratio α. In modes with high reflection coefficient R the output power P_{out} and the corresponding efficiencies η_{out} and $\eta_\perp$ have a

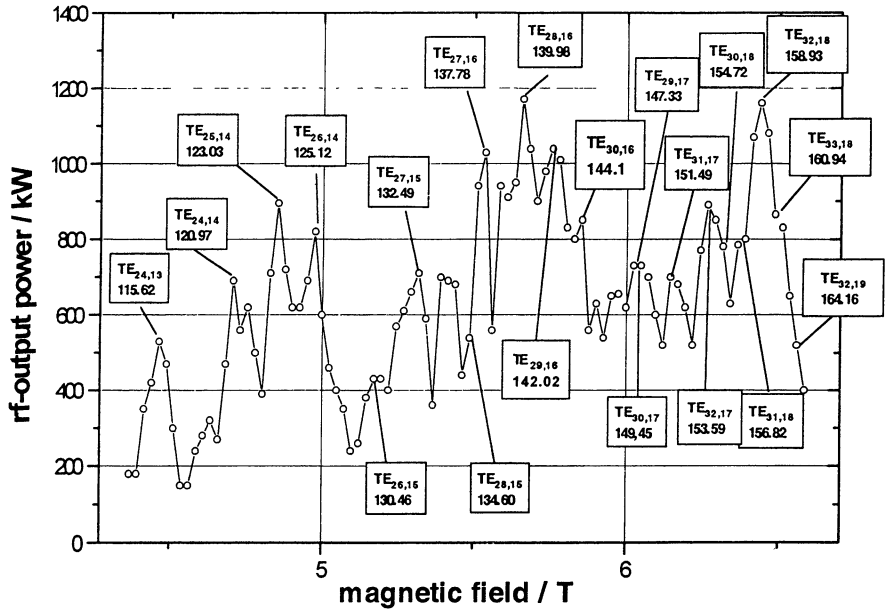

Fig. 7: RF output power versus magnetic field. $I_b = 50$ - 52 A. Constant magnetic compression with $R_b = 10.0$ mm except for the $TE_{28,16}$ - mode. Each point represents stable single mode operation with maximum power in the indicated mode.

a minimum. For these modes the gun could not be operated at the desired voltage because of beam instabilities, probably due to leakage of reflected and converted rf power towards the gun. This resulted also in reduced α values. Some influence on P_{out} is also due to the constant beam radius which has not been adjusted for optimum beam-rf interaction in the different modes. It is therefore expected that in a radial version with an appropriate broadband q.o. output coupling system any of the possible oscillating modes shown in Fig. 7 will have an output power and efficiency similar to modes at frequencies without window reflections. In some modes the transverse efficiency is as high as about 60%. Using a single-stage depressed collector a total efficiency around 50% is expected even with the relatively low α. At frequencies above the design value the maximum achievable α is reduced below the design value due to the need of higher magnetic field and the fact that the gun is of diode type.

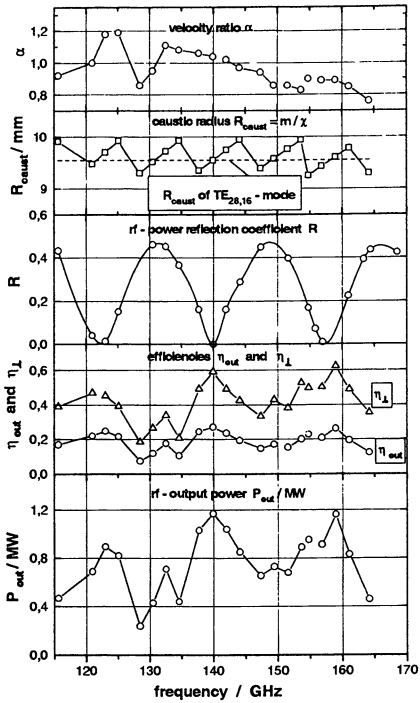

Fig. 8: RF - output power P_{out} , output and transverse efficiency η_{out} and $\eta_\perp$, reflection coefficient R , caustic radius R_{caust} and velocity ratio α versus frequency. Each point corresponds to one mode. Experimental conditions as in Fig. 7.

3. 165 GHz, $TE_{31,17}$ coaxial gyrotron with axial output

3.1 Selection of the operating mode and cavity design

There are two main limitations in the design of the coaxial gyrotron under description. The first is the use of the sc magnet existing at FZK, which can reach a maximum field of around 6.6 T, and the second is the use of the IMIG of the 140 GHz-$TE_{28,16}$ coaxial gyrotron. Due to the first limitation and the requirement of an operating frequency in the range of 165 to 170 GHz, the acceleration voltage has to be reduced close to 75 kV, in order to increase the cyclotron frequency through a reduced relativistic mass factor γ. The reduction of the voltage from 90 to 75 kV and the increase of the cavity magnetic field from 5.54 to 6.5 T result in a

considerably reduced value of the velocity ratio α. The only available way to increase the value of α is the increase of the magnetic compression through the reduction of the gun magnetic field. This means a smaller electron beam radius in the cavity, which in turn is limited by the diameter of the non-removable part of the inner conductor (16 mm), which is fixed to the IMIG and ends up just before the cavity.

Assuming a minimum acceptable beam radius in the resonator of 9 mm, only modes of the azimuthal families $m = 30$ (beam radius $R_b = 9.12$ mm) and $m = 31$ ($R_b = 9.41$ mm) were found to result in reasonable values of α, 1.40 and 1.10 respectively, according to EGUN simulations. In view of the next version of the tube with a lateral output, the modes with azimuthal index $m = 30$ are excluded because non of them is degenerate with a WGM $TE_{m,2}$, in which the cavity mode should be transformed before the dual-beam output launcher [7]. From the modes of the azimuthal family $m = 31$ only the $TE_{31,17}$ mode ($\chi = 94.62$) is degenerate with a WGM mode, the $TE_{83,2}$ mode ($\chi = 94.69$). Therefore the $TE_{31,17}$ mode was selected as the operating mode of the 165 GHz coaxial gyrotron [8].

A coaxial resonator has been designed, according to the design principles presented in [2] and [8], to oscillate in the $TE_{-31,17}$ mode at 165 GHz. The cut-off section of 22 mm length is tapered by 3.0° and it is connected to the 22 mm long cylindrical midsection with parabolic roundings of 4 mm for reduced mode conversion. Power transmission towards the gun is practically zero and the mode purity of the downtaper is 99.3%. The linear part of the uptaper is 30 mm long with an angle of 1.5°. A non-linear uptaper was designed and optimized to increase rapidly the diameter to 100 mm in a distance of 330 mm from the middle of the resonator with negligible mode conversion (output mode purity 99.8%). The radius of the cylindrical part of the resonator is 27.38 mm = 15 λ, where λ is the free-space wavelength. The inner conductor has a radius of 7.32 mm at the middle of the cylindrical part of the resonator, and it is downtapered by 1° towards the output. The wall of this conductor is longitudinally corrugated with 72 rectangular slots of 0.35 mm width and 0.38 mm depth, a value which is close to 0.21 λ ensuring effective mode discrimination and reduced problems from possible mode competition from second cyclotron harmonic interaction. The normalized impedance w varies in the cylindrical part of the resonator from 2.03 to 2.14, and along the total resonator from 1.93 to 2.31. The negative slope of the

mode eigenvalue curve along the cylindrical part results in a slight decrease of the diffractive Q of the mode by 8% from the Q value in an equivalent regular cylindrical resonator with length 22 mm.

The cold-cavity resonant frequency and diffractive Q of the $TE_{31,17}$ mode are f = 164.976 GHz and Q = 3010. The relatively high Q value is a result of the increased cavity length ($\approx 12\,\lambda$), which is necessary to compensate the moderate accelerating voltage ($\approx$ 75 kV) and the low electron velocity ratio α ($\approx$ 1.0). The equivalent Gaussian length L_g of the cold-cavity field profile is 24.5 mm, which corresponds to a normalized interaction length $\mu = \pi\alpha\beta_\perp L_g / \lambda$ close to 16. The frequency separation between the operating mode $TE_{-31,17}$ and its azimuthal neighbours $TE_{-30,17}$ and $TE_{-32,17}$ is 2.268 GHz and 2.283 GHz, while their diffractive Q is 2685 and 3254, respectively. Assuming an rf power of 1.5 MW in the cavity, the peak loading of the outer wall is found to be 1.15 kW/cm^2, and at the inner conductor it is limited to 0.17 kW/cm^2 (ideal copper at room temperature).

3.2 Experimental results and comparison with numerical simulations

The 165 GHz-$TE_{31,17}$ mode coaxial gyrotron has been tested in pulsed operation with 0.15 ms pulse length and 1 Hz repetition rate. However, in single pulses the gyrotron has been operated up to 0.5 ms.

The design operating point with an output power of 1.36 MW and 36.7 % efficiency was not accessible because of beam instabilities at high velocity ratio α (high cathode voltage) due to high velocity spread. The beam was often observed unstable and the operation of the tube was difficult towards the high-power region. With the increase of the beam radius in the cavity (lower compression, lower beam α) the beam was more stable and vice versa. This is an additional indication for development of beam instabilities due to reflected electrons at high beam α in the magnetic mirror before the cavity. In order to operate stably the tube at higher voltage and current the second gun-coil ES2 was energized instead of the ES1, resulting in lower beam α and velocity spread. The experimentally achieved maximum output power versus the cathode voltage is presented in Fig. 9. The cavity magnetic field is 6.63 T and the beam radius is 9.63 mm. The beam α is 0.5 at U_c = 45 kV cathode voltage and increases to 0.92 at U_c = 92 kV, according to the adiabatic dependence. The beam current starts at 41 A at 45 kV and reaches 52 A at

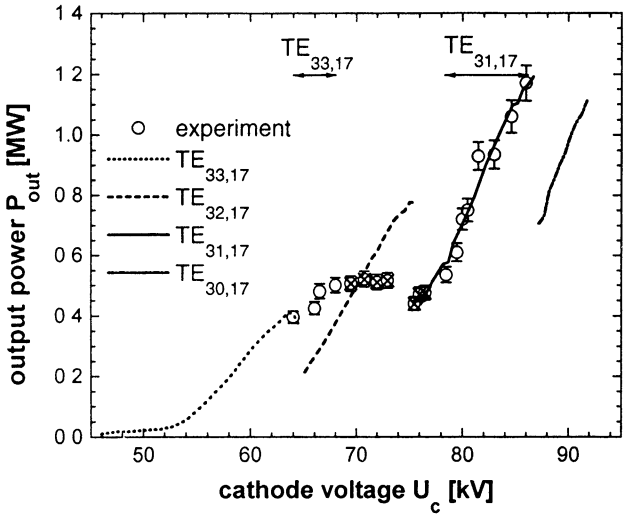

Fig. 9: Output power of different modes versus cathode voltage. B_o=6.63T, R_b=9.63 mm, $\delta\beta_{\perp rms}$ =3.5 % and α = 0.84 at U_c = 77 kV and I_b = 40A. Open/crossed circles show single/multi mode operation.

92 kV. At U_c = 84 kV cathode voltage and I_b = 50 A current the beam α is equal to 0.84 and the rms velocity spread is 3.5%, according to EGUN computations. The beam was stable up to 52 A. Experimentally only two frequencies were measured in single-mode operation: 168.52 GHz ($TE_{33,17}$ mode) and 164.99 GHz ($TE_{31,17}$ mode). In an extended cathode voltage range (70 to 77 kV) multimoding of these two frequencies and the $TE_{32,17}$ mode at 167.27 GHz was observed. The agreement between the numerical and experimental results of the operating $TE_{31,17}$ mode is excellent. Experimentally the mode was found to oscillate up to 86 kV cathode voltage and 51 A current with 1.17 MW output power and 26.7% efficiency. Assuming 7% internal losses (ohmic losses in cavity and output waveguide, window absorption) and 1.7 kV voltage depression, an electronic efficiency of 29.2% is computed. The beam α is 0.86 and the transverse electronic efficiency is 68.6%. This operating point is 2.5 kV inside the hard excitation region, which starts close to 83.5 kV cathode voltage. Numerically the $TE_{31,17}$ mode was found to oscillate stably up to 86.7 kV with 1.19 MW output power and 27.1% total efficiency. It was not possible in the experiment to increase U_c to more than 86 kV because of high-voltage power supply limitations. In general, the operation of the tube with the ES2 gun-coil energized was very smooth and easy, because of the low beam α and the absence of beam instabilities.

The tube was also operated at higher frequencies by controlling the magnetic field and the cathode voltage. The maximum power achieved is given in Table 2. Megawatt level output power (1.02 MW) was measured at a frequency of 167.14 GHz frequency with 26.8% efficiency in the $TE_{32,17}$ mode. The far field pattern of the 165 GHz-$TE_{31,14}$ coaxial gyrotron output is shown in Fig. 10 where 62 minima and maxima are easily recognized.

Tab.2: Frequency tunability of the 165 GHz coaxial gyrotron.

mode TE_{mp}	**$TE_{31,17}$**	**$TE_{32,17}$**	**$TE_{33,17}$**	**$TE_{34,17}$**
frequency / GHz	164.98	167.14	169.46	171.80
magnetic field / T	6.63	6.62	6.62	6.62
beam radius / mm	9.63	9.70	9.75	9.82
cathode voltage / kV	86	76	70	57
beam current / A	51	50	50	46
output power / MW	1.17	1.02	0.63	0.35
total efficiency / %	26.7	26.8	18.0	13.3

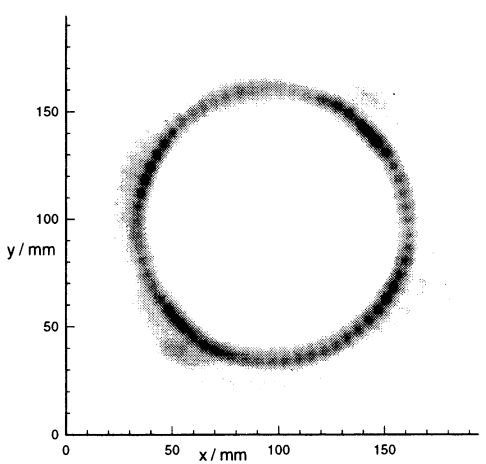

Fig. 10: Measured far-field pattern of the 165 GHz-$TE_{31,17}$ coaxial gyrotron output with stopped rotation.

4. Gyrotron with radial dual-beam rf-output and single-stage depressed collector

A gyrotron relevant for cw-operation with a radial dual rf-beam output and a depressed collector (Fig. 11) is under construction. Components as output windows, double-beam launcher and single-stage depressed collector are already available. The mirrors and the mirror box are under fabrication.

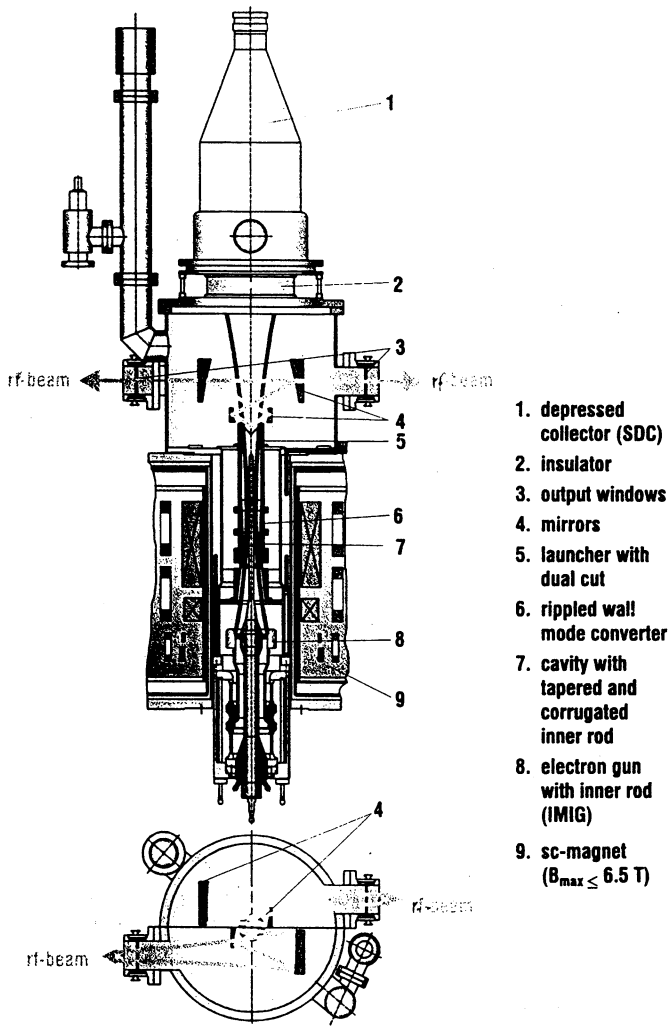

Fig. 11: Schematic layout of the coaxial cavity gyrotron with dual rf-beam output.

For operation with two rf output windows a q.o. mode converter system based on a two-step mode conversion scheme, $TE_{-28,16}$ to $TE_{+76,2}$ to TEM_{00}, which generates two narrowly-directed (60° at the launcher) output wave beams has been designed [7] as shown in Tab. 3. High conversion efficiency is expected (94 %). If one employs, as in conventional hollow waveguide cavity gyrotrons, a q.o. mode converter for the operating volume mode of the cavity, the dimensions of the mirror system are excessively large for a dual beam output since the azimuthal angle of divergence φ of the radiation in geometric optical approximation is quite large, e.g. $\varphi = 2 \arccos(m/\chi_{mp}) = 142.6^0$ for the $TE_{28,16}$ mode. For a high-order WGM of the type $TE_{m,2}$ the azimuthal angle of divergence φ of the radiation is sufficiently small, e.g. $\varphi = 2 \arccos(m/\chi_{mp}) = 59.1^0$ for the $TE_{76,2}$ mode, since the representing rays from its caustic are located closer to the waveguide wall. Thus a double-cut q.o. launcher can generate two diametrically opposed narrowly-directed output wave beams. However, it should be pointed out that the two step mode conversion works properly only for the design mode and cannot be used if the possibility of frequency tuning is considered.

The conversion of the cavity mode to the degenerate WGM is achieved by introduction of longitudinal corrugations in the output taper (1.5°) consisting of $\Delta m = 104$ slots according to the formula:

$$R_w = R_{w,0}(z) + \rho \cos(\Delta m \phi)$$

where $R_{w,0}(z)$ is the mean radius of the output waveguide wall, $\rho =$ 0.05 mm is the amplitude of corrugations and $\Delta m = 104$.

The quasi-optical (q.o.) converter will use an improved dimple double-beam launcher with $\Delta m_1 = 2$ and $\Delta m_2 = 6$ perturbations for longitudinal and azimuthal bunching of the two mm-wave beams [7].

Tab. 3: Two-step mode conversion sequence for coaxial gyrotron.

$TE_{-28,16}$	$TE_{+76,2}$	TEM_{00}
volume mode	whispering gallery mode	wave beam
degenerate modes longitudinal $\Delta m = 104$, waveguide mode converter		q.o. dual-beam output through two rf output windows

Acknowledgements

The work was supported by the European Fusion Technology Program (ITER Task No: G 52 TT 03 94-08-03 FE, ID No: T 24) under the Project Kernfusion of the Forschungszentrum Karlsruhe (FZK). We gratefully acknowledge H. Baumgärtner, H. Budig, P. Grundel, W. Leonhardt, N. Münch, J. Szczesny, and R. Vincon of the FZK Gyrotron Team technical staff for the mechanical design, the precise machining and the careful assembly of the tube as well as for their assistance during the experiments.

References

[1] S. N. Vlasov, L. I. Zagryadskaya and I. M. Orlova, *Radio Engineering and Electronic Physics,* **21**, pp. 96-102, 1976.

[2] C. T. Iatrou, S. Kern and A. B. Pavelyev, *IEEE Transactions on Microwave Theory and Techniques,* **41**, pp. 56-64, 1996.

[3] V. A. Flyagin, V. I. Khishnyak, V. N. Manuilov, A. B. Pavelyev, V. G. Pavelyev, B. Piosczyk, G. Dammertz, O. Höchtl, C. T. Iatrou, S. Kern, H.-U. Nickel, M. Thumm, A. Wien, and O. Dumbrajs, *19th International Conference on Infrared and Millimeter Waves,* Conference Digest JSAP 941228, pp. 75-76, Sendai, Japan, 1994.

[4] J. J. Barroso and R. A. Correa, *International Journal of Infrared and Millimeter Waves,* **12**, pp. 717-728, 1991.

[5] B. Piosczyk, O. Braz, G. Dammertz, C. T. Iatrou, S. Kern, A. Möbius, M. Thumm, A. Wien, S. C. Zhang, V. A. Flyagin, V. I. Khishnyak, A. N. Kuftin, V. N. Manuilov, A. B. Pavelyev, V. G. Pavelyev, A. N. Postnikova, and V. E. Zapevalov, *20th International Conference on Infrared and Millimeter Waves,* Conference Digest, pp. 423-424, Lake Buena Vista (Orlando), Florida, USA, 1995.

[6] V. K. Lygin, V. N. Manuilov, A. N. Kuftin, A. B. Pavelyev and B. Piosczyk, *International Journal of Electronics*, **79**, pp. 227-235, 1995.

[7] M. Thumm, C. T. Iatrou, A. Möbius and D. Wagner, *21th International Conference on Infrared and Millimeter Waves,* Conference Digest, paper AM6, Berlin, 1996, ISBN 3-00-000800-4.

[8] C. T. Iatrou, *IEEE Transactions on Plasma Science*, **24**(3), 1996.

[9] O. Braz, A. Arnold, M. Losert, A. Möbius, M. Pereyaslavets, M. Thumm, *21th International Conference on Infrared and Millimeter Waves,* Conference Digest, paper ATh6, Berlin, 1996, ISBN 3-00-000800-4.

[10] S. Kern, *21th International Conference on Infrared and Millimeter Waves,* Conf. Digest, paper AF2, Berlin, 1996, ISBN 3-00-000800-4.

Development and applications of submillimeter wave gyrotrons

T.Idehara, T.Tatsukawa, I.Ogawa, Y.Shimizu, N.Nishida and K.Yoshida
Faculty of Engineering, Fukui University, Fukui 910, Japan

Development and applications of high frequency, medium power gyrotrons in Fukui University (Gyrotron FU series) are described. The latest gyrotron in the series, Gyrotron FU IV has achieved a frequency tunability up to 847 GHz. The previous gyrotron, Gyrotron FU III achieved third harmonic operations in single mode, amplitude modulation and frequency step switching. The early gyrotron, Gyrotron FU II has demonstrated mode competition and mode cooperation. The former is not convenient for high frequency, harmonic gyrotrons and should be removed. Gyrotron FU II has been applied to plasma scattering measurement of Compact Helical System (CHS) at National Institute for Fusion Science (NIFS). Gyrotron FU I , FU E and FU IV are being used for ESR experiment as millimeter to submillimeter wave sources.

1. Introduction

The development of gyrotrons are proceeding in two directions. One is the development of high power, millimeter wave gyrotrons as the power sources for electron cyclotron heating of the plasma, for electron cyclotron current drive of tokamaks and for ceramic sintering. At the present, 120-170 GHz, 1 MW, pulsive gyrotrons are delivered for plasma heating and current drive[1-5] and 30 GHz, 15 kW, cw gyrotron for ceramic sintering.[6,7]

The other is the development of high frequency, medium power gyrotrons[8,9] as millimeter to submillimeter wave sources for plasma

scattering measurement,[10,11] ESR experiment[12] and so on. Such gyrotrons operate at the fundamentals, the second harmonics of electron cyclotron resonance and even at the third harmonics under high magnetic field whose intensity is over 10 T. They have many advantages which other conventional sources do not possess, for example, frequency tunability and moderately high power output. Gyrotrons developed in Fukui University are ones of the latter, that is, high frequency, medium power gyrotrons covering a wide frequency range in millimeter to submillimeter wavelength. We call a series of these gyrotrons 'Gyrotron FU series'. The latest gyrotron of the series, Gyrotron FU IV[13] has achieved a frequency tunability from 160 GHz to 847 GHz by many single mode operations at the fundamentals and the second harmonics of electron cyclotron frequency. The gyrotron is being used for a high frequency ESR experiment as a radiation source.

The previous gyrotron, Gyrotron FU III[14] has also achieved a frequency tunability up to 636 GHz by operations at the fundamentals, at the second harmonics and even at the third harmonics. The gyrotron demonstrated an amplitude modulation and a frequency step switching of its output, which are useful for its applications to the infrared spectroscopy as a radiation source.

The early gyrotron Gyrotron FU II[15] is the first submillimeter wave gyrotron in the series, whose maximum frequency is 402 GHz. It is being used for a plasma scattering measurement of Compact Herical System (CHS) in National Institute for Fusion Science (NIFS) at Nagoya. Around 100 watt output power at 352 GHz is transmitted by circular waveguide system, converted into a quasi-Gaussian mode and injected into CHS plasma. A scattered signal is analyzed using a homodyne detection system. The measurement confirmed an excitation of low frequency drift wave during NBI or ICRF heating. Such informations are important for achievement of the best plasma confinement.

The first gyrotron, Gyrotron FU I is frequency-tunable from 70 GHz to 200 GHz and is being used as a radiation source for ESR experiment.

At the present, we have constructed a new gyrotron Gyrotron FU

IVA[8], using a 17T superconducting magnet. The cavity has a nonlinear up-taper region and smooth connection parts in the beginnings of the cutoff down-taper and the output up-taper, to minimize the mode conversion from the main cavity mode to its competing modes. The gyrotron has just begun to operate. It will achieve the breakthrough of the wall of 1 THz in near future. In this monograph, we will summarize the development of Gyrotron FU series and their applications to plasma scattering measurement and ESR experiment.

2. Development of Gyrotron FU series

2.1 Designs and constructions of high frequency, harmonic gyrotrons

Gyrotron FU series is including 7 gyrotrons. Each gyrotron consists of a sealed-off gyrotron tube and a superconducting magnet except Gyrotron FU III, which has a demountable tube. Table 1 summarizes the present status of gyrotrons included in the series.

Table 1 Present status of Gyrotron FU series

Gyrotron FU I	70-200 GHz	Radiation source for ESR experiment
Gyrotron FU E	90-300 GHz	Radiation source for ESR experiment
Gyrotron FU IA	38-215 GHz	Radiation source for plasma scattering measurement of WT-3
Gyrotron FU II	70-400 GHz	Radiation source for plasma scattering measurement of CHS
Gyrotron FU III	100-640 GHz	3rd harmonic operations in single modes, Amplitude and frequency modulations
Gyrotron FU IV	160-850 GHz	cw stable operations of gyrotron Radiation source for ESR experiment
Gyrotron FU IVA	300-1,324 GHz	Higher frequency operations at 3rd harmonics, High purity mode operations

(a) Gyrotron FU IV[13]

The design was carried out by computer simulations. We selected narrow cavities to get a good mode separation and then to

operate the gyrotron in many single modes at the fundamentals, second harmonics and even at the third harmonics. Such a situation is important for our high frequency, harmonic gyrotrons. For example, the diameter of the latest gyrotron, Gyrotron FU IV, is only 3.23 mm, as shown in Fig. 1.

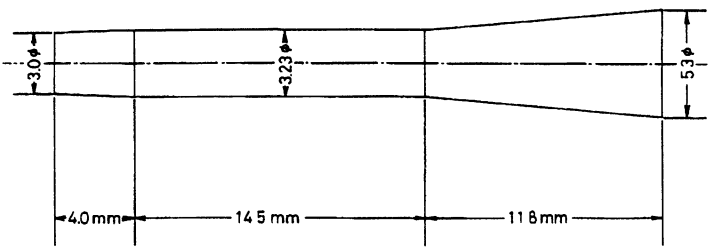

Fig. 1 The shape of a cylindrical cavity installed in Gyrotron FU IV.

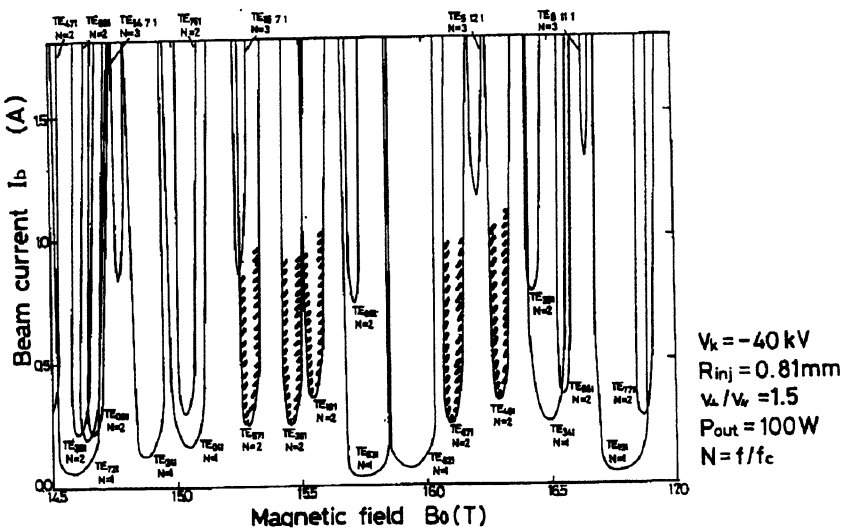

Fig. 2 Computer simulation results for beam currents I_b to sustain 100 W output power for many cavity modes as functions of magnetic field intensity B_0. A parameter N shows harmonic number.

In Fig. 2, beam currents to sustain 100 W output powers are plotted for many cavity modes as functions of the magnetic field intensity B_0. A parameter N ($=f/f_c$, f and f_c are a operation frequency and an

electron cyclotron frequency) shows harmonic number. 17 T superconducting magnet is used for Gyrotron FU IV. As seen in the figure, there are many candidates for single mode operations at fundamentals (N=1), second harmonics (N=2) and even third harmonics (N=3) in the field intensity region from 14.5 T to 17 T. If we adjust field intensity B_0 at its optimum value, we can operate second harmonics hatched in Fig. 2, suppressing the mode competitions with any fundamentals of higher output power. We can expect the maximum frequency at second harmonic is around 850 GHz by single mode operation of $TE_{4,8,1}$ cavity mode. The other gyrotrons in Gyrotron FU series are designed along the same line as Gyrotron FU IV.

(b) Gyrotron FU IVA[8]

A schematical drawing of a new gyrotron, Gyrotron FU IVA is shown in Fig. 3. The gyrotron consists of a 17 T superconducting magnet and a sealed-off tube. A triode magnetron injection type gun operates in the magnetic field leaking from a superconducting magnet. The mirror ratio, that is the ratio of the main field intensity at the cavity region to the intensity at the cathode of electron gun, is about 45. A computer simulation result shows that we can control the ratio α ($= v_\perp / v_{//}$, $v_\perp$ and $v_{//}$ are the perpendicular and the parallel velocity components) only by adjusting the anode voltage V_a in the wide field intensity range from 5 T to 17 T. A cavity whose diameter and length are only 3 mm and around 7 mm is installed in the gyrotron. Fig. 4 shows the shape of the cavity. It has a nonlinear up-taper in the output region and smooth

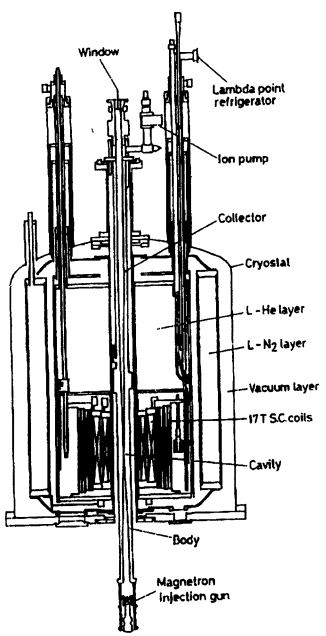

Fig. 3 A schematical drawing of Gyrotron FU IV A.

connection parts in the beginnings of cutoff down-taper and up-taper at the output to minimize a mode conversion from the main cavity mode to its competing modes. The cavity has also a small iris at the output end to increase a quality factor and then to decrease a starting current for each cavity mode. The design of this cavity was carried out precisely by D.Wagner from University of Stuttgart and M.Thumm from Forschungszentrum Karlsruhe.

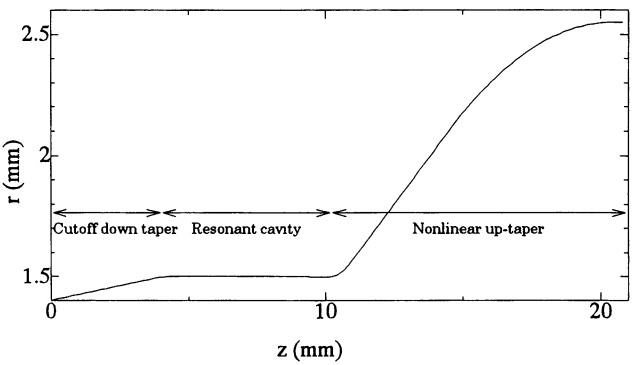

Fig. 4 The shape of a cavity installed in Gyrotron FU IVA.

Fig. 5 shows, a computer simulation results for mode conversion from the main cavity mode $TE_{2,6,1}$ to its competing modes $TE_{2,5,1}$, $TE_{2,7,1}$ and so on, which occurs in the nonlinear up-taper region. A part of the main mode is converted to $TE_{2,5,1}$ and $TE_{2,7,1}$ modes in the middle of the up-taper region, but almost all power returns back to the main mode at the end of up-taper. A calculation results show 99.3 percent of total power can penetrate the up-taper region as the main mode.

Fig. 6 shows a computer simulation results for equi-oscillation-efficiency-lines of third harmonic operations (N=3) of $TE_{2,10,1}$ and $TE_{9,7,1}$ modes together with fundamental operation (N=1) of $TE_{9,1,1}$ mode. The vertical and horizontal axes are an injection point of beam electron in the cavity and field intensity B_0, respectively. Hatched region are the injection region of electrons in the present device. Single mode operations at third harmonics (N=3) are possible only by adjusting field intensities B_0 at the optimum conditions. The frequencies of $TE_{2,10,1}$ and $TE_{9,7,1}$ modes are 1022 and 1034 GHz. Therefore, we expect this gyrotron will achieve

the breakthrough of 1 THz.

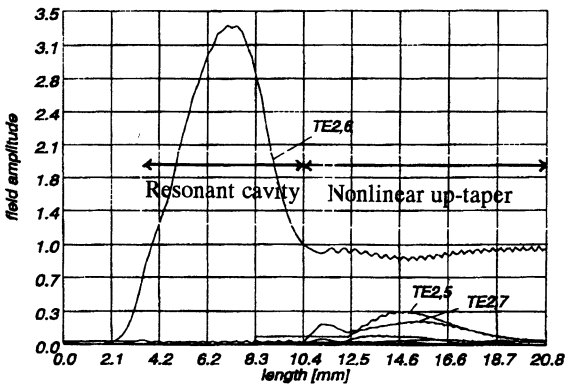

Fig. 5 Computer simulation result for mode conversions from the main cavity mode $TE_{2,6,1}$ to its competing modes $TE_{2,5,1}$, $TE_{2,7,1}$ and so on, which occur in the nonlinear up-taper region.

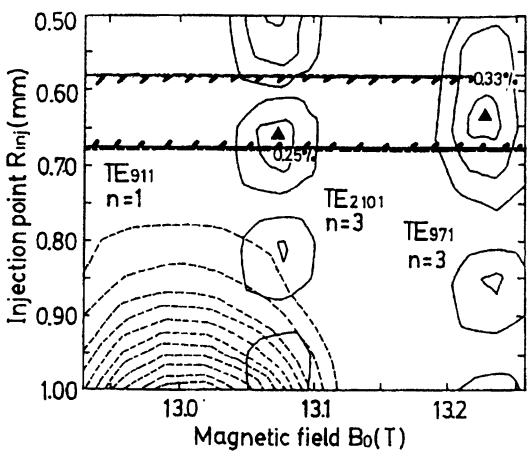

Fig. 6 Computer simulation result for equi-oscillation-efficuency-lines of third harmonic operations of $TE_{2,10,1}$ and $TE_{9,7,1}$ modes together with fundamental operation of $TE_{9,1,1}$ mode.

2.2 Experimental results of high frequency, harmonic gyrotrons (Gyrotron FU series)

As shown in Table 1, gyrotrons included in Gyrotron FU series are frequency step-tunable sources which cover a wide wavelength range from millimeter to submillimeter. The output powers are not so high, that is, from several hundred watt to several ten kilowatt at the fundamental operations and from several ten watt to several kilowatt at the second harmonic operations. The main results which Gyrotron FU series has achieved up to the present are summarized as follows.

(a) Frequency tunability from 38 GHz to 850 GHz[13-16]

6 gyrotrons in the series except Gyrotron FU IVA have achieved frequency step-tunabilities in the ranges shown in Table 1. Fig. 7 shows a typical result of frequency measurement for Gyrotron FU IV using a Fabry-Perot interferometer. There are many instances for single mode operations at fundamentals (Fig. 7(a)) and at second harmonics (Fig. 7(b)). Each interferometer pattern corresponds to field intensity B_0 indicated by an arrow. Measured wavelengths, corresponding frequencies and cavity modes are denoted in the figure. The highest frequency observed up to the present is 847 GHz by single mode operation of $TE_{4,8,1}$ cavity mode at the second harmonic (N=2).

Table 2 is a list of all observed frequencies, together with corresponding field intensities, cavity modes and a number of output powers measured by a water load. Frequency step-tunability is achieved from 160 to 850 GHz by both fundamental and second harmonic operations. Output powers are several hundred watts at the fundamentals and several ten watts at the second harmonics.

Similar frequency tunability is achieved by each gyrotron in the series, as shown in Table 1. The Gyrotron FU series covers wide frequency range from 38 GHz to 850 GHz.

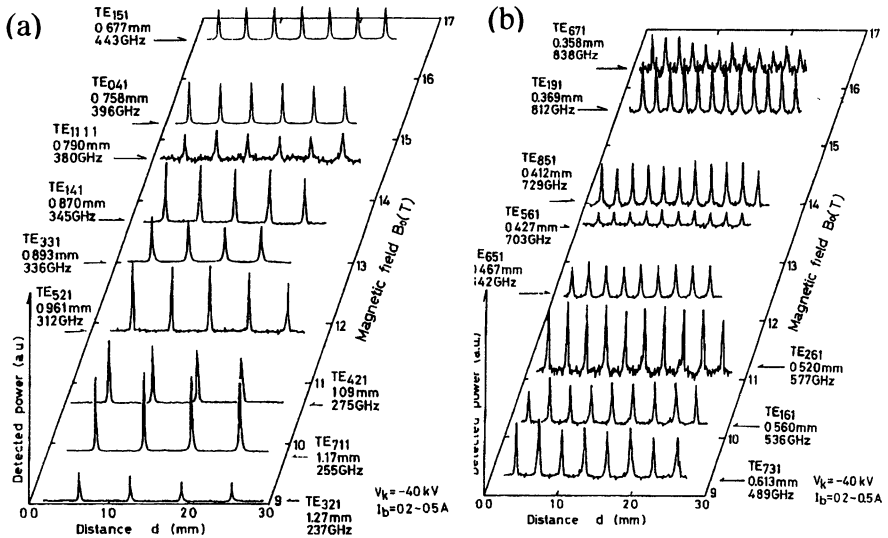

Fig. 7 A typical result of frequency measurement for Gyrotron FU IV using a Fabry-Perot interferometer. Interferometer patterns for (a) the fundamentals and (b) the second harmonics are shown in the figure.

Table 2 List of all frequencies observed for Gyrotron FU IV , together with corresponding field intensities, cavity modes and a number of output powers measured by a water load.

B_0 (T)	$f=f_c$ (GHz)	$f=2f_c$ (GHz)	P (W)	TE m n
6.23	159			1 2
6.55		336		3 3
6.73		346		1 4
7.31		376		4 3
7.38	190			5 1
7 64	199		403	2 2
8 13	208			0 2
8.34		443		3 4
8 52	221			6 1
8.77		455		9 2
9 27		486		0 5
9 34		489		7 3
9 35	237		456	3 2
9 58	253			1 3
9.86	255			7 1
9.97		521		11 2
10 14		529		3 5
10.20		536		1 6
10.76	278		253	4 2
11.00	281			8 1
11.05		577		2 6
11.15	293			2 3
11.38	301			0 3

B_0 (T)	$f=f_c$ (GHz)	$f=2f_c$ (GHz)	P (W)	TE m n
11.85	309			5 2
12.42	316			9 1
12 44		647		6 5
12.74	337		107	3 3
13 40	346			1 4
13 49		703		5 6
13.55	356		55	6 2
13.68		714		3 7
13.90		718	51	1 8
13.96		729		8 5
14.25	372		107	4 3
14.63	378			11 1
14.79	390			2 4
14 97	396			0 4
15 57		802		3 8
15.62	414			5 3
15 71		812	63	1 9
15.80	417			8 2
16.30		838		6 7
16.32		847		4 8
16.52	431			3 4
16 67	443			1 5

(b) Higher harmonic (N≧3) operations[17,18]

Higher harmonic (N≧3) operations enable us to save magnetic field intensity and develop high frequency gyrotrons. Therefore, those are necessary for the development of high frequency, medium power gyrotrons as submillimeter wave sources. Gyrotron FU I, FU II and FU III have achived third (N=3) and fourth (N=4) harmonic operations.

We used Michelson interferometer combined with a signal analyzer for Fast Fourier Transformation (FFT) to obtain frequency spectrum of gyrotron output. A block diagram of the measurement system is shown in Fig.8. Gyrotron output is fed to beam splitter 1 and splits in two ways. After a number of reflections, the two beams emerge at beam splitter 2. Beam splitters 1 and 2 are metal meshes (60 lines/in.). Mirrors 1 and 2 are metal plates. The phase shifter is composed of two metal plate mirrors. When the phase shifter is driven at a constant speed v, the detected interference signal alternates with frequency $f' = 2v/\lambda = 2vf/c$, where λ and f are the wavelength and the frequency of the gyrotron output. The signal from the pyroelectric detector was amplified and Fourier analyzed by a signal analyzer. The observed frequency (f') spectrum can be easily converted to real gyrotron frequency (f) spectrum by using the above relation between f and f'. Fig. 9 (a) is a typical instance of interferometer pattern observed for

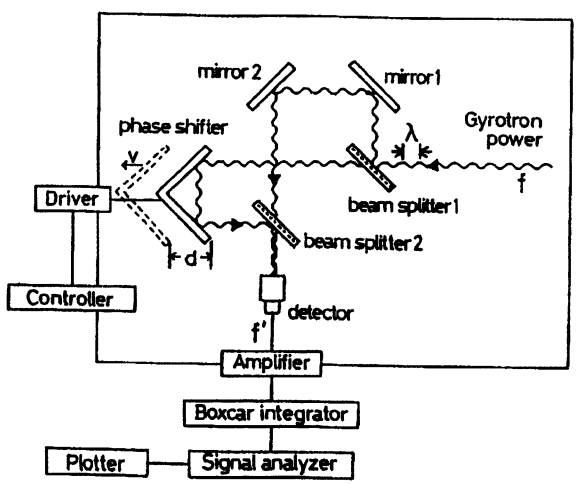

Fig. 8 Block diagram of frequency measurement system using a Michelson interferometer.

Gyrotron FU II and Fig. 9 (b) corresponding frequency spectrum obtained by FFT of the interferometer pattern. It is seen that intense third harmonic operation occurs together with intense fundamental and weak second harmonic operations. In another case, the weak operation even at the fourth harmonic occurs with the fundamental, the second and the third harmonic operations of more intense output powers. Fig. 10 summarizes frequencies observed on the spectra as functions of field intensity B_0. Solid lines are the fundamental, the second, the third and the fourth harmonic resonances. Higher harmonic operations enable us to operate Gyrotron FU II at high frequency modes up to around 600 GHz.

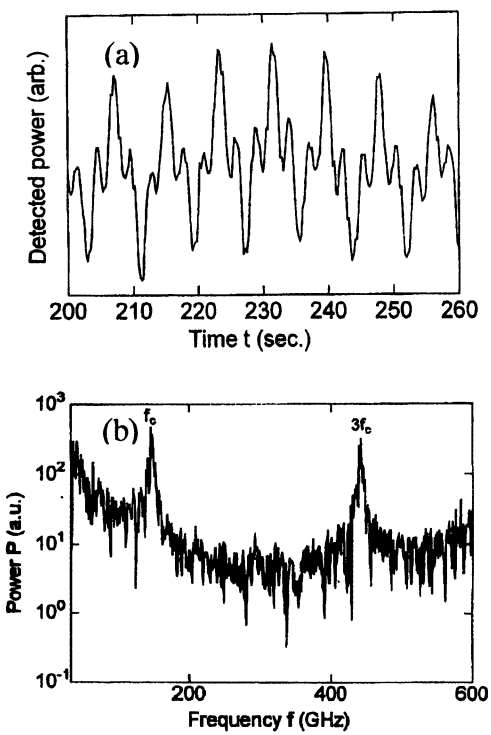

Fig. 9 A typical result of frequency measurement using a Michelson interferometer. (a) Interference pattern for Gyrotron FU II. (b) Frequency spectrum obtained by FFT of the interference pattern. B_0=5.68 T, V_k=-40 kV, I_b=050 A, f=145 GHz($TE_{1,2,1}$, $f=f_c$) and f=440 GHz($TE_{1,6,1}$, $f=3f_c$)

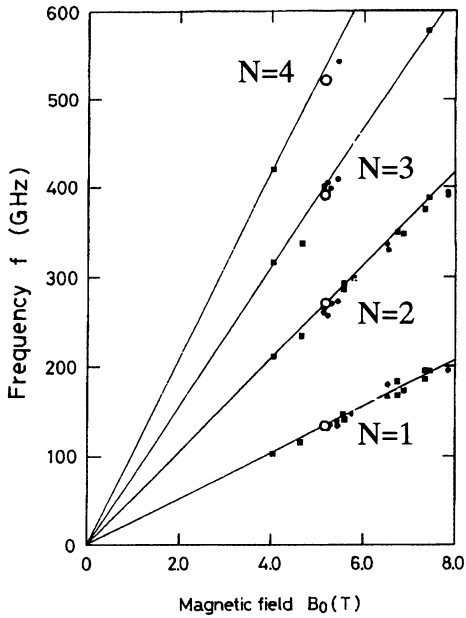

Fig. 10 All frequencies observed on spectra of the output of Gyrotron FU II as functions of B_0.

(c) Mode competition and mode cooperation[19,20]

Sometimes, mode competition between the fundamental (N=1) and the second harmonic (N=2) operations occurs in our high frequency gyrotrons. In such a case, higher frequency mode (N=2) is suppressed by excitation of lower frequency mode (N=1) of higher output power. This phenomenon is not convenient for high frequency, harmonic gyrotrons and should be removed.

Fig. 11 shows a typical features of the mode competition. Solid and dotted lines are output powers at the second harmonic operations of $TE_{2,6,1}$ cavity mode and at the fundamental operations of $TE_{2,3,1}$ mode as functions of beam current I_b with field intensity B_0 as a parameter. For each field intensity, the second harmonic, single mode operation starts at lower threshold beam current I_{b1}. However, when I_b is increased, the fundamental operation starts at

higher threshold current I_{b2} and its output power increases. The second harmonic operation is suppressed completely, when the fundamental becomes intense. Therefore, a single mode operation at the second harmonic occurs in the beam current range from I_{b1} to I_{b2}. This single mode operation is useful, when we apply our high frequency, harmonic gyrotrons as submillimeter wave sources.

In some circumstances, one mode helps the other mode to become established. One could describe this as 'mode cooperation'. A phenomenon observed in Gyrotron FU II suggests phase bunching due to the second harmonic operation acts as a prebunching to enhance the fundamental operation, which results in a reduced starting current for fundamental operation.

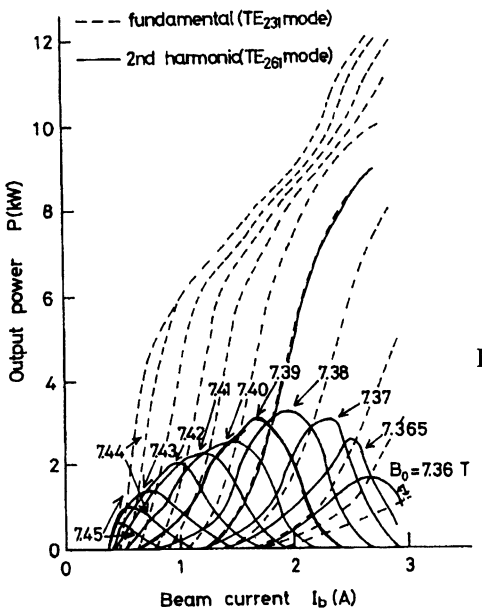

Fig. 11 Output powers of Gyrotron FU II at the fundamental (broken lines) and the second harmonic (solid lines) as functions of beam current I_b with field intensity B_0 as a parameter.

Fig. 12 shows calculated output power for the $TE_{2,6,1}$ mode at the second harmonic (solid lines) and for $TE_{2,3,1}$ mode at the fundamental (broken lines) as functions of beam current I_b for a magnetic field B_0=7.32 T. Thick and thin lines show both the case of simultaneous excitation of fundamental and second harmonic (really occurring) and the case of each single mode excitation (not really occurring, only assuming). The dotted line shows the total

power of both excitations. Though other low-power branches appear in the simulation for single mode excitations of the fundamental and the second harmonic, they are removed in the figure, because we can treat them as spurious modes.

Comparison between these give some interesting insights. (1) When the second harmonic is present, the starting current for fundamental operation falls from point A to B. (2) In the region between these points, total power is greater than it would be if there was only second harmonic operation. So, when mode cooperation occurs, more power is extracted from the electrons. When B_0=7.32 T and I_b=1.1 A the total power increases by more than 80 %.

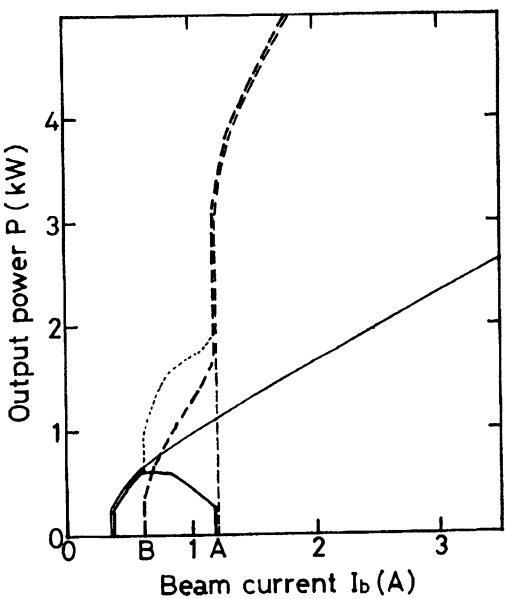

Fig. 12 Calculated output power P for the $TE_{2,6,1}$ mode at the second harmonic (solid lines) and for the $TE_{2,3,1}$ mode at the fundamental (broken lines) as functions of beam current I_b. Thick and Thin lines show both the case of simultaneous excitation of fundamental and second harmonic (really occurring) and the case of each single mode excitation (not really occurring, only assuming). The dotted line shows the total power of both simultaneous excitations. The field intensity is fixed at B_0=7.32 T. Between both currents denoted by A and B, the mode cooperation occurs.

In Fig. 13(a), the range of beam currents for mode cooperation derived from the experimental results is shown as a function of the magnetic field B_0. Fig. 13(b) shows the corresponding calculated results. In both figures, the curves labeled B show the starting current for the fundamental and the curves labeled A show the current for complete suppression of the second harmonic. Slightly weaker field intensity in the experimental results than that in the simulation comes from the inaccuracy of our gaussmeter.

Computer simulation results[20] indicate the possibility of mode cooperation, where a gyrotron operation at the second harmonic provokes excitation of another mode at the fundamental cyclotron resonance, and these two modes may coexist. The prebunching of beam electrons in gyration phase introduced in the initial stage by the second harmonic, may enhance the operation at the fundamental, which could not rise up without the help of the second harmonic operation. This mechanism results in the decrease of the starting current of operations at the fundamental and perhaps offers a more efficient way of achieving useful output powers from a gyrotron operating at lower voltages

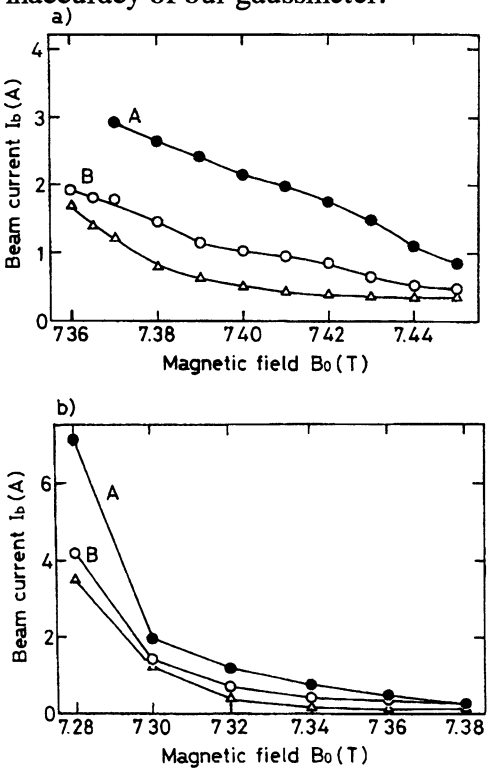

Fig. 13 Beam current range for mode cooperation as functions of field intensity B_0. (a) Experimental result and (b) simulation result. △ shows the starting current for the second harmonic.

and currents.

(d) Amplitude modulation of submillimeter wave gyrotron output[21]

An amplitude modulation and frequency modulation of submillimeter wave gyrotrons are useful for their applications to wider fields as radiation sources. Gyrotrons FU III and FU IV have achieved amplitude modulation of its output. A modulation of the anode voltage V_a will modulate the velocity distribution of electron beam, which, in turn, will modulate the gyrotron output.

Fig. 14 shows a typical results of modulating the submillimeter wave gyrotron, with the modulation level of anode voltage V_a expressed as the ratio $\Delta V_a/V_a$ as a parameter. The gyrotron, in this instance, is operating at the fundamental of the cyclotron frequency. The cavity mode is $TE_{6,2,1}$, the frequency is 349 GHz, and the output power is about 60 W. The modulating frequency is 5 kHz and modulation mode is square wave.

The upper traces show the high voltage pulse applied to the anode. The small

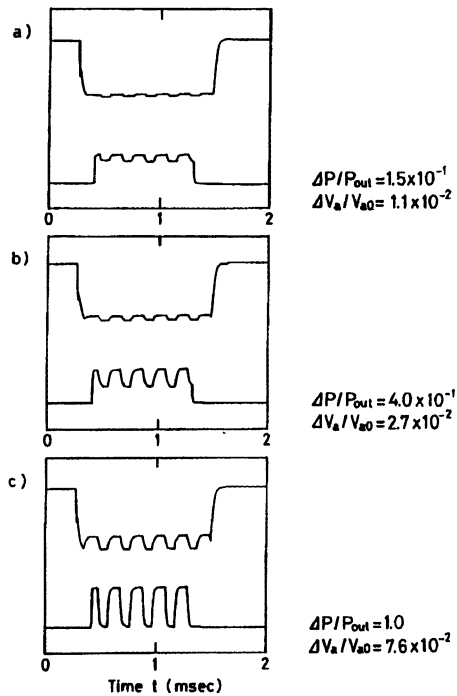

Fig. 14 Amplitude modulation result for Gyrotron FU III. Upper traces are high voltage pulses applied to the anode and lower traces are output powers of the gyrotron. Operation conditions; $TE_{6,2,1}$ mode at the fundamental, modulation frequency is 5 kHz and modulation mode is square wave, the frequency f =349 GHz, unmodulated beam voltage V_b=40 kV and beam current I_b=0.3 A.

square wave modulation signal is visible in the traces. The lower traces show the output power of the gyrotron. The modulation rate $\Delta P_{out}/P_{out}$ of gyrotron output increases with the modulation rate $\Delta V_a/V_a$ of the anode voltage. The 100 % modulation of the output ($\Delta P_{out}/P_{out}$=1.0) is attained when $\Delta V_a/V_a$ is only several percent ($\Delta V_a/V_a \sim 0.076$). Experimental results show the modulation rate $\Delta P_{out}/P_{out}$ of output is almost linearly proportional to $\Delta V_a/V_{a0}$. This means the sinusoidal modulation of output power is possible by the sinusoidal modulation of anode voltage. Sinusoidal modulation of P_{out} at the modulation frequency up to 600 kHz has been achieved with the low $\Delta V_a/V_a$ value of 1.1×10^{-3}.

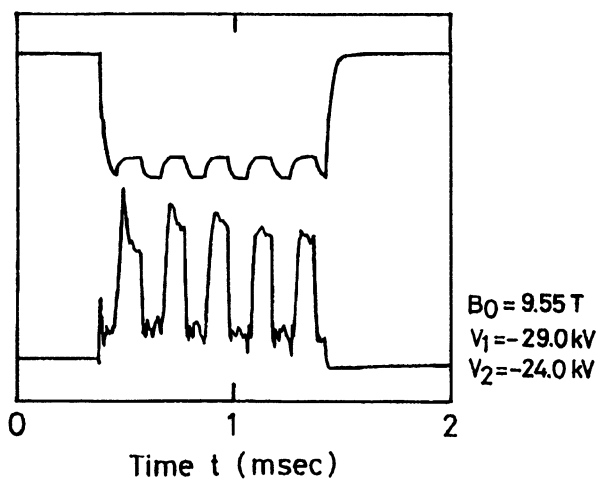

Fig. 15 Upper trace; High voltage pulse applied to the electron gun cathode, modulated by a 5 kHz square wave. The magnetic field is B_0=9.55 T, V_1=29.0 kV and V_2=24.0 kV. Lower trace; Output power measured by a pyroelectric detector.

(e) Frequency step switching due to switching of operating cavity mode[22]

One kind of frequency modulation that is possible is obtained by step switching from one cavity mode to another, by modulating the energy of the electron beam. It is still useful for many applications of gyrotrons, for example, plasma heating at several frequencies (a simultaneous heating at the electron cyclotron fundamental and the second harmonic resonances), heat pulse propagation experiments at two different frequencies, and so on. The principle of frequency step switching the gyrotron output is as follows. Usually, gyrotrons operate at a frequency near the electron cyclotron frequency ω_c or its harmonics n ω_c. The electron cyclotron frequency is $\Delta\omega_c = eB_0/(\gamma m_0)$, where e is the electric charge unit and m_0 the rest mass of the electron, B_0 the static magnetic field and $\gamma=(1-v^2/c^2)^{-1/2}$ the relativistic factor.

When the energy of an electron is changed, γ, which is related to the beam voltage V by $(\gamma-1)m_0c^2=eV$ changes and, as a consequence, the electron cyclotron frequency ω_c changes. If the cathode voltage is switched from V_1 to V_2, the electron cyclotron frequency changes from ω_{c1} to ω_{c2} and the frequency step is $\Delta\omega_c=\omega_{c2}-\omega_{c1}=\omega_{c0}eV_1(1-V_2/V_1)/(m_0c^2)$, where ω_{c0} is the geometric mean of ω_{c1} and ω_{c2}. If there are two cavity modes whose operating conditions are very close, it becomes easy to switch from one to the other. In this way, rapid frequency step switching of a gyrotron can be realized. In the experiment, V_1=30 kV, V_2/V_1=0.75, so, $\Delta\omega_c/\omega_c=1.47\times10^{-2}$. If at least two cavity modes lie in the range $\Delta\omega_c$ of electron cyclotron frequency, frequency step switching occurs when operation changes from one mode to the other.

Fig. 15 shows a typical result for frequency step switching between two fundamental modes. The upper trace shows the high-voltage, 1 ms pulse applied to the cathode of the electron gun. The anode voltage is obtained using a resistive voltage divider. The modulation superimposed on the high-voltage pulse was a 5 kHz

squire wave. In the case, V_1=29.0 kV, and V_2/V_1=8.28$\times 10^{-1}$, so $\Delta\omega_c/\omega_c$=9.80 $\times 10^{-3}$. The lower trace shows the gyrotron output pulse. Modulation of the energy of electron results in the modulation of gyrotron output. The drastic variation of output power observed in the figure occurs, because a beam efficiency changes when cavity mode is switched. In the case, both powers are several hundred watts. It is possible to get nearly equal powers for both modes by controlling injection point of electron beam in a cavity.

Frequency modulation is confirmed by sampling the output first when the voltage is V_1 and again when it is V_2 and measuring the frequencies by a Fabry-Perot interferometer. The measured frequencies are f_1= 257GHz and f_2=260 GHz.

Similar frequency step switching is possible between a fundamental and a second harmonic, when the frequency of the latter is nearly equal to twice the frequency of the formar. The submillimeter wave gyrotron is used as a radiation source for plasma scattering measurement and ESR experiment in our laboratory. The advantages of frequency step switching, as well as amplitude modulation, will be useful in those applications.

3. Application of Gyrotron FU series

3.1 Application to plasma scattering measurement[10]

Aa shown in Table 1, Gyrotron FU II is being used for plasma scattering measurement of Compact Helical System (CHS) in National Institute for Fusion Science (NIFS) as a radiation source. The gyrotron is well suited source for plasma scattering measurement, because of its capacity for high powers at submillimeter wavelength range. Gyrotron FU II delivers long pulses (pulse width is changed up to 0.6 s) of moderately high power ($\sim$110 W) at submillimeter wavelengths ($f\sim$354 GHz, λ=0.847 mm). Its application enables us to improve the S/N ratio of the measurement and to observe density fluctuation with a low level.

Fig. 16 shows installation of scattering measurement system on CHS. The gyrotron output is transmitted by conventional over-sized

circular waveguids and converted to two-dimensionally focused, linearly polarized, quasi Gaussian beam, before it is injected into plasma. Scattered wave from plasma is received by horn antennae installed in plasma vessel and is converted into low frequency signal by homodyne detection system.

The scattering measurements with scattering angles of 4.4^0 and 8.8^0 are carried out in NBI heated plasma and ICRF heated plasmas. Fig. 17 shows a typical result of scattering measurement with the angle of 8.8^0 for NBI heated plasma. The trace shows one frequency spectrum of scattered signal after another. Each spectrum covers the frequency region from 0 to 1 MHz and was obtained in 20 msec. The plasma is initiated by microwave pulse for electron cyclotron

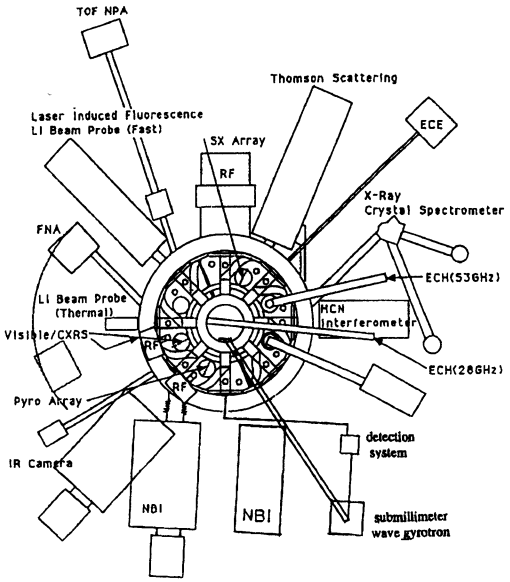

Fig. 16 Schematical drawing of installation of scattering measurement system using a submillimeter wave gyrotron, Gyrotron FU II on CHS.

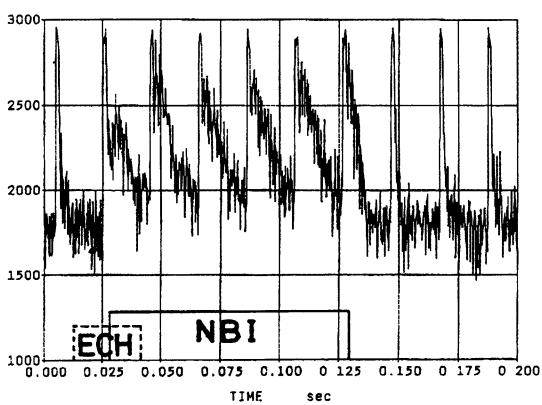

Fig. 17 Time evolution of frequency spectrum of scattered signal. Time intervals of ECH and NBI pulses are indicated.

heating (ECH) and heated by neutral beam injection (NBI) pulse. It is seen the broadening of the spectrum occurs during NBI heating. After NBI pulse, the broadening cannot be observed. It is found up to 600 kHz and is possibly due to scattering by drift waves excited spontaneously by NBI heating.

Fig. 18 shows (a) scattering measurement result for ICRF heated plasma, together with (b) the corresponding reflection measurement using a reflectmeter. The plasma is fired at the time of 10 msec by ECH pulse and ICRF heating pulse is applied in the time interval from 40 to 90 msec. Each curve shows time evolution of scattered wave power for respective frequency interval. The scattering angle of 8.8^0 corresponds to wavenumber of 11.4 cm^{-1}. The increase in scattered wave power is followed by the ICRF heating. The results of reflection measurement is reasonable with that of scattering measurement, which supports the availability of both measurements.

Observed scattered signals suggest that some instability concerning with the drift wave occurs during NBI or ICRF heating. This phenomenon will be dangerous for a well plasma confinement. We will continue the measurement under

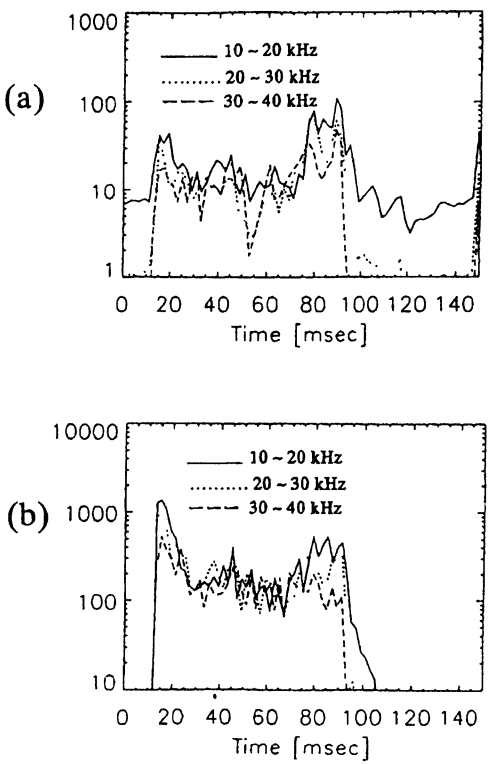

Fig. 18 (a) Time evolution of scattered wave power for respective frequency interval. (b) Time evolution of reflected wave power for respective frequency interval.

various plasma parameters, to study the effect of this instability on plasma confinement.

(b) Application to ESR experiment [12]

Gyrotrons FU I, FU E and FU IV are being used for ESR spectroscopy as radiation sources. The gyrotrons have important advantages as millimeter to submillimeter wave sources, which other conventional sources never possess, for example, frequency tunability in wide range and moderately high output power. Because of such advantages, our gyrotrons are useful for ESR spectroscopy in the millimeter to submillimeter wavelength range to study nonlinear phenomena of ESR.

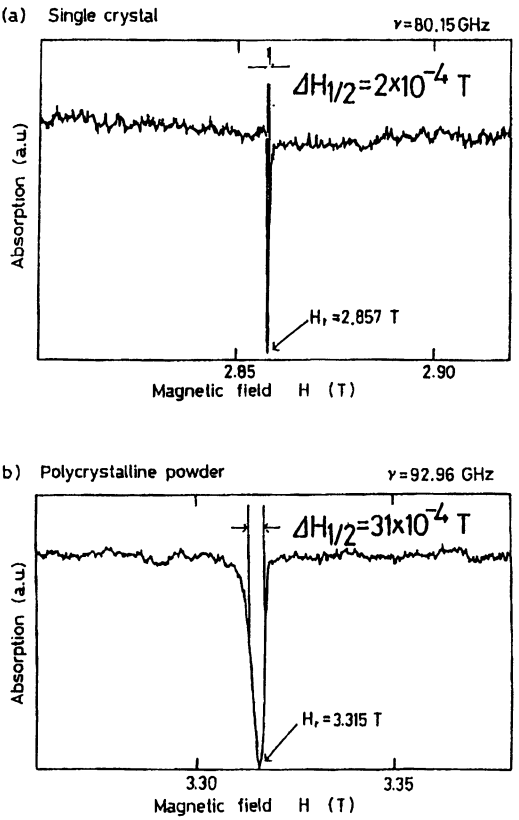

Fig. 19 ESR resonant absorption patterns for standard samples DPPH. (a) for a single crystal sample and (b) for polycrystalline powder sample.

We have constructed an ESR spectometer using Gyrotron FU I as a radiation source. The output power of the gyrotron is transmitted by oversized circular waveguide and drives the specrometer. The main part of the spectrometer consists of W-band waveguide system. The superconducting magnet generates high magnetic field up to 8.5 T at the sample holder. A transmitted power is detected by a crystal detector. The spectrometer covers a wide frequency range in

millimeter wave region, because Gyrotron FU I is a frequency tunable source.

Fig. 19 shows typical patterns demonstrating ESR resonant absorption for a standard sample DPPH. For (a) single crystal sample, a sharp resonance is observed. The half value width ΔH is equal to $2 \cdot 10^{-4}$ T. The value is comparable with the theoretical prediction. On the other hand, for polycrystalline powder sample, the resonance is broadened, because of an anisotropy of g-value.

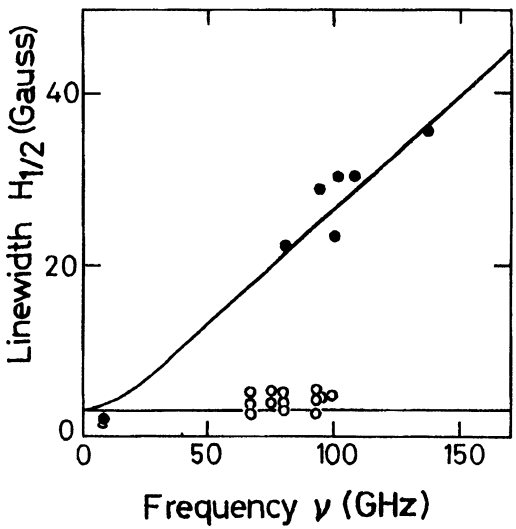

Fig. 20 The observed half value widths of the resonant absorption lines as functions of the frequency ν. Solid lines show theoretical predictions taking an anisotropy of g-values into account. ○ and ● correspond to the cases of single crystal sample and polycrystalline powder sample, respectively.

Fig. 20 shows observed half value widths of the resonance lines as functions of frequency ν. Solid circles are the results for single crystal sample and hollow circles for polycrystalline powder sample. Solid lines show theoretical predictions taking an anisotropy of g-values into account and are good agreement with experimental results.

The study of ESR using Gyrotron FU IV is under way. In near future, we will try the ESR experiment in the wide frequency range in submillimeter wave.

4. Summary

Gyrotron FU series in Fukui University consists of 7 gyrotrons. Each of them is designed to get many single mode operations at the fundamentals, the second harmonics and even at the third harmonics of electron cyclotron resonance. Such a design results in a high frequency, medium power gyrotron covering wide frequency range from millimeter to submillimeter wavelength. The results which Gyrotron FU series has achieved are as follows,

(1) These gyrotrons have achieved frequency tunability from 38 GHz to 850 GHz.

(2) The output powers are moderately high, that is, from several hundred watt to several ten kilowatt at the fundamental operations and from several ten watt to several kilowatt at the second harmonic operations.

(3) Higher harmonic operations up to fourth are demonstrated. This is necessary for development of high frequency gyrotrons covering the whole submillimeter wavelength range.

(4) Mode competition and cooperation between the fundamental and the second harmonic are studied in detail. The former is not convenient for our high frequency, harmonic gyrotron.

(5) Amplitude modulation and frequency step switching of gyrotron output have been achieved for its application to wider field.

Gyrotron FU II has been already applied for plasma scattering measurement of CHS in NIFS, and Gyrotron FU I, FU E and FU IV for ESR experiment to study nonlinear phenomena of ESR.

At the present, the newest gyrotron Gyrotron FU IVA has just operated. The gyrotron will achieve a breakthrough of 1 THz, in near future.

Acknowledgment

The study was carried out under collaborations with University of Sydney in Australia, Forschungszentrum Karlsruhe and University of Stuttgart in Germany. It was supported by Grant in Aids (Scientific Research Program A, Developmental Scientific Research Programs and Monbusho International Scientific Research Programs) from Ministry of Education, Science, Sports and Culture

in Japan and International Joint Research Project and Bilateral Exchange Program from Japan Society for Promotion of Science.

References

[1] B.Pioscyk, O.Braz, G.Dammertz, C.T.Iatrou, S.Kem, M.Kuntze, A.Moebius, M.Thumm, V.A.Flyagin, V.I.Khishnyak, A.N.Kufttin, V.I.Malygin, A.B.Pavelyev, and V.E.Zapelov, *Proc. of 21st Int. Conf. on Infrared and Millimeter Waves*, Berlin, Germany, edited by M. von Ortenberg and H.U.Mueller (Humboldt University zu Berlin) AM2.

[2] K.Sakamoto, A.Kasugai, M.Tsuneoka, K.Takahashi, T.Imai, T.Kariya, Y.Okazaki, K.Hayashi, Y.Mitsunaka and Y.Hirata, ibid. AT1.

[3] V.E.Mjasnikov, M.V.Agapova, V.V.Alikaev, A.S.Borshchegovsky, G.G.Denisov, V.A.Flyagin, A.Sh.Fix, V.I.Ilyin, A.P.Keyer, V.A.Khmara, A.N.Kostyna, V.O.Nichiporenko, L.G.Popov and V.E.Zapevalov, ibid. ATh1.

[4] K.Felch, P.Borchard, C.Cahalan, T.S.Chu, H.Jory, C.M.Loring, C.P.Moeller, ibid. AM16.

[5] T.Kimura, J.P.Hogge, R.Advani, D.Denison, K.E.Kreischer and R.J.Temkin, ibid. AM1.

[6] Antakov, I.G.Gachev, V.I.Kurbatov, E.BV.Sokolov, E.A.Solujanova and E.V.Zasypkin, ibid. AM3.

[7] H.Asano, T.Kikunaga, K.Memmi, F.Sato and T.Tsukamoto, ibid. AM5.

[8] T.Idehara, T.Tatsukawa, I.Ogawa, Y.Shimizu, K.Kurahashi, N.Nishida and K.Yoshida, ibid. AT9.

[9] K.D.Hong, G.F.Brand and T.Idehara, J. Appl. Phys., 74, 5250 (1993).

[10] I.Ogawa, K.Yoshisue, H.Ibe, T.Idehara, K.Kawahata, Rev. Sci. Instrum., **65**, 1788 (1994).

[11] P.W.Fekete, G.F.Brand and T.Idehara, Plasma Phys. and Controoled Fusion, **36**, 1407 (1994).

[12] T.Tatsukawa, T.Maeda, H.Sasai, T.Idehara, M.Mekata, T.Saito and T.Kanemaki, Int. J. Infrared and Millimeter Waves, **16**, 293

(1995).
[13] T.Idehara, Y.Shimizu, K.Ichikawa, S.Makino, K.Shibutani, T.Tatsukawa, I.Ogawa, Y.Okazaki and T.Okamoto, Phys. Plasmas, **2**, 3246 (1995).
[14] Y.Shimizu, S.Makino, K.Ichikawa, T.Kanemaki, I.Ogawa, T.Tatsukawa, T.Idehara, Phys. Plasmas, **2**, 2110 (1995).
[15] T.Idehara, T.Tatsukawa, I.Ogawa, H.Tanabe, T.Mori, S.Wada, G.F.Brand, M.H.Brennan, Phys. Fluids B, **4**, 267 (1992).
[16] T.Idehara, T.Tatsukawa, H.Tanabe, S.Matsumoto, K.Kunieda, K.Hemmi and T.Kanemaki, Phys. Fluids B, **3**, 1766 (1991).
[17] T.Idehara, T.Tatsukawa, I.Ogawa, S.Wada, K.Yoshisue and F.Inoue, Phys. Fluids B, **4**, 769 (1992).
[18] T.Idehara, T.Tatsukawa, I.Ogawa, Y.Yamagishi and T.Kanemaki, Appl. Phys. Lett., **62**, 832 (1993).
[19] T.Idehara, T.Tatsukawa, I.Ogawa, T.Mori, H.Tanabe, S.Wada, G.F.Brand and M.H.Brennan, Appl. Phys. Lett. **58**, 1594 (1991).
[20] T.Idehara and Y.Shimizu, Phys. Plasmas, **1**, 3145. (1994).
[21] T.Idehara, Y.Shimizu, S.Makino, K.Ichikawa, T.Tatsukawa, I.Ogawa, G.F.Brand, Phys. Plasmas, **1**, 461 (1994).
[22] T.Idehara, Y.Shimizu, S.Makino, K.Ichikawa, T.Tatsukawa, I.Ogawa, G.F.Brand, Phys. Plasmas, **1**, 1774 (1994).

DESIGN CRITERIA FOR STEP TUNABLE LONG-PULSE GYROTRONS

G. Dammertz, O. Braz[1], M. Kuntze, B. Piosczyk, M. Thumm[1]

Forschungszentrum Karlsruhe, ITP, Association EURATOM-FZK,
P.O. Box 3640, D-76021 Karlsruhe, Germany
[1]and Univ. Karlsruhe, Inst. für Höchstfrequenztechnik und Elektronik,
Kaiserstr. 12, D-76128 Karlsruhe, Germany

The necessity of step-tunable gyrotrons for fusion reactors requires the excitation of different modes at different frequencies. For a $TE_{m,n}$ gyrotron the $TE_{m\pm3,n\pm1}$ mode can be excited at very high output powers by the variation of the magnetic field as these modes have approximately the same caustic radius and thus also the same coupling between the electron beam and the rf-field. Due to the same caustic radius the gyrotrons can be operated with the same quasi-optical mode converter. For long pulse operation at high output powers an efficient cooling of the resonator is very important. An optimisation for the wall thickness depending on the heat-transfer coefficient between copper and water has to be performed. In general, the heat-transfer coefficient is not known, and also difficult to estimate. From the frequency dependence caused by thermal expansion of the cavity during long pulse operation the heat-transfer coefficient and the Ohmic loss density can be derived.

1. Introduction

A main goal of the gyrotron development program at the Research Centre Karlsruhe (FZK) is the design, construction and test of high-power gyrotron oscillators for electron cyclotron wave applications in fusion plasmas.
At FZK gyrotrons with an output power exceeding 1MW and a frequency of up to 170 GHz are under development. In particular a conventional gyrotron with a hollow waveguide cavity operating in the $TE_{22,6}$-mode with a design output power of 1 MW was tested at short pulses. The possibility of stepwise frequency tuning in a frequency range between 115 and 165 GHz was verified.
The frequency behaviour of a gyrotron during long pulses was investigated in a $TE_{10,4}$ gyrotron. With a simple theoretical model the temperature distribution and the expansion of the cavity was calculated. Comparing the experimentally observed frequency change during a pulse with the theoretical one, it is possible to estimate the peak Ohmic loss density and the heat-transfer coefficient between the cavity and the cooling liquid.

2. Stepwise Frequency Tunability

The possibility of slow stepwise-frequency tuning was demonstrated with our $TE_{22\,6}$ gyrotron. This gyrotron was designed for an output power of 1 MW at a cathode voltage of 80 kV and a beam current of 40 A. The gyrotron is built up from a diode type magnetron injection gun with a LaB_6 emitter. The beam tunnel is made of alternating copper and rf-absorbing ceramic discs [1].

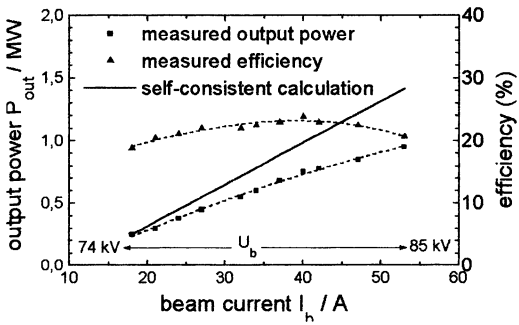

Figure 1: Dependence of output power and efficiency on beam current

During the measurements two different quasi-optical mode converters had been used, either a simple non-improved one without any internal perturbations at the launcher, or a second one with an improved launcher containing mirrors in the waveguide [2,3].

The window was either a single disc boron nitride or a quartz window.

The results of our experiment with the non-improved launcher and the boron nitride window are shown in Figure 1. The highest output power was measured to P_{out}=0.94 MW at a cathode voltage U_b= 85 kV and a beam current I_b=53 A. The highest efficiency (without depressed collector) of η=24% was obtained at 80 kV and 42 A. The difference to the theoretical output powers and efficiencies are assumed to be at least partly caused by the diffraction losses. A total power loss of about 30% was estimated.

To avoid the diffraction losses and to achieve the design value of 1 MW an improved launcher had been installed, but the highest output power was only 600 kW. Spurious oscillations with a frequency of 40 MHz in the beam tunnel could be observed. However, this does not seem to be the reason for the reduced power, as a further experiment with the non-improved launcher again yielded an output power of about 900 kW, though spurious oscillations were present.

We assume that the interaction of the electron beam with the rf-field inside the cavity is changed by reflections at the launcher. Due to the large perturbations inside the launcher competing modes with the wrong direction of rotation might be reflected and change the interaction.

Table 1: Experimental results for different modes

f (GHz)	mode	r^2	α	power (kW)
117.9	19.5	.41	1.2*	750
136.1	21.6	.31	1.53	810
140.1	22.6		1.4	780
144.2	23.6	.25	1.3	770
147.6	24.6	.41	1.2	910
151.2	25.6	.33	1.15	760
162.3	25.7	.38	1.02	970

The possibility of slow frequency step tuning by variation of the magnetic field

is shown in Table 1. The tube was operated at a cathode voltage U_b=80 kV and a beam current I_b=40 A. The frequencies, the power reflection coefficients r^2 at the output window, the velocity ratios α, and the corrected output powers for the different modes are given. The output powers are corrected here according to $P_{corr}=P_{meas}\ (1+r^2)$, as the reflections vary by more than 40 % over the frequency range. The magnetic field distribution and hence the compression ratio was kept constant during these measurements except for the $TE_{19\,5}$ mode. As the velocity ratio increases with decreasing frequency, for the $TE_{19\,5}$ mode the velocity ratio was too high for stable operation because of reflected electrons. The value of 1.2 was achieved by a change of the cathode magnetic field or better to say by a change of the compression ratio.

As the α-value changes with the magnetic field, for a step-tunable gyrotron it would be desirable to have a triode gun. The α-value could be adjusted at a constant compression ratio by changing the voltage of the modulation anode.

In a cw-tube built for frequency tuning, a window without reflections for the desired modes has to be installed. This is possible with a window matched to the desired frequencies. But this choice restricts the frequencies strongly. A better solution is given by a window installed in the beam line under the Brewster angle. This allows to get out all modes without any reflections.

3. Long-pulse operation of the $TE_{10,4}$ gyrotron

The $TE_{10,4}$ gyrotron was designed for an output power of 500 kW at U_b=80 kV and I_b=25 A. A triode gun with a M-type impregnated tungsten emitter was used. For a modulation voltage of 23 kV the velocity ratio α was calculated to be 1.1 [4]. The peak Ohmic loss density at the inner surface of the cavity was calculated to 5.9 kW/cm² at the design output power. However, during the experimental period the geometry of the cavity had changed (Figure 2). The radius of the cavity at the centre (z=0 mm) was reduced by about 15 µm, at the end (z=±7.5 mm) no change had occurred. For the new geometry, the Q-value was decreased and the Ohmic loss density was calculated to be about 3.6 kW/cm².

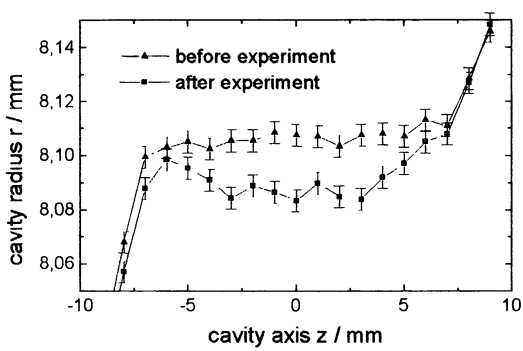

Figure 2: Geometry of cavity before and after long-pulse experimental period

The heating of the cavity due to the Ohmic losses influences the expansion of the cavity. The temperature in the cavity wall is described by the differential equation

$$\frac{d^2T}{dr^2}+\frac{1}{r}\frac{dt}{dr}+\frac{d^2T}{dz^2}=\frac{\rho c_p}{\lambda}\frac{dT}{dt} \qquad (1)$$

with the specific density ρ, the heat capacitance c_p and the heat conductivity λ. These values are dependent on the temperature, thus the differential equation can only be solved numerically. For T<500°C, the ratio $\rho c_p/\lambda$ is constant within 10 %, and even for temperatures up to 1000°C the error is less than 20%. So for an approximate solution this differential equation can be solved by treating the ratio $\rho c_p/\lambda$ to be constant. The integration constants are determined by the boundary conditions.

Introducing a thermoelastic displacement potential Φ the differential equation

$$\frac{d^2\Phi}{dr^2}+\frac{1}{r}\frac{d\Phi}{dr}+\frac{d^2\Phi}{dz^2}-\alpha\frac{1+\nu}{1-\nu}T=s(t) \qquad (2)$$

can be derived for the expansion of the cavity [5], with an integration constant s(t), the thermal expansion coefficient α and the Poisson number ν. The expansion is obtained from the thermoelastic displacement potential by

$$\Delta z=\frac{d\Phi}{dz} \quad \text{and} \quad \Delta r=\frac{d\Phi}{dr}.$$

The calculations were performed for a cylindrical structure which extends along the axis from -L to L. The Ohmic loss density is taken as Gaussian, with a power drop to 10% at the end of the cavity thought to extend from $-l_c$ to l_c. The ratio between cylindrical tube and cavity length usually was chosen to be 10.

The radial heat flow at the inner surface is given by the distribution of the Ohmic loss density; at the outer surface the heat flow out of the copper equals the heat flow into the water. For mathematical reasons the arrangement is taken to be periodic with a periodicity of 2L. This means that either the thickness d of the tube is small compared to the tube length 2L, or the axial heat flow at the end of the tube is zero, for example in case of poor heat conductivity.

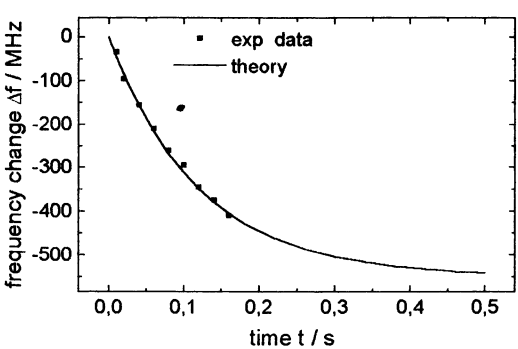

Figure 2: Frequency change during a pulse

For the expansion we further assume, that the tube can move freely into all directions. In radial direction this is always true. The expansion into axial direction also can be taken as free, as $\Delta L/L$ is small even if the cavity expands.

Figure 2 shows a comparison of the measured frequency change with the approximate theory. The points present the

frequency taken from a continuous measurement [6]. The space charge neutralisation time in this experiment is only 30 ms, so the influence can be neglected. From the frequency dependence it is possible to obtain two very important parameters: the Ohmic loss density and the heat-transfer coefficient α_t. The latter one can be calculated from the time constant, and the Ohmic loss density is determined by the total frequency shift. The frequency change of the experiment could best be fitted with P_Ω= 3.7 kW/cm² and α_t=8.5 W/cm²/K.

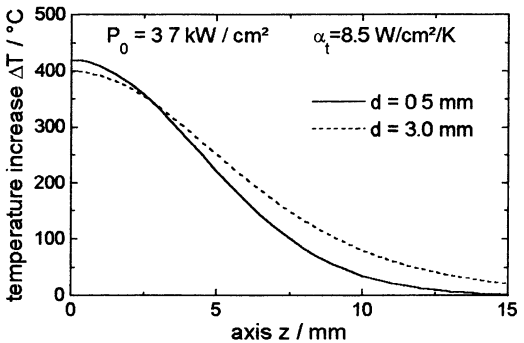

Figure 3: Temperature distribution on the inner surface along axis

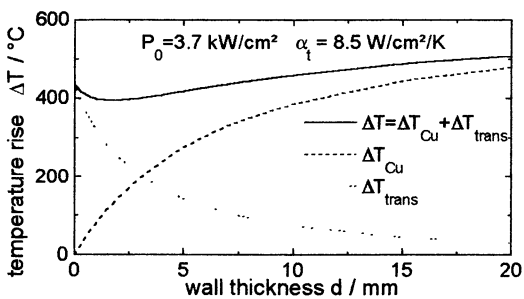

Figure 4: Transition temperature and temperature difference between inner and outer surface

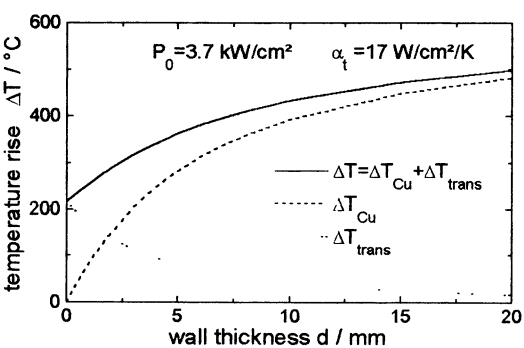

Figure 5: Transition temperature and temperature difference between inner and outer surface

Figure 3 shows the temperature increase of the stationary solution on the inner surface along the axis for two different thicknesses. Far away from the centre of the cavity the temperature increases with increasing wall thickness, but in the centre this behaviour is reversed. The temperature on the inner surface is higher for thinner walls.

The reason for this effect is seen in the axial heat flow. The temperature at the inner surface adds from two terms: the temperature difference ΔT_{Cu} between inner and outer surface of the cavity and the transition temperature ΔT_{trans} between the outer copper surface and cooling water. Due to the inhomogeneous power distribution along the axis an axial heat flow takes

place, and this reduces the radial heat flow into the water. With increasing wall thickness the transition temperature decreases, whereas the difference between inner and outer surface increases (Figure 4-5). The transition temperature depends on the heat-transfer coefficient. For α_t=8.5 W/cm²/K the decrease in transition temperature is higher than the increase of the temperature difference, for α_t=17 W/cm²/K the effect is reversed (Figure 5).

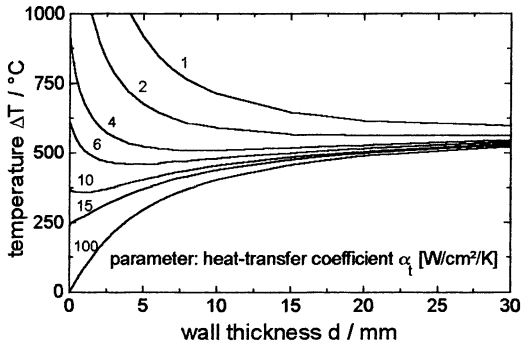

Figure 6: Dependence of temperature on wall thickness

The temperatures of the inner surface at the centre of the cavity are shown in Figure 6 for different heat-transfer coefficients. For small values one finds an optimum wall thickness with smallest temperature increase, whereas for heat-transfer coefficients exceeding 10-15 W/cm²/K the temperature increases with increasing wall thickness.

To explain the frequency shift from the temperature distribution, the expansion of the cavity has to be calculated. For free expansion into all directions the expansion along the axis is given in Figure 7 for two different wall thicknesses. For thin walls the deformation is much higher than for thick walls, though the temperature on the inner surface in these two cases was about the same. The reduced value for thicker walls is caused by the rigidity of the wall material. The neighbouring parts inhibit the cavity to expand as they are at lower temperature than at the centre. Another important point is that the difference of deformation between the centre of the cavity (z=0 mm) and the end of the cavity (z=7.5 mm) is reduced for thicker cavity walls. For d=3mm the difference is only 4 µm, whereas for d=0.5 mm the difference is about 20 µm. So the change in Q-value and in Ohmic loss density is reduced for thick cavity walls. Also from this point of view an optimisation procedure concerning the wall thickness should be considered.

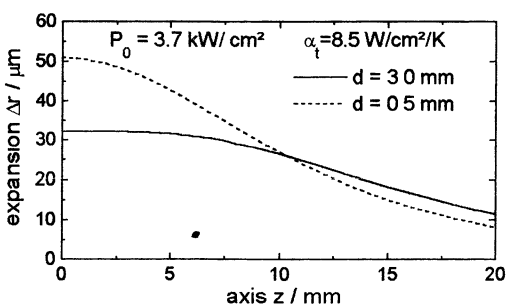

Figure 7: Expansion of cavity along axis

4. Conclusions

Wide frequency step tuning of gyrotrons is possible but one needs a broadband window preferable a Brewster window. A triode gun is preferable for a free choice of the α-value.

To reduce the deformation of the cavity during long pulses, a thick wall of the cavity is preferable. For low heat-transfer coefficients this agrees with the optimisation concerning low temperature increase.

References:

[1] M. Thumm, O. Braz, G. Dammertz, C. T. Iatrou, M. Kuntze, B. Piosczyk and G. Soudée, "Operation of an Advanced, Step-Tunable 1 MW Gyrotron at Frequencies between 118 and 162 GHz", 20th Inter. Conf. on Infrared and Millimeter Waves, Orlando, Florida, pp. 199-200, 1995

[2] A. Möbius and J. Pretterebner, "Avoidance of edge diffraction effects of WGM-fed quasi-optical antennas by feed-waveguide deformation", 16th Inter. Conf. on Infrared and Millimeter Waves, Lausanne, Switzerland, pp. 531-532, 1991

[3] M. Thumm, E. Borie, G. Dammertz, G. Gantenbein, M.Kuntze, A. Möbius. H.-U. Nickel, B. Piosczyk and A. Wien, "Development of high-power 140 GHz gyrotrons for fusion plasmas applications", 2nd Inter. Workshop on High Power Microwaves in Plasmas, Moskau-Nizhny Novgorod, Russia, Vol.2, pp.670-689, 1993

[4] G. Dammertz, O. Braz, C.T. Iatrou, M. Kuntze, A. Möbius, B.Piosczyk and M.Thumm, " Highly efficient long-pulse operation of an advanced 140 GHz 0.5 MW gyrotron oscillator", 20th Inter. Conf. on Infrared and Millimeter Waves, Orlando, Florida, 285-286, 1995

[5] S.P.Timoshenko and J.N.Goodier, "Theory of Elasticity", McGraw-Hill Kogakusha Ltd, Tokyo, pp. 476-484

[6] G. Gantenbein, T. Geist and G. Hochschild, „Instantaneous frequency measurements on a gyrotron output signal", 14th Inter. Conf. on Infrared and Millimeter Waves, Würzburg, Germany, pp. 221-222, 1989

COMMISSIONING OF THE 8 GHZ, 1 MW GYROTRONS OF THE FTU LH SYSTEM

F. Mirizzi, S. Di Giovenale, T. Fortunato, C. Gourlan, G. Maffia, S. Podda, M. Roccon, A. A. Tuccillo

Associazione EURATOM-ENEA sulla Fusione,
Centro Ricerche Frascati
C.P. 65 - 00044 Frascati, Rome, Italy

Abstract

The Lower Hybrid (LH) system for FTU is designed to generate a total amount of 9 MW at the nominal frequency of 8 GHz, allowing Heating and Current Drive operations at high plasma density.

Due to the lay-out of the terminal section of the transmission line, it is necessary to control the output power and frequency of the rf source, a 1 MW gyrotron, with a very high accuracy.

After the "pioneering" work made during the commissioning of the two prototypes: the 1 MW Thomson TTE and the 500 kW Varian Ass.es gyrotrons, an intense effort has been done in the commissioning of the series tubes, the Thomson gyrotrons, to fully understand, from the engineering point of view, the behaviour of these tubes and to define an essential, but comprehensive, theory, sufficient to manage the output power and frequency according to the experimental requirements.

Introduction

The Frascati Tokamak Upgrade (FTU) is a machine included in the European Thermonuclear Fusion Program aimed at investigating high density plasmas subject to powerful radiofrequency (RF) fields (Lower Hybrid, Ion Bernstein Waves, Electron Cyclotron Resonance Heating).

The Lower Hybrid system will generate, at full performances, a total amount of 9 MW at the nominal frequency of 8 GHz, in pulsed regime (pulse length = 1 s, duty cycle = 1/600).

The system has a modular configuration; each module is powered by a gyrotron able to produce up to 1 MW for 1 second in the TE_{01} circular mode. The output power is transmitted through an oversized circular waveguide (C-18) over a distance of about 30 meters, converted into TE_{10} rectangular mode and split to feed a 12 x 4 waveguides conventional grill.

Each gyrotron and its associated transmission line, down to the rectangular waveguides, has been extensively tested on dummy loads to

define the influence of the main controllable input parameters (beam voltage V_k, beam current I_k, gun-anode voltage V_{gk}, main focusing coil current I_{fp}) on the output power and frequency.

The experimental results of this work are analysed in the frame of an essential but comprehensive gyrotron theory, enabling the definition of an operations map for each gyrotrons that greatly increases the capability and flexibility of the system in its exploitement during the experimentation.

The LH system for FTU

Each LH module (fig. 1) is based on a conventional 1 MW gyrotron with output mode TE_{51} in circular waveguide. A 90° bend connects the vertical output of the gyrotron to the horizontal transmission line. To reduce the transmission losses the TE_{51} mode is converted to the TE_{01} low losses mode and transmitted through a standard C 18 (Ø = 114.58 mm), oversized circular waveguide.

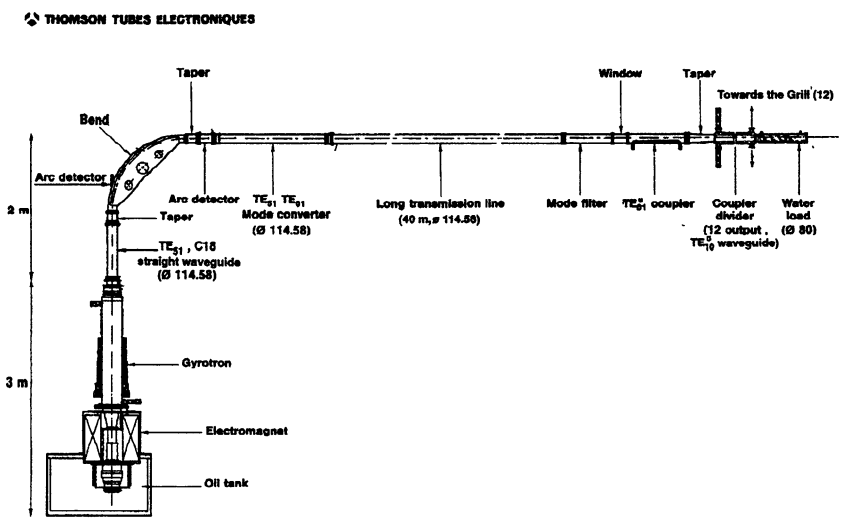

fig. 1 - Lay-out of the 8 Ghz, 1 MW LH module for FTU

The direct and reflected power in this section is detected by selective directional couplers to have a qualitative evidence of the behaviour of the gyrotron.

At the end of the circular section of the line the rf power is split in twelve WR 137 rectangular waveguides and, at the same time, its e.m. mode is converted to the fundamental TE_{10} mode by means of a suitable

coupler/divider.

Twelve phase-shifters control the phase in each output branch of the coupler to assure the correct spectrum at the output of the antenna: a grill of 12 x 4, reduced section (28 x 3.6 mm), rectangular waveguides.

After the phase-shifter a 1:4 power divider permits the right feeding of the four waveguides of each grill column.

The overall transmission losses, from the gyrotron output to the gill mouth, are about 40%, so that the power at the grill mouth is about 600 kW with a power density of $10 \div 12$ kW/cm^2.

A multiwindow, an array of 12 x 4 alumina windows, assembled on a titanium alloy frame, separate the FTU vacuum from the pressurised grill.

A more comprehensive system description is reported in [1] and [2].

Commissioning and experimental evidences

To have the correct $n_{//}$ spectrum at the grill mouth, because of the different path lengths of the twelve transmission lines, in WR 137, connecting the power divider to the grill, it is essential to control the gyrotron output frequency within $\pm$ 4 MHz.

Moreover the high power density at the grill ($\geq$ 10 KW/cm^2) requires to control the gyrotron output power within the range $0.5 \div 1$ MW to optimise the coupling to the plasma in all the operating scenarios.

The above two requirements bring to a foregoing work of characterisation for each tube on dummy loads before its connection to FTU; this work permits to define a multi-dimensional operating space and, within this space, the best operating point of the gyrotron in terms of output power and frequency.

On the basis of the diagrams resulting from this work it is also possible to obtain the variational dependences among the gyrotrons parameters.

The 1 MW Thomson gyrotrons for the FTU LH system present seven independent input parameters:

- cathode voltage (V_k),
- gun anode voltage (V_{gk}),
- main focusing coil current (I_{fp}),
- heater current (I_f),
- gun coil current (I_{cg}),
- cavity gradient coil current (I_{gc}),
- gun gradient coil current (I_{gg}).

According to our operative experience the two output parameters: power and frequency, are mainly influenced by the first four above parameters, while the last three have a secondary influence.

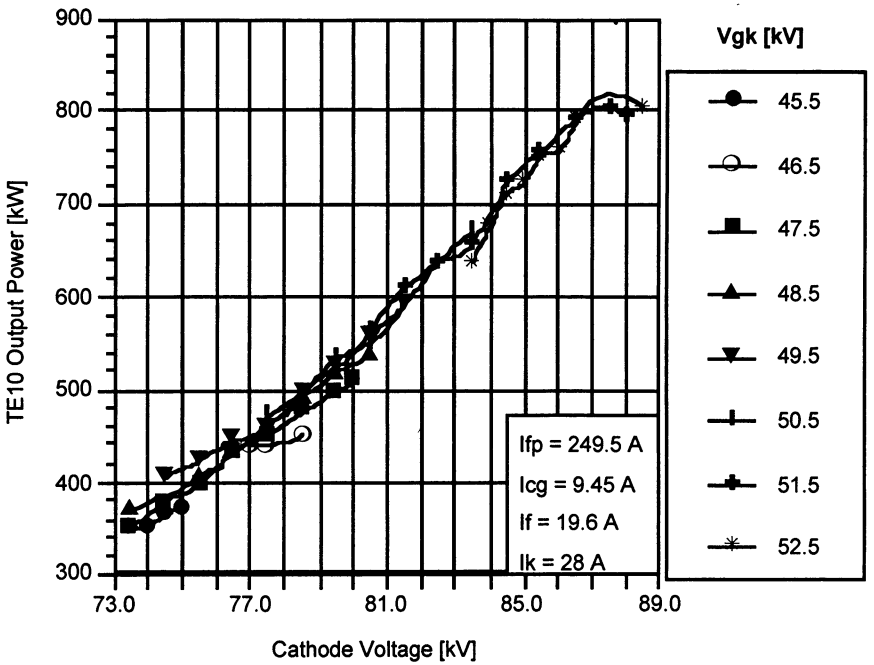

fig. 2 - Gyrotron n. 6: Power vs. Cathode voltage

The chart in fig. 2 reports a set of curves $P_{out} = f(V_k)$ with gun anode voltage as parameter. The power, in the TE_{10} mode, is the sum of the mean output power in the twelve branches of the coupler/divider.

From the diagram it is possible to make the following considerations:

- the output power of the gyrotron may be controlled over a wide range of values of cathode voltage;
- the output power increases with the cathode voltage;
- for a given cathode voltage, the output power is weakly dependent on the gun voltage;
- for a given gun voltage the tube may oscillate only over a limited range of values of cathode voltage;
- the maximum power at the output of the coupler/divider is about 800 kW for $V_k \approx 87$ kV;
- for $V_k \leq 85$ kV a good approximation of the whole set of curves is given by a first order polynomial:

$$P_{out} = 34\left(V_k - 63.6\right); \qquad (1)$$

where V_k is in kV and P_{out} in kW.

- according to this approximation the output power is null at $V_k \approx 64$

kV;
- for $V_k > 87$ kV the output power is in saturation;
- the maximum variation rate of the output power, at $V_k = 85$ kV, is about 42 kW/kV;
- the mean variation rate, according to (1), is 34 kW/kV.

These considerations are analysed in the last part of this paper in the frame of an essential theory.

The output frequency as a function of cathode voltage, for the same points of fig. 2, is displayed in the chart in fig. 3.

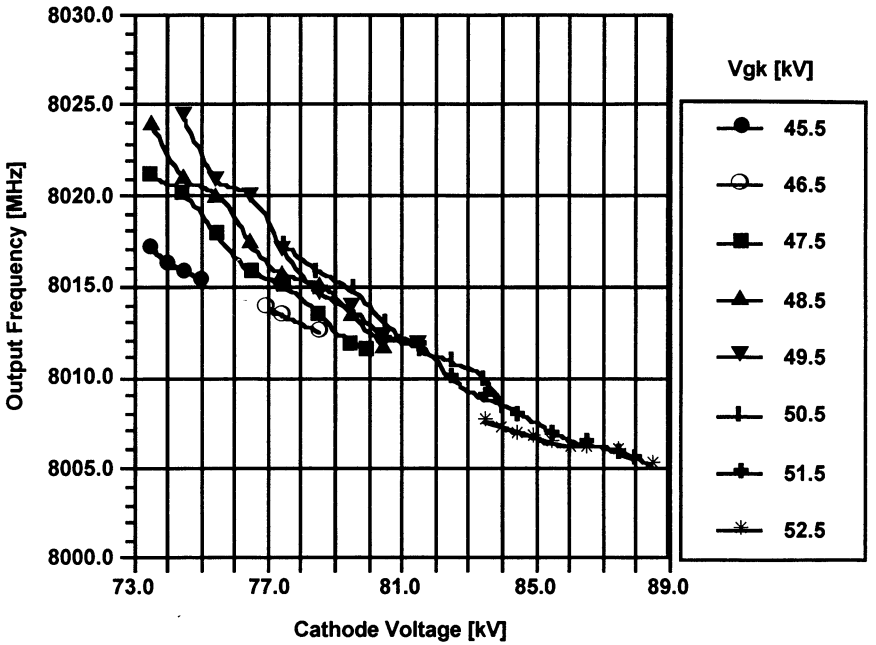

fig. 3 - Gyrotron n. 6: Frequency vs. Cathode Voltage

The following considerations may be done:
- for low values of cathode voltage (≤ 80 kV) the frequency is dependent on the gun voltage;
- for $V_k > 80$ kV this influence is strongly reduced;
- the curves converge to a minimum of 8005 MHz at about 90 kV;
- the maximum relative frequency variation, at $V_k = 73.5$ kV, is about $\pm 0.11\%$;
- in the range of variation of V_k (73 ÷ 89 kV) the relative frequency variation is about 0.24%.

Even if these values are significantly small in absolute, to guarantee the required $n_{//}$ spectrum, it is necessary to change the phase in the twelve WR 137 sections when the output frequency of the gyrotron,

because of an imposed output power variation, varies more than 4 MHz.

In the fig. 4 the parameter is the main focusing coil current I_{fp}.

The diagram is very useful in the definition of the value of I_{fp} that permits to control the output power on the widest range of V_k.

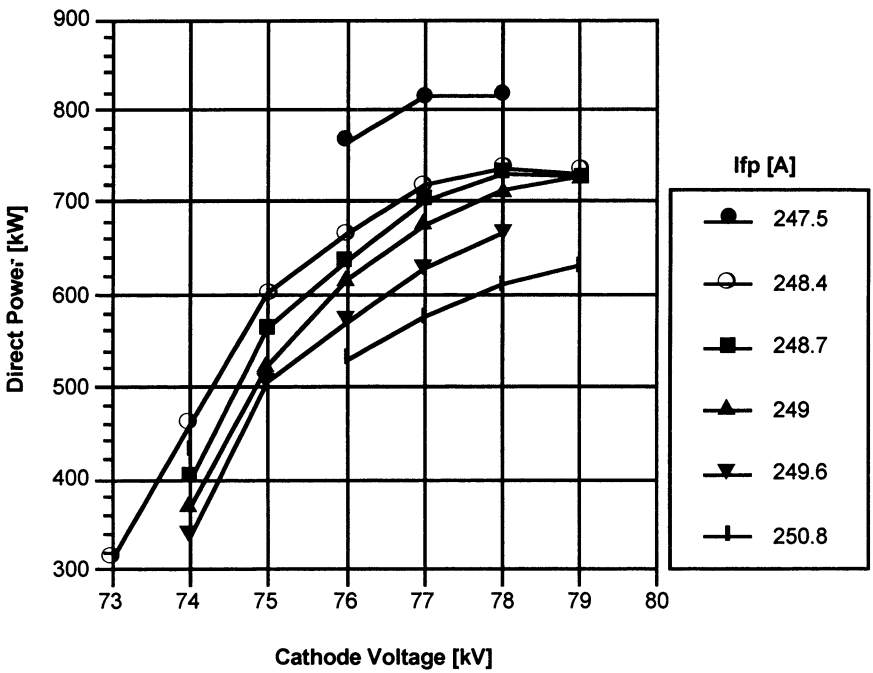

fig. 4 - Power vs. main focusing coil current

For the gyrotron examined in fig. 4 it is possible to use several values of I_{fp} with a good control on the output power over a wide range of V_k; the value of 247.5 A permits to have the maximum output power in absolute, but in a very narrow range of cathode voltage.

The influence of the beam current on the output power is shown in the diagram in fig. 5.

From this diagram it is evident that the cathode current determines limited variation of output power (< 10%) so that it could be used only for small adjustment.

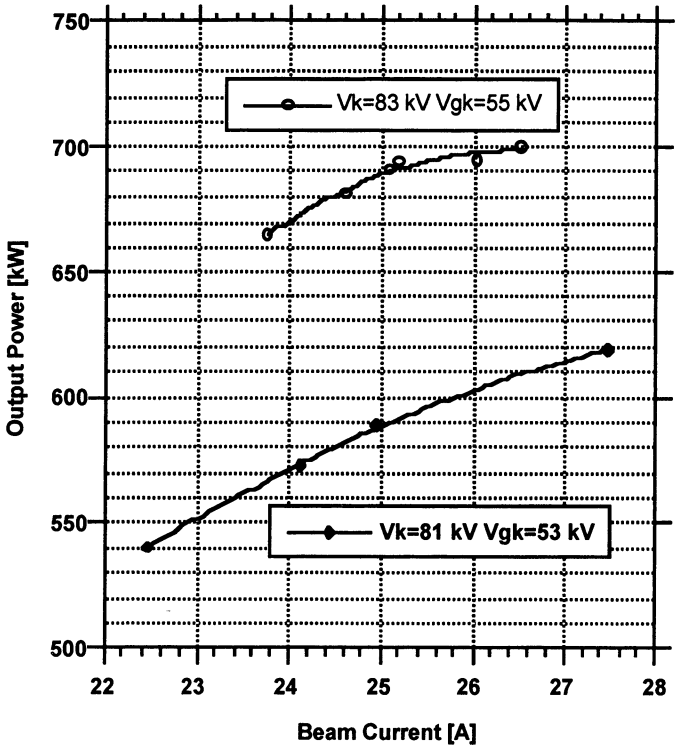

fig. 5 - Power vs. Beam Current

Theoretical considerations

The gyrotron is based on the transfer of energy between weakly relativistic electron beams and high frequency electromagnetic (e.m.) fields.

The electron kinetic energy depends only on the cathode voltage; it has the following expression in eV:

$$W = V_k = (\gamma - 1) W_0 \qquad (2)$$

where W_0 = 511 keV is the electron energy at rest and γ the relativistic correction factor.

The gyrotron cavities are generally designed to work in a Te_{mnp} mode, so that only the transverse energy of the electrons is available to be

transferred to the e.m. field.

The transverse to total kinetic energy ratio is:

$$\frac{W_\perp}{W} \approx \frac{\beta_\perp{}^2}{\beta^2} = \frac{\alpha^2}{1+\alpha^2} \tag{3}$$

where "β" are the electron velocities normalised to the light velocity and

$$\alpha = \frac{\beta_\perp}{\beta_{//}} \tag{4}$$

is the transverse to axial velocity ratio.

The value of α affects the performances of the gyrotron: the FTU gyrotron has been designed to give the best performances at $\alpha = 2$, that is for a 4/5 energy ratio.

The transverse velocity at the input of the cavity is given by the following relation:

$$\beta_\perp = \frac{1}{\gamma} K V_{gk} \sqrt{\frac{B}{B_k{}^3}} \tag{5}$$

where B and B_k are the static magnetic fields respectively in the cavity and in the cathode region; K is a constant dependent only on the dimensions of the cathode and of the gun anode.

The FTU gyrotrons work at a cathode voltage of about 80 kV, therefore its electron beam can be considered weakly relativistic.

According to (2) the total electron velocity is:

$$\beta = \sqrt{2\frac{V_k}{W_0}} \tag{6}$$

so that the energy ratio in (3) becomes:

$$\frac{W_\perp}{W} = K^2 \left(\frac{W_0}{2V_k} - 1 \right) V_{gk}{}^2 \frac{B}{B_k{}^3} \tag{7}$$

This relation evidences the dependence of the energy ratio on the gun and cathode voltage and permits to explain in the fig. 2 the limited range of cathode voltage at $V_{gk} = \text{cost.}$

The electron cyclotron frequency is given by:

$$\Omega_c = \frac{eB}{m} \tag{8}$$

where B is the cavity static magnetic field, and could be expressed in term of electron energy as follow:

$$\Omega_c = \Omega_0 \frac{W_0}{W_T}; \tag{9}$$

in this expression $W_T = mc^2$ is the total electron energy.

In the interaction region, a resonant circular cavity, the electron gives up part of its energy to the e.m. field, hence, according to (9), its cyclotron frequency grows.

If Ω_{ci} and Ω_{cf} are the cyclotron frequencies respectively at the input and at the output of the cavity, the total energy transferred to the high frequency e.m. field in the interaction region is:

$$\Delta W = W_0 \Omega_0 \left(\frac{1}{\Omega_{ci}} - \frac{1}{\Omega_{cf}} \right). \tag{10}$$

In the cavity, and hence at its output, the field parameters and the electron beam parameters are linked by the following relation:

$$\Omega_c = \omega - k_{//} v_{//} \tag{11}$$

where ω, the frequency of the e.m. field, and $k_{//}$, the axial propagation constant, are dependent only on the mechanical characteristics of the cavity, while $v_{//}$ is the axial velocity of the electron.

The energy of the electron would be completely extracted if $\Omega_{cf} = \Omega_0$, that is an ideal upper limit.

Instead the transfer of energy is null when:

$$\Omega_{cf} = \omega - k_{//} v_{//} = \Omega_{ci} \tag{12}$$

According to the above discussion, to have a positive energy transfer from the electrons to the e.m. field, the field frequency must be in the following range:

$$\Omega_{ci} < \omega < \Omega_0 \tag{13}$$

In weakly relativistic conditions the Doppler correction factor $k_{//} v_{//}$ in (12) can be neglected with respect to the field frequency, so that the energy variation is:

$$\Delta W = W_0 \Omega_0 \frac{\omega - \Omega_{ci}}{\omega \Omega_{ci}} \qquad (14)$$

The electron cyclotron frequency at the input of the cavity depends on both the cavity magnetic field B and the cathode voltage:

$$\Omega_{ci} = \frac{\Omega_0}{\gamma} \approx \Omega_0 \left(1 - \frac{V_k}{W_0}\right) \qquad (15)$$

so that:

$$\Delta W = W_0 \left(1 + \frac{V_k}{W_0} - \frac{\Omega_0}{\omega}\right) = V_k - W_0 \frac{\Omega_0 - \omega}{\omega} \qquad (16)$$

The output power has a linear link with the energy variation of the electrons, that is:

$$\begin{aligned} P_{out} &= M \Delta W \cdot N = \\ &= M\left(V_k - W_0 \frac{\Omega_0 - \omega}{\omega}\right) - N = M V_k - N_1 \end{aligned} \qquad (17)$$

This last formulation gives a formal interpretation of the diagram in fig. 2, and hence, in the limits of weakly relativistic conditions, the linear dependence of the output power of a gyrotron on the cathode voltage has a general validity.

Status of the LH system

Currently the first out of the three launching structures, each one made up by three grills mechanically connected and fed by three gyrotrons, is in operation on FTU; the lower grill of the second structure is fed by a fourth gyrotron.

The total RF power now available on FTU is therefore about 2 MW.

A fifth gyrotron has been completely characterised on dummy loads and is now ready to be connected to the middle grill of the same

structure; for a sixth gyrotron the characterisation is started by the end of July 1996.

According to this schedule, by the end of the current year two coupling structure will be operative on FTU.

The seventh 1 MW gyrotron actually available in ENEA has been assembled and is going to replace, after a complete commissioning, the prototype tube in the module 7, that is reaching its "end of life".

Conclusions

The first 4 modules of the 8 GHz, 9 MW, pulsed LH system are working on the FTU. The experimental work is in progress and the results are encouraging.

The preliminary characterisation of the tubes during the commissioning and the comprehension of their behaviour has been very useful during the experimental phase because, on the base of the map of operative points, it has been always possible to set the gyrotron parameters for the best performances according to the characteristics of the plasma.

The experience and the large amount of data accumulated during the commissioning of these tubes have enabled us to fully understand the gyrotrons from the point of view of the users, and to derive an essential gyrotron theory.

The commissioning of further tubes will hopeful permit to refine and to extend this theory.

References

[1] L. Baldi et al.: Proc. of the 23rd EuMC, Madrid (Spain), 1993.

[2] Tuccillo et ali.: Proc. of the 2nd Intern. Workshop Strong Microwaves in Plasmas, Nizhny Novgorod (Russia), 1993

[3] S. Digiovenale et al.: Proc. of the 17th Symposium on Fusion Technology, Rome (Italy), 1992

[4] R. Andreani et al.: Proc. of the17th Symposium on Fusion Technology, Rome (Italy), 1992

[5] P. Garin et al.: Proc. of the17th Symposium on Fusion Technology, Rome (Italy), 1992

[6] L. Alladio et al.: Proc. of the 10th Topical Conference on Radiofrequency Power in Plasmas. - Boston (U.S.A.), 1993

[7] V. A. Flyagin et al.: IEEE Trans. on Microwave Theory and Thecnics, vol MTT 25, n. 6, June 1977.

[8] V. A. Flyagin et al.: Proc. of the IEEE, vol 76, n. 6, June 1988.

[9] G. Mourier: AEÜ Archiv für Elektronik und Übertragungstechnik, band 34, 1980, 473

[10] I. I. Antakov et al.: International Journal of Infrared and Millimeter Waves, vol. 14, n. 5, 1993.
[11] K. E. Kreischer et al.: International Journal of Infrared and Millimeter Waves, vol. 1, n. 2, 1980.
[12] K. E. Kreischer et al.: International Journal of Infrared and Millimeter Waves, vol. 2, n. 2, 1981.

Ka-BAND AND W-BAND 10 KW CW HIGH EFFICIENCY GYROTRONS FOR MATERIALS PROCESSING

I. I. Antakov, I. G. Gachev, V. I. Kurbatov, E. V. Sokolov, E. A. Solujanova and E. V. Zasypkin

GYCOM Co. Ltd, 46 Ulyanov Str., 603600,
Nizhny Novgorod, Russia

Abstract

A new application of powerful microwave radiation is material processing including bonding and coating of ceramics, bonding of plastic and composite materials and so on. For experimental study of action of mm-wave radiation upon dielectric materials, a 30-GHz 10 kW CW second-harmonic gyrotron, and also 37-and 84-GHz 15-20 kW CW gyrotrons operating at the fundamental cyclotron frequency were developed at IAP and GYCOM. This paper presents the design of 35- and 94-GHz CW compact gyrotrons operating at the fundamental and using a relatively low - voltage electron beam. The results of the hot test of the 35-GHz gyrotron are also presented. Output power of 9-10 kW CW with 35-40% efficiency was observed in the TE_{02} mode.

Introduction

Material processing using microwave radiation is being developed actively in the whole world. This technology has been demonstrated successfully for such applications as bonding and coating of ceramics, bonding of plastic insulation and protective coatings to pipe, and bonding of composite [1], [2]. For the experimental study of action of mm-wave radiation upon dielectric materials, gyrotron oscillators at frequencies 30-300 GHz with power outputs from 1 to 30 kW CW are required. Additional requirements to microwave sources are reliability, high efficiency, simplicity, small size and low cost. Recently, a 30-GHz 10 kW CW second-harmonic gyrotron has been developed at IAP [3]. This tube is a key component of the Gyrotron Heating System (GHS) designed specially for high temperature processing of materials with

mm-wave radiation [4]. For experiments on materials processing at IAP and Los Alamos the similar GHS with the 37-and 84 GHz gyrotrons producing 15-20 kW CW with 20-kV, 3-A electron beam is used [4], [5]. These oscillators have an internal mode converter for shaping output radiation as a Gaussian wave-beam. A cryogenic magnet is necessary to operate these tubes.

This paper presents the design and performance characteristics of the 35-GHz compact gyrotron operating at the fundamental, using a relatively low voltage electron beam ($\leq$ 30 kV) and producing power output up to 10 kW CW with 35-40% efficiency. A compact cryogenic magnet for this tube is being designed now.

Gyrotron Design

Several criteria were used in the design of the gyrotron. First, this device should produce 10 kW CW with an efficiency more than 30-35%. Second, beam voltage should not exceed 30 kV. Finally, to use this oscillator as a component of the GHS designed at IAP, the operating mode and output waveguide radius are desired to be the same as those for the IAP's second-harmonic gyrotron [3]. The gyrotron utilizes a triode thermionic magnetron injection gun (MIG) energized by a 30 kV, 1 A dc power supply. MIG produces an annular electron beam, where pitch angle α is controlled by adjusting intermediate anode voltage. Gun simulations using EPOS code predicts transverse velocity spread of 5-8% with a pitch angle of 1.4 when the cathode-anode voltage is equal to 9-12 kV.

35-GHz gyrotron. The diameter of the emitter is 16 mm, its width is 3 mm, and the beam diameter in the circuit is about 5.3 mm. The emitter is being fabricated from LaB_6. The nominal magnetic field in the cirquit 1.3 T is produced by a cold - bore superconducting magnet with magnetic compression ratio of 9.1. The interaction of an electron beam with the RF field occurs in a cylindrical cavity 40 mm long operating in the TE_{021} mode. The optimized cavity shape has been designed using the nonlinear gyrotron theory [6]. Simulation predicts cavity *Q*-factor of about 700. The electron beam is injected into the first radial maximum of the cavity RF field.

94-GHz gyrotron. Emitter diameter is 16 mm as in the 35-GHz tube, beam diameter in the cirquit is 1.9 mm. The dc magnetic field in

the circuit is 3.7 T, magnetic compression ratio is about 18. Electron beam interacts with the RF field of the TE_{421} mode inside a cylindrical cavity 20 mm long. Cavity Q-factor is 1200, it means that expected ohmic losses in the cavity wall will be at the level of 250 W/cm^2 at 10 kW CW output power. After passing through the cavity the beam and the output microwave travel through a 4° output uptaper to a 39-mm diameter circular output waveguide and then through a BN barrier window to the calorimeter. The spent electron beam is collected on the cooled wall of the output waveguide. Design beam loading on a collector wall is 200-300 W/cm^2. A permanent magnet is positioned at the end of the beam dump region to ensure that no electrons can strike the output window.

Results of 35-GHz gyrotron test

Three 35-GHz gyrotrons having the same design were tested.

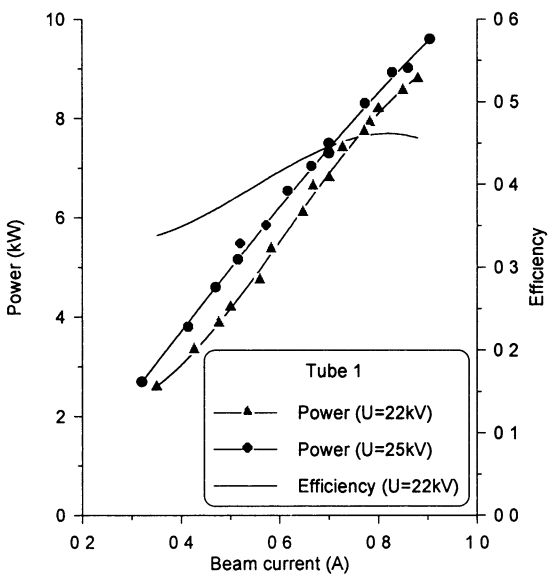

Fig. 1. Output power and efficiency as a function of beam current for tube 1.

The objective of these tests was to demonstrate the stable, efficient and reliable gyrotron operation at the output power level of 10 kW CW. The approach taken in this study was to optimize experimentally the gun and cavity shape in order to attain maximum of the output power and efficiency.

Tube 1 was tested at 0.3-0.9 A beam current and beam voltage up to 25 kV. The main obstacle for its operation at larger beam voltage was a high-voltage breakdown in the cathode-anode gap of the gun arisen due to low vacuum provided by a built-in discharge pump. Figure 1 shows the dependencies of the output power and efficiency on the beam current measured at 22 and 25 kV of the beam voltage. For each point of these curves, the anode voltage and magnetic field in cavity were adjusted to optimize power output. Maximum power of about 9.7 kW with 43% efficiency occured at 0.9-A beam current and 25 kV beam voltage. The peak efficiency of 46% with the power level of 8 kW was attained at 0.8-A and 22 kV.

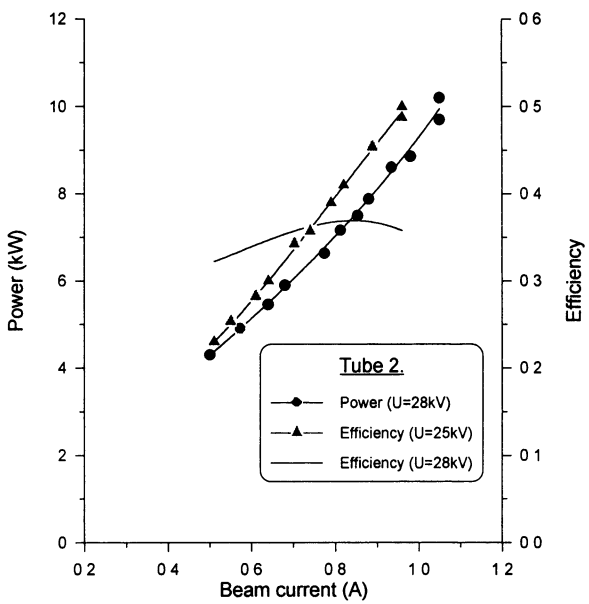

Fig. 2. Output power and efficiency vs. beam current for tube 2.

Further, the vacuum inside next two tubes was improved due to the use of a built-in discharge pump having other design. It made it possible to achive stable gyrotron operation at beam voltage of 28 kV and current up to 1.2 A. Figure 2 indicates the output power as a function of a beam current for 25-and 28 kV beam voltage obtained with tube 2. Maximum output power of 10 kW with an efficiency of about 37% was attained at 1-1.2 A beam current. According to our evaluation, the decrease in peak efficiency was caused by deterioration of the beam quality due to uncontrolled shifting of the cathode in regard to the anode.

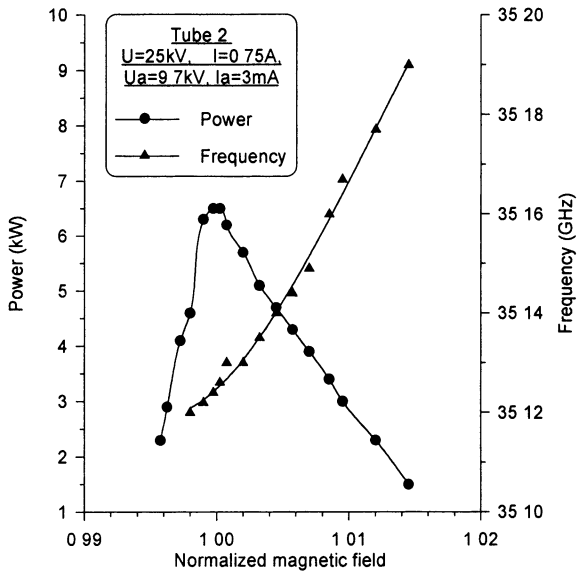

Fig. 3. Output power vs. cavity magnetic field for tube 2.

Figure 3 is the plot of the output power versus cavity magnetic field for tube 2. The measurement was performed with 25-kV, 0.75-A beam. In a peak of the curve all experimental parameters were optimized to achieve maximum output power. Further only the strength of the magnetic field was varied. It was found that the best performance occured when the magnetic field in the output cavity was 1.32 T. The optimal frequency 35.125 GHz was nearly 100 MHz above the cold cavity resonant

frequency. Operating frequency was tuned from 35.12 to 35.18 GHz due to the magnetic field variation.

The dependence of the output power on the anode voltage for tube 2 measured at 0.7 A and 20 kV is shown in Fig. 4. All other parameters were set at the maximum efficiency point. Figure 4 shows a sharp growth of the output power with the anode voltage, with the maximum of 4.5 kW at 9 kV. Output power enlargement is accompanied by the appearance of the anode current growing monotonously from zero to 7 mA. Saturation in the output power at anode voltages over 9 kV may be attributed to the beam instability which usually appeared when pitch angle α exceeds some boundary value. At voltages over 9.2 kV, a high-voltage breakdown in the gun and a burst of microwave radiation occured. It is important to note that unlike in the majority of powerful CW gyrodevices, in our tubes an uncontrolled increase of a beam current has not been observed.

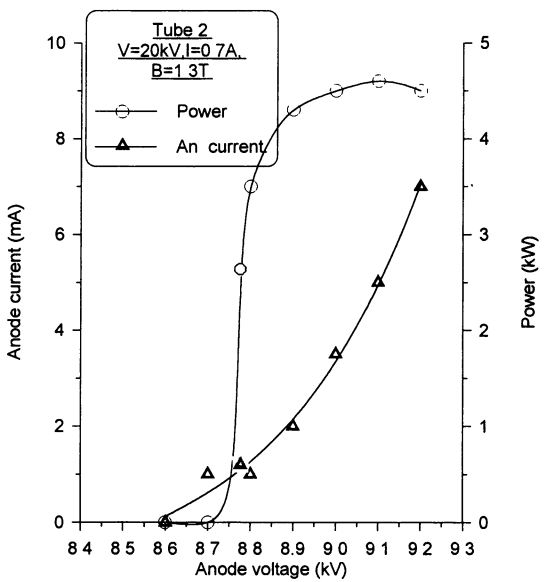

Fig. 4. Dependence of the output power and anode current on anode voltage for tube 2

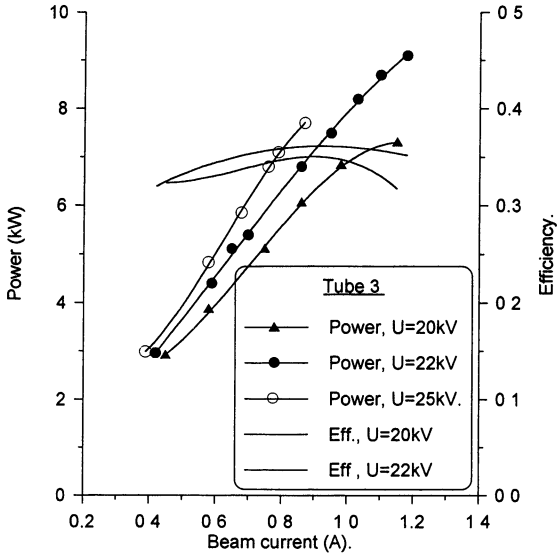

Fig. 5. Output power and efficiency as a function of beam current for tube 3

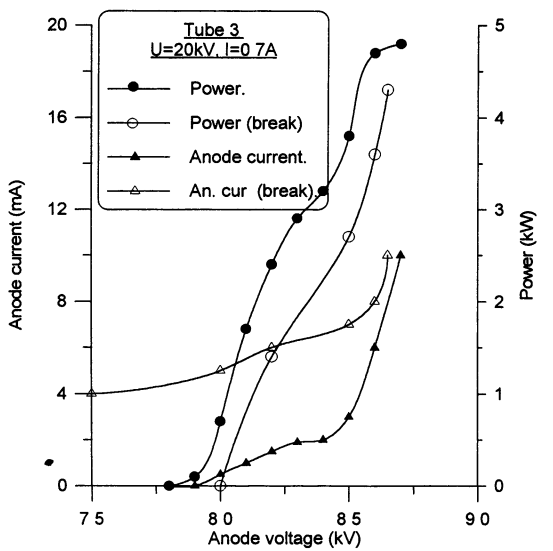

Fig. 6. Output power and anode current vs anode voltage before and after strong breakdown in the gun (tube 3)

In the third tube the cathode-anode gap was smaller in comparison with the both previous tubes. The output power of about 9.1 kW with 35% efficiency has been obtained with a 22-kV, 1.2-A electron beam (see Fig. 5). At 25 kV, the tube could operate only at the beam current less than 0.9 A. At a higher beam current a high-voltage breakdown in the gun occured. Figure 6 shows the output power and anode current as a function of the anode voltage measured at the same beam parameters (20 kV, 0.7 A) as in tube 2. A growth of the output power with anode voltage is smoother than in the previous tube, however the value of saturation power was the same as in tube 2. In Fig. 6, the dependencies of the output power and anode current on anode voltage marked as "break" were measured after a strong breakdown in the gun. To our opinion, the main reason of the efficiency drop and anode current enlargement is spraying of LaB_6 from the emitter surface to the other parts of the cathode. So, from our last experiment it follows that reduction of the cathode-anode gap does not lead to improvement of gyrotron performance while the breakdown problem become more troublesome. Therefore, in the future we plan to use the gun utilized in tubes 1 and 2.

Conclusion

Both 35-and 94-GHz CW efficient compact gyrotrons for materials processing have been designed at GYCOM. Three 35-GHz tubes have been manufactured and tested. Output power of 9-10 kW CW with 35-40% efficiency was observed at 22-25-kV, 1-1.2-A operation in the TE_{02} mode. The output power and efficiency was limited by a high-voltage breakdown in the gun. The phenomenon of uncontrolled increase of a beam current has not been observed in these tubes. It is necessary to note that this oscillator is the first from a set of powerful gyrotrons operating within the frequency range 30-230 GHz. Today 94- and 230-GHz gyrotrons for materials processing applications are being developed.

References

1. V. E. Sklyarevich, and R. F. Decker, "Super high frequency microwave processing of materials - a basis for developing new technologies", Industrial Heating, pp. 54-56, October (1991)

2. W. H. Sutton, "Microwave processing of ceramics - an overview", Material Research Society Symposium Proceedings, 1992, vol. 269, pp. 3-20
3. Flyagin et al, "CW 10 kW technological gyrotron in the range 15-20 GHz, ITG-Fachbericht, Garmisch-Partenkirchen, 132, (1995), pp. 187-191
4. Yu. Bykov et al, "The gyrotron system for ceramics sintering", Microwaves: Theory and Application in Materials Processing III, Ceramic Transactions, Westerwille, Ohio, 1995, vol. 59, pp. 133-140
5. Katz, and D. E. Rees, "Quasi-optical gyrotron materials processing at Los Alamos", Microwaves: Theory and Application in Materials Processing III, Ceramic Transactions, Westerwille, Ohio, 1995, vol. 59, pp. 141-147
6. Gaponov et al, "Powerful millimetre-wave gyrotron", Int.J.Electron., vol.51, pp. 277-302, 1981

MODELING OF WIDEBAND GYRO-AMPLIFIERS

*M. Blank, B. Levush, B.G. Danly, P.E. Latham**

Naval Research Laboratory, Washington, D.C., U.S.A.
*Omega P, Inc., New Haven, CT, U.S.A.

Abstract

The Naval Research Laboratory is currently investigating wideband gyro-amplifiers as high power sources for millimeter wave radars. A theoretical model was developed to analyze the cyclotron maser interaction in the gyrotwystron configuration [1]. Recently, the simple bunching model described in ref. 1 has been improved, and the theory now includes explicit modeling of the buncher cavities. A numerical code, based upon the model, was written and a W-band gryotwystron design is presented as an example. Studies show that careful design of the traveling wave section is necessary to minimize the backward wave interaction over a wide bandwidth.

Introduction

It is well known that devices based on the cyclotron maser instability are capable of efficiently generating high power radiation at millimeter wave frequencies in both amplifier and oscillator configurations. In the amplifier configuration, the gyro-TWT has demonstrated wide band performance at moderate output power levels. For example, a Ka-band two-stage tapered waveguide gyro-TWT achieved 8 kW peak output power at 20% instantaneous bandwidth [2]. Another Ka-band gyro-TWT demonstrated 50 kW peak power at 7.5% bandwidth [3]. However, gyro-TWT operation at higher output powers is made difficult by oscillations that arise as the output power is increased. On the contrary, gyroklystron amplifiers provide high power stable operation at limited bandwidth. A 94 GHz multi-cavity gyroklystron achieved 65 kW with 0.3% bandwidth [4]. Much like its conventional counterpart [5], the gyrotwystron configuration, consisting of one or more buncher cavities followed by a traveling wave output section, represents a compromise between the high power, narrow band gyroklystron and the lower power, wide band gyro-TWT. Theoretical studies [6,7] have shown that the gyrotwystron is capable of high power, wide band operation. A C-band gyrotwystron experimentally demonstrated 80 kW output power at 23% efficiency with a -3 dB bandwidth of 1.6% [8]. Gyrotwystron experiments at the fundamental in X-band and the second harmonic in Ka-band have achieved 22 MW at 22% efficiency and 12 MW at

12% efficiency, respectively [9]. In these experiments, the gyrotwystrons were being studied as potential drivers for next generation linear colliders, so bandwidth was not required and, thus, not optimized.

Gyrotwystron Modeling

A theory was developed to model the cyclotron maser interaction in the gyrotwystron configuration (fig. 1). The model [1] includes both forward and backward wave interactions with the beam in the tapered traveling wave section. A tapered magnetic field and electron beam velocity spread are also included in the formalism. Recently, the simple bunching model described in ref. 1 has been improved, and the theory now includes explicit modeling of the buncher cavities. The drive cavity is represented by a $Q_{external}$ and Q_{loss}, which leads to frequency dependent input power coupling, resulting in a frequency dependent field amplitude in the cavity. The complex field amplitude in the drive cavity, *a,* is given by:

$$|a|^2 = \frac{P_{in}}{P_o}\frac{Q_t^2}{Q_{external}}\frac{1}{W\left|\frac{1}{2}+i\Delta-g\right|^2}, \qquad (1)$$

where P_{in} is the input power in kilowatts; $P_O=m^2c^3/q$=17045.511 kW; $1/Q_t=1/Q_{external}+1/Q_{loss}$; W is the stored energy; g is the complex gain function, and

$$\Delta = Q\frac{\mathrm{Re}\{\omega_c\}-\omega_{drive}}{\omega_{drive}}. \qquad (2)$$

The complex gain function, g, is calculated assuming a Gaussian axial field profile.

As an example, the improved theory was used to design a W-band gyrotwystron amplifier. The interaction between the TE_{01} mode and a 65 kV, 5 A electron beam with α=1.3 was studied. An input power of 1.5 kW was used. The gyrotwystron under study consists of an input cavity, with $Q_{external}=Q_{loss}$=150, a drift region cut-off to the TE_{01} mode in W-band, and a tapered traveling wave output section. The magnetic field was also tapered. Although velocity spread is included in the formalism, an ideal beam was used to simplify the comparison between the frequency independent drive cavity model and the improved model.

Figure 2 shows theoretical power and efficiency as functions of frequency for the W-band gyrotwystron. The squares indicate the

simple model and the circles indicate results from the improved model, which includes a frequency dependent drive cavity field amplitude. The peak efficiency is 22% corresponding to 71 kW output power. The bandwidth of the traveling wave section, calculated with the simple theory, is 6.5%. The improved model shows a realizable bandwidth of 2% for an input cavity with Q_{total}=75.

The model was also used to study the backward wave interaction for various traveling wave circuits. Figure 3 shows the normalized amplitude of the forward and backward waves for a W-band gyrotwystron driven at 94 GHz. For the circuit used in fig. 3, the final radius of the nonlinear transition section (see fig. 1) is 0.195 cm. Figure 4 shows the forward and backward waves for a circuit with a final transition radius of 0.192 cm. All other beam and circuit parameters were held fixed. A comparison of figs. 3 and 4 indicates the sensitivity of the backward wave amplitude to the exact circuit dimensions. In particular, the tapered transition section must be carefully designed to minimize the backward wave interaction.

Next, the effect of drive cavity Q on bandwidth was studied. In all cases, critical coupling ($Q_{external}$=Q_{loss}) was assumed. Figure 5 shows the theoretical predictions for -3 dB instantaneous bandwidth with varying drive cavity Q. In the modeling, all other parameters, including circuit dimensions, beam parameters, and input power, were fixed. Figure 5 confirms the expected result; instantaneous bandwidth is inversely proportional to drive cavity Q.

Summary

A theoretical model was developed to study the gyrotwyston interaction. Based on the model, a numerical code was written and, as an example, a W-band gyrotwystron was designed. A simple theory of bunching, with a frequency independent bunching parameter, was compared with the improved, frequency dependent model. As expected, the more realistic frequency dependent model showed the bandwidth significantly reduced from the simple model, which predicts the bandwidth of the traveling wave section alone. Furthermore, a study of the effect of drive cavity Q on bandwidth produced the expected result, namely that bandwidth is inversely proportional to Q. Perhaps the most important result came from investigation of the backward wave interaction. Studies showed that the amplitude of the backward wave is highly sensitive to dimensions of the traveling wave circuit. As shown in figs. 3 and 4, a 0.003 cm change in the final radius of the tapered transition section resulted in a 3 fold increase in the backward wave amplitude. Thus, the traveling wave section must be designed carefully to reduce the backward wave excitation over a wide bandwidth.

References

[1] P.E. Latham and G.S. Nusinovich, Phys. Plasmas, Vol. 2, No.9, 1995, pp. 3494-3510.
[2] G.S. Park *et al.*, Phys. Rev. Lett., Vol 74, No. 12, 1995, pp.2399-2402,
[3] K.R. Chu *et al.*, IEDM Technical Digest, 1990, pp. 669-702.
[4] I.I. Antakov *et al.*, 18th International Conference on Infrared and Milimeter Waves, Conference Digest, 1993, pp. 466-467,.
[5] A. Staprans, E.W. McCune, and J.A. Ruetz, Proc. IEEE, vol. 61, 1973, pp. 299-327..
[6] M.A. Moiseev, Izvestiya Vysshikh Uchebnykh Zavedenii, Radiofizika, Vol. 20, No. 8, 1977, pp. 1218-1223.
[7] S.I. Viravoy, G.N. Rapoport, Izvestiya Vuzov CCCP, Radioelektronika, Vol. 16, No. 10, 1973, pp. 96-105.
[8] P.M. Malouf *et al.*, IEEE Trans. Electron Devices, Vol. 42, No. 9, pp. 1681-1685, 1995.
[9] W. Lawson *et al.*, IEDM Technical Digest, pp. 247-250,1994.

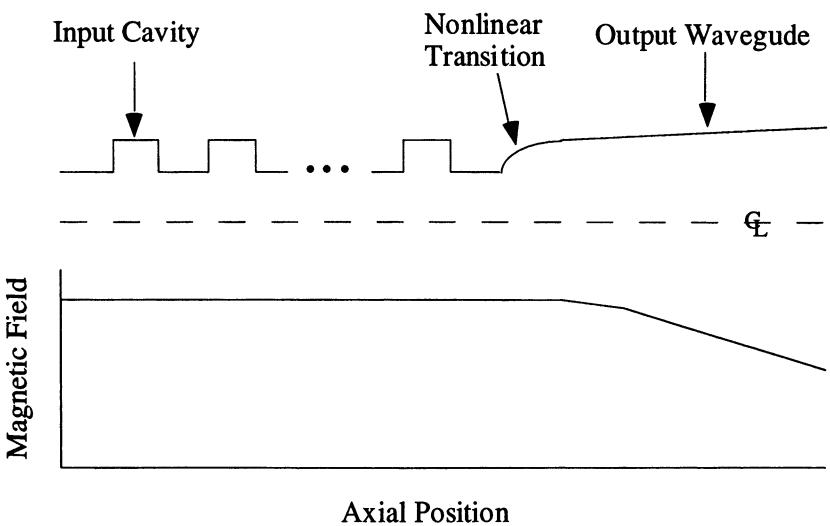

Figure 1 Schematic of the gyrotwystron amplifier.

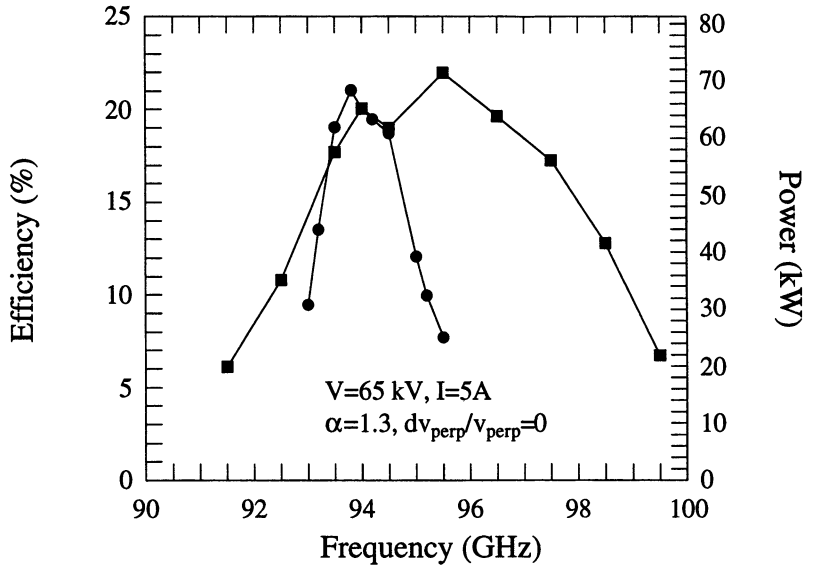

Figure 2 Theoretical results for W-band gyrotwystron amplifier. The squares indicate the simple drive cavity model and the circles indicated the improved model with frequency dependent drive cavity field amplitude.

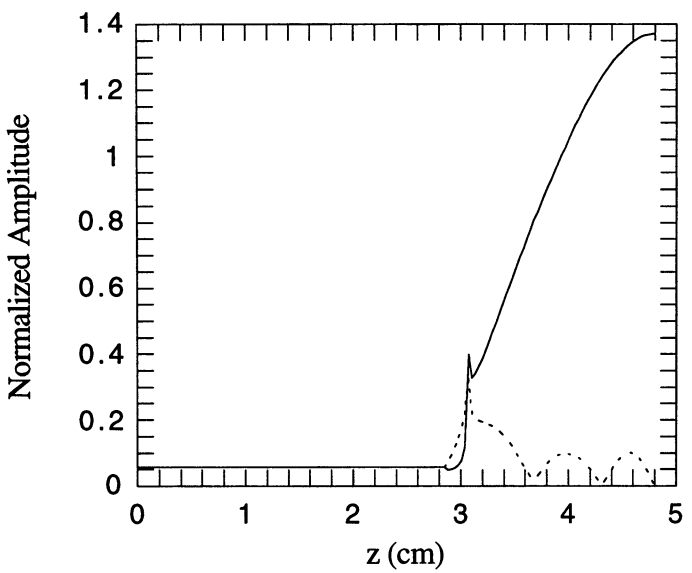

Figure 3 Normalized amplitudes of forward wave (solid line) and backward wave (dashed line) at 94 GHz drive frequency . The traveling wave circuit has a nonlinear transition section with a final radius of 0.195 cm.

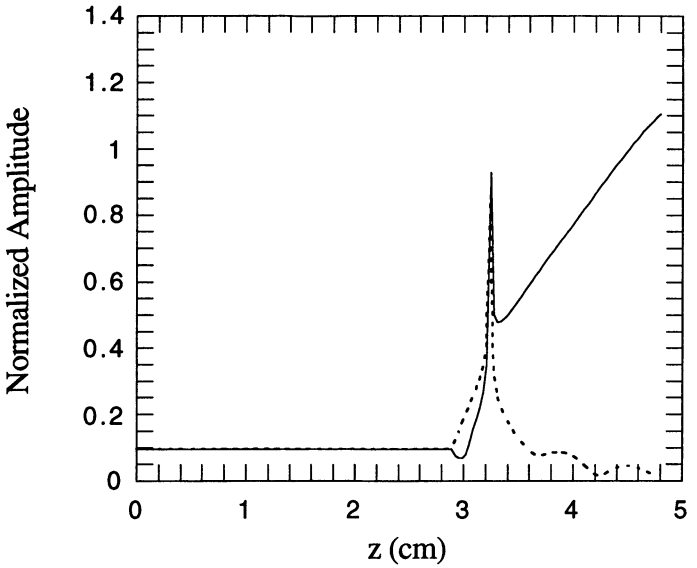

Figure 4 Normalized amplitudes of forward wave (solid line) and backward wave (dashed line) at 94 GHz drive frequency . The traveling wave circuit has a nonlinear transition section with a final radius of 0.192 cm.

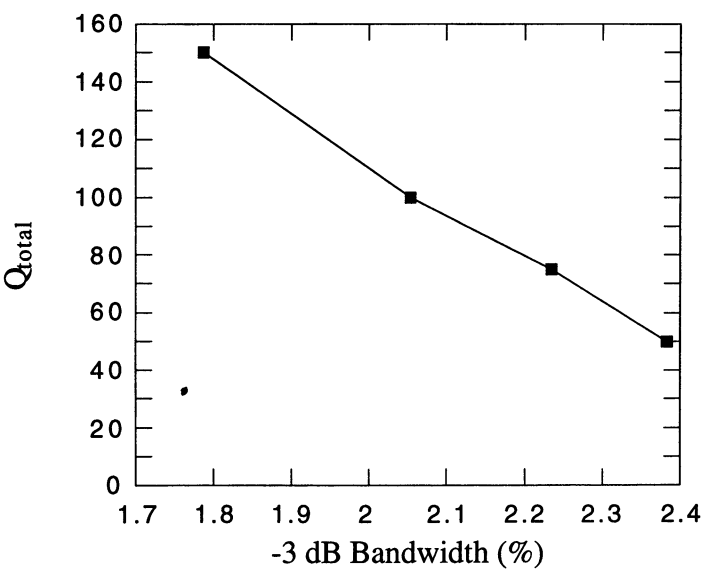

Figure 5 Bandwidth as a function of drive cavity Q. All other parameters, including circuit dimensions, beam parameters, and drive power, were fixed.

INITIAL TESTS AND OPERATION OF A 110 GHz, 1 MW GYROTRON WITH EVACUATED WAVEGUIDE SYSTEM ON THE DIII–D TOKAMAK

John Lohr, Dan Ponce, L. Popov, J.F. Tooker, Daqing Zhang,***

General Atomics, San Diego, California, USA
*Gycom, Nizhny Novgorod, Russia
**Institute of Plasma Physics, Academia Sinica, Hefei, PRC

A gyrotron producing nominally 1 MW at 110 GHz has been installed at the DIII–D tokamak and operated in a program of initial tests with a windowless evacuated transmission line. The alignment and first test operation were performed in an air environment at atmospheric pressure. Under these conditions, the tube produced rf output in excess of 800 kW for pulse lengths greater than 10 msec and power near 500 kW for pulse lengths of about 100 msec into a free space dummy load. The gyrotron was operated into evacuated corrugated waveguide in the full power parameter regime for pulse lengths of up to 500 msec injecting greater than 0.5 MW into DIII-D for a preliminary series of experiments. Generated powers greater than 900 kW were achieved. A parasitic oscillation at various frequencies between 20 and 100 MHz, which was generated during the pulsing of the gyrotron electron beam, was suppressed somewhat by a capacitive filter attached to the gyrotron itself. Addition of a magnetic shield intended to alter the magnetic field geometry below the cathode eliminated internal tube sparks. Rework of the external power and interlock circuitry to improve the immunity to electromagnetic interference was also done in parallel so that the fast interlock circuitry could be used. The latest results of the test program, the design of the free space load and other test hardware, and the transmission line will be presented.

I. INTRODUCTION

Extrapolation of size scaling for tokamak fusion reactors from the present devices to those capable of sustained net energy output has led to designs for power plants operating at high plasma currents and large magnetic fields. In the present economic equation with relatively inexpensive fossil fuels, such large and expensive installations are not as attractive as other electrical generation options with lower capital cost. The picture has been changed in the past few years by

the discovery of tokamak operating regimes with substantially improved parameters which extrapolate to smaller and less expensive system designs. These new regimes, called collectively Advanced Tokamak (AT) regimes, rely on the control of the current density profile, and hence the profile of the magnetic shear, across the plasma discharge. In particular, AT operation requires substantial off-axis current in contrast to normal tokamak operation where the current density profile is peaked in the plasma center.

Operation in the AT regimes has heretofore been achieved transiently by taking advantage of the very slow flux penetration into a hot plasma, however a power production reactor must be able to operate in the AT regime essentially continuously and therefore will rely on non-inductive current drive methods.

On DIII–D, a major effort is underway to investigate Electron Cyclotron Current Drive (ECCD) for producing and sustaining AT geometry. Initial steps in a program which could lead to installation of up to 10 MW of electron cyclotron heating and current drive power call for installation of three rf systems operating at 110 GHz, the second harmonic resonance frequency on DIII–D, each of which will generate nominally 1 MW for two seconds or longer. The three systems will use one Gycom gyrotron and two CPI (formerly Varian) gyrotrons all with windowless evacuated transmission lines. The Gycom gyrotron [1] has been installed at DIII–D and is in a test program leading to routine operation. As of July 1996 at least 500 kW rf power has been injected into DIII–D for 500 msec long pulses on a routine basis and up to 900 kW has been generated. This paper describes the system configuration and reports on the results of the tests of the Gycom Centaur gyrotron to date.

II. RF SYSTEM OVERVIEW

The rf system is a unique combination of the gyrotron and an evacuated waveguide transmission line without any vacuum window except for the boron nitride single disk window on the gyrotron itself. The overall system is presented in Fig. 1. The 31.75 mm diameter corrugated aluminum waveguide carries the HE_{11} mode. The waveguide diameter represents a compromise between power handling capability and the requirement that the line be somewhat insensitive to misalignment, thermal expansion and motion. The rf beam exits the gyrotron slightly off-center (about 4 mm) and slightly off perpendicular (about 0.3 degrees up tilt). The arbitrary specification that mode conversion at the entrance to the waveguide be less than 2% yields the requirement that the beam be centered at the input to the waveguide to within 0.5 mm and be coaxial to within 0.1 degree [2,3]. The beam exiting the gyrotron is phase corrected to the free space Gaussian and focused by a pair of mirrors in the evacuated Mirror Optics Unit (MOU). The MOU was aligned to the measured beam using a specially constructed and adjusted input bellows assembly and is floating on springs so

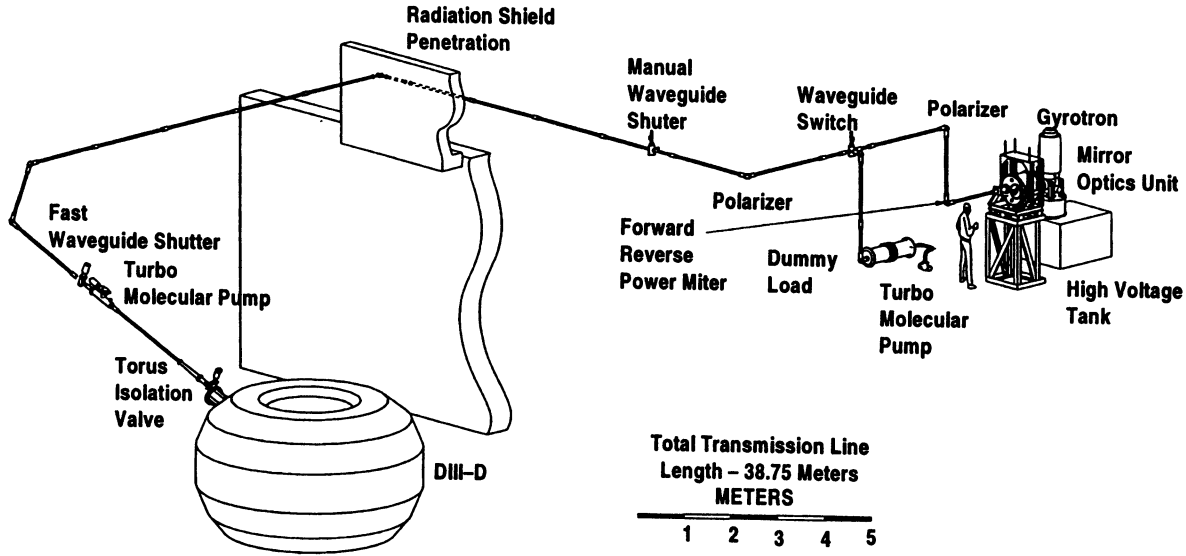

Fig. 1. Schematic diagram of the evacuated windowless waveguide system for the 110 GHz installation on the DIII–D tokamak. The line is 38.75 m long and the diameter of the corrugated circular waveguide is 31.75 mm.

thermal expansion of the gyrotron and the waveguide assembly does not place mechanical strain on the gyrotron. Two photographs of the installation are shown in Fig. 2, one with an anechoic chamber used in initial testing, and the other with the MOU in place.

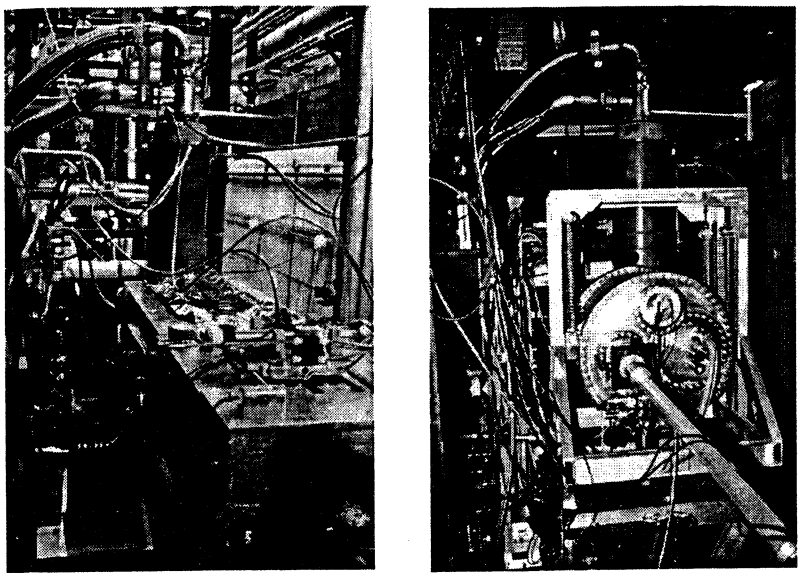

(a) (b)

Fig. 2. Photographs of the anechoic chamber (a) used to house the planar octanol load during the initial tests of the Centaur gyrotron at DIII–D and the final installation (b) with the Mirror Optics Unit in place; the MOU replaced the anechoic chamber for vacuum waveguide operation. and contains the phase correction and focusing mirrors

The interface between the waveguide and the MOU is accomplished by a short section of waveguide attached to an x–y translating stage which is bolted to the MOU. This permits the actual point at which the beam enters the waveguide be accurately positioned. The powers in the forward and reflected waves are measured at the first mitre bend located approximately 2 m past the MOU. This miter bend has a series of several coupling holes sealed with a quartz lens which carries a fraction of the forward and reflected power to detectors. To facilitate gyrotron optimization and ECH experiments, a waveguide switch is used to shuttle the rf power between a dummy load and the DIII–D tokamak without breaking vacuum. Polarization control of the launched rf power is accomplished by a set of polarizing mirrors mounted in two of the mitre bends. By appropriate

rotation of the two mirrors, any elliptical polarization desired can be obtained. Inside the tokamak vacuum vessel is a focusing mirror and a flat turning mirror, permanently angled 19 degrees off the major radius line, which can be tilted vertically to direct the beam poloidally. This allows the power deposition region to be placed off-axis without changing the magnetic field.

The entire waveguide system contains six miter bends and is 38.75 meters long with estimated loss of 2% in the waveguide and 0.6% in each miter bend. The miter bend losses are from mode conversion, 0.5%, and from ohmic loss, 0.1%. The line is evacuated to a pressure of approximately 1×10^{-5} torr by a turbomolecular pump at the MOU, by a turbopump pumping through small holes in the waveguide in the final section leading to the tokamak and by the tokamak itself. The dummy load also has a pumping port with turbo pump which maintains its base pressure at 1×10^{-6} torr. Vacuum protection for the tokamak is provided by a fast shutter system installed in the waveguide three meters in front of the tokamak. The pressure sensor for this shutter is at the MOU, and any increase in pressure above 1×10^{-3} torr there results in closure of the fast shutter in less than 10 msec. The fast shutter was primarily intended to protect the tokamak from the coolant in the case of fracture of a double disk gyrotron window, not the situation in the case of the Centaur gyrotron, which has a single disk window. Two complete waveguide lines have now been installed on DIII–D and the launchers for four systems are in place inside DIII–D.

III. INITIAL OPERATION

The initial testing of the gyrotron at DIII–D was done at atmospheric pressure into a specially constructed free space dummy load, shown in Fig. 3, capable of absorbing the full gyrotron output power for 50 msec. The load is about 35 cm square and consists of two parallel sheets of dielectric filled with 1-octanol [$CH_3(CH_2)_7OH$]. The entrance surface is teflon with pyramidal facets presenting a 60 degree conical absorber, which is ten free space wavelengths deep, to the incoming beam. The circulating octanol has an attenuation of 13 dB/cm [4] and the attenuation of the entire load is about 40 dB. The back surface of the teflon is also faceted to a depth of five wavelengths in octanol. The back surface of the load is made from a flat sheet of TPX (polymethyl-pentene). The teflon and TPX sheets were mounted on an aluminum spacer which contained the flow fittings and calorimetry block. The load was scribed with fiducials so that detailed measurements of the beam could be made using thermally sensitive paper mounted directly on the load.

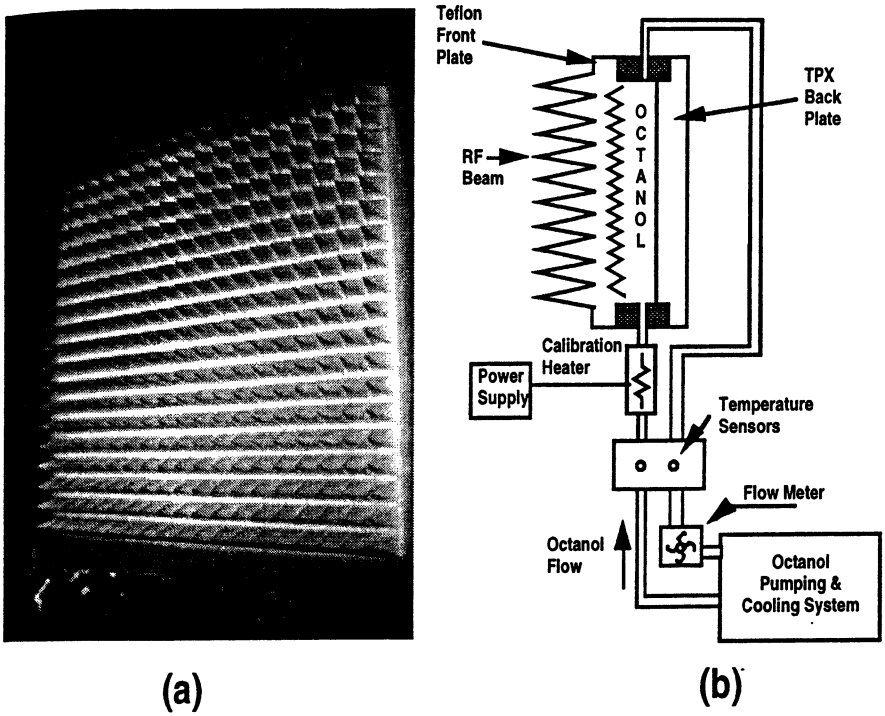

Fig. 3. Photograph (a) and sketch (b) of the planar octanol load used for free space calorimetry and beam quality measurements at atmospheric pressure. The load can withstand the full 1 MW gyrotron output power for about 50 msec. The load is 35 cm square and provides about 40 dB attenuation.

The dummy load was housed in a wooden anechoic chamber with dimensions $1 \times 1 \times 2$ meters which was lined with microwave absorber and purged with dry nitrogen as protection against fire. The load could be moved axially within the box, and this capability was used to determine the direction and position of the beam as it propagated out from the gyrotron window. Thermally sensitive paper was used to diagnose the beam and in Fig. 4 the free space beam patterns are shown for the near field close to the window and the far field 1.7 m past the window There was good qualitative agreement with calculations [5].

The anechoic chamber was used both with the gyrotron launching into free space and with the phase correction and focusing mirrors in the MOU. The

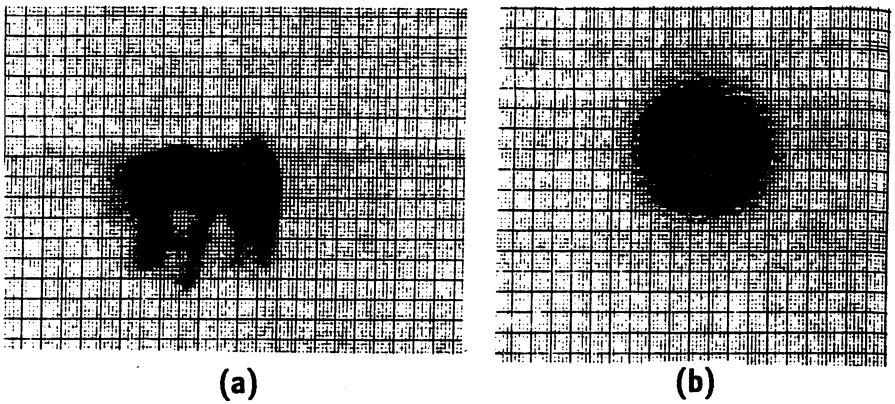

Fig. 4. Free space power profile measurements using thermally sensitive paper in the near field (a) at 31 cm from the gyrotron window and the far field (b) at 173 cm from the window. The beam exiting the gyrotron window is a flattened Gaussian to spread the power more uniformly over the window surface. The major divisions on the paper are 1 cm apart.

initial measurements with the gyrotron only were used to build an adapter flange to connect the MOU to the gyrotron so that the beam propagated through the MOU on the designed path. The MOU output waveguide, a section of 31.75 mm diameter guide with x–y translation and tilt capability, was then installed on the MOU and was adjusted slightly to center the beam.

The beam was accurately centered on the waveguide following the MOU as indicated by the thermal paper patterns in Fig. 5. The MOU output waveguide is 70 cm long and the beam is seen to be well centered both at the input and the output of this section of waveguide. The power measured following the output waveguide was approximately the same as the free space measurements. Tuning mechanically to eliminate possible tilt of the beam axis with respect to the waveguide axis has not yet been done.

Power measurements were performed calorimetrically using the octanol load, either by pulsing repetitively at constant frequency but for different duty cycles (to eliminate uncertainty from the turn-on of the gyrotron), or by analyzing the octanol response to a single pulse. The calorimetry was calibrated using a heater immersed in the flow which delivered a known power to the octanol.

Following the initial tests, the output waveguide was connected to a vacuum dummy load capable of absorbing the full gyrotron output power for 1 second. This experimental arrangement was used to verify the coupling of the power to the dummy load using approximately 4 meters of corrugated evacuated waveguide and two miter bends. Calibrated calorimetry was performed on the water cooling for the gyrotron output window, the MOU mirror and housing and

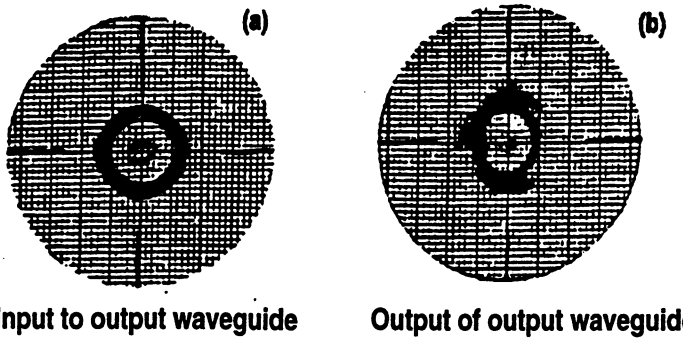

Fig. 5. Thermal paper beam patterns at the input and output of the first 70 cm long piece of waveguide at the output of the Mirror Optics Unit. The dark circle marks the edge of the deposition region due to evaporation of the ink in the high power center.

the high power dummy load. RF monitors were located on the MOU, at the first miter bend for forward and reflected measurements, and on the dummy load. The total power generated by the gyrotron was estimated during repetitive pulses using the temperature increase in the gyrotron output window assuming absorption data supplied by Gycom. The rf monitors were used as a guide to the mode purity and the calorimetry was used to perform power accountability checks.

In initial operation, the short pulse free space maximum power output from the gyrotron of about 850 kW was reproduced using the evacuated line to the dummy load. Of this power, approximately 25% appeared in the MOU, 65%-70% in the dummy load, 4% in the window and the rest was absorbed in the waveguide and the miter bends. Although the calorimetry accuracy is limited to between 5% and 10%, the power accountability was good. The power absorbed by the MOU cooling water was higher than expected by about a factor of two. The efficiency was 35% for 110 GHz power generation and better than 95% for the transmission line.

Measurements of the output frequency of the gyrotron as a function of pulse length were made using a wavemeter on the forward power monitor at the first miter bend. These measurements, shown in Fig. 6, reproduced tests performed in Moscow and provided design parameters for a notch filter being built to protect the heterodyne ECE diagnostic from the gyrotron power. The gyrotron operates at 110.10 GHz early in the pulse and the output frequency decreases to 109.9±0.02 GHz after about 80 msec of full power output. The final frequency is 109.75±0.02 GHz, or 350 MHz lower for long pulses than at the beginning of the pulse.

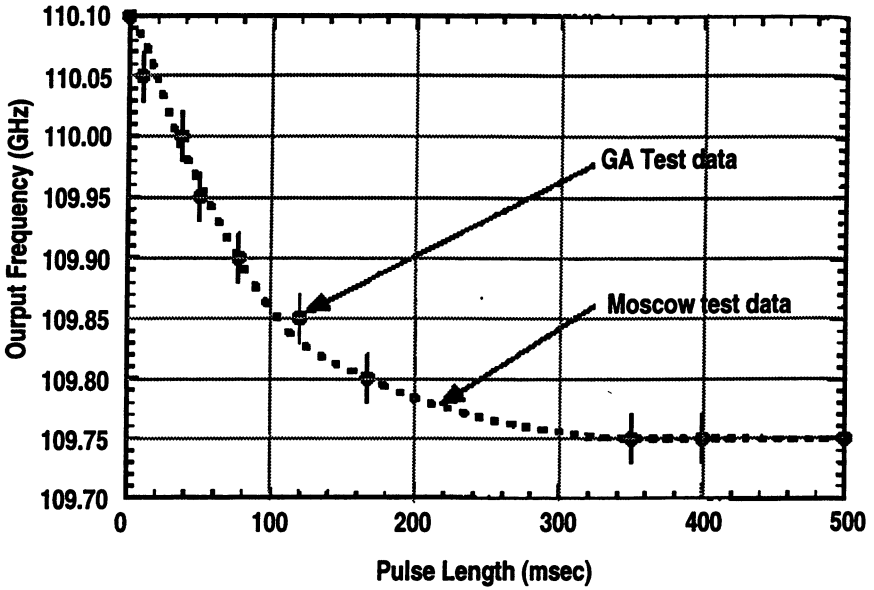

Fig. 6. Gyrotron output frequency as a function of pulse length. The measurements at DIII–D agreed with the tests performed in Moscow.

The transmission line operated with no sign of any waveguide arcing and with transmission loss of less than 5%, which was at the limit of the accuracy of the the calorimetry. Although pulse length was initially limited by rf interference from a parasitic oscillation, pulses of 500 msec in length, the administrative limit, were produced reliably with dummy load power greater than 500 kW, approximately 150 kW absorbed in the MOU cooling circuit, and generally good power accountability.

IV. LOW FREQUENCY PARASITE

The operation of the gyrotron has been accompanied by a low frequency parasitic oscillation which caused severe problems for the protective interlock circuitry despite the fact that the basic operation of the gyrotron at 110 GHz was relatively unaffected. Several measures which collectively made it possible to operate were undertaken to obviate the effects of this parasite.

The initial operation of the gyrotron during acceptance testing in Moscow was without a strong parasitic oscillation. After some days of operation in San Diego, a parasitic oscillation began to be observed first on the calorimetry signals and then on virtually all signals. The parasite frequency initially was in the 20 MHz range with harmonics out to 150 MHz. The parasite had the characteristics that it was about 5 MHz wide at –3 dB, did not appear to be connected

with the external circuit parameters, and was present whenever the beam was present in the tube (independent of rf generation at 110 GHz).

Several direct measures were undertaken on the gyrotron in an attempt to reduce the amplitude of this parasite. A capacitive filter, Fig. 7, was connected across the gyrotron accelerating gap. This filter provided a 1 nF short across the tube insulator, with uniform electric field gradient maintained by a voltage divider chain. An iron collar was installed at the top of the tube insulator to eliminate the possibility of a magnetic well with a trapped electron population below the cathode, which might be causing the parasite. The actual effect produced by this collar was to eliminate small internal gyrotron sparks which had been observed during operation in the presence of the parasite, however its effect on the parasite itself was minimal. Additional work on understanding the parasite is in progress [6].

The tube filter installation resulted in a substantial change in the character of the instability. The new spectrum has a small peak at 4.7 MHz with a satellite at 5.7 MHz, plus a strong peak at 96 MHz with sidebands and structure between 88 and 106 MHz. Harmonics out to the third are observed. The 96 MHz peak had not been observed before the installation of the gyrotron filter. The rf spectrum, estimated to have a total power of several kW, is shown in Fig. 8.

This parasite is still observed during normal operation of the gyrotron. There has not been any evidence that the amplitude of the parasite has decreased during the course of gyrotron operation to date. Despite the installation of the tube filters, it continued to be impossible to run the gyrotron without spurious interlock trips and other control and monitoring problems. Therefore a comprehensive program of rf interference suppression, both in the gyrotron system and in other DIII–D systems, was undertaken, which enabled operation in the presence of the parasite.

It has occasionally happened that during normal gyrotron operation the parasite suddenly has become more severe. Reducing the gun coil current by about 10% has permitted return to normal operation and following conditioning the normal operating regime can be restored. The present situation is that the parasite is a serious but generally manageable problem.

V. INITIAL OPERATION INTO DIII–D

Although thus far experimental time has been limited, the gyrotron and transmission line system have been operated into DIII-D plasmas and the principal features of the systems have been checked. The launcher injects the rf power at a fixed angle of 19 degrees off perpendicular to the toroidal field and can be scanned poloidally, as indicated in Fig. 9. Calculations of the spot size in the plasma predict that 98% of the rf power will be distributed across an area with diameter 12.8 cm at a distance of 1.00 m from the final poloidally scanning

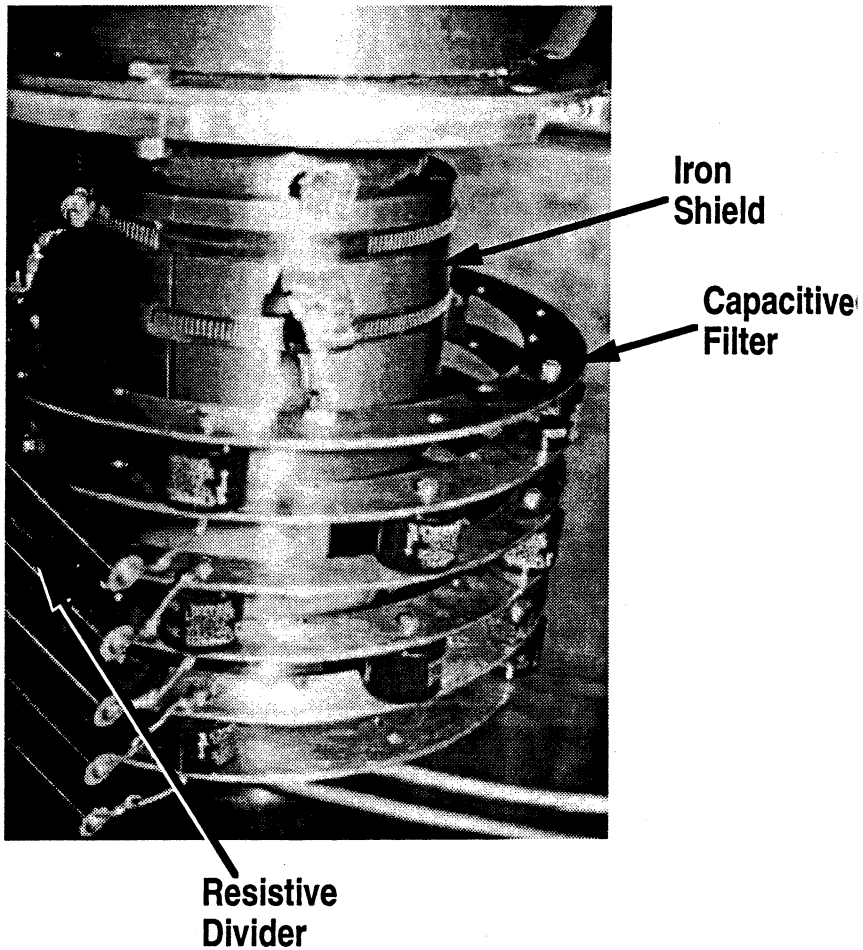

Fig 7. Photograph of the capacitive filter and magnetic collar mounted on the gyrotron inside the high voltage tank. Five planes connected with 5 nF are arranged in series for a total 1 nF filter. The iron collar is mounted on the upper, anode, portion of the gyrotron.

mirror. The calculated spot size increases to 16.3 cm diameter at a distance of 1.25 m from the final mirror. The actual power deposition profile was estimated from the change in the time derivative in the ECE T_e signals at the termination of the rf pulse. These measurements are summarized in Fig. 10, where the power deposition profile is seen to be broader than expected and with substantial

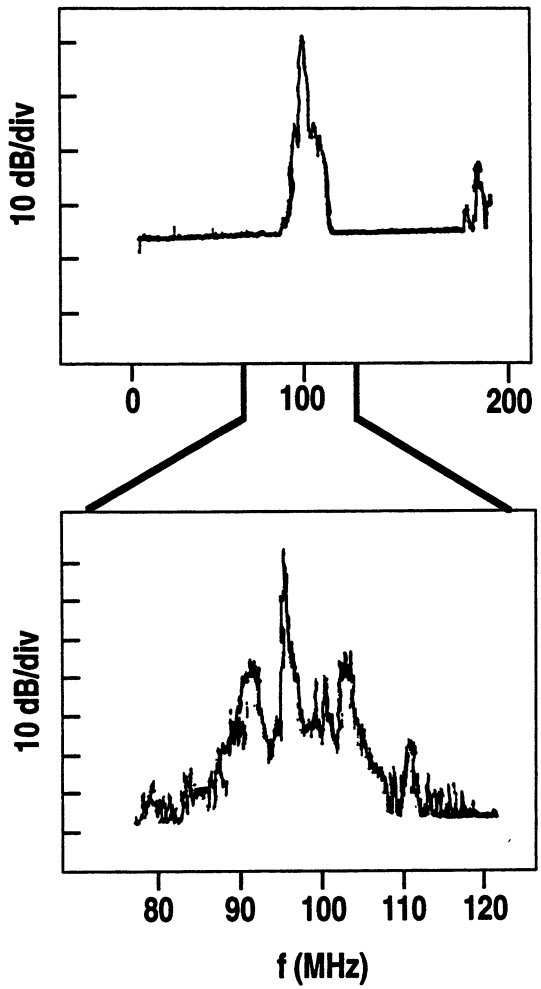

Fig. 8. Spectrum of the low frequency parasitic oscillation after installation of the filter and collar. The center frequency is about 96 MHz and sidebands are visible. The second harmonic is 35 dB below the fundamental.

wings. The FWHM is 14 cm but appreciable power is absorbed within a broader region with 30 cm radius, for absorption centered about 10 cm off the magnetic axis. Fourier analysis of modulated rf injection indicated an even broader power

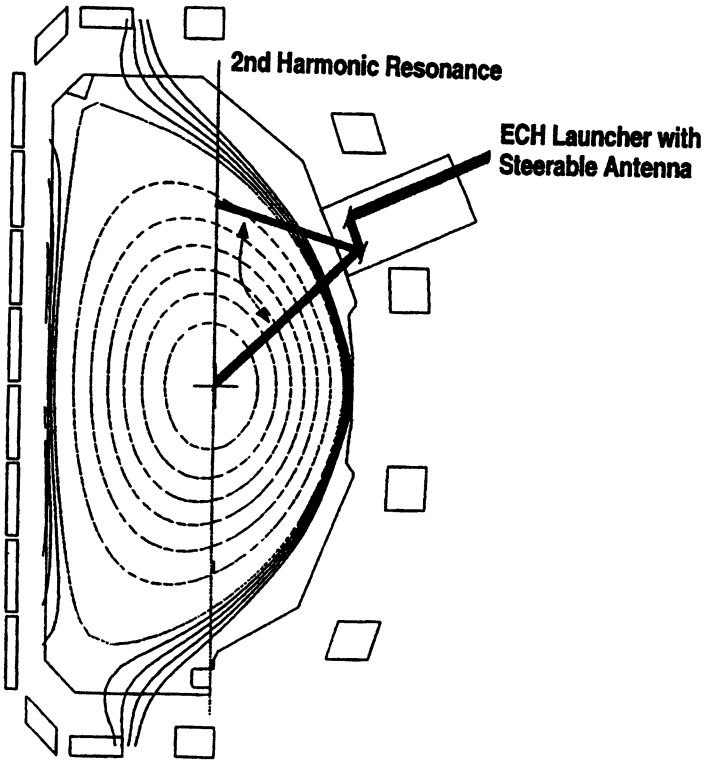

Fig. 9. Cross section of the DIII–D chamber showing the poloidal scan of the injected rf power.

deposition profile. Presently, measurements of the elliptical polarization of the beam launched into DIII–D are being performed under the assumption that an admixture of O–mode is present.

It is characteristic of the operation of this system that there is some reflected power measured at the first miter bend during the first 100 msec of the rf pulse. The forward power measurement has a maximum value during this part of the pulse and then drops, reaching a steady value after about 200 msec. The reflected power decreases to unmeasurable levels after the first 100 msec. An rf monitor on the MOU is also available to indicate the rf power reflecting in the MOU and not a part of the Gaussian beam. These rf monitor traces are shown in Fig. 11, both for an unmodulated and a modulated case. For the modulated case, the high voltage, the collector sweep coil current and the window arc detector

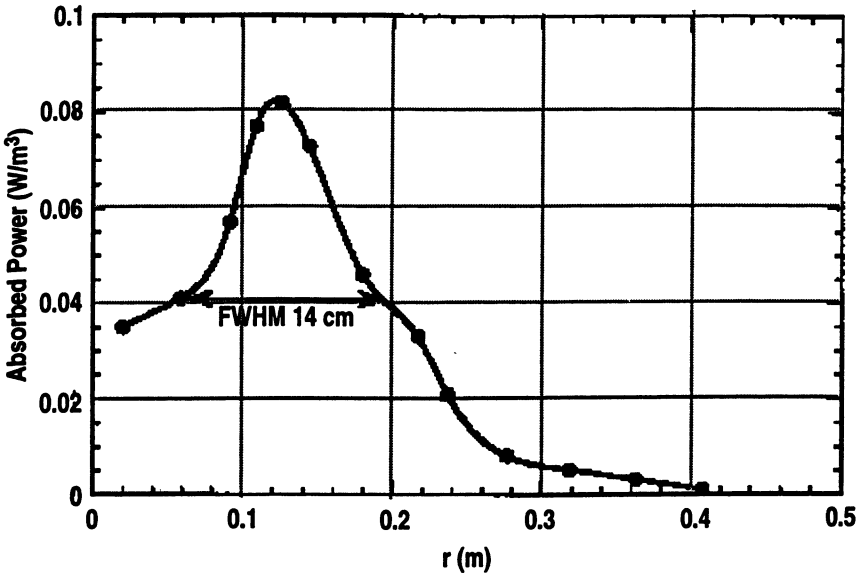

Fig. 10. Power deposition profile measured from the time derivative of the ECE T_e signal upon termination of the rf pulse. The profile is broader than calculated from the optics of the launcher.

signal are also displayed. The beam voltage is modulated approximately 13% to obtain greater than 60% modulation of the generated rf power. These traces were for injection into DIII–D plasmas for the full 500 msec long pulses.

Injection of approximately 500 kW into DIII–D plasmas at low density has resulted in electron temperatures as high as 12 keV. Traces of the discharge with the highest T_e are shown in Fig. 12 along with the electron temperature profile from the Michelson interferometer, the heterodyne radiometer and Thomson scattering. The radiometer data show a suprathermal electron population at these low densities.

VI. CONCLUSION

The Gycom Centaur gyrotron is now running routinely at DIII-D with generated power in all modes at 110 GHz of approximately 900 kW, pulse lengths up to 500 msec and good power accountability. The efficiency is 35% for 110 GHz rf power generation and better than 95% for the evacuated windowless transmission line to the tokamak. Approximately 15%–25% of the power generated by the gyrotron, as inferred from window calorimetry, appears in the MOU.

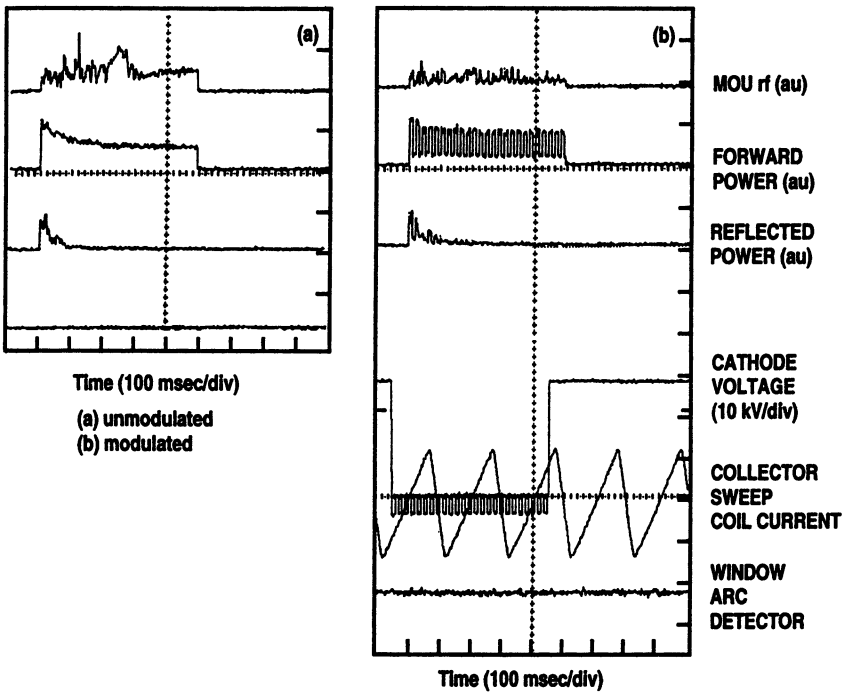

Fig. 11. The rf monitor signals for unmodulated and modulated 500 msec long pulses. The sawtooth signal is the collector sweep coil current. A 13% modulation of the cathode high voltage yields a 60% rf output modulation for transport studies.

Initial injection into DIII–D plasmas has been performed for 500 msec pulses. The MHD measurements of plasma energy indicated that about 550 kW was absorbed in the plasma for about 800 kW generated. Initial transport experiments using modulation of the 110 GHz rf have been performed and ECH synergy for fast wave current drive was investigated.

ACKNOWLEDGMENT

The authors are grateful to Max Austin for providing the T_e profile data and to R.E. Brambila for technical support.

This is a report of work supported by U.S. Department of Energy Contract DE-AC03-89ER51114

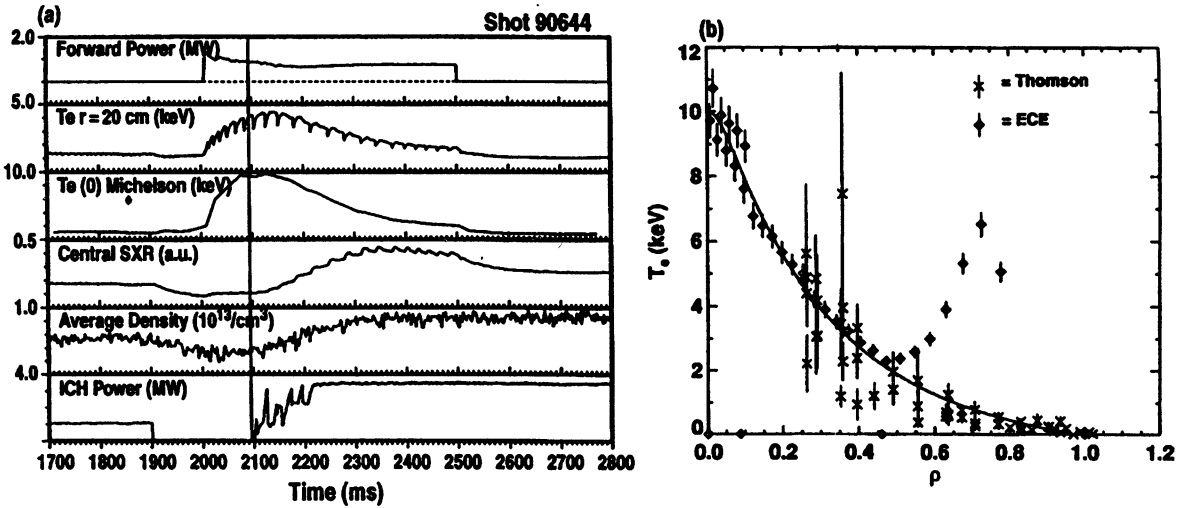

Fig. 12. Time dependence of the forward rf power and several diagnostic traces during ECH/fast wave synergy experiments: (a) the electron temperature profile (b) from ECE and Thomson scattering is shown at the time indicated by the vertical line on the time plots. The density increase associated with the injection of ICH power at 2100 msec decreases the T_e value. Comparison of the ECE and Thomson data at $\rho \sim 0.7$ indicates a superthermal electron velocity distribution function during the low density portion of the discharge.

REFERENCES

1. M.V. Agapova, V.V. Alikaev, L.A. Axenova, *et.al.*, Proc. 20th Int. Conf. on Infrared and Millimeter Waves, Ed. R. Temkin, Coca Beach, Florida, 205, 1995.
2. K. Ohkubo, Proc. U.S./Japan RF Technology Exchange, unpublished (1995).
3. John L. Doane, Infrared and Millimeter Waves, **13**, 123, 1985.
4. H. Stickel, Int. J. Electronics, **64**, 63, 1988.
5. V. Zapevalov, private communication.
6. V.E. Myasnikov *et al.*, these proceedings.

CW 10 kW TECHNOLOGICAL GYROTRON IN THE RANGE 15-50 GHz

V.A.Flyagin, A.N.Kuftin, V.K.Lygin, A.G.Luchinin, O.V.Malygin, V.N.Manuilov, Sh.E.Tsimring, V.E.Zapevalov

Institute of Applied Physics, Russian Academy of Sciences, Nizhny Novgorod, Russia

Abstract

This report describes the design concept and experimental parameters of the developed 30 GHz gyrotron with output power 10 kW, which operates at the second harmonic of the cyclotron frequency. As the magnetic system, an oil-cooled solenoid is used. According to the experimental data, parameters of the gyrotron, as well as thermal loads of the anode, collector, and energy output window correspond to the calculation models. The chosen design version may be used as the basis for further development of technological CW gyrotrons operating in the range of 15 through 50 GHz with output power up to 30 kW.

Introduction

One of the important problems of modern high-power electronics is development of efficient sources of microwave radiation in the range of 15 through 50 GHz for industrial purposes [1]. Specifically, of interest is application of microwave radiation to processing of dielectric materials with relatively low losses (baking and production of ceramic materials, formation of ceramic items, production of composite materials, outbaking of semiconductors, etc.). The above tasks require microwave generators operating in the continuous regime with output power up to 30 kW in the range of 15 through 50 GHz. The most promising type of the generator with the said parameters is the gyrotron.

IAP scientists made a technological gyrotron complex for microwave processing of materials [2]. The concept of the complex is based on the idea of making a parametric series of gyrotrons with fixed frequencies in the range of 15 through 50 GHz. The developed basic technological gyrotron complex includes:

- gyrotron (P = 10 kW, f = 30 GHz),
- magnetic system (solenoid) with a cooling system,

- equipment set for electric supplies of the gyrotron and magnetic system,
- electrodynamic system for conversion and transportation of microwave radiation,
- microwave oven that provides operation in a controlled gas atmosphere or vacuum at the temperature up to 2.500°C,
- diagnostic equipment,
- system for automatic/manual control over the temperature regime of microwave processing.

The technological gyrotron complex makes it possible to use all the advantages of microwave processing associated with volume absorption of microwave energy (lower energy consumption, significantly shorter processing time, selective material heating, etc.).

Further the gyrotron design is described, and experimental parameters of the magnetic system and the basic gyrotron prototype for the technological microwave complex are given.

Magnetic system

The magnetic system that provides gyrotron operation consists of four axially symmetric solenoids (one main and three auxiliary ones) with independent current control. The main solenoid coiled with copper wire of rectangular cross-section is equipped with an oil-water cooling system. The calculated parameters of the main solenoid agree well with the experimental data:

- maximum magnetic field 1 T,
- length of the homogeneous section in the resonator region at the level ≤ 0.3% 100 mm,
- internal diameter of the solenoid case bore 60 mm,
- coolant consumption (transformer oil) 3.6 m^3/h,
- water consumption for oil cooling 7–10 m^3/h.

The power consumed depends on the temperature and oil-cooling water consumption, and may vary within 10%. At the level of the inductance of the magnetic field 0.57 T ($n = 2$, $\lambda = 10$ mm), the main solenoid consumes 14.3 kW of power.

Additional solenoids are used to correct the value of the magnetic field at the cathode and collector.

Gyrotron design

The choice of the operating mode is based on the requirements to gyrotron energy parameters and efficiency estimates [3]. In the current case we considered a small-sized gyrotron operating in the continuous regime with output power 5 through 25 kW (beam power 15–90 kW, accelerating voltage 20–30 kV, and beam current, respectively, 0.5–3 A). This power level cancels the necessity to use large transverse cross-sections of the interaction space, which causes the use of spatially developed electrodynamic systems. The operating mode was chosen to be the H_{021} mode, the wavelength was $\lambda = 10$ mm ($n = 2$) and the simplest resonator was made as a section of a cylindrical waveguide with cone transitions ($Q_{dif} = 3200$). When operating at the second harmonic of the cyclotron frequency, the power consumed by the main copper-coiled solenoid is 14.3 kW (for the first harmonic, 57 kW), the problem of heat removal from the solenoid coiling is solved much easier, and at the set value of the output microwave power, 5–15 kW, efficiency of the whole complex is essentially higher. Estimated dependencies of the output power of the gyrotron on the accelerating voltage and beam current are shown in Fig. 1.

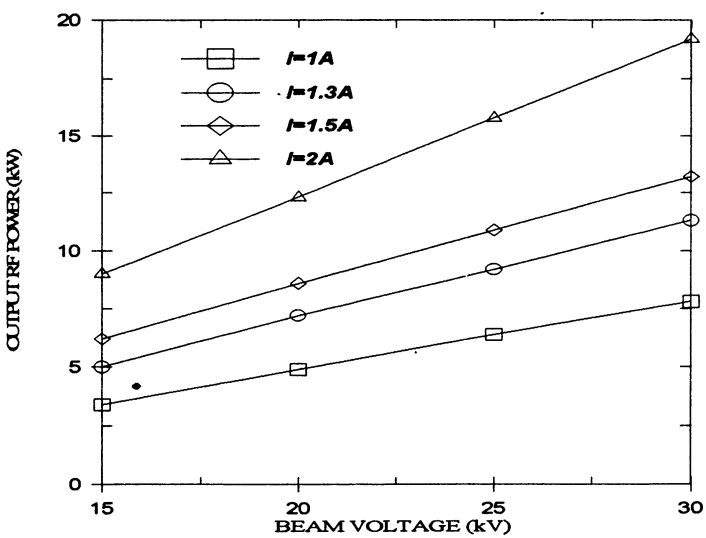

Fig.1. Estimated dependencies of the output power of the gyrotron vs. the accelerating voltage and beam current.

The problem of electron beam formation required numerical modeling of the optimized adiabatic magnetron-injection gun of the triode type. The system operating in the following regime was considered:

- accelerating voltage 30 kV,
- anode voltage 24 kV,
- operating beam current ≤ 3 A,
- pitch-factor $g = V_\perp/V_\parallel$ 1.5.

Trajectories of the electron beams were analyzed by means of the EPOS application program [4]. Variation of the values of velocity spread and oscillatory energy in dependence on the beam current is shown in Fig. 2. According to the data of the trajectory analysis, in this system in the regime of $I = 0$ the values of oscillatory energy of electrons passing from the left side of the emitter to the right one grow. As the beam current increases under the effect of the space charge field, oscillatory velocities of electrons level out, which in the long run provides lower velocity spread, $\delta V_\perp$ (Fig. 2).

The collector system of the technological gyrotron should provide landing of an electron beam with specific power density $P_{sp} \leq 1.2$ kW/cm^2 on the cylindrical collector with radius $R = 19.5$ mm at the above parameters of the electron beam. The adiabatic calculation of the collector system by equations given in [5] yields mean power density $P_{sp} \approx 0.7$ kW/cm^2. Power density distribution over the collector surface is essentially inhomogeneous, the mean value of power density is twice as low as the maximal value, $P_{max} \approx 1.47$ kW/cm^2. The collector of the technological gyrotrons has successfully passed long-term tests operating with the maximal load of 85 kW.

The gyrotron is designed as a metal-ceramic sealed unit. Required vacuum is provided by a built-in electro-discharge pump that operates in the scattered field of the magnetic system of the gyrotron. During storage the electro-discharge pump can be turned on by means of an additional magnetic system on permanent magnets, which is dismounted before the gyrotron is installed in the operating magnetic system. Energy output is a BN disk of the required thickness. The magnetron-injection gun forms the required electron beam and provides operation life time in the HEATER-ON regime over 1000 h; high-temperature emitting materials stable to breakdowns and sharp changes in operation regimes are used.

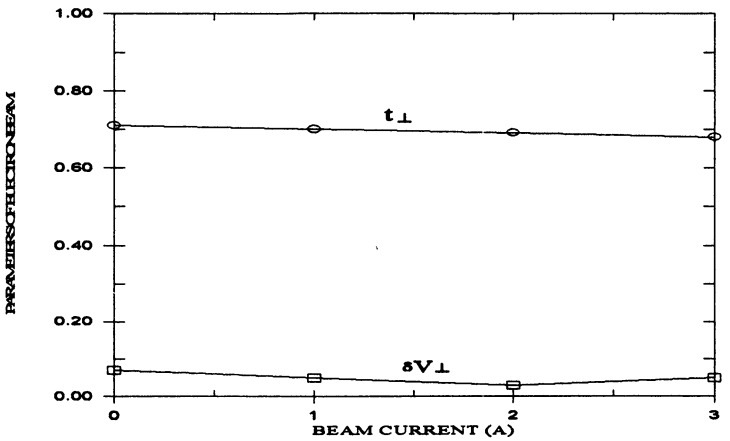

Fig.2. Velocity spread $\delta V_\perp$ and oscillatory energy of electrons $t_\perp$ as a function of beam current.

Experimental results

Experimental studies of the generation regimes of the technological gyrotron as a part of the complex had the following objectives:

- to test operability of the complex power supply system,
- to determine optimal regimes for gyrotron operation,
- to eliminate the dependencies of the power and efficiency of the gyrotron on the current and voltage of the electron beam,
- to determine optimal ways to control the output power of the gyrotron.
- to measure thermal loads on the anode, resonator, collector and window of the gyrotron.

The experiments demonstrated stable generation of continuous power 6–10 kW at the frequency of 30.4 GHz. Optimal regimes for gyrotron operation and ways to control its output power were found; that is required for further development of microwaves application to processing of dielectric materials with various heating scenarios. Figure 3 shows typical graphs for gyrotron power versus current and voltage of the electron beam. As follows from these results, the gyrotron is a widely tunable device with respect to current and voltage. During reconstruction of the magnetic field of the main solenoid, stable generation of microwave power was observed, at the level of 5–7 kW (U_b = 27 kV, I_b = 1A) with radiation wavelengths λ = 7.4 mm, 6.8 mm (n = 2) and λ = 16.5 mm (n = 1).

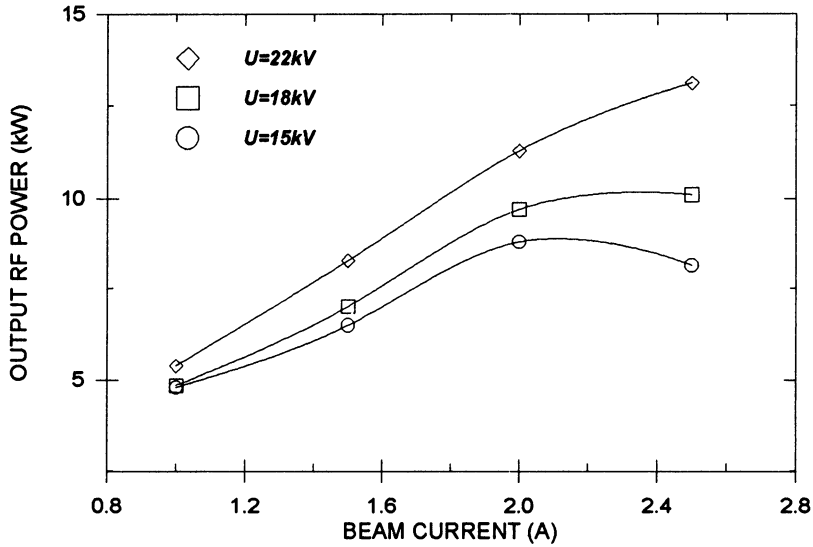

Fig.3. Measured power vs. current and voltage of the electron beam.

Thermal loads were measured with water meters of absorbed power, special temperature-sensitive sensors set at the corresponding gyrotron components and a special IF camera. As shown by the experimental data, the thermal loads on the anode, resonator, collector and window correspond to the calculated models, and the chosen design version can be used for further development of the CW gyrotrons that produce up to 30 kW of power in the range of 15–50 GHz.

References

1. Application of High-Power Microwaves. Ed. A.V. Gaponov-Grekhov, V.L. Granatstein. Artech House, Boston & London.
2. Bykov Yu., Eremeev A., Holoptsev V., Proc. 4th Symp. Microwave Processing of Materials, Mat. Res. Soc., ed. M. Iskander, R. Lauf, W. Sutton, Pittsburgh, 1994, 347, p. 585.
3. Flyagin V.A., Gaponov A.V. et al., IEEE Trans. Microwave Theory Tech., 1977, 25, p. 514.
4. Lygin V.K., Manuilov V.N., Tsimring Sh.E., Elektronnaja Tekhnika, Ser. 1, Elektronika SVCh, 1987, 7, p. 36 (in Russian).
5. Tsimring Sh.E., Lectures on Microwave Electronics, Saratov, 1974, 4, p. 5 (in Russian).

DEVELOPMENT OF THE PROTOTYPE 170 GHZ/1 MW GYROTRON FOR ITER AT IAP

G.G.Denisov, V.A.Flyagin, A.N.Kuftin, V.K.Lygin, M.A.Moiseev, V.E.Zapevalov

Institute of Applied Physics, Russian Academy of Sciences, Nizhny Novgorod, Russia

The paper presents the results of calculation, design and experimental study of the prototype 170 GHz/1 MW gyrotron for ITER. The dependence of gyrotron parameters on the beam current, accelerating voltage and magnetic field is analyzed. The experimental results are compared with the calculated data.

Electron-cyclotron heating and current control in the planned plasma set-up ITER require gyrotrons with CW power up to 1 MW and frequency 170 GHz. The possibility to make such gyrotrons is proved by calculations and experiments. In the framework of ITER activities two versions of the 1 MW gyrotron at 170 GHz frequency with pulse duration up to CW have been developed [1]. The main parameters of the planned gyrotrons with operating mode $TE_{28\,7}$ ($TE_{31\,8}$) are presented in the table below:

Operating frequency	170±0.5 GHz
Wavelength, λ	1.763 mm
Output power	1.0 MW
Pulse duration	several seconds to CW
Accelerating voltage	80 kV
Maximum beam current	45 A
Magnetic field at resonator center	6.8 T
Resonator radius	15.86 (17.9) mm
Mean beam radius in resonator	8.26 (9.13) mm
Mean cathode radius	45.2, 47.5 (51.13) mm
Resonator Q-factor	1000
Specific density of losses in resonator	2.5 (2.3) kW/cm^2
Pitch-factor	1.25
Calculated maximum (electron) efficiency	0.4
Calculated relative oscillatory energy	0.62
Structure of output radiation	narrowly-directed wave beam

Usually our work on a new gyrotron includes the following stages:

- calculation and design;
- test of the experimental version of the tube in a short-pulse regime;
- work on the industrial prototype operating in the full-scale regime.

The gyrotron has the same principal design concept as the earlier developed 140 GHz./0.5 MW/3 s and 110 GHz/1 MW/2 s gyrotron. The magnetic system of the tube includes a main superconducting solenoid and a cathode coil for fine adjustment of electron beam parameters

In terms of electron optics the main efforts go along the following lines:

- development of the theory describing formation and transportation of helical electron beams (HEBs) of high intensity, including study of instabilities and methods of their suppression;
- experimental investigation of HEB properties in modeling regimes;
- development of efficient thermoemitters and control of their quality (homogeneity, temporal stability of characteristics, etc.).

Achievement of 1MW output power of a 170 GHz gyrotron with operating voltage U_b =80 kV and the efficiency ≈ 35 % is required to produce a beam with current I_b ≈40 A and a pitch-factor g ≈1.25 ($g = v_\perp / v_z$, $v_\perp$ and v_z are oscillatory and longitudinal velocity in the operating space, respectively). Thus, a magnetron-injection gun (MIG) should provide formation of a beam with such parameters.

The allowable radius of the cathode for the chosen operating mode is defined by the value of the acceptable electrical field on the cathode, E_c, which, as a rule, must not exceed 6 kV/mm. Width of the emitter is selected with the account of extreme allowable density of emission current (usually it is not recommended to exceed 3 A/cm^2). When selecting of an optimum configuration of electrodes the value of velocity spread $\delta v_\perp$ was taken not to exceed 30 %. The specified restrictions were considered for particular guns of gyrotrons with different operating mode. Below results of investigations of the three possible versions of guns are presented.

For operating mode $TE_{31\,8}$ in terms of limitations on an electrical field E_c, the optimum radius of the cathode is R_c =51mm. Thus on the cathode E_c ≈5.8 kV/mm. Numerical simulation yielded dependencies of velocity spread $\delta v_\perp$ *(l)* and ratio of the oscillatory energy to the total one $t_\perp$ *(l)* as in the model with zero initial velocities (EPOSR [2]) and taking

into account initial velocities (EPOS-V [3]). Evolution of transverse velocity distribution function, $f(v_\perp)$, is traced with the growth of beam current. The sensitivity of the beam parameters to influence of thermal deformations of the gun and possible technological errors is investigated. We shall note, that it is possible to use the cathode with R_c =50mm, but in this case for required pitch-factor g a regime with $E_c \approx 6.3$ kV/ mm is necessary.

For gyrotron with operating mode $TE_{28\,7}$ two versions of guns with different radii of the cathode were designed. In the first version a gun with R_c =45.2mm was used. The necessary g value requires an increased electrical field on the cathode, E_c ≈6.3 kV/mm. In the second variant the reduction of E_c to 5.5-5.7 kV/mm was achieved by using of the cathode with an increased average emitter radius (R_c =47.5 mm). For the both variants dependencies $\delta v_\perp$ *(I)* and $t_\perp$ *(I)* and evolution $f(v_\perp)$ are investigated.

The transformation of distribution function $f(v_\perp)$ can serve as one of attributes of the loss of beam stability [4]. In the considered guns infringement unimodality of oscillatory velocity distribution function is not registered at currents of a beam, even exceeding design value of current (I=40A). The specified circumstance gives grounds to hope , that the offered MIG will provide formation of a stable beam with acceptable parameters.

For experiments the method of a retarding field [5] was used. The measurements were carried out for a gun with R_c =45.2 mm in the scale-down regime on automated installation [6], both at presence of influence electrons catched in the adiabatic trap between the cathode and magnetic mirror, and at excepting such electrons. The received dependencies, $\delta v_\perp$ and $t_\perp$, are compared with results of numerical simulation and good correlation is observed.

The problem of provision of stable single-mode generation in an oversized resonator at sufficiently high efficiency and near-1MW level of the output power becomes more complicated at highs working frequency. An essential circumstance here is that this problem has to be solved within a number of limitations. The basic one is the limitation of density of ohmic losses in resonator walls - the energy load is limited by possibilities of the cooling system, which are, as a rule, not higher than 2–3 kW/cm^2. The

stability of operation is analyzed theoretically for more and more accurate models with consideration of two-mode and three-mode interaction. Besides stability of stationary regimes, nonstationary processes of mode interactions are studied, including those under variation of the electron beam parameters.

Parameters of RF radiation from the cavity have been computed basing on the advanced non-linear theory of interaction of the electron beam with the RF field of the cavity mode. For the optimized cavity profile, results of calculations of the output power P_{out}, efficiency η and thermal load of the cavity p_{ohm} depending on the electron beam current I are presented by Fig. 1. The calculations were done taking into account velocity spreads $\delta v_\perp$ in the electron beam. The thermal load is given for the cavity center where it is maximal. From investigations of the electron gun velocity spread $\delta v_\perp$ in the electron beam is expected to be near 0.3. Calculations show the possibility to attain the 1 MW output at the beam current below 40 A with an acceptable thermal load in the cavity. Special theoretical investigation has confirmed stability of operation of the $TE_{28\,7}$ ($TE_{31\,8}$) mode at its high-efficiency regimes.

The calculation has shown that in the optimized up-tapering waveguide connecting the cavity with the mode converter a parasitic RF power transformation of the $TE_{28\,7}$ ($TE_{31\,8}$) mode to other is below 1%.

The mode converter is a part of the internal electrodynamic system of the tube including the cavity as well. The converter separates RF radiation from the worked-out electron beam, transforms a complicated cavity mode to an easier transportable wave beam and allows to minimize the harmful action of possible reflections of RF power to a gyrotron. Optimization of a built-in converter in modern gyrotrons means now the optimization of RF field structure over the output window as well, in order to increase its permittivity, in addition to high efficiency of mode conversion. In the gyrotron, the converter consists of an irradiator and 3 mirrors.

The output window is a single boron nitride disk brazed into a metal cylinder with an output flange. The disk is cooled along its edge by flowing water. The main variant of the output window for 1 MW CW gyrotrons at frequencies 170 GHz is considered now a sapphire cryogenic window. Some other materials, e.g., high-purity and doped silicon, are under investigation as well.

Experimental investigations of a short-pulse prototype of the 170 GHz gyrotron were made on the automation set-up and dependencies of gyro-

tron parameters on the beam current, accelerating voltage and magnetic field are analyzed. The experimental results are compared with the calculated data. Results of measurements of the output power, P_{out}, and efficiency η depending on electron beam current I for the short-pulse experimental model of this gyrotron are presented in Fig. 2. Calculation and experimental data are in good correlation.

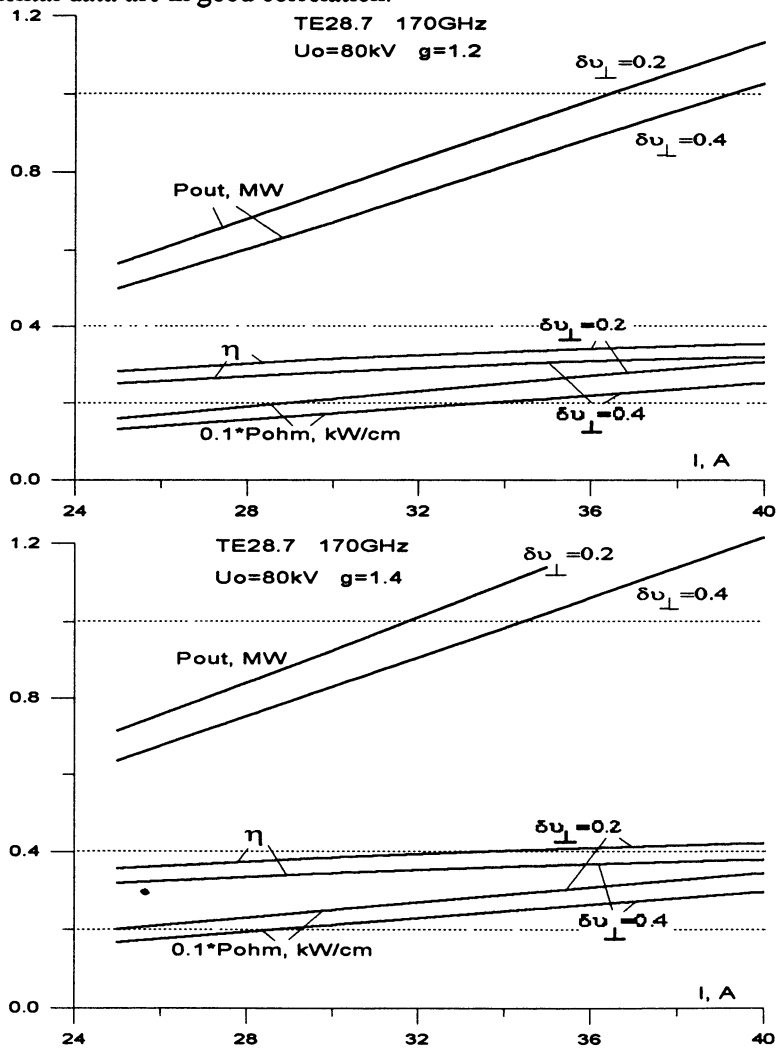

Fig. 1. Results of calculations of the output power P_{out}, efficiency η and thermal load of the cavity p_{ohm} vs. beam current I.

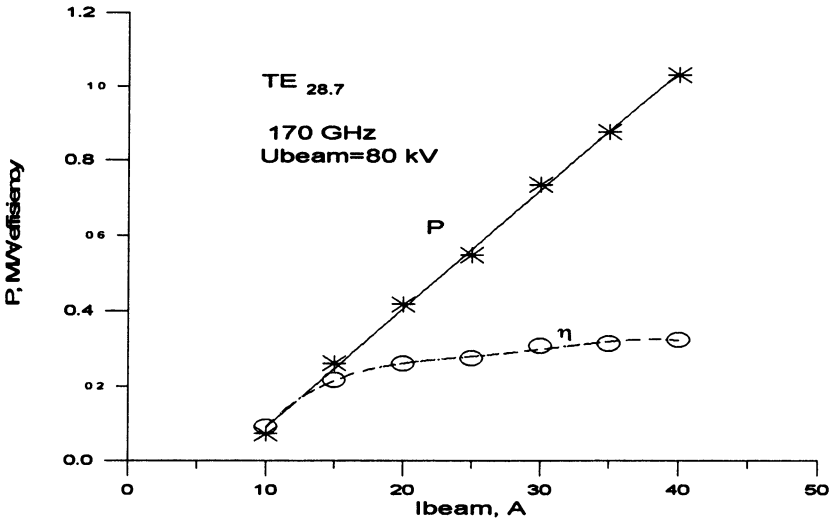

Fig.2. Results of measurements of the output power, and efficiency vs. beam current for short pulse experimental model of gyrotron.

The possibility to make the 170 GHz/1 MW gyrotron for ITER is proved by calculations and experiments. Numerical modeling and a series of experiments allowed creation of an electronic gun ensuring formation of an electron beam with parameters, necessary for the 170 GHz/1MW gyrotron. Calculation results and experimental data for the prototype 170 GHz/1 MW gyrotron for ITER are in good correlation. The successfully tested short-pulse prototype is a reliable ground for development of an industrial tube operating in the full-scale regime.

References

1. Denisov G.G., Flyagin V.A., Zapevalov V.E. Proc. 20 Int. Conf. on IR&MM waves. Orlando, USA, 1995, 197.
2. Kuftin A.N., Lygin V.K., Tsimring Sh.E., Zapevalov V.E. Int. J. Electronics, 72, (1992), 1145.
3. Lygin V.K. Int. J. of Infrared and Millimeter waves, 16(1995), 363.
4. Flyagin V.A., Goldenberg A.L., Zapevalov V.E. Proc. 18 Int. Conf. on IR&MM waves. Colchester, UK, 1993, v.2104, 581.
5. Goldenberg A.L., Avdoshin E.G. Izvestiya Vysshikh Uch. Zavedenii, Radiofizika, 16(1973), 1605 (in Russian).
6. Andronov A.N. et al. Proc. 20 Int. Conf. on IR&MM waves. Orlando, USA, 1995, 141.

SEPARATION OF ENERGETIC FRACTIONS OF ELECTRON BEAM BY CUSPED MAGNETIC FIELD

I.S.Kulagin, V.N.Manuilov, M.I.Petelin, N.I.Zaitsev

Institute of Applied Physics, Russian Academy of Sciences, Nizhny Novgorod, Russia

To increase the efficiency of a high-power microwave generator, one may split the spent electron beam into energetic fractions and collect each fraction at an electrode of a properly depressed potential. The larger is the number of separated fractions and of collecting electrodes, the higher is the efficiency (see, e.g. [1]).

If a tubular beam is confined magnetically, it can be split by a cusp formed with a counter co-axial solenoid. Indeed, electrons moving at the axis are not affected by the field. Evidently, electrons moving not far from the axis pierce the cusp as well. But if the energy of the non-axial electrons becomes small, they move adiabatically along magnetic lines and are deflected in radial direction (Fig. 1). These simple considerations allow us to hope that spent electrons can be separated at least into two fractions.

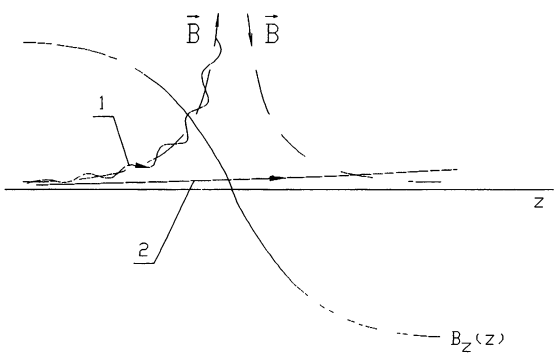

Fig. 1. Scheme of separation of electrons depending on their energy in the cusp magnetic field: 1 - trajectory of a small-energy electron; 2 - trajectory of a high-energy electron.

The separation effect was verified experimentally at the system shown in Fig. 2. An axisymmetric glass vessel covered on inside with luminophor was placed in a cusped magnetic field formed by coils 1 and 3, and reverse-field coil 2. At the homogeneity region the field was equal to 1 T. This vacuum tube had a widened electron-collecting section 120 mm in diameter. A Pierce-type electron gun producing an electron beam 1 mm in

diameter was placed at 5 mm from the axis. The accelerating voltage was changed in the range from 0 to 20 kV.

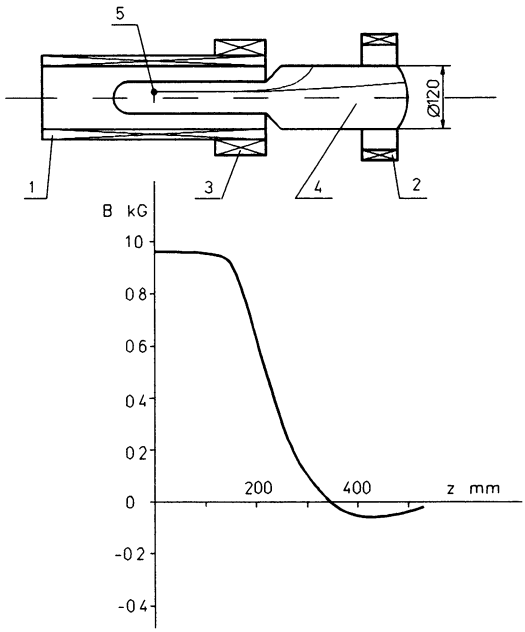

Fig. 2. Scheme of the experiment and corresponding profile of the magnetic field: 1 - main coil; 2 - reverse-field coil; 3 - additional coil; 4 - cathode-ray tube; 5 - electron gun.

Calculated electron trajectories for different energies are presented in Fig. 3. Trajectories differ by initial radial location changing within the range of 1 mm (from 4.5 to 5.5 mm). Sometimes this difference leads to essential distinctions between electron trajectories. All electrons with energies over 8 keV pass through the reverse region. If the energy is from 4 to 8 keV, a part of electrons being initially farther from the axis is reflected before the reverse magnetic field reaches its maximum. After the reflection some electrons settle on tube side walls immediately and the rest, after several longitudinal oscillations. The part of the latter electrons and the number of their longitudinal oscillations grow as the electron energy drops. If the electron energy is less than 4 kV, all electrons are reflected and finally settle on side walls of the tube. If the electron energy is of the order of 100 eV, the electrons become "adiabatic" and move along the magnetic field line and settle on a side wall of the tube near the reverse

plane. It should be noted that the area of "adiabatic" electrons is entirely overlapped by the area of oscillatory electrons.

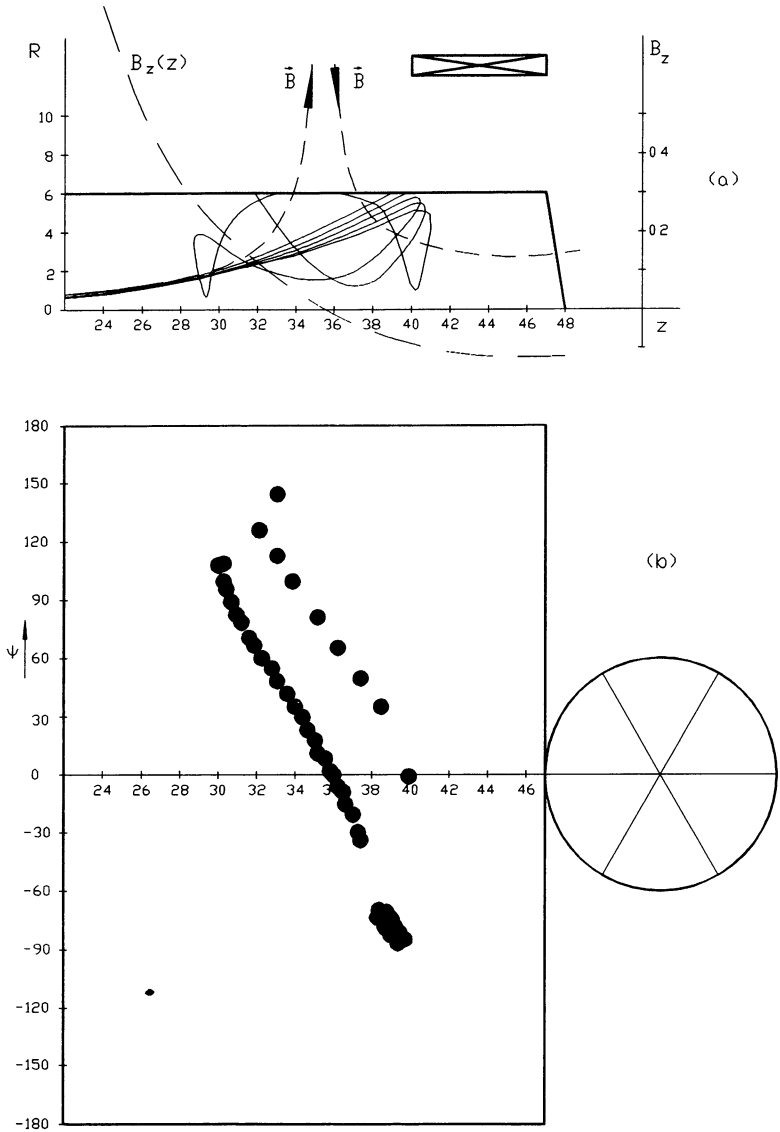

Fig. 3,a. Calculated trajectories (a) and traces (b) on the tube development at the accelerating voltage 4 kV. View of the development from inside. ψ=0° is the cathode azimuth.

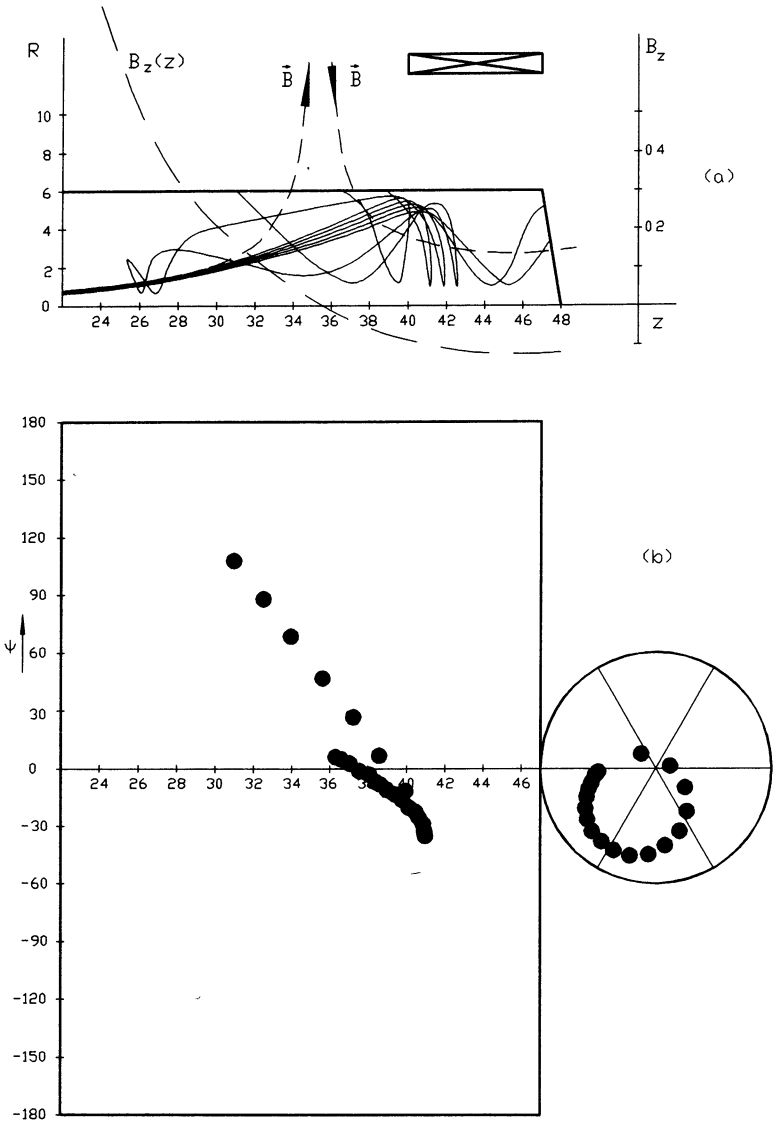

Fig. 3,b. Calculated trajectories (a) and traces (b) on the tube development at the accelerating voltage 6 kV. View of the development from inside. ψ=0° is the cathode azimuth.

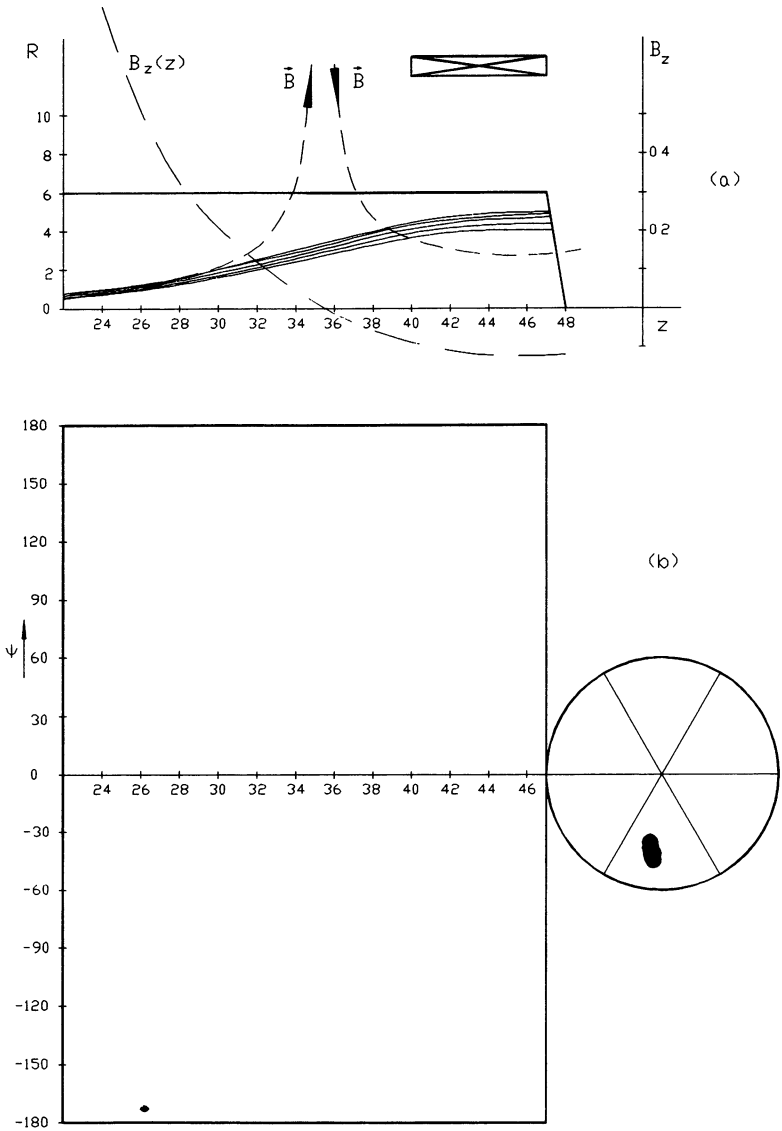

Fig. 3,c. Calculated trajectories (a) and traces (b) on the tube development at the accelerating voltage 20 kV. View of the development from inside. ψ=0° is the cathode azimuth.

Typical beam traces on the tube surface seen in the experiment are presented in Fig. 4. High-energy electrons pass through the cusp region and make an arc-like trace on the tube end. As the energy of electrons

drops, a part of electrons is reflected and then makes some strips on the tube side wall. Different strips correspond to different numbers of longitudinal oscillations, their locations are in good agreement with the numerical simulation.

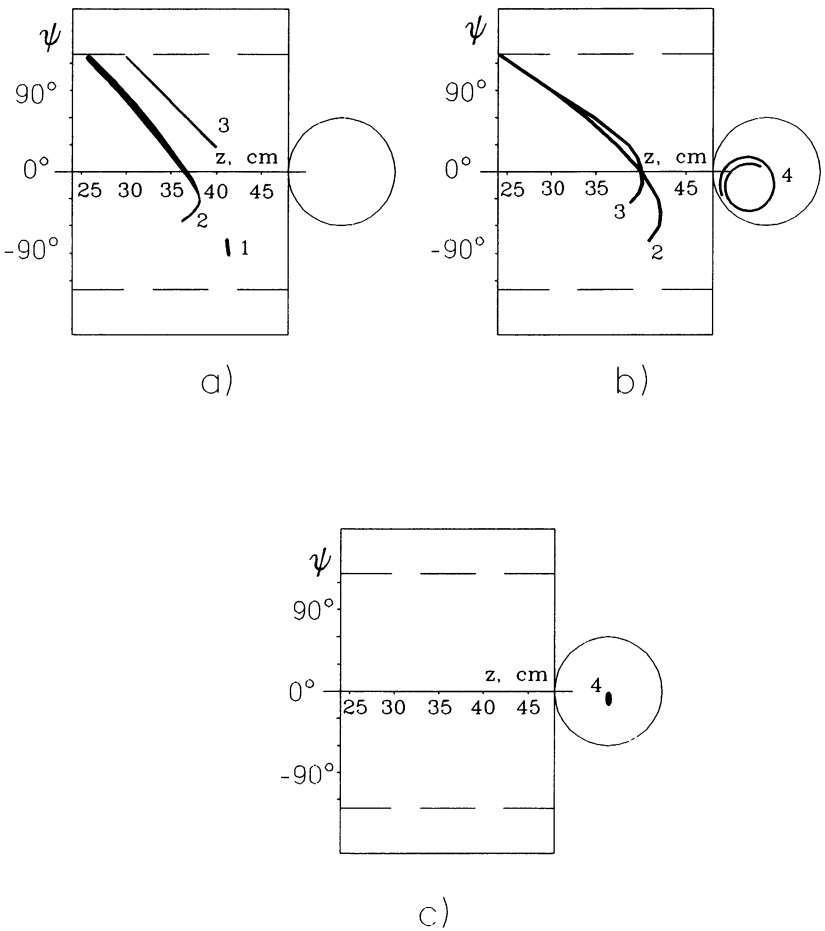

Fig. 4. Electron beam traces on the tube surface development; view from inside through the luminophor-free window, its border is marked by dashed lines; ψ=0° is the cathode azimuth: (a) - U=5 kV: (b) - U=10 kV; (c) - U=20 kV. Kinds of traces: 1 - near-"adiabatic" electrons; 2,3 - non-adiabatic oscillatory electrons after one (2) or two (3) reflections in the magnetic field; 4 - non-adiabatic electrons piercing the cusp.

Thus, the beam is separated by the cusped magnetic field at least into two energetic fractions. In microwave generators this effect can be used to develop a collector consisting of two sections with different potentials, both being lower than the potential of the RF interaction space (see Fig. 5).

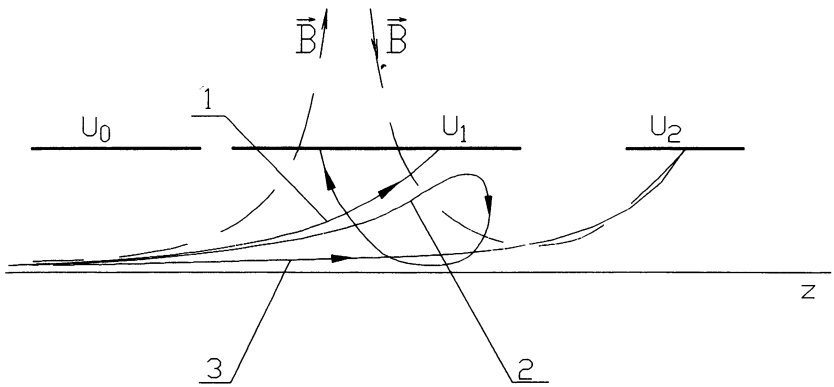

Fig. 5. Scheme of a depressed collector. Trajectories of electrons with different energies ($W_1<W_2<W_3$) are shown: 1 - energy W_1; 2 - energy W_2; 3 - energy W_3. U_0-U_2 - electrode potentials ($U_0<U_1<U_2$).

Note that the development of depressed collector based on the described separating system must be carried out taking into account the decelerating electric field and secondary electrons emitted from the collector surface.

Reference

1. Borodachova T.V., Goldenberg A.L., Manuilov V.N. In: Gyrotrons. IAP, Gorky, 1989, pp.161-180.

HIGH-POWER MICROWAVE PRODUCTION BY GYROHARMONIC CONVERSION AND CO-GENERATION

J. L. Hirshfield,[*§] *M. A. LaPointe,*[*] *R. B. Yoder,*[§] *A. K. Ganguly,*[*] *Changbiao Wang*[§] *and B. Hafizi*[*]

[*]Omega-P, Inc., 202008 Yale Station, New Haven, CT 06520
[§]Physics Department, Yale University, New Haven, CT 06511

ABSTRACT

An rf accelerator that adds significant gyration energy to a relativistic electron beam, and two mechanisms for extracting coherent radiation from the beam, are described. The accelerator is a cyclotron autoresonance accelerator (CARA), underlying theory and experimental tests of which are reviewed. These illustrate the utility of CARA in preparing beams for high harmonic gyro interactions. Examples of preparation of gyrating axis-encircling beams of ~400 kV, 25 A with $1 < \alpha < 2$ using a 2.856 GHz CARA are discussed. Generation of MW-level harmonic power emanating from a beam prepared in CARA into an output cavity structure is also described, including measurements of rf spectrum and power. The potential for gyroharmonic conversion (GHC) at higher powers and higher frequencies is discussed, in view of the results described here. A new radiation mechanism, closely related to GHC, is also described. This mechanism, dubbed "co-generation", is based on the fact that the lowest TE_{sm} mode in a cylindrical waveguide at frequency $s\omega$ with group velocity nearly identical to group velocity for the TE_{11} mode at frequency ω is that with $s = 7$, $m = 2$. This allows coherent radiation to be generated at the 7th harmonic co-existent with CARA and in the self-same rf structure. Conditions are found where co-generation of 7th harmonic power at 20 GHz is possible with overall efficiency greater than 80%. It is shown that operation of a cw co-generator can take place without need of a power supply for the gun. Efficiency for a multi-MW 20 GHz co-generator is predicted to be high enough to compete with other sources, even after taking into account the finite efficiency of the rf driver required for CARA.

INTRODUCTION

Considerable interest exists in new concepts for producing high peak power (>150 MW), narrow band, low duty-cycle, low pulse repetition frequency (~1 kHz) pulsed rf amplifiers operating at 1.0 GHz or higher frequency for use in large electron/positron linear colliders. For these devices, electrical efficiencies greater than 45% are considered essential. As a result, effort is underway for development of rf sources to meet this need, including klystrons [1], relativistic klystrons [2], cluster klystrons [3], gyroklystrons [4], magnicons [5] and gyro-harmonic converters [6]. Much of the klystron development is at 11.424 GHz, where the Next Linear Collider Test Accelerator (NLCTA) is to be operated at SLAC. A new magnicon design at 11.424 GHz has recently been perfected [6], in which higher power and efficiency are predicted than have been achieved with klystrons. A relativistic klystron [2] and second harmonic gyroklystron [4] are being investigated for operation at 17.136 GHz. But little effort has gone into study of sources at higher frequencies, even though it has been pointed out [7] that high energy colliders (>1 TeV) will probably have to operate at 20 GHz or above. For example, a study for a 5 TeV center-of-mass collider shows that operation at 34.3 GHz could allow a loaded acceleration gradient of 150 MV/m to be sustained, leading to an active accelerator length of 17 km [8]. It will not be argued either way in this paper whether or not construction of a machine of this magnitude will be practical in the forseeable future. But it is clear that demonstration of an acceptable rf source at a frequency of 20 GHz or higher is essential for the rational planning of such a machine.

This paper describes recent progress on experimental and theoretical understanding of gyroharmonic conversion (GHC) and co-generation. These processes could have the potential for efficient production of high-power cm-wavelength radiation suitable for collider applications. In GHC, low frequency rf drive power is used to energize an electron beam in a magnetic field, and the beam is then allowed to selectively emit coherent radiation at a harmonic of the drive frequency [6]. As with the magnicon, no bunching is induced on the beam in GHC, and all electrons can experience nearly identical forces from the rf fields. This can lead to high conversion efficiencies, computed to be above 70% at the 5th harmonic under ideal conditions [6]. With efficient energy recovery from the spent beam using a depressed collector, the electrical efficiency might be as high as 85%. If a 150 MW rf drive pulse at 2.9 GHz were used, such as that produced with DESY klystrons [9], one finds 100 MW and 300 J/pulse to be produced at the harmonic. This is sufficient energy/pulse to drive ~11 m of a 34 GHz multi-TeV collider. If the efficiency of the rf drive source is 53%, one finds that GHC can have an overall efficiency of 45%, as required. This crude estimate defines the goals that must be achieved for GHC to be a serious contender for future collider applications. Herein, a progress report is presented on work to date on

GHC, with experiemtal results of 4th harmonic conversion at 11.4 GHz. In addition, a new approach for efficient utilization of a CARA beam for 7th harmonic co-generation at 20 GHz is described, wherein efficiencies exceeding 80% are predicted.

CYCLOTRON AUTORESONANCE ACCELERATION (CARA)

A sketch of the Yale/Omega-P GHC experimental device is given in Fig. 1. The device has three major parts: (i) a Pierce-type diode electron gun that injects a pencil beam; (ii) a cyclotron autoresonance accelerator (CARA) that

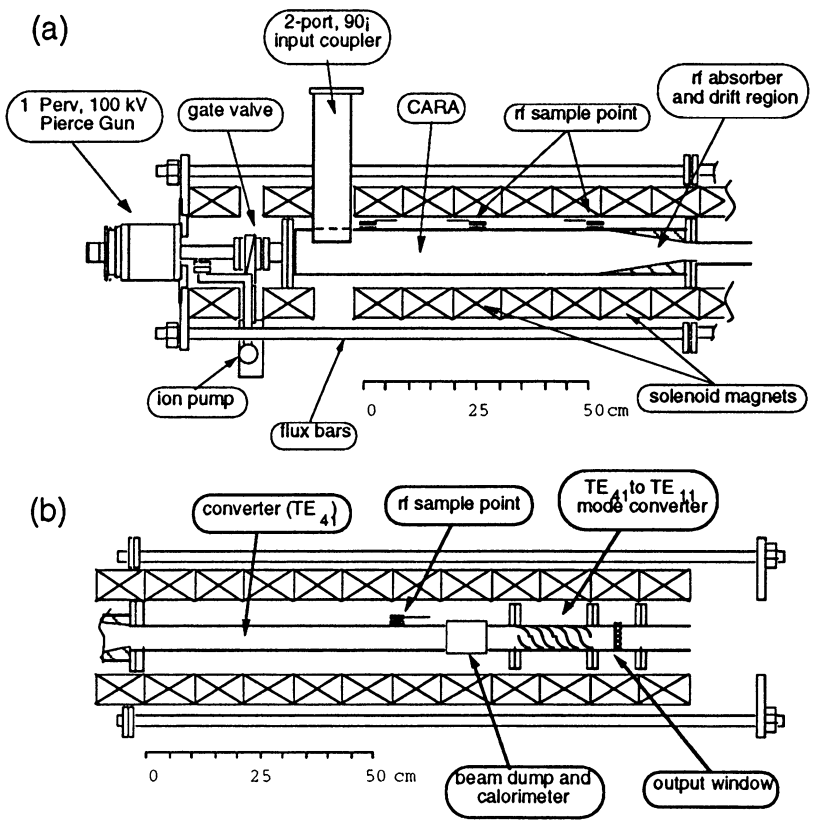

Fig. 1. Schematic diagram of the Yale/Omega-P cyclotron autoresonance accelerator (a) and gyroharmonic converter (b). During measurements, the GHC is terminated either with a radiating horn or with a calorimeter.

energizes the beam and produces axis-encircling gyrating orbits that rotate in time at the CARA drive frequency; and (iii) a converter waveguide or cavity in which coherent radiation is generated by the beam at harmonic of the CARA drive frequency. In the Yale/Omega-P apparatus, CARA is driven at 2.856 GHz, using a former SLAC XK-5 klystron that produces up to 24 MW, 3 μsec pulses at up to a 10 Hz repetition rate. The 1.0 μPerv injector gun operates up to 100 kV, with a current of up to 31 A. The guide magnetic field is produced by up to 20 individually-energized coils whose power supplies are externally-programmed to produce desired field profiles. Here, measurements of CARA performance are described in which a beam collector with a built-in calorimeter is substiuted for the converter section shown in the bottom half of Fig. 1.

Prior theory and simulation studies for CARA predict that high efficiency transfer of rf power to beam power can occur, provided that the injected beam does not have too large an axial velocity spread, and provided the magnetic field profile is judiciously adjusted [10,11]. To date, ~25 A beams of up to ~10 MW beam power have been produced, with efficiency values of between 90% and 96%. Higher beam powers might seem possible, since 24 MW of rf power is

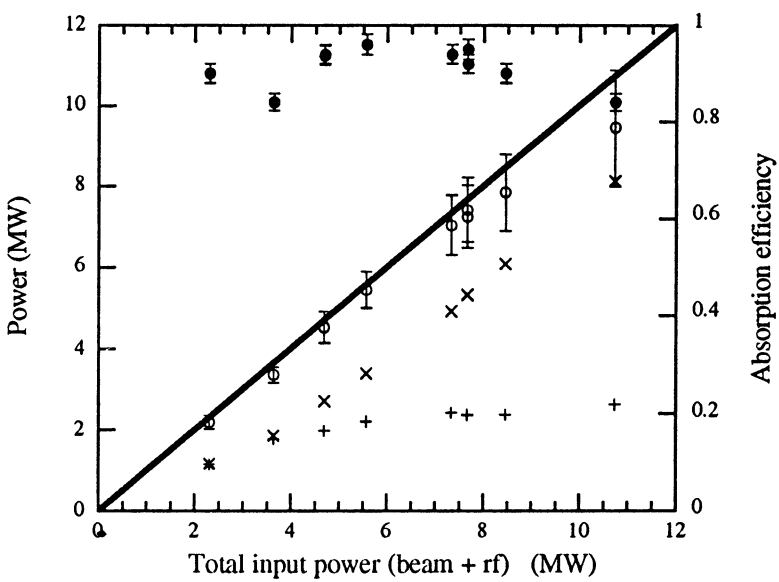

Fig. 2. Beam power and efficiency for the Yale/Omega-P CARA. Key to the symbols: (+) initial beam power; (×) initial rf power; (o) final beam power; (•) efficiency.

available, but this is not the case, since the upper energy limit in CARA for 100 kV injection is about 435 keV for beam matching into GHC at grazing [11]. A summary of the data for CARA operation is given in Fig. 2, where total input power (beam + rf) is the independent variable, with output beam power and efficiency are the dependent variables. Details of this experiment are found in two recent publications [12,13], and will not be restated here. Significant points established by the measurements include (a) confirmation of theory regards high rf power transfer efficiency; (b) observed resilience to detrapping when the actual magnetic field profile deviates from the ideal profile; and (c) an achievement of final beam energies in accordance with theoretical predictions.

These measurements add evidence to earlier contentions [6] that CARA is well suited for preparation of beams for injection into GHC output structures for generation of harmonic output power. In experiments to be described in the next section of this paper, the rf power levels are limited, since the maximum CARA beam power achieved is about 10 MW. By comparison, injection of a 350 kV, 200 A beam into an upgraded CARA, driven with 140 MW of rf from a DESY klystron, would allow a 1.0 MeV, 200 MW beam to be produced and injected at grazing into a GHC.

GYROHARMONIC CONVERSION (GHC)

Theoretical and computational studies have shown that the efficiency of gyroharmonic conversion (GHC) is sensitive to the quality of the injected beam, and to the strength of competing rf modes in the output structure [6]. In the Yale/Omega-P apparatus, the injected beam (up to 100 kV, 31 A) is computed to have an rms axial velocity spread of 0.10%, based on simulation studies using the relativistic DEMEOS code [14]. The axial velocity spread is magnified in CARA, and upon entrance to the rf output structure it can reach rms values in the range 0.5% - 1.0%, depending upon the magnitude of the magnetic guide field up-taper between CARA and the output section. The growth of axial velocity spread can be controlled to some extent, by use of a small detuning away from exact resonance of the magnetic field profile in CARA [15]. For an axis-encircling cold beam at grazing, theory predicts that no output radiation is coupled into TM modes, and that radiation at the s-th harmonic is coupled only into TE_{sm} modes, where m = 1,2,3.... The most dangerous competing mode in a waveguide output section has been shown to be the one lower than the design mode, if it is not cutoff; otherwise, it is at the next higher harmonic. In a cavity output section designed to operate in the TE_{411} mode, for example, 4th harmonic competition could be anticipated from the TE_{412} and TE_{413} modes, if these are so closely spaced so as to be within the beam's gain spectrum.

Experiments have been conducted with 50-cm and 20-cm long output sections, with output radiation passing through a mode converter designed to transform the TE_{41} rotating mode at 11.424 GHz into a TE_{11} rotating mode. The radiation then passed a single-disk alumina window and was either broadcast by a horn and detected in an anechoic chamber, or absorbed in a calorimeter. Initital experiments were with a copper output waveguide of length 50 cm and radius 2.323 cm. This radius is 0.8% smaller than the cutoff radius at 8.568 GHz (3rd harmonic) in the TE_{31} mode, and 4.5% larger than the cutoff radius at 11.424 GHz (4th harmonic) in the TE_{41} mode. Yet only 3rd harmonic radiation was detected. It was concluded that dielectric pulling by the beam lowered the TE_{31} mode cutoff frequency by about 1%, thereby allowing the 3rd harmonic to dominate. A modified output section--also 50 cm in length--was then employed, but with a radius of 2.205 cm, namely 0.8% smaller than the cutoff radius at 11.424 GHz for the TE_{41} mode, but 5.8% smaller than the cutoff radius for the TE_{31} mode at 8.568 GHz. This section, fabricated from stainless steel, had a 1.3 deg up-taper in radius to the 2.323 cm output waveguide. For this structure, no 3rd harmonic radiation was observed, but the spectrum of emission near 11.4 GHz was unacceptably broad. It is possible that the dense spectrum of TE_{41n} modes were so closely spaced that, each with relatively low ohmic Q's attributal to the stainless steel walls, the lower-order modes merged, yielding a non-selective frequency response [16]. A third modification was then substituted, a copper section of length 20 cm, radius 2.205 cm, also with a 1.3 deg taper to the 2.323 cm outpfut waveguide. Preliminary observations with this circuit showed generally higher output powers than with the previous circuits, easily detectable with the calorimeter. Narrow spectra centered on the 3rd or 4th harmonics were observed, depending on the magnetic field profile chosen. At this writing, measurements continue, and output cavity modifications are underway with the goal of maximizing output at 11.424 GHz.

Analysis and computations have been carried out for cavity output sections as employed in the aforementioned experiments. Simulation of the mode properties of the 20-cm long copper circuit showed that the TE_{411} and TE_{412} modes have cold resonant frequencies of 11.53 and 11.59 GHz; and Q's of 1,061 and 264, respectively. An example of a particle simulation study is shown in Fig. 3 for conditions not greatly dissimilar from those of the experiments. Details of the underlying theoretical considerations and computational method will be discussed in a forthcoming publication [17]. The parameters for the simulation are listed in the figure, including a cavity radius of 2.2257 cm, which was chosen to simulate the loaded cutoff frequency of the actual 2.205 cm cavity in the presence of the beam. The computation shows an output efficiency of 34.8%, corresponding to a power output of 2.55 MW plus 0.15 MW lost in the cavity walls. Other computations show that the output efficiency can be higher for a shorter cavity. But it does not appear likely that

practical conditions can be found with efficiencies above 50% for cavity gyroharmonic conversion at the 4th harmonic or above as described here.

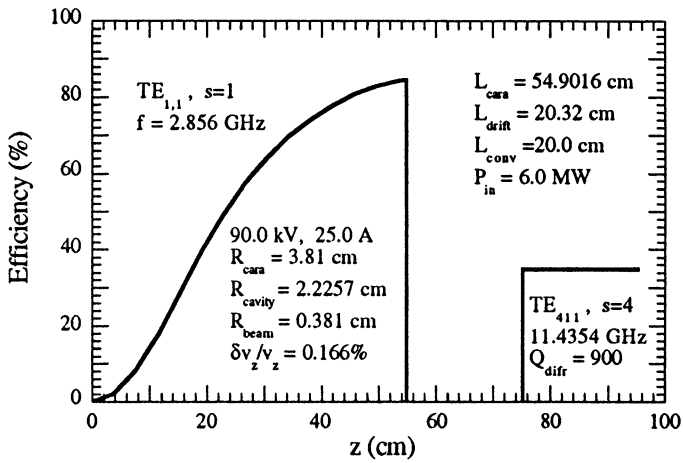

Fig. 3 Efficiency for CARA (left) and for GHC with cavity output (right). Parameters are as indicated in the figure. Computed power output is 2.55 MW.

SEVENTH-HARMONIC CO-GENERATION

It has not generally been noted that certain $TE_{s\ell}$ electromagnetic modes of a cylindrical waveguide at frequency $s\omega$ exhibit coincidental near matching between their group velocities and those of the TE_{11} mode at frequency ω. This basic characteristic of the simplest closed guided wave structure may allow the excitation of strong s-th harmonic radiation when a fundamental injected wave interacts with a nonlinear medium in the waveguide. Group velocity matching can allow classical parametric interactions to occur [18] but, as will be shown here, it may also allow coupling in which the nonlinear medium supplies and receives significant power to and from the waves. The nonlinear medium for the work presented here is a relativistic gyrating electron beam; the fundamential TE_{11} mode excites cyclotron autoresonance acceleration (CARA) of the beam [2]; and the lowest mode for which a near match in group velocity obtains is the $TE_{7,2}$ at the seventh harmonic. It will be shown that high efficiency production of multi-megawatt power at 20 GHz is possible through this "co-generation" mechanism, when a beam is energized using 2.856 GHz power. Other high

power microwave TE-mode fast-wave harmonic interactions may also be enhanced by this matching phenomenon, including the gyro traveling-wave amplifier, gyroklystron and waveguide free-electron laser [19]. Similar matching phenomema for TM-modes may enhance other types of harmonic interactions, such as in the frequency-doubling magnicon [5].

The term "co-generation" is used here to signify that harmonic power is generated in the self-same structure where CARA acceleration (and deceleration) of the beam occurs. Since the interaction to be discussed occurs in a traveling-wave structure, injected rf power that does not become transformed into the harmonic wave can be recovered, recycled and perhaps used in a subsequent co-generator stage. Energy in the spent electron beam emerging from the interaction can also be recovered with high efficiency, since the energy spread on the beam induced in the acceleration and generation processes can be small. It is these unusual features that permit overall 7th harmonic co-generation efficiencies greater than 80% to be predicted, as is illustrated below.

The requirement for group velocity matching for efficient power transfer between two guided waves that interact with an electron beam near gyroresonance and its harmonics can be easily appreciated. Below are written the resonance conditions that must be satisfied for simultaneous acceleration due to the CARA mechanism, and for deceleration due to the generation of radiation near the s-th gyroharmonic, namely

$$\omega = \frac{\Omega}{\gamma} + ck_{z,11}\beta_z, \tag{1}$$

and

$$s\omega = \frac{s\Omega}{\gamma} + ck_{z,s\ell}\beta_z. \tag{2}$$

In Eqs. (1) and (2), ω is the radian frequency at which CARA is operated, $\Omega = eB_o/m$ is the rest gyrofrequency for electrons of mass m and charge e in a magnetic field B_o, γ and $c\beta_z$ are the relativistic energy factor and the axial velocity for the beam electrons, and $k_{z,s\ell} = (s\omega/c)\left(v_{g,s\ell}/c\right) = (s\omega/c)n_{s\ell}$ is the axial wavenumber, itself proportional to the normalized group velocity $n_{s\ell}$ for each wave; for CARA, $s = \ell = 1$. Clearly, Eqs. (1) and (2) cannot be satisfield simultaneously unless

$$\frac{k_{z,s\ell}}{s} = k_{z,11} \qquad \text{or} \qquad n_{s\ell} = n_{11}\ , \tag{3}$$

namely equal group velocities for the two modes, when the frequency of the $TE_{s\ell}$ mode is s times that of the TE_{11} mode. This is consistent with the selection rule for gyroharmonic conversion with an axis-encircling beam in a cylindrical waveguide, namely that power at the s-th harmonic can flow cumulatively from the beam only into $TE_{s\ell}$ modes [6]. A measure of the degree to which $TE_{s\ell}$ modes satisfy Eq. (3) can be seen by substituting into it the relation $n_{s\ell} = \sqrt{1-(j'_{s\ell}c/s\omega R)^2}$, where $j'_{s\ell}$ is the ℓ-th zero of the Bessel function derivative $(d/dx)J_s(x)$, and where R is the waveguide radius. When $n_{s\ell} \approx n_{11}$, one can derive the approximate relationship

$$\frac{n_{s\ell}}{n_{11}} \approx 1+(1-r_{s\ell})\left(\frac{1}{n_{11}^2}-1\right), \tag{4}$$

where $r_{s\ell} = j'_{s\ell}/sj'_{11}$. In Fig. 4 are plotted values of $r_{s\ell}$ for modes with ℓ (the radial index) up to 6, and s (the azimuthal index) up to 30. It is seen that $r_{s\ell}$ is within the range 1.00 ± 0.005 for the $TE_{7,2}$, $TE_{13,3}$, $TE_{24,5}$ and $TE_{30,6}$ modes. This suggests that one might find conditions where a prescribed magnetic field profile allows efficient CARA acceleration, and simultaneously

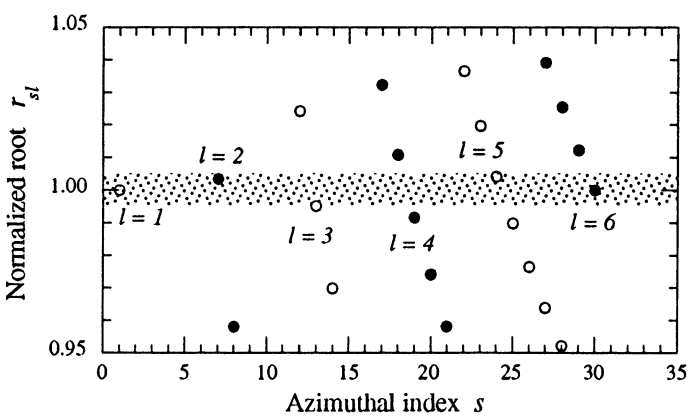

Fig. 4. Ratio of Bessel function roots $r_{s\ell}$. In shaded area $0.995 < r_{s\ell} < 1.005$.

allows strong radiation at one or more of the 7th, 13th, 24th and 30th harmonics. Since succesively higher beam energies are required to obtain

significant coupling as s increases, there is reason to expect that conditions might be found where only one of these modes will be excited at a time. In a rectangular waveguide, group velocity matching is much more prevalent, occuring (for example) between the TE_{01} and all TE_{0s} modes at the s-th harmonics. This situation could lead to serious mode competition at high harmonics; moreover, the aforementioned selection rule for axis-encircling beams does not apply for rectangular waveguides. Thus, only cylindrical waveguides are appropriate for co-generation.

In this paper, we examine co-generation only at the 7th harmonic, but possible competing modes are also considered. We take the rf source frequency to be 2.856 GHz, corresponding to the frequency of the 65 MW klystrons (type 5045) that drive the Stanford Linear Collider (SLC), so that the 7th harmonic is at 19.992 GHz. A calculation could be made for any rf source frequency, but we purposely have chosen 2.856 GHz in anticipation of conducting experiments using an existing rf source, and in conceiving of the rf driver system for a future multi-TeV electron-positron collider being built using existing mature rf technology, including type 5045 klystrons. Thus to examine in detail the co-generation of harmonic radiation within CARA, particle simulation studies were carried out with rf and injected beam powers corresponding to Yale/Omega-P experimental capabilities, namely for an rf source power level at 2.856 GHz of 10.0 MW, and an injected beam of 100 kV, 25 A.

Results to illustrate the principle of co-generation are shown in Fig. 5 for an ideal "cold" beam, i.e., a beam with no initial axial momentum spread or guiding center spread. Fig. 5a shows the evolution along the axis in CARA of rf power in the TE_{11} and $TE_{7,2}$ modes at 2.856 GHz and 19.99 GHz in a waveguide of radius 3.65 cm (n_{11} = 0.5374 and $n_{7,2}$ = 0.5329); Fig. 5a also shows the variation in imposed resonant axial magnetic field, according to Eq. (1). A pronounced recurrence phenomenon is observed, with rf power shifting back and forth between the fundamental and the 7th harmonic waves. At z = 84.0 cm, where the 7th harmonic power has reached 3.32 MW, the fundamental power is 6.22 MW, and the sum of the two is only 5% less than the 10.0 MW fun fundamental power injected initially. Fig. 5b shows the ensemble-average beam energy factor $\langle\gamma\rangle$, the relative rms energy spread $\delta\gamma/\langle\gamma\rangle$, and the ratio of the ensemble-average gyration radius to waveguide radius $\langle r_g/R\rangle$. The beam energy at z = 84.0 cm is 100.4 kV, so the beam is seen to have acted essentially as a catalyst by exchanging power with the rf modes up to this point, but returning nearly to its original state. At z = 167.2 cm, the fundamental rf power level has risen to 9.45 MW, and only 0.31 MW resides in the 7th harmonic wave; again the beam energy is back to 99.9 kV. In the course of this

one full reccurence cycle, the magnetic field varies quasi-sinusoidally between 0.86 and 1.55 kG. Fig. 5c shows the rf power at the 6th harmonic in the $TE_{6,2}$

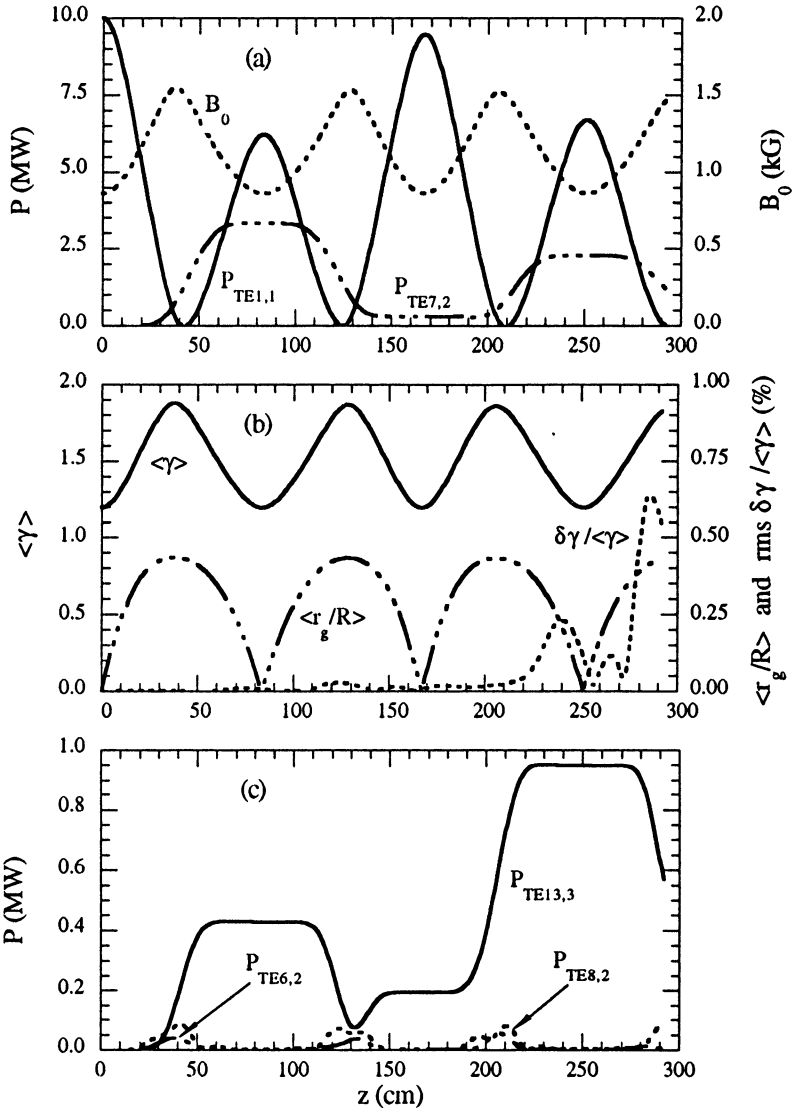

Fig. 5. Parameters for 7th harmonic co-generation for an initially cold beam. Parameters are described in text.

mode, at the 8th harmonic in the $TE_{8,2}$ mode, and at the 13th harmonic in the $TE_{13,3}$ mode. The maximum total of 6th and 8th harmonic power is 0.13 MW, the 13th harmonic power is seen to reach 0.427 MW at z = 84.0 cm, and 0.949 MW at z = 251 cm. The fact that the $TE_{13,3}$ mode is the only serious competitor to the $TE_{7,2}$ enforces the claim made above that group velocity matching is a major factor in co-generation, since $n_{13,3}$ = 0.5438. More power appears at the 13th harmonic during the second recurrence cycle because of injection of finite power from the first cycle. Were the device to be terminated at z = 84.0 cm, rf power could be extracted with about one-third at the 7th harmonic and two-thirds at the fundamental; the beam power could in principle be largely recovered using a depressed collector. The 6.22 MW of extracted fundamental power could, in principle, be used (with an additional 3.78 MW) to drive a second CARA identical to the first, and the sequence continued indefinitely. Such a system would have a nearly ideal conversion efficiency, the net effect of which is to convert rf power from the fundamental to the 7th harmonic. Losses in this system arise from finite conductivity in the waveguide walls, from imperfect beam power recovery at a depressed collector, and from power converted to competing harmonics. But these can each be small fractions of the total 12.5 MW in circulation. Of course, an injected beam with zero axial velocity spread is an idealization that cannot be met in practice.

Results of a computation for an injected beam with a finite rms axial velocity spread of 0.10% are shown in Fig. 6, with the various quantities displayed as in Fig. 5. The basis for employing this value of axial velocity spread is a design study using the DEMEOS code [14] for the moderate convergence, perveance $K = 1.0\times10^{-6}$ A-V$^{-3/2}$ Pierce-type electron gun that is in operation on the Yale/Omega-P CARA. Two significant additional features are present in this example, namely a detuning of the axial magnetic field from exact resonance, and a finite amplitude injected signal at the 7th harmonic. Without magnetic field detuning, co-generation is found to be severely weakend by velocity spread. The optimum detuning parameter $\Delta = \Omega/\omega\gamma\beta_z - 1/\beta_z + n_{11}$ for this case was found to be -0.02. Injection at the CARA input of 0.10 MW of 7th harmonic power in the $TE_{7,2}$ mode was found to yield a 7th harmonic power level at z = 82 cm of 1.99 MW, as shown in Fig. 3a. To achieve this result, it was necessary to optimize the phase of the injected initial 7th harmonic power; a relative phase of 0.6π maximized the production of 7th harmonic power. If the injected 7th harmonic power level is increased from 0.1 to 1.0 MW, the 7th harmonic output increases to 3.9 MW, for gain of an additional 1.0 MW. Injection can be accomplished by re-circulating to the input a portion of the 7th harmonic output power.

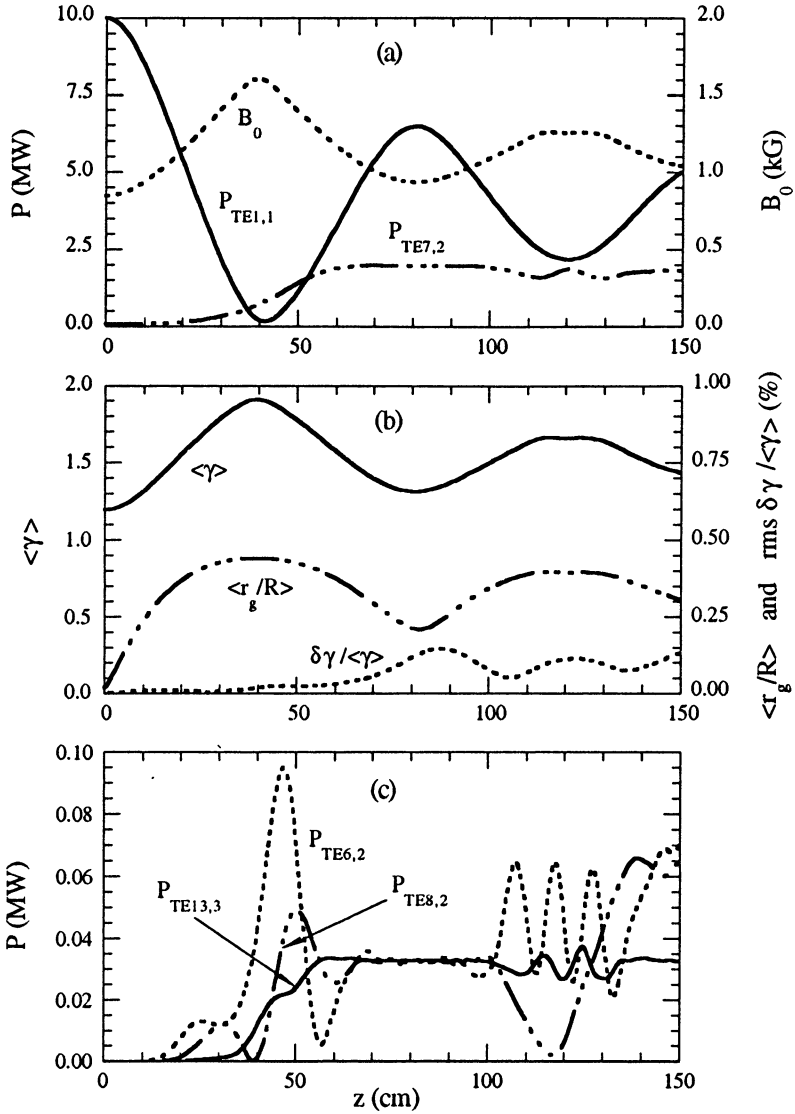

Fig. 6. Same as Fig. 5, except for a beam with an initial rms axial velocity spread of 0.10%.

If a device based on the results shown in Fig. 6 were terminated at z = 82 cm, one could extract 1.99 MW of 7th harmonic power, 6.47 MW of fundamental harmonic power, and 0.098 MW of power in competing harmonics. The efficiency for utilization of rf power then follows as η_{rf} = (1.99 + 6.47)/10.10 = 83.8%. If energy in the spent electron beam is included (3.86 MW), one would have η_{total} = (8.46 + 3.86 η_{rec})/12.6, where η_{rec} is the efficiency for recovery of beam power using a depressed collector. One can define $\eta_{rec} = (\gamma_r - 1)/(\langle\gamma_s\rangle - 1)$ as an ideal recovery efficiency for a single-stage depressed collector, where $\gamma_r = 1 + e|V_r|/mc^2$ is the energy factor corresponding to the collector retarding potential V_r, and where $\langle\gamma_s\rangle$ is the average energy factor of the spent beam particles. To avoid undesirable beam reflection at the collector, γ_r is taken to be the lowest value of beam energy factor in the spent beam. For the beam at z = 82 cm in Fig. 6, computations have been performed that yield η_{rec} = 63.0%. Using this gives η_{total} = 86.4%. This figure embodies several idealizations, but it seems high enough to provide strong motivation for further study of co-generation.

DISCUSSION

Experiments on CARA show that gyration energy can be imparted to a high power electron beam with efficiency values that exceed those for other fast-wave interactions. Copious radiation from energetic beams prepared in CARA has been observed, mainly near the 3rd gyroharmonic, with reactive pulling of overmoded output cavity structures evidently introducing unforeseen challanges for cavity design. Efforts continue on the experiments described in this paper. However, the concept of gyroharmonic co-generation suggests that it may be not unreasonable to conceive of high power 20 GHz co-generators with a total power efficiency of greater than 80%. These could be driven using existing SLC klystrons and associated modulators. The examples presented in this paper are for a 10 MW rf driver, namely at the level where experimental tests are planned. So further studies are required to optimize a system using 65 MW input pulses such as type 5045 klystrons provide. But it does not seem unreasonable for each co-generator in such a system to provide 50-60 J output pulses at 20 GHz with an overall rf system efficiency, including the klystron drivers, that would exceed 50%. This system could constitute the sought-after rf source for a future multi-TeV electron-positron collider. Co-generation interactions with other fast-wave interactions should also be possible, as shown by preliminary experiments on 7th harmonic generation in a waveguide FEL amplifier [19]. Needless to say, the potential and practicalilty of co-generation will not be fully confirmed until additional experiments and design studies of this new mechanism are carried out.

ACKNOWLEDGEMENT

This research was sponsored in part by the US Department of Energy and in part by the US Office of Naval Research.

REFERENCES

1. G. Caryotakis, *IEEE Trans. Plasma Science* **22**, 756 (1994).
2. J. Haimson, B. Mecklenburg and B. G. Danly, in *Pulsed RF Sources for Linear Colliders*, AIP Conf. Proc. **337**,146, R. C. Fernow, ed. (Amer. Inst. of Phys, New York, 1995).
3. R. B. Palmer, *et al*, ibid., p. 94; H. Wang, *et al*, ibid., p. 103.
4. J. P. Calame, *et al*, ibid., p. 195.
5. O. A. Nezhevenko, ibid., p. 172; S. H. Gold, B. Hafizi and A. W. Fliflet, ibid., p. 184.
6. A. K. Ganguly and J. L. Hirshfield, *Phys. Rev.* E **47**, 4364 (1993).
7. G. S. Nusinovich and V. L. Granatstein, ibid., p. 16.
8. P. B. Wilson, ibid., p. 293.
9. D. Sprehn, R. M. Phillips and G. Caryotakis, ibid., p. 43.
10. B. Hafizi, P. Sprangle, and J. L. Hirshfield, *Phys. Rev.* E **50**, 3077 (1994).
11. C. Wang and J. L. Hirshfield, *Phys. Rev.* E **51**, 2456 (1995).
12. M. A. LaPointe, R. B. Yoder, C. Wang, A. K. Ganguly and J. L. Hirshfield, *Phys. Rev. Lett.* **76**, 2718 (1996).
13. J. L. Hirshfield, M. A. LaPointe, A. K. Ganguly, R. B. Yoder and C. Wang, *Phys. Plasmas* **3**, 2163 (1996).
14. R. True (private communication).
15. J. L. Hirshfield, A. K. Ganguly and C. Wang, in *Pulsed RF Sources for Linear Colliders*, AIP Conf. Proc. **337**, 200; R. C. Fernow, ed. (Amer. Inst. of Phys, New York, 1995).
16. The authors are indebted to M. I. Petelin and A. L. Goldenberg for clear enlightenment on this issue.
17. A. K. Ganguly, to be published.
18. See, for example, A. Yariv, *Quantum Electronics* (Wiley, New York, 1967). Ch. 22.
19. Y.-H. Liu and T. C. Marshall, *Proc. 11th Intl. Conf. on High-Power Particle Beams*, Prague, June 1996 (to be published). In the experiment reported in this paper, a 24 GHz TE_{11}-mode waveguide FEL amplifier exhibited output at the 2nd, 3rd and 7th harmonics, but the 7th was the strongest when the beam was diverted off axis, even for beam energies much lower than required to maximize 3rd harmonic output.

CYCLOTRON AUTORESONANCE MASERS AND RELATIVISTIC GYROTRONS

V.L.Bratman, Yu.K.Kalynov, N.G.Kolganov, V.N.Manuilov, M.M.Ofitserov, A.V.Savilov, S.V.Samsonov and A.B.Volkov

Institute of Applied Physics, Russian Academy of Sciences,
Nizhny Novgorod, Russia

Abstract

Experiments with cyclotron autoresonance masers, including the auto-oscillator operating in the millimeter region of wavelengths with the efficiency close to the theoretical prediction, here revieved. Preliminary results of an experiment with the relativistic Large Orbit Gyrotron are presented; selective excitation of the 1st-5th cyclotron harmonics at the wavelengths from 14 mm down to 4 mm with power about 100 kW is achieved. Some opportunities for further increase of the efficiency of the both devices, which could make them more advanced in the submillimeter wavelength region, are discussed.

1. Introduction

This report is devoted to the two relativistic varieties of the cyclotron resonance masers, which are the closest relatives to the subrelativistic gyrotrons. As is well known, operation of the gyrotron is based on the relativistic effect completely, namely, on the dependence of the cyclotron frequency on the electron energy. However, from this point of view it would be a hasty judgment to conclude that the increase of the particle energy up to relativistic values is surely useful for this device. Indeed, first of all the energy increase decreases the cyclotron frequency and, consequently, the radiation frequency at the fundamental. In addition, if one does not take any special measures, the relativistic electrons go out of the cyclotron resonance with the wave, having lost a small part of their energy. There are at least two known methods for compensation of these evident defects of the relativistic gyrotron.

1. It is possible to use the Doppler effect if one makes the electrons interact with a wave propagating not across but almost along their translational motion [1-4]. In this case, like in the FEL, the radiation

frequency, ω, can be significantly higher than the electron oscillation frequency, i.e. the cyclotron frequency, ω_H:

$$\omega \approx \omega_H / \left(1 - \beta_{z_0} / \beta_{ph}\right).$$

Here β_{z_0}, β_{ph} are the longitudinal electron velocity and the phase velocity of the wave normalized to the speed of light. Simultaneously, due to the change of the electron translational momentum the regime close to the autoresonance [5,6] takes place, when the electron keeps in resonance with the wave even if it loses a significant part of its initial energy. Hence the electron efficiency in such a regime can be high. These possibilities are realized in Cyclotron Autoresonance Masers (CARMs) [1-4].

2. It is possible to use the non-dipole interaction of the relativistic electrons with a wave and excite higher harmonics in the relativistic gyrotrons [7-9]:

$$\omega \approx s\omega_H .$$

In principle, such a gyrotron can also have a high efficiency if one uses a profiled magnetic field.

Even taking account no of the difficulties connected with using high voltage it is clear at once that both the CARM and high harmonic relativistic gyrotron are more complicated and delicate devices than the subrelativistic gyrotron. Both devices require electron beams with higher quality for their operation. Besides, the problem of discrimination of parasitic modes is more acute for the both devices than for the subrelativistic gyrotron.

2. High-Efficiency CARM

The CARM with high Doppler frequency up-shift was suggested about 20 years ago [1,2]. The first experiments were accomplished in 1982 [10]. Since then, many successful experiments with oscillators and amplifiers at the wavelengths from 2 cm to 1.2 mm were carried out in our country and abroad [10-22]. Simultaneously, much more effort was spent on FEL realization. According to our experience in investigations of the both devices, at millimeter-submillimeter waves it is easier to realize the CARM than the FEL.

Our experimental results in the field of the CARM are shown in Table 1. All the experiments were carried out using high-current electron accelerators with explosive-emission injectors, which provided the current

pulses tens nanoseconds long and the electron energy from 0.5 to 1.2 MeV. We achieved generation at 2 mm already in 1982 [10]. But after that we tried to improve the CARM operating at longer waves, from 4 to 8 mm. One of our best results obtained in collaboration with the High-Current Electronics Institute was the amplifier at the wavelength of 8 mm with power of 10 MW and amplification of 30 dB [19]. The highest radiation power (30-50 MW) and the Doppler frequency up-conversion (about 8) were obtained in the experiment, which was carried out in collaboration with the Joint Nuclear Research Institute, at their LIA [20]. In this CARM operating at the wavelength of 4 mm, the high Doppler up-conversion had allowed the magnetic field to be as small as 11 kOe, which was more than two times smaller than for the weakly-relativistic gyrotron.

Table 1. Experiments with the CARM performed at IAP and in collaboration with other Institutions

λ mm	Mode	P MW	η %	Ampl dB	τ ns	Institution and Comments	Year
2-4	$TE_{1,1}$ $TE_{4,1}$ $TE_{2,1}$	6-15	2-4		50	IAP IAP+Lebedev Phys. Inst.	1982
8	$TE_{5,1}$	30	10		15	IAP	1993
4 6	$TE_{1,1}$	50 30	8 10		30	IAP+JINR (Induction Linac)	1991
8	$TE_{1,1}$	13	26		15	IAP	1995
8	$TE_{1,1}$	10	4	30	20	IAP+HCEI	1986

Table 2 contains some experimental results obtained in other laboratories. One has to mention the amplifier, realized at MIT [18]. Its output parameters are close to the above parameters of our amplifier, but the efficiency is higher. At MIT the first CARM with the thermocathode has been also realized [17]. At Livermore, on the basis of LIA the CARM with the shortest wavelength (1.2 mm) has been studied [11]. Recently at the Strathclyde University the first CARM operating at the second cyclotron harmonic has been realized [21]

Table 2. Some experiments with the CARM performed in other laboratories.

λ mm	Mode	P MW	η %	Ampl dB	τ ns	Institution and comments	Year
1.2		50	3		20	LLNL (Induction Linac)	1990
10		0.1	2			MIT (Thermo-cathode)	1992
21	$TE_{2,1}$	0.5	6		100	Univ. of Strathclyde (2nd harmonic)	1995
8	$TE_{1,1}$	12	7	32	15	MIT	1989

Thus, a lot of experiments demonstrate high-frequency and selective properties of the radiation generated by CARMs. However, in these experiments the CARM efficiency is not higher than 10%. This value is too small, several times smaller than the efficiency, predicted by the theory for the CARM with the ideal electron beam. In order to show that the main cause of such low efficiency is low quality of the used electron beams (too large spread in electron longitudinal velocity), in 1995 we carried out a special experiment at relatively long wavelengths, which should demonstrate the possibility of realization of high-efficiency CARM [22] In this experiment (Fig. 1) selection of the "most rectilinear" particles by a narrow anode outlet similar to that realized earlier for the FEL [23] was used to form the electron beam. Besides, the beam quality was additionally improved by means of the non-adiabatic magnetic field produced by a special correcting coil [24]. An operating rotary velocity was imparted to electrons in a kicker introducing small additional spread. At the same time, sensitivity of the oscillator to the velocity spread was reduced maximally by using a very short microwave system, in which electrons underwent only 4-5 gyrorotations.

Along with the beam quality, another serious problem in CARM realization is connected with excitation of parasitic modes, especially dangerous of which are near-cut-off (gyrotron) and backward waves. To prevent this, the operating mode was chosen to be the lowest transverse $TE_{1,1}$ mode of a cylindrical waveguide in the regime of grazing dispersion characteristics of the beam and wave. In this case the danger of transverse

parasitic mode excitation (at least at the fundamental cyclotron harmonic) disappears.

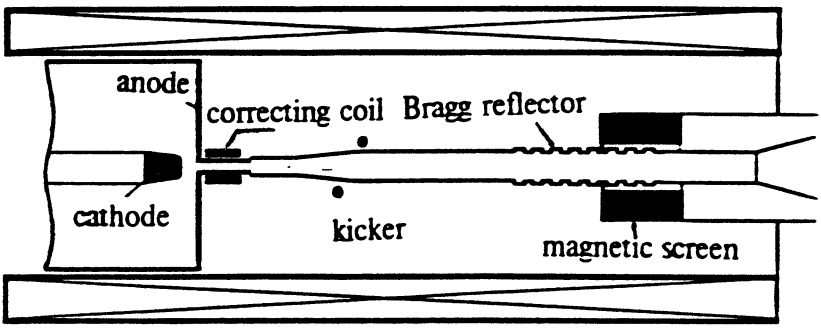

Fig.1. The schematic of the high-efficiency CARM.

The experiments were carried out at the high-current direct-action "Sinus-6" accelerator with a field-emission cathode. This accelerator can provide an electron beam with energy of 300-600 keV, total current of 3-8 kA and pulse duration of about 20 ns. The diameter of the beam used in the experiment was 2.5 mm. The current of a beam was 100 A at the particle energy 500 keV and the 10 ns flat-top of a voltage pulse. The axial magnetic field exceeded 9 kOe. For the chosen gun parameters the accelerator operated in the regime close to the matched one and the total diode current amounted to 3-5 kA. In order to eliminate undesirable action of the anode electrostatic lens, we used a small correcting coil generating a pulsed magnetic field with intensity on-axis controlled within 0-2 kOe and the radial component concentrated near the coil borders in two short (as compared to the Larmor step of electrons) regions. If the coil is placed down-stream from the anode aperture at the distance of a quarter of the Larmor step, has the length of half of the Larmor step and generates the magnetic field on the axis of direction opposite to the guiding one with certain intensity, then the radial field of the coil practically compensates the spurious transverse velocity for all particles of the paraxial beam.

The initially rectilinear beam after the electron gun was pumped by means of a kicker in the form of a rectangular current frame sloping at 60° to the z-axis, generating the transverse magnetic field with its distribution close to the homogeneous one near the beam so, it was weakly

sensitive to the particle position spread. The kicker imparted to electrons the necessary rotary velocity in a broad band of the guiding magnetic field.

The microwave system was made up of a cavity with the operating section in the form of a smooth cylindrical waveguide 7.8 mm in diameter and 60 mm long. The cavity was bounded on the cathode side by a cut-off waveguide 4.4 mm in diameter, which reflected the $H_{1,1}$ mode at wavelengths longer than 7.5 mm. At the collector side the wave was reflected from a Bragg reflector formed by a section of a corrugated waveguide with the corrugation period of 5.5 mm. The reflection coefficient for the Bragg reflector without the electron beam proved to be maximal at the wavelength of 8.45 mm. The frequency difference between the longitudinal modes of the cavity $\Delta f \approx 1$ GHz was approximately equal to the frequency band width of the Bragg reflector, which allowed us to select only one longitudinal mode with the Q-factor 1.5-2 times higher than those of the neighbouring modes by slightly tuning the length of the operating section.

According to the simulations, the maximum efficiency for the operating CARM parameters and an ideal rectilinear initial beam amounted to 30%. For the operating velocities $\bar{\beta}_\perp = 0.4 \div 0.55$ initial oscillations $\beta_{\perp 0} = 0.05$ led to spread 7`÷5% and to 20÷15% efficiency reduction, and for value $\beta_{\perp 0} = 0.1$ the spread is $4 \div 10\%$ and the efficiency decreases by almost two times.

In the experiment switching on of the correcting coil with the calculated value and direction of the current led to 10-20% broadening of the generation band on the magnetic field, as well as to the increase of the radiation pulse duration caused apparently by reduction of the start current of the oscillator due to the improvement of the beam quality. In this case, ın the optimal regime the radiation power was 20-30% higher but the beam current was practically the same.

The maximum power at the wavelength of 7.9±0.1 mm amounted to 13±2 MW for the following set of parameters: accelerating voltage - 500 kV, beam current - 100 A, guiding magnetic field - 12.4 kOe, transverse particle velocity - $\beta_\perp = 0.55$. The corresponding electronic efficiency of the CARM oscillator reached 26% with absolute accuracy $\pm 5\%$.

The performed experiment proved the fact that corresponding to the theoretical predictions, the use of an electron beam with a small

velocity spread raises CARM efficiency at least to the level of efficiency of the FEL. It is also clear from theory [25] (see Sect. 4) that by tapering magnetostatic and HF field distributions it is possible to enhance electronic efficiency of a CARM further. However, it should be borne in mind that in this work, as well as in the works describing experiments with high efficiency FELs (excepting [26,27]), only a part of the initial electron beam was used. To obtain really high efficiency, it should be necessary to make up an electron-optical system providing high quality of the whole beam. Results of the experiment on forming an electron beam for the ubitron [26,27] and preliminary estimations show that this problem can be solved by using thermo-emitters; moreover, it can be solved not only for the millimeter but also for the submillimeter wavelength ranges. If this is true, then using enhanced magnetic fields and high-selective low-loss microwave systems of the open type [28] one can hope for creation of effective, relatively low-voltage (300-500 kV) sources generating coherent submillimeter radiation suitable for solution of the problems of fusion plasmas diagnostics, solid-state physics and spectroscopy researches.

3. High-Harmonic Relativistic Gyrotrons

Already at subrelativistic electron energies the gyrotron provides giant radiation power up to 1 MW with pulse duration of a few seconds at short-millimeter waves [29], as well as about 100 kW of power with pulse duration of tens of microsecond at the wavelengths shorter than 0.5 mm [30]. The subrelativistic gyrotron operating at the higher cyclotron harmonics is proved to be able to produce the radiation at the wavelengths as short as 0.3 mm [31], which makes it promising for the spectroscopy. Basing on these results and the theory [7-9] we are trying to develop a powerful submillimeter gyrotron operating at moderately relativistic electron energies 200-300 keV instead of 3-6 MeV for the FELs. Already at the mentioned comparatively low particle energies coupling of the electron beam having a large pitch-factor with cavity modes at higher harmonics is practically as strong as at the fundamental. Using high pulsed magnetic fields up to 20-30 T and providing selective excitation of the separate modes for the resonances up to the 5-10th harmonics it would be possible to obtain from a single device coherent radiation with broadband frequency step-tuning.

As a first modeling step to a sub-millimeter gyrotron, we have started our experiments at millimeter waves with well-known [9] Large

Orbit Gyrotrons (LOGs). Due to a certain symmetry of the system where a thin electron beam encircles the axis of an axisymmetric cylindrical cavity the significant mode separation takes place; namely, in a LOG only the modes having the azimuthal index equal to the number of the resonant harmonic can be excited. If the electron beam has a small velocity spread, then it provides selective excitation of a single cyclotron harmonic. Starting from the LOG we are realizing the known method of parasitic mode discrimination. At the same time we paid the main attention to the formation of helical electron beam using the same methods as we applied to the CARM.

A general theory of electron-wave interaction in the relativistic gyrotron at the cyclotron harmonics was developed in Refs.[7-9,32] as direct generalisation of the well-known theory (see, e.g. [33]) of the subrelativistic gyrotron. According to the theory for a uniform magnetostatic field the maximum electron efficiency for the resonance at the s-th harmonic is determined by the following estimation:

$$\Delta\gamma / \gamma_0 \sim 1 / sN ,$$

where N is the number of electron gyrooscillations inside the cavity $(N >> 1)$, and γ is the electron Lorentz factor. At comparatively large beam current for which the cavity length and correspondingly the number, N, can be chosen not very large: N~5-10, efficiency at the higher harmonic (s~5-10) amounts to a few percent, which is sufficient for a number of applications.

In order to achieve the mentioned efficiency it is necessary to have an electron beam with small energy spread, $\Delta\gamma / \gamma_0 < 1 / sN$, and comparatively large initial transverse velocity of the electrons. In addition, to provide a single mode generation at a higher harmonic, the parasitic modes should be effectively suppressed. In principle, it can be achieved using only electrodynamical methods but it is more efficient to use them in combination with electron methods controlling the coupling coefficient between the electron beam and the mode. The last method is used in the LOG [9], where a thin electron beam encircling the axis of an axisymmetric cylindrical cavity excites only the modes having the azimuthal index equal to the number of the resonant harmonic, namely, rotating transverse-electric TE_{spq} modes. The field structure of these modes near the cavity axis coincides with the structure of the corresponding rotating multipoles (2s-poles).

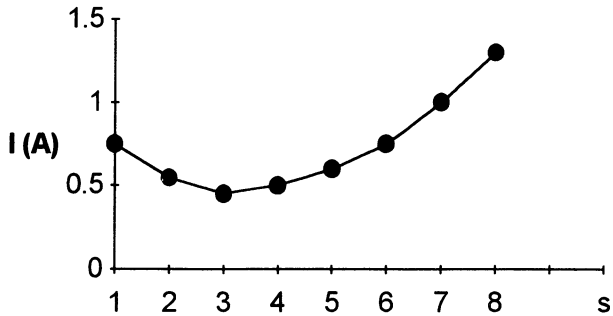

Fig.2. Starting current of the LOG-1 versus cyclotron harmonic number

Increasing of the electron-wave coupling for high transverse electron velocities and increasing of diffraction Q of the fixed gyrotron cavity with increase of the harmonic number lead to a significantly smaller difference in the operating currents of the different harmonics as compared to the subrelativistic situation. Moreover, even with the account for the increase of the ohmic losses at shorter millimeter waves, the minimal starting current of a LOG with a large electron pitch factor corresponds to a higher harmonic rather than to the fundamental. For example, already for moderate electron energy 250 keV, a pitch-factor $g = 2$, and the cavity length corresponding to N=5 of electron gyrorotations inside the cavity, the 3rd harmonic has the minimal starting current, and the starting current for the 6th harmonic is equal to that for the fundamental (Fig. 2). It is important to emphasize that according to calculations the frequency non-equidistance of the first $TE_{m,p,1}$ modes is sufficiently large; thus, having the electron beam with a small velocity spread one can expect selective excitation of the cavity modes from s=1 to s=7.

In order to check predictions of the theory we designed two gyrotrons of the millimeter wavelength range, LOG-1 and LOG-2, with the thermionic and the explosive emission cathodes, correspondingly.

LOG-1 was designed for operation at the new high-voltage installation described in [34] and intended for study of two types of relativistic devices, namely, gyrotrons and CARMs. The operating electron voltage and current are 250 kV and 10 A at pulse duration 10 μs The diode-type quasi-Pierce electron gun with a spherical thermionic cathode and tapering guiding magnetic field permits compression in diameter of the

electron beam from 20 mm at the cathode, where the magnetic induction is equal to only 1.4 mT, to 1.2 mm in 0.4 T magnetic field with a sufficiently low amplitude of radial pulsations, when predicted transverse velocity in the beam does not exceed 0.05 c. In the magnetic field of 0.4 T the beam is pumped to the operating transverse velocity by a kicker in the form of a current frame slopping to the axis of the guiding field. Then this transverse velocity is increased to 0.6 c by adiabatic tapering of magnetic field to 1.6 T. A traditional gyrotron cavity with the operating $TE_{5,1,1}$ mode with the wavelength of 2 mm excited at the 5th cyclotron harmonic is used as a microwave system. The designed power at the 2 mm wavelength with a microsecond pulse duration is more than 100 kW. Now fabrication of the LOG-1 components is nearly finished.

LOG-2 has been designed for operation at the high-current "Sinus-6" accelerator. The operating electron voltage and current, passing into the cavity, are 300-350 kV and 25-35 A at pulse duration about 20 ns. In the LOG-2 we use our experience in producing a high quality helix beam obtained with CARMs (see Sect. 2). In order to produce a thin rectilinear electron beam with a small velocity spread from an explosive emission cathode we select only a small central part with diameter 1.5 mm from a high current beam. The above mentioned values of the current were obtained for uniform magnetic fields 0.7-1.2 T. After pumping in the kicker similar to the kicker of LOG-1, electrons with the pitch factor $g = 1.3 \div 1.5$ enter a traditional gyrotron cavity with diameter 8.2 mm and length of its cylindrical part of 42 mm bounded by the input and output conical taperings 1.6° and 3.4°, correspondingly. In the experiment, when decreasing the operating magnetic field, we clearly observed successive selective excitation of the $TE_{s,1}$ modes at the fundamental and the cyclotron harmonics from s=1 to s=5, which was confirmed by measurements of the radiation frequency by means of a set of cut-off waveguide filters. The measured values of the operating magnetic fields and the frequencies corresponded to the calculations very well (see Tables 3 and 4). We observed also maximums of the received signal at the magnetic fields corresponding to the 6th and 7th harmonics, but the wavelengths of radiation for those fields have not yet been measured. Up to now we received the radiation using only the horn and semiconductor detector calibrated at the wavelengths about 8 mm. The maximum signal was registered at the 3rd cyclotron harmonic when the wavelength of the radiation was equal to 6.1 mm at the output power not less than 100 kW.

The radiation power at the second harmonic, when λ=8.4 mm, was about 50 kW. The most important is that the signal at the 5th harmonic, when λ=4mm, was not weaker. Taking into account the decrease of the detector sensibility at higher frequencies it means that the power radiated at the 5th cyclotron harmonic was not less than 100 kW.

Table 3. Calculations for LOG-2.

Harmonic Number, *s*	1	2	3	4	5	6
Wavelength, mm	13.9	8.4	6.1	4.8	4.0	3.4
Resonant Magnetic Field, kOe	12.2	10.1	9.3	8.8	8.5	8.3

Table 4. Preliminary experimental results for LOG-2.

Harmonic Number, *s*	1	2	3	4	5
Operating Mode	TE_{11}	TE_{21}	TE_{31}	TE_{41}	TE_{51}
Wavelength, mm	14.0	8.4	6.1	4.8	4.0
Magnetic Field, kOe	11.8-10.0	10.0-9. 8	9.8-8.6	8.6-8.3	8.3-8.1

4. Opportunities of the efficiency increase

As shown by the above demonstration experiments, it is very important to study some alternative schemes of such devices, which should increase efficiency and decrease sensitivity to the beam quality in CARMs and relativistic gyrotrons. One of possible ways to increase efficiency in both devices is realization of the regime of trapping and adiabatical deceleration of electrons [35,36,25], being analogous to that which has been already realized experimentally in FELs [37]. For the cyclotron resonance masers, the main idea of such a regime is to provide prolonged

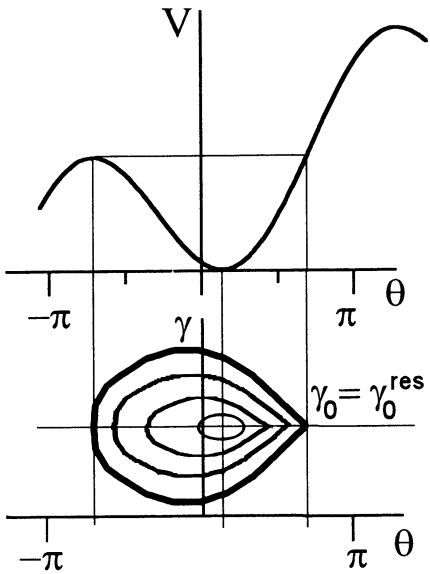

Fig.3. Effective potential well and phase plane.

synchronous interaction between the wave and the main part of the electron beam by tapering the guiding magnetic field. In the beginning of the region of electron-wave interaction, particles are trapped by the wave and oscillate in the effective potential well (Fig. 3). On the "energy-phase" plane this corresponds to synchrotron oscillations of the trapped electrons inside the so-called "bucket". The point of equilibrium (the "bucket" center) corresponds to the electron, which has the phase respect to the wave, θ, close to π ("zero" of the wave field) and the relativistic Lorentz factor, corresponding to the exact cyclotron resonance between an electron and the wave, $\gamma \approx \gamma^{res}$. Thus, the averaged (over synchrotron period) energy of the trapped particles coincides with the "resonant" energy. Due to the decrease of the magnetic field, the resonant energy decreases with the longitudinal coordinate. Correspondingly, on the phase plane the "bucket" with the trapped electrons becomes lower (Fig. 4). Therefore, all trapped electrons lose simultaneously their energies so that the average electron energy is defined by the expression

$$\langle \gamma(z) \rangle \approx K \gamma^{res}(z),$$

where K is the share of particles which are trapped by the potential well. It is important to notice that for effective realization of the regime of trapping, one needs to provide only a slow decrease of the magnetic field (large length of the interaction space), but the law of the magnetic field decrease may be arbitrary (for example, linear). It is also important that for the gyrotron the same profile of the magnetic field provides the regime of trapping for various cyclotron harmonics (while the resonant magnetic fields are certainly different for different harmonics because of the non-equidistant spectrum of the transverse cavity modes).

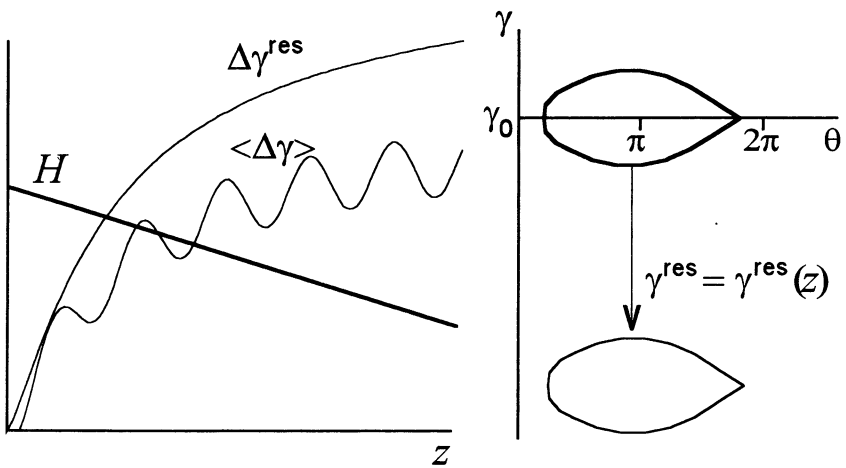

Fig.4. Electron energy extraction during the process of the adiabatic deceleration of the trapped particles.

There are two differences of the regime of trapping in comparison with the usual regime of compact electron bunching, realized in the above experiments: the magnetic field profiling and the length of the electron-wave interaction region; for the regime of trapping this length should correspond to many periods of the synchrotron oscillations. At the same time, in the regime of trapping the mechanism of the electron bunching significantly differs from the mechanism of compact bunching. This leads to the important peculiarity of the regime of trapping: the sensitivity to the spread in electron velocity is smaller than in the regime of compact electron bunching, while the interaction region length is essentially larger [25]. Actually, the electron efficiency is mainly defined by the efficiency of trapping at the beginning of the interaction region. Then, during the motion through this region, the behaviour of the trapped particles with various

initial pitch-factor is practically the same: they lose their energies with the decrease of the resonant energy.

Another method of the efficiency increase, which can be used in CARMs and gyrotrons [38] operating in the CW or long-pulse regimes, is the depressed collector method and recovery by the power supply of the electron energy, which is saved by particles at the output of the electron-wave interaction region. This is the well-known technical method, having been utilized in various RF electron devices, including the gyrotron [39-41] and the FEL [42,43]. But for the CARM and the gyrotron, energy recovery can be principal in their competition with the very efficient gyrotron. The most attractive scheme of the recovery is the simplest, single-step depressed collector. In this case the voltage is the difference between the accelerating voltage, U_0, and the recovery voltage at the collector, U_{rec}. Then, the electron energy recovery provides the increase in the total efficiency of the device by factor

$$\eta_{\text{rec}} = \frac{U_0}{U_0 - U_{\text{rec}}} > 1 ,$$

called recovery efficiency.

As it has been shown [38], such a scheme allows the efficiency of CARMs and gyrotron, operating in the usual regime of the compact electron bunching, to be increased significantly. For the gyrotron, the recovery efficiency decreases with the increase of the cyclotron resonance number. Nevertheless, since it is more difficult to obtain high electron efficiency at higher harmonics, the energy recovery in this case can be even more attractive than at the fundamental. For the CARM with low electron efficiency, the recovery efficiency is proportional to the reversed electron efficiency. The total efficiency practically does not depend on the electron efficiency and can exceed 25%.

It could be very attractive to combine the both methods of the efficiency increase, which has been reviewed above. Actually, the regime of trapping provides the increase not only in electron efficiency, but also in the possible recovery efficiency, which is induced by smaller RF amplitude and, therefore, smaller spread in output electron energy [38]. For instance, in the CARM operating in the regime of trapping, the total efficiency is higher than in the regime of electron bunching and can be about 50%.

References

1. Petelin M.I., Radiophys. Quantum Electron., 1974, **17**, 686.
2. Bratman V.L., Ginzburg N.S., Conf. Digest of 9th All-Union Conf on HR Electronics, Kiev, 1979, 107.
3. Bratman V.L., Ginzburg N.S., Petelin M.I., Optics Commun., 1979, **30**, 409.
4 Vomvoridis J.L., Int. J. Electronics, 1982, **53**, 555.
5. Kolomensky A.A., Lebedev A.N., DAN SSSR, 1962, **145**, 1259.
6. Davydovsky V.Ya., Zh. Eksper. Teoret. Fiz., 1962, **43**, 886.
7.Bratman V.L., Ginzburg N.S., Nusinovich G.S., Pis'ma v Zh. Tekhn. Fiz., 1977, **3**, 961.
8. Ginzburg N.S., Nusinovich G.S., Izv. Vuzov- Radiofiz., 1979, **22**, 754.
9. McDermott D.B., Luhmann N.C., Kupiszewski A., Jory H.R., Phys. Fluids, 1983, **26**, 1936.
10. Botvinnik I.E., Bratman V.L., Volkov A.B. et al., Pis'ma v Zh. Eksper. Teoret. Fiz., 1982, **35**, 418.
11. Caplan M., Kulke B., Westenskow G.A. et al., LLNL, Livermore, CA, UCRL-55689-90.
12. Choi J.J., Gilgenbach R.M., Spenger T.A., Int. J. Electronics, 1992, 72, 1045.
13. Fliflet A.W., McCowan R.B., Sullivan C.A. et al., Nucl. Instr Meth. Phys. Res. A., 1989, **A285**, 233.
14 Bratman V.L., Denisov G G., Int. J. Electronics, 1992, **72**, 969.
15. Alberti S., Danly B.G., Gulotta G. et al., Phys. Rev. Lett., 1993, **71**, 2018.
16. Bratman V.L., Gubanov V.P., Denisov G.G. et al., Digest of 6th All-Union Symp. on High-Current Electronics, Novosibirsk, 1986, part 3, 6.
17. Pendergast K.D., Danly B.G., Menninger W.L. and Temkin R.J., Int. J. Electronics, 1992, **72**, 983.
18. Bekefi G., DiRienzo A., Leibovitch C., Danly B.G., Appl. Phys. Lett., 1989, **54**, 1302.
19. Bratman V.L., Gubanov V.P., Denisov G.G. et al., Relativistic HF Electronics (IAP, Gorky), 1990, **6**, 206.
20 Bratman V.L , Denisov G.G., Ofitserov M.M. et al., Int. J. IR and MM Waves, 1992, **13**, 1857.
21. Cooke S.J., Spark S.N., Phelps A.D.R. et al., Digest of 18th Int. Conf on IR and MM Waves, Colchester, 1993, 462.

22. Bratman V.L., Denisov G.G., Kol'chugin B.D., Samsonov S.V., Volkov A.B., Phys. Rev. Lett., 1995, **75**, 3102.
23. Conde M.E., Bekefi G., IEEE Trans. Plasma Sci., 1992, **20**, 240.
24. Samsonov S.V., Int. J. IR and MM Waves, 1995, **16**, 753.
25. Bratman V.L., Ginzburg N.S., Savilov A.V., Relativistic High-Frequency Electronics (IAP, N.Novgorod), 1992, **7**, 22.
26. Kaminsky A.A., Kaminsky A.K., Sarantsev V.P. et al., Nucl. Instr. Meth. Phys. Res. A, 1996, **A375**, 215.
27. Kaminsky A.A., Kaminsky A.K., Rubin S.B. et al., Relativistic High-Frequency Electronics (IAP, N.Novgorod), 1992, **7**, 60.
28. Bratman V.L., Denisov G.G., Samsonov S.V., Proc. of 2nd Int. Workshop "*Strong Microwaves in Plasmas*", N.Novgorod, 1993, 690; Bratman V.L., Denisov G.G., Ofitserov M.M., Petelin M.I., Samsonov S.V., Nucl. Instr. Meth. Phys. Res. A, 1995, **A385**, 135.
29. V.E.Myasnikov, M.V.Agapova, A.S.Borshchegovsky, G.G.Denisov, V.A.Flyagin et al., Proc. of 21st Int. Conf. on Infrared and Millimeter Waves, Berlin, 1996, ATh1.
30. Flyagin V.A., Luchinin A.G., Nusinovich G.S., Int. J. IR & MM Waves, 1983, **4**, 629.
31. Idehara T., Brand G.F. *Submillimeter wave gyrotron development and applications*. Fukui University, Japan, 1995.
32. Bratman V.L., Ginzburg N.S., Nusinovich G.S., Petelin M.I., Strelkov P.S., Int. J. Electronics, 1981, **51**, 541.
33. Flyagin V.A., Gaponov A.V., Petelin M.I., Yulpatov V.K., IEEE Trans. on MTT, 1977, **25**, 514.
34. Bratman V.L., Botvinnik I.E., Grom Yu.D., Kalynov Yu.K., Ofitserov M.M., Proc. SPIE of XVI Int. Symp. on Discharges and Electrical Insulation in Vacuum, Moscow-St.Peterburg, Russia, 1994, 538.
35. Ginzburg N.S., Izv. Vuzov - Radiofiz., 1987, **30**, 1181.
36. Nusinovich G.S., Phys. Fluids B., 1992, **4**, 1989.
37. Orzechowski T.J., Anderson B., Clark J. et al., Phys. Rev. Lett., 1986, **57**, 2172.
38. Bratman V.L., Denisov G.G., Savilov A.V., Int. J. IR and MM Waves, 1995, **16**, 459; Bratman V.L., Phelps A.D.R., Savilov A.V., Proc. of 21st Int. Conf. on IR and MM Waves, Berlin, 1996,), AW3; Bratman V.L., Phelps A.D.R., Savilov A.V., Phys. Plasmas, 1997, in press.

39. Sakamoto K., Tsuneoka M., Kasugai A. et al., Digest of 19th Int. Conf. on IR and MM Waves, Sendai, 1994, 63; Sakamoto K., Tsuneoka M., Kasugai A. et al., Phys. Rev. Lett.,1994, **73**, 3532.
40. Dammertz G. , Braz O., Iatrou C.T., Kuntze M., Möbius A., Piosczyk B., Thumm M., Digest of 20th Int. Conf. on IR and MM Waves, Orlando, 1995, 285.
41. Benediktov N.P., Glyavin M.Yu., Kuftin A.N., Zapevalov V.E., Izv.Vuzov - Radiofizika, 1996, in press.
42. Ellias L.R, Ramian G., Phys. of Quant. Electron., 1982, **9**, 603.
43. Verhoeven A.G.A., Bongers W.A., Best R.W.B. et al., Digest of 17th Int. Conf. on IR and MM Waves, Passadena, 1992, 126; Urbanus W.H., Verhoeven A.G.A., Bongers W.A. et al., Nucl. Instr. Meth. Phys. Res., 1993, **A331**, 235.

STATUS OF THE 1 MW, TUNABLE, FREE ELECTRON MASER

A.G.A. Verhoeven, W.A. Bongers, V.L. Bratman, M. Caplan**, G.G. Denisov*, G. van Dijk, B.S.Q. Elzendoorn, C.A.J. van der Geer, S.W.T. de Kroon, P. Manintveld, A. Poelman, J. Pluygers, R. Prins, M.Yu. Shmelyov*, A.B. Sterk, W.H. Urbanus, M. Valentini, M.J. van der Wiel*

FOM-Instituut voor Plasmafysica 'Rijnhuizen', Association EURATOM-FOM, tel.: (31)30-6096999, fax: (31)30-6031204, e-mail: verhoeve@rijnh.nl
P.O. Box 1207, 3430 BE Nieuwegein, the Netherlands
*Institute of Applied Physics, Nizhny Novgorod, Russia
**Lawrence Livermore National Laboratories, Livermore, CA, USA

1. Introduction

A free electron maser is being built for ECW applications on future fusion research devices such as ITER. A unique feature of the Dutch Fusion FEM is the possibility to tune the frequency over the entire range from 130 to 260 GHz at an output power exceeding 1 MW.

The assembly of the FEM was started. It uses a 12 A thermionic electron gun and a 2 MeV electrostatic accelerator. The undulator and mm-wave system are located inside a terminal at 2 MV level. The terminal is placed inside a steel vessel of 11 m length and a diameter of 2.6 m, filled with SF_6 at 7 bar. After interaction with the mm waves in the undulator, the energy of the electron beam is recovered by means of a decelerator and a multi-stage depressed collector. This will bring the overall efficiency above 50%.

The electron beam line is entirely straight from gun to collector. This is done to minimize the current losses to a value lower than 20 mA. The mm waves are directed sideways from the electron beam. This is achieved by means of a stepped waveguide, a symmetrical step in the transverse dimension of a low-loss HE_{11} waveguide, just behind the undulator. Furthermore, an adjustable reflector enables adjustment of the feedback power.

In the first phase of the project, a so-called inverse set-up is used. The electron gun is mounted inside the high-voltage terminal. The 2 MV accelerating-voltage power-supply was tested without break-down up to 2.3 MV. The electron gun and the undulator were tested successfully earlier. Very encouraging tests were performed on the mm-wave system, both at low power at Rijnhuizen and at high power at IAP. In the autumn of '96 the test of the electron gun together with the accelerating structure up to 2 MV level was performed.

2. Application of a FEM to ITER

A Free Electron Maser (FEM) combines the advantages of high-power, high-frequency mm-wave sources for ECW applications, such as gyrotrons, with the additional advantages of continuous tunability, a higher frequency and -eventually- a higher power per unit. The specifications for the Fusion-FEM are optimized for ECW applications to ITER. For ITER at this moment a total additional heating power of 100 MW is foreseen, of which, most probably, 50 MW will be supplied by ECW-sources.

The frequencies (130-260 GHz) are chosen such that for ITER (with a toroidal magnetic field of up to 5.7 T on axis) both fundamental on-axis heating at 160 GHz and off-axis heating between 140 and 200 GHz can be achieved. Furthermore, the ideal frequencies for EC current drive are from 220 to 260 GHz. The FEM is constructed in such a way that it can be used for start-up at 130 GHz; in addition the same installation can be tuned within less than one minute to give again over 1 MW of power for heating or current drive at any desired plasma position. The specifications can be modified at any time to meet other requirements.

Now, a maximum pulse length is 100 ms foreseen. The major modification from the current project to a FEM for application on ITER is to extend the pulse length to CW. Furthermore, since a total ECW-power of 50 to 100 MW is foreseen, an upward scaling of the power per unit from 1 MW to 4 or 5 MW seems feasible [1]. Compared to fixed-frequency high-power sources, a source with an adjustable frequency has a number of additional advantages [2].

3. Basic layout

The basic layout of the FEM is largely determined by the requirement for high overall efficiency. This together with fast tunability and CW operation determines the choice for a DC acceleration and deceleration system rather than an RF system. The choice for a maximum electron energy of 2 MeV and a beam current of 12 A has been made on the basis of simulations of the interaction between the electron beam and the mm waves. The main parameters of the Fusion-FEM are given in Table 1. The required high system-efficiency demands an efficient recovery of the electron beam leaving the undulator. For this purpose a decelerator and a depressed collector are incorporated.

Table 1. Design parameters of the Fusion-FEM.

mm-wave frequency	130-260 GHz
mm-wave output power	1 MW
Electron energy	1.35-2 MeV
Electron beam current	12 A
Electron loss current	< 20 mA
Normalized beam emittance (xx')	50 π mm mrad
Pulse length	100 ms
Duty cycle	10^{-3}
Overall efficiency (mains to P_{mmw})	> 50%
Linear gain	7 - 10
Gain in saturation	3.5
Waveguide mode	HE_{11}
Type of waveguide	rectangular corrugated
Cross section of primary waveguide	15*20 mm^2
Separation mmw beam, electron beam via stepped waveguide	
Undulator period	40 mm
Undulator gap	25 mm
Peak undulator field, section 1	0.2 T
Number of full cells, section 1	20
Gap between undulator sections	60 mm (adjustable)
Peak undulator field, section 2	0.16 T
Number of full cells, section 2	14
Total number of cells (incl. matching)	38
Length of undulator	1.58 m

The undulator and the mm-wave system are located at high voltage level, for two reasons. The cathode of the electron gun is placed at earth potential, and the electrodes of the depressed collector at low voltages. The power supplies that are connected to the collector, with a total current of 12 A, are located outside the pressure tank at earth potential, while components that need little or no power are inside the high-voltage terminal. This results in the basic layout of the Fusion-FEM as shown in fig. 1.

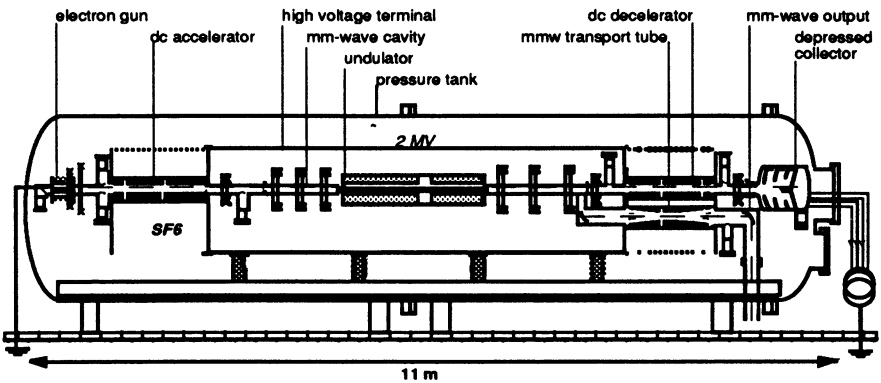

Fig. 1 Schematic layout of the Fusion-FEM.

The accelerating voltage in the FEM is much higher than in other high-power mm-wave sources such as gyrotrons and CARMs (Cyclotron Auto Resonant Masers). However, in our case, the 2 MV power supply has to deliver only the current lost during transport. Since the electrons are collected at the reduced voltages of the depressed collector the main current has to be supplied at a voltage of no more than a few hundred kV.

The FEM is a medium-gain oscillator with an intrinsic extraction efficiency (i.e., electron beam power to mm-wave power) of around 5 %. The gain is sufficiently high to ensure both a fast start-up of the mm-wave power and a manageable level of the total inter-cavity power. The above mentioned value of the intrinsic extraction efficiency is determined by two factors. On the one hand, it has to be sufficiently high otherwise the electron beam power would have to be very high. On the other hand, to avoid a large energy spread of the unspent electron beam, the extraction efficiency should not be too large. Too much energy spread makes it difficult to achieve a good electron-beam transport and efficient energy recovery.

4. Simulation of the interaction between electron beam and mm waves.

The interaction between the electron beam and the mm waves inside the fusion FEM has been simulated using several codes. In the beginning, most often the CRMFEL-code was used, later on the GPT code was preferred. CRMFEL is a fully 3-D, non-linear, general-purpose particle-pusher code. Until recently these simulations were done with a single-frequency, stationary version of this amplifier code [3,4]. Simulations for three different energies indicated that the net mm-wave power generated at a frequency of 130 GHz (at 1.35 MeV) is 1.1 MW, at 200 GHz (at 1.75 MeV) 1.3 MW and at 250 GHz (at 2 MeV) 1.2 MW.

The undulator consists of two sections with a different magnetic field. In the first undulator section the net mm-wave power (i.e., the total power minus the injected feedback power of 400 kW) grows to 700 kW at 200 GHz and saturates at the end of the first undulator section. In the second undulator section the electron energy, which is now lower due to the interaction with the mm waves, matches the lower undulator strength and the mm-wave power grows to 1.3 MW, saturating at the end of the second undulator section.

Simulations with a modified non-stationary (space-charge included) code developed at the University of Maryland indicate that a parameter regime can be found with a pure single-frequency operation, without any sidebands. The reflection coefficient of the mm waves, the size of the electron beam and especially the distance between the two undulator sections have a strong effect on the FEM behaviour [4,5].

In the mean time, a fully 3D code MFF, has been developed at Rijnhuizen [6]. The code is based on a multi-frequency model in the continuous beam limit with a 3D description of the electron beam. Space-charge forces are included by a Fourier expression. These forces strongly influence the spectrum generated. The simulations show that the linear gain is high - of the order of 10 - so that the system quickly reaches the non-linear regime. In saturation the gain is still more than a factor 3. For an optimised reflection coefficient and drift gap between the undulator sections, the spectrum evolves as shown in fig. 2. Initially, in the linear regime, the spectrum shows three bands.

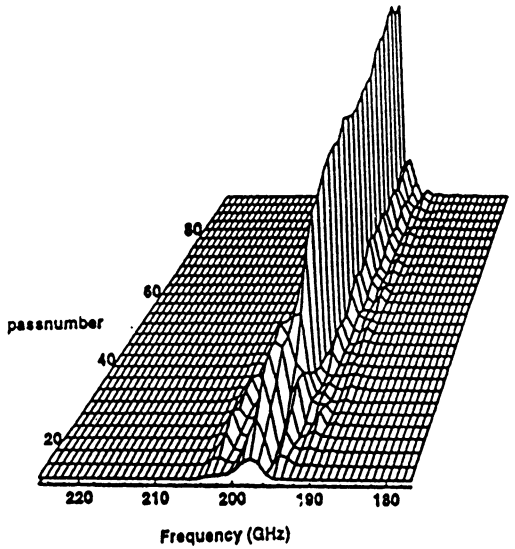

Fig. 2 Evolution of the mm-wave power during start-up of the FEM. The frequency spectrum is shown as a function of the number of times that the mm waves interact with the electron beam. It is seen that, once in saturation, the spectrum evolves into one single peak.

At growing power the system saturates and space charge becomes more important because the electron beam is stronger bunched. Then the sidebands vanish and a single peak grows to more than 1 MW.

It is clear from all simulations that the reflection coefficient (i.e., the amount of mm-wave power that is fed back to the input) is a very important parameter. Therefore, we have chosen for adjustability of this parameter for the Fusion-FEM project. This gives also the possibility to operate over the full frequency range.

5. Electron beam line

The electron beam line of the Fusion-FEM consists of a 12 A, 80 kV thermionic electron gun, the 2 MV electrostatic accelerator, the mm-wave cavity, the electrostatic decelerator and the depressed collector, see fig. 3. The electron beam line is kept straight to ensure the lowest possible electron-beam loss.

Several diagnostics have been developed to monitor the position and cross section of the electron beam. The cross section is measured via an Optical Transition Radiation (OTR) screen, which can be placed at several positions along the beam line. The position of the centre of mass of the electron beam is measured by electrostatic pick-up electrodes. The pick-up electrodes are integrated in the walls of the waveguides of the mm-wave cavity. In this manner, the electron beam position can be determined inside the cavity, without disturbing the mm-waves.

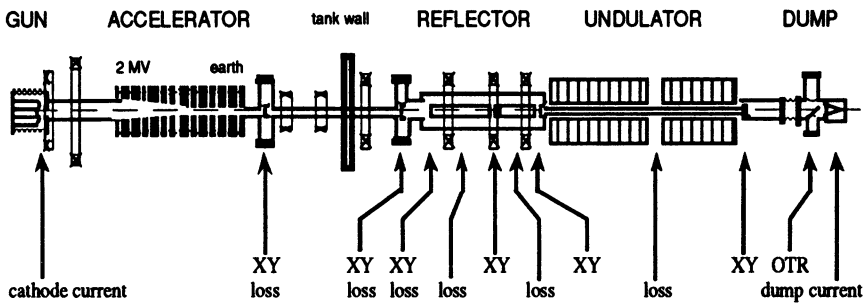

Fig. 3 Schematic lay-out of the electron beam line from electron gun up to the beam dump (presently mounted right after the undulator. The electron beam diagnostics are indicated by XY (electrostatic beam position monitors) and loss (beam loss current detection

6. Electron gun

The triode-type electron gun, especially developed by Varian/CPI, for the Fusion-FEM project has its cathode at earth potential, the anode at + 80 kV and in between a modulation electrode to switch the beam on (+10 kV) or off (-12 kV). In order to limit the halo current special precautions were taken. Around the cathode a thin ring is mounted, which suppresses emission from the edge of the cathode. In addition, a focus electrode, which is mounted very close to the cathode suppression ring, can be biased at just a few Volt to influence the electric field distribution at the cathode edge and thus the edge emission.

The gun parameters are specified in such a way that the electron beam has a so-called top-hat profile, i.e., a uniform current distribu-

tion for 99.8 % of the electrons. Measurements show that the total normalized emittance is only 20 to 60 π mm mrad. This means that at least 99.8% of the beam current can be transported loss-free and therefore the loss current can be sufficiently low. Beam-profile measurements of the prototype gun show an extremely uniform current distribution, a steep decline of the current density at the edge of the beam and little halo current.

Behind the gun a solenoid lens focuses the beam into the accelerator, in such a way that at the exit side of the accelerator the beam envelope is sufficiently small for further transport. A bucking coil, close to the gun, makes both the magnetic field and its gradient zero at the center of the cathode in order to minimize the emittance growth.

7. Design of the electron beam optics

The most important issue of the beam transport system is to transport the beam with very low loss current, of the order of mA's. Early simulations, done to get a basic design, were performed with an envelope code. These simulations run fast but the accuracy is limited. To obtain more accurate results, two approaches were used.

The GPT (General Particle Tracking) [7] code was used to perform detailed multi-particle simulations. The results are accurate for the bulk of the beam but the simulations are time-consuming. Further, particle tracking codes have statistical difficulties in taking into account thermal electrons that have a velocity much higher than the Gaussian electrons, which can translate into a small percentage of beam current outside the nominal beam edge.

The importance of ensuring 99.8 % transmission motivated the development of a relativistic version of the Herrmann optical theory of thermal velocity effects [5,8,9]. This theory determines current distribution functions semi-analytically everywhere along the beam line, allowing the determination of beam envelopes containing up to 99.9% of the beam current. An initial uniform distribution in real space and a Gaussian distribution in velocity space is assumed. Actual gun characterisation measurements show that the uniform distribution in real space is a very good approximation [10].

A result obtained with the GPT code is shown in fig. 4. From left to right it shows the beam starting at the electron gun then passing through the accelerator tube. A set of solenoids focus the beam into a waist at the position of the downstream mirror of the mm-wave cavity. A periodic-focusing system, transports the beam into the mm-wave cavity and focus it down to the matched radius at the undulator entrance.

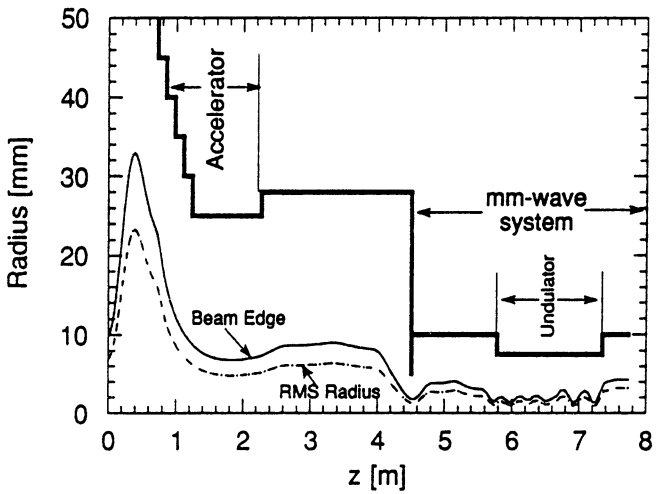

fig. 4. Layout of the beam line from the gun (far left) to the entrance of the undulator (far right). The 3D GPT code simulates the 12 A electron beam, which is accelerated to 2 MeV and has an emittance of 80 π mm mrad. The lenses are not drawn to scale.

A comparable plot, obtained with the Herrmann optical theory, is shown in fig. 5. Shown are the beam contours containing 95.0 %, 99.0 %, 99.5 % and 99.9 % of the beam current. The 95.0 % contour corresponds well with the result obtained with the GPT code.

Again shown in this plot are the undulator and the electron-beam contours here-in. The 99 % contour of the beam diameter is less than 8 mm, whereas the minimal transverse dimension of the beam pipe is 15 mm in total.

A first design of the electron beam line from the exit of the undulator up to the depressed collector has also been made. In this beamline section the energy of the unspent electron beam will be recovered in the final set-up of the project.

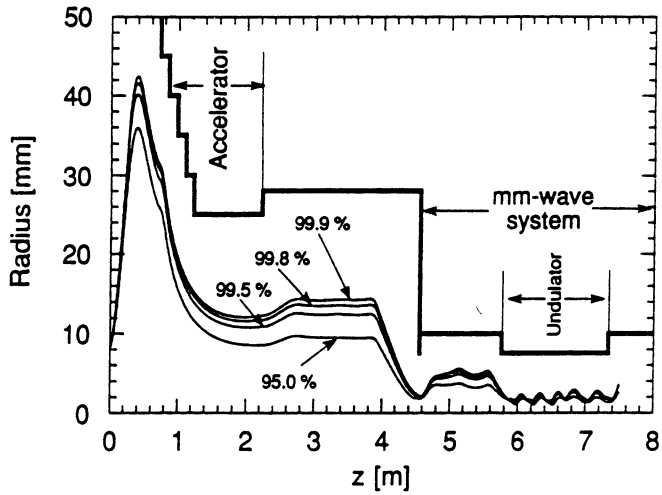

Fig. 5. Beam envelopes for the situation given in fig. 5. The envelopes are calculated by the Herrmann optical theory and show the contours which contain 95 %, 99.5 %, 99.8 % and 99.9 % of the beam current.

The deceleration and transport section after the undulator is roughly the opposite of the beam line from the gun to the undulator entrance. However, before the undulator the beam is almost mono-energetic, while after the undulator the energy spread is around 12 %.

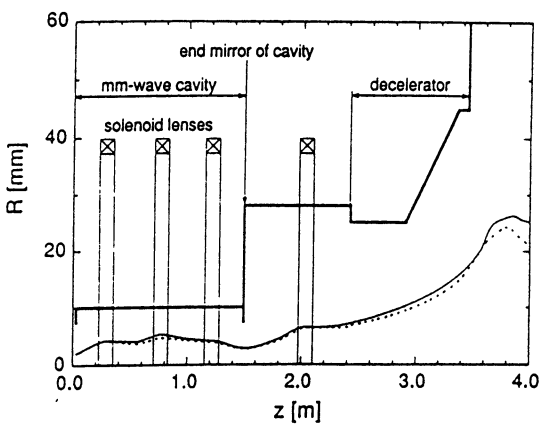

Fig. 6. Layout of the electron beam line between the undulator and the collector. Beam-envelope simulations for an electron beam with energy spread (solid line) and for a mono-energetic beam of 1.92 MeV with identical starting conditions (dotted line). The total emittance and energy spread of the beam are 90 π mm mrad and 12 %, respectively.

The layout of the beam line after the undulator is shown in fig. 6. The beam is transported through the mm-wave system by three rotationally symmetric lenses. A fourth lens focuses the beam into the decelerator tube. In the simulation result in fig. 6 the initial energy of the beam ranges from 1.8 to 2.05 MeV. In this case the beam is decelerated by 1.75 MV.

The influence of energy spread can be seen in fig. 6, which shows also the envelope of a mono-energetic beam with an initial energy of 1.92 MeV. The plot illustrates that the influence of energy spread is marginal.

8. Depressed collector

After passing the undulator the electron beam is decelerated and the energy of the electrons is recovered in the depressed collector. In the design of the multi-stage depressed collector earlier designs for so-called parabolic shadow-side collectors are followed [11,12]. A schematic drawing of the depressed collector is shown in fig. 7.

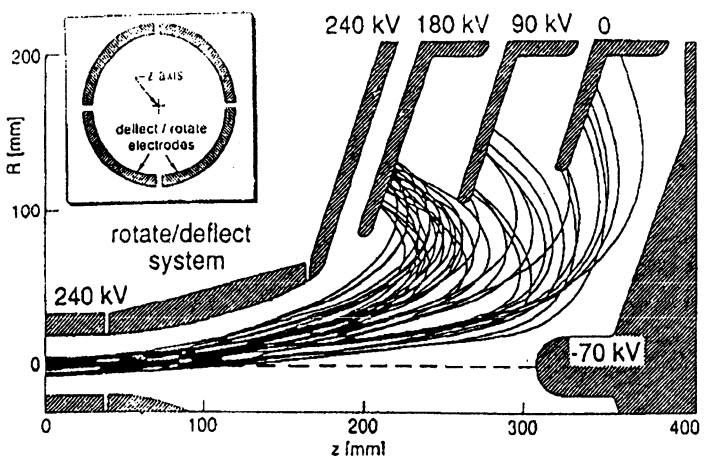

Fig. 7. Schematic drawing of the depressed collector and the beam rotation-deflection system. The beam-rotating system is located just in front of the actual depressed collector. The electron beam axis is indicated.

In this set-up the electrons are decelerated to a very low axial velocity. Simultaneously, the entire beam is bent off-axis by an additional rotating transverse electric field to avoid excessive local heating

on the collector plates. Then, the electrons are slightly accelerated backwards and collected. The advantage of the path reversal is that secondary electrons are forced to return to the collector plates and cannot escape and be accelerated towards the undulator. The electron beam is collected on three electrodes, on large circular areas. The system is rotationally symmetric with respect to the dashed line (R=0).

The energy distribution of the unspent electron beam as calculated with the CRMFEL code ranges from -200 keV to +60 keV relative to the initial energy of 2 MeV. The simulation results are used in fig. 7. At z=0 the beam is convergent and has a diameter of 14 mm.

Recently, the energy distribution has been calculated with the GPT code. The result is shown in fig. 10, for the case of a 12 A electron beam with an initial energy of 1.75 MeV. The energy spread is shown for the case of optimum interaction with the mm-waves; the electron beam is injected on axis [14].

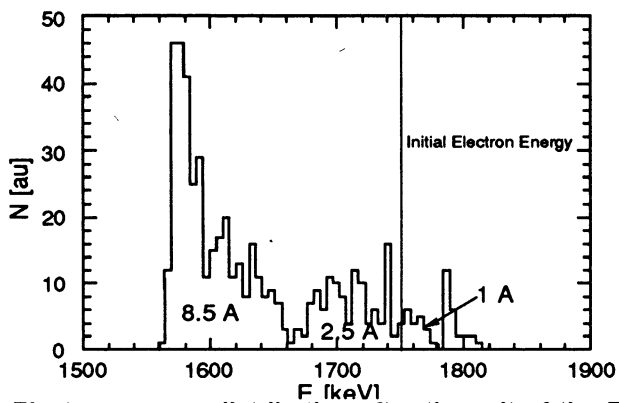

Fig. 8 **Electron energy distribution after the exit of the FEM in case of optimised FEL interaction, as calculated by the CRMFEL code. Three main peaks can be distinguished, having each a current as indicated.**

At the moment the technological aspects of the design of the depressed collector are under investigation, such as the construction of the cooling systems of the collector electrodes, which must handle 600 kW during 100 ms pulses, the 250 kV high-voltage feed-throughs and the vacuum aspects [13]. The design is now based on a separate depressed-collector vacuum vessel at earth potential. Separate feed-throughs for each of the electrode voltages are foreseen, see fig. 9.

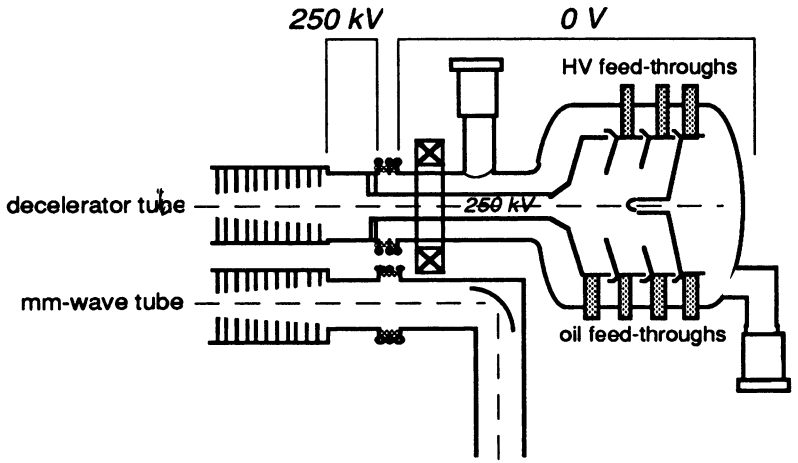

Fig. 9. The new design for the depressed collector. On the right side the electrons enter via the decelerator tube (upper). The lower tube is the mm-wave output-beam transport-tube.

9. Undulator

For proper transport of the 12 A, 2 MeV electron beam through the narrow waveguide inside the undulator, transverse focusing in both the x-z and y-z plane is required. After having compared several types of undulators, we have opted for an undulator geometry as developed at the RRC Kurchatov Institute in Moscow [15], see fig. 10.

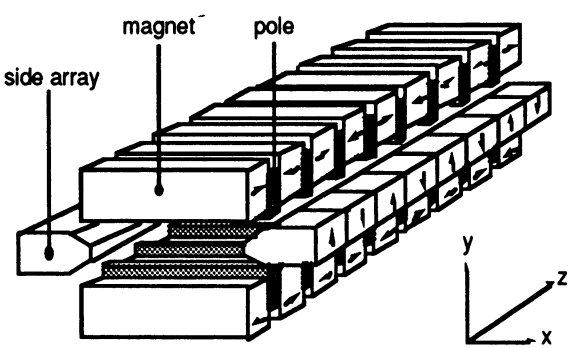

fig. 10. The undulator with its side magnets.

This undulator consists of two planar magnet units and two magnetic side arrays. The side arrays shape the undulator field profile for

focusing in the wiggling plane, while at the same time, the main field is enhanced. An additional advantage of the side magnets is that field shaping, and thus the transverse focusing strength, can be tuned very accurately, and can be changed when required.

10. Millimeter-wave System

The FEM is configured as a mm-wave oscillator, consisting of a waveguide amplifier section (inside the undulator) and a feedback and outcoupling system. Since the electron beam line is completely straight the mm waves have to be coupled out sideways. Further, the fraction of the electron current intercepted in the mm-wave system should be as small as possible, which means that there should be enough transverse space for the electron beam. After taking all requirements into account a rectangular corrugated waveguide was chosen, carrying the very low-loss hybrid mode HE_{11}, with the E-field parallel to the broad side of the waveguide [16].

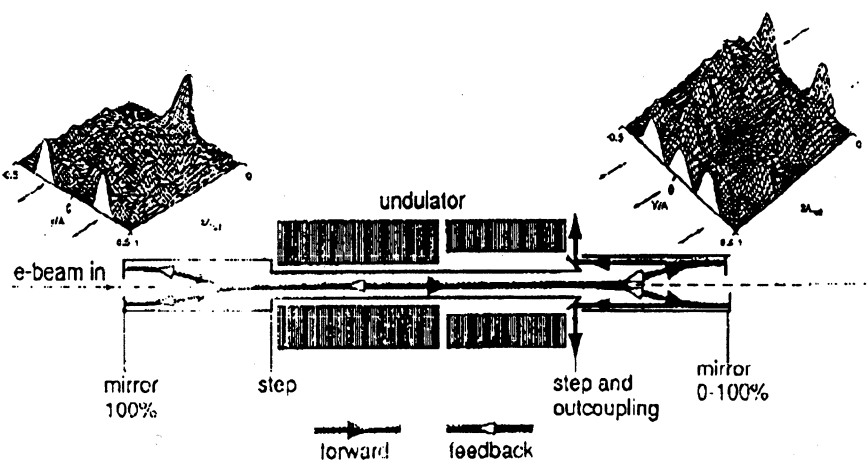

Fig 11 Schematic layout of the mm-wave system. Left of the undulator the 100 % reflector and on the right side of the undulator the splitter system is given. This splits the feedback power (going through the primary waveguide back to the 100 % reflector) from the output power.

Outcoupling and reflection systems are incorporated through a stepped waveguide, as follows. Both before and after the undulator the

Outcoupling and reflection systems are incorporated through a stepped waveguide, as follows. Both before and after the undulator the transverse cross section of the waveguide changes step-wise from 15*20 mm^2 to 60*20 mm^2 (for a frequency of 260 GHz), where the 60 mm direction is parallel to the undulator magnetic field. This ensures that the primary HE_{11} mode is fully separated into two off-axis beams. These beams have identical profiles and plane wave fronts.

Full separation of the beams takes place after a distance $L=a^2/n\lambda$ from the step, with a is the height of the waveguide after the step and n is the number of parallel beams, respectively [17]. At the position of the widest separation two mirrors are placed, which reflect the two mm-wave beams, while the electron beam passes on axis through the opening between the mirrors, see fig. 11. On the left side simulation results show the field intensities of an HE_{11} beam, propagating in a stepped waveguide. Here it splits into two identical beams. The two beams merge into one HE_{11} beam after reflection on the two mirrors. In this way the 100 % reflector is formed. The power in the aperture is < -30 dB.

Outcoupling and feedback of the mm waves is realised by a similar stepped waveguide behind the undulator. By giving one of the two mirrors a small displacement in z-direction, the reflected beams have a phase difference and one on-axis and two off-axis backward-propagating beams are formed. By variation of the phase difference, i.e., by translating one of the mirrors, the reflected on-axis power can be varied from 0 to 100 % of the output mm-wave power. The on-axis beam propagates back all the way through the primary waveguide. In this way part of the mm-wave power is fed back. The two off-axis beams are coupled out by way of 45° miter bends. On the right side of fig. 11 simulation results can be seen for the outcoupling system. In a similar way, the two output beams are combined to one in a parallel mounted combiner system.

Without changing any of the dimensions a fast tunability around the chosen central frequency can be achieved by varying only the electron energy. However, to adjust the frequency over the entire frequency range of 130 GHz to 260 GHz, it is necessary to make a variation of a, the height of the waveguide after the step.

By using a quasi-optical confocal mirror system the single mm-wave beam is transferred in vacuum to the insulator tube between 2 MV and ground potential. This is a tube very similar to the accelerator tube. However, to let the mm waves pass from the 2 MV level to earth potential a wider -tapered- aperture is used for controlling the electrostatic field.

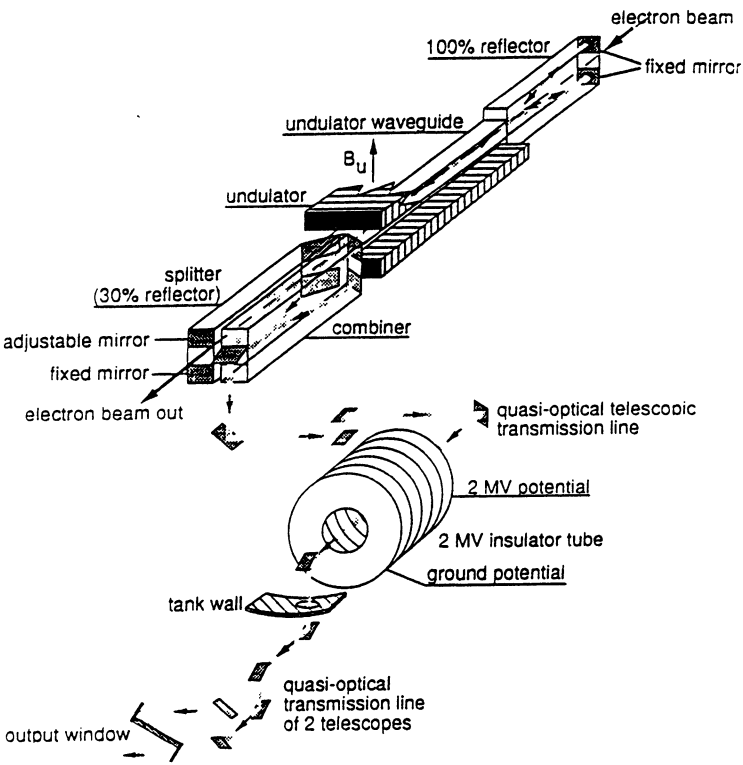

Fig. 12. Schematic layout of the mm-wave system of the Fusion-FEM project. On the upper right side is shown the 100 %-reflector, then the primary waveguide inside the undulator and the adjustable reflector and outcoupling system via confocal telescope quasi-optical mirror systems.

11. Broadband output window

Since the frequency of the FEM has to be varied over a very wide frequency range, it is necessary that the vacuum barrier is broadband as well. We have chosen for a window at the Brewster angle [18,19],

since this is the only possibility for a real broad-band solution over a band as wide as one octave. A disadvantage, however, is the large angle between the incoming mm waves and the normal to the window surface. For the first stage of the Fusion-FEM project a single-disc, edge-cooled boron-nitride Brewster-angle window with a diameter of 140 mm.is sufficient to withstand the 100 ms pulses.

12. Status of the project

The first experiments are done in the inverse set-up [20]. Here, the electron gun is mounted inside the high voltage terminal. The undulator and waveguide system are outside the pressure vessel at earth potential for easy adjustments and fine tuning of the entire system. As a consequence the decelerator and depressed collector cannot be used yet, which means that the FEM pulse duration will be limited to 10 μs.

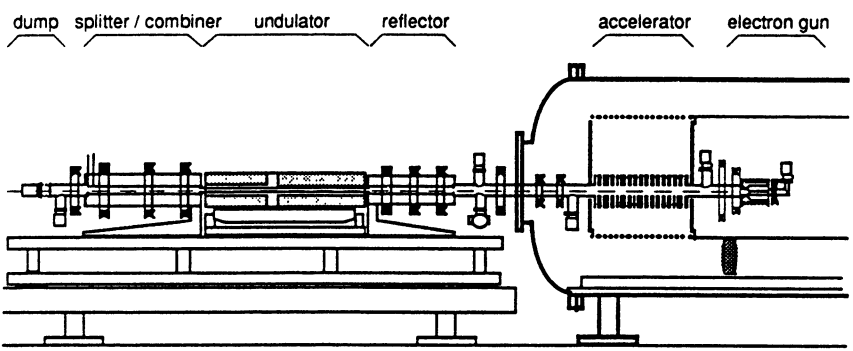

Fig. 13. Schematic layout of the inverse set-up

The entire high-voltage system, consisting of the Insulated Core Transformer (ICT), the high-voltage terminal and the accelerator column, have been tested up to -2 MV. The control and communication systems have been installed and implemented. Special care has been given to prevent electromagnetic interferences between the electrical systems and control and computer systems inside the high-voltage terminal.

During initial electron-beam tests in October 1996, in which the gun was operated at 35 kV, a beam current of 3 A has been accelerated to 1.5 MV in 5 μs pulses. In fig.14 both the cathode current is shown and current on the dump after acceleration up to 1.5 MV.

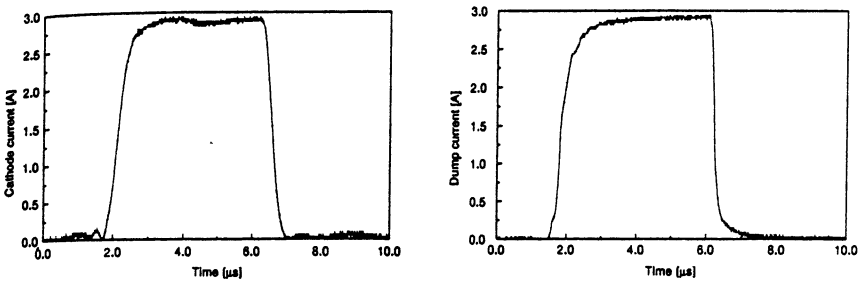

Fig. 14. Measured current on the cathode (left) and dump (right)

The current is lower than expected, due to poisoning of the thermionic cathode because of insufficient vacuum quality (in the 10^{-7} range). Nevertheless, this low current was sufficient to test the beam diagnostics and beam focusing and alignment systems, successfully. The beam centre of mass position and loss currents were measured using 4-plate electrostatic pick-ups and apertures, respectively. For the same pulse as given in fig. 15 the measured current on one of the apertures is given. During current rise and fall the electron optics are not at the optimized values, due to the gate voltage slopes. During the flat top of the pulse virtually no current is measured on the aperture.

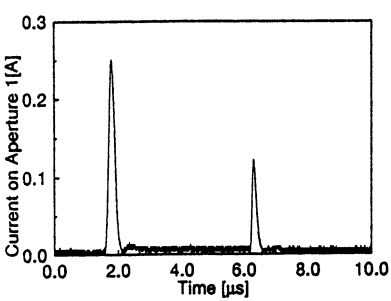

Fig. 15. Measured current on the aperture

Separately the cathode current is measured as a function of anode voltage at two different filament power levels, now the beam is dumped before it enters the accelerator tube, see fig. 16.

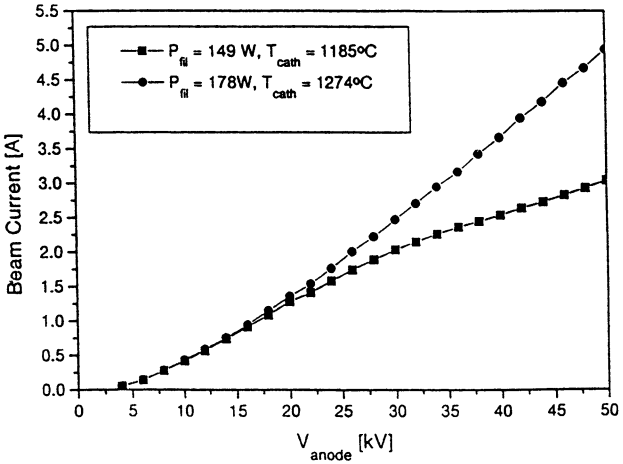

Fig. 16. Beam current as a function of anode voltage

13. Conclusions

The construction and the commissioning of the accelerating part of the Fusion FEM beam line is in progress. The complete high-voltage system is routinely operated up to 1.8 MV. Very encouraging results were achieved during intermediate tests with an electron beam of 3 A that has been accelerated to 1.5 MV, during 5 μs. Due to poisoning of the thermionic cathode, the beam current was limited. Now the undulator is being installed and the electron-beam transport through the undulator will be tested soon.

14. Acknowledgements

The authors are grateful to the many people who had very valuable contributions to this report:
W. Kooijman, G. Land, A. Putter, F. Wijnoltz, *Rijnhuizen*
A. Tulupov, *Russian Res. Centre, Kurchatov Inst. Moscow, Russia*
H.-U. Nickel and M. Thumm, *Kernforschungszentrum Karlsruhe,*
A.A. Varfolomeev, S.N. Ivanchenkov, A.S. Khlebnikov and
A.V. Smirnov, *RRC, Moscow,*
W. Kasparek, G. Müller, D. Wagner, *Inst. für Plasmaf, Stuttgart*

A. Krasnykh, *JINR, Joint Inst. for Nuclear Research, Dubna, Russia.*
M. Cattelino and G. Miram, *CPI/Varian, Palo Alto, USA*
P.C.T. van der Laan, P. van Deursen and J. Wetzer, *T.U. Eindhoven*

The work described here was performed as part of the research programme of the association agreement between the "Stichting voor Fundamenteel Onderzoek der Materie" (FOM) and Euratom, with financial support from the "Nederlandse Organisatie voor Wetenschappelijk Onderzoek" (NWO) and Euratom.

15. References

[1] M. Caplan, et al,. Jan. 95, Proc. 9th Workshop on ECE and ECRH, EC9, World Scientific, 333-341.
[2] A.G.A. Verhoeven, *et al.,* "Proc. of the Int. Worksh. on Strong Microwaves in Plasmas, IAP, N. Novgorod, (1993) p.616-631
[3] M. Caplan, T.M. Antonsen, B. Levush, A.V. Tulupov, W.H. Urbanus. Nucl. Instr. and Meth. **A358** (1995)174.
[4] A.V. Tulupov, W.H. Urbanus, A.G.A. Verhoeven, M.J. van der Wiel, M. Caplan. Nucl. Instr. and Meth. **A341** (1994) 305.
[5] M. Caplan, C.A.J. van der Geer, M. Valentini, and W.H. Urbanus, Nucl. Instr. and Meth. **A375** (1996) 91.
[6] P.J. Eecen, T.J. Schep and A.V. Tulupov, Nucl. Instr. and Meth. **A375** (1996) 190.
[7] S.B. van der Geer, J.F.G. van der Geer and M.J. de Loos, private communications, 1995.
[8] G. Herrmann, J. of Applied Physics, Vol. **29**, No. 2, (1958) 127
[9] C.C. Cutler, and M. Hines, Inst. Radio Eng. **43** (1955) 307.
[10] M.J. Cattelino, J. Atkinson, Varian Internal Techn Rep. 1993.
[11] L.R. Elias and G.J. Ramian, IEEE **NS-32**, No. 2 (1985) 1733.
[12] I. Kimel, L.R. Elias and G.J. Ramian, Nucl. Instr. and Meth. **A250** (1986) 320.
[13] G. Poorter, ISBN 90-5282-694-3. Technical. Univ. Eindhoven
[14] M. Valentini, et al., FEL96, Rome
[15] A.A. Varfolomeev, *et al.,* Nucl. Instr. and Meth. **A341** (1994) p. 466
[16] G.G. Denisov, *et al.,* Proc. of Workshop on FEM-mm waves, Rijnhuizen, The Netherlands 1992.
[17] L.A. Rivlin, Laser Focus (1981) 82.
[18] H.-U. Nickel, H. Massler and M. Thumm, Proc. 18th Int. Conf on IR & MMWs, Colchester, 1993, p. 172
[19] G.G. Denisov, and M. Yu. Shmelyov , Proc. 21th Int. Conf on IR & MMWs 1996, Berlin, BF3
[20] Urbanus, et al., Nucl. Instr. and Meth. **A375** (1996) 401

HIGH-EFFICIENCY OPERATION OF THE JINR-IAP Ka-BAND FEL-OSCILLATOR

*N.S. Ginzburg**, A.A. Kaminsky*, A.K. Kaminsky*, N.Yu. Peskov**, S.N. Sedykh*, A.P. Sergeev*, A.S. Sergeev***

*Joint Institute for Nuclear Research, Dubna, Moscow region, Russia
**Institute of Applied Physics RAS, Nizhny Novgorod, Russia

A narrow-band high-efficiency FEL-oscillator with a Bragg resonator was designed basing on a linear induction accelerator which formed a 1 MeV, 200 A, 200 ns electron beam. At the frequency of 31 GHz radiation with power 31 MW and efficiency 25% was measured. High efficiency and narrow spectrum width was achieved due to selective properties of the Bragg resonator in combination with the high quality of the helical electron beam formed in the reversed guide field regime.

Introduction

The aim of this work was to design, build and construct a high-efficiency, narrow-band spectrum FEL-oscillator which operated in the millimeter wavelength range. To achieve this, the high selective property of Bragg resonators [1] was combined with the advantages of operating the FEL in the so-called reversed guide magnetic field regime. When operating in this regime, previous investigations of FEL-amplifiers [2, 3] demonstrated the possibility of forming a helical electron beam with a low spread of parameters and, thus, the possibility to achieve high efficiency. At the first stage of JINR-IAP experiments the FEL-oscillator with the record efficiency of 19% for the millimeter wavelength FEL-oscillators has been realized [4]. At this stage we optimized parameters of Bragg cavity that allowed to increase efficiency of the FEL up to 25%.

Experimental set-up

An experimental study of the FEL was performed on the LINAC-3000 (JINR, Dubna) (Fig. 1) which generated electron energies up to 1 MeV and a 200 A beam current pulse of duration ~200 ns at a repetition rate up to 2 Hz. The helical wiggler with period of 6 cm and amplitude of the transverse magnetic field on the axis up to 3.5 kG was used to pump the oscillation velocity to the electrons. The wiggler field was slowly up-

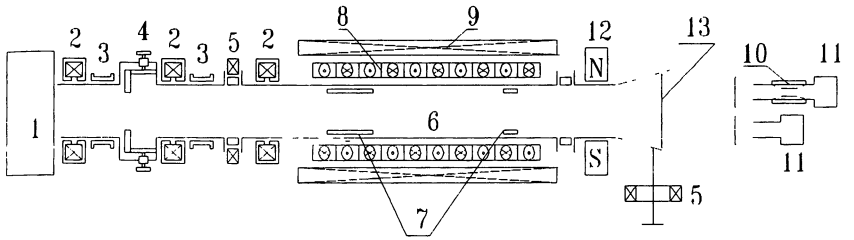

Fig. 1. Scheme of the FEL-oscillator with Bragg resonator:
1 - driver beam injector (induction linac); 2 - magnetic lens; 3 - two-direction beam position corrector; 4 - beam scraper; 5 - beam current monitor; 6 - interaction region; 7 - RF Bragg mirrors; 8 - undulator; 9 - solenoid; 10 - cut-off waveguide filter; 11 - RF detector; 12 - deflecting magnet; 13 - RF window.

tapered over the initial six periods providing an adiabatic entrance for the electron beam. The wiggler was immersed in a uniform axial magnetic field generated by a solenoid. The strength of this field could be varied up to 10 kG. Also, it was possible to vary the direction of the guide field.

Free Electron Laser operation in the reversed guide magnetic field regime (marked by "-" sign) was studied. In such a regime the direction of rotation of the electrons in the uniform axial guide field is opposite to its rotation in the wiggler field. An advantage of operating the FEL in the reverse guide magnetic field regime, far from the cyclotron resonance regime is the ability to form a high-quality helical electron beam with low spread of parameters.

Microwave system of the FEL

To provide the narrow-band spectrum of radiation a two-mirror Bragg resonator was designed and made for the FEL experiment. The cavity consisted of two Bragg reflectors separated by a central uniform cylindrical waveguide with its inner diameter 22 mm. The Bragg reflectors were constructed by machining 0.3 mm deep and 5.4 mm period corrugations on the inner wall of the waveguide. A 16.2 cm long Bragg reflector was positioned at the cathode side of the cavity with Bragg reflectors of different lengths positioned at the collector side of the FEL. In agreement with calculations, three effective reflections of the operating $TE_{1,1}$ wave of the circular waveguide into backward waves were observed

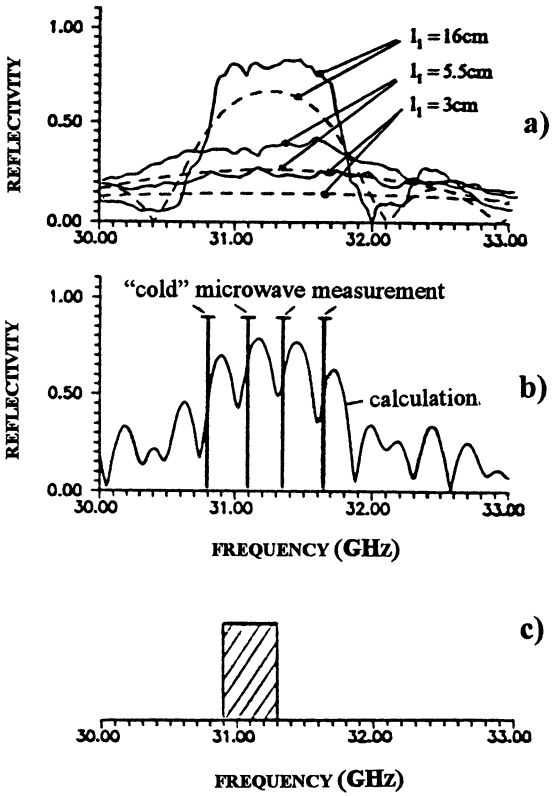

Fig. 2.
a) Reflection coefficient of separate Bragg mirrors having different lengths versus frequency (for feedback circle $TE_{1,1} \leftrightarrow TM_{1,1}$): solid line corresponds to "cold" microwave measurements, dotted line corresponds to the calculations.
b) Reflection coefficient of two-mirror Bragg resonator (l_1 = 16 cm, l_0 = 40 cm, l_2 = 3 cm) versus frequency. Minimum of the reflection coefficient correspond to eigenmodes of the Bragg resonator. Eigenfrequencies measured in "cold" microwave experiment are shown.
c) Upper estimation of radiation spectrum in "hot" experiments measured by means of a set of cut-off waveguide filters.

in "cold" microwave measurements of the Bragg reflectors. For a launched $TE_{1,1}$ wave at a frequency of ~29 GHz, the backward $TM_{1,1}$ and $TM_{2,1}$ waves at the frequency of ~31.5 GHz and ~38.5 GHz respectively were measured. Dependence of the reflectivity of the Bragg mirrors as a function of frequency is shown in Fig. 2a. The number of high-Q-factor longitudinal modes for every reflection zone was 3-7 (Fig. 2b) when a regular cavity section 30 cm to 70 cm long was used.

Numerical simulation of excitation of a FEL with Bragg resonator

Preliminary, dynamics of FEL operation with a two-mirror Bragg resonator was studied theoretically. Time domain analysis taking into consideration the dispersion properties of the Bragg reflectors was used. The numerical simulation of excitation of a FEL by a relativistic electron beam and oscillation build-up was performed. Analysis of the frequency spectrum and the dependence of the output power on time indicates a two stage transient process. The first stage of the transient process is accompanied by large oscillations of efficiency and output power (Fig.3a). Such oscillations are caused by excitation of all longitudinal modes

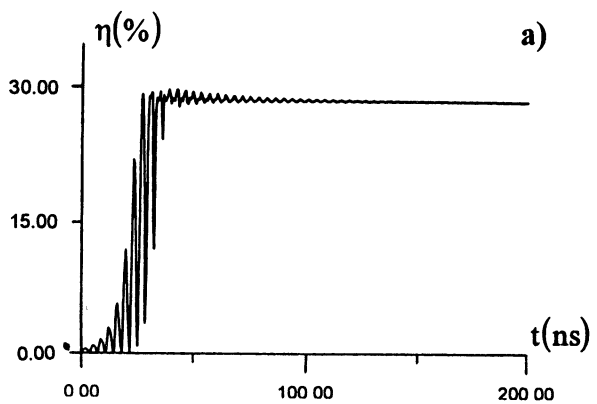

Fig. 3. Computer simulation of oscillations build-up in the FEL-oscillator with two-mirror Bragg resonator under optimal experimental conditions (E_{beam} = 0.8 MeV, I_{beam} = 150 A, f = 31 GHz, B_0 = -2 kG, $B_\perp$ = 1 kG, Q = 450)
a) time dependence of efficiency;

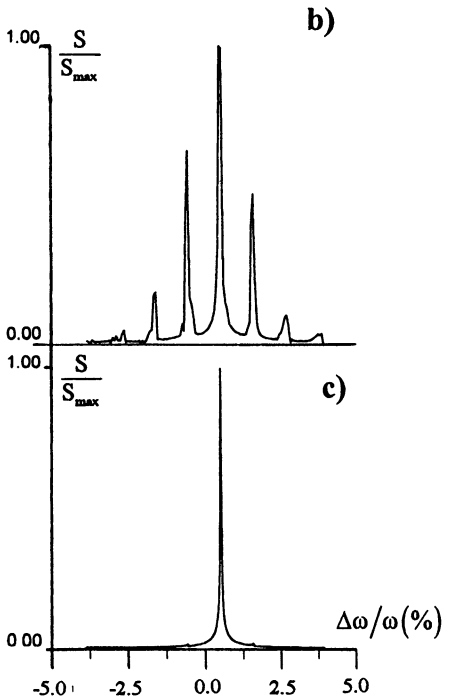

Fig. 3 (continuation).
b) spectrum of radiation in the transient stage (t < 50 ns);
c) spectrum of radiation in the stationary regime (t > 50 ns).

disposed at the zone of Bragg reflections (Fig. 3b). Later at the second stage one of the longitudinal modes grows and suppresses other modes due to a nonlinear mode competition mechanism. This results in a single mode being established (Fig. 3c) and, consequently, stationary single frequency operation.

Also, parameters of the Bragg cavity were optimized and optimal parameters of the resonator was found. Increasing reflectivity of Bragg mirrors above the optimal value led to lower electron efficiency and increasing width of radiation spectrum. When the Q-factor of the resonator greatly exceeded the starting value the multifrequency self-modulation regimes were observed in the FEL.

Experimental results

As result of the experiment, radiation at the designed circularly polarized $TE_{1,1}$ wave and separate frequencies corresponding to all the feedback waves mentioned above was detected. Selection of the feedback regime was achieved by changing both the wiggler and guide fields. The duration of the RF pulse measured was approximately 100 ns (Fig. 4). The radiation frequencies detected were in good agreement with the measured reflection bands of Bragg mirrors (Table 1). The highest radiation power (measured by means of a calorimeter and calibrated semiconductor detectors) as well as the narrowest bandwidths were measured at the frequency of 31 GHz. Reflection coefficients of the Bragg mirrors and, consequently, the Q-factors of the longitudinal modes corresponded to the optimal value calculated from the computer simulation. Initially a 10.8 cm long output Bragg reflector was used which was later decreased in length to 3 cm. Calculations indicated that FEL efficiency should increase the length of the output Bragg reflector is made shorter At the same time the length of the central regular waveguide section was increased from 30 cm to 70 cm. By measuring the radiation spectrum width and power for the different Bragg cavity configurations mentioned above it was discovered that the both remained relatively constant. These experiments demonstrate that this type of FEL is a flexible system which maintains high efficiency and high selectivity over a large range of cavity configurations.

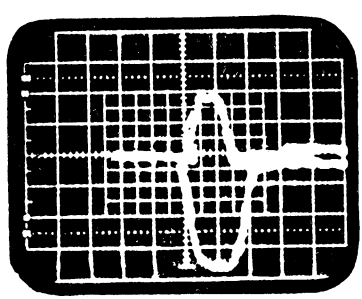

Fig. 4. Typical oscilloscope traces of beam current (lower signal, 50 A/div) and RF power (upper signal, 15 MW/div); horizontal scale 100 ns/div .

The spectrum of the radiation was determined by means of a set of waveguide cut-off filters which were used to measure the wavelength in the band 0.7 - 1.2 cm to the accuracy of 1%. The measured spectrum width of the output radiation in all cases did not exceed the reflection band width of the Bragg mirrors. Comparison of the measured spectrum of radiation (Fig. 3c) with that measured in the "cold" microwave experiments (Fig. 3b) shows that only one eigenmode of the cavity lies inside the measured frequency region of the radiation. Computer simulations predict that the electron beam does not shift the frequency of the radiation from the eigenfrequency of the cavity. Thus, experimental measurement does not contradict the theoretical prediction of realization of single-mode single-frequency operation of the FEL.

An atmosphere break-down was observed when output radiation was focused with a spherical mirror placed at the distance about 1.5 m from the output window of the FEL (Fig. 5). The break-down was observed at all the feedback circles regimes. The measured on the break-down photographs the wavelength was in good agreement with measurements of the spectrum.

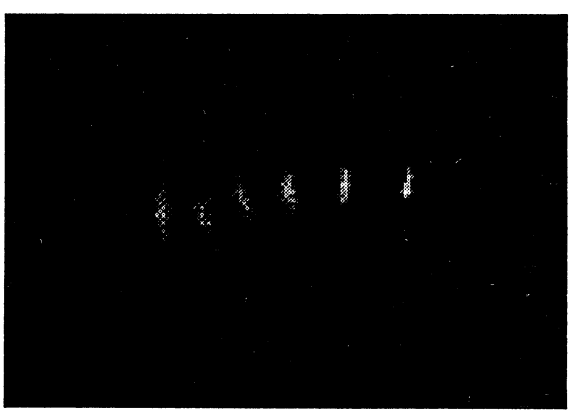

Fig. 5. Potograph of the atmospheric RF-breakdown.

Conclusion

A narrow band FEL-oscillator with a reversed guide magnetic field which generated microwave radiation at different feedback regimes of the Bragg resonator was realized. The FEL parameters under which microwave generation was observed were in good agreement with numerical simulation. Measured radiation frequencies coincided with the results of "cold" microwave experiments. At the frequency of 31 GHz the output power was 31 MW which corresponded to FEL efficiency of ~25%. The efficiency achieved outstrips the efficiency of previous FEL-oscillator experiments which used a guide magnetic field. It is important to note that high efficiency was realized at the full current produced by the accelerator (without the need to reduce the current in the beam).

The observed frequency band width was less than 1%. The radiation spectrum most probably consisted of one resonator mode or, perhaps, two such modes. This rather narrow spectrum width was possible because of the high quality of the helical electron beam formed in the reversed guide field regime as well as the excellent selective properties of the Bragg resonator. We believe that here only upper estimation of the real frequency bandwidth is presented. In later experiments more accurate measurement of the spectrum will be attempted.

This work was supported by grants N:94-02-04481 and N:95-02-05697 from Russian Foundation for Fundamental Research.

Table 1. Summary of experimental results (E_{beam} = 0.8 MeV, I_{beam} = 150 A)

Interaction region length (cm)	40	70	40	30	40
Output reflector length (cm)	10.8	5.4	3.0	5.4	10.8
Undulator field (G)	1100	900			610
Solenoid field (G)	-2200	-1800			-1440
Radiation frequency (GHz) (corresponding backward wave)	29.3±0.3 $TE_{1,1}$	31.1±0.2 $TM_{1,1}$			38.2±0.9 $TM_{1,2}$
Output power (MW)	6	20	31	23	3
Efficiency (%)	5±1	16±3	25±5	19±4	2.5±0.5

References

1. Bratman V.L., Denisov G.G., Ginzburg N.S. and Petelin M.I., IEEE J. of Quant. Electr., 1983, QE-19, 282.
2. Kaminsky A.A., Kaminsky A.K., Rubin S.B. e.a., Particle Accelerat., 1990, 33, 189.
3. Conde M.E., Bekefi G., Phys. Rev. Lett., 1991, 67, 3082.
4. Kaminsky A.K., Kaminsky A.A., Sarantsev V.P. e.a., Nucl. Instr. and Meth., 1996, A375, 215.

EXPERIMENTAL OBSERVATION OF SUPERRADIANCE IN THE MILLIMETER-WAVE BAND

A.D.R.Phelps, A.W.Cross, S.J.Cooke, N.S. Ginzburg, A.S. Sergeev*, I.V. Zotova*, Yu.V.Novozhilova*, N.Yu.Peskov*. I.V.Konoplev*, V.G.Shpak**, M.I.Yalandin**, S.A. Shunailov**, and M.R. Ulmaskulov***

Department Physics and Applied Physics University of Strathclyde. Glasgow, G4 0NG, UK
*Institute of Applied Physics, Russian Academy of Science Nizhny Novgorod, Russia
**Institute of Electrophysics, Russian Academy of Science Ekaterinburg, Russia

Introduction.

In recent years much attention has been given to theoretical considerations of superradiance (SR) from space-localized non-equilibrium ensembles of electrons [1-14]. This phenomenon includes features which are present in both stimulated (selfbunching and coherence) as well as spontaneous processes (absence of threshold). It is reasonable to consider SR in a specific situation when the electron pulse length essentially exceeds the operating wavelength (otherwise effective traditional spontaneous emission .) while at the same time is less or comparable with the interaction length (in contrast with traditional mechanisms of stimulated emission of quasi-continuous electron beams which are used extensively in microwave electronics - TWT, BWO, CRM. FEL, etc). Coherent emission from the entire electron pulse can only occur when a selfbunching mechanism typical for stimulated emission develops. Another natural condition of coherent emission is the mutual influence of different fractions of the electron beam pulse. In the absence of external feedback such influences can be caused by slippage of the wave with respect to the electrons due to a difference between the electron drift velocity and the electromagnetic wave group velocity.

Superradiance can be associated with several different mechanisms of stimulated emission: bremsstrahlung, cyclotron, Cherenkov.

etc. The first part of this report is devoted to the theoretical description of cyclotron and Cherenkov superradiance in waveguides. In the second part we present results of the first experimental observation of cyclotron, undulator and Cherenkov SR from an isolated electron bunch in the millimeter-wave band.

1. Basic theoretical description.

1.1 Cyclotron superradiance in the group synchronism condition.

The cyclotron SR [10-14] involves the process of azimuthal self-bunching and consequent coherent emission in an ensemble of electrons rotating in a uniform magnetic field. It was demonstrated in [14,15] that conditions of group synchronism when the electron-bunch drift velocity $v_{||}$ coincides with the e.m. wave group velocity v_{gr} is the most favourable regime for cyclotron type of SR. In fact, this regime includes some of the advantages of gyrotrons [16] as far as in the moving reference frame, electrons as in gyrotrons radiate at quasi-cutoff frequencies. The regime of group synchronism is realized during waveguide propagation of radiation when dispersion curves of the wave, $k = c^{-1}\sqrt{\omega^2 - \omega_c^2}$, and of the electron flux, $\omega - kv_{||} = \omega_H$, are tangent (Fig.1(a)). In this case the cutoff frequency ω_c and relativistic gyrofrequency $\omega_H = eH_0/\gamma mc$ satisfy $\omega_H = \omega_c\gamma_{||}^{-1}$, where $\gamma_{||} = (1 - v_{||}^2/c^2)^{-1/2}$, $\gamma = (1 - v_{||}^2/c^2 - v_\perp^2/c^2)^{-1/2}$ and $v_\perp = \beta_\perp c$ is the electron transverse velocity.

It is reasonable to analyze SR under the group synchronism condition in a reference frame K' moving with the electron bunch of length b'. Using Lorentz transformations, we easily find that the longitudinal wave number k' and the transverse component of the magnetic field in the K' frame tend to zero. As a result we have an ensemble of rotating electrons, with zero translational velocity, which radiates at a quasi-cutoff frequency (Fig.1(b)) i.e. in a gyrotron-like regime.

Under the assumption that the transverse structure of the radiation $\vec{E}'_\perp(\vec{r}'_\perp)$ is the same as that of the waveguide mode, we present the radiation field as

$$\vec{E}' = Re[\vec{E}'_\perp(\vec{r}'_\perp)A'(z',t')\exp(i\omega_c t')],$$

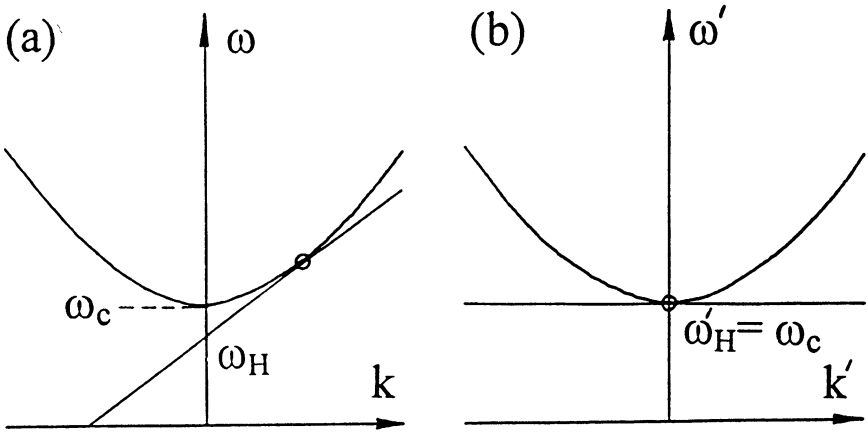

Fig.1. Dispersion characteristics corresponding to grazing regime in (a) laboratory and (b) moving reference frame.

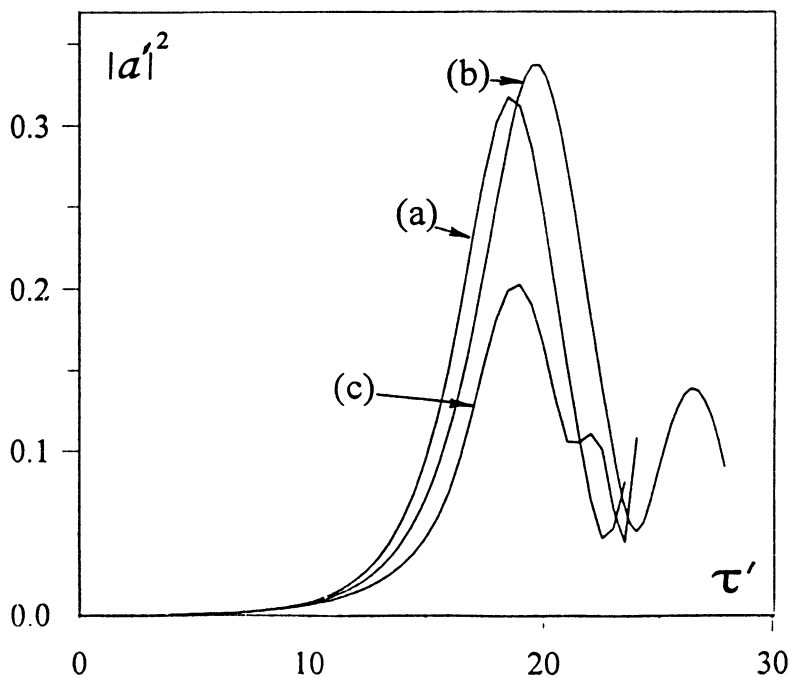

Fig.2. Time dependence of the square of the amplitude of the electric field of the SR pulse in the moving frame:
(a) Δ=0, (b) Δ =-0.4 ,(c) Δ=1.

where the evolution of the longitudinal field distribution is described in accordance with the dispersion relation by a parabolic equation

$$i\frac{\partial^2 a'}{\partial Z'^2} + \frac{\partial a'}{\partial \tau'} = 2if(Z')G\langle\beta'_+\rangle_{\Theta_0} \qquad (1)$$

The azimuthal self-bunching is caused by the dependence of the gyrofrequency on the electron energy and described by the equation

$$\frac{\partial \beta'_+}{\partial \tau'} + i\beta'_+(|\beta'_+|^2 - \Delta - 1) = ia'. \qquad (2)$$

Under the assumption that in the initial state the electrons are distributed uniformly in cyclotron-rotation phases, aside from small fluctuations ($r \ll 1$), we can write the initial conditions on system (1),(2) as follows

$$\beta'_+|_{\tau'=0} = \exp[i(\Theta_0 + r\cos\Theta_0)],\ \Theta_0 \in [0, 2\pi],\ a|_{\tau'=0} = 0.$$

Here $\beta'_+ = (\beta'_x + i\beta'_y)/\beta'_{\perp 0}$ is the normalized transverse electron velocity; $Z' = z'\beta'_{\perp 0}\omega_c/c$, $\tau' = t'\beta'^2_{\perp 0}\omega_c/2$, $a' = \dfrac{2eA'}{mc\omega_c\beta'^3_{\perp 0}} \cdot J_{m-1}(R_0\omega_c/c)$, $\Delta = 2(\omega'_H - \omega_c)/\omega_c\beta'^2_{\perp 0}$ is the detuning of the unperturbed gyrofrequency from the cutoff frequency,

$$G = \frac{1}{2\pi} \cdot \frac{eI_0}{mc^3} \cdot \frac{1}{\beta^4_{\perp 0}\beta_{\|0}\gamma^3_{\|}} \cdot \frac{\lambda_c^2}{\pi R^2} \cdot \frac{J^2_{m-1}(R_0\omega_c/c)}{J^2_m(\nu_n)(1 - m^2/\nu_n^2)}$$

is a form-factor written under the assumption that the electron bunch is hollow with an injection radius R_0; I_0 is the total current in the lab frame; R is the radius of the waveguide; m is the azimuthal index of the operating mode; J_m is a Bessel function and ν_n is the n-th root of the equation $dJ_m/d\nu = 0$. The function $f(Z')$ describes the distribution of the electron density along the longitudinal coordinate. We assume further that $f(Z')$ is a rectangular function of normalized width $B = b'\beta'_{\perp 0}\omega_c/c$.

Based on the Eqs. (1),(2) we simulate cyclotron SR with the normalised parameters $G = 1.5$ and $B = 10$, corresponding to the experimental values: operating mode TE_{21}, waveguide radius $R = 0.5cm$, beam injection radius $R_0 = 0.2cm$, pitch factor $g = \beta_\perp/\beta_\| \sim 1$, total

current $I_0 = 150A$, pulse length $b = b'/\gamma_{||} = 7cm$. The dependence of the radiation power in the moving frame K' on time, for different values of the detuning parameter, are plotted in Fig.2. Note that the maximum growth rate corresponds to the grazing condition $\Delta = 0$. However SR also occurs for both negative and positive Δ. The possibility of radiation under negative Δ is caused by electron frequency detuning; although ω'_H is less than ω_c, the radiation frequency exceeds the cutoff frequency. Such detuning, however, can support radiation only in a limited range and for $\Delta < -1$ the SR instability ceases. At the same time for positive Δ, assuming an ideal bunch instability the radiation persists for any Δ. The growth rate only slightly falls with increasing Δ.

However it is reasonable to expect that this dependence will be much sharper in the case of real bunches with a finite spread of longitudinal velocities. In the moving frame for such a bunch different electrons can drift with respect to each other. The longitudinal mutual displacement will essentially influence the radiation if the displacement exceeds the waveguide wavelength $\lambda' = 2\pi/k'$. In the exact group synchronism regime, when $\Delta = 0$, k' tends to zero (Fig.1(b)) and λ' to infinity and longitudinal displacement of the electrons is not important. As we increase Δ and go away from the grazing regime k' decreases, λ' falls and the same displacement can strongly reduce the radiation. Such behaviour has been actually observed in the following experiments.

Results are plotted in Fig.2 corresponding to the radiation power in the comoving frame K' where the electron bunch radiates isotropically in the $\pm z'$ directions along the waveguide axis. However in the laboratory frame the situation is totally different and both components will propagate in the same $+z$ direction. To find the radiation which affected the observation point (detector) it is appropriate, using Eqs.(1) and (2), to determine the field on the line $z' + v_{||}t' = const$ along which the detector is moving in the K' frame. Using such a method the temporal dependencies of the radiation power in the laboratory frame are presented in Fig.3(a), for the case $\Delta = 0$. We see that the radiation appears as a set of two pulses. The first pulse is created by photons emitted in the K' frame in the $+z'$ direction, while the second is by photons emitted in the opposite direction. The de-

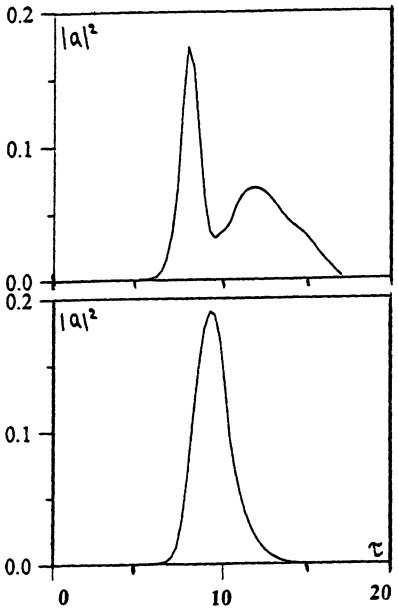

Fig.3. Time dependence of the square of the amplitude of the electric field and the instanteneous frequency of the SR pulse in the laboratory frame: (a) Δ=0, (b) Δ=-0.4.

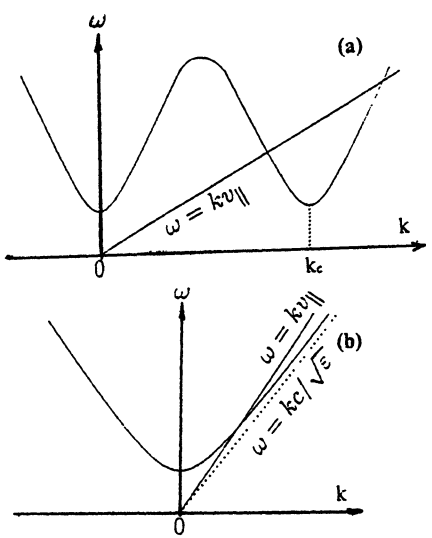

Fig.4. Dispersion diagrams for Cherenkov synchronsm (a) with backward wave in a periodically corrugated waveguide and (b) with forward wave in dielectric-loaded waveguide.

tector will overtake the second packet of photons if its velocity, which in the K' frame equals the bunch velocity $v_{||}$, exceeds v'_{gr} (note that the group velocity of radiation v'_{gr} in the K' frame is extremely low, being proportional to the small detuning of the radiation frequency above cutoff). Naturally due to the Doppler effect the frequency in the first pulse exceeds the frequency of the second pulse. For the same reason the peak power of the first pulse is essentially greater than that of the following pulse and the duration of the first pulse is less than the duration of the second pulse.

It is also important to remark that for negative Δ, the group velocity v'_{gr} becomes so small that the divergence between photons emitted in the $\pm z'$ direction is negligible and for a given observation distance in the laboratory frame the signal received by the detector will look like a monopulse (Fig.3(b)).

Experimental data presented in Sect.2.1 generally confirms the results of these theoretical considerations.

1.2 Cherenkov superradiance.

Cherenkov SR occurs when an electron bunch moves through a slow-wave system in the form of periodically corrugated metallic waveguides, as well as regular dielectric loaded waveguides. In the first case the emission is mainly associated with the excitation of the backward wave under Cherenkov-type synchronism with a slow spatial harmonic (Fig.4(a))

$$\omega = (-k + k_c)v_{||}, \tag{3}$$

where ω and k are the wave frequency and longitudinal number respectively, $k_c = 2\pi/\lambda_c$, and λ_c is the corrugation period.

In the case of the dielectric-loaded waveguide the emission is associated with a forward propagating wave under the Cherenkov synchronism condition (Fig.4(b))

$$\omega = kv_{||}. \tag{4}$$

In the both cases the longitudinal electric field of the synchronous wave can be presented in the form

$$E_z = Re[E_z^s(\vec{r}_\perp)A(z,t)\exp(i\omega(t - z/v_{||})],$$

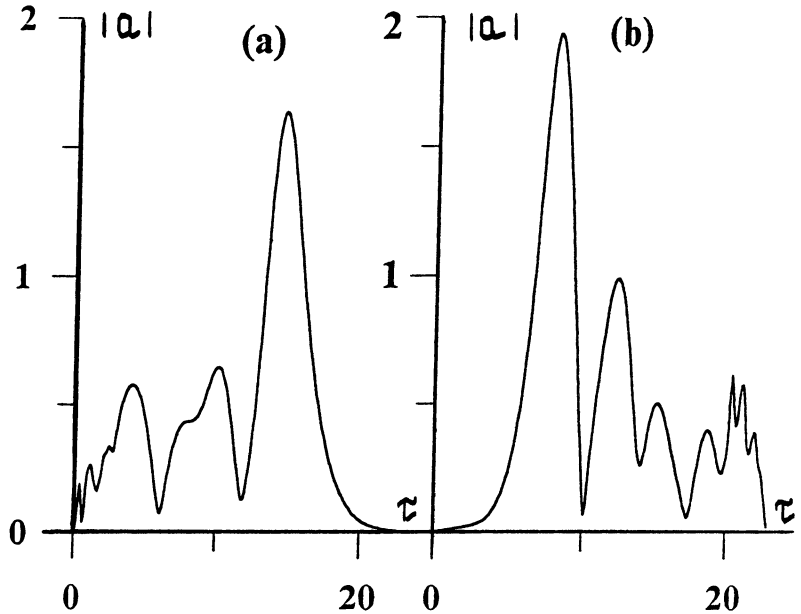

Fig.5. Dependences on time amplitude of electromagnetic field in the cases of SR in dielectric-loaded waveguide (a) and periodical waveguide (b)

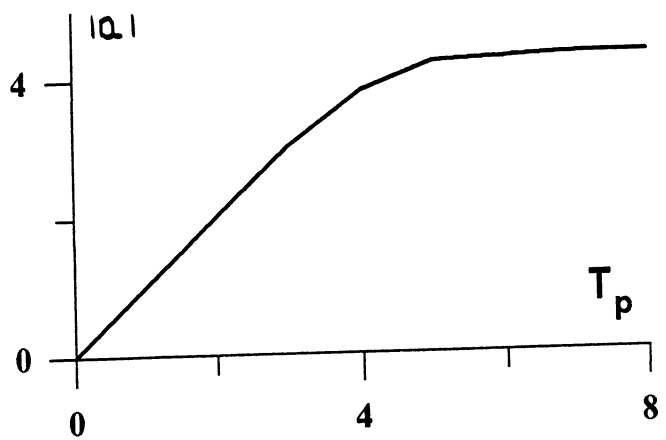

Fig.6. Dependence of maximal pulse amplitude on the electron pulse duration in the case of backward SR.

where $E_z^s(\vec{r}_\perp)$ describes the transverse distribution and $A(z,t)$ describes the temporal evolution of the longitudinal distribution. The interaction of the electrons with the radiation can be described by the following equations

$$\left(\frac{\partial}{\partial\zeta} \mp \frac{\partial}{\partial\tau}\right) a = J, \quad J = 1/\pi \int_0^{2\pi} \exp(-i\Theta) d\Theta_0$$
$$\frac{\partial^2\Theta}{\partial\zeta^2} = Re\,(a\exp(i\Theta)) \tag{5}$$

with the boundary conditions

$$\Theta|_{\zeta=0} = \Theta_0 + r cos\Theta_0, \quad \left.\frac{\partial\Theta}{\partial\zeta}\right|_{\zeta=0} = 0, \quad \Theta_0 \in [0, 2\pi], \quad a|_{\zeta=L} = 0.$$

Here we are using dimensionless variables:

$$\zeta = \beta C z. \quad \tau = \omega C(t - z/v_{||}) \left(1 \pm \frac{v_{||}}{v_{gr}}\right)^{-1}, \quad a = \frac{eAE_z^s(\vec{r}_{\perp 0})}{\beta^3 C^2 \gamma^3 mc^2}.$$

$C = \left(\frac{eI_0|E_z^s(\vec{r}_{\perp 0})|^2}{\gamma^3 \beta^3 N_s}\right)^{1/3}$ is the Pierce parameter, I_0 is the electron current, N_s is the norm of the waveguide mode, $\Theta = \omega t - k_s z$ is the electron phase with the respect to synchronous wave, where $k_s = k_c - k$ for backward and $k_s = k$ for forward wave propagation. The upper and lower signs correspond to interaction with the backward and forward waves respectively. Note that Eqs.(5) coincide with equations describing undulator SR in the frame of a uni-directional model [1-4].

The results of numerical simulation are presented in Fig.5. In both situations we see formation of a short superradiant pulse with duration of approximately several HF oscillations.

In the case of backward SR, the dependence of maximal pulse amplitude on the pulse duration is plotted in Fig.6. It is important to note that for a short duration electron bunch the peak amplitude grows according to a linear law. It corresponds to a squared dependence of the radiation power with respect to the number of electrons. So for short bunches all electrons radiate coherently.

2. Experimenal results.

A RADAN 303 accelerator with a subnanosecond slicer was used to inject typically 0.3-0.5 ns, 0.2-1 kA, 250 keV single electron pulses [17, 18]. These electron pulses were generated from a magnetically insulated coaxial diode which utilized a cold explosive emission cathode. Ã typical oscillogram of the electron bunch current is presented in Fig.7. The fast rising e-beam current and accelerating voltage pulses were measured using a Faraday cage strip line current probe and an in line capacitive voltage probe respectively, with both signals recorded using a 7 GHz Tektronix 7250 digitizing oscilloscope. To change the electron current a special collimator was used. High cur-

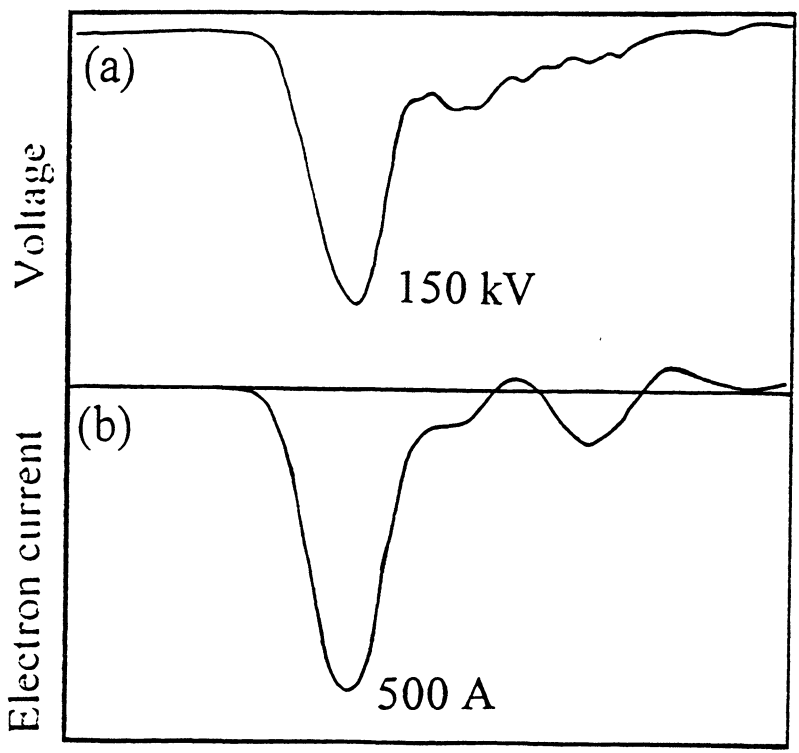

Fig.7. Oscillograms: (a) pulse output voltage, (b) electron bunch current.

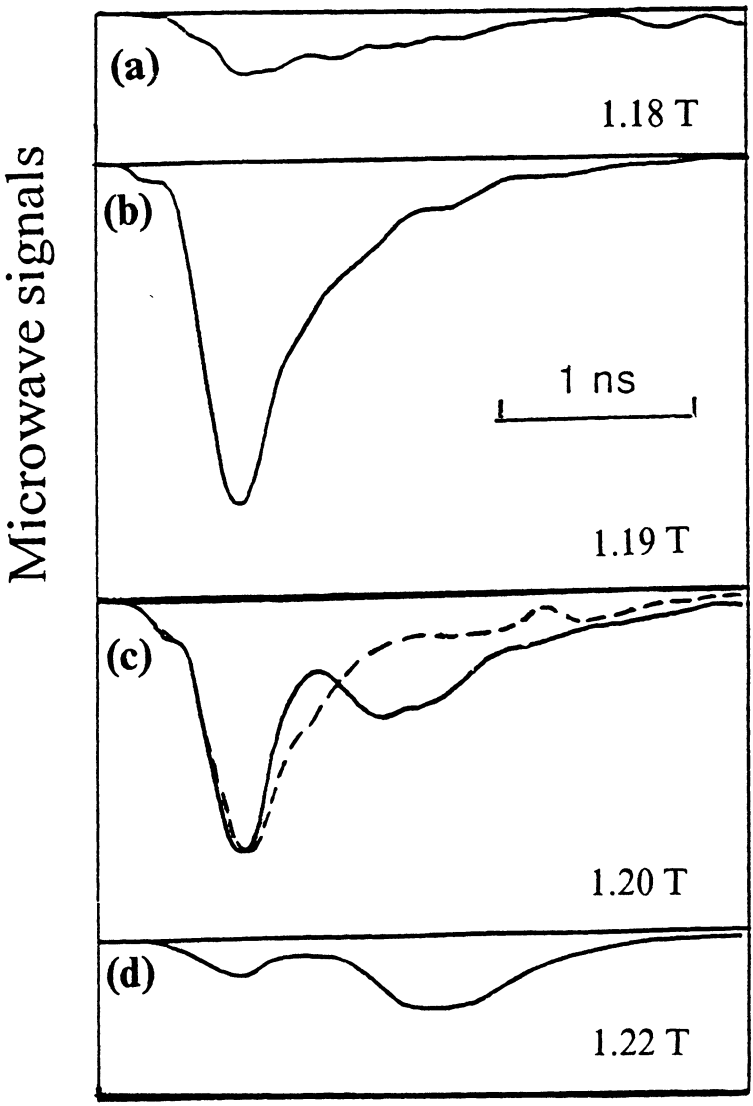

Fig.8. Oscillograms of cyclotron SR pulses for different values of magnetic field. Dashed line on the oscillogram (c) corresponds to the signal passed through a filter with cut-off frequency 33.3 GHz.

rent electron pulses were transported through the interaction space over a total length of up to 30 cm in a longitudinal guiding magnetic field of up to 2 T. For measurement of the radiation a hot-carrier germanium detector which had a transient characteristic of 200 ps was used.

2.1 Observation of cyclotron and undulator SR.

To observe the cyclotron emission transverse momentum, corresponding to a pitch factor g of about unity, was imparted to the electrons by the kicker installed immediately after the collimator.

Cyclotron SR was observed in a rather narrow range of detuning of the uniform magnetic field corresponding to grazing conditions with TE_{21} and TE_{01} modes. It was thus proven that the regime of group synchronism is optimal for cyclotron emission.

The oscillograms presented in Fig.8. confirm the behaviour described above. The radiaton is a monopulse with duration less than 0.5 ns, when the magnetic field is smaller than the value corresponding to the grazing condition $H \sim 1.2T$ (Fig.8(a)) and is converted to a double pulse when the magnetic field exceeds this value (Fig.8(b)). The fast decline of the microwave signal for smaller values of the magnetic field. less than 1.18 T, is obviously caused by violation of the synchronism conditions (large negative Δ), while the similar decrease in signal for larger magnetic fields, exceeding 1.22T, (large positive Δ) is related to the mechanism. discussed above, of increasing sensitivity to the spread of the electron drift velocities.

To prove that for the double pulse regime the frequency in the first pulse exceeds the frequency in the second pulse, a set of cut-off waveguide filters was used. The dashed line on the oscillogram Fig.8(b) illustrates suppression of the second low frequency pulse for the filter with cut-off 33.3 GHz. In general, measurements carried out showed a very broad radiation spectrum and in this case covered the band 28.6-36.4 GHz. Thus the relative spectrum width amounted to 20%.

Important confirmation of the stimulated nature of the observed emission can be found from the dependencies of the peak power on the emission distance (in fact, on the interaction time). The graphs plotted in Fig.9. have been obtained by variation of the length of the

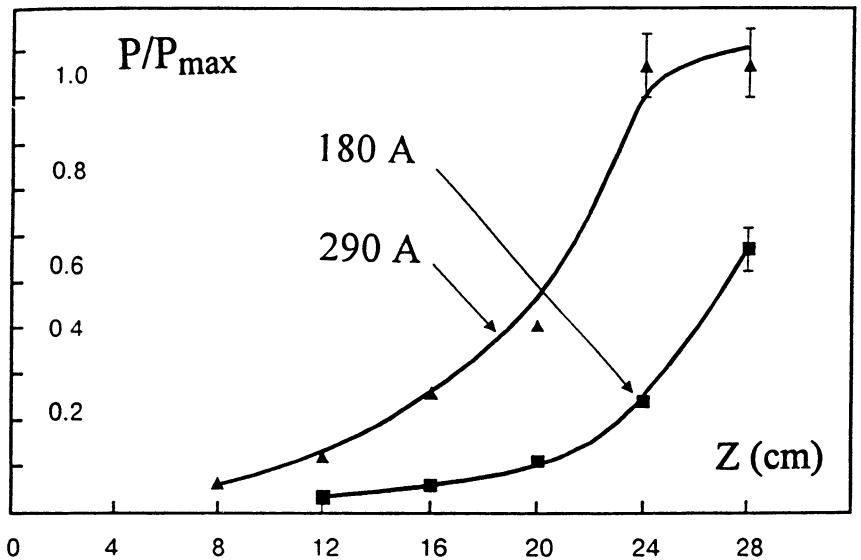

Fig.9. Peak power of a cyclotron SR pulse as a function of the interaction distance of the electron bunch, for two different values of the electron current. The magnetic field is 1.2 T.

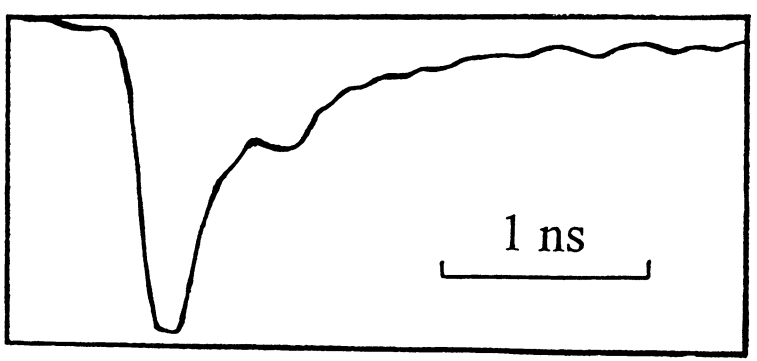

Fig.10. Oscillogram of SR pulse from the electron bunch passing through the undulator.

homogeneous magnetic field for two different values of the electron current. In the initial stages the peak power grows according to an exponential law. The corresponding gain was approximately two times less than the predictions of a computer simulation for an ideal bunch. Such a discrepancy can be easily explained by the electron velocity and energy spread. Note that if the emission was caused only by the initial modulation of the electrons over azimuthal phases (without subsequent selfbunching) near the cut-off regime the power should grow as the square root of the emission distance.

In the case of 290 A current, saturation of the growth of the peak power was observed. For a smaller current of 180 A saturation for the given maximum length was not achieved. The absolute radiation power was estimated by integrating the detector signal over the radiation pattern. For the TE_{21} mode this power exceeded 200 kW, which corresponded to an efficiency of energy transformation of more than one percent.

Note that superradiance under the group synchronism condition with the operating TE_{11} mode also has been observed in the case of a bunch passing through an undulator immersed in a guide magnetic field. Adiabatically tapering of the undulator entrance was used to provide excitation of bounce-oscillations. The SR was recorded for both group I and group II stationary orbits [19]. The first group of orbits corresponds to the so called reverse guide magnetic field regime at a magnetic field strength of 1 T while the second group of orbits was obtained using a forward magnetic field of strength 1.3 T, which slightly exceeded the cyclotron resonance value. The maximum peak power was observed for the second case for the amplutude of undulator field 0.2 T. A typical oscillogram for this case is presented in Fig.10.

2.2 Observation of Cherenkov SR.

In Fig.11 results of the observation of short pulse radiation emission from an electron bunch passing through a periodical waveguide of total length 10 cm are presented. The period of corrugation of the slow wave structure was 3.3 mm and the corrugation depth was 0.8 mm and had a mean radius of 3.6 mm. The observed microwave

signal consisted of several peaks. The first small peak corresponded to the high frequency radiation propagating in the same direction as the electron beam (TWT mechanism), while the second larger peak corresponded to the designed counter-propagating emission mechanism. Subsequent bursts are related with reflection of radiation from the edges of the slow-wave system. Note that the total electron bunch length ~10 cm is comparable with the interaction length and was insufficient for operating the normal BWO feedback mechanism [20],[21].

The main peak has a duration of up to 0.3 ns. Frequency measurements made using a set of cut-off waveguides showed that the main peak had a central oscillating frequency of approximately 40.5 GHz. While the first peak in Fig.11 had a higher oscillating frequency of greater than 43 GHz. However the frequency of this peak was less than predicted from the calculated Doppler up-shift in the case of excitation of the TM_{01} mode by electrons with energy 250 keV. Such a discrepancy indicated that this peak was generated by lower energy electrons (200 keV) at the front of the beam current pulse.

The radiation had a polarization corresponding to the TM_{01} mode which only has a radial component of electric field. This is shown in Fig.11 in which the comparison of the solid and dashed graphs, illustrates the drastic decrease in the microwave signal when the receiver horn was turned through an angle of 90 degrees. The measured radiation pattern also corresponded with good accuracy to the excitation of the TM_{01} mode. This measurement allowed the absolute peak power to be estimated by integrating the detected signal from the detector over its radial position. The estimated peak power was ~1 MW. Additional confirmation of the rather high level of radiation power was obtained from the flashing of a neon bulb panel when the radiation signal illuminated the panel at a distance of 10 cm from the output horn.

The typical feature of SR is the squared dependence of the radiation power with respect to the number of electrons due to the coherent nature of this radiation. The accelerator did not provide the possibility for independent variation of the total electron current without variation of the accelerating voltage amplitude and pulse duration. However it was possible to collimate the tubular electron beam and

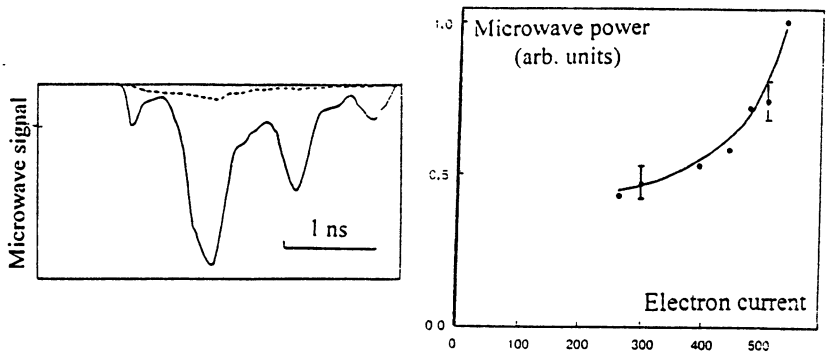

Fig.11. Microwave pulse in the case of periodical wave guide.Solid and dashed lines correspond to different orientation of receiver horn.

Fig.12. Dependence of peak microwave power on electron bunch current, in the case of periodical waveguide.

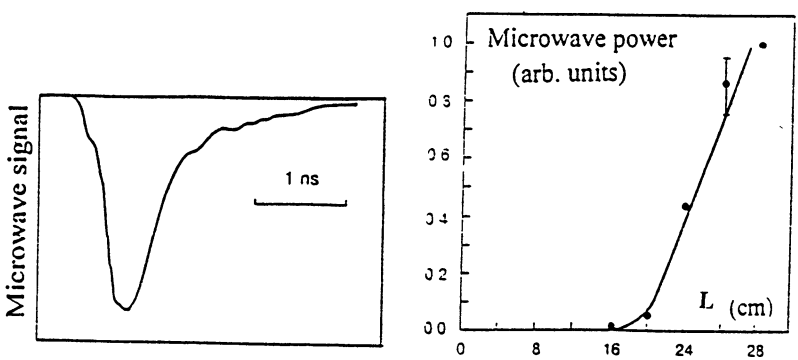

Fig.13. Oscillogram of microwave pulse for forward radiation in the case of dielectric-loaded waveguide.

Fig.14. Dependence of peak microwave power on interection length, in the case of dielectric-loaded waveguide.

to change, by variation of the strength of the guide magnetic field, the current passing through the slow-wave structures. The dependence of peak power on the electron beam current obtained by such a method was close to the above-mentioned squared scaling as shown in Fig.12.

In a second series of experiments a slow-wave structure in the form of a dielectric loaded waveguide was used. In this series of experiments two separate dielectric inserts were investigated. The dielectric material used was Mylar and Teflon in tubular form of wall thickness 2 mm inserted inside the metallic circular waveguide of inner diameter 10 mm and total length 25 cm. The best results were obtained for the Mylar insert which was constructed from multilayers of 0.05mm film. The dielectric constant of this material is 2.5-3. The typical SR pulse of duration 0.5 ns associated with the forward propagating wave in the Mylar loaded waveguide is presented in Fig.13. The peak power was also estimated to be between 1 to 2MW, and is comparatively high for the electron current passing through the cavity was measured to be less than 200 A.

The frequency spectrum measurements using cut-off waveguides and metallic grids with different mesh sizes showed that higher frequency radiation was generated in the dielectric-loaded waveguide as compared to the metallic slow wave structure and that this radiation had a rather large spectral width $\geq$ 10 GHz. According to calculations this frequency range correspond to excitation of the TM_{01} and hybrid HE_{11} modes. As a result the radiation pattern had a frequency dependence and thus had a rather complicated profile, which became narrower with the increase in the frequency band measured.

The important confirmation of the stimulated nature of the observed radiation is the dependence of the peak power on interaction length, as shown in Fig.14. This figure clearly shows that the radiation power is very small for short interaction lengths and increases drastically as the interaction length is increased. This means that at the initial stage self-bunching of electrons developed and the radiation power exceeded the threshold of the detector's sensitivity only after formation of the electron bunches. Note for comparison that in the case of traditional spontaneous emission caused either by density perturbation inside the electron pulse or by radiation from the sharp

front edge of the pulse the power should not depend on the interaction length.

Conclusion.

Summarising the results presented, we believe that the radiation observed was related with a novel mechanism of stimulated coherent emission of short electron bunches, namely superradiance. Of course, the results discussed here give only a rather general physical picture of superradiance, which needs further investigation, which would specifically concentrate on more accurate measurements and comparison with theoretical simulations. However even at the this early stage it must be emphasized that the radiation, especially in the case of BWO-like regimes, was characterized by a high level of stability and reproducibility from pulse to pulse. The efficiency of energy transformation amounted to 1% for the backward wave mechanism and up to 3% for the forward mechanism. The unique characteristic of microwave pulses such as duration (0.3-0.5ns) in combination with Megawatt power levels is encouraging for future applications in areas such as novel diagnostics and the studying of nonlinear phenomena in plasmas. Another advantage of the RADAN subnanosecond accelerator and consequently any associated experiments is that the whole system is in the form of a table-top system. In addition this accelerator is capable of operation in the repetitive, up to 100 pps regime.

This work was supported by the Russian Fund of Fundamental Research, grant 95-02-04791 and by the United Kingdom DRA and EPSRC.

Reference.

[1] R. Bonifacio, C. Maroli, and N. Piovella, Opt. Comm. **68**, 369 (1988).

[2] R. Bonifacio, N. Piovella, and B. W. J. McNeil, Phys. Rev. A **44**, 3441 (1991).

[3] R. Bonifacio, F. Casagrande, G. Cerchiony, L. De Salvo, P. Pierini, and N. Piovella, Riv. Nuovo Cimento **13**, N9 (1990)

[4] R. Bonifacio, R. Corsini, L. De Salvo, P. Pierini, and N. Pi-

ovella, Riv. Nuovo Cimento **15**, N11 (1992)

[5] N. S. Ginzburg, Sov. Tech. Phys. Lett. **14**, 197 (1988).

[6] N. S. Ginzburg and A. S. Sergeev, Sov. Phys. JETP Lett. **54**, 446 (1991).

[7] A. Gover, F. V. Hartemann, G. P. Lesage, N. C .Luhmann, R. S. Zhang, and C. Pellegrini, Phys. Rev. Lett. **72**, 1192 (1994).

[8] N. Piovella, P. Chaix, G. Shvets, and D. Jaroszynski, Phys. Rev. E **52**, 5470 (1995).

[9] V. V. Zheleznyakov, V. V. Kocharovsky, and Vl. V. Kocharovsky, Usp. Fiz. Nauk **159**, 194 (1989).

[10] N. S. Ginzburg and I. V. Zotova, Sov. Tech. Phys. Lett. **15**, 573 (1989).

[11] N. S. Ginzburg and A. S. Sergeev, Sov. Phys. JETP **99**, 171 (1991).

[12] N. S. Ginzburg and A. S. Sergeev, Opt. Comm. **91**, 140 (1992).

[13] G. R. M. Robb, B. W. J. McNeil, and A. D. R. Phelps, 19th Int. Conf. on Infrared and Millimeter Waves, Sendai, Japan, JSAP No.AP941228, p.155 (1994).

[14] N. S. Ginzburg, I. V. Zotova, and A. S. Sergeev Sov. Phys. JETP Lett. **60**, 513 (1994).

[15] N. S. Ginzburg, I. V. Zotova, I. V. Konoplev, A. S. Sergeev, V. G. Shpak, S. A. Shunailov, M. R. Ul'maskulov, and M. I. Yalandin, Sov. Phys. JETP Lett. **63**, 331 (1996).

[16] V. A. Flyagin, A. V. Gaponov, M. I. Petelin, V. K. Yulpatov, IEEE Trans. on Microwave Theory and Techniques **MTT-25**, 514 (1977).

[17] G. A. Mesyats, V. G. Shpak, M. I. Yalandin, and S. A. Shunailov. Proc. 8th Int. Pulsed Power Conf. USA, San-Diego, p.73 (1991).

[18] V. G. Shpak, S. A. Shunailov, M. I. Yalandin, and A. H. Dyad'kov Prib. Tekh. Eksp. **1**, 149 (1993).

[19] H.P.Freund Phys.Rev.A 27 (1983) 1977

[20] C. D. Korovin, G. A. Mesyats, V. V. Rostov et al. Pis'ma v ZhTF **11**, 1972 (1985) .

[21] K. L. Felch, K. O. Busty, R. W. Layman et al. Appl. Phys. Lett. **38**, 601 (1981).

REDUCTION OF FOCUSING MAGNETIC FIELD IN RELATIVISTIC CHERENKOV OSCILLATORS

E.B.Abubakirov, M.I.Fuchs, N.G.Kolganov, N.F.Kovalev, A.V.Palitsin, A.B.Volkov

Institute of Applied Physics, Russian Academy of Sciences,
Nizhny Novgorod, Russia

Relativistic Cherenkov microwave oscillators operating in the repetitive pulse regime are attractive for different application, such as plasma chemistry, linear colliders, radar sets and others. However, the great power consumption for creation of required strong focusing magnetic fields by means of non-cryogenic cooling solenoids or the use of superconductive ones is significant limitation for several applications, particularly for radar systems [1]. To find out the possibilities of operation of Cherenkov generators with weak focusing magnetic fields we consider both mechanisms of electron beam interaction with electromagnetic fields in such generators and resources of electron optics.

Reasons for influence of the magnetic field on output radiation

Operation of Cherenkov devices is based on synchronous interaction of a straight-forward electron beam with a spatial harmonic of the operating eigenmode of the microwave electric field

$$\vec{E}(\vec{r},z,t) = \sum_n \vec{E}_n(\vec{r}) \exp i(\omega t - h_n z) . \qquad (1)$$

of the periodic electrodynamic system, when longitudinal velocity v_e of electrons and a phase velocity $v_{ph} = \omega/h_n$ of the harmonic are closed

$$\left| v_{ph} - v_e \right| / v_e < \pi/kL . \qquad (2)$$

Here ω and $h_n = h_0 + n\bar{h}$ are cycle frequency and longitudinal wave number of the operating harmonic, $\bar{h} = 2\pi/d$, d is period of the electrodynamic system , n is number of the spatial harmonic $k = \omega/c = 2\pi/\lambda$, c is light velocity, and L is length of the interaction space. Cherenkov stimulated radiation of electrons moving rectilinearly does not depend on

the value of the magnetic field. Therefore, at a glance it seems that it suffices to provide transportation of the electron beam through the interaction space, i.e. to counterbalance the space charge force with the Lorenz force. The value of the external magnetic field for suppression of Coulomb repulsion is not too high:

$$H_z > [(mc\gamma\omega_p/e)^2 - H_\theta^2]^{0.5}. \qquad (3)$$

Here $H_\theta = 2J/cr$ is azimuth eigen magnetic field of the electron beam, ω_p is plasma frequency, $\gamma = (1 - v_e^2/c^2 - v_{e\perp}^2/c^2)^{0.5}$ is relativistic factor, and e, m and $v_{e\perp}$ are charge, rest mass and transverse velocity of electron. For example, in X-band generators it is sufficient to apply the external magnetic field of 1 - 1.5 kOe for transportation of electrons taking into consideration both the characteristic diameter of the electron beam which is of the order of the operating wavelength λ in relativistic generators, and the characteristic impedance of the electron beam which is of the order of 100 Ohm.

However, the typical dependence of the radiation power on the focusing magnetic field is more complicated, in particular for BWO. Generalization of the data obtained in various experiments with relativistic generators would show a dependence (Fig. 1), which has non-monotonous character with several deep and shallow pits. It is necessary to choice the minimum value of the magnetic field, at which the microwave power achieves its maximum. Usually for an X- band BWO it takes place when the value of magnetic field value exceeds 20 kOe [2,3].

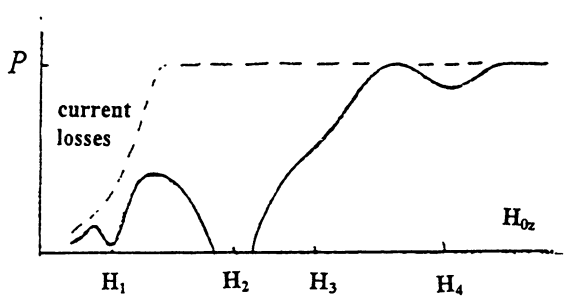

Fig. 1. Generalized dependence of radiation power of relativistic generators on value of external magnetic field

The applied magnetic field excites fast and slow cyclotron waves in the electron beam [3] with the following dispersion characteristics

$$\omega = h_n v_{ell} \pm l\omega_H . \qquad (4)$$

Here $\omega_H = eH_0/mc\gamma$ is cyclotron frequency, $H_0 = (H_{0z}^2 + H_{0\theta}^2)^{0.5}$ is total magnetic field, l is number of the cyclotron harmonic. The complicated dependence (Fig. 1) is due to the influence of cyclotron waves on operation of relativistic generators and amplifiers. This influence is especially great when conditions (2) and (4) are fulfilled simultaneously.

It is convenient to consider peculiarities of interaction of electromagnetic waves with cyclotron waves and space-charge ones in relativistic generators for characterized regions of double resonances.

Classification of resonances can be shown on the Brillouen diagram (Fig. 2). For example, let us consider a relativistic BWO. As a rule, electromagnetic radiation is taken from the collector edge of the BWO by a wave which is the operating backward wave reflected from the cut-off section on the cathode edge of the interaction space. Fig. 2 show cyclotron resonances with both the backward and the forward waves.

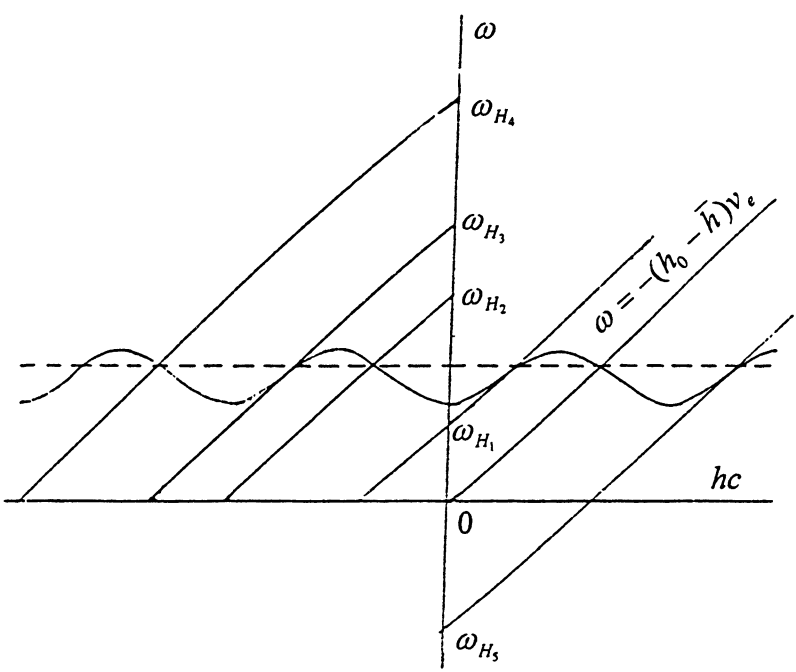

Fig. 2. Dispersion characteristics of electromagnetic, space charge and cyclotron waves in BWO.

We assume that initial transverse velocities of electrons in the interaction space are absent, therefore resonances at cyclotron harmonics ($l \neq 1$) are not taken into consideration.

Along with Cherenkov synchronism of the electron beam with spatial harmonic $n = -1$ of the operating mode which propagates in the direction opposite to the electron beam,

$$\omega \approx -(h_0 - \bar{h})v_e \qquad (5)$$

there are cyclotron resonances of the fast cyclotron wave with harmonics of the operating mode, namely: with fundamental harmonic $n = 0$ near the value H_2 of the magnetic field:

$$\omega + h_0 v_e \approx \omega_{H_2}; \qquad (6)$$

with harmonic $n = +1$ near the value H_4:

$$\omega + (h_0 + \bar{h})v_e \approx \omega_{H_4}. \qquad (7)$$

There are also some regions of the magnetic fields corresponding to cyclotron resonances with harmonics of the forward wave:
with fundamental harmonic $n = 0$:

$$\omega - h_0 v_e \approx \omega_{H_1}; \qquad (8)$$

with harmonic $n = -1$:

$$\omega - (h_0 - \bar{h})v_e \approx \omega_{H_3}. \qquad (9)$$

At last there is resonance of a slow cyclotron wave with the harmonic $n = +1$ of the forward wave (interaction on the abnormal Doppler effect)

$$\omega - (h_0 + \bar{h})v_e \approx -\omega_{H_5}. \qquad (10)$$

The cyclotron waves exert the strongest influence on BWO operation in the zone of the resonant (6) magnetic field, H_2. Both the experiments (Fig. 1) and numerical calculations (Fig. 3) of the self-consistent system of equations (44) - (48) (see Appendix) show the absence of the output radiation in a wide region of magnetic field values. When the value of the magnetic field approaches this region, on its smooth slopes electromagnetic energy transforms to transverse electron velocities. As follows from (5), (6), the resonant condition of "cyclotron absorption" [3,4],

$$\omega_{H_2} = \bar{h} v_e \qquad (11)$$

is independent on individual signs of modes, i.e. this phenomenon is present for all modes simultaneously. Achievement of the maximum output power requires a strong focusing magnetic field which exceed sharply

resonant value (6). It is confirmed by numerous experimental data (see, for example, [2,3]). One should have in mind the presence of the "cyclotron absorption" zone in strong magnetic field $H_4 \approx 2H_2$ near resonance (7) of the fast cyclotron wave with (+1)-spatial harmonic of the operating backward wave. Usually resonance (7) exerts the weak influence on interaction process but some situations are found when the microwave radiation disappears completely. Such deep resonance was found by authors for one of axial magnetic field directions in BWO which operates on mode TE_{41} of an electrodynamic system with triple-start helical corrugation. In this region of the magnetic field for opposite direction there was a small decrease of the output power only.

The fast cyclotron wave interacts with the fundamental harmonic of the forward wave (reflected by the cut-off section) in the region of the weak magnetic field, when resonance condition (8) is fulfilled. The zone of interaction with the forward wave is essentially narrower than the zone for the backward wave (Fig. 3) as follows from equations (44) - (48).

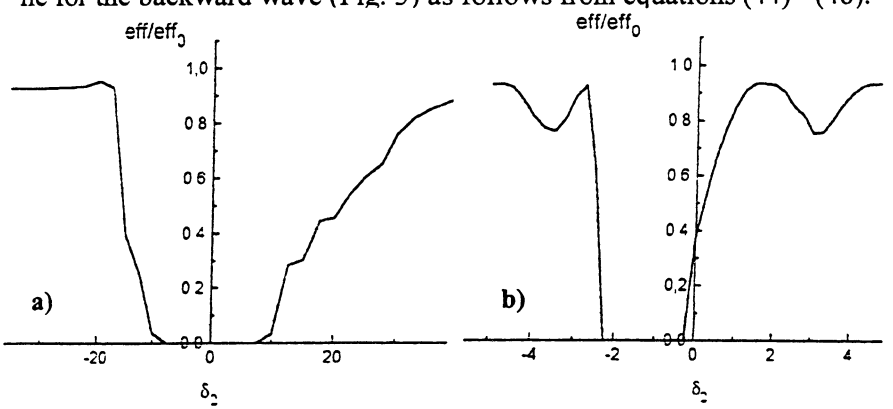

Fig. 3. Calculated zones of "cyclotron absorption": a): for backward wave, b): for forward wave of BWO (eff$_0$ is efficiency when cyclotron absorption is absent, δ_2 is linear function of magnetic field - see Appendix)

In X-band BWOs the pit corresponding to condition (8) usually overlaps the region of the magnetic field in which current losses become considerable (Fig.1). Here magnetic field H_θ of the electron beam is a considerable part of total field H_0, and so condition (8) depends on the electron position. It is the reason of incomplete disappearance of radiation in the zone (in experiments).

Resonance (9) reveals itself weakly and is hardly recognized. In X-band BOW it takes place on the slope of the zone corresponding to condition (11).

Besides, there is resonance (10) in the region of the weak magnetic field but practically the whole of a high frequency field of a slow cyclotron wave is concentrated inside the electron beam, and therefore interaction of the wave is insignificant in the abnormal Doppler condition.

What possibilities can be used to reduce the operating magnetic field?

Methods to reduce strength of magnetic field

1. Exclusion of resonant cyclotron interaction

A resonant cyclotron interaction can be effectively excluded with use of method proposed in [3,4] for a mode selection in oversized microwave systems. The method of cyclotron-resonant mode selection permits to operate in the region of the magnetic field corresponding to resonant condition (11). Although the energy of all modes is absorbed by the fast cyclotron wave, according to equations (37) - (43) intensity of absorption is proportional to factor $J^2_{\nu\pm1}(\mu r/R)$ where ν is azimuth index of the operating backward wave, μ is root of the Bessel function for TM-waves and of derivation of the Bessel function for *ET*-modes, R is average radius of the electrodynamics system. For *TM*-modes except TM_{01}, and for TE -modes with radial indexes more than unity there are distinguished radii r_b when

$$J^2_{\nu\pm1}(\mu r_b/R) = 0. \qquad (12)$$

For non-symmetric rotating modes these radii are different for the opposite directions of the longitudinal magnetic field (sign + or - in (12) accordingly). For several lowest modes the disposition of these radii is shown in Fig. 4. If one of such modes is chosen as operating mode of BWO and the radius of the hollow electron beam is chosen from condition (12), then in the region of the resonant magnetic field for the operating mode the Cherenkov interaction is provided without losses and the same time for other modes the output power is absent owing to "cyclotron absorption". Disposition of the electron beam must be sufficiently accurate to correspond to distinguished radius r_b, deflection from the ra-

dius or displacement from the axis of the electron beam lead to an increase in the start current.

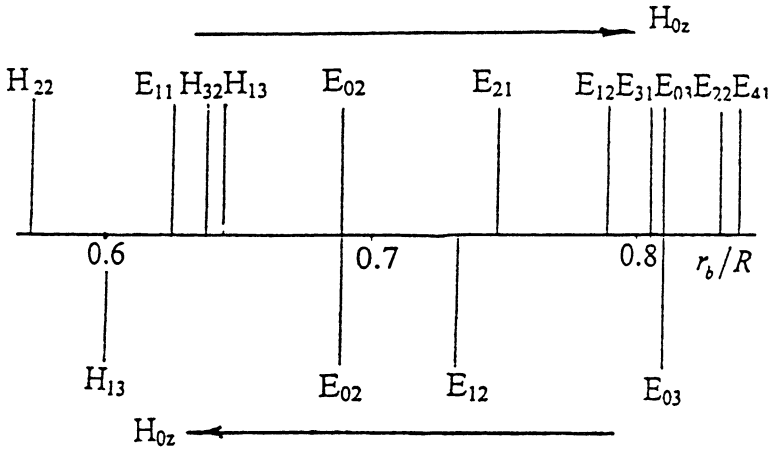

Fig. 4. Disposition of electron beam radii for lowest modes corresponding to cyclotron absorption absence.

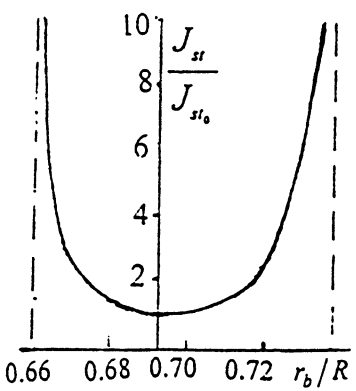

Fig. 5. Dependence of start current on electron beam radius for BWO on mode TM_{02}

Fig. 5 shows the dependence of start current J_{st} on the electron beam radius for operating mode TM_{02} which indicates that deflection from required radius must not be more than 0.5 mm. In IAP the X-band BWO with cyclotron mode selection operating on mode TM_{02} was successfully tested [3]. Near the resonant magnetic field 12 kOe the radiation power achieves 2 GW with efficiency 10 % when the ratio of the electron beam radius to the average radius of the electrodynamic system is 0.693.

2. Improvement of electron optics

The next step to decrease the focusing magnetic field is to improve the forming system of the electron beam in order to provide its transportation across the interaction space without current losses and to

transportation across the interaction space without current losses and to reduce the electron transverse momentum spread which must not be less than

$$\Delta p_{\perp} << 1 \qquad (13)$$

required for efficient operation of a microwave generator [5].

It would be appropriate to remember here the first Russian and American experiments [6,7] in 1973-1974 which demonstrated high efficiency (over 10 %) of high-power Cherenkov generators (namely BWO) driven by relativistic electron beams. In these experiments the focusing magnetic fields were of the order of 1.5 - 3 kOe and the forming systems of the electron beam were made as planar diodes with foil anodes. In the planar diode electric and magnetic fields are parallel (Fig. 6a). It provides a quasi-laminar moving of electrons with low transverse velocities. Owing to the use of low-perveance electron beams in the BWO stratification of electron energies is insignificant even in solid beams. However, such forming systems had a significant defect. It was a short lifetime of the foil anode which was destroyed after one or several shots.

These forming systems were not used very long and soon were replaced by magnetically insulated coaxial diodes without foil (Fig. 6b). So, the problem of short lifetime was solved, but there appear other problems which hampered the use of a weak magnetic field. In the electron beam injected by such diodes one can distinguish two electron fractions: one of them is born on a side surface of the cylindrical cathode, the other fraction starts on the cathode edge.

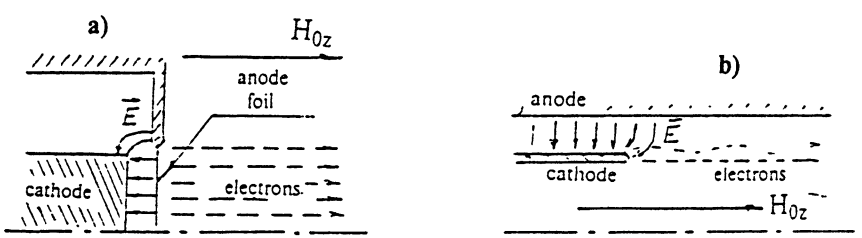

Fig. 6. Configuration of electric and magnetic fields in: a) planar diode and b) coaxial magnetically insulated diode.

Electron trajectories in typical configurations of coaxial diodes which are used in relativistic microwave devices are shown in Fig. 7. The first fraction forms in cross tangential magnetic $H_0 = \sqrt{(H_{0z}^2 + H_{0\theta}^2)}$ field (H_{0z} is external axial component and $H_{0\theta}$ is azimuthal one produced by the inherent current of the electron beam) and radial electric E_0-field.

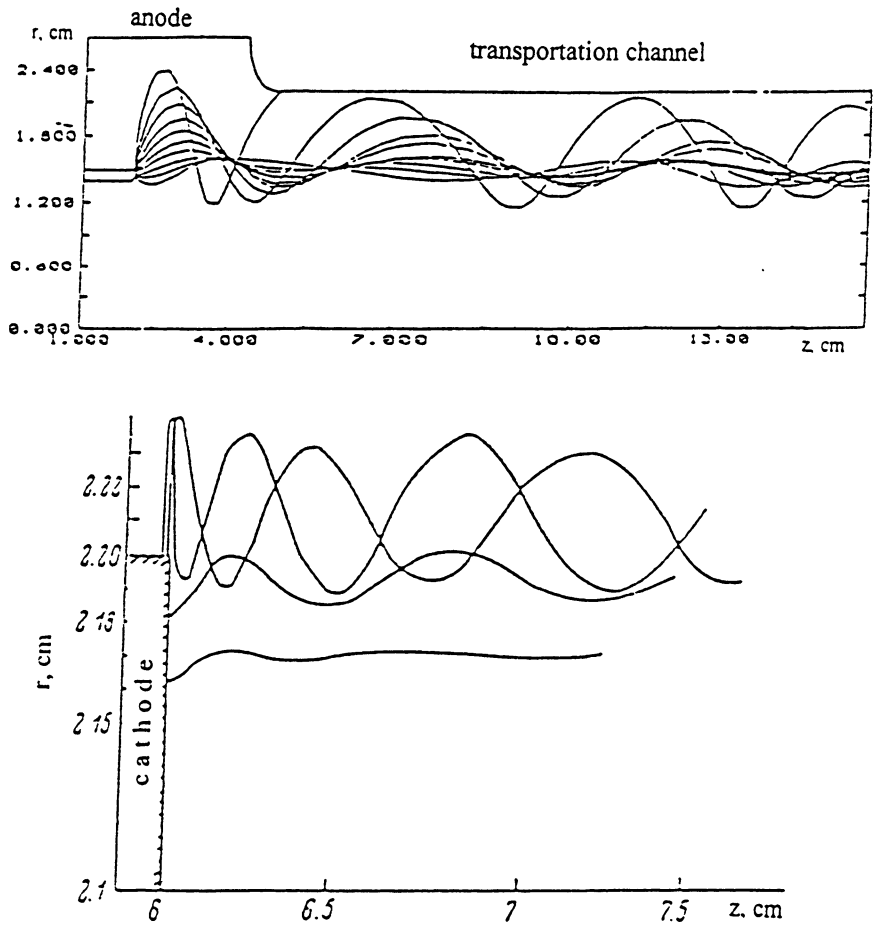

Fig. 7. Electron trajectories in coaxial diode with magnetic insulation.
Top: tubular cathode [8], U = 0.5 MV, J = 6.4 kA, H = 3.8 kOe, R_a = 2.7 cm, radius of transportation channel is R = 2.1 cm.
Bottom: end-type cathode [9], U = 1 MV, J = 9.8 kA, H = 15 kOe, R_a = R = 4.5 cm.

As it is evident from Fig. 7, the first fraction has the greatest transverse velocity spread. Electron trajectories of the second fraction are smoother. When the magnetic field is much stronger than the electric one, $H_0 >> E_0$, the basic part of the electron current is transferred by the second fraction which is a quasi-laminar flow and has a small electron velocity spread. In the region of the weak magnetic field the basic current part is determined by the first fraction. For configuration which is shown in Fig. 7 (bottom) this part up to 80 % of whole current near cut off regime. Taking into attention that in a homogeneous magnetic field electron transverse oscillations are closed to Larmour diameters $2R_L$ on the cathode (Fig. 7), for providing of the condition (13) the magnetic field must be

$$H_0(kOe) >> \frac{0.2I(kA)}{R_b(cm)} f(\gamma_R) \qquad (14)$$

where $f(\gamma_R) = (\gamma_R - 1)/(\gamma_R - \gamma_0)\beta_0$, $\beta_0 = (1 - \gamma_0^{-2})^{0.5}$,

$\gamma_R = 1 + eU/mc^2, \gamma_0 = (2\gamma_R + 0.25)^{0.5} - 0.5$.

In the region of weak magnetic fields there is another important condition to provide the electron beam transportation without current losses. It is necessary to secure $R_b + 2R_L < R$ or

$$H_0^2(kOe) > 2.5J(kA/cm^2) f(\gamma_R). \qquad (15)$$

The estimation for X-band 1 MV generator shows that $H_0 > 4kOe$.

The evident method to improve the electron optics is creation of an electron gun, in which electric and magnetic fields are parallel, for example, when configuration of electrodes are closed to planar design (diaphragm is closed to cathode cut).

However, even for the electron beam which is formed in the coaxial diode with magnetic insulation it is possible to provide the low transverse velocity spread and the electron beam transportation without current losses in the region of weak magnetic fields by using a magnetic decompression, when the magnetic field on the cathode, H_{0c}, is more than the field in the interaction space $\alpha = H_{0c}/H_0 > 1$. When the inhomogeneous magnetic field uses conditions (14) and (15) for the magnetic field in the electrodynamic system of a microwave generator are accordingly transformed to

$$H_0(kOe) >> \frac{0.2I(kA)}{\alpha R_b(cm)} f(\gamma_R), \quad H_0^2(kOe) > \frac{2.5J(kA/cm^2)}{\alpha} f(\gamma_R) \quad (16)$$

X-band and K-band were tested on IAP BWOs with homogeneous magnetic fields and with an use of decompression. The previous results show that the use of decompression permits essentially to decrease an energy expenditure on creation of the focusing magnetic field in the interaction space. For example, radiation power of the X-band 0.5 MV 3 kA BWO is 200 MW when the strength of the homogeneous magnetic field exceeds 25 kOe. Using decompression α = 4 the same power is achieved when in the interaction space the magnetic field strength is 2.5 kOe only. Basically the same progress is achieved by decreasing current losses (Fig. 8). When the magnetic field is 3 kOe, radiation power disappears because of the cyclotron absorption of the forward wave TM_{01} which is reflected from the cut-off cross section.

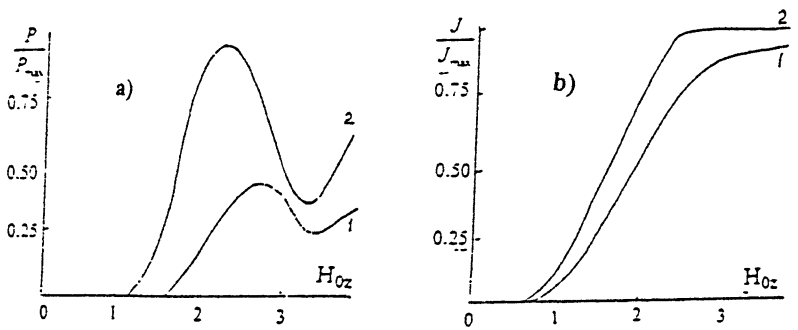

Fig. 8. Dependence of a) radiation power and b) beam current in the interaction space on magnetic field strength; 1.- in homogeneous magnetic field, 2.- with decompression α=4.

3. Modification of cyclotron absorption zone in forward wave

There are possibilities to change or to move the zone of cyclotron absorption of the forward wave which radiates the microwave energy. It can realize by several methods:

1.To use a jump of a cyclotron phase by change of a magnetic field on a part of the interaction space. As calculation of equations (43) - (47) shows (Fig. 9a), in the center of the zone a radiation appears when the change of the phase is equal π. For a backward wave such method is not

effective because this type of interaction is accompanied with a strong dynamic mismatch of the cyclotron resonance.

2.To use the drift channel of the BWO output when Cherenkov interaction is absent but cyclotron interaction continues. It leads to narrowing of the zone (Fig. 9b);

To change the structure of the wave removing the electromagnetic energy from the BWO. It permits one to move the zone to the desired direction and at the same time to produce the required radiation pattern. This method was tested at IAP on the BWO used earlier as the electron beam modulator for X-band amplifier [10]. The cut-off cross section of the BWO was replaced on the Bragg reflector converting the operating backward TE_{41} mode to the forward mode, TE_{11}. Due to this conversion, the experimental radiation pattern in the form of a Gaussian wave beam is obtained.

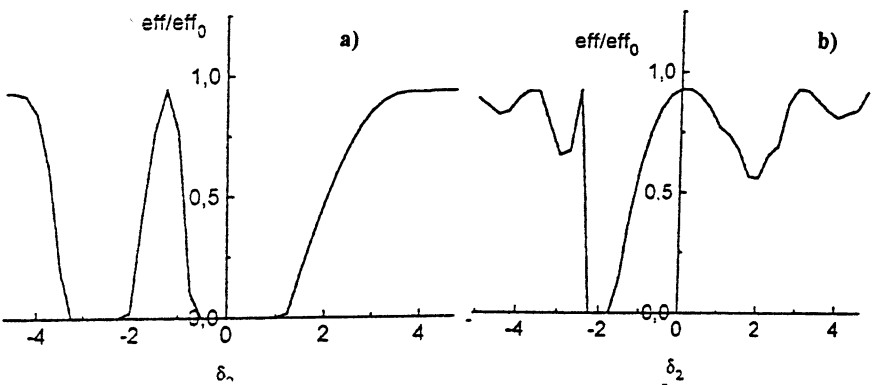

Fig. 9. a) Modification of "cyclotron absorption" zone Fig. 4b when the change of the cyclotron phase is equal to π ; b) change of the zone Fig. 4b when path for the forward wave is doubled.

Appendix

Non-linear analysis of the phenomenon for resonant devices with a fixed field structure (for example, orotron) was done in [11]. In BWO the microwave field is formed by the electron beam, therefore it is necessary to investigate a self-consistent system of equations including both the equation of electron motion in electromagnetic fields which are formulated in [11] and the equation of the electromagnetic field excitation by microwave current [12].

$$\frac{dC_s}{dz} = \frac{1}{N_s} \int_{S_-} \vec{j}_\omega \vec{E}_{-s} dS, \qquad (17)$$

where C_s are amplitudes of eigenmodes E_s of an electrodynamic system in representation of the electromagnetic field as the following sum

$$\vec{E} = \sum_s C_s \vec{E}_s e^{-i\omega t}, \qquad (18)$$

$$N_s = \frac{c}{4\pi} \int_{s_\perp} \{[\vec{E}_s \vec{H}_{-s}] - [\vec{E}_{-s} \vec{H}_s]\} d\vec{S} \qquad (19)$$

is wave norm,

$$j_\omega = \frac{1}{\pi} \int_0^{2\pi} j(t) e^{i\omega t} d(\omega t) \qquad (20)$$

is complex amplitude of monochromatic current density. Taking into account the law of charge conservation.

$$\rho v_e dt dS = \rho_0 v_0 dt_0 dS_0, \qquad (21)$$

the integral (17) transforms to

$$\frac{dC_s}{dz} = \frac{1}{\pi N_s} \int_{S_\perp} \int_0^{2\pi} j_0 F(r)\, d(\omega t_0) dS_0, \qquad (22)$$

where

$$F = E_{II} + \frac{\vec{p}_\perp \vec{E}_\perp}{p_{II}} = F(S(S_0)) \qquad (23)$$

is function of electron disposition determined from the motion equation with initial condition $r(z=0) = r_0$, j_0 is current density in the input cross section S_0 of the interaction space (under $z = 0$) where electron transverse velocities are absent, t_0 is moment of an electron flight into the interaction space, p_{II} and $p_\perp$ are longitudinal and transverse components of relativistic electron momentum $\vec{p} = m\gamma\vec{v}_e$ determined from equation of an electron moving, E_{II} and $E_\perp$ are longitudinal and transverse components of the electric field $\vec{E}_{-s}$. Owing to representation of the field $\vec{E}_{-s}$ as sum (1) of spatial harmonics, function (23) can be written as

$$F = \sum_n F_n(x,y)\, e^{ih_n z}\,. \qquad (24)$$

The motion of electrons can be represented as the motion of Larmour orbit center and cyclotron rotation

$$r = R + ae^{i\psi}\,, \qquad (25)$$

where

$$\psi = \int \frac{\omega_H}{v_e} dz + \psi_0 \qquad (26)$$

is phase of cyclotron rotation,

$$a = cp_\perp / eH_0 \qquad (27)$$

is radius of one. The amplitude F_n of each spatial harmonic is an infinite sum of cyclotron harmonics:

$$F_n(X + a\cos\psi, Y + a\sin\psi) = \sum_m F_{m,n}(X,Y) e^{-im\psi}\,, \qquad (28)$$

where

$$F_{m,n}(X,Y) = \frac{1}{2\pi}\int_0^{2\pi} F_n e^{im\psi} d\psi\,. \qquad (29)$$

Neglecting non-synchronous interaction, function F can be represented by two terms

$$F = F_{1,0} e^{i\theta} + F_{0,1} e^{i\varphi} \qquad (30)$$

with slow varying phases:
cyclotron phase

$$\theta = \omega t - h_0 z - \psi\,, \qquad (31)$$

and Cherenkov one

$$\varphi = \omega t - h_1 z \qquad (32)$$

when double resonance (5), (6) takes place. Other part of sum (24) gives the least contribution after averaging fast varying phases.

Following the method of [13] we find terms $F_{0,1}$, $F_{1,0}$ using (23), (29) and representing microwave fields via electric and magnetic Hertz vectors expanded on plane waves

$$\Pi^{e,m}(x,y) = \frac{1}{2\pi}\int_0^{2\pi} f^{e,m}(\psi)\, e^{ig(x\cos\psi + y\sin\psi)} d\psi\,, \qquad (33)$$

where $g=(k^2-h^2)^{05}$ is transverse wave number. For example, using the integral form of the Bessel function

$$J_\nu(z)=\frac{i^{-\nu}}{2\pi}\int_\alpha^{\alpha+2\pi}e^{i(z\cos\phi+\nu\phi)}d\phi \tag{34}$$

and denoting $\hat{L}^{(k)}=(\frac{\partial}{\partial X}+i\frac{\partial}{\partial Y})^k$ we can write the amplitude of the fundamental Cherenkov harmonic of longitudinal electric field which is synchronous with the fast cyclotron wave of the electron beam:

$$\begin{aligned}E_{0,1}^{(z)}&=\frac{1}{2\pi}\int_0^{2\pi}g_0^2\Pi^e(x,y)e^{i\theta}d\theta=\\&=\frac{g_0^2}{2\pi}\int_{-\pi}^{\pi}f^e(\psi)e^{ig_0(X\cos\psi+Y\sin\psi)}e^{i\psi}[\int_{-\phi}^{2\pi-\phi}e^{ig_0a\cos(\theta-\varphi)}d(\vartheta-\phi)]d\phi=\\&=\frac{1}{ig_0}J_0(g_0a)\hat{L}E_0^{(z)}(X,Y)\end{aligned} \tag{35}$$

Similarly one can obtain other components of electromagnetic field. So, the equation of the electromagnetic field excitation by microwave current is

$$\begin{aligned}\frac{dC_s}{dz}=\frac{1}{\pi N_s}\int_{S_\perp}\int_0^{2\pi}j_0\{&[I_0(|g_1|a)E_z^1(\vec{R})+iI_1(|g_1|a)\frac{kp_\perp}{g_1p_z}H_z^1(\vec{R})]e^{i\varphi}+\\&+[(J_1(g_0a)+\frac{kp_\perp}{2g_0p_z}(J_0(g_0a)+J_2(g_0a)))\frac{L^{(1)}E_z^0}{g_0}-\\&-i\frac{kp_\perp}{2g_0^2p_z}(J_0(g_0a)-J_2(g_0a))L^{(1)}H_z^0(\vec{R})]e^{i\theta}\}d(\omega t_0)dS\end{aligned} \tag{36}$$

which must be solved for BWO with boundary condition $C_s=0$ when $z=L$. Here L is length of an interaction space, $\vec{R}(X,Y)$ is disposition of electron-rotation centers in polar coordinates.

Note: when electrons have transverse velocities at the input of the interaction space it should be average the right part of equation (36) over initial cyclotron phases.

Besides equation (36), the total system of equations defining processes of interaction in Cherenkov devices with non-fixed electromagnetic field structure when double resonances take place, includes [11]:
the equation for Cherenkov phase

$$\frac{d\phi}{dz} = \frac{k}{\beta_z} - h_1, \tag{37}$$

the equation for cyclotron phase

$$p_\perp \frac{d\theta}{dz} = \frac{p_\perp}{\beta_z}\left(k - h_0 - \frac{\omega_H}{c}\right) -$$

$$-\frac{e}{c\beta_z}\mathrm{Re}\left\{\left[\frac{\beta_z p_\perp}{p_z} I_0(|g_1|a)H_z^1 - i\frac{h_1 - \beta_z k}{|g_1|} I_1(|g_1|a)E_z^1\right]e^{-i\varphi} + \right. \tag{38}$$

$$\left. + \left[\frac{1}{g_0}\left(\frac{\beta_z p_\perp}{p_z} - \frac{k - \beta_z h_0}{g_0^2 a}\right) J_1(g_0 a)\hat{L}H_z^0 + i\frac{h_0 - \beta_z k}{g_0^2}\frac{dJ_0(g_0 a)}{d(g_0 a)}\hat{L}E_z^0\right]e^{i\theta}\right\},$$

the equation for electron energy

$$\frac{d\gamma}{dz} = -\frac{e}{mc^2}\mathrm{Re}\left\{\left[I_0(|g_1|a)E_z^1 + iI_1(|g_1|a)\frac{kp_\perp}{p_z|g_1|}H_z^1\right]e^{-i\varphi} + \right.$$

$$+ \left[\left(J_1(g_0 a) - \frac{h_0 p_\perp}{2p_z g_0}(J_0(g_0 a) + J_2(g_0 a))\right)\frac{\hat{L}E_z^0}{g_0} - \right. \tag{39}$$

$$\left. \left. - i\frac{h_0 p_\perp}{2p_z g_0}(J_0(g_0 a) + J_2(g_0 a))\hat{L}H_z^0\right]e^{-i\theta}\right\},$$

equation for electron transverse momentum

$$\frac{dp_\perp}{dz} = \frac{e}{c\beta_z}\mathrm{Re}\left\{-iI_1(|g_1|a)\frac{k - \beta_z k}{g_0}H_z^1 e^{-i\varphi} + \right.$$

$$\left. + \frac{1}{g_0^2}\left[\frac{h_0 - \beta_z k}{g_0 a}J_1(g_0 a)\hat{L}E_z^0 + i(k - \beta_z h_0)\frac{dJ_1(g_0 a)}{d(g_0 a)}\hat{L}H_z^0\right]e^{-i\theta}\right\}, \tag{40}$$

and equations for coordinates of electron orbit centers

$$\frac{dX}{dz} = -\frac{1}{\beta_z h_0}\mathrm{Re}\left\{\left[-\frac{iI_0(|g_1|a)}{g_1^2}\left((h_1 - \beta_z k)\frac{dE_z^1}{dY} - (k - \beta_z h_1)\frac{dH_z^1}{dX}\right) - \right.\right.$$

$$-\frac{\beta_z p_\perp}{|g_1| p_z} I_1(|g_1|a)\frac{dH_z^1}{dY}\Big]e^{-i\varphi}+\Big[i\frac{\beta_z p_\perp}{2p_z}\Big(J_0(g_0a)H_z^0-\frac{J_2(g_0a)}{g_0^2}\hat{L}^2H_z^0\Big)-$$

$$-\frac{iJ_1(g_0a)}{g_0^2}\Big((h_0-\beta_z k)\frac{d}{dY}\hat{L}E_z^0-(k-\beta_z h_0)\frac{d}{dX}\hat{L}H_z^0\Big)\Big]e^{-i\theta}\Big\};\ (41)$$

$$\frac{dY}{dz}=-\frac{1}{\beta_z h_0}\mathrm{Re}\Big\{\Big[\frac{iI_0(|g_1|a)}{g_1^2}\Big((h_1-\beta_z k)\frac{dE_z^1}{dX}+(k-\beta_z h_1)\frac{dH_z^1}{dY}\Big)+$$

$$+\frac{\beta_z p_\perp}{|g_1| p_z} I_1(|g_1|a)\frac{dH_z^1}{dX}\Big]e^{-i\varphi}+\Big[\frac{\beta_z p_\perp}{2p_z}\Big(J_0(g_0a)H_z^0+\frac{J_2(g_0a)}{\cdot g_0^2}\hat{L}^2H_z^0\Big)+$$

$$+\frac{iJ_1(g_0a)}{g_0^2}\Big((h_0-\beta_z k)\frac{d}{dX}\hat{L}E_z^0+(k-\beta_z h_0)\frac{d}{dY}\hat{L}H_z^0\Big)\Big]e^{-i\theta}\Big\}.\ (42)$$

In the region of weak magnetic fields where one can expect large transverse oscillations it is necessary to analyze the total system of equation. The system can be made essentially simpler when Larmour radii are small $|g_{0,1}|a<<1$, the electron beam is thin (we neglect by inhomogeneous of microwave field structure on cross section of the electron beam), all electrons have ultrarelativistic energies $\gamma^2>>1$ and energy changes are small:

$$\frac{db}{d\varsigma}=I\int_0^{2\pi}(e^{i\varphi}+\rho f e^{i\theta})d\varphi_0 \qquad (43)$$

$$\frac{d\rho}{d\varsigma}=-\mathrm{Re}(bfe^{-i\theta}) \qquad (44)$$

$$\frac{dU}{d\varsigma}=\mathrm{Re}(\rho bfe^{-i\theta}+be^{-i\varphi}) \qquad (45)$$

$$\frac{d\varphi}{d\varsigma}=2U-\delta_1+\rho^2 \qquad (46)$$

$$\frac{d\theta}{d\varsigma}=\delta_2+2U(1-\varepsilon)+n\rho^2+\mathrm{Re}(i\frac{\varepsilon bf}{\rho}e^{-i\theta}) \qquad (47)$$

where $b = \frac{e}{mc^2}\frac{C_s E_z^1}{k\gamma_0^2}$, $\rho = \frac{p_\perp}{\sqrt{2\gamma_0^2}}$, $U = \frac{1-\gamma/\gamma_0}{\sqrt{2\gamma_0^2}}$ are desired functions; $\varsigma = \frac{kz}{\sqrt{2}\gamma_0}$, and parameters are $\varepsilon = \gamma_0^2(1-n\beta_0)$, $n = \frac{h_0}{k}$, $I = \frac{e}{mc^2}\frac{j_0 S(E_z^1)^2}{\pi^2\sqrt{2}k^2\gamma_0 N_s}$, $f = \frac{2\alpha g_0}{b\sqrt[3]{2\gamma_0^2}}$, for E-waves $\alpha = \frac{\left|\hat{L}E_z^0\right|}{\sqrt[3]{2\gamma_0^2}}$, for H-waves $\alpha = \frac{e}{mc^2}\frac{\left|\hat{L}H_z^0\right|}{2g_0^2}$, Cherenkov synchronism mismatch is $\delta_1 = \gamma_0\sqrt{\frac{2}{b}}\left(-1+\frac{h_1}{k}-\frac{1}{2\gamma_0}\right)$, the cyclotron resonance mismatch is $\delta_2 = \gamma_0\sqrt{\frac{2}{b}}\left(1-\frac{h_0}{k}+\frac{1+eH_0/mc\omega}{\gamma_0^2}\right)$. When $z=0$ we consider that the initial Cherenkov phases are uniformly distributed $\varphi_0 \in [0,2\pi)$, normalized electron energy $U=0$, in the interaction space electrons fly without transverse velocities, i.e. $\rho = 0$, $\varphi = 0$. The amplitude of the operating spatial harmonics is equal to zero ($b=0$) on other end of the interaction space, when $\varsigma = \varsigma_0$

Acknowledgments

This work is supported by the Russian Interdisciplinary Scientific and Technological Program "Physics of Microwaves" and Russian Foundation of Basic Researches, Grant No. 95-02-04281.

References

1. Mesyats G.A., Petelin M.I., Osipov M.L. et al. An experimental high power short-pulse radar. Abstracts of III Intern. Workshop on Strong Microwaves in Plasmas. IAP RAS, Nizhny Novgorod, Russia, August 7-14, 1996, S-2.
2. Bykov A.M., Gubanov V.P., Gunin A.V. et al. Relativistic repetitive-pulse X-band generators. In: Relativistic microwave electronics. Gorky: IAP AS USSR, 1988, 5, 101-124.
3. Abubakirov E.B., Belousov V.I., Varganov V.N. et al. Experimental realization of the cyclotron-resonant mode selection method in rela-

tivistic electron microwave Cherenkov generators. Pis`ma v ZhTF, 1983, vol.9, no.9, pp.533-536.
4. Abubakirov E.B., Ginzburg N.S., Kovalev N.F., Fuchs M.I. Influence of fast cyclotron waves on operation of Cherenkov microwave devices driven by relativistic electron beam. Radiotechnics and electronics (Russian), 1989, vol.34, no.9, pp.1058-1066.
5. Kovalev N.F., Petelin M.I., Raizer M.D., Smorgonski A.V. O-type devices based on stimulated Cherenkov and transient radiation of electrons. In: Relativistic microwave electronics. Gorky, IAP AS USSR, 1979, 1, 76-113.
6. Kovalev N.F., Petelin M.I., Raizer M.D. et al. Generation of high-power pulses of electromagnetic radiation by relativistic electron beam. Pis`ma v ZETF, 1973, vol.18, no.4, pp.232-235.
7. Carmel Y., Ivers J., Kribel R.E., Nation J. Intense coherent Cherenkov radiation due to the interaction of a relativistic electron beam with a slow-wave structure. Phys.Rev.Lett., 1974, vol.33, no.21, pp.1278-1282.
8. Korovin S.D., Pegel I.V. Numerical modeling of forming of high-current electron beam in coaxial magnetic insulated diode. Proc.IX Symp. on High-Current Electronics, 1992, pp.110-111.
9. Gorshkova M.A., Il`in V.P., Nechaev V.E. et al. Structure of high-current relativistic electron beam forming by coaxial gun with magnetic insulation. ZhTF, 1980, vol.50, no.1, pp.109-114.
10. Volkov A.B., Zaitsev N.I., Ilyakov E.V. et al. Realization of high gain of high power microwave amplifier with explosive emission gun. Pis`ma v Zh.T.F., 1992, vol.18, no.12, pp.6 - 10.
11. Abubakirov E.B., Ginzburg N.S., Kovalev N.I., Fuchs M.I. Influence of fast cyclotron waves on operation of Cherenkov microwave devices driven by relativistic electron beams. Radiotechnics and Electronics (Russian), 1989, vol.34, no.5, pp. 1058-1066.
12. Vainshtein L.A., Solntsev V.A. Lectures on microwave electronics. Moscow: Soviet Radio, 1973.
13. Petelin M.I., Yulpatov V.K. Masers on cyclotron resonance. Lectures on microwave electronics. Part 4. Saratov: Saratov University, 1974, pp.96-178.

EFFICIENCY INCREASE OF HIGH-POWER MICROWAVE SOURCES BASED ON MULTIWAVE CERENKOV GENERATORS

V.I.Koshelev, M.P.Deichuly, A.S.Zavyalov, A.I.Klimov, A.A.Petkun, V.M.Tarnovsky

High Current Electronics Institute, Siberian Division of the Russian Academy of Sciences, Tomsk, Russia

Abstract

Possibilities to increase the efficiency of high-power microwave sources based on multiwave Cerenkov generators (MWCG) due to MWCG generator efficiency increase and power losses decrease when radiation is taken out of generator into atmosphere and output radiation is transformed into linearly polarized wave beam have been investigated in a 3-cm-wavelength range.

Introduction

For practical application, high-power microwave sources with linearly polarized wave beams and high output efficiency are necessary. The efficiency of both in power and in energy is important. The latter condition corresponds to the requirement to obtain microwave radiation pulses with the duration similar to the one of the electron beam current pulse.

To generate gigawatt-power-level, centimeter- and millimeter-wavelength-range radiation, an MWCG [1] was used. The investigations [1] that have been carried out allowed to mark out problems which are in the way of creation the effective microwave sources based on MWCG: 1) essential part (up to 30 %) of radiation power with φ-polarization not transforming into the linear one resulting in decrease of microwave source output efficiency; 2) high power losses ($\leq$ 50%) due to the reflection from a thick dielectric window and radiation into side lobes of a pattern; 3) essential (30 - 40%) power losses when θ-polarization radiation is transformed into a linear one. As usual, the important task is to increase the radiation generation efficiency in MWCG which decreases when electron energy decreases [2].

MWCG Generation Efficiency

Two-sectional uniform (nonuniformity periods in the sections are equal) overmoded ($D / \lambda >> 1$, D is the diameter, λ is the radiation wavelength) slow-wave structures (SWS) [1, 2] are usually used in MWCG. A drift tube is of great importance in increasing the efficiency of generation radiation. It ensures : 1) more smooth bunching of electrons; 2) tuning of a slow-wave phase of high-frequency field and electron bunch at the input into the second section at the expense of the field phase shifting owing to the jump of a phase wave velocity in the drift tube; 3) increase of effective energy output of high-frequency field out of generator owing to the decrease of the slow-wave structure Q ; 4) selection of optimum starting generation frequency.

A shortcoming of MWCG with a two-sectional uniform SWS is related to the difficulty of simultaneous using of all the possibilities of the drift tube. The choice of optimum combinations of the merits mentioned results in limitation of their efficiency. Using of multisectional nonuniform (nonuniformity periods in the sections differ from each other) SWS in MWCG promote not only the elimination of the defect indicated as a part of the drift tube functions in this case is implemented by the sections but also to the efficiency increase of the above-stated possibilities.However, for effective optimization of a complex MWCG SWS it is insufficient to have only a conceptual approach and experimental investigations. In this connection a simplified nonlinear MWCG model has been developed taking into account electron beam space charge by particle-in-cell method and preliminary numerical calculations have been carried out.

Experimental investigations were carried out at a "SINUS-7M" accelerator at the diode voltage U_d = 1 MV, beam current I_b = 10 kA, pulse duration τ_p = 40 ns. A hollow beam diameter varied in the limits of 10 ÷ 11.8 cm. Magnetic field B = 5 ÷ 15 kG. Radiation power was determined by patterns in two (θ- and φ-) polarizations measured in atmosphere. Radiation power losses in a transmitting antenna were not controlled. Radiation spectrum was measured by band-pass filters with a 0.5-percent band width.

Several MWCG variants with a three-sectional SWS and D = 13cm were investigated experimentally. The results of investigations of one of them with the periods in the sections l_1 = 1.45 cm, $< l_2 > \approx$ 1.5 cm, $< l_3 > \approx$ $\approx$1.4 cm are presented below. The sign $< >$ means averaging of a period along the section length. Radiation pulses with the power P_θ = 2.3 GW, P_φ= 0.2 GW, 30-ns duration and < 1% spectrum width were obtained in

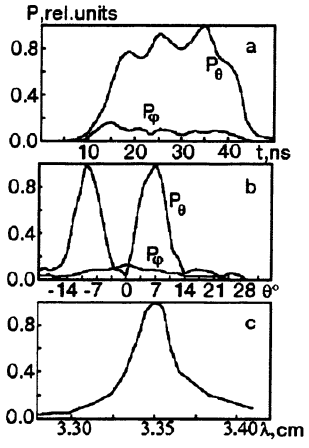

Fig.1. Pulse oscillograms (a), patterns (b), and radiation spectrum (c).

MWCG with such SWS at the wavelength λ = 3.35 cm. Fig. 1 a,b,c presents the corresponding oscillograms, patterns, and radiation spectrum. Radiation power instability $\Delta P_\theta / P_\theta \approx$ ≈15% at the instability of the beam power up to 20%. The efficiency of generation radiation with θ-polarization equals to 25%, not taking into account power losses in a transmitting antenna, that is two times higher than the efficiency of MWCG with a uniform two-sectional SWS at U_d = 1 MV (radiation spectrum width is <1%) and corresponds to the MWCG efficiency (by radiation taken out into atmosphere) at U_d = 2MV [1] but five times less power relation $P\varphi / P_\theta$ and less instability of radiation power.

Injection of Radiation from Generator into Atmosphere

As it was already mentioned above, power losses when injecting radiation from MWCG into atmoshpere can be divided to the losses due to reflections from a thick dielectric window and radiation spreading at high angles to a horn antenna axis (diffractional losses).

When the thickness of a plane-parallel window $d = (2n + 1)\ \lambda / 4\varepsilon^{1/2}$ (n is the integer, ε is the capacitivity), power losses due to wave reflection reach 14% [3]. At optimum wavelength λ_{opt} satisfying the relation $d=n\lambda_{opt} / 2\varepsilon^{1/2}$, transmission coefficient is close to 1. Expansion of a frequency passband is possible due to the using of layers with a smooth changing of capacitivity in the layer thickness from 1 to the value ε corresponding to the window material. It can be achieved by turning a triangular profile grooves with the depth ~ (0.5 ÷ 1) λ_{opt} and base width ~λ_{opt} /4 in one or two mutually perpendicular directions. As a result, ribbed or tenon-like surfaces are formed from both sides of the window.

Properties of a plane window with such matching layers were investigated in a 3-cm range on the samples made of polyethylene which

were placed in a 72 x 34- mm cross-sectional waveguide. Measurements

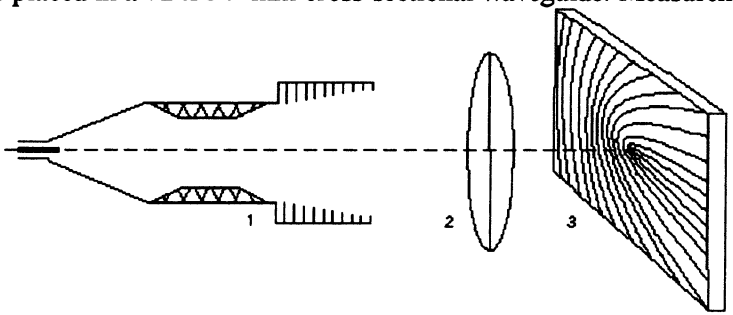

Fig.2. Experimental setup. 1 - MWCG model, 2 - lens, 3 - polarization transformer.

have shown that the wave transmission coefficient in a $\lambda = (0.8 \div 1.2)\ \lambda_{opt}$ - wavelength range was close to 1.

To suppress pattern side lobes , it was suggested to use a diaphragmed waveguide, installed after a microwave generator SWS, with smooth decrease of the groove depths from $\lambda_0/2$ to $\lambda_0/4$, where λ_0 is the operating wavelength at which the highest side lobes radiation supression is achieved. Experimental investigations were carried out at a MWCG model presented schematically in Fig. 2. Generator model presented a SWS in the form of $\approx 4\lambda_0$ -diameter cylindrical waveguide with a thin polyethylene layer.Smooth or diaphragmed horns with $\approx 3.5\lambda_0$ - length and $\approx 4.5\lambda_0$ -aperture diameter were connected to the waveguide. Wave field presenting a sum total of surface and space waves was excited by a short pin feeded from a standard generator. Angle distribution of power flow density $S(\theta)$ was measured and a part of power $P(\theta)/P_{max}$ placed inside a spatial angle corresponding to a θ angle was computed in the investigations. The latter allowed to compare the powers concentrated in the main and side lobes.

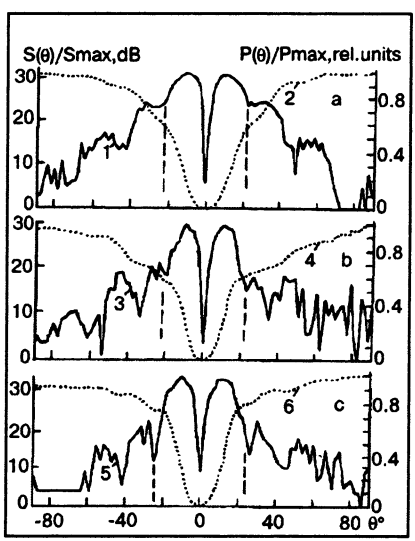

Fig. 3. Patterns (1, 3, 5) and integrals of radiation intensivity on the patterns versus upper limit (2.4,6) of a waveguide open end (a), smooth (b) and diaphragmed (c) horns.

The efficiency of side lobes radiation suppression depended on the field structure. Essential significance had a length b of a smooth waveguide part between a dielectric SWS and diaphragmed horn. Fig. 3 presents measurement results at $\lambda = \lambda_0$ and $b = 4\ \lambda_0$. From comparison of the curves 2, 4, 6 , essential redistribution of power between the main and side lobes is seen. The power concentrated in the side lobes of a diaphragmed horn is ~ 20% less than that of a smooth one. Side lobes supression by a diaphragmed horn is realized in a wavelength band $\Delta\lambda/\lambda_0 \approx 3\%$.

Transformation of a Multiwave Radiation Polarization

To transform MWCG radiation with θ-polarization into a linearly polarized wave beam, it is suggested to use a device based on a metallic mirror as well as a system of arched conductors placed at a distance of approximately a quarter of a radiation wavelength from the mirror [4], the angle of the mirror plane inclination to the generator axis being equal to 45°. The conductors are located on a dielectric substrate. A theory of such transformers which takes into account the influence of the angle θ_0 between the directions of radiation incidence and a normal to the mirror, capacitivity and thickness of a substrate, the distance between the conductors on the phase relation between the components of the reflected wave has been developed. The conductors are a system of parabols $x=y^2/4b-b\cos\theta_0$ where b is the parameter of the system.

Investigations of the transformer were carried out at a setup presented in Fig. 2. Radiation created by a MWCG model was collected into a parallel beam by a 40-cm-diameter and 26-cm-focuse distance lens and was incident to the polarization transformer with 40x60-cm cross-sectional dimensions at the angle $\theta_0 = 45°$. Radially polarized radiation powers immediately behind the lens and linearly-polarized radiation powers after the transformer were determined by the patterns measured. Figs. 3a and 3b present distribution of a power flow density for a wave with the main polarization and a cross-polarized one, respectively.

The power in a cross-polarized wave at an operational wavelength $\lambda_0 = 3.27$ cm was equal to 10 ± 2% from a common power reflected from the transformer. Power losses in a substrate dielectric (a sheet of 0.7mm-thick getinax) equaled to 8 ± 2%. The efficiency of radially-polarized radiation transformation into a linearly-polarized wave beam for a given model equaled to 82 ± 2%.Using of dielectrics with small losses should result in decreasing of both losses and cross-polarization radiation level, i.e.

to a marked increase of the polarization transformer efficiency. Measurements have shown that the given transformer model preserves its features in a 8 ÷ 9.5 GHz-frequency range and when the angle of θ_0 varies in the limits of ± 2°.

Fig. 4. Distribution of power flow density for a main (a) and cross-polarized (b) field components.

Conclusion

A complex of theoretical and experimental investigations that have been carried out demonstrated the possibilities of increasing the efficiency of high-power microwave sources based on MWCG from radiation generation to obtain linearly-polarized wave beam.

The research described in this publication was made possible in part by Grant NY 6300 from International Science Foundation and Russian Government.

References

1. Bugaev S.P., Cherepenin V.A., Kanavets V.I., Klimov A.I., Kopenkin A.D., Koshelev V.I., Popov V.A., Slepkov A.I. IEEE Trans. Plasma Science, 1990, 18, 525.
2. Chernyavsky I.A., Deichuly M.P., Koshelev V.I., Pikunov V.M. SPIE Proc. Series, 1994, 2259, 542.
3. Born M., Volf E. Principles of Optics. Pergamon Press, 1968.
4. Kaloshin V.A., Ermolaev S.V., Shishlov A.V. Antenna: Author's Certificate 1376150 USSR, Bulletin of Inventions. 1988, 7, 222.

NUMERICAL EXPERIMENT WITH THE RELATIVISTIC BWO USING KARAT CODE

*S. D. Korovin, I. V. Pegel, and V. P. Tarakanov**

High Current Electronics Institute, Tomsk, Russia
*High Temperature Institute, Moscow, Russia

Introduction

The Relativistic Backward Wave Oscillator (RBWO, Fig. 1, [1]) with the operating wave TM_{01} is a well-accepted powerful microwave device realized on the base of high current electron accelerators. The necessity of its time-dependent simulations results from the existence of non steady-state regimes of generation [2] and from the fact that usually the RBWO is driven by high current electron beams with nanosecond pulse duration which is comparable with the oscillation establishment time.

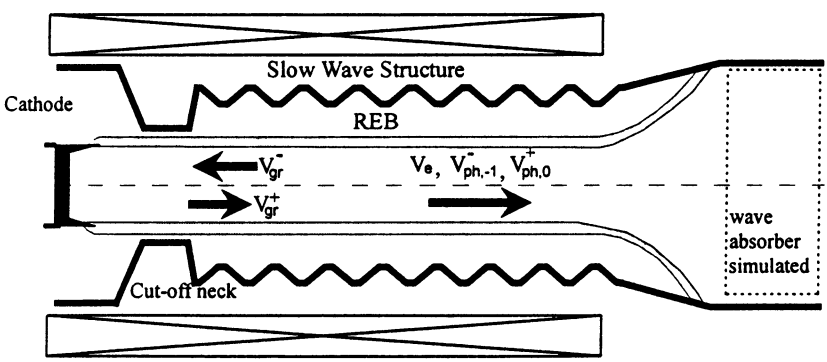

Fig. 1. Schematic of Relativistic BWO

In the earliest 1D time-dependent BWO model [3], hydrodynamic approach was used to describe the electron beam. This did not allow to account kinetic phenomena like particle reflection which actually occur in high-efficiency microwave devices. Also, all temporal dependencies were considered averaged over the beam transit time. The kinetic Particle-In-Cell method used in the fully electromagnetic 2.5&3D code KARAT [4] is free of this lack.

Formulation of the Problem

The 2.5D axisymmetric version of the code was used. Both the BWO with coaxial feeding diode and the BWO with the electron beam injected in the cut-off neck have been simulated. The voltage to the diode was led in the form of a TEM-pulse through the coaxial line like in actual experiments. A coil has been considered producing magnetic field of up to 40 kOe.

To match the generated radiation, an absorber has been simulated at the right edge of the device with a uniform or linearly increasing conductivity so that the power reflections did not exceed 1%. To avoid the high-frequency Alias-Cherenkov instability, digital filtration of both the charge and current densities and the electromagnetic fields has been used. In the contrary to time-biased field solvers, this does not cause any depression of physical oscillations. The filtration also prevented the system from the «explosive» instability of boundary conditions at the left opening of diode coaxial.

The main parameters corresponded to the X-band BWO [5] realized on the base of high current nanosecond electron accelerator «SINUS-6», with the total length of 13.32 cm, having eight main ripples (half-depth of corrugation 2.25 mm) and one matching ripple (half-depth 1 mm). The coupling impedance for the (-1)st spatial harmonics increases from 1.6 Ohm at the cathode edge of the slow wave structure to 2.1 Ohm at the output edge (at operation frequency) due to magnetic field profile. In the simulations, the electron energy was about 450 keV with the beam current varied from zero up to ~7 kA.

Effects of Space Charge in the BWO

The simulation showed that the BWO output power has a maximum as a function of beam current (Fig. 2). As the analysis indicated [7], this is caused by the changes in the amplitude and phasing of high-frequency current due to space charge of high current electron beam. This, in particular, confirms earlier conclusions made by N. Kovalev. A lower start current value was

obtained in the simulation than predicted by the formula for the classic BWO obtained with the account of (-1)st spatial harmonics of backward wave only. This is explained by the effect of nonsynchronous but strong field of fundamental harmonics of the forward wave [6]. Note that in the simulation the electromagnetic field was described as it is with no separation in spatial harmonics.

A distinctive feature of high-efficiency RBWO is the backward electron current reaching 0.1 from the injected beam current. It appears jump-wise at some beam current level and decays gradually along with the generation power (Fig. 2). The backward electrons have high energies (reaching the injection energy) and transverse velocities. The backward current curve is not symmetric around its maximum, in the contrary to the generation power. That indicates that its appearance is not directly determined by the high amplitude of operating wave. The analysis showed that the reason of backward current is the short-wavelength destruction of compact electron bunches due to strong space charge fields. As a result of intense thermalization, the electrons get significant energy changes, both positive and negative. A part of slow electrons then gain negative velocities under the action of backward and forward (reflected) electromagnetic waves.

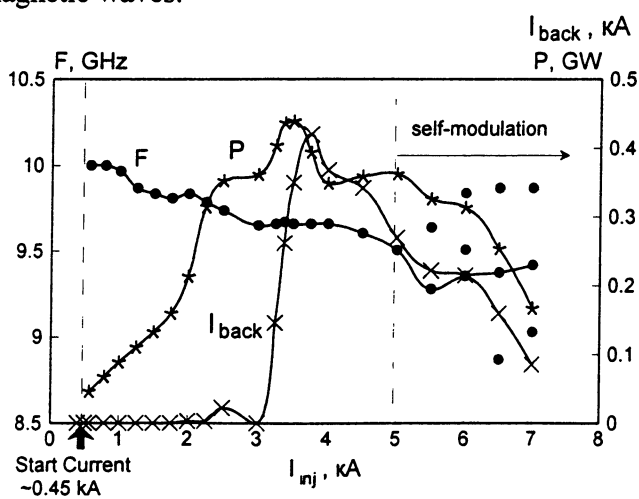

Fig. 2. Generation power and frequency and the backward electron current vs injected beam current

The simulation showed that the backward current in the BWO depends on the guiding magnetic field. It appears on the right-hand slope of the cyclotron downfall (see Fig. 3 and also Fig. 4 for generation power) and than decreases while the microwave power remains almost constant. This indicates the significant role of transverse motion in the formation of backward flow.

Passing through the cut-off neck, the backward electrons input additional charge into the diode and this increases the diode impedance in relation to the main electron beam. The Figure 3 illustrates the behavior of impedance of separated diode and the diode loaded with the BWO. In low magnetic fields these curves are coincident but to the right from the cyclotron downfall where the backward current appears the impedance of BWO-loaded diode is 10% higher. The fact of observation of this effect in an experiment must be a simplest sign of backward current presence.

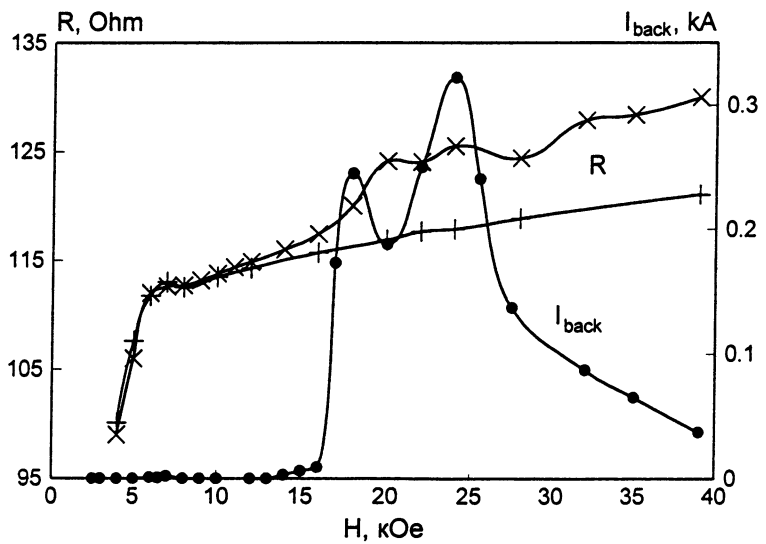

Fig. 3. Backward current, generation power and the impedance of separate (+) and BWO-loaded (x) coaxial diode vs magnetic field

Effects of Magnetic Field in the BWO

The numerical experiment confirmed the effect of cyclotron suppression of generation known in the BWO experiments and

explained by N. F. Kovalev in terms of cyclotron resonant absorption of the backward wave on its fundamental harmonics. The corresponding resonant magnetic field is

$$H_R = \frac{mc^2}{e} k \gamma \left(1 + \beta_{e\|} / \beta_{ph}\right) \qquad (1)$$

where $\beta_{e\|} = V_{e\|}/c$, γ is the electron mass-factor, $k = \omega/c$, β_{ph} and ω are the wave phase velocity and cycle frequency.

In the simulation, the beam energy and the current were 450 keV and 3.5 kA in the injection regime and, in the case with the diode, the incident TEM-pulse was constant but the diode impedance varied slowly with the magnetic field causing slow changes in beam energy and current.

In both cases, an expressed minimum of microwave power appeares at the magnetic field corresponding to (1). In the high fields, the power saturates and the generation is steady-state in the contrary to the slopes of the cyclotron downfall and the low fields.

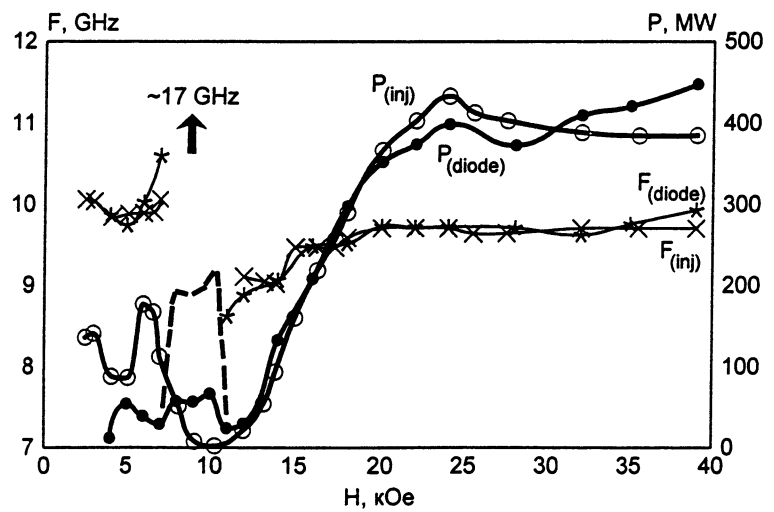

Fig. 4. Dependencies of RBWO forward and backward (dashed line) emission power and frequency on the magnetic field

The low power level in the low magnetic fields is the consequence of intense pumping of transverse velocities of beam

electrons due to operating wave, and their dumping to the wall. This effect is considered to be a principal limitation of generation efficiency in the low magnetic field. A specific self-modulation was observed here also caused by beam dumping in the cut-off neck.

On the bottom of cyclotron downfall, a high frequency TM_{01} generation appears in the case when the BWO with the diode is simulated. Note that the main portion of power is therewith emitted in backward direction (~200 MW vs 50 MW in forward direction, see dashed line in the Fig. 4). The anode neck does not cut the high frequency backward wave and also it is not cyclotron-absorbed in this range of magnetic field. Entering the diode, the wave produces a modulation of the diode voltage as deep as 10% which results in beam pre-bunching and therefore assists the generation excitation. The establishment of this oscillation is twice as long as in the regular regime. The high frequency generation (the device of which is not discussed here) has not been observed when the diode was separated from the slow wave structure by means of a foil transparent for the electrons but reflecting electromagnetic waves.

Note however that the non-axisymmetric waves have not been considered in these simulations which probably can be in a concurrence with this high-frequency oscillation. We hope that the results of 3D BWO simulation will be obtained in the nearest future with the use of 3D version of KARAT code.

In the conclusion, note that the simulation results are in a good agreement with the actual BWO experiments. The numerical experiments are now intensively used at HCEI to design powerful Cherenkov microwave oscillators.

References

1. Carmel Y. *et al.* Phys. Rev. Lett., 1974, **33**, p. 21
2. Ginzburg N. S., Kuznetsov S. P. Relativistic High Frequency Electronics. Gorki: IAP AS USSR, 1981, p. 101.
3. Ginzburg N. S. *et al.* Radiofizika, 1978, **21**, p. 1037.
4. Tarakanov V.P. User's manual for code KARAT / BRA, VA, 1992.
5. Roitman A. M. *et al.* / Abstr. ICOPS'94, p. 194.
6. Korovin S. D. *et al.* / Lett. J. Tech. Phys. (Sov.), 1994, **20**, N 1, p. 12.
7. Pegel I. V. To appear in "Soviet Physics Journal", 1996, **11**

EFFECTS OF NONLINEAR BLEACHING IN MICROWAVE RELATIVISTIC DEVICES

E.B.Abubakirov, A.V. Savelyev

Institute of Applied Physics, Russian Academy of Sciencies,
Nizhny Novgorod, Russia

There are special regimes in electron microwave devices with distributed interaction which, when using the eigenwave description, refer to coherent summing of the eigenwaves. One of the simplest examples of such regimes is the suppression of the input signal in the TWT (Kompfner deep condition). The absence of an output signal in this case occurs due to coherent summing of the three eigenwaves (see, e.a. [1]). The similar situation takes place in the BWO. Boundary condition $E = 0$ at the collector end of this type generator can be satisfied also when coherent summing of few eigenwaves happens. Suppression of the output signal in the Bragg reflector filled with a relativistic electron beam [2], which may be regarded as a modification of the Kompfner suppression, belongs to the same class of phenomena.

All these states take place at low amplitudes of interacting waves. At the same time, their evolution as the input signal grows is the subject of special interest. The peculiarity of the phenomena of this type is that first of all nonlinear effects influence phase constants of the eigenwaves [3]. That means that at the output (or input) of a microwave device the condition of mutual compensation or coherent summing of eigenwaves will be disturbed. In the case of suppression of the output high-frequency signal (in TWT) the growth of input signal amplitude leads to *bleaching* of the microwave element. For Bragg reflector with electron beam or regenerative BWO-amplifier (BWO near the self-excitation threshold) the opposite process will take place: the transmission coefficient of these devices will fall down as the input signal grows.

To analyze these effects on the base of the Cherenkov-type relativistic microwave devices we can use the following nonlinear equations, which describe the interaction between the electron beam and the synchronous electromagnetic wave [4]:

$$\frac{dw}{d\zeta} = \mathrm{Re}\{(F + i\sigma \int_0^{2\pi} e^{-i\vartheta} d\vartheta_0) e^{i\vartheta}\}, \quad \frac{d\vartheta}{d\zeta} = \frac{1}{w^2} - \delta, \qquad (1)$$

$$\frac{dF}{d\zeta} = \pm\alpha \int_0^{2\pi} e^{-i\vartheta} d\vartheta_0, \qquad (2)$$

Here $w = \gamma/\gamma_0$, $\gamma_0 = \left(1-(v_0/c)^2\right)^{-1/2}$, v_0 is initial velocity of electrons; $\zeta = kz/2\gamma_0^2$, $\delta = 2\gamma_0^2(h/k-1)$ is synchronism mismatch; $\sigma = 4\gamma_0 T\left(eI/mc^3\right)/\pi\left(\gamma_0^2-1\right)^{-3/2}$ is space charge parameter, T is depression coefficient; $F = \left(2\gamma_0 e/mc\omega\right)E_z$, $\alpha = 2\gamma_0^3 ZIe/mc^3\pi$ is coupling parameter and Z is coupling resistance.

Kompfner deep condition

First of all let us take a look at the well-known situation of signal suppression of in TWT (Kompfner deep condition). At some values of synchronism mismatch in a TWT there is no output signal (Fig. 1).

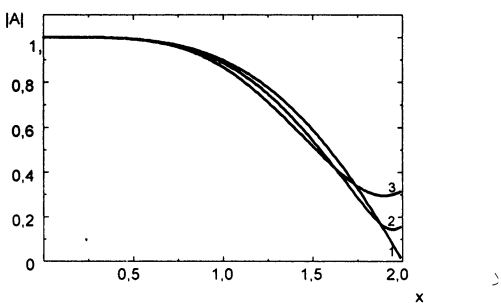

Fig. 1 Appearance of signal at the output of TWT

The increase of amplitude leads to appearance of signal at the output - to *bleaching* of TWT. We can explain it by "misphasing" of eigenwaves what happens due to nonlinear corrections to the phases of these waves, so compensatory conditions are no longer valid and the sum of eigenwaves which represents the field in the tube is not zero at the output.

Bragg reflector with relativistic electron beam

Considered on the examples of such classical devices as TWT and BWO, the state analogous to the above mentioned can be discovered in the case of the Bragg reflector with a relativistic electron beam. The Bragg-type reflectors designed on the basis of slightly corrugated

waveguides are well known for their ability to provide single-mode regimes in oversized systems. Transportation of powerful electron beam directly through the volume occupied by electromagnetic fields in the reflector influences reflector characteristics and can lead to suppression of the reflected wave. Evolution of this compensatory state with the growth of input amplitude is considered similar to the above cases.

For calculations the following nonlinear equations, which are combined with relativistic TWT equations (1) and coupled waves equations,

$$\frac{df_2}{d\zeta} = i\varepsilon \cdot f_1 - \alpha \cdot \int_0^{2\pi} e^{-i\theta} d\theta_0, \quad \frac{df_1}{d\zeta} = -i\varepsilon \cdot f_2 - id \cdot f_1 \cdot, \qquad (3)$$

are used. Here $d = 2\gamma_0^2\left(\bar{h} - h_1 - h_2\right)/k$ is signal mismatch with respect to the central frequency of reflector, $\bar{h} = 2\pi/l$, l is period of reflector wall corrugation; $\delta = 2\gamma_0^2\left(h_2/k - 1\right)$ is synchronism mismatch between wave 2 and the beam; h_j is longitudinal wave number; ε is coupling parameter for waves in the reflector (it is proportional to the corrugation depth in reflector); $f_{1,2}$ refer to incident and reflected waves accordingly. The compensatory state in this case arises when the reflected wave is suppressed completely (Fig. 2, point d=0).

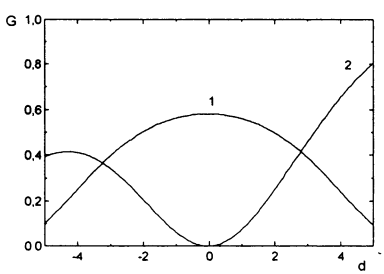

Fig. 2. Deformation of frequency curve in the presence of relativistic electron beam: 1 - "cold" reflector, 2 - reflector with a beam;

$$G = \left|f_2(1)/f_1(1)\right|^2, d = \left(\bar{h} - h_1 - h_2\right)L.$$

Such a state is characterized by similar non-linear evolution (Fig. 3). The reflected wave primarily (at low amplitude) suppressed by the electron beam starts to appear with the increase of the amplitude. Similar to previous cases, it is caused by disturbing of the compensatory conditions which are responsible for the zero of amplitude of the reflected wave at the output of the device.

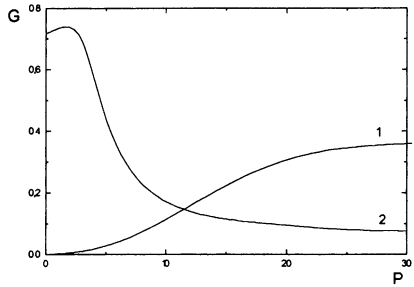

Fig. 3 Dependencies of reflection (curve 1) and transmission (curve 2) coefficients versus input power

TWA with a combined input signal

In the case of combined excitation of TWT both by an electromagnetic signal and a modulated electron beam the initial amplitude of the growing wave in TWA depends on correlation between amplitudes and phases of the input signal, high-frequency current and its derivative. So the situation when the initial amplitude of the growing wave drops to zero is possible. And as the amplification is mainly defined by this eigenwave we can speak here about amplification blocking in TWA. Note that such a compensatory state refer to one of the eigenwaves while previously considered states relate directly to the high-frequency field.

To explore evolution of this state when nonlinear effects appear we will base our analysis on a sectioned amplifier where a TWT-section is excited by the electron beam modulated in previous sections (Fig. 4).

Fig. 4. Scheme of a sectioned amplifier

Let us estimate efficiency of excitation of the TWT-section with an initial amplitude of eigenwave with exponential growth. This value in the case of the combined input signal is calculated as:

$$A_1 = \frac{x_1^2 - q}{(x_1 - x_2)(x_1 - x_3)} \left\{ A_0 - C(x_2 + x_3)(ix_1 CJ + J') \right\}, \qquad (4)$$

where $C=(2\pi\alpha)^{1/3}$ is amplification parameter (analogue of Pierce parameter in the theory of traditional TWT), $q=2\pi\sigma/C^2$ characterizes space charge, J and J' are high-frequency current and its derivative at the input of TWT section, x_i is solution of the TWT dispersion equation:

$$(x+d)(x^2-q)-1=0, \qquad (5)$$

$d=(\delta-1)/C$. Further the excitation coefficient is taken as the squared ratio of initial amplitude of the growing wave to the amplitude of the input signal in amplifier $G=|A_1/A_{in}|^2$. This coefficient characterises the efficiency of excitation of the TWT and is a periodic function of the drift space length (Fig. 5).

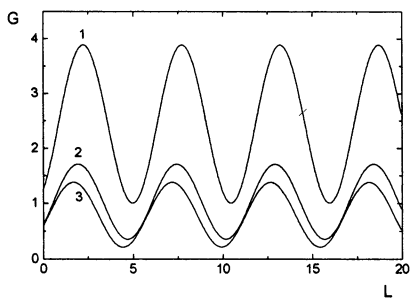

Fig. 5 Dependencies of excitation coefficient $G=|A_1/A_0|^2$ versus drift space length at different values of mismatch parameter in TWT

The periodicity of the curves is explained by the fact of beating of two eigenwaves with different phase velocity. These eigenwaves correspond to the fast and slow space charge waves in the beam which form the stationary wave in the drift space. When changing the length of the drift space, the input of the TWT periodically goes through a node or antinode that corresponds to the minimum or maximum efficiency of excitation.

Considering the state with the minimum efficiency of excitation as the compensatory state formed by coherent summing of two eigenwaves, we can explore the evolution of this state with the growth of amplitude of the input signal (Fig. 6). The increase of amplitude leads to expansion of the curve, which is caused by nonlinear corrections to propagation constants of the eigenwaves. When the drift space region is sufficiently long, hese corrections may lead to significant contribution to phase of the stationary wave, so its node may be replaced with antinode. If primarily (at

low amplitude) the system was configured to minimum of excitation coefficient than, with the growth of amplitude, excitation coefficient can rise up to the maximum.

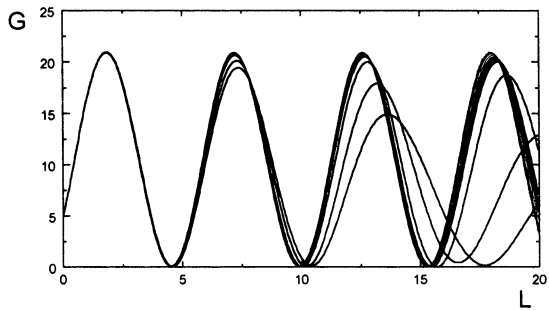

Fig. 6. Evolution of $G = \left|iCx_1 J(\zeta) + J'(\zeta)\right|^2 / F_{in}^2$ with the growth of input amplitude

Considered examples are just a small part of the cases in which some compensatory states can be realised. In fact, practically any distributed system may have such a state. So, the appearance of nonlinear effects (with the growth of input amplitude as in the considered cases) leads to distortion of compensatory conditions which destroys the state. By this such states can be called "*nonrough*" states which means that small non-linearity causes disturbing of the compensatory conditions.

The analyzed effects considered on the examples of real devices may have practical importance. The compensatory basis of above mentioned states which determines their high sensitivity to amplitude variation makes it possible to create special amplification characvteristics (e.a., threshold amplification), to provide small rise-up times in oscillators, to increase efficiency of microwave devices, etc.

References:

1. W.Kleen, K.Poschl, "Einfuhrung in die mikrowellen electronik". S.Hirzel Verlag Stuttgart, vol.2, 1958
2. E.B.Abubakirov, *Radiotechnika i electronika*, vol.35, No.12, p.1234, 1991.
3. L.D.Landau, E.M.Livshits, Theoretical Physics, vol.1. Moscow: Nauka, 1965.
4. N.F.Kovalev, A.V.Smorgonsky, *Radiotechnika i electronika*, vol.20, No.6, p.1305, 1975.

GENERATION OF POWERFUL MICROWAVES BY EXCITATION OF A PLASMA RESONATOR

V.I.Chelpanov, A.L.Babkin, S.M.Galkin, V.G.Kornilov, V.D.Selemir, V.S.Zhdanov

(RFNC-VNIIEF, Sarov, Russia)

Introduction

The variety of practical application determines constant attention to theoretical and experimental researches of interaction of relativistic electron beams (REB) with plasma. For us use of plasma-beam interaction for transformation of REB energy in energy of electromagnetic radiation is of interest. There are all basis to believe, that on a line of parameters (width of amplification and generation band, opportunity of frequency tuning, progress in area of shorter wave lengths, compactness) the plasma sources of microwave radiation are represented more perspectiv, than vacuum analogues [1, 2]. The most widespread real system, used as slow-wave structure, represents a piece of smooth metal waveguide, partially or completely filled by plasma. Just for such system a generation problem is theoretically solved and such important parameters as generation starting conditions, frequency of generation and its growth rate, interaction efficiency, condition of the optimum coupling of plasma system with an output tract [3] are found. These theoretical representation qualitatively and quantitatively have proved to be true by experimental work [4]. Just this on this concept of the plasma generator we are guided in our work as on basic. At the same time the certain interest represents filling by plasma of conventional slow-wave structures (dielectric and corrugated ones).

Engineering of experiment

One of the basic technical problems of experimental realization of a plasma microwave electronics is creation of plasma-filled electrodynamic structures. As a rule, it is metal cylindrical waveguide with length up to several tens of centimeters, partially or completely filled by plasma of density of $10^{12}...10^{13}$ cm^{-3}. We have chosen, as it

seems, more simple and reliable way of plasma creation - direct high-current discharge in low pressure gas.

The discharge was formed in a waveguide, which can be smooth, corrugated, with presence of tubular dielectric. The discharge cathode was located at the electrodynamic structure output strictly on its axis. A15 μm copton film served for the anode, dividing high-vacuum diode area from the discharge one. In number of cases the anode was served by a metal round plate with a diameter smaller than the waveguide one, located coaxial with the discharge cathode and carried with it on distance, which determines the length of a plasma column. The disharge was formed in a strong magnetic field about 10^4 G. Working pressure needed for discharge changed from $3 \cdot 10^{-3}$ up to $3 \cdot 10^{-2}$ Torr. Length of the discharge gap was electrodynamic structure electrodynamic structure electrodynamic structure usually 40cm, cathode voltage was 15...20kV. Under such conditions the discharge stablly occured up to pressure $2 \cdot 10^{-2}$ Torr. The discharge had the cylindrical form with the cross size, conterminous to the cathode one, that is fixed by photographing of discharge luminescence(Fig.1). In the given experiments the waveguide diameter was 5.2cm, diameter of the cathode - 4cm. The discharge luminescence photo shows, that its diameter about coincides with cathode by the size.

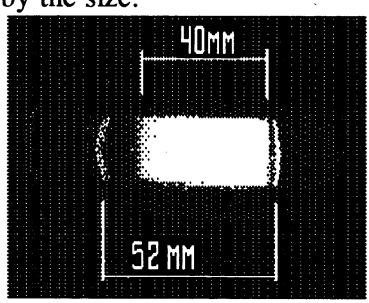

Fig.1

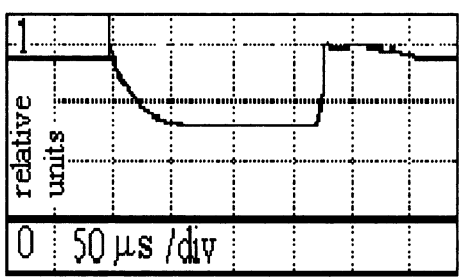

Fig.2

Microwave probing by frequency 10 GHz, for which critical plasma density makes 10^{12} cm^{-3}, has shown, that plasma density lays just in this region. The conclusion was made on microwave signal passing through plasma. Oscilloscope trace of a passed signal is shown in Fig.2. A discharge current in these experiments made 300 A, resistance limiting a current 50 Om, pressure in the chamber 10^{-2} Torr.

The basic way of plasma density change was determined by dependence of plasma concentration on the discharge current, which is in turn proportional to limiting resistance in the discharge circuit. It was confirmed by probe measurements. They were carried out with double Lengmure probe, working in the ion saturation regime. The probe could move in a radial direction in a plane, laying on distance of 2cm from an axis of microwave probing beam (Fig.4). A strong magnetic field does not allow to speak about absolute meanings of plasma concentration. However uniting the probe indication with data of microwave probing, we can speak that changing resistance limiting a current from 50 up to 1Om, we receive plasma with density from 10^{12} up to 10^{14} cm^{-3}. Dependence of probe value on discharge current are shown on Fig.3. Pressure in the chamber was $1 \cdot 10^{-2}$ Torr.

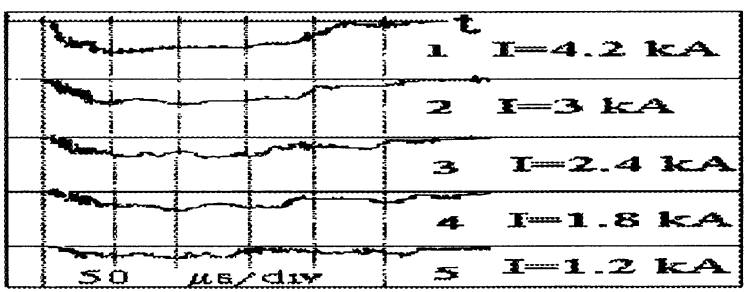

Fig.3

In this series of experiments the cathode of the round form was made from graphite and had a diameter 4cm. Use of stainless steel cathodes of the ring form resulted in worse radial uniformity of plasma, not changing as a whole above-stated dependence. Thus, researches have shown, that the received plasma has good uniformity, reproducibility and on the basic parameters is close to that, which is required for realization of generation experiments.

The experimental stand, a schematic view of which is submitted on Fig.4, was developed allowing to carry out plasma-beam interaction researches not only in smooth plasma-filled waveguide, but also in di-electric and cjrrugated ones, i.e. to look all variants of conventional slow-wave structures in which presence of plasma can result in advantageous effects on emitted power and (or) frequency.

In the experimental stand an opportunity of realization amplifying systems was laid. For coupling of an external signal special section was

constructed with four , turned from each other on 90° waveguide vacuum inputs with a band 8...12 GHz. If necessary they can be replaced by the waveguide with a higher pass band. The input of more low-frequency radiation can be organized by a resonance cavity method, using space between slowing down structure (∅5,2cm) and external chamber (∅10cm), on which system of a magnetic field is installed. Technically simple modification of the output microwave horn allows to realize on the stand klystron type amplifying system, which concept is submitted in paper[5].

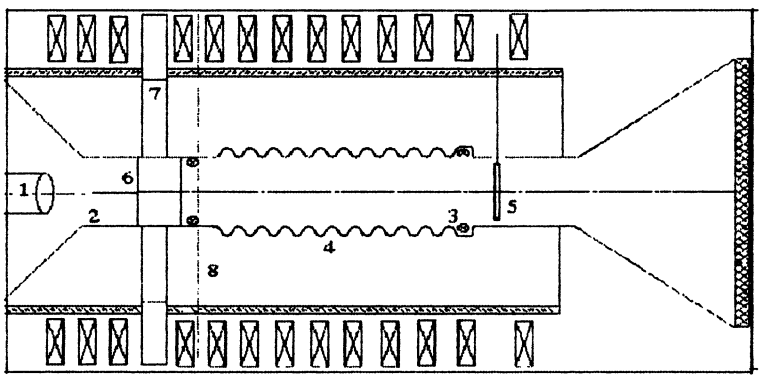

Fig.4. 1- cathode of the accelerator, 2- anodes of the accelerator, 3- Rogovsky belts, 4- slow-wave structure, 5- discharge cathode, 6- copton film, 7- sections for input of external radiation, 8- axes of probing microwave beam

Experimental research

The first experiments on plasma-beam interaction were carried out on plasma-filled corrugated slow-wave to structure, as in the laboratory generation of microwave radiation on corrugated vacuum structures have been already investigated [6].

Similarly to these researches, the experiments were carried out on the accelerator "I-3000". The electron beam energy - 2.4 MeV, beam current 10...20 kA. The beam had the tubular form with average radius 1.75 cm and thickness not exceeding 0.2 cm at the entrance of structure. Slow-wave structure had an average diameter 5.2 cm, corrugation depth - 0.8 cm, its period - 1.5 cm. The general ideology of realization of

experiments was those. Dependence of the generated power level in vacuum regime was investigated on gradual addition in the generator construction the elements necessary for plasma mode regime (copton film, discharge cathode located at the structure output, pressure needed for discharge function). All these factors can result in essential decrease of generation efficiency and even to its failure. Consecutive fulfilment of these steps has revealed, that the set of the listed factors does not influence generation power in vacuum regime. However, it is necessary to note, that the level of capacity was 5...6 times lower, than in paper[6], despite of identity of structure.

After a preliminary stage experiments on plasma-filled structure were carried out. The diameter of the discharge cathode was 4 cm and beam passed inside the plasma column. The pressure did not exceed $2 \cdot 10^{-2}$ Torr. The resistance, limiting discharge current in this series was chosen to be 50 Om and did not vary. On our estimations, the plasma density under such circumstances was about 10^{12} cm^{-3}.

By carrying out a few series of experiments, consisting of 4 ...6 accelerator pulses (on the average, such amount of pulses maintained copton film), appreciable influence of plasma presence on the generation power level was found out. It expressed in decrease of the generated power. Achieving careful coaxialness of the discharge cathode, specifying plasma column in the waveguide, and REB with structure axis it was possible to remove the reasons of the destructive phenomena. The level of generation power thus has increased 2 times in comparison with that received in vacuum experiments. Oscilloscope traces of generated microwaves, registrated in a distant zone, correspondent to the plasma and vacuum regimes of generator operation are shown on Fig. 5,6.

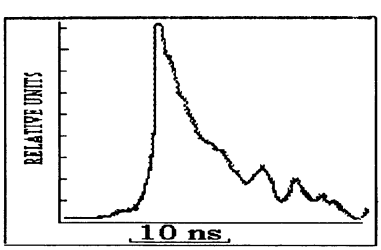

Fig. 5

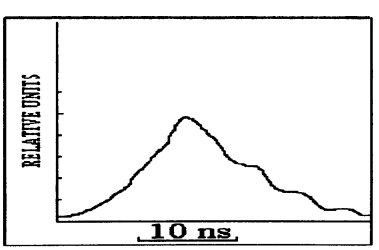

Fig. 6

The generation frequency did not vary and laid in a band 9.5...10 GHz. The signals of Rogovsky belts testify an absence of current indemnification in plasma experiments (indirect confirmation of a correct estimation of plasma density) and provisional equality of a current in both experimental modes.

Numerical modeling

In the given section we represents the results of computer modeling, with use of a code KARAT [7]. A series of numerical experiments was carried out with the generating system parameters which can be realized on the described above stand. Complete system length - 40 cm, plasma column length -35 cm, its diameter - 3.6 cm, waveguide - 5.2 cm. The set parameters of the beam were close to those that could receive on the accelerator "I-3000", electron energy - 1.5 MeV or 2.5 MeV, beam current -15 kA. On Fig. 7-11 results of the most successful numerical experiment are submitted. Plasma density was $2 \cdot 10^{12}$ cm^{-3}, electron energy - 1.5 MeV ($\gamma=4$), beam current - 15 kA.

The received data specifies the fact that for given plasma column length and beam current 1.5 MeV beams are preferable in comparison with beams of higher energy. It is well explained by the dependence of plasma-beam instability growth rate on REB energy.

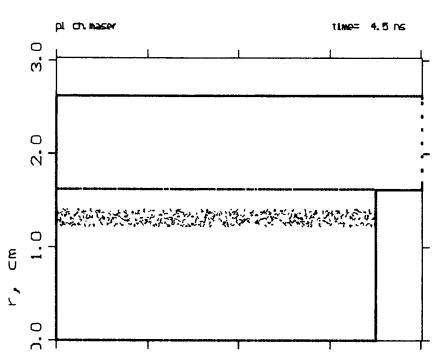

Fig.7. Schematic plot of computer modeling

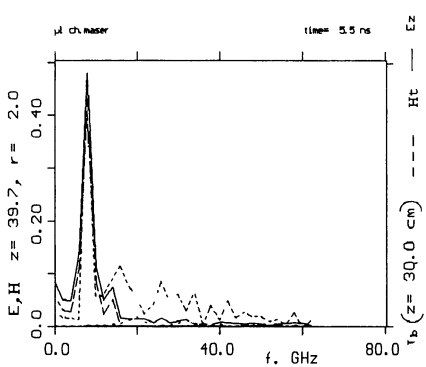

Fig.8. Excited wave components spectrum

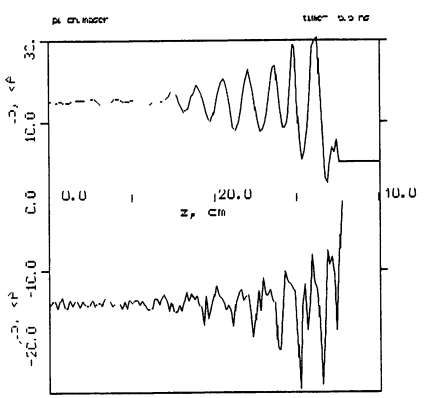

Fig.9. Dependance of plasma Ip and Ib currents on Z, t=5,5 ns

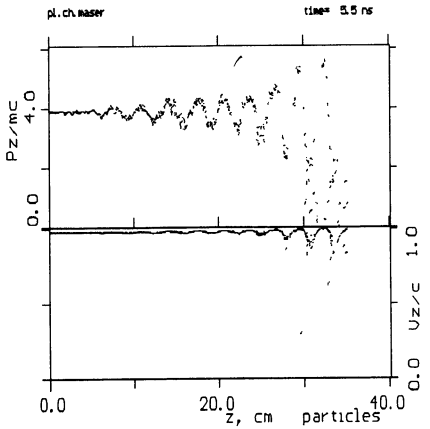

Fig.10. Phase portrait of electron on P_zZ and V_zZ planes, t =5,5ns

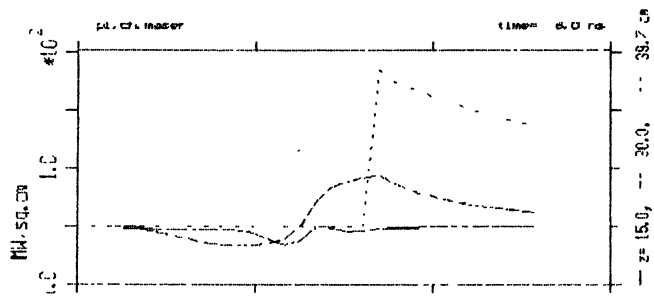

Fig.11. Energy flow density at the resonator output, z = 40 cm, t = 6.0 ns

Conclusion

We submit the first results of researches of microwave generation at the excitation of plasma-filled electrodynamic structures by REB. Performed method of filling of conventional vacuum structures with plasma of given density and experimental stand enable us to investigate generating and amplifying systems. Results of numerical modeling of generating system taking into account real geometry and other parameters of the beam and plasma are represented. The experiments on the interaction of REB with plasma-filled corrugated waveguide was

carried on. It was found out, that on the basic frequency of generation laying in a band 9.5...10 GHz microwave power level has increased about twice in comparison with vacuum variant.

References

1. Bogdankevich L.S. et al., UFN, 1981, **133**, 3
2. Rukhadze A.A. et al., *Physics of High Current Relativistic Electron Beams*, Moscow, "Nauka", 1980
3. Kuzelev M.V., Rukhadze A.A., *Electrodinamics of Dense Electron Beams in Plasma*, Moskow, "Nauka", 1990
4. Kuzelev M.V. et al., ZETF, 1982, **83**, 1358
5. Han S. Uhm, Phys.Fluids B5, 1993, **6**, 1877.
6. Pavlovsky A.I., Bosamykin V.S., Gordeev V.S.,Selemir V.D. et al., *Rel. High-Frequency Electronic, issue* **7**, 1995, 301
7. Tarakanov V.P.,*User's Manual for code Karat,* Berkley Reserch Associate, Inc., Springfield, VA, 1992

THE PLASMA INSTABILITY IN THE POWERFUL BEAM — PLASMA MICROWAVE AMPLIFIERS

Yu.Bliokh, M.Lyubarskii, V.Podobinskii

Institute of Plasma Electronics, National Science Center "KFTI", Kharkov, Ukraine

Introduction

In the non-relativistic microwave plasma electronics the most intensive development get generators and amplifiers with hybrid plasma – filled slow – wave structures [1 - 5,7]. They are vacuum slow – wave structure (SWS) which is filled partially by plasma. In this case the regions of electromagnetic energy propagation and beam – wave interaction are separated. That allows to reduce the microwave's fields in the plasma under large electromagnetic energy flux in all structure. The necessity of fields strength reducing in the plasma is connected with discovered experimentally [6,7] low – frequency instabilities, which arise in plasma if microwave fields exceed some threshold magnitude. In the plasma – beam microwave generators and amplifiers such instabilities determine the natural spectrum line width and spectrum homogeneity in the stochastic generation regimes [8].

Plasma may be examined as a wave decelerating medium. From this point of view beam – plasma instability (BPI) is the same as a charged particles beam instability in the vacuum SWS. However, it is the set of sufficient distinctions in the physics of processes which take place under beam – wave interaction in the plasma and in the vacuum SWS. In this report only such specific electrodynamical properties of hybrid structures will be considered, which has no analogies in the vacuum ones. This peculiarities are connected with that the plasma is the moving medium as opposed to vacuum structures.

The plasma electrodynamical properties — dispersion relations, wave's field topography etc. — are defined by plasma characteristics: density, geometrical form etc.. It is sufficient that these parameters, strictly speaking, depend on magnitude and space distribution of microwave's fields in the plasma. This is the sufficient distinction that is the subject of this work.

One of the reasons, that dictates the connection between plasma parameters and electromagnetic fields excited by beam, is the HF-pressure. This pressure "press out" plasma from regions with increased microwave fields level. Therefore HF-pressure forces may change sufficiently the longitudinal plasma density distribution. In its turn BPI is very sensitive to the plasma homogeneity degree. Therefore plasma density redistribution affects excited waves amplitude and, consequently, changes HF-pressure profile. In such a way the process of BPI requires, strictly speaking, joint description of plasma motion and excited fields.

The self-consistent dynamic of plasma and microwave fields not necessarily leads to some steady – state. Under some conditions the regular or stochastic automodulation regimes may appear. In a great degree it is explained by that plasma density perturbations propagate as slow plasma waves. The last preserve during some time information about plasma perturbations and carry it over space. In such a way the connection between plasma parameters and microwave fields excited by beam has non-local space-time character.

Mathematical model and results of investigations

In this report we shall consider the system in which manifestations of all other effects are minimized. Let us consider the TWT-amplifier with plasma-filled SWS. It will be assumed that the beam current is small and TWT operates in the linear regime. The current smallness means also that region of a resonance wave's phase velocities is narrow and even small variations of dispersion properties leads waves out from resonance with beam. Therefore the plasma density variations, that influence on dispersion characteristics, are small enough and it is possible to describe their dynamics in the linear approximation.

If the system is located in a strong longitudinal magnetic field, then one-dimensional model of a plasma motion is applicable. The plasma density perturbations, which are induced by high-frequency pressure (HFP) of excited microwave fields, may be described by equation:

$$\frac{\partial^2 \Delta x}{\partial t^2} - v_s^2 \frac{\partial^2 \Delta x}{\partial z^2} = -\frac{e^2}{M m \omega^2} \frac{\partial |E|^2}{\partial z}. \qquad (1)$$

Here Δx is displacement of plasma element from its equilibrium position, v_s is the ion-sound velocity, E is the complex-valued amplitude

of a wave with frequency ω. The plasma density is connected with Δx by expression $n \equiv n_0(1+\eta) = n_0(1 - \partial\Delta x/\partial z)$, where n_0 is non-disturbed plasma density.

The Equation (1) describes slow long-scales plasma density variations. The typical space and time scales are defined by ion-sound velocity v_s. In the practically interest cases this velocity is small as compared with wave's phase and group velocities. Besides it is naturally to regard that the time of a microwave field relaxation under BPI is much short than the time of a plasma density profile change. Let us simplify the problem assuming that plasma density variation space scale is large as compared with reciprocal BPI increment $\delta k(n_0)^{-1} \equiv \delta k_0^{-1}$ (the scale of E variation). In this case it is possible to find $E(z)$, using WKB-approximation. It means that instability increment $\delta k(n(z,t))$ is defined by local plasma density. It allows to express the right side of (1) as a function of a density, that makes this equation isolated:

$$\frac{\partial^2 u}{\partial \tau^2} - \frac{\partial^2 u}{\partial \xi^2} = -\sigma \frac{\partial}{\partial \xi} \left\{ e^{2\delta k_0 L[\int_0^\xi \kappa(\xi',\tau)d\xi' - 1]} \right\}. \qquad (2)$$

Here L is plasma longitudinal dimension, $\xi = z/L$, $\tau = tv_s/L$, $u = \Delta x/L$, $\kappa = \delta k(n(\xi',\tau))/\delta k_0$, σ is the ratio of densities of output microwave energy w and thermal plasma energy $n_0 T_e$.

Eq. (2) remains rather complex for analytical investigation, which allows to find connection between system parameters and conditions of low-frequency instability rising. To this end let us consider the case when amplification coefficient, or BPI increment, is large:

$$\delta k_0 L \gg 1. \qquad (3)$$

This condition means that field E reaches its final value on the short part at the end of a system. HFP force is concentrated, in the main, at this final part also. Therefore the model may be simplified once more. It is possible to suppose that all distributed along system HFP force is applied to the right boundary and in plasma this force is absent. In such a way connection between plasma disturbances $u_0 \equiv u(0,\tau)$ and $u_1 \equiv u(1,\tau)$ on the boundaries can be found. Let us adduce, omitting intermediate calculations, the equations obtained

in this way :

$$\alpha u_0(\tau) + \beta \frac{du_0(\tau)}{d\tau} + \alpha u_1(\tau - 1) + \gamma \frac{du_1(\tau - 1)}{d\tau} = F(\tau - 1),$$
$$\alpha u_1(\tau) + \beta \frac{du_1(\tau)}{d\tau} + \alpha u_0(\tau - 1) + \gamma \frac{du_0(\tau - 1)}{d\tau} = F(\tau). \quad (4)$$

Here F is the whole HFP force that acts on the plasma column:

$$F(\tau) \sim \sigma \exp\left\{2\delta k_0 L \left(\int_0^1 \kappa[\eta(\xi,\tau)](1 - \eta(\xi,\tau))d\xi - 1\right)\right\},$$

α, β and γ are some coefficients that describe plasma boundary conditions. The function η is a solution of homogeneous wave equation and can be represented in the form of linear combination of u_0, u_1 and its time derivatives that are calculated in retarded times $\tau - \xi$, $\tau + \xi - 1$ etc..

Instead of simplifications which were made the equations (4) have preserved the main property of initial problem: non-local connection between functions that describe it. The fact that force is removed from volume to its boundaries allows to express the space non-locality through time one and pass from partial differential equation to only two integro-differential equations with retarded argument.

The results of analytical and numerical investigations of equations (4) are presented briefly below. The automodulation of plasma density and output amplifier signal appear if the output electromagnetic energy density w exceeds some threshold w_* value:

$$w_* \simeq \frac{n_0 T_e}{A k_0 L}\left(1 + \frac{\delta k_0^2 L}{A k_0}\right). \quad (5)$$

Here $A \sim \frac{\omega_p \partial D/\partial \omega_p}{\omega \partial D/\partial \omega}$, $D(\omega, k; \omega_p) = 0$ is the dispersion equation of waves in hybrid system, k_0 is the resonance wave number. The expression (5) has qualitative character and factors of order unit are omitted here.

Functional dependence of w_* on parameters was verified numerically using both Eq. (2) and Eq. (4). These verifications are in good agreement one with another and with analytical expression (5). Non-linear stage of plasma instability was investigated numerically

using both these equations also. The results of calculations have shown that if the microwave power density w weakly exceeds threshold value w_*, then regular periodic automodulation of plasma density and output amplifier signal arise. Strong dependence of BPI increment on plasma density leads to deep output signal automodulation under weak plasma density variations. Further power w increasing leads to stochastic automodulation origin. If the boundary reflection coefficient of ion-sound waves is small, then plasma density variations has form of waves, that propagate in the opposite to beam direction and practically do not change their shape. It means that distributed along system HFP force acts, on the whole, on the short final length of plasma column, as it was assumed under transformation Eq. (2) to Eqs. (4). The example of such behavior of a system under consideration is represented on Fig. 1.

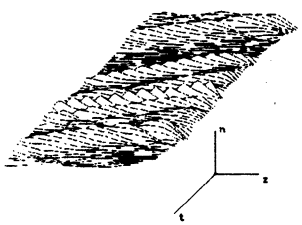

Figure 1: Stochastical space – time dynamic of the plasma density

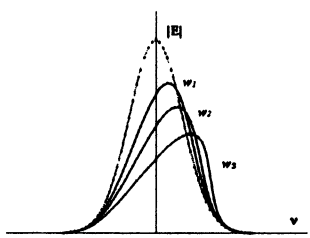

Figure 2: Amplifier AFC, $w_1 < w_2 < w_3$. Dotted line – AFC for homogeneous plasma.

The properties of the amplifier with hybrid SWS beginto change themselves if $w < w_*$ also. Nonhomogeneity of plasma density in the stationary state leads to amplification coefficient decreasing and strong distortion of amplifier amplitude – frequency characteristic (AFC) (See Fig. 2).

Conclusion

The magnitude of threshold power w_* depends on used SWS. Let us compare the set of amplifiers that are intended for operating in

the same frequency band and used electron beams with similar parameters. For such devices the differences in the w_* magnitudes are connected, in the main, with value of parameter A that determined the "sensitivity" of hybrid structure electrodynamical properties to plasma density variation. It is natural that the most "sensitive" structure is the plasma wave-guide, for which $A \sim 1$. If as a SWS used hybrid one, small part of which is filled by plasma (for example, the set of inductive connected resonators [1 - 3]), then the parameter A magnitude may be evaluated as $A \sim \omega_p^2/\omega^2 \cdot S_p/S_w$, where S_i are the cross-sections of plasma and wave-guide. The sensitivity of such structure is much less than for plasma wave-guide. It should be pointed that plasma volume decreasing leads to device efficiency drop. Therefore, in order to choice the optimal structure parameters it is necessary to take into account both low-frequency plasma instability and deterioration of energetic characteristics of microwave device when the plasma role in the synchronous wave forming is reduced.

This work is supported by Sciense and Technology Center of Ukraine (Grant No. 277).

References

1. Yu.Bliokh, Ya.Fainberg, M.Lyubarskii et.al.,Ukr Dok.Ak.Nauk, (1990), No.11, P.55

2. Yu.Bliokh, Ya.Fainberg, M.Lyubarskii et.al.,Pl.Phys.Rep., (1994), V.20, No.9, P.681.

3. Yu.Bliokh, Ya.Fainberg, I.Onistchenko et.al., 10th Int.Conf. High Power Beams, 1994,V.1,P.260

4. A.Antonov, Ya.Fainberg, Yu.Bliokh, Pl.Phys.Rep., (1994), V.20, No. 9, P.777

5. M.Zav'jalov, L.Mitin, V.Perevodtchikov et al., Pl.Phys.Rep. (1994), V.20, No. 7, P.

6. E.Kornilov, O.Kovpik, A.Krivorutchko et al., JETPf Let., (1972), V.15, P.501

7. Yu.Bliokh, Ya.Fainberg, E.Kornilov L.Mitin, Pl.Phys.Rep., (1994), V.20, No.9, P.767

8. Yu.Bliokh, Ya.Fainberg, M.Lyubarskii et al., Pl.Phys.Rep., (1994), V.20, No.8, P.675.

THE RESULTS OF 7 GHz PULSE MAGNICON INVESTIGATION[1]

G.N. Ostreiko, E.V. Kozyrev, I.G. Makarov, O.A. Nezhevenko, B.Z. Persov, G.V. Serdobintsev, S.V. Shchelkunoff, V.V. Tarnetsky, V.P. Yakovlev, and I.A. Zapryagaev

Budker Institute of Nuclear Physics,
Novosibirsk, Russia

Introduction

The magnicon [1,2,3,4] belongs to a new class of microwave amplifiers – deflection-modulated devices. The first magnicon was built and tested in the 1980's in INP [2] During the first tests the magnicon showed efficiency exceeding that of klystrons achieved in the course of over 50 years of its development.

This paper presents the results of testing the advanced version of magnicon, which was described in detail at previous International Workshop (RF94) [5] and developed in INP as a prototype of the microwave power source for linear colliders.

A schematic diagram of the device is shown in Fig.1. The magnicon consists of the following basic units: an electron source, RF system, magnetic system and a collector. RF system consists of two parts: the deflecting system for beam modulation and the output cavity for conversion of the beam energy into the RF energy. A magnetic system provides a long-term interaction between beam electrons and RF fields in the cavities as well as beam focusing.

The tube is an amplifier operating at frequency of 7 GHz in frequency-doubling mode .

On all the deflection system cavities the circularly-polarized TM_{110} mode (Fig.1) oscillations are excited. The drive cavity 3 is excited by the drive generator. The passive (gain) cavities 4 and 5 are excited by a deflected beam. The penultimate cavity 5 consists of two coupled cavities in which the beam excites the opposite-phase (π-mode) oscillations, thereby enabling

[1] The research described in this publication was made possible in part by grant NQH000 from the International Science Foundation.

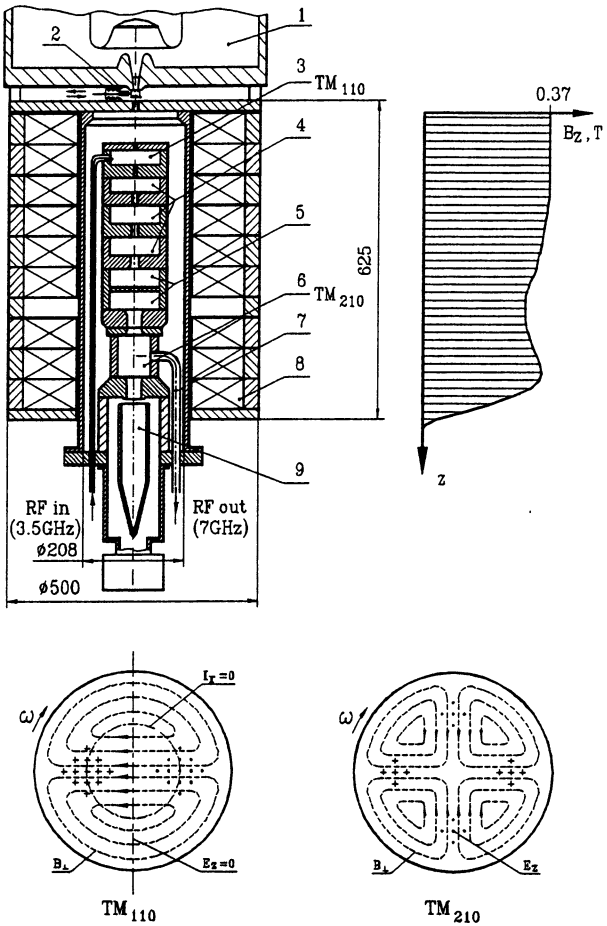

Figure 1: Schematic layout of the magnicon: 1 — electron source; 2 — vacuum valve; 3 — drive cavity; 4 — gain cavities; 5 — penultimate cavity; 6 — output cavity; 7 — waveguide (×2); 8 — solenoid; 9 — collector

the realization of the deflection angle "summing" mode of operation [1]. This enables one to attain a deflection angle $\alpha>50^{\circ}$ (which is necessary for reaching high efficiency) at a cavity surface RF field $E\approx 250$ kV/cm. In the output cavity 6 the modulated beam excites the TM_{210} mode (Fig.1) with a frequency two times larger than the drive frequency. All the cavities are located inside the solenoid 8, which produces a longitudinal magnetic field. For an effective beam deflection and interaction in the output cavity it is necessary for the cyclotron frequency of electron rotation in the solenoid field to be 1.5–2 times higher than the drive frequency [2,4,7]. The output cavity is more than 8 cm long that provides $E\approx 250$ kV/cm.

The design parameters of this magnicon version are listed below:

Operating frequency	7 GHz	Drive frequency	3.5 GHz
Output power	55 MW	Gain	53 dB
Pulse duration	1.5 μs	Beam voltage	420 kV
Repetition rate	5 pps	Beam current	240 A
Efficiency	56 %		

The results of the beam behavior simulations in the process of deflection and deceleration are shown in Fig.2.

The design is based on the detailed preliminary numerical simulations [8]. The physical model considers a beam of finite transverse size, real space distribution of DC magnetic field and real RF fields of the cavities. Those fields were calculated by SAM and SuperLANS2 codes [9,10]. We do not take into account space charge effects and finite beam emittance. The numerical model is based on macro particle methods. We have created the codes for both steady state and time dependent simulations. A self-consistent solution during the steady state simulation is obtained by choice of the cavity RF field amplitudes and phases to achieve an overall power balance. Steady state simulations were used for magnicon optimizing and stability analysis. Time dependent code has been applied for transient process investigations.

Experimental Studies

The problems and requirements to the magnicon elements revealed and formed during the previous magnicon versions investigation [4,5,6,11,12] were took into account in present design.

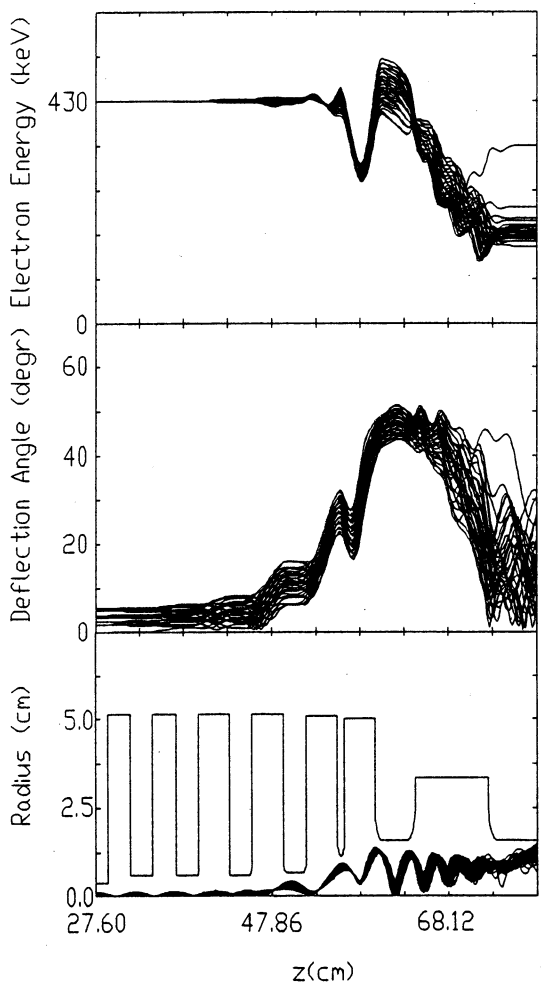

Figure 2: Simulation of the magnicon for a 3 mm diameter beam

1. At the present time, the initial tests of the latest magnicon version (Fig.1) have been carried out. The parameters obtained are listed below:

Frequency	7.006 GHz	Drive frequency	3.503 GHz
Power	30 MW	Gain	55 dB
Pulse width	0.7 μs	Beam voltage	401 kV
Repetition rate	3 pps	Beam current	210 A
Efficiency	35 %		

The oscillograms presented in Fig.3 are: beam voltage (U), signal from the penultimate cavity (PC4) and output signal (OUT1). The output signal (peak power) calibration was carried out by the calorimetric measurements of average RF power.

The magnicon cavities consist of separated copper parts connected with one another by indium seals. This design allows to replace the RF system parts operatively but does not allow to bake-out the cavities up to high temperatures. This leads to long RF condition times for the cavities.

In the described experimental studies during the deflecting cavities conditioning the self-excitation was observed at different frequencies. After dismantling of the tube autographs of electric discharges were found almost in all the cavities. The discharges autographs indicate the self-excitation of various modes (symmetric and non-symmetric). However, these self-excitations disappeared during conditioning and were not observed at the operating range of drive signals.

The main problems were concerned with conditioning of the output cavity, waveguides and loads, that are a single vacuum chamber (there are no ceramic windows). During conditioning self-excitation in the output cavity appeared and after a time disappeared at various frequencies (11.8 GHz, 5.92 GHz and 12.04 GHz, one after another). The first two frequencies disappeared during conditioning, however the self-excitation at the frequency 12.04 GHz is still here and limits the pulse width at a power over 20 MW (at lower power the output signal duration is 1.5 μs). Results of simulation and measurements at atmosphere proved the presence of a resonance at this frequency. Oscillations present also in the output cavity and penultimate cavity. The oscillation mode has a field distribution with a quadrupole nature. The mechanism of this mode exciting is under investigation now.

2. The main causes of decreasing efficiency with respect to the designed value are a thicker beam (than the calculated one) and the non-optimal loaded Q-factor.

In the course of work on the 7 GHz magnicon we examined 7 cathodes. Depending on the cathode quality and gun assembling the beam diameter varies somewhat, however the average d_{max}=2.8 mm. However, in the present magnicon version the magnetic field of solenoid (8, Fig.1) is 0.37 T rather than 0.45 T, which is the projected value for operating gun [6].

This magnetic field decreasing by 20 % leads to the beam diameter increasing up to d_{max}=4 mm. The calculated efficiency value versus beam diameter d_{max} is shown in Fig.4. It is clear from Fig.4, that at d_{max}=4 mm efficiency cannot exceed 42 % and for the projected value of 56 % it is necessary to have the beam with $d_{max} \approx 3$ mm. Moreover, the coupling between the output cavity and load was equal to 200 and was have been chosen optimal for the efficiency of 56 %. In the case of the beam with a large cross-size the efficiency decreases and it takes a higher loaded Q-factor value to obtain a maximal output power.

Thus the measured efficiency is 80 % of the calculated value for the real beam available now.

To improve the situation a new focusing electrode for the gun has been developed, and for the best matching the beam into the solenoid magnetic field the distance between the gun and solenoid was extended. This work is done now and experiments proved the validity of this decision. The measured maximal beam cross-size at the accompanying magnetic field of 0.37 T is less than 3 mm.

3. Another cause leading to decreasing efficiency is the RF fields distribution distortion in the output cavity due to presence of coupling apertures with waveguides. The field maps (2D simulation [10]) for orthogonal TM_{210} modes, superposition of which defines the RF fields distribution in output cavity, are presented in Fig.5. For compensation of the coupling apertures with the waveguides 1 effect there are two protrusions 2 in the present design output cavity, however, their effect is inadequate. One can see that field distribution of these two modes differs sufficiently. The loaded Q-factors of these modes also somewhat differ (180 and 220). As a result the interaction with the beam is found to be irregular along the azimuth that

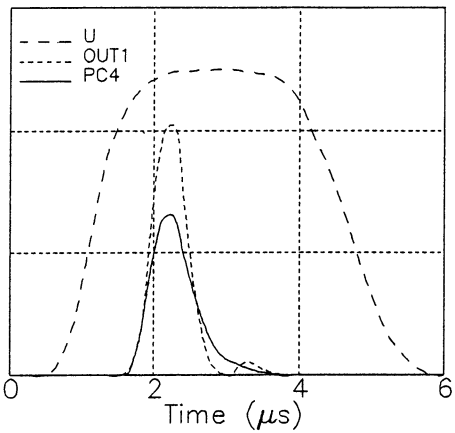

Figure 3: The oscillograms

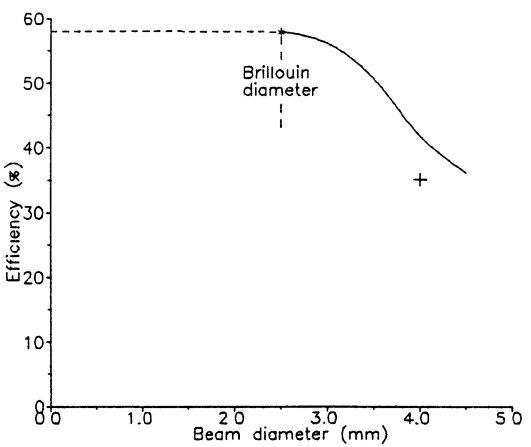

Figure 4: The efficiency versus the beam diameter; the experimental point is marked with +

leads to the decreasing efficiency.

This problem can be solved by increasing the number of protrusions. The improved cavity version is being developed now. We also think that improved cavity design can better the situation with the parasitic modes self-excitation firstly through decreasing the coupling between the beam and non-symmetric parasitic modes.

4. The measured dependence between the output power and drive signal (Fig.6) is in quite good agreement with the simulation results.

It is traditional (beginning with gyrocon) for the oscillations with circular polarization obtaining that the deflection cavity is driven by two signals of equal amplitude through two power inputs separated in azimuth by 90° [1]. These signals must also be shifted in phase by 90°. In magnicon the beam is magnetized and its gyrotropic properties lead to the circular deflection "self-stabilization" effect, i.e. if oscillations with an elliptical polarization are excited in the cavity, the ellipticity is reduced in the presence of the beam [1,2]. The experimental tests have verified that in the present magnicon version this wholesome effect shows itself so strongly that one can drive the deflection cavity by one signal (like a klystron) without a loss in output power and efficiency.

Summary

In the course of 7 GHz frequency-doubling magnicon amplifier investigation a peak power of 30 MW and efficiency of 35 % have been obtained in a pulse of 0.7 μs width. The drive frequency is 3.5 GHz and gain is 55 dB. This performance establishes the magnicon as an attractive candidate for linear collider applications.

During investigations many effects interfering with normal device operating were revealed. They are: self-excitation of the penultimate cavity (TM_{010} and TM_{110} modes), harmonics generation, instability in penultimate and output cavities [5,11,12].

After eliminating these problems the device behavior is in good agreement with theoretical predictions and simulation results. The main causes of the difference between obtained efficiency and design value of 56 % are the relatively thick beam (diameter is 4 mm instead of 3 mm) and RF fields non-symmetry in the output cavity. We are going to eliminate these drawbacks and obtain parameters approaching the designed ones in the nearest future.

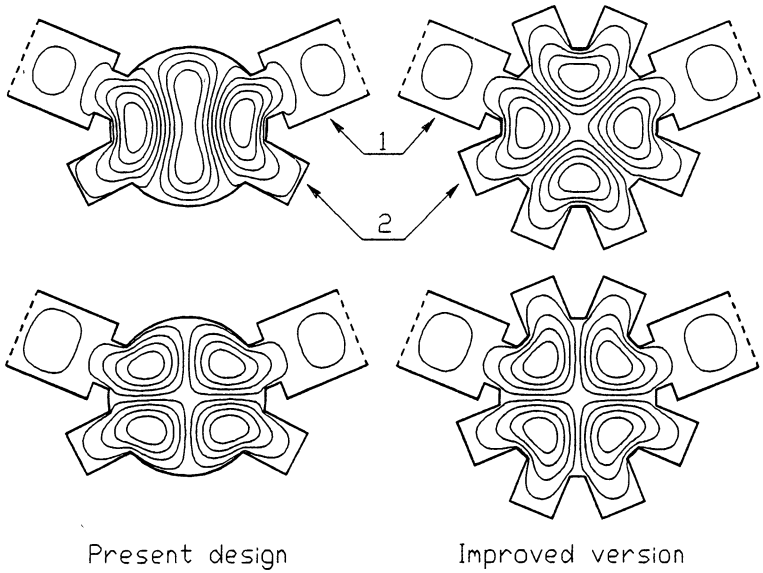

Figure 5: Field maps in the output cavity: 1 — waveguides, 2 — protrusions

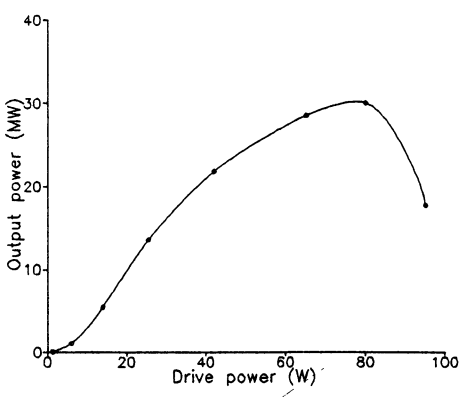

Figure 6: The output power versus drive signal

References

1. O.A. Nezhevenko, "Gyrocons and Magnicons: Microwave Generators with Circular Deflection of the Electron Beam," in *IEEE Trans. of Plasma Science* vol. 22, No. 5, October 1994, pp. 756–772.

2. M.M. Karliner et al., "The Magnicon – an Advanced Version of the Gyrocon," NIM-A, vol. A 269, No. 3, 1988, pp. 459–473.

3. V.E. Akimov et al., "High Power X-Band Pulse Magnicon," in *Proc. EPAC 90*, Nice, 1990, vol. 1, pp. 1000-1002, World Scientific, 1992.

4. O.A. Nezhevenko, "The Magnicon: a New Power Source for Accelerators," in *Proc. IEEE Part. Accel. Conf.*, San Francisco, 1991, vol. 5, pp. 2933–2942.

5. O.Nezhevenko et al., "7 GHz Pulsed Magnicon," in *AIP Conf. Proc. 337 (RF94 Workshop)*, Montauk, NY, 1994, pp. 174–183.

6. Y.V. Baryshev et al., "A 100 MW Electron Source with Extremely High Beam Area Compression," NIM-A, vol. A 340, 1994, pp. 241–258.

7. M.M. Karliner et al., "An Approximate Theory of the Magnicon," Preprint INP 88–66, Novosibirsk, 1988 (in Russian).

8. V. Yakovlev et al., "Numerical Simulation of Magnicon Amplifier," in *Proc. Part. Accel. Conf.*, Dallas, 1995, (to be published).

9. B. Fomel, M. Tiunov and V. Yakovlev, "Computer-Aided Electron Gun Design," in *Proc. XIII Int. Conf. on High-Energy Acc.*, vol. 1, 1987, pp. 353–355.

10. D. Myakishev and V. Yakovlev, "The New Possibilities of SuperLANS Code," in *Proc. Part. Accel. Conf.*, Dallas, 1995, (to be published).

11. O.A. Nezhevenko et al., "First Test of the X-Band Pulsed Magnicon," in *Proc. IEEE Part. Acc. Conf.*, Piscataway, NJ: IEEE, vol. 4, 1993, pp. 2650–2652.

12. I. Zapryagaev et al., "Status of the X-Band Pulsed Magnicon," in *Proc. Europ. Part. Acc. Conf.*, vol. 3, 1994, pp. 1927–1929.

VIRCATOR WITH A PLASMA ANODE

A.L. Babkin, V.I. Chelpanov, A.E. Dubinov,
V.G. Kornilov, V.D.Selemir, A.V.Sudovtsov, V.S. Zhdanov

RFNC - VNIIEF, Sarov, Russia

Since 1994 the experimental investigations, aimed at the rising of microwave radiation of generators, based on vircator effect, by changing metal anodes with plasma layer, are carried out in VNIIEF. First experiments with plasma anode diodes [1] is showed the possibility of high-voltage (up to 350 kV) high-current (up to tens kiloamperes) electron beam generation in microsecond duration range. However, it is not clear, if vircator regime of generation is possible with plasma anode, what are its properties and if numerous plasma instabilities suppress it. This work is devoted to the solution of this problems.

Computer simulation

Authors carried out the computer simulation of vircator with plasma anode. The passage of applied programs on the basis of 2.5-dimensional "KARAT" PIC-code, created by V.P.Tarakanov and described in [2] was used.

Model of region geometry: diameter of plane cathode - 70 mm, diode gap - 30 mm, plasma layer depth - 20 mm, diameter of diode anode and tube drift - 180 mm. The plasma concentration in simulation was equal to $7 \cdot 10^{11}$ cm^{-3}, ion mass corresponded to carbon ions. It was assumed, that the voltage of 300 kV with the front in the shape of step was applied to the diode gap. In this case the diode current was 35 kA.

The evolution of phase portrait of all particle group is shown on fig.1, and it is clear, that the virtual cathode, vibration of which could be the source of powerful microwave radiation, is formed behind the plasma layer. The flight current here has oscillating component.

Also the dynamic of plasma ion component is very interesting: part of ions is captured by virtual cathode to collective motion. The analysis of fig.1 allows define the law of motion of the virtual cathode motion, as whole, as together with it the law of motion of front of captured ion beam. The diagram, with shows the laws of motions of

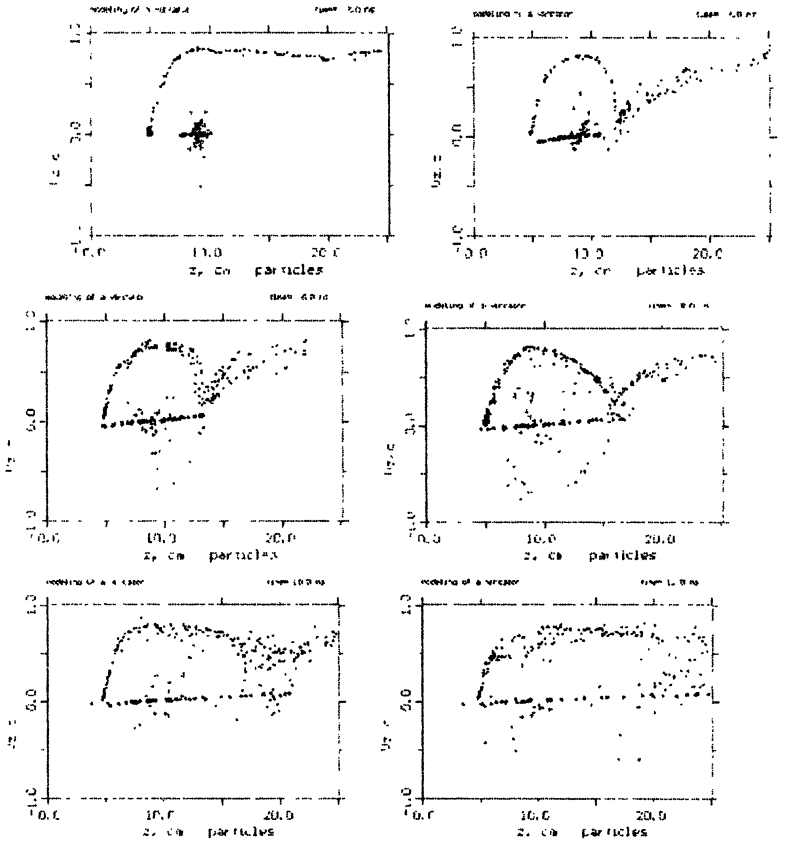

Fig.1. Phase portraits of particles collective (• - beam's electrons, + - plasma's electrons, * - plasma's ions):

a) t = 2 ns; b) t = 4 ns; c) t = 6 ns;

d) t = 8 ns; e) t = 10 ns; f) t = 12 ns.

virtual cathode and ion beam front is shown on fig.2. It is clear, that both motions happen approximately uniformly, however the front of ion beam outruns the virtual cathode. The similar results was obtained in [3] on one-dimensional numerical model of electron injection with ultra-ultimate current into moderate density gas. Besides, the analysis of evolution of spatial distribution of ions testifies to the effective focusing of captured ion beam.

Hence, the results of simulation of vircator type with plasma anode tell about the possibility of its use as for microwave radiation powerful pulses generation, as for collective acceleration of positive ions.

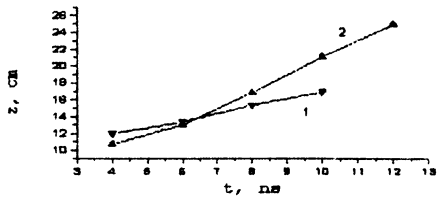

Fig.2. The diagrams of a movement laws: 1 - virtual cathode, 2 - front of ion beam.

Experimental investigation

"KOVCHEG" facility (see fig.3) consists of capacity storage 1 on the basis of four Marx generators of total capacity 1.28 μF, coaxial transferring line 2 with inductance up to 1 μH, diode section 3, plasma anode unit 4, drift tube 5, with radiation turn mesh 6 and output window 11. At the accelerating diode plasma layer substituted flat anode, and electron beam is injected to the drift chamber. The flange, positioned between accelerator output and drift pipe was used as a body of plasma anode. Radial channels - external electrodes of coaxial plasma sources , were drilled in this flange. Gas is fed with the help of high-speed electrodynamics valve, and through the channels at the second electrode goes to injector discharge gap. The formation of disk-shaped plasma structure is made with the help of two ring-shaped plates of special profile. Double Langmuir probes were used to measure the plasma density distribution in plasma jets. Maximum plasma density, which corresponds to the current of saturation, at subaxial region on the distance of 115 mm from the nozzle was $6 \cdot 10^{12}$ cm^{-3}. . Plasma density on the distance of 15 mm from the center on the direction to the small axis is 15 times less, than at the centre. The jet speed on the axis of coaxial plasma source in this conditions is equal $1.2 \cdot 10^{6}$ cm/s. Central hole of plasma anode unit with diameter 160 mm limits the transversal dimension of accelerator anode plasma part. At the described series of experiments there were three symmetrically positioned injectors. The current on the transmission line input I_a, diode current Id, "vircator" current I_v, overflight current I_{out} on the input into radiation turn unit were monitoring by Rogovsky belt

(7,8,9,10) correspondingly. The signal recording was performed in KAMAK standard with the discrete 25 ns.

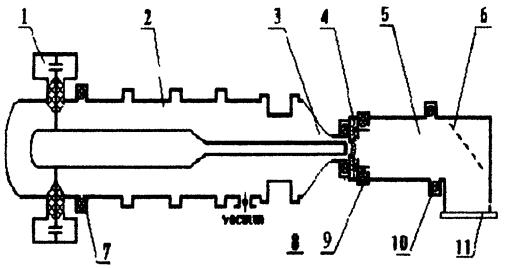

Fig.3. The "KOVCHEG" scheme.

The delay between triggering of injector battery and Marx generators, fed the electron diode, influence on the character of device operation. Experiments with diode gap of 80 mm are discussed below. Nitrogen was as a plasma-forming gas in injectors. Long (> 2 μs) current impulse is generated. With small delays (11...13 μs). In this regime the current Iv appears with small delay relatively to I_a and I_d. With big delays (≥20 μs) on the initial stages, the accelerator works in the regime of plasma-filled diode with the subsequent disconnection and generation of high-voltage (up to 500...700 kV) electron beam.

The instability of electron current generation is found out at the intermediate delays. Current Iv is similarly modulated in the area of x-ray signal modulation. Nonstationary work of the diode with plasma anode at high speeds of accelerating voltage rising is found out in the work [4] for conditions of electron beams generation with energy up to 40 keV and current up to 2 kA. In our experiments nonstationarity was not connected with speed of accelerating voltage change. Optimum delay, at which the largest microwave radiated, was ~ 16 μs.

The signals chronograms at generation experiment with diode gap 80 mm are presented on the fig.4. The behaviour of current oscillograms in the vircator with plasma anode is similar to, investigated by us, regime of vacuum diode with anode mesh, i.e. physical processes in the diode with the metal mesh are identical. However the duration of current impulse of accelerated electrons in the diode with plasma anode is more, then in usual diode with mesh anode. So, the influence of anode plasma is the first case is essentially reduced. It is clear from the fig.4, that the formation of virtual cathode in the drift tube and returning electron

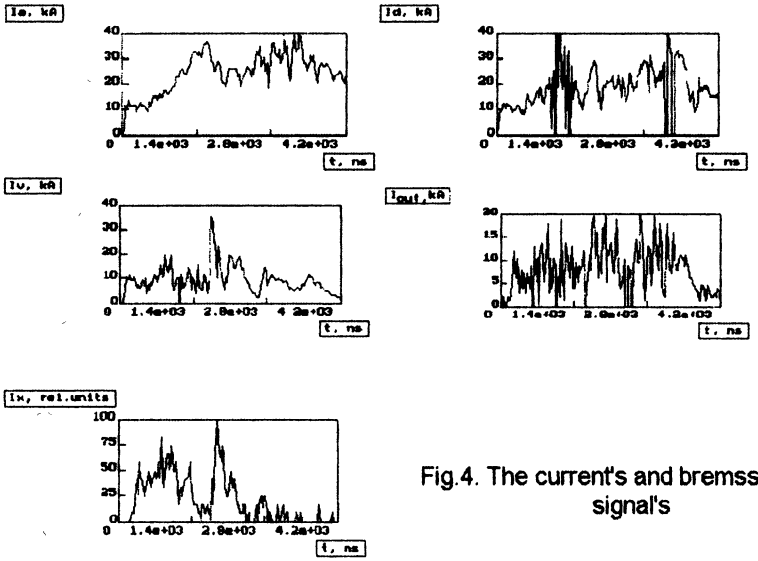

Fig.4. The current's and bremsstrahlung signal's

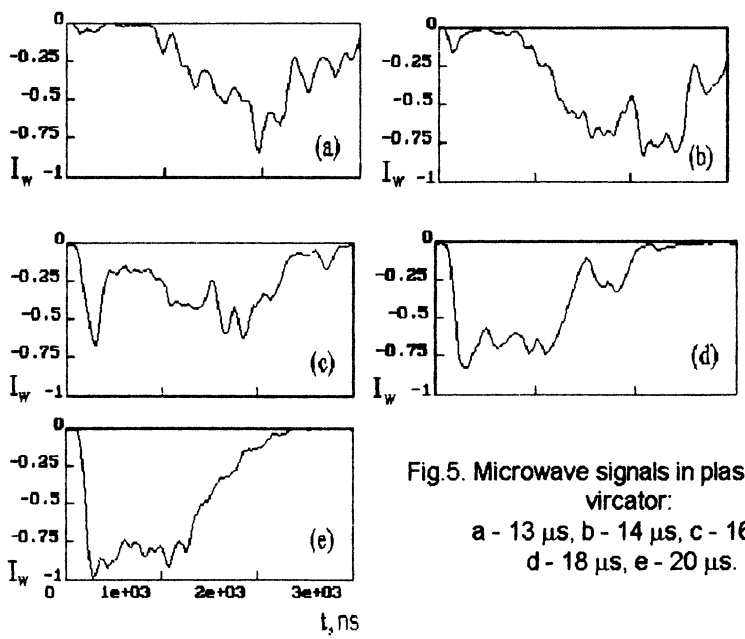

Fig.5. Microwave signals in plasma anode vircator:
a - 13 μs, b - 14 μs, c - 16 μs,
d - 18 μs, e - 20 μs.

current leads to the appearance of regions with stabilised impedance on the current chronograms. The value of current I_{out} is move than 10 times exceeds the limiting vacuum current. It is possible to explain by the compensation of electron charge of overflight current by plasma ions, accelerated in virtual diode. At that the differential signal of electron and ion current is monitored. The generation of accelerated ion beam from the anode plasma by the relativistic electron flux, was investigated in [5].

The chronograms of microwave signals, obtained with the different delays of Marx generator triggering relatively to the triggering of injector batteries, are presented on the fig.5. It is clear, that at the delays ≤ 14 μs the microwave radiation appears with the delay up to 800 ns relatively to current signals (the zero time of chronograms is corresponds to the beginning of current flow in diode). The increasing of the delay leads to the appearance of microwave generation on the initial current region. At delay more than 18 μs the microwave radiation ends for the time <2 μs from the beginning of current flow. The maximum duration of microwave radiation was not less than 2.5 μs.

At investigated regimes with the use of other plasma-forming gases the general character of the device work was similar to described above. The decreasing of diode gap leads the necessity to decrease the delay of accelerating voltage triggering.

The work performed according to the project RFFI 96-02-17047a.

References

1. Babkin A.L., Chelpanov V.I., Dubinov A.E. et al. Int. Symp. "BEAMS TECHNOLOGIES (BT'95)", Dubna, Febr. 28 - March 4, 1995, p. 8.
2. Tarakanov V.P. User's manual for code Karat, Berkley Research Associate, Inc., Springfield, VA, 1992.
3. Khodataev K.V., Shakhanova E.V. Preprint of M.V.Keldysh Inst. Appl. Math. USSR Acad. of Sci. 1986, No. 79.
4. Ozur G.E., Nazarov D.S., Proskurovsky D.I. 1st International Symposium Beam Technologies (BT`95). Dubna, Russia.
5. M.Reiser. IEEE Trans. on Nucl. Sci. 1981, **NS-28**, 3, p. 3555.

CONVERSION OF "PARAXIAL" WAVEGUIDE MODE TO GAUSSIAN BEAM

S.V.Kuzikov, M.I.Petelin

Institute of Applied Physics, Russian Academy of Sciences, Nizhny Novgorod, Russia

1. Introduction

Some microwave generators produce at their output high-order modes, the cut-off frequency of which is much below the carrier frequency. For example, this may happen in a high-power electron device having a collector space much broader than an interaction space.

Such a kind of modes is composed of paraxial rays which propagate at a small angle relative to the waveguide (this angle is called the Brillouin angle). Thus, the distance between two subsequent ray reflections from the waveguide wall, called the Brillouin length, must be large:

$$L_B = 2R \cdot \sqrt{1-(\frac{m}{\mu})^2} \cdot \mathrm{ctg}(\beta), \qquad (1)$$

where β is Brillouin angle, L_B is Brillouin length, R is radius of waveguide, m is azimuthal index of mode, and μ is root of an equation $J_m'(\mu)=0$. So, any converter based on conversion by means of a waveguide wall deformation [1,2,3] must be the longer, the smaller is Brillouin angle.

Nevertheless, a small parameter (Brillouin angle) for the given problem may play positive role, if one uses a mirror installed across the waveguide [4]. This way allows, in principle, to transform the fields using the length less than one Brillouin length.

2. Quasi-optical wave converters based on conical reflectors

The main idea is based on two-stage conversion. In order to obtain a Gaussian beam for a case of the circular waveguide it is necessary to convert initial mode into a wave with enough large Brillouin angle, using a transverse mirror in the form of a conducting axis-symmetrical cone. Then the reached wave has to be converted into a Gaussian beam by means of any traditional method.

Let us introduce one of possible schemes (Fig. 1) which is based

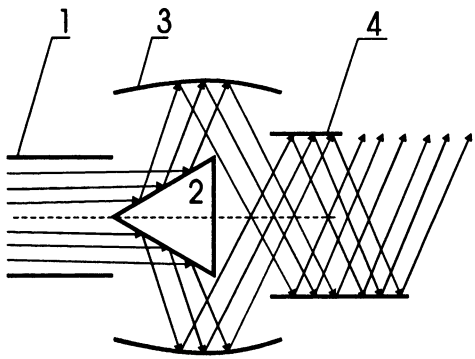

Fig. 1. Principal scheme of the converter based on the conical reflector: 1 - input circular waveguide, 2 - reflecting cone, 3 - barrel, 4 - conventional vizor converter

on this idea. The cone (2) changes the angle of initial ray propagation essentially. The barrel (3) returns a wave flow to the next waveguide (4) compensating the field divergence caused by flow propagation from the initial waveguide to the next waveguide. It is assumed that the last waveguide has at the output a converter based on a vizor with a quasi-parabolic mirror [2]. In this case the mentioned converter is efficient because it operates with the wave having acceptable Brillouin angle. At the output of the converter the field structure is to consist of a beam of parallel rays which is close to the Gaussian beam. For the presented scheme the Gaussian content of the beam power may reach up to 80%.

In order to increase the efficiency it is necessary to prepare inside the required converter a Gaussian-like amplitude field structure which will be radiated to the free space. For these goals it is certainly natural to apply the dimpled converter [3] behind the cone and the barrel. This converter consists of an alternating set of focusing and defocusing deformations. It bunches a field along both coordinates (longitudinal and azimuthal ones) providing at the output a quasi-Gaussian amplitude distribution. Therefore, the proposing converter should be assembled of three parts, as it is shown in Figs. 2-3. The first axis-symmetrical part is the cone with the barrel, the second asymmetrical part is the dimpled converter, and the last part is a quasi-parabolic mirror which compensates radial divergence of the final Gaussian beam.

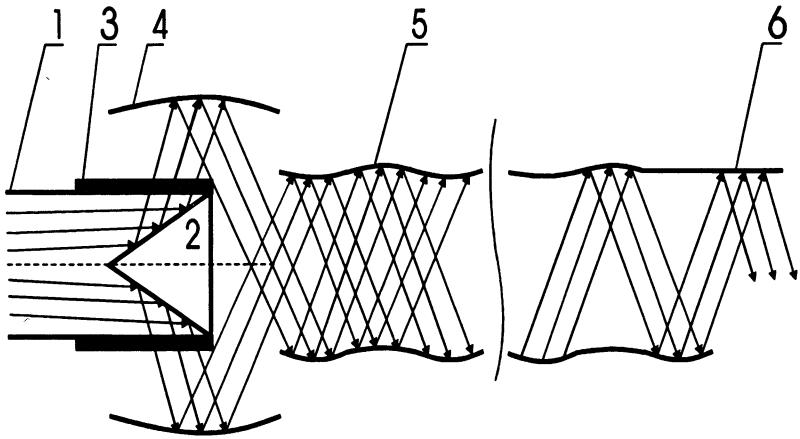

Fig. 2. Principal scheme of the converter based on a conical reflector and a dimpled converter: 1 - input circular waveguide, 2 - reflecting cone, 3 - resonant window, 4 - barrel, 5 - dimpled converter, 6 - quasi-parabolic mirror

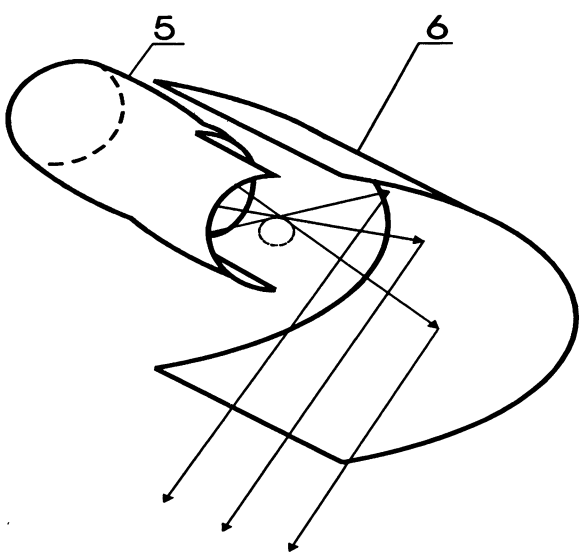

Fig. 3. Principle of operation of the quasi-parabolic mirror

The described principle has a sufficiently common character and, probably, it may be applied for a wide class of modes with electric and magnetic fields closed to zero at the top of the cone to avoid scattering losses.

In this point of view, among the most convenient modes are TE_{0n} waves. First of all, they satisfy the mentioned requirement. Besides, these waves are scattered weakly into modes of the TM type providing a low level of cross-polarization at the output of the converter. So, let us consider some examples of converters which operate with TE_{0n} modes.

3. Converters of the TE_{01} mode to Gaussian beams

The lowest TE_{0n} mode has one unique property in comparison with other modes with n>1. In the simplest scheme (Fig.1) a given mode, which has transverse distribution of the electric field described by Bessel function $J_1(\mu r)$, after the barrel excites a field structure which has been bunched already along the longitudinal coordinate. The TE_{01} wave is well matched with the eigenmode of axisymmetrically corrugated waveguide (see Fig. 4). The mentioned eigenmode consisting of TE_{0n} modes of the cylindrical waveguide has a quasi-Gaussian field structure

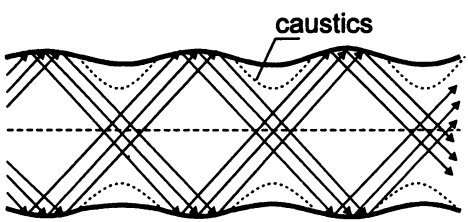

Fig.4: Field structure of corrugated waveguide eigenmode which is excited by TE_{01} mode behind the cone

at concave sections of the corrugated waveguide. Efficiency of power excitation for this mode may reach 97%. Therefore, to convert the TE_{01} mode it is necessary to bunch a field in the second part of the converter (dimpled converter) along its azimuth only. The bunching along the longitudinal coordinate must be kept by means of constant corrugation for which the given field structure is actually an eigenwave.

The calculations were performed by the method of coupled modes [5] for two kinds of the output field structures:

a) converter of the TE_{01} mode to a single Gaussian beam

In this case the profile of wall deformation in the second part of the converter has to be chosen in a form containing two terms:

$$\sigma(r,z) = l_1 \cdot \cos(2\pi \cdot z / d_1) + l_2 \cdot \cos(\varphi) \cdot \cos(2\pi \cdot z / d_2), \quad (2)$$

where z is longitudinal coordinate, and φ is azimuthal angle. The first term corresponds to the corrugation that retains the existing longitudinal field structure, the second term leads to mixing of TE_{1n} modes which provide bunching on the azimuth.

The result of calculation of the field at the wall of a dimpled converter is presented in Fig. 5. At the input the field has longitudinal bunching only, but at the output it has quasi-Gaussian distribution on both coordinates.

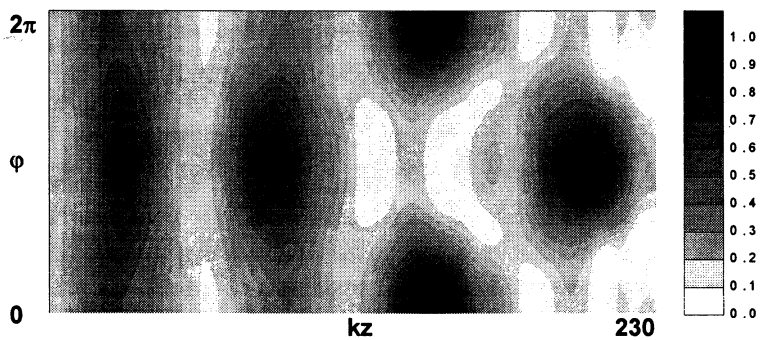

Fig. 5. Distribution of field (H_z) on the wall of the TE_{01} - single Gaussian beam converter. kd_1=58.1, kd_2=174.2, kl_1=0.77, kl_2=0.39

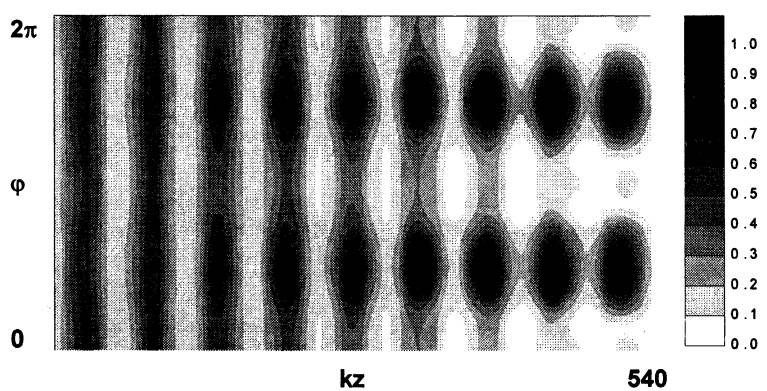

Fig. 6. Distribution of field (H_z) on the wall of the TE_{01} - double Gaussian beam converter. kd_1=58.1, kl_1=0.77, kl_3=0.10

b) converter of the TE_{01} mode to a double Gaussian beam

For some cases extraction of radiation in the form of two independent Gaussian beams is more preferable. In order to provide such a kind of output it is necessary to use the following deformation in the second part of the converter:

$$\sigma(r,z) = l_1 \cdot \cos(2\pi \cdot z / d_1) + l_3 \cdot \cos(2\varphi), \qquad (3)$$

This deformation can provide the field distribution at the output in the form of two Gaussian beams (Fig. 6) due to partial conversion of the initial axis-symmetrical wave into modes with m=2 azimuthal indices.

The described converter being one of the simplest was tested at frequency 92 GHz. The converter started from the TE_{01} mode in the waveguide 30 mm diameter. The resulting quasi-Gaussian beams propagated at relative angle ~80°. Measured field distribution of one of the resulting beams at the distance of 100 mm from the waveguide end is shown in Fig. 7. Converter efficiency obtained from analysis of mutual convolution of the measured field distribution and the calculated one is 92% with accuracy 2%.

Fig. 7. Measured field distribution of one of output beams. Contour levels: 0.1, 0.2,...,0.9

4. Conversion of high-order TE_{0n} modes

Highest TE_{0n} modes have more complicated field structure, so that in the simplest scheme with the quadratically profiled shape of a cone and a barrel the exciting wave in the input of the second part is far from the Gaussian field structure on the both coordinates. Of course, this

wave can be converted to the Gaussian beam using a dimpled converter with corresponding complicated deformation. However, a simpler way is to convert the initial wave into the same eigenmode of a corrugated waveguide as the previous case using axisymmetrical small perturbation of surfaces of the cone and the barrel. These perturbations should play the role of phase correctors. Their profile may be found, for example, using the synthesis procedure suggested in [6]. If the necessary profile has been found, the second part of the proposed converter may be produced using the same way as for the converters of the TE_{01} mode (see part 3).

Input data for the synthesis procedure are initial amplitude distribution at the window, the final amplitude distribution at the barrel, and the operator, which couples fields at the window and the barrel. Since distance between the open end of the initial waveguide and the window satisfies condition $L<<kR^2$ ($k=w/c$), one can take amplitude distribution of a given TE_{0n} wave as the required initial amplitude distribution at the window. It is natural to assume that the desirable amplitude distribution at the barrel is Gaussian in accordance with the field distribution of the corresponding eigen wave of corrugated waveguide (see Fig. 4). The operator which allows to calculate the field $U(r,z)$ at one cross-section from the field $U(r_0,z)$ at another one can be obtained using expansion of the given field on cylindrical waves. In particular, for the axisymmetrical case it leads to the following formulas:

$$U(r,z) = \int_{-\infty}^{\infty} A(h) \cdot H_1^{(1),(2)}(\sqrt{k^2 - h^2} \cdot r) \cdot \exp(jhz)dh,$$
$$A(h) = \frac{1}{2\pi \cdot H_1^{(1),(2)}(\sqrt{k^2 - h^2} \cdot r_0)} \cdot \int_{-\infty}^{\infty} U(r_0,z) \cdot \exp(-jhz)dz, \quad (4)$$

where $H_1^{(1),(2)}$ is Hankel function (upper index 1 corresponds to condition $r>r_0$, index 2 corresponds to case $r<r_0$).

a) converter of the TE_{02} mode to the Gaussian beam

Basing on the described method the converter of TE_{02} mode was calculated (Fig. 8). Maximum power convolution at the barrel between the desirable field and the achieved one is about 99%. It is provided by the shaping of the cone and the barrel in the following forms:

$$R_c(z) = \mathrm{tg}(\Theta) \cdot z + \Delta_1(z)$$
$$R_b(z) = R_0 + \Delta_2(z), \quad (5)$$

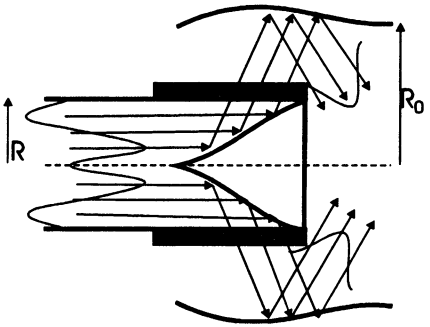

Fig. 8. Scheme of conversion of the TE_{02} mode to the bunched axisymmetrical field structure

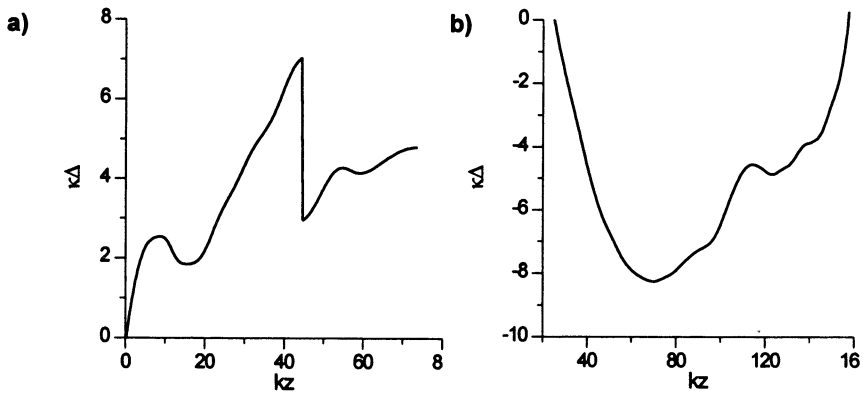

Fig. 9. Synthesized perturbations of the cone (a) and barrel (b) profile to provide desirable field distribution at the output

correspondingly, where Θ is angle of the unperturbed cone. The calculated dependencies of $\Delta_1(z)$ and $\Delta_2(z)$ are shown in Fig. 9.

5. Summary

The method proposed is acceptable for a wide class of paraxial modes, and it may be used for high-power electron devices. The method allows to reduce converter length essentially providing various possible output Gaussian structures. The tested converter of the TE_{01} mode showed the possibility to achieve high efficiency using a sufficiently simple electrodynamic system. The new hybrid technique of converter design for highest TE_{0n} modes based on the synthesis procedure makes it

possible to achieve high efficiency, and it may be applied for a wider class of wave converters.

References

1. N.F.Kovalev et al, Radio Physics and Quantum Electronics, No. 11, 1968, pp. 449-450.
2. S.N.Vlasov et al, Radio Engineering and Electron Physics, No. 20, 1975, pp. 14-17.
3. G.G.Denisov et al, Conference Digest of 17-th Int. Conf. on IMMW, Pasadena, California, Dec. 14-17, 1992, pp. 124-125.
4. B.W.Stallard et al, Int. Journal of Inf. and M. Waves, Vol. 11, No. 9, pp.1011-1032.
5. B.Z.Katsenelenbaum, Theory of Nonuniform Waveguides with Slowly Varying Parameters, Moscow: Akad. Nauk SSSR, 1961. (in Russian)
6. B.Z.Katsenelenbaum et al, Radiotekhnika i Electronika, No. 12, 1967, pp.244-251. (in Russian)
7. N.L.Aleksandrov et al, Optics Communication, Vol. 115, 1995, pp. 449-452.

THE DESIGN, CONSTRUCTION AND TESTING OF AN EXPERIMENTAL HIGH POWER, SHORT-PULSE RADAR

D.Clunie[1], *G.Mesyats*[2], *M.L.Osipov*[3], *M.I. Petelin*[4], *P.Zagulov*[5], *S.D.Korovin*[6], *C.F.Clutterbuck*[7], *B.Wardrop*[8]

1. Ministry of Defence, London, England
2. Institute of Electrophysics, RAS, Ekaterinburg, Russia
3. ALMAZ Design Bureau, Moscow, Russia
4. Institute of Applied Physics, RAS, Nizhny Novgorod, Russia
5. Scientific Instrument Special Design Bureau, RAS, Ekaterinburg, Russia
6. Institute of High Current Electronics, RAS, Tomsk, Russia
7. Defence Research Agency, Malvern, England
8. GEC-Marconi Research Centre, Chelmsford, Essex, England

ABSTRACT

The detection of small, fast moving targets travelling just above the sea surface poses particular difficulties for microwave radars. This paper describes an experimental equipment designed and built by a consortium of Russian organisations, under contract to the United Kingdom, to collect data relevant to such a task. The radar experiment is novel in that it provides high range resolution, and adequate energy for detection, by means of a short duration pulse (5ns) of high peak power (500 MW). Operating at a pulse repetition frequency of 150 Hz, clutter returns are suppressed by subtracting the returns from adjacent pulses, although a variety of signal processing algorithms are available to be applied to the signal. The equipment has a comprehensive data recording and display system, and has recently been deployed at a UK coastal test site to gather data on clutter and targets for further analysis.

1. INTRODUCTION

Conventional pulse-Doppler radars encounter problems if used for the detection of low cross-section targets approaching at low level. These problems arise from the conflict between minimising the radar range cell to reduce the masking clutter, whilst ensuring that the range cell is sufficiently large to contain the target during several coherent bursts of illu-

mination. The latter are required to overcome aliasing of the Doppler-processed returns and target fading effects. The generation of short duration pulses in space, of sufficient energy to provide useful detection, has not been a practical option until the advent of a suitable transmitter in the form of a microwave relativistic backward-wave oscillator.

As has been reported by Mesyats (1,2) and Osipov (3), in 1985 a radar experiment, using a 10 GHz generator as the transmitter, was conducted at the Kulyman test range overlooking the Ob river in Western Siberia. The experiment was the outcome of a joint effort between the Russian Academy of Sciences and industry. Due to logistical and financial problems the test programme was severely curtailed, but sufficiently encouraging experimental results were obtained to demonstrate proof of concept.

Under a collaborative arrangement between the UK MoD and GEC-Marconi, the main participants in the original radar programme were contracted in early 1993 to design and build a second system, incorporating improvements to the original design, for delivery to the UK as an experimental test bed.

2. PROGRAMME OVERVIEW

The Programme was contractually started in March 1993. A phased approach was taken, and the work successfully progressed from the initial feasibility study (which relied heavily upon the 1985 experiment), through equipment design, sub-system manufacture, and integration phases, to the delivery in May 1995 of the two containers (transmitter cabin and operations container) to a specially prepared test site at Bezvodnoye, some 20 km east of Nizhny-Novgorod. Here, system integration, commissioning, safety checks and a limited trials programme were carried out. The trials demonstrated the essential characteristics of the equipment, and showed the resolution and target detection potential of the radar against static targets, boats and a helicopter. The trials were witnessed by a UK delegation, and the equipment accepted for transportation to the UK.

After careful documentation of the equipment for customs clearance, in the autumn of 1995 the containers were placed on board a chartered Ilyushin 76 heavy transport aircraft, which flew them, with the chassis and turntable for the transmitter cabin, to Stansted airport in the UK. From Stansted the equipment was conveyed by raod to a DERA test site

near Portsmouth. From January to March 1996 an Anglo-Russian team then assembled and commissioned the radar, with GEC-Marconi engineers being trained to operate and maintain the equipment. Formal acceptance of the radar by the UK coincided with a visit by Prof Gennady Mesyats (Russian Academy of Science) in May 1996, and a programme of UK measurements and trials is now underway.

3. CONCEPT

The heart of the experimental radar is the transmitter, which employs a high efficiency backward-wave oscillator operating at 10 GHz, capable of producing a peak power of 500 MW with a pulse duration of 5 ns. To avoid Doppler-aliasing, incoherent detection is used, and to suppress slowly changing clutter returns, over-period subtraction is employed. By using a wide transmitted bandwidth, the range cell is reduced such that the principal scattering centres of the target are resolved, considerably reducing the interference effect causing target fading, as well as reducing the clutter return. Target detection is a function of the total energy on the target, i.e. the product of peak power, pulse duration, and number of pulses. Hence if the pulse duration is reduced, the peak power must be correspondingly increased to compensate.

In more conventional radars, in order to decouple pulse duration and range resolution, use is often made of a long transmitted pulse having intra-pulse coding. By using a matched filter on reception, the range resolution inherent in the transmitted waveform can be largely recovered at the expense of processing complexity and the presence of range sidelobes. The sidelobes of the matched filter process, and the apparent range of the target, can also be degraded by target motion during the extended pulse width. The use of a high peak-power transmitter obviates the need for pulse compression and its attendant limitations. To emulate, by pulse compression, the energy and resolution of the waveform of the experimental system described in this paper would require a 50 kW transmitter, a 40 μs pulse, a 250 MHz frequency excursion within the pulse, and a 10,000:1 pulse compression ratio.

4. SYSTEM OVERVIEW

The experimental system has been kept very simple in radar terms, as it is designed to be a vehicle for research into propagation, clutter and

target characteristics, and not a prototype for any specific type of radar. Consequently it has few of the features of a modern radar system, and the block diagram is very basic. This is shown in Fig 1, and can be partitioned as follows:

- Transmitter power supply
- Microwave source
- Microwave antennas
- Receiver
- Data capture, signal processing, and display

These are each discussed in more detail below. A schematic of the transmitter cabin is shown in Fig 2.

Transmitter power supply

The mains supply to the transmitter comes via a motor generator, which is needed to provide isolation from adjacent equipment and a low impedance source.

The power supply must produce a stable train of high voltage, high current pulses to the cathode of the microwave source. These are produced by a modulator (a SINUS generator), in which a Tesla transformer charges a coaxial pulse-forming line to 660kV. The line is discharged by a triggered gas-gap switch into an oil-filled transmission line. The reduced impedance of the connected circuits produces a voltage on the transmission line of one-half of the charging voltage. The transmission line has a slowly changing impedance so that at the cathode end it has an impedance of 120 Ohms, matching the impedance of the diode formed by the cathode, and delivers a 600kV negative pulse with a duration of 10 ns.

Microwave source

The microwave source is a relativistic backward-wave oscillator designed to operate at 10 GHz, and using Cherenkov radiation to supply the electromagnetic field. The periodic structure is realised as a circularly symmetric quasi-sinusoidal corrugation of the stainless steel waveguide wall, close to which the tubular beam of electrons propagates at near the velocity of light. The interacting electromagnetic wave is the E_{01} mode, which propagates in the opposite direction to the electron beam. By placing a cut-off waveguide section between the interaction space and the cathode, the wave is reflected, and passes again through the corrugated waveguide, but without interacting with the electrons. Using a

relativistic electron beam, the phase velocity of the synchronous electromagnetic wave needs to be slowed only slightly, and the increased electron mass means that substantial energies can be transferred to the electromagnetic wave with small changes in electron velocity, enabling relatively high efficiencies together with high output powers to be achieved.

The electron beam generated by the tubular cathode carries some 2.5 GW of pulse power. To sustain the explosive electron emission involved in these power levels, a graphite cathode is used. Micro-points on the cathode surface are vaporised by the current, and a plasma is formed from which the large operating current can be drawn. After about 10^7 pulses, sufficient material has been removed from the cathode to affect the cathode-anode gap, the diode impedance, and hence the operating regime of the generator.

In order to constrain the electrons to a trajectory close to, but not connecting with the periodic structure, a high axial magnetic field of 3 Tesla is required. This is generated by a low-temperature superconducting magnet. The use of too low a magnetic field would have two deleterious effects. One would be to encourage cyclotron resonance interaction between the electrons and the electromagnetic field, resulting in power transfer back into the electron stream. The second effect would be the introduction of inhomogeneities in the emission from the cathode surface, which results in an axially asymmetric beam current.

Having passed through the interaction region, the electrons are deflected onto a water-cooled surface of the anode, where they generate intense X-rays, which are absorbed by lead shielding.

The output electromagnetic wave then traverses a precisely contoured section of waveguide (the mode-converter) where the mode is changed from E_{01} to H_{11} with a conversion efficiency in excess of 95%.

Microwave Antennas

The oversize waveguide terminates at a vacuum window through which the Gaussian-shaped excitation illuminates an offset, underfed, 1.2m parabolic reflector, forming a pencil beam with a nominal beamwidth of 3 degrees.

The receiving dish is a similar offset-feed parabolic dish, 0.9m in diameter, with a pyramidal horn feed, shielded from the transmitting dish to reduce feed-through into the receiver. The isolation is in excess of 50 dB.

Both transmit and receive feeds are fixed, with vertical polarisation, but limited azimuthal scan of the radar beams is achieved by turning the two reflectors in synchronism over $\pm 7.5^0$ via a stepper motor, allowing $\pm 15^0$ of scan, which is sufficient for experimental purposes. A video camera with zoom facility is also coupled to the mechanism, so that operators can observe local activity around boresight.

As has been noted, the radar suppresses clutter by subtracting the signals from adjacent pulses. However, the transmitter and receiver chains introduce timing and amplitude jitter which limit the cancellation which can be achieved. To ameliorate this, a sample of each transmitted pulse is taken by means of a small probe aperture in the transmitter dish, and amplitude detected to form a reference pulse.

Receiver

Even with the provision of an isolating screen, the high peak-power levels result in several kW of power entering the receive horn. To protect the receiver, a special protection device is used. This has two sections, a vacuum-beam device followed by a solid-state amplifier. When the input power exceeds 200mW, the electron-beam coupling between input and output is disrupted, resulting in progressive attenuation of up to 60 dB. The solid-state section also provides blanking. Since saturation effects are avoided, the front-end attenuation is removed within nanoseconds of the transmitter pulse falling below the threshold level.

The receiver downconverts the main signal with a balanced mixer to a 2.25 GHz IF where it undergoes amplification and filtering prior to rectification and video amplification. The nominal bandwidth of the receiver chain is 300 MHz. Computer-controlled attenuators are provided within the IF path to enable the overall receiver gain to be controlled either by the operator, or to provide a time-varying swept gain according to a pre-defined law.

The video signal is passed from the transmitter cabin to the control cabin along specially shielded cable, after which it is combined with the reference video pulse and applied to the data capture unit.

Data capture, signal processing and Display.

The video signal is converted to digits by a commercial 8-bit 500 MHz analogue-to-digital converter which resides in a PC slot. Due to the limitations of on-board storage and data transfer, data processing is lim-

ited to a 2.5 km window, which can be either static or set to move in range to follow a target of interest.

In parallel with being processed and displayed, the data is written to hard disk, and can be transferred to magnetic tape for off-line archiving.

As well as the 'raw' signal, a variety of processing algorithms can be applied to improve target detectability. The two most commonly used are the MTI algorithm, using simple subtraction of returns from adjacent pulses, and the compensated-MTI algorithm, where the data from the synchronisation pulses are used to compensate for amplitude fluctuations and timing jitter.

Two real-time displays are available to the operators: the first is a conventional "A"-scope display, and the second is a waterfall display with sequential A-traces being scrolled downwards. These are shown in Fig 3 and Fig 4 respectively.

A third display, showing a map of the surveillance area with the superimposed radar beamwidth, is also available for use in post-trials analysis.

5. RADAR PARAMETERS

Power

The power output of the generator, within the pulse, is a strong function of the tube operating parameters, both electrical and mechanical. For a given mechanical configuration (cathode condition and spacing from the anode, the profile of the slow-wave structure etc), the tube operating voltages and currents can be adjusted to provide maximum efficiency, but these parameters also have an effect on the spectrum of the radiated pulse. In a radiating experiment, such as the one described here, the operating frequency must be constrained in order to meet local frequency allocation criteria (10 GHz in this instance), and this results in the tube being operated at slightly less than optimum efficiency.

The power was measured in two ways: by a simple calorimeter swung in front of the transmitting antenna, intercepting 60% of the power, and by a calibrated vacuum diode detector placed on the rear of the transmitting dish, fed through a small aperture. These measurements indicate a peak output of 400 MW, although somewhat less than this is available for radar detection, due to the extended nature of the rf spectrum, and the band-pass characteristics of the receiving chain.

Radio-Frequency Spectrum

The pulse rf spectrum was measured during the Russian trials phase using an HP 8562A spectrum analyser, and the measurement was repeated in the UK during the commissioning checks on the equipment. Whilst in both cases the spectral peak had been set to 10GHz, to match the receiver band-pass, and the spectral spread was similar, the shape was different in the two cases, arising from the different tube geometries (different cathodes, and different slow-wave structure profiles). Fig 5 shows the spectrum measured in the UK.

Pulse Characteristics

a) Shape. The transmitted pulse shape is a function of the tube operating parameters, and small adjustments were made in commissioning to provide the optimum for radar operation. The received pulse is a good replica of the transmitted pulse, and the shape can been seen in the figures in the echoes from point targets. The rise time is approximately half that of the decay time, and the 3 dB width from the tube in the trials configuration is 7.3 ns.

b) Amplitude Stability. Variations in the pulse amplitude from pulse to pulse are to be expected in a tube of this nature due to variations in the emitting surface of the field-emission cathode. Amplitude variations have been kept to less than 2% through careful design, and the measured rms power stability is also better than 2%.

c) Timing Stability. The energy from the pulse-forming line is transferred to the cathode via a high pressure (20 atmospheres) nitrogen gas-switch, fired by a triggatron. The gas is circulated to remove the ionisation products, and restore ambient conditions for the next pulse. Above a prf of 150 Hz (6.7 ms intervals), the ionisation is not completely removed between pulses, and the timing stability approaches 7 %. At the 50 Hz prf used for the majority of trials, the stability is better than 4 %.

6. OPERATING THE RADAR

Setting Up

The major factor in setting up the radar after transportation or storage, is establishing the vacuum system and cooling the cryomagnet from ambient. The latter exercise can take 48 hrs, as it involves liquid nitrogen and helium, and requires specialist handling procedures. Once the

cryomagnet is established, the radar can be brought to operation within 20 minutes, which is the time to establish the waveguide vacuum.

Safety Aspects

Before the equipment could be operated as a radar, extensive enviromental checks were carried out, particularly with respect to X-rays and the rf field strength. The X-ray emissions were measured at full power and at the highest prf (150 Hz) using TLD (integrating) dosimeters, and a Eberline R 010 ion chamber dosimeter. The emissions were found to be well contained by the lead shielding of the tube, but a 20m exclusion zone was placed around the transmitter cabin to provide a safety margin and allow for any "hot-spots".

The average rf field was measured using a NARDA isotropic probe and electromagnetic radiation monitor, and the ground level safety zone for biological hazard was found to be contained within the X-ray exclusion zone.

Transmitter Control

The run-up of the transmitter is under computer control, with safety locks on all critical functions. All parameters are monitored and displayed in the operations cabin. The prf is set at this stage.

The start-up sequence is simply:

- Prepare vacuum
- Switch on Motor Generator
- Secure doors and interlocks
- Switch on transmitter power supply
- Activate transmitter from control computer

Radar Operation

The operator can select a number of screen options, among which the following are the most useful during trials activity:

a) A-scope Display. This display showing either the linear signal as a function of range, or a logarithmic version of it, see Fig 3. The operator can control the range at which the 2.5 km processing window is set; the automatic range-rate for keeping moving targets with the processing window (the rate can be adjusted at any time); and the range and amplitude display scales. Different MTI processing algorithms can be selected at any time.

b) Waterfall Display. This has similar operator options to the A-scope display, but shows a time sequence of A-scope traces superimposed. See Fig 4.

c) The Antenna Pointing Display. This display enables the operator to set the pointing direction of the radar beam, relative to boresight, in the azimuth plane. Elevation cannot be remotely controlled by the operator. This display is used in conjunction with the video camera monitor, which is slaved to the antennas, and gives an indication of the field-of view of the radar.

d) Analysis Displays. The A-scope and waterfall displays are available to the operator for post trials analysis of recorded data. In addition, a geographical display is available which shows the radar track of a target superimposed upon the downloaded GPS data, if available. In the majority of trials, a global positioning system (GPS) receiver was used on the target vehicle to record the absolute position of the platform at 1 sec intervals during the trial. The GPS log can then be down-loaded into the display computer together with the trials data file, and the actual flight profile plotted. The data for specific points in the flight can be called up and displayed. The map display with GPS data is shown in Fig 6.

7. INITIAL TRIALS ACTIVITY

The experimental trials that have been undertaken in the UK can be separated into five groups:

Detection and resolution of static targets
Detection of fixed wing aircraft
Detection of helicopters
Detection of boats
Gathering of clutter data: land, sea and precipitation.

Static Targets

In the static tests, two 10 m^2 Luneberg lenses on posts were deployed on a sandbank some 2 km from the radar. The A-scope display is shown in Fig 3. The horizontal scale is 5 m/div, and the two lenses can be seen on the extreme left. The small target some 8m behind the lenses is a dog being exercised on the beach, with a person about 8 m to the rear of the dog. The responses on the left half of the display are from vegetation to the rear of the beach.

Fixed Wing Aircraft

Two types of aircraft were deployed in the initial trials phase, a single engined light aircraft, a Piper PA 28, and a twin propeller short-haul transport aircraft, a Pilatus Britten-Norman Defender. Two-way communication was maintained with both aircraft, and GPS data-logging was used to assist with the trials analysis. Due to airspace restrictions, neither aircraft was able to fly to the maximum range of the radar, but initial calculations show the detection range of the radar is in keeping with the measured parameters.

Helicopter Trials

Helicopter trials included a flight by a Bell JetRanger. The A-scope display of Fig 7 shows a single-pulse range profile with the helicopter approaching the radar. The strong returns from the cockpit and rotor can be seen together with the rear rotor, the total extent of the return of 9m being consistent with the physical dimension of 9.5m.

Some 20 km from the radar there is a large fixed tower, and in Fig 4 a waterfall display of the helicopter returning past the tower can be seen, the tower being the vertical trace on the right. The acceleration of the helicopter can be clearly seen. What is not so clear, is that the range profile of the helicopter changes markedly from pulse to pulse. At the low prf used in the data-collection, the main-rotor and tail-rotor blades will be randomly oriented pulse-to-pulse, and large fluctuations in radar cross section are to be expected.

Ship Detection

The cross-channel ferries have proved to be very convenient targets of opportunity, and have been observed out to ranges in excess of 50 km. A range profile of the Portsmouth-Le Havre ferry is shown in Fig 8, measuring some 140 m in extent. The masking of the longer range superstructure due to the end-on view can be clearly seen.

A dedicated trial was also held, using a high-speed inflatable powerboat. Two Luneburg lenses were attached across the boat, with a separation of 2 m, and these could be clearly resolved when the boat was side on.

Clutter and Precipitation

The radar site is sheltered, and sea-states greater than sea-state 3 were not observed during the initial trials phase. The radar antennas are situated about 8 m above mean sea level, and clutter was rarely observed

beyond ranges of 10 km. Data were collected during a number of rain storms, but have not yet been analysed. The recorded data will provide the basis for future MTI algorithm development.

7. FUTURE UPGRADES AND DEVELOPMENT POTENTIAL

It is apparent from the above discussion that the experimental system described provides a unique opportunity for radar and propagation experimentation, but that further development work in a number of areas would be beneficial. A number of Research and Development options are being considered at the present time, most of them aimed at microwave generator. The following sections briefly outline the development areas where changes would bring the greatest benefits from a radar perspective.

Microwave Generator

The current design of the gas switch limits the maximum pulse repetition frequency of the generator to about 150 Hz. Improvements to the cooling and to the gas flow would allow higher prf to be sustained. High prf is not essential with the staring configuration of the current experiment, but would be needed in surveillance or tracking environments.

The cathode life needs to be extended beyond the current figure of 10^8 pulses. This may be possible through the use of improved materials for the cathode, replacing the current graphite material. Stainless steel and ceramic materials have been tried in the past, but composites may be the more promising way ahead.

From a logistics point of view, perhaps the cryomagnet is the area of greatest inconvenience, but direct replacement by a more conventional electro-magnet would only be possible if the magnetic field requirements of the tube could be reduced at the same time. This would need a redesign of the tube geometry, to avoid the problems mentioned in Section 4.

Antennas/Scanning

The current experimental system has the very simple antenna configuration of a fixed, overmoded, feed, and moveable antenna dish. A more flexible radar configuration requires a high-power rotating joint, or some other method of scanning the beam, such as a passive array of phase-shifters. A number of options are currently being considered.

Receiver/Signal Processing

The PC-based system used on the system is adequate for experimental purposes, but limited to a processing window of only 2.5 km, due to the very large number of range cells to be processed. The current problem is one of data transfer during the radar-off periods, rather than the data acquisition rate. There is little doubt that an economic solution to these problems will be available in the near future.

8. CONCLUSIONS

This three-year programme has culminated in the successful delivery and commissioning of a unique Russian radar on the UK trials site. Initial UK trials have started to gather data which will enable the effectiveness of this type of radar in detecting small targets to be quantitatively evaluated, and further research objectives to be identified.

ACKNOWLEDGEMENTS

This work has been supported and sponsored by the UK Ministry of Defence, and by GEC-Marconi.

The authors gratefully acknowledge the contributions made to the programme by: the Almaz team, led by Vadim Skosyrev; the Russian Academy of Sciences teams from Tomsk, Ekaterinburg, and from Nizhny-Novgorod. The role of Nikolai Kovalev - who also led the Russian team in the UK - in equipment design, testing and resolving logistical problems, deserves a special mention. We also gratefully acknowledge the major efforts by the staff of the GEC-Marconi Research Centre, and of the DERA test site at Fraser.

REFERENCES

1. Bunkin B V et al: "Beams-92, 9th International Conference on High Power Particle Beams", Washington DC, Abstracts, p.269
2. Manheimer W M, Mesyats, G, Petelin, M I:"Applications of High-Power Microwave Sources to Enhanced Radar Systems", Chapter 5 of "Applications of High-Power Microwaves", Artech House, 1994.
3. Osipov M L:"Superwide-Band Radar", Telecommunications and Radio Engineering 49(9), 1995, pp 42-47.

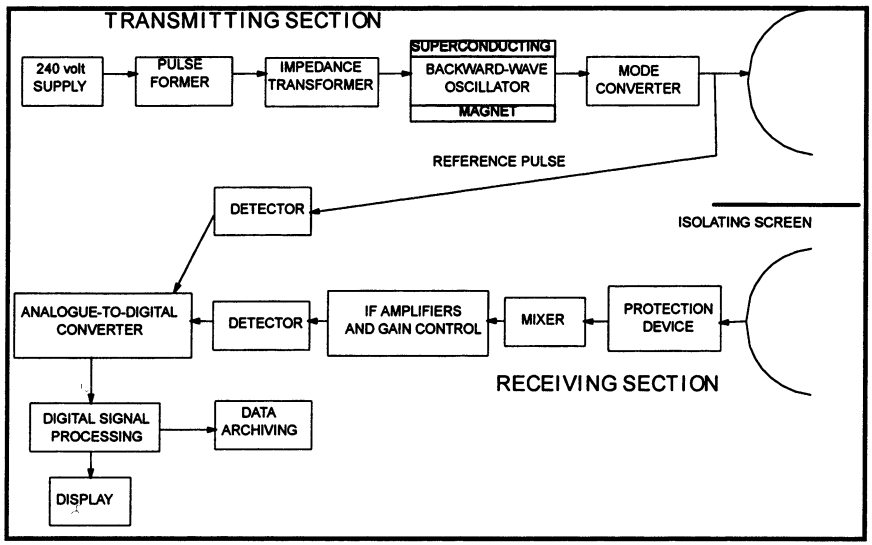

Fig 1 System Block Diagram

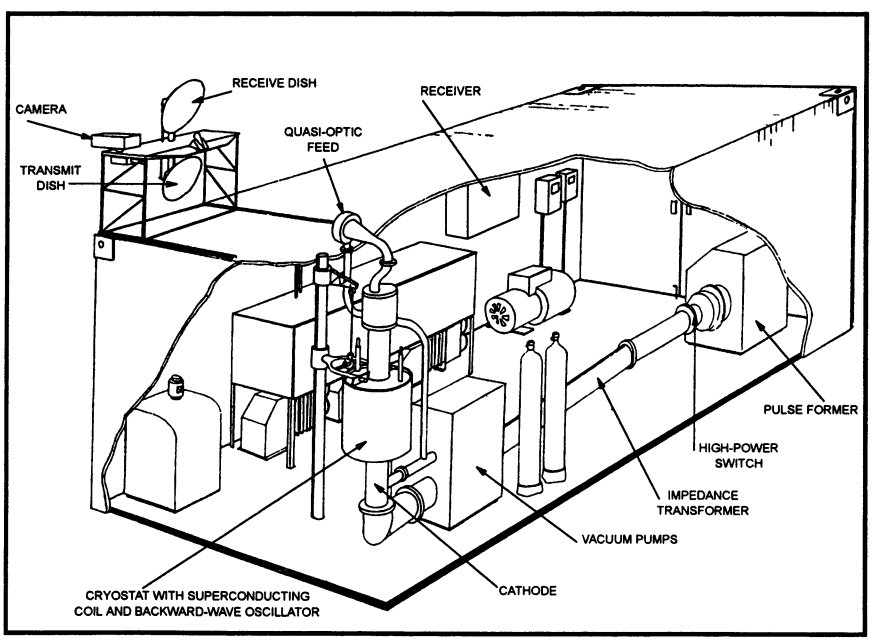

Fig 2 Transmitter Cabin Layout

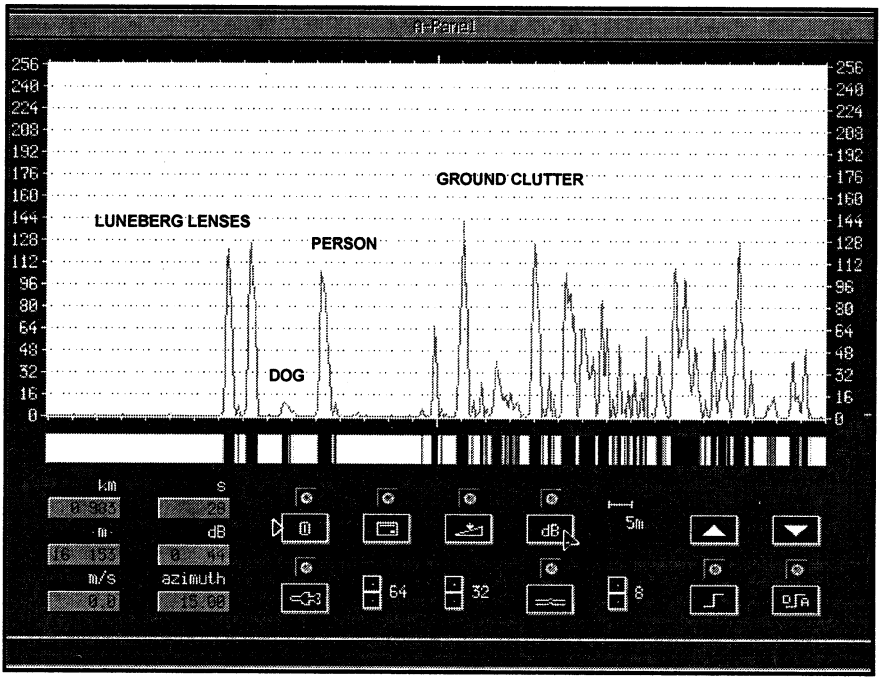

Fig 3 A-Scope Display (static targets)

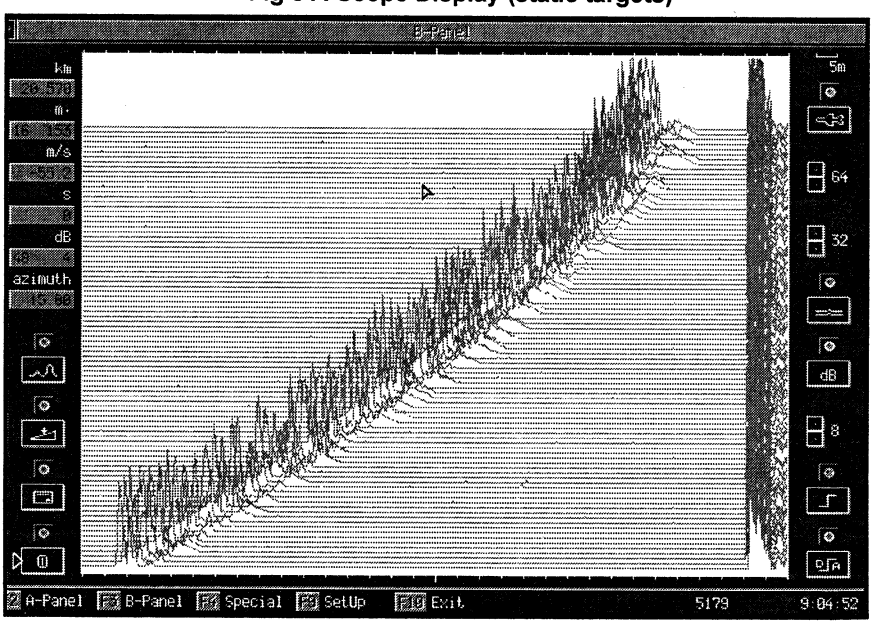

Fig 4 Waterfall Display (Helicopter past tower)

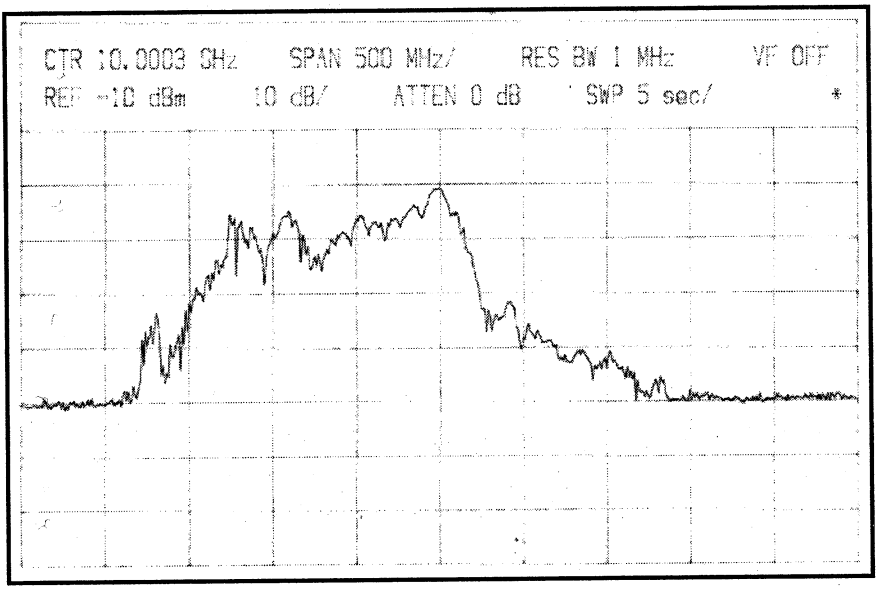

Fig 5 Radio Frequency Spectrum in England

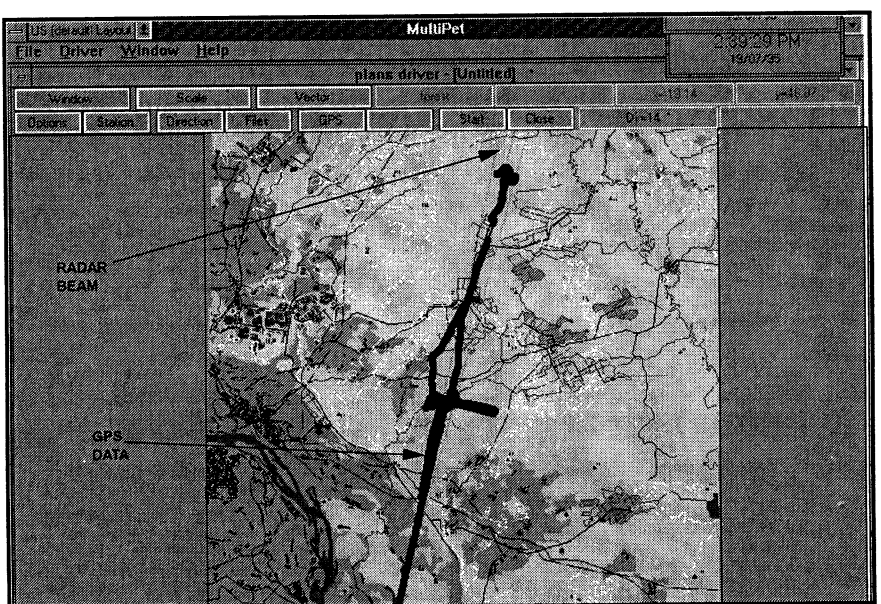

Fig 6 Geographical Display with superimposed GPS data

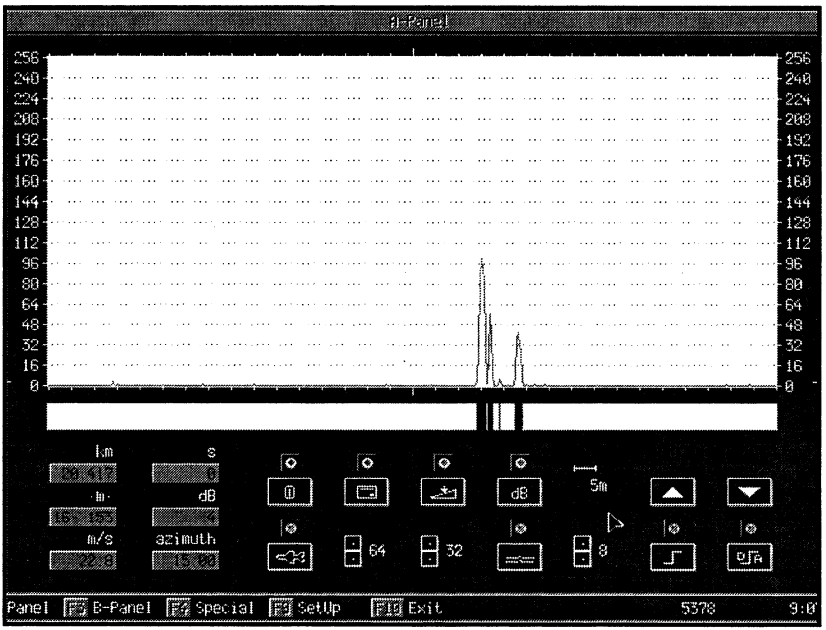

Fig 7 A-Scope display of Helicopter profile

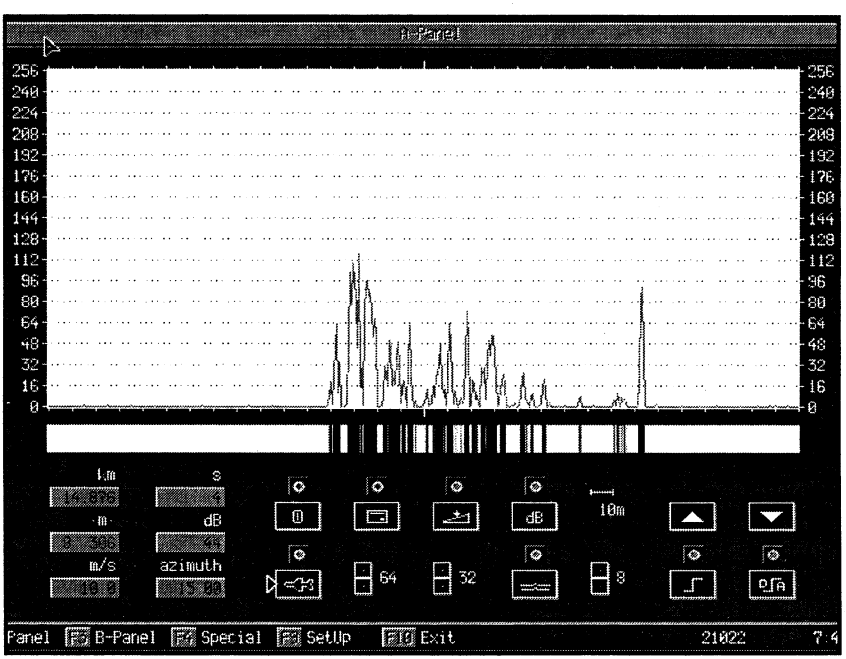

Fig 8 A-Scope display of Ferry profile

MICROWAVE PULSE COMPRESSORS

M.I.Petelin

Institute of Applied Physics of Russian Academy of Sciences,
Nizhny Novgorod, Russia

It is known that the cost of pulses produced by microwave generators and amplifiers depends not only on the pulse energy: if the latter is fixed, the cost grows rapidly with the pulse power. So it seems attractive to produce a long pulse of relatively low power and then compress it (if, of course, the compression method will be not too expensive).

This obvious idea was realized at first in the radar: a patent for use the pulse compression to enhance the space resolution without reduction of the target detection range was given in Germany in 1940 to E.Hattmann who proposed to emit a chirped (frequency modulated) pulse and after reflection from the target compress it in the receiver at the intermediate frequency.

Today there is a need to compress pulses immediately at the radio frequency: ultra-high-power microwave pulses are used to study nonlinear phenomenae in the plasma, are planned for use in a new generation of the particle accelerators and would be applicable to high range resolution (clutter rejection) radars as well, if the compression were not accompanied with side lobes (some versions of compressors discussed below have a good chance to satisfy the last condition).

Microwave pulse compressors are divided into passive and active.

Passive compressors

Passive compressors do not contain elements with time dependent (externally controlled or non-linear) electrodynamic parameters; but any compressor of the sort implies a special modulation of the primary pulse. As an example we can take a piece of usual metallic tube (Fig. 1). The wave group velocity in such a tube is known to depend on the wave frequency. So, if the input microwave pulse is frequency modulated, each part of the pulse travels with its own velocity. With a proper modulation (monotonically growing frequency) we can arrange a situation when all parts of the pulse will arrive to the waveguide output simultaneously.

Such a compression process is analogous to the electron bunching in the klystron (analogy universal for all passive compressors) and to the

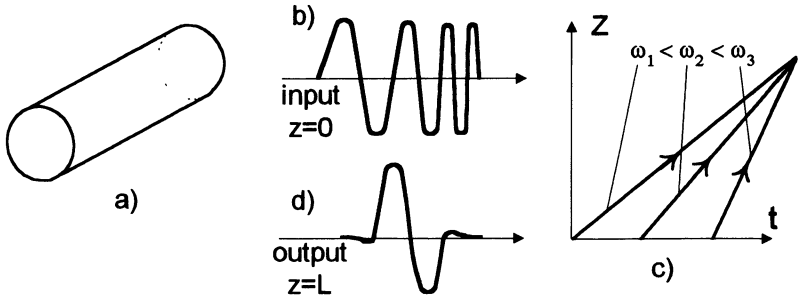

Fig.1. Cylindrical waveguide (a) as a pulse compressor: the input pulse should be frequency- modulated (b) so that after travelling through the tube, all frequency fractions arrive to the output simultaneously (c) and compose a pulse of reduced duration (d).

wave beam focusing (photon bunching) by the lens (Fig.2). The latter analogy gives a spectrum criterion for the pulse compression: (Fig.3) the ideal compressor should conserve intensities $|f_\omega|^2$ of all spectral components f_ω of the primary pulse (no ohmic losses and reflections) and only "rectify" the spectrum phase on frequency dependence, i.e. to minimize $d^2 \arg f_\omega / d\omega^2$ at all frequencies.

The cylindrical waveguide (Fig.1) possesses a large frequency dispersion only near the cut-off, which limits its use to relatively low frequencies, low powers and relatively short primary pulse durations. However more complicated waveguides are capable for a better performance. For example let us mention about an irregular adiabatic mode converter proposed for the pulse compression by N.F. Kovalev. The device (Fig.4) represents an axisymmetric waveguide corrugated with a period d slowly changing in the axial direction z. The waveguide cross section is chosen so, that in the operating frequency band there are only two propagating modes: e.g. TE_{01} and TE_{02}. In a region, where the propagation wave numbers h_1 and h_2 satisfy resonant scattering condition

$$h_1 - h_2 = 2\pi / d, \qquad (1)$$

the primary mode, let it be TE_{02}, is converted to the secondary mode, in this case TE_{01}. As h_1 and h_2 depend on frequency and d depends on z, the conversion region position determined by (1) is a function of frequency. As the group velocities of the two modes are essentially different, fractions of different frequencies travel from the input to the output during different

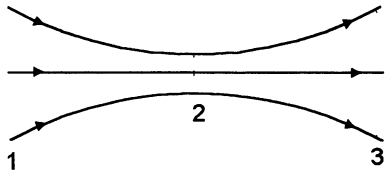

Fig.2. Propagation of converging flow (1) in the free space; after the focal spot (2) the wave flow expands (3).

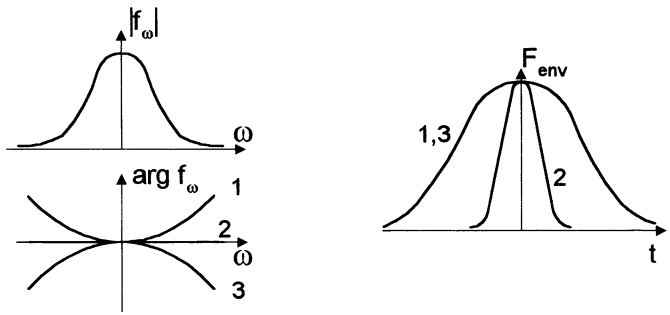

Fig.3. Spectrum evolution of the pulse propagating through a lossless dispersive medium: the spectrum intensity remains coserved, whereas the spectrum phase changes; in an intermediate cross section (2), where $d^2 \arg f_\omega / d\omega^2 = 0$, the pulse duration is minimum.

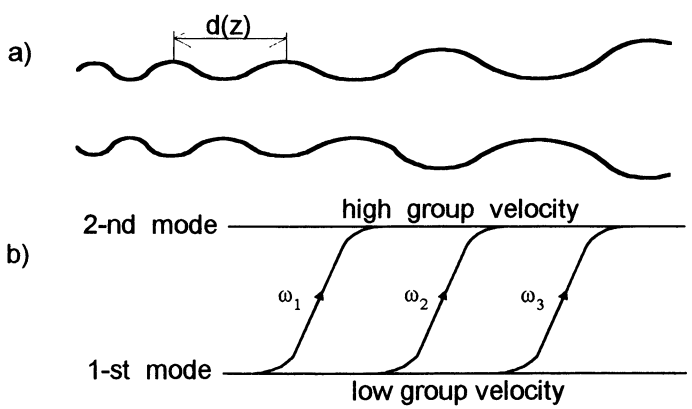

Fig.4. Irregular adiabatic mode converter (a) and schematic trajectories of different frequency fractions (b).

times, which, basing on the "klystron" method, can be used for the pulse compression.

To compress very long (narrow band) pulses, it is necessary to use either sufficiently long waveguides or, to keep the compressor in a limited volume, highly dispersive elements, namely, resonant cavities.

A convenient version is the ring cavity exemplified with a system of three mirrors, one of them being semi-transparent (Fig.5). If the loaded Q is much less than the ohmic one, losses are negligible and, so, the microwave energy incident to the cavity is reflected totally, only with a delay, in a direction different from the incidence one; the delay time being proportional to Q. Neglecting losses, for the spectrum transmission coefficient $K_s(\omega)=F_+(\omega)/F_-(\omega)$ we have

$$|K_s(\omega)| = 1. \qquad (2)$$

On the other hand, the transmission coefficient should have a resonant singularity in the complex frequency plane at the cavity eigen-frequency $\omega_s=\omega'_s(1+i/2Q_s)$. The latter condition combined with (2) gives

$$K_s = (\omega - \omega^*_s) / (\omega - \omega_s), \qquad (3)$$

which corresponds to the following equation

$$dF_+/dt - i\Omega_s F_+ = dF_-/dt - i\Omega^*_s F_- \qquad (4)$$

for the complex amplitudes F_+ and F_- of input and output pulses. $f_\pm=\mathrm{Re}\{F_\pm\exp(i\omega_0 t)\}$ in Eq(4) $\Omega_s=\omega_s-\omega_0$ where ω_0 is a reference frequency close to ω'_s.

Single ring cavity compressors (equivalent to that shown in Fig 5 [1,2][1]) are usually fed with a pulse which has the resonant frequency $\omega_0=\omega'_s$, the Π-envelope and one π-step of the RF pulse. In this case, as follows from (4), the maximum power gain is equal to 9, but (because of the precursor losses and a part of the microwave energy remaining in the cavity) it would be achieved at zero energetic efficiency. A reasonable compromise is realized, with efficiency near 70%, at the power gain 4-5 [1, 2].

A better combination of parameters can be obtained with a chain of ring cavities (Fig.6) which Q-factors compose a monotonous function of eigen-frequencies. The input pulse should be frequency modulated so that each fraction of the pulse delayed by its "own" resonant cavity arrives at

[1] Options for concrete type of ring cavities are quite numerous.

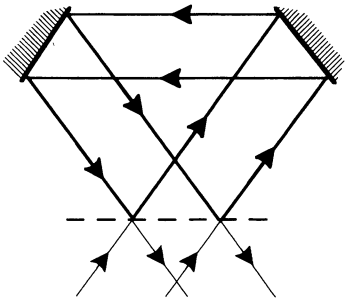

Fig.5. Ring cavity: a quasi-optical version.

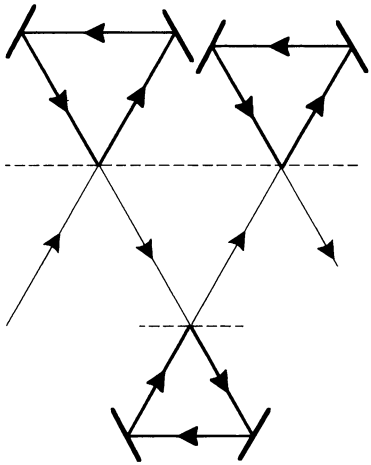

Fig.6. Microwave pulse compressor representing a chain of ring cavities.

the chain output simultaneously with other fractions. The compressor with 3 cavities at efficiency near to 70% has the power gain 8-10.

Active compressor

If the microwave energy is injected into a cavity (Fig.7) during a long time[2] and then extracted during a short time, the microwave power is obviously enlarged. For such a performance the Q-factor in the accumulation phase should be much higher than in the extraction phase and the both should be much less than the ohmic one.

---

[2] If a cavity is filled from a waveguide with a Π-shaped pulse, the maximum energy accumulation efficiency is known to be 81.4%. The efficiency can be enlarged to 100%, if the pulse envelope is exponential: $P \propto \exp(\omega_s' t / Q)$ - the proof based on the reciprocity principle is so trivial, that an article by N.F. Kovalev, M.I. Petelin and I. E. Ronin on the subject (with some generalizations) was not accepted by a magazine.

Note that the amplitude modulation of microwave source does not reduce its efficiency only if a multy-sectioned depressed collector is used.

The simplest output switch represents a T-junction of standard waveguides with a gas discharge gap in one of elbows (Fig.8). In the microwave energy accumulation phase, the standing wave structure in the shirt-circuited elbow is orthogonal to the eigen-mode of the output waveguide and, so, no energy is radiated. When the gas in the gap is

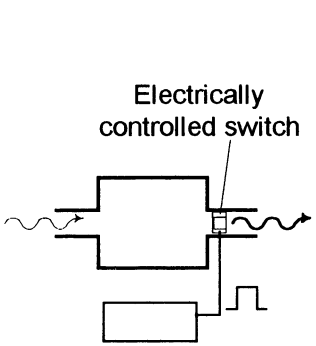

Fig.7. Microwave pulse compression by Q-modulated cavity

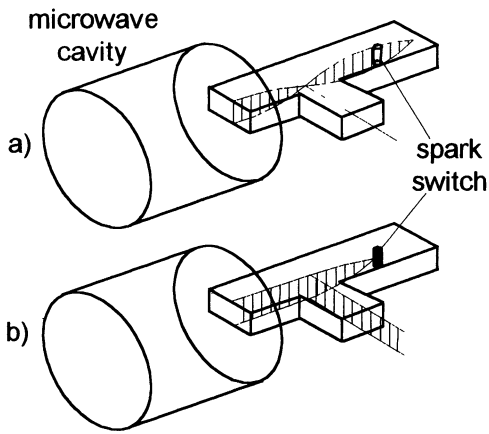

Fig.8. Output switch of microwave pulse compressor and structures of RF field during accumulation (a) and extraction (b) of energy.

broken and turned to plasma, the RF field structure in the shirt-circuited elbow becomes shifted to allow radiation into the output waveguide. This method was successfully used in experiments performed in Tomsk, where power gains up to 70 in the single compressor and up to 600 in a three-stage scheme were obtained [4, 5]. It is extremely important that in one of Tomsk experiments the mutual phase coherence of two pulses produced by two parallel compressors was demonstrated.

The compressors based on standard waveguides undergo obvious limitations on the carrier frequency, feeding pulse duration and output power. A better performance can be expected with compressors composed of oversized electrodynamic structures and distributed switches. Two options are discussed [6]:

- the ring mirror cavity with an array of gas discharge tubes distributed over one of reflectors (Fig.9)

and

- the quasi-cylindrical cavity with Bragg reflectors containing a system of gas discharge tubes impregnated into the corrugated surface (Fig.10).

The breakdown in the gas discharge tubes

- in the first case (Fig.9) enlarges the effective corrugation depth of the controlled reflector,

- in the second case (Fig.10) shifts the wave propagation number to outside of the Bragg reflection band, thus providing the necessary modulation of the cavity Q-factor.

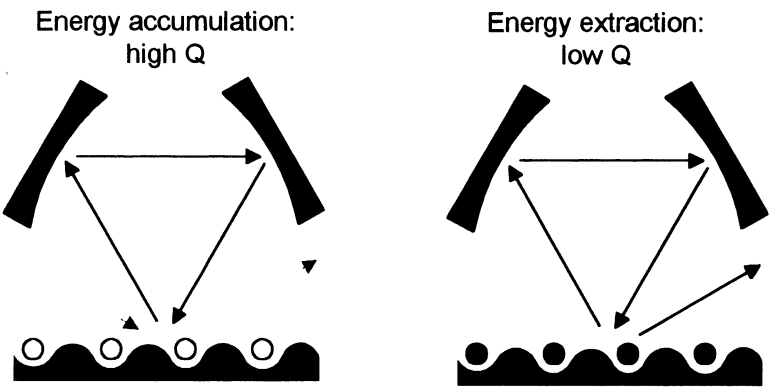

Fig.9. Pulse compression by a mirror cavity with electrically controlled reflection.

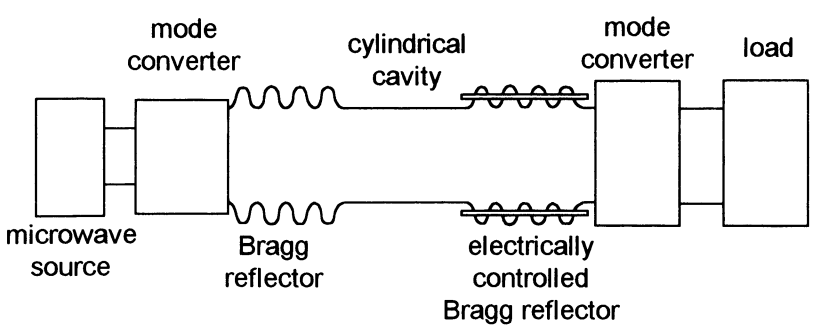

Fig.10. Schematic diagram of microwave pulse compressor with Bragg reflectors.

Problems to solve

For all pulse compressors projected to produce enhanced microwave powers basing on use of oversized electrodynamic components, there are common problems of coupling to input and output waveguide systems. Such a coupling can be provided with mode converters similar to those developed for the microwave plasma heating experiments.

The active pulse compressors need electrically controlled switches which would realize a reasonable compromise: to be breakdown-proof at the energy accumulation phase and provide a short breakdown time at the transition to the energy extraction phase.

From the last viewpoint passive pulse compressors seem more simple, but they cannot produce the same high gains as the active compressors. Thus, at this stage it seems likely that in future the both classes of compressors will have separate application domains.

References

1. Wilson P., in "Application of High-Power Microwaves", ed. A.V.Gaponov-Grekhov, V.L.Granatstein, Artech House, Boston-London, 1994, 229
2. Balakin V.E., Syrachev I.V., Proc. 3th Europeran Part. Accel. Conf., 1992, 1173
3. Petelin M.I., Tai M.I., Proc. of AIP Conference 337, Pulsed RF sources for linear colliders, Montauk, NY, 1994, 303
4. Didenko A.N., Ushkov Yu.G., Powerful microwave pulses of nanosecond duration, Moscow, Atomizdat, 1984
5. Didenko A.N., Novikov S.A. et. al., Doklad AN, 1991, **321**, 518
6. Vikharev A.L., Kovalev N.F., Petelin M.I., Pis'ma v Zh. Tech. Fiz., 1996, **22**, N19, 41

POWERFUL MICROWAVE COMPRESSORS OF RF-PULSES

Yu.G.Yushkov, V.A.Avgustinovich, S.N.Artemenko
V.L.Kaminsky,S.A.Novikov, S.V.Razin, P.Yu.Chumerin

Scientific Research Institute of Nuclear Physics
of Tomsk Polytechnical University, Tomsk, Russia

The report introduces main results of the investigation of high power microwave pulse compressors carried out in Scientific Research Institute of Nuclear Physics. A simplified version of the compressor operation is the storing of electromagnetic energy in a resonant cavity and the following rapid extraction of this energy to a some kind of a load. The attractive feature of resonant microwave compressors (RMC) resides in that a travelling wave power in a common single-mode copper cavity having double travelling time per length of a cavity 10^{-9} - 10^{-8} s can exceed a power of an exciting generator as 10 - 20 dB and in multimode cavity 20 -30 dB or more. In superconducting cavities the increase may achieve 50 - 60 dB and 60 -70 dB respectively. Best present technologies permit to obtain an electrical field strength in microwave elements or systems up to several hudreds of kV/cm and the travelling wave power corresponding to this electric component could be the order of 10^8W in single mode copper cavities and of 10^9W in multimode cavities. These levels of power will be followed by an output pulse power if one makes available an extraction time close to a double travelling time per length of a cavity. An increase of an extraction time will lead to a decrease of output pulse power. Therefore short extraction times are main objectives for elaboration of microwave compressors.

Now two methods support a rapid energy extraction. The first is implemented in SLED system having the switching in the microwave external circuit, the second in resonant systems supplied by interference switches which are the output elements designed for example as a waveguide T-junction with a short circuited straight arm or a side one. Here the second method is considered as it provides higher power gains and operation schemes of compressors having a single- or multimode storing cavity and the ones integrated with an exciting tube are considerd as an examples of its realization.

Single mode cavity RMC

Usual schematic design of the single mode cavity RMC is presented on fig.1a. The cavity has the output tee element one of its arm being short circuited and the switch located at the distance of fourth of a waveguide wavelength from a short circuit plate. The switch changes the storing regime of a compressor into the one of extraction. RMC of this design can operate within wavelength interval 3 - 100 cm. Storing cavities for 3 cm and 10 cm wavelength bands are manufactured of standard waveguides of a correspondent frequency band and for 30 cm and 100 cm bands of coaxial lines with a coaxial interference switch.

Decoupling of the cavity and a load during energy accumulation process is achived by the choice of a defined length of a short circuited arm of a tee when phases of waves propagating to a load from a cavity volume and the tee arm are reversed. If the switch is turned on it changes the electrical lenth of the arm by fourth of wavelenth which results in waves to be in phase and consequently in extraction of energy. Switches are usually gaseous waveguide ones. Electrical isolation is maintained by a gas (nitrogen, argon, SF_6, air) of excess pressure of several atm. Table 1 presents typical parameters of RWCs of the geometry of fig.1a.

Table 1.

f,GHz	P_{in}, MW	P_{out}, MW	T_{out}, ns	M^2, dB	Q_0 x 10^4	η, %	L, m
1.0	0.3	20	10	18.5	2.0	21	1.5
2.8	1.3	190	4.2	21.6	1.2	22	0.9
2.8	1.0	22	20	13.4	1.4	18	2.5
9.4	0.05	2.5	3.2	17	1.4	18	0.35

Here f -frequency, P_{in} -input power, P_{out} -output pulse power, T_{out} - output pulsewidth, M^2 - power gain, Q_0 - intrinsic quality factor, η - efficiency, L -length of a cavity.

As Table 1 shows for output pulsewidth values 3 -20 ns P_{out} can reach of several megawatts in 3 cm wavelength band and tens and hundreds megawatts in 30-cm and 10 -cm bands respectively. The transient attenuation of the cavity output element during the process of exciting makes up - 40 -45 dB. The relativly low η of this type of RMC can be attributed to the reflection of energy during a transient process of exciting, to the losses in cavity walls and in the switch. Typical envelopes of microwave pulses shaped by this way are shown on fig. 1b.

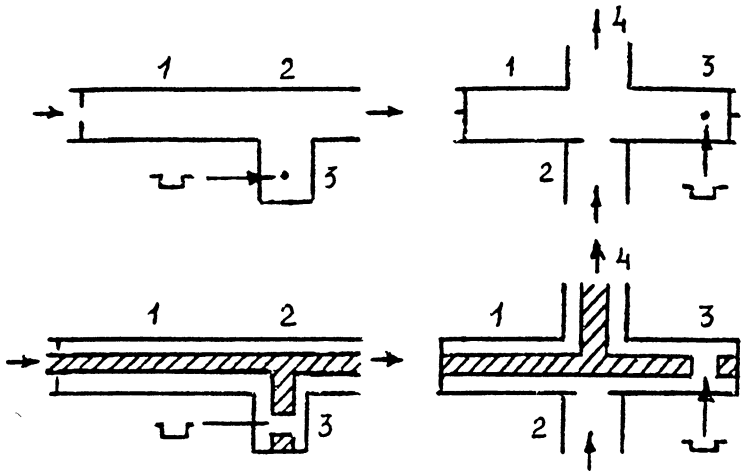

Fig.1a. Single-mode cavity. Interference switch.
1- cavity, 2 - T -junction, 3- switch, 4- output arm.

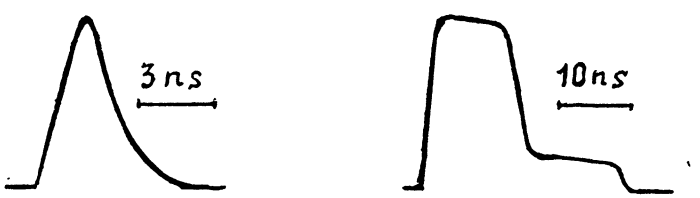

Fig.1b. Envelopes of output pulses.

For some applications of high power nanosecond RF -pulses the coherent summing of output pulses of different RMC in a common load is of definit interest.The study of this question was begun by experiments of summing up output radiation of two compressors fed by the single common generator. The scheme of laboratory set is presented on fig.2a. the magnetron driver was used and it had the output pulse power of 1.3 MW and the pulsewidth of 3.5 mcs. Construction of the two cavities were identical and each one designed as a double symmetrical waveguide tee ("magic tee") with two short-circuited arms. The gaseous microwave switch was located in one of the arms. Synchronized starting of the extraction regime was maintained by voltage pulses having the risetime of 5 ns and amplitude of up to 10 kV which were applied to triggering gaps of the switches. Output sygnals of the compressors were summed up in phase in the load by H-plane tee as the phase relation was matched by lengthes of this tee arms. Cavity volumes were filled by argon at the pressure of 5 atm. Oscillograms of one of summand pulses and the total one are shown on fig. 2b. The peak output power of each cavity was 5 10^7W and their summation gave a bit less 10^8W. The increase of the total pulsewidth was due to statistic dispersion of microwave switch startings but nevertheless the jitter was within several nanoseconds. The spread did not exceed 1 - 1.5 ns with the probability of 70 %.

This experiment showed the possibility of coherent operation of synchronized RMC which may lead to developing of multiple cavity system under condition that exciting generators are phase locked.

The peak power of short microwave pulses with the pulsewidth of several cycles of field oscilations can be increased over the thresholds of a single cavity by another procedure. One may decrease the energy storing time along the corresponding increase of input pulse power or use the series compression the last stages of which operate under said condition. The scheme illustrating series compression is presented on fig. 3a. The first stage cavity was made of standard waveguides but the design of following stages was affected by desired output pulsewidth. Here the second and third cavities were coaxial as a coaxial tee has wider frequency bandwidth than the waveguide one. The first cavity operated with the stimulated switchout but selfdischarges were used for switching in coaxial cavities. The first stage gave the peak power of 21 MW and pulsewidth of 30 ns, the second - 310 MW and 1.4 ns, the third - 630 MW and 0.4 ns. Fig.3b shows output signals of the second and third stage. The total efficiency was about 7%.

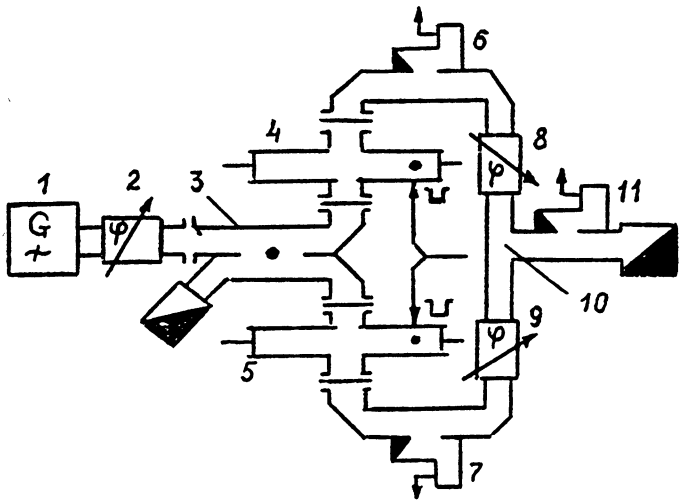

Fig.2a. Scheme of parallel compressors operation.

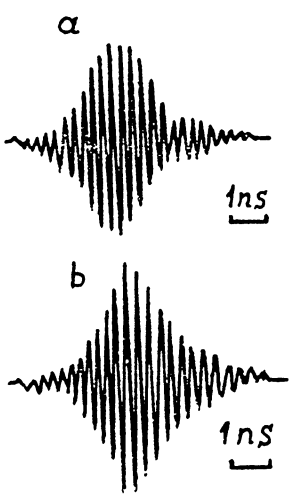

Fig.2b. Microwave oscillograms.
a- output pulse of separate compressor, b- total pulse.

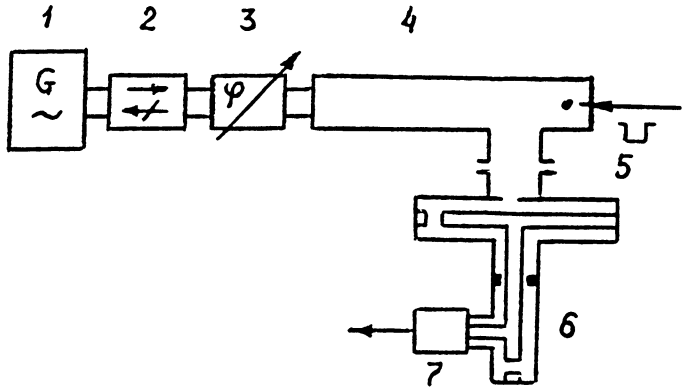

Fig.3a. Series compressors operation.
1 - generator, 2 - circulator, 3 - phase shifter,
4, 5, 6 - compressors, 7 - matched load

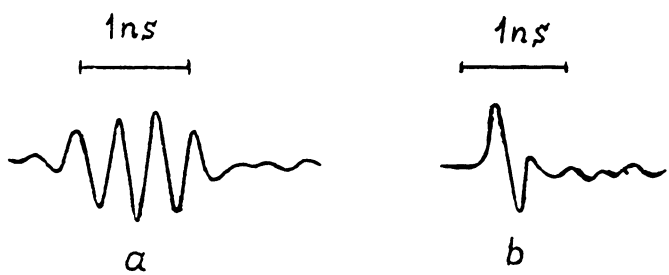

Fig.3b. Microwave oscillograms.
a - output pulse of compressor 5, b - output pulse of compressor 6.

The results showed this prosedure may allow to gain a microwave pulse power of the order of 1 GW using standard generators of 10 cm wavelength band.

A relativistic generators can serve as a pumping ones in RMC in spite of their usually short pulsewidth 10^{-8} - 10^{-7} s. In this case RMC might improve the coherence of radiation of a relativistic tube as it becomes coupled to a high Q -value circuit. The experiments were done with the vircator developed in the institute laboratory as well.

The scheme of the installation is shown on fig.4a. The vircator gave microwave pulse power of 350 MW and the frequency range (2.7 - 3) GHz and at -3dB level. The envelope of this pulse is presented on fig.4b. The part of the vircator output power was transmitted through the horn into the input guideline of the storing cavity. By this way the maximum value of input power was 20 MW. The mode H_{01n} was exited in the cavity at the resonant frequency 2.83 GHz. Electrical isolation of input line of the cavity was supported by SF_6. The cavity was designed as a double waveguide tee and had the loaded Q_L value 4 10^3. Its volume was isolated by the mixture of nitrogen and SF_6 at the pressure of 1.6 atm. The vircator pulsewidth and consequently the storing time were 25 - 30 ns and at the end of the transient the switch came into action due to selfdischarge. The compressor output power was 400 MW and its oscillogram is shown on fig.4c. So the power gain was not less than 13 dB and the relative frequency stability defined by Q_L was 2.4 10^{-4}.The efficiency did not exceed 6%.

Multimode cavity RMC

The devices described above give the high peak power but relatively low energy in a pulse. The pulse energy may be increased only by using large cavity volumes which are multimode ones. If the electric field strength 150 - 500 kV/cm is achieved in a cavity of the volume 1 m^3 then the stored energy will be of several kilojoules. Microwaves of this energy extracted by 10 - 100 ns would have given the pulsepower of 1 -10 GW. But that raises the problem of the rapid energy extraction.

Evaluations showed that the system of fig.5a is capable to provide the power gain 10 - 15 dB with the output pulsewidth 20 - 200 ns and the peak power 1 -100 MW. It is assumed that the cavity volume is 10^{-2} -10^{-1} m^3 correspondently.

The cavity of this configuration was tested in 3-cm and 10-cm wavelength bands. The storing cylindrical copper cavities had the volume of 2 10^{-2} - 5 10^{-2} m^3 and intrinsic Q value of (0.7 - 1.1) 10^5 of working

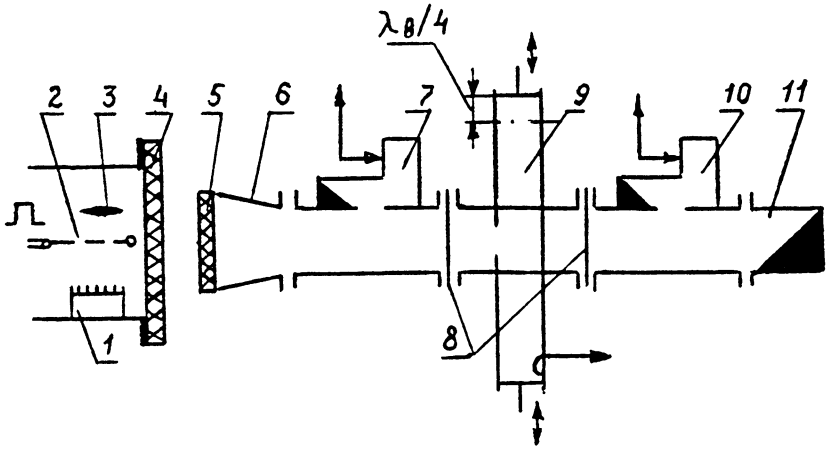

Fig.4a. Vircator - compressor system.
1- cathode, 2- anode, 3- virtual cathode, 4, 5, 8- dialectric windows, 6- an tenna, 7,10- directional coupler, 9- storing cavity, 11- matched load.

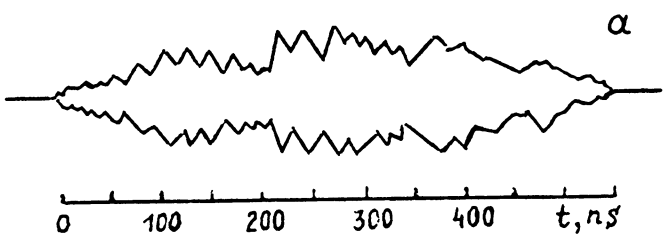

Fig.4b. a- vircator output pulse envelope,
b- oscillogram of output compressor pulse

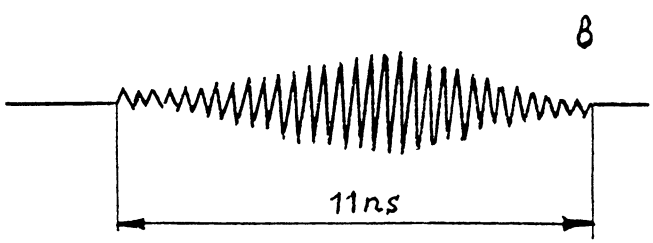

modes $H_{01(n)}$ or $H_{11(m)}$ .The interference switch made of a standard waveguide was attached to one of end plates in the region of maximum of the magnetic component. The drive microwave pulse has the power of 1 MW and the pulsewidth of 3 10^{-6}s. The switch was triggerd by starting voltage pulses. The typical envelope of the pulse obtained is presented on fig.5b. Its pulsewidth is 100 -150 ns at -3 dB level and the power 5 - 10 MW. The power gain was 7 - 10 dB and efficiency 40 - 45%. The compressor of these dementions and configuration allows to encrease an output power up to 40 - 50 MW by propotional increasing of an input power.

The similar compressor of 3-cm band operating at $H_{01(9)}$ mode had following parameters: volume 1.5 10^{-3} m^3, pulsewidth 20 ns at -3 dB level, pulse power 1.3 MW and microwave efficiency 48%.

The another procedure of energy extraction for multimode cavities is the transformation of a working mode into a one strongly coupled with an external load. Practically one can use the $H_{01(n)}$ working mode and modes $E_{11(n)}$ or $H_{11(m)}$ to transform into. The energy could be transmitted through an output cylindrical waveguide which critical frequency of H_{01} wave is over working frequency and of H_{11} is under it. The waveguide is attached to one of the end plates as shown on fig.6a. The high but resonable tolerances of dimentions give a transient attenuation at storing regime not higher than the traditional waveguide tee. The procedures for an instant increase of the amount of intermode coupling may be different. In particular it may be done by the microwave discharge spark on the finite length of angular (φ) electrical component in the region of its maximum. This type of switching was experimentally studied in 3-cm and 10-cm wavelength bands. The microwave discharge arc was triggerd in the cavity volume at the maximum of φ electric component at the first longitudinal variation nearest to the output port. The cross section diameter of the output waveguide was 0.2 - 0.3 that of the cavity. The obtained power gain was 9 - 13 dB for normal conducting copper cavities of Q_0= 10_5 and 27 - 30 dB for the superconducting niobium cavity at the pulsewidth 20 - 80 ns. An output envelope is presented on fig.6b. The efficiency did not exceed 35%. This procedure benefits from the distruction of many stray modes by the output aperture and the attached waveguide.

The developing of the construction presented on fig.7a is attributed to desire to extract energy of a multimode cavity by possible shortest times 10 - 100 ns. Studies were made to obtain switching in axial symmetric big volume cavities by the multimode coaxial line. Fig.7a shows field distribution charts as well. Here the axial wave (H_{01} or TEM) of the line interferes with the axial wave travelling out of the radial gap in the internal coaxial conductor.Diameters of coaxial line conductors and dimentions of the the

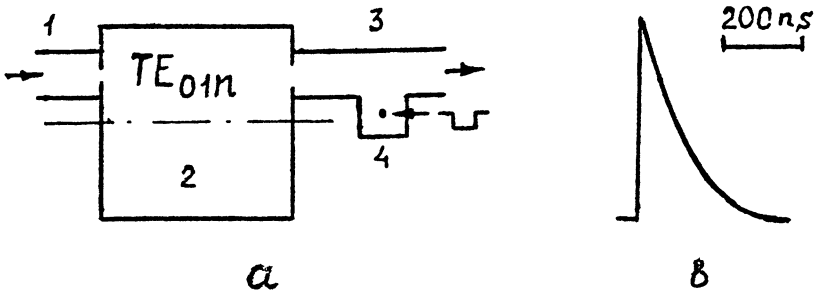

Fig.5. Multimode cavity. Interference switch.
a- schematic configuration, b- output pulse envelope.
1- input waveguide, 2- cavity, 3- T junction, 4- switch.

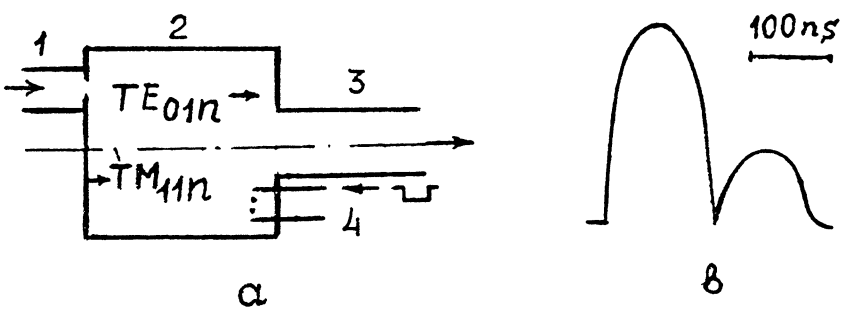

Fig.6. Multimode cavity. Mode transformation.
a- schematic configuration, b- output pulse envelope.
1- input waveguide, 2- cavity, 3- output waveguide, 4- switch.

gap should supply the equality of amplitudes of these waves and their phaseshift 180° during energy storing. Besides the diameters have to provide a single mode operation of the coaxial line. Switching occurs due to inversion of the phase of the wave travelling from the radial gap. The microwave arc in the gap is formed along φ electric component for H_{01} wave and along the axis for TEM wave.

Experimental testings were made. The cavity in 10-cm band had $H_{01(11)}$ working mode, 2.84 GHz resonant frequency and the volume about $7\ 10^{-2}$ m^3. Diameters of internal and external conductors were 0.16 m and 0.3 m respectivly. The gap had length of 0.07 m and was excited at H_{011} mode. The mesured Q- value was $3\ 10^4$ at the calculated one $8\ 10^4$.

The cavity in 3-cm band of fig.7b was excited by falling TEM mode through the circle coupling aperture around internal conductor. At the resonant frequency 9.31 GHz the working mode was $TEM_{00(21)}$ in the cavity avd E_{020} in the radial line of the gap. The Q- value was $1.2\ 10^4$ and that is 20% less than for ordinary coaxial cavity dead shorted on both ends. The switching was brought about by the arc of microwave selfdischarge along the axis of the gap. The envelope of the microwave pulse is drawn on fig.7c. The pulse power was 1.2 MW which is 15 times as the input pulse power.

RMC of direct storing of electron beam energy

It is known any generator is some kind of storung oscillation system which is strongly coupled to an external load. Such storing system does not principally differ from the one of RMC. So it was interesting to integrate a tube and RMC in a single device where an oscillation circuit might be opened rapidly for energy extraction. This approached was induced by low efficiency of ordinary RMC, by circulator to be used and so on.

The schematic drawing of the integrated tube and RMC is on fig.8a. The coaxial self sustained oscillator was in 30-cm band and well matched to coaxial RMC. The cathode-grid circuit was the quarter-wavelength coaxial resonator. The tube was fed by voltage pulses of 5 kV and of pulsewidth 5 mcs. The anode current was 1 A. After the switch gap was broken down the pulses were detected at the output of the device. Their peak power was 50 kV and pulsewidth 5 ns at -3 bB level. The envelope is presented on fig.8b. The power gain was 10 dB, the efficiency 30 - 35%. A more powerfull tube will allow to increase the output power up to 1 MW. If the coaxial tee is opened partially the device can operate in standard regime of continuous oscillations or regime of microsecond pulse generation. The distinctive feature of the integrated device is in-

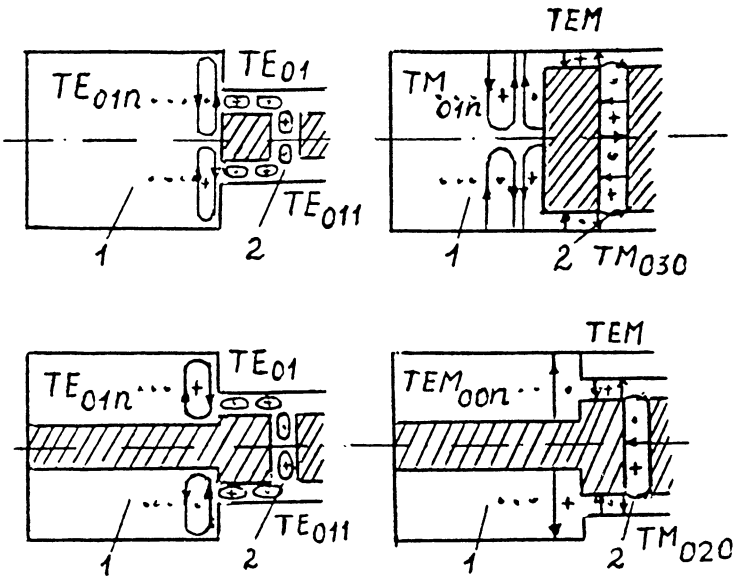

Fig.7a. Multimode cavity. Multimode coaxial switch.
1- cavity, 2- radial line of switching gap.

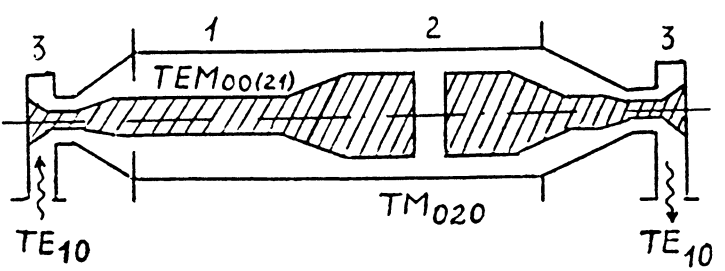

Fig.7b. Experimental model of coaxial compressor.
1- cavity, 2- multimode coaxial switch, 3- coaxial-waveguide coupler.

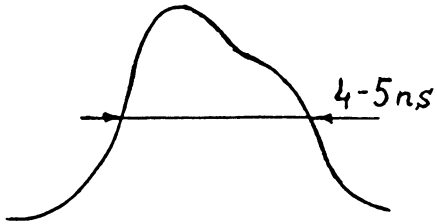

Fig.7c. Output pulse envelope.

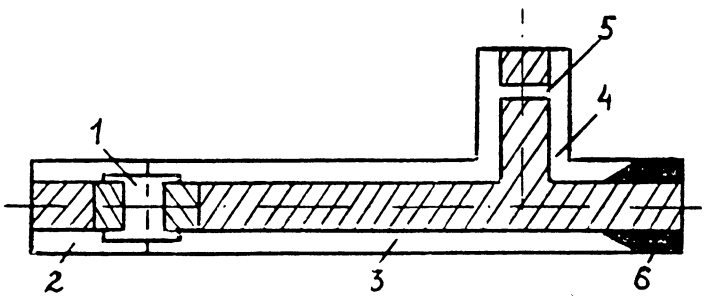

Fig.8a. Integrated system of tube and compressor.
1- vacuum tube, 2- cathode-grid circuit, 3- anode-grid circuit (storing cavity), 4- coaxial tee, 5- switching gap, 6- output load.

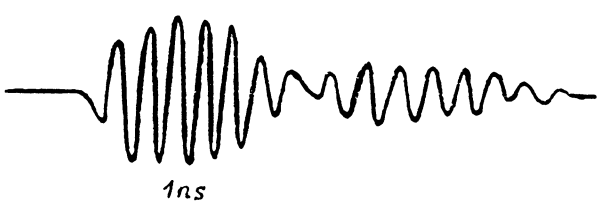

Fig.8b. Output pulse oscillogram.

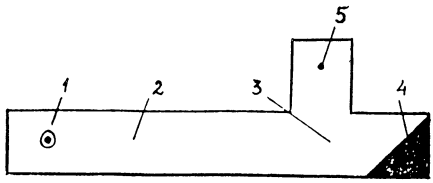

Fig.8c. Integrated system of monotron and compressor.
1- electron beam, 2- cavity, 3- waveguide tee, 4- load, 5- switch.

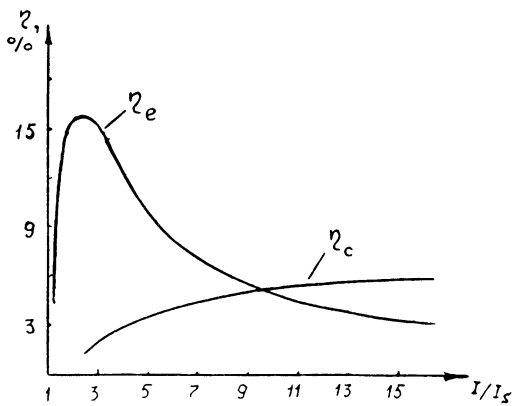

Fig.8d. Plots of efficiency - working current relations.
η_e- efficiency of monotron, η_c- efficiency of integrated system,
I_s - starting current.

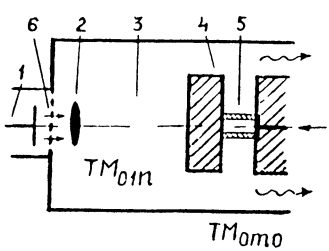

Fig.8e. Integrated system of vircator and compressor.
1- cathode, 2- virtal cathode, 3- cavity, 4- multimode coaxial line, 5- radial line of switching gap, 6- anode.

creased dementions of an output oscillation circuit. Therefore problems may rise in exciting of oscillations as a life time of electromagnetic field fluctuations is finite and an increase of the time for reaching the steady feedback state causes increasing the time for reaching the steady state oscillations. A lot of high power generators operate in the pulse regime and an increase of transient excitation time may lead to oscillations in resonant circuit to have no chance to begin during an action of high voltage pulse applied. But in this case the device does not need a long time operation in the steady state and the coming up to this state is enough to switch at the moment to an energy extraction. That means that efficiency of nanosecond pulse shaping will be considerably affected by transient dynamics of an excitation and supression of the oscillations and not by characteristics in the steady state. Studying of the device of fig.8c showed that it should have the current pulsewidth an order less than a generator for ordinary pumping of the cavity. The short current pulsewidth may allow the device to operate with a higher feeding voltage. According to evaluations the power of a travelling wave in the resonant circuit could be 0.1 - 10 GW at the current 10^2 - 10^3 A, working voltage amplitude 10^5 - 10^6 V and efficiency 0.4 - 0.5. The average power consumed by the device will be equal to that consumed by a generator with output microwave power 1 - 10^2 MW and total efficiency 15 - 20%. Fig.8d showes an electron efficiency - working current relation of the monotron and the same for a monotron integrated with a compressor. Stationary region values of η_c are 3-4 times smaller than the maximum value of η_e and are depent on decrease of the efficiency due to current increase and on decrease of the part of the electron beam energy dissipated on a collector due to decrease of the time of oscillation excitation.

Fig.8e gives the example of possible configuration of the relativistic tube integrated with the compressor.

So the microvave devices using the accumulation of external generator energy in a resonant cavity may be suitable and efficient sources of pulsed radiation. They have the simple design and might be installed to operative generators for uncreasing the pulse power without considerable expenses. Technical difficulties of compressors with direct storing of electron beam energy are the same order as of common tubes.

CONTENTS OF VOLUME 2

NONLINEAR PROCESSES IN PLASMAS

HIGH-POWER MICROWAVE SOURCES